ZONATION IN TOURMALINE FROM GRANITIC PEGMATITES
&
THE OCCURRENCE OF TETRAHEDRALLY COORDINATED ALUMINUM AND BORON IN TOURMALINE

by

Aaron J. Lussier

A Thesis submitted to the Faculty of Graduate Studies
of

The University of Manitoba

in partial fulfilment of the requirements of the degree
of

DOCTOR OF PHILOSOPHY

Department of Geological Sciences

University of Manitoba

Winnipeg

ABSTRACT

[1] Four specimens of zoned tourmaline from granitic pegmatites are characterised in detail, each having unusual compositional and/or morphologic features: (1) a crystal from Black Rapids Glacier, Alaska, showing a central pink zone of elbaite mantled by a thin rim of green liddicoatite; (2) a large (~25 cm) slab of Madagascar liddicoatite cut along (001) showing complex patterns of oscillatory zoning; and (3) a wheatsheaf and (4) a mushroom elbaite from Mogok, Myanmar, both showing extensive bifurcation of fibrous crystals originating from a central core crystal, and showing pronounced discontinuous colour zoning. Crystal chemistry and crystal structure of these samples are characterised by SREF, EMPA, and ^{11}B and ^{27}Al MAS NMR and Mössbauer spectroscopies. For each sample, compositional change, as a function of crystal growth, is characterised by EMPA traverses, and the total chemical variation is reduced to a series of linear substitution mechanisms. Of particular interest are substitutions accommodating the variation in $^{[4]}$B: (1) ^{T}B + ^{Y}Al $\leftrightarrow$ ^{T}Si + ^{Y}(Fe, Mn)$^{2+}$, where transition metals are present, and (2) $^{T}B_2$ + ^{Y}Al $\leftrightarrow$ $^{T}Si_2$ + ^{Y}Li, where transition metals are absent. Integration of all data sets delineates constraints on melt evolution and crystal growth mechanisms.

[2] Uncertainty has surrounded the occurrence of $^{[4]}$Al and $^{[4]}$B at the *T*-site in tourmaline, because B is difficult to quantify by EMPA and Al is typically assigned to the octahedral *Y*- and *Z*-sites. Although both $^{[4]}$Al and $^{[4]}$B have been shown to occur in natural tourmalines, it is not currently known how common these substituents are. Using ^{11}B and ^{27}Al MAS NMR spectroscopy, the presence of

$^{[4]}$B and $^{[4]}$Al is determined in fifty inclusion-free tourmalines of low transition-metal content with compositions corresponding to five different species. Chemical shifts of $^{[4]}$B and $^{[3]}$B in ^{11}B spectra, and $^{[4]}$Al and $^{[6]}$Al in ^{27}Al spectra, are well-resolved, allowing detection of very small (< ~0.1 *apfu*) amounts of *T*-site constituents. Results show that contents of $0.0 < {}^{[4]}\text{B}, {}^{[4]}\text{Al} < 0.5$ *apfu* are common in tourmalines containing low amounts of paramagnetic species, and that all combinations of Si, Al and B occur in natural tourmalines.

ACKNOWLEDGEMENTS

I extend my most sincere gratitude to my advisor, Dr. Frank C. Hawthorne for granting me the opportunity to participate in the research that I have so-enjoyed, and for sharing his enthusiasm and insight into all things mineralogic and crystallographic. I would also like to express my appreciation to the members of my advisory committee: Drs. Norman M. Halden, Scott Kroeker, Elena Sokolova, and Mario Bieringer for their insightful comments over the past years; and to Dr. Lee A. Groat for agreeing to act as external examiner.

I am very grateful to the members of the technical, research and support staff in the Department of Geological Sciences: Mr. M. A. Copper, Mr. N. Ball, Dr. Y. Abdu, Dr. P. Yang, Dr. R. Shidu, Mr. R. Chapman, Mr. S. Meijia, Dr. M. Schindler, Ms. D. Danyluk, Ms. Brenda Miller. I am particularly grateful to Mr. M. Cooper and Dr. M. Schindler for the many helpful conversations over the past years, and to Sasha Herwig for assistance with data *X*-ray data collection. I also thank C. Francis at the Mineralogical Museum at Harvard University for donating the Madagascar liddicoatite.

I appreciate the collaborative support received from the MAS NMR lab in the Department of Chemistry at the University of Manitoba: Drs. S. Kroeker, P. M. Aguiar, and V. K. Michaelis. I also wish to thank Drs. R. C. Ewing and J. Zhang at the University of Michigan for access to, and assistance with, the TEM.

I acknowledge financial support to me from: (1) the Natural Sciences and Engineering Council of Canada in the form of a PGS-D; (2) the University of Manitoba in the form of a Graduate Fellowship Award; and (3) The Province of Manitoba in the form of Manitoba Graduate Fellowship.

I express great thanks to my wife, Kathryn Sexton, my mother, Eileen Lussier, and my father, Mark Lussier for their understanding, support, and patience over the years.

For

Kathy

&

Mom & Dad

TABLE OF CONTENTS

CHAPTER 6

CRYSTAL CHEMISTRY OF TOURMALINE

LIST OF TABLES

LIST OF FIGURES

CHAPTER 1

INTRODUCTION

1.1 TOURMALINE: TOWARD A ROBUST PETROLOGIC TOOL

The potential of tourmaline minerals to serve as petrologic indicators is tremendous. This is because they are found in a wide variety of geologic environments, show extensive compositional variability (even on the scale of a single crystal), and are stable over wide ranges of temperature and pressure (see London 2011; van Hinsberg *et al.* 2011). For example, major- and trace-element variations in tourmalines have been used as effective recorders of the geochemical evolution of metamorphic rocks (Henry & Dutrow 1992, 1996; Henry & Guidotti 1985; Povondra & Novak 1986) and crystallization sequences in pegmatitic rocks (Aurisicchio *et al.* 1999; Dyar *et al.* 1998; Jolliff *et al.* 1986; London 1986, 1992, 1999; Neiva *et al.* 2007; Novak & Povondra 1995; Novak *et al.* 1999; Selway *et al.* 1998 1999*a*,*b* 2000*a*,*b* 2002; Tindle et al., 2002, 2005). Similarly, the compositional variation in even a single, zoned crystal may contain significant petrogenetic information (Agrosi *et al*. 2006; Dutrow & Henry 2000; Henry *et al.* 1999; van Hinsberg & Marschall 2007a,b; van Hinsberg & Schumacher 2007; van Hinsberg *et al.* 2006), as the very slow rates of solid-state diffusion (*e.g.*,von Georne *et al.* 1999), and the refractory nature of tourmaline makes crystals resistant to resetting by thermal and fluid events. In addition, tourmaline minerals are the most common boron-bearing minerals in the crust of the Earth, and therefore play an important role in the B-cycle.

Over the past two decades, there has been considerable work done on the characterization (*e.g*. Hawthorne *et al.* 1993; Burns *et al.* 1994; Grice & Ercit 1993; Grice *et al.* 1993; Taylor *et al.* 1995; Bloodaxe *et al.* 1999; Kalt *et al.* 2001; Cámara *et al.* 2002; Schreyer *et al.* 2002a,b; Ertl & Hughes 2002; Ertl *et al.* 2003a,b, 2004, 2005; Hughes *et al.* 2000, 2004; Marschall *et al.* 2004; Bosi & Lucchesi 2004; Bosi *et al.* 2004, 2005) and understanding (Hawthorne 1996, 2002; Bosi & Lucchesi 2007; Bosi 2011) of site-occupancy in tourmaline. However, the complete derivation of site populations (and accurate bulk compositions) is not trivial, and our knowledge of the crystal chemistry and thermodynamic properties of all tourmaline minerals is still far from complete.

1.2 GENERAL FORMULA AND CRYSTAL STRUCTURE

The general formula of tourmaline can be written as:

$$^{[9]}X\ ^{[6]}Y_3\ ^{[6]}Z_6\ [^{[4]}T_6O_{18}]\ [^{[3]}BO_3]_3\ ^{[3]}V_3\ ^{[3]}W$$

where[1]

X = Ca, Na, K, ☐ (vacancy), Pb, Ag (syn.)

Y = Li, Mg, Fe^{2+}, Mn^{2+}, Al, Cr^{3+}, V^{3+}, Fe^{3+}, Ti^{4+}, (☐)

Z = Mg, Al, Fe^{3+}, V^{3+}, Cr^{3+}, Fe^{2+}

T = Si, Al, B

B = B

V = OH, O, [≡O(3)]

W = OH, F, O^{2-}, [≡O(1)].

The structure of tourmaline, projected onto (001) is illustrated in Figure

[1] Throughout this work, italicized symbols (*e.g.*, *X*, *Y*, *Z*) will designate sites in the tourmaline structure, whereas non-italicized symbols (*e.g.*, X, Y, Z) will designate specific cations or groups of cations (e.g., T = Si_6, T = $(Si,B)_6$.

1.1. There is one tetrahedrally coordinated site, labelled *T*, which is predominantly occupied by Si but may also contain Al and B. Six TO_4 tetrahedra join corners to form a $[T_6O_{18}]$ ring, and all tetrahedra point in the -*c* direction (Figure 1.2), giving the structure a polar character. There are two octahedrally-coordinated sites labelled *Y* and *Z*. The *Z*-octahedra share edges forming infinite $[Z\Phi_4]$ chains (Φ = unspecified anion) parallel to the *c*-axis. Six of these chains are linked by corners, and surround three *Y* octahedra which share edges to form a $[Y_3\Phi_6]$ trimer. There is one triangularly coordinated site that is occupied by B, and these BO_3 groups provide additional linkage between *Y*- and *Z*-octahedra (Figure 1.1). The *X*-site is [9]-coordinated and is located on the 3-fold axis between the basal plane of the $[T_6O_{18}]$ ring and the $[Y_3\Phi_6]$ trimer.

Two anion sites, O(1)- and O(3)-sites, have variable occupancy. The [3]-coordinate O(3)-site is common to two *Z*- and one *Y*-octahedra; it is typically occupied by (OH), but may also be occupied by O^{2-}. The [3]-coordinate O(1)-site is common to three *Y*-octahedra; it is occupied by (OH), F, and O^{2-}. Where O(1) and O(3) are occupied by (OH), the bonds extend in the +*c* and -*c*-directions, respectively (Figure 2.2). The distance between H [at O(3)] and O(5) is ~2.2 Å, and it has been suggested that a weak H-bond forms between these two ions (Robert *et al.* 1997).

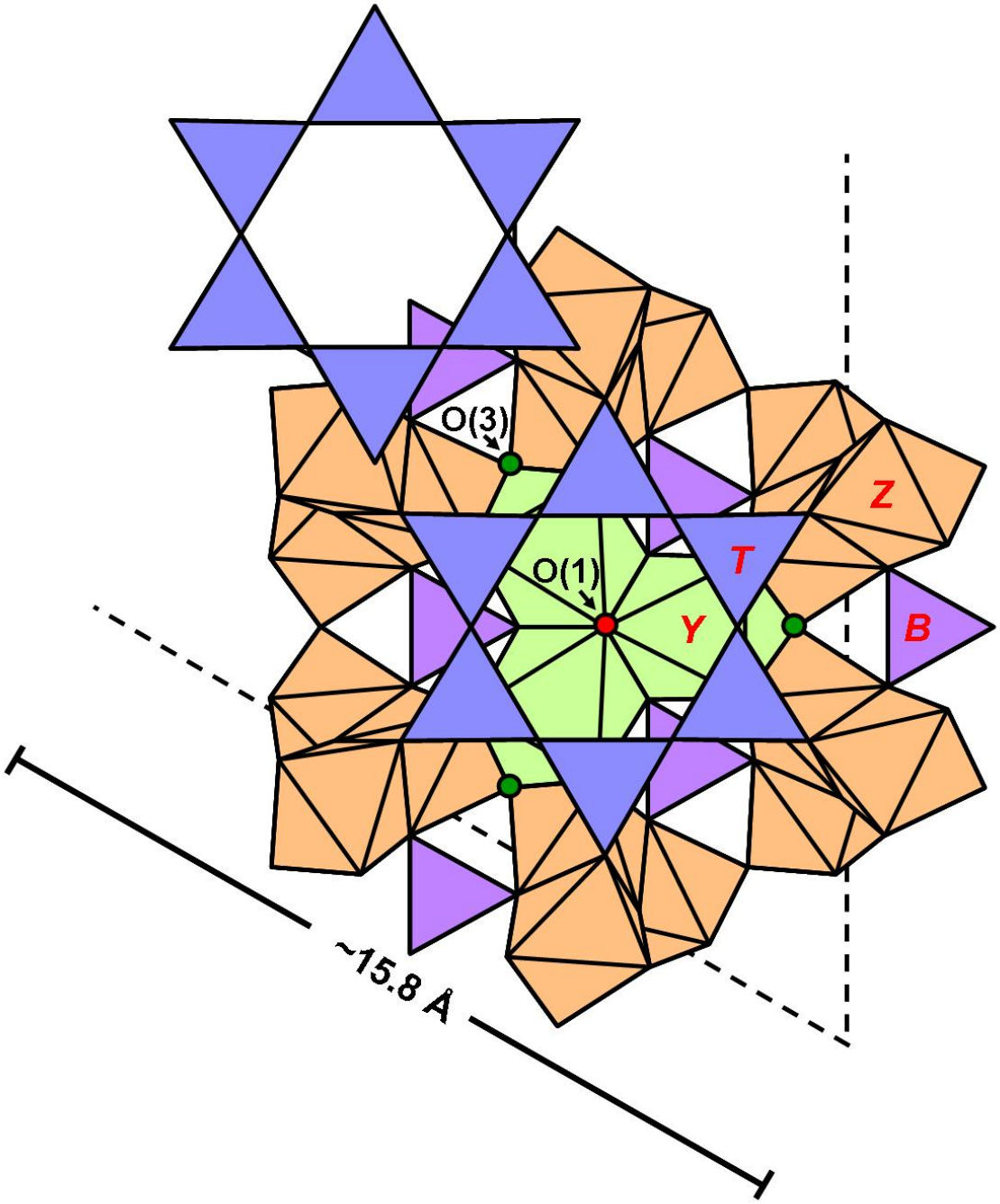

Figure 1.1 Fragment of the tourmaline structure projected onto (001); *X*-site cation is not shown. Dotted-lines correspond to *a*-cell edges.

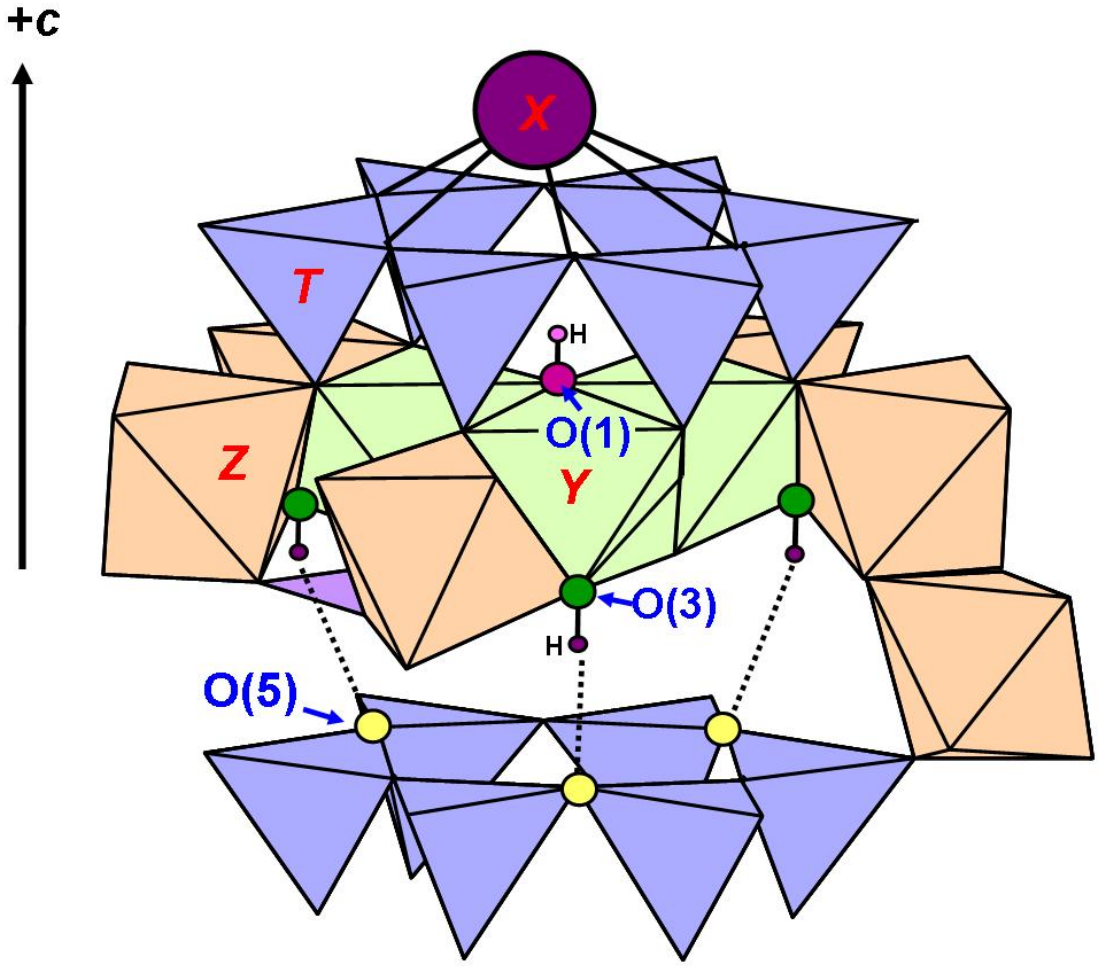

Figure 1.2 Fragment of tourmaline structure projected (approximately) on (100) showing variable anion positions O(1) and O(3) occupied by (OH). Note opposing directions of O-H bonds. Dotted lines represent H-bonds to O(5) anions.

1.2.1 Space-group symmetry

Most tourmalines have trigonal symmetry (space group *R*3*m*). However, the occurrence of anomalous biaxial optics in some tourmalines is well-known (*e.g.*, Braun 1881; Madelung 1883; Foord & Cunningham 1978; Takano & Takano 1959; Foord & Mills 1978; Akizuki *et al*. 2001; Shtukenberg *et al.* 2007; Hughes *et al.* 2011; Lussier *et al.* 2011). Shtukenberg *et al.* (2007) and Hughes *et al.* (2011) both report tourmaline crystals (of elbaite-liddicoatite and dravite, respectively) where significantly better agreement is observed where *X*-ray intensity data are merged with triclinic as opposed to trigonal Laue symmetry. Their final refinements in the triclinic space group *R*1 show ordering within the *Y*-site trimers. However, Lussier *et al.* (2011) observed large *2V* angles [up to 20.5(9)°] in a Madagascar liddicoatite, yet a detailed investigation into X-ray merging across mirror planes in *R*3*m* showed no substantial deviation from trigonal symmetry, indicating that the physical nature of ordering and symmetry reduction may be very subtle.

1.3 TOURMALINE NOMENCLATURE AND CLASSIFICATION

Since it was initially published, the classification scheme proposed by Hawthorne & Henry (1999) has been widely used. However, the Subcommittee on Tourmaline Nomenclature of the International Mineralogical Association (STM-IMA) has recently produced a new nomenclature for the tourmaline-supergroup minerals. The recommendations of the STM-IMA presented in Henry

et al. (2011) are followed throughout this work, and a brief outline of the classification procedure is presented here.

1.3.1 Tourmaline groups

Henry *et al.* (2011) recognize tourmaline minerals as forming a supergroup consisting of "two or more mineral groups, which have essentially the same structure and composed of chemically similar elements" (Mills *et al.* 2009). These *primary* groups are divided on the basis of the most abundant species at the *X*-site (Na (+K), Ca, □). Arithmetically, these groups are defined as:

Alkali: $^{X}(Na + K) \geq {}^{X}Ca$ and $^{X}(Na + K) \geq {}^{X}\square$; and

Calcic: $^{X}Ca \geq {}^{X}(Na + K)$ and $^{X}Ca > {}^{X}\square$

X-vacant: $^{X}\square \geq {}^{X}(Na + K)$ and $^{X}\square > {}^{X}Ca$

and correspond to the fields of the ternary system shown in Figure 1.3*a*.

Furthermore, a general series of tourmaline species is defined on the basis of *W*-site occupancy. The *W*-site can be occupied by three distinct anions: O^{2-}, F^{-}, and $(OH)^{-}$, and depending on the relative abundance of each form *oxy*-, *hydroxy*-, and *fluor*- species. Arithmetically, these groups are defined as:

Hydroxy: $^{W}OH + {}^{W}F \geq {}^{W}O$ and $^{W}OH \geq {}^{W}F$;

Fluor: $^{W}OH + {}^{W}F \geq {}^{W}O$ and $^{W}F \geq {}^{W}OH$; and

Oxy: $^{W}O > {}^{W}OH + {}^{W}F$.

and correspond to the fields of the ternary system shown in Figure 1.3*b*.

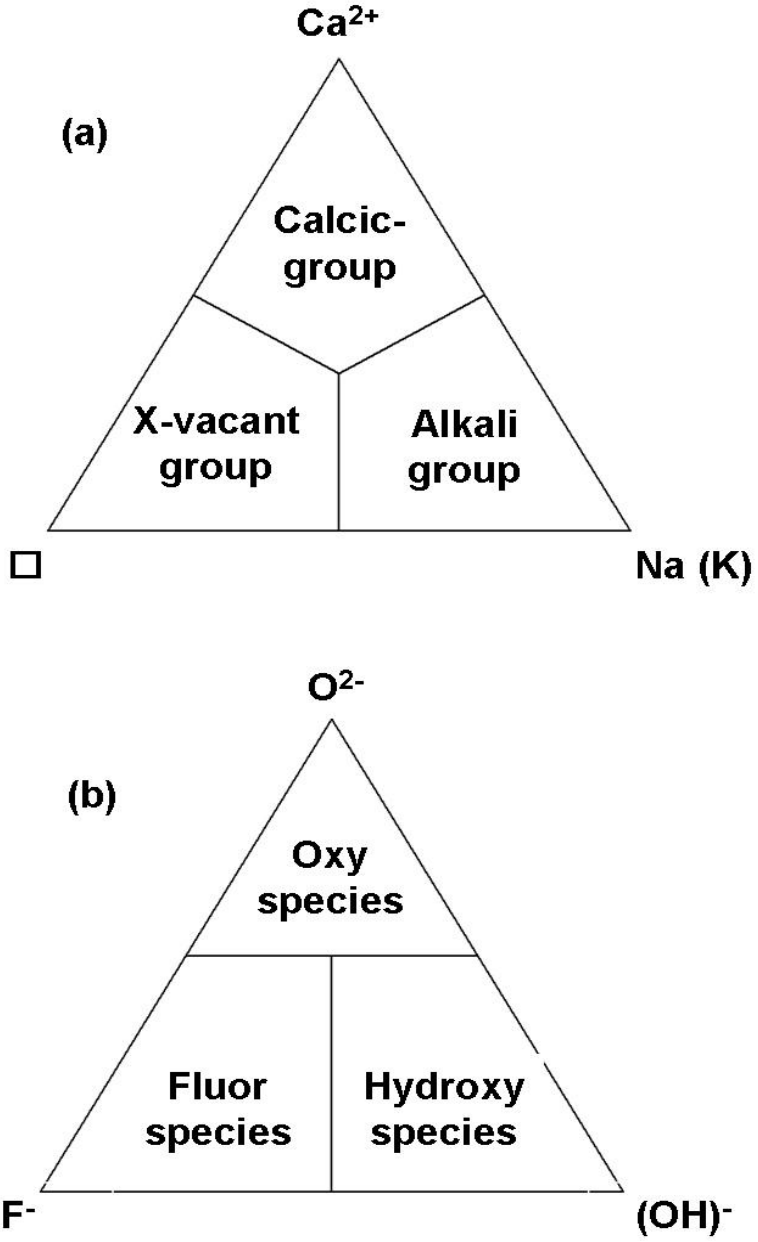

Figure 1.3 Ternary systems for determination of (a) primary tourmaline groups based on X-site occupancy; and (b) general series of tourmaline species based on O(1)-site occupancy (from Henry *et al.* (2011), used with permission).

1.3.2 Tourmaline species

Within each *X*-site group, Henry *et al.* (2011) define subgroups. Subgroup 1 is defined as the *fundamental subgroup* and generally, contains the largest number of species. The operation of common heterovalent coupled substitutions (Table 1.1) on the species in subgroup 1 generates the additional subgroups. For example, operation of substitution (3) on subgroup 1 of the alkali-species in Table 1.2 will generate the compositions found in subgroup 2 (and so on). The resulting structural formulae for both recognized (given in bold font) and prospective tourmaline species are given for the *alkali*-group (Table 1.2), the *calcic*-group (Table 1.3), and the *X-site vacant* group (Table 1.4). Species that are within a given subgroup are related by the operation of homovalent substitutions that may result in extensive solid solution (*e.g.*, schorl-dravite).

1.3.3 Tourmaline classification

The (OH)-dominant species is the '*root composition*'. For the purposes of classification, a tourmaline is named on the basis of the dominant constituents of the dominant valence state. For example, a tourmaline with the general formula: $^{X}Na\ ^{Y}[Al_{0.6}Li_{0.6}Fe^{2+}{}_{1.05}Mg_{0.75}]\ ^{Z}Al_6\ [^{T}Si_6O_{18}]\ [BO_3]_3\ ^{V}(OH)_3\ ^{W}(OH)$ would be an alkali tourmaline, but would be classified as a schorl because the dominant valance state at the *Y*-site is divalent, and Fe^{2+} is the dominant divalent cation. As stated in Henry *et al*. (2011), tourmalines are "named for the dominant species in the dominant subgroup" in Tables 1.2 to 1.4. The series of discrimination diagrams given in Figure 1.4 facilitates classification of tourmalines (where T = Si_6 *apfu*).

TABLE 1.1 SIGNIFICANT TOURMALINE HETEROVALENT COUPLED SUBSTITUTIONS AND ASSOCIATED EXCHANGE VECTORS (*after* Henry *et al.* 2011)

	Generalized coupled substitutions	Corresponding exchange vector	Resulting actions
(1)	$^{X}R^{1+} + R^{2+} \leftrightarrow {}^{X}\square + R^{3+}$	$(^{X}\square R^{3+})(R^{1+}R^{2+})_{-1}$	relates alkali-vacant groups
(2)	$^{X}R^{1+} + R^{3+} \leftrightarrow {}^{X}Ca + R^{2+}$	$(^{X}CaR^{2+})(R^{1+}R^{3+})_{-1}$	relates alkali-calcic groups
(3)	$^{Y}2R^{2+} \leftrightarrow {}^{Y}Li + {}^{Y}Al^{3+}$	$(LiAl)(2R^{2+})_{-1}$	relates incorporation of Li in all groups
(4)	$R^{2+} + (OH)^{-} \leftrightarrow R^{3+} + O^{2-}$	$(R^{3+}O^{2-})(R^{2+}(OH)^{-})_{-1}$	relates deprotonation in all groups
(5)	$½Li + (OH)^{-} \leftrightarrow ½{}^{Y}Al + O^{2-}$	$(Al_{0.5}O)(Li_{0.5}(OH))_{-1}$	relates deprotonation in Li species
(6)	$R^{2+} + {}^{T}Si^{4+} \leftrightarrow R^{3+} + {}^{T}R^{3+}$	$(R^{3+}R^{3+})(R^{2+}Si^{4+})_{-1}$	relates Tschermak-like tetrahedral-octahedral substitution in all groups

R represents cations such as: R^{+} = Na, K, R^{2+} = Mg, Fe^{2+} Co, Ni, Zn; R^{3+} = Al, Fe^{3+}, Cr^{3+}, V^{3+}, $^{T}B^{3+}$. No site designation may represent multiple sites.

TABLE 1.2 GENERALIZED STRUCTURAL FORMULAE FOR RECOGNIZED OR PROSPECTIVE TOURMALINE SPECIES LISTED BY X-SITE ALKALI-GROUP TOURMALINE (*after* Henry *et al.* 2011)

	X	*Y*	*Z*	T_6O_{18}	$(BO_3)_3$	V_3	*W*
Alkali subtype 1	R^{1+}	$R^{2+}{}_3$	$R^{3+}{}_6$	$R^{4+}{}_6O_{18}$	$(BO_3)_3$	$S^-{}_3$	S^-
Dravite	Na	Mg_3	Al_6	Si_6O_{18}	$(BO_3)_3$	$(OH)_3$	(OH)
Schorl	Na	$Fe^{2+}{}_3$	Al_6	Si_6O_{18}	$(BO_3)_3$	$(OH)_3$	(OH)
Chromium-dravite	Na	Mg_3	Cr_6	Si_6O_{18}	$(BO_3)_3$	$(OH)_3$	(OH)
Vanadium-dravite	Na	Mg_3	V_6	Si_6O_{18}	$(BO_3)_3$	$(OH)_3$	(OH)
"Fluor-dravite"	Na	Mg_3	Al_6	Si_6O_{18}	$(BO_3)_3$	$(OH)_3$	F
"Fluor-schorl"	Na	$Fe^{2+}{}_3$	Al_6	Si_6O_{18}	$(BO_3)_3$	$(OH)_3$	F
"Potassium-dravite"	K	Mg_3	Al_6	Si_6O_{18}	$(BO_3)_3$	$(OH)_3$	(OH)
"Tsilaisite"	Na	$Mn^{2+}{}_3$	Al_6	Si_6O_{18}	$(BO_3)_3$	$(OH)_3$	(OH)
Alkali-subtype 2	R^{1+}	$R^{1+}{}_{1.5}R^{3+}{}_{1.5}$	$R^{3+}{}_6$	$R^{4+}{}_6O_{18}$	$(BO_3)_3$	$S^-{}_3$	S^-
Elbaite	Na	$Li_{1.5}Al_{1.5}$	Al_6	Si_6O_{18}	$(BO_3)_3$	$(OH)_3$	(OH)
"Fluor-elbaite"	Na	$Li_{1.5}Al_{1.5}$	Al_6	Si_6O_{18}	$(BO_3)_3$	$(OH)_3$	F
Alkali subtype 3	R^{1+}	$R^{3+}{}_3$	$R^{3+}{}_4R^{2+}{}_2$	$R^{4+}{}_6O_{18}$	$(BO_3)_3$	$S^-{}_3$	S^{2-}
Povondraite	Na	$Fe^{3+}{}_3$	$Fe^{3+}{}_4Mg_2$	Si_6O_{18}	$(BO_3)_3$	$(OH)_3$	O
Chromo-alumino-povondraite	Na	Cr_3	Al_4Mg_2	Si_6O_{18}	$(BO_3)_3$	$(OH)_3$	O
"Oxy-dravite"**	Na	Al_3	Al_4Mg_2	Si_6O_{18}	$(BO_3)_3$	$(OH)_3$	O
"Oxy-schorl"	Na	Al_3	$Al_4Fe^{2+}{}_2$	Si_6O_{18}	$(BO_3)_3$	$(OH)_3$	O
"Na-Cr-O root name"	Na	Cr_3	Cr_4Mg_2	Si_6O_{18}	$(BO_3)_3$	$(OH)_3$	O
"Potassium Povondraite"	K	$Fe^{3+}{}_3$	$Fe^{3+}{}_4Mg_2$	Si_6O_{18}	$(BO_3)_3$	$(OH)_3$	O
Alkali-subtype 4	R^{1+}	$R^{1+}{}_1R^{3+}{}_2$	$R^{3+}{}_6$	$R^{4+}{}_6O_{18}$	$(BO_3)_3$	$S^-{}_3$	S^-
"Na-Li-O root name"	Na	$LiAl_2$	Al_6	Si_6O_{18}	$(BO_3)_3$	$(OH)_3$	O
Alkali subtype 5	R^{1+}	$R^{3+}{}_3$	$R^{3+}{}_6$	$R^{4+}{}_6O_{18}$	$(BO_3)_3$	$S^-{}_3$	S^-
Fluor-buergerite	Na	$Fe^{3+}{}_3$	Al_6	Si_6O_{18}	$(BO_3)_3$	O_3	F
Olenite	Na	Al_3	Al_6	Si_6O_{18}	$(BO_3)_3$	O_3	(OH)
"Buergerite"	Na	$Fe^{3+}{}_3$	Al_6	Si_6O_{18}	$(BO_3)_3$	O_3	(OH)
"Fluor-olenite"	Na	Al_3	Al_6	Si_6O_{18}	$(BO_3)_3$	O_3	F
Alkali subtype 6	R^{1+}	$R^{3+}{}_3$	$R^{3+}{}_6$	$R^{3+}{}_3R^{4+}{}_3O_{18}$	$(BO_3)_3$	$S^-{}_3$	S^-
"Na-Al-Al-Al root name"	Na	Al_3	Al_6	$Al_3Si_3O_{18}$	$(BO_3)_3$	$(OH)_3$	(OH)
"Na-Al-Al-B root name"	Na	Al_3	Al_6	$B_3Si_3O_{18}$	$(BO_3)_3$	$(OH)_3$	(OH)
"Fluor-Na-Al-Al-Al root name"	Na	Al_3	Al_6	$Al_3Si_3O_{18}$	$(BO_3)_3$	$(OH)_3$	F
"Fluor-Na-Al-Al-B root name"	Na	Al_3	Al_6	$B_3Si_3O_{18}$	$(BO_3)_3$	$(OH)_3$	F

TABLE 1.3 GENERALIZED STRUCTURAL FORMULAE FOR RECOGNIZED OR PROSPECTIVE TOURMALINE SPECIES LISTED BY X-SITE CALCIC-GROUP TOURMALINE (after Henry et al. 2011)

	X	*Y*	*Z*	T_6O_{18}	$(BO3)3$	V_3	*W*
Calcic-subtype 1	*Ca*	$R^{2+}{}_3$	$R^{2+}R^{3+}{}_5$	$R^{4+}{}_6O_{18}$	$(BO_3)_3$	$S^-{}_3$	S^-
Fluor-uvite	Ca	Mg_3	$MgAl_5$	Si_6O_{18}	$(BO_3)_3$	$(OH)_3$	F
Feruvite	Ca	$Fe^{2+}{}_3$	$MgAl_5$	Si_6O_{18}	$(BO_3)_3$	$(OH)_3$	(OH)
Uvite	Ca	Mg_3	$MgAl_5$	Si_6O_{18}	$(BO_3)_3$	$(OH)_3$	(OH)
"Fluor-feruvite"	Ca	$Fe^{2+}{}_3$	$MgAl_5$	Si_6O_{18}	$(BO_3)_3$	$(OH)_3$	F
Calcic-subtype 2	*Ca*	$R^{1+}{}_2R^{3+}$	$R^{3+}{}_6$	$R^{4+}{}_6O_{18}$	$(BO_3)_3$	$S^-{}_3$	S^-
Fluor-liddicoatite	Ca	Li_2Al	Al_6	Si_6O_{18}	$(BO_3)_3$	$(OH)_3$	F
Liddicoatite	Ca	Li_2Al	Al_6	Si_6O_{18}	$(BO_3)_3$	$(OH)_3$	(OH)
Calcic-subtype 3	*Ca*	$R^{2+}{}_3$	$R^{3+}{}_6$	$R^{4+}{}_6O_{18}$	$(BO_3)_3$	$S^-{}_3$	S^{2-}
"Ca-Mg-O" room name	Ca	Mg_3	Al_6	Si_6O_{18}	$(BO_3)_3$	$(OH)_3$	O
"Ca-Fe-O" room name	Ca	$Fe^{2+}{}_3$	Al_6	Si_6O_{18}	$(BO_3)_3$	$(OH)_3$	O
Calcic-subtype 4	*Ca*	$R^{1+}{}_{1.5}R^{3+}{}_{1.5}$	$R^{3+}{}_6$	$R^{4+}{}_6O_{18}$	$(BO_3)_3$	$S^-{}_3$	S^{2-}
"Ca-Li-O root name"	Ca	$Li_{1.5}Al_{1.5}$	Al_6	Si_6O_{18}	$(BO_3)_3$	$(OH)_3$	O

TABLE 1.4 GENERALIZED STRUCTURAL FORMULAE FOR RECOGNIZED OR PROSPECTIVE TOURMALINE SPECIES LISTED BY X-SITE VACANT TOURMALINE (after Henry et al. 2011)

	X	Y	Z	T_6O_{18}	$(BO_3)_3$	V_3	W
□-*subtype 1*	□	$R^{1+}{}_2R^{3+}$	$R^{3+}{}_6$	$R^{4+}{}_6O_{18}$	$(BO_3)_3$	$S^{-}{}_3$	S^{-}
Foitite	□	$Fe^{2+}{}_2Al$	Al_6	Si_6O_{18}	$(BO_3)_3$	$(OH)_3$	(OH)
Magnesio-foitite	□	Mg_2Al	Al_6	Si_6O_{18}	$(BO_3)_3$	$(OH)_3$	(OH)
□-*subtype 2*	□	$R^{1+}R^{3+}{}_2$	$R^{3+}{}_6$	$R^{4+}{}_6O_{18}$	$(BO_3)_3$	$S^{-}{}_3$	S^{-}
***R*ossmanite**	□	$LiAl_2$	Al_6	Si_6O_{18}	$(BO_3)_3$	$(OH)_3$	(OH)
□-*subtype 3*	□	$R^{2+}R^{3+}{}_2$	$R^{3+}{}_6$	$R^{4+}{}_6O_{18}$	$(BO_3)_3$	$S^{-}{}_3$	S^{2-}
"□-Mg-O" room name	□	$MgAl_2$	Al_6	Si_6O_{18}	$(BO_3)_3$	$(OH)_3$	O
"□-Fe-O" room name	□	$Fe^{2+}Al_2$	Al_6	Si_6O_{18}	$(BO_3)_3$	$(OH)_3$	O
□-*subtype 4*	□	$R^{1+}{}_{0.5}R^{3+}{}_{2.5}$	$R^{3+}{}_6$	$R^{4+}{}_6O_{18}$	$(BO_3)_3$	$S^{-}{}_3$	S^{2-}
"□-Li-O root name"	□	$Li_{0.5}Al_{2.5}$	Al_6	Si_6O_{18}	$(BO_3)_3$	$(OH)_3$	O

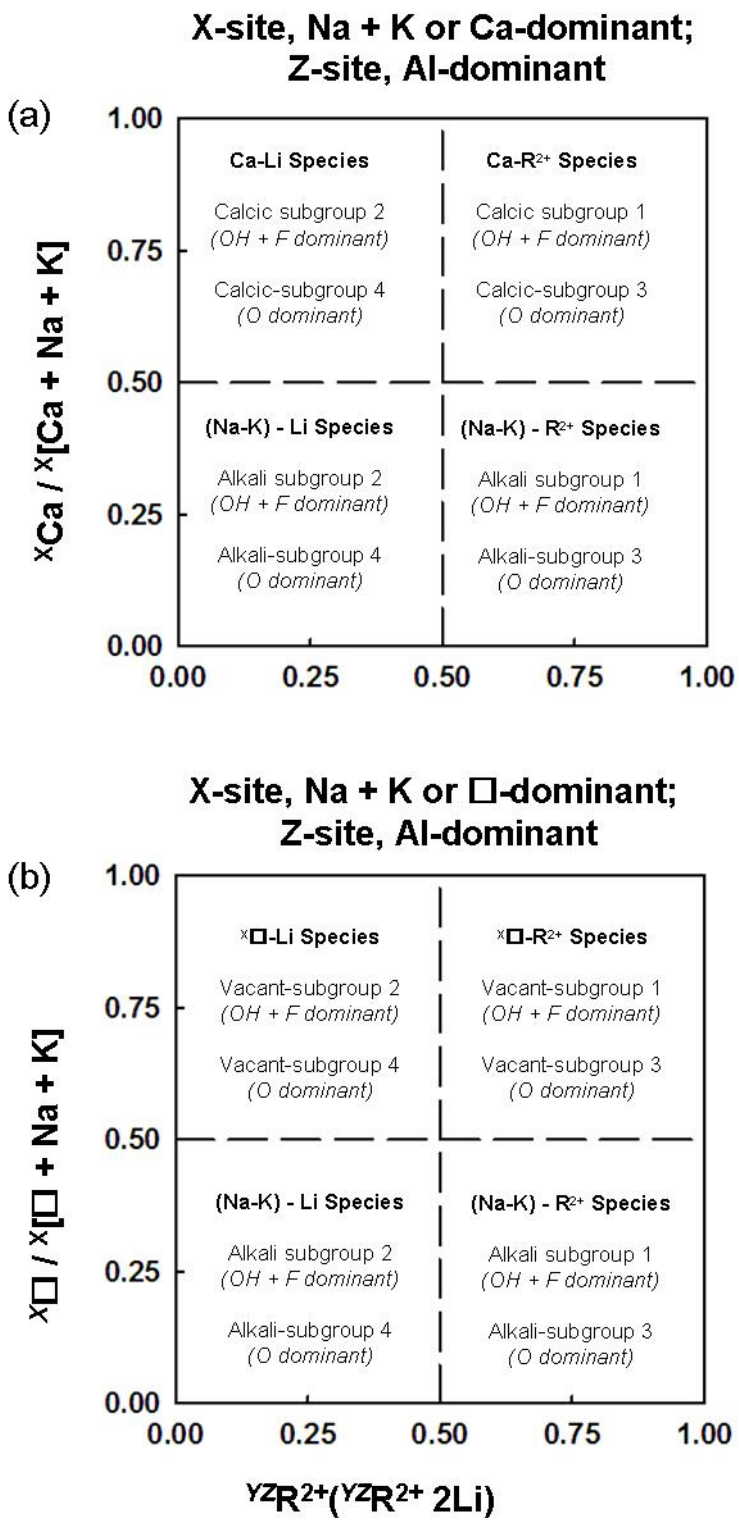

Figure 1.4 Diagrams to classify tourmalines in the appropriate subgroups. Determinations of subgroups 1-4 for: (a) alkali- and calcic-group tourmalines; (b) alkali- and *X*-vacant groups tourmalines; and (c) alkali-, calcic-, and X-site vacant tourmalines; (from Henry *et al.* (2011), used with permission).

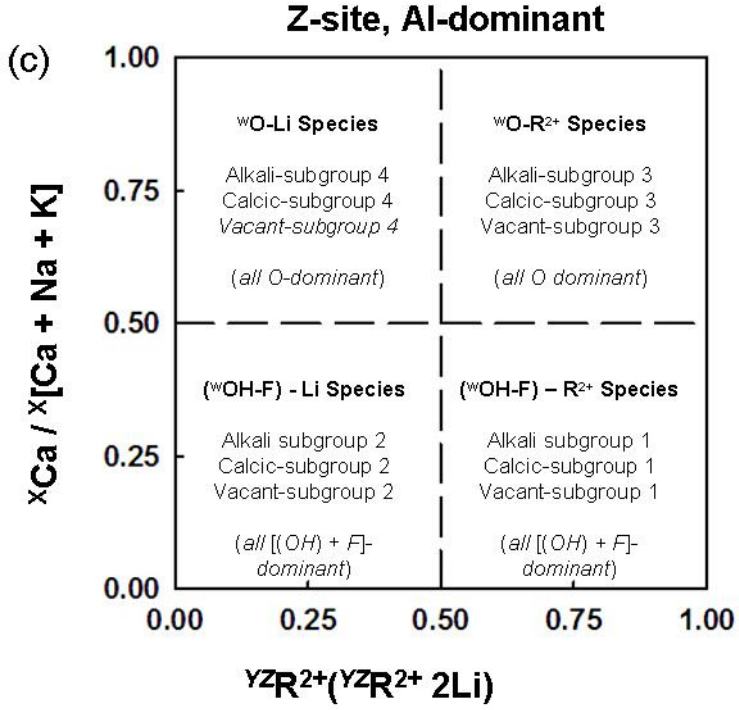
Z-site, Al-dominant
(c)
1.00
0.75
0.50
0.25
0.00
0.00
0.25
0.50
0.75
1.00
^{X}Ca / ^{X}[Ca + Na + K]
$^{YZ}R^{2+}$($^{YZ}R^{2+}$ 2Li)
^{W}O-Li Species
Alkali-subgroup 4
Calcic-subgroup 4
Vacant-subgroup 4
(all O-dominant)
^{W}O-R^{2+} Species
Alkali-subgroup 3
Calcic-subgroup 3
Vacant-subgroup 3
(all O dominant)
(^{W}OH-F) - Li Species
Alkali subgroup 2
Calcic-subgroup 2
Vacant-subgroup 2
(all [(OH) + F]-dominant)
(^{W}OH-F) – R^{2+} Species
Alkali subgroup 1
Calcic-subgroup 1
Vacant-subgroup 1
(all [(OH) + F]-dominant)

If necessary, prefixes may be added to the root name in the sequence: *X*-site modifier, *Y*-site modifier, *Z*-site modifier, *T*-site modifier, and *W*-site modifier. For example, a schorl in which K was the predominant R^{1+} cation at *X* and F was the predominant S^{1-} anion at *W* would be termed “potassium-fluor-schorl”.

1.4 SELECTED PHYSICAL PROPERTIES OF TOURMALINE

Tourmalines minerals have an average hardness of 7 - 7.5 on Mohs scale (*e.g.*, Deer *et al.* 1992; Klein & Dutrow 2008). Cleavage is described as very poor on {110} and {101}, and twinning on {101} and {401} is rare (Deere *et al*. 1992; Dietrich 1985). Densities of most tourmalines are ~3.1, with specific values for common species being: dravite (3.03-3.18), schorl (3.18-3.22) and elbaite (2.90-3.10) (Deer *et al*. 1992). Owing to the acentricity of the structure, tourmalines are both pyroelectric and piezoelectric and develop electric charges when the opposite ends of a crystal are subjected to different heats and pressures, respectively.

1.4.1 Crystal form and habit

Tourmaline minerals crystallize in the, “ditrigonal pyramidal (3*m*) class of the trigonal subsystem of the hexagonal crystal system” (Deitrich 1985). Morphologically, crystals are commonly euhedral and may show a wide variety of trigonal pyramidal forms (which may occur on both the analogous (-*c*) and antilogous (+*c*) ends) and prismatic forms. Readers are referred to Deitrich (1985) for a more detailed discussion of tourmaline crystal morphology.

In this work, tourmalines with the prismatic and fibrous habits are encountered. In general, massive and prismatic habits are those most commonly observed in tourmaline, occurring in both crystals igneous and metamorphic origin. These crystals range in size from microscopic up to ~2 m in maximal dimension (*e.g.*, Rowley 1942; Lyckberg 1997), and are commonly euhedral to subhedral. Fibrous habits are relatively common in pegmatitic tourmalines (*e.g.*, Mitchell 1964; Pezzotta *et al.* 1996; Selway *et al.* 1999; Yavuz *et al.* 1999; Dutrow & Henry 2000; Ertl *et al.* 2007). These are thin prisms elongated along *c*, and are commonly grouped in parallel, divergent or fibrous masses (Deitrich 1985). Fibres may extend outward from a single crystal at the sample base, appearing to bifurcate along their length (*e.g.*, Furbish 1968; Lussier *et al.* 2008a,b).

1.5 SELECTED OPTICAL PROPERTIES OF TOURMALINE

Tourmaline is most commonly uniaxial negative. Deer *et al.* (1992) report the following ranges of optical parameters. Indices of refraction for natural tourmalines range from 1.634-1.661 (dravite) 1.660-1.671 (schorl), and 1.633-1.651 (elbaite) for ω, and 1.612-1.632 (dravite) 1.635-1.650 (schorl) 1.615-1.630 (elbaite) for ε. Birefringence (δ) ranges from 0.021-0.029 (dravite), 0.025-0.035 (schorl), and 0.017-0.021 (elbaite). Dispersion in tourmaline is generally weak, whereas pleochroism and dichroism are typically strong, with absorption $\omega > \varepsilon$ (Deer *et al*. 1992). Commonly, prism faces have subadamantine to vitreous luster whereas terminations have subvitreous to dull luster (Deitrich 1985).

1.5.1 Colour and colour zoning

Some tourmalines, particularly elbaite and liddicoatite, show brilliant and complex colour zoning with a wide range of colours, including, white, colourless, brown, blue, black, orange, pink, green, yellow, purple and red, as well as complex combinations of different hues (*e.g.*, Dunn *et al.* 1977, 1978; Dietrich 1985; Benesch 2000; Dirlem *et al.* 2002; Rustemeyer 2003). Several types of colour zoning occur in tourmaline and some of the most common are: (1) *oscillatory zoning*, where successive layers, each of different colour, alternate in a rhythmic manner (see images in Benesch 2000; Dirlem et al. 2002); (2) *colour sector zoning*, where colour differences correspond to different crystal sectors (*e.g.*, Rustemayer 2003; Henry *et al.* 1999; Akizuki *et al.* 2001; van Hinsberg *et al.* 2006; van Hinsberg & Marschall 2007); (3) *gradational zoning*, common in , for example, 'watermelon' tourmalines, wherein red slowly changes to colourless which slowly changes to green along the length of the crystal prism; (4) *irregular (or patchy) zoning* (Deitrich 1985), which shows an irregular distribution of colours; and (5) *discontinuous colour zoning*, where abrupt changes in colour not necessarily associated with different growth sector boundaries are observed (*e.g.*, Dutrow & Henry 2000; Lussier *et al*. 2008b, 2011b,c).

1.5.2 Important causes of colour

The specimens investigated in detail in this work show complex patterns of colour zoning. Compositional data typically show correlations between colour and major constituents, for example, Mn and pink, and Fe and green. The amount of compositional change required to result in a visually pronounced colour change may be small (*i.e.*, << 0.1 *apfu*).

Colour in tourmaline originates mainly from transition elements (*e.g.*, Fe^{2+}, Fe^{3+}, Mn^{2+}, Mn^{3+}, Cu^{2+} and Ni^{2+}) present as either major or minor constituents at the *Y*- and *Z*-octahedral sites. The simplest colour-causing mechanisms are *d*-*d* electron transitions in a specific atom (*e.g.*, Cu^{2+} in brilliant blue Paraiba-type tourmalines; Laurs *et al.* 2008).

Inter-Valence Change Transfer (IVCT) occurs in tourmaline where absorption of an incident light photon results in an electron hopping between members of a charge-coupled pair, both located in edge-sharing octahedra (see Burns 1981; Hawthorne 1988). Such pairs may be homonuclear, such as $Fe^{2+} + Fe^{3+} \leftrightarrow Fe^{3+} + Fe^{2+}$, which results in brown-to-black colouration (Faye *et al.* 1974; Smith & Strens 1976; Smith 1978*a*,*b*; Mattson & Rossman 1987; Taran *et al.* 1993), or heteronuclear, such as $Fe^{2+} + Ti^{4+} \leftrightarrow Fe^{3+} + Ti^{3+}$, which results in a brown colouration (Rossman & Mattson 1986; Taran *et al.* 1993) and $Mn^{4+} + Ti^{3+} \leftrightarrow Mn^{3+} + Ti^{4+}$, which results in yellow-green colouration (Rossman & Mattson 1986).

1.6 SOLID SOLUTIONS IN TOURMALINE

Solid solutions are commonly observed between several species of natural tourmaline. There are complete solid solutions between schorl-elbaite and schorl-dravite (Dietrich 1985; Bosi & Lucchesi 2004; Bosi *et al.* 2005b). Additionally, partial to complete solid solutions have also been observed to operate between dravite-chromdravite (Bosi *et al.* 2004), schorl-olenite (Kalt *et al.* 2001) elbaite-liddicoatite (Ertl *et al.* 2006a), dravite-uvite, dravite-povondraite, feruvite-uvite (Dietrich 1985) and elbaite-dravite (Novák *et al.* 1999; Ert *et al.* 2010).

1.7 CONTRIBUTION OF THIS WORK

1.7.1 Review of tourmaline crystal chemistry

There are presently ~200 tourmaline structures in the published literature, and over 80% have appeared in the last 15 years. The most recent assessments of relations between *Y*-site occupancy and <*Y*-*Φ*> and *Z*-site-occupancy and <*Z*-*Φ*> (where <> denotes mean values) date to before 1996 (*e.g.*, Grice & Ercit 1993; Hawthorne *et al.* 1993; Burns *et al.* 1994; MacDonald & Hawthorne 1995a). Furthermore, more recently published relations between *T*-site occupancy and
<*T*-O> show considerable disagreement (*e.g.*, MacDonald & Hawthorne 1995a; Hughes *et al.* 2004; Ertl *et al.* 2006a). These relations are re-examined and updated here using a selected database of compiled structures.

1.7.2 Crystal chemistry of the T-site

It has been definitively shown that both Al (*e.g.*, Povondra 1981; Grice & Ercit 1993; MacDonad & Hawthorne 1995a) and B (*e.g.*, Ertl *et al.* 1997; Marler & Ertl 2002; Hughes *et al.* 2004; Tagg *et al.* 1999; Schreyer *et al.* 2002a,b) may occur in the *T*-sites of tourmalines. However, a general understanding of their frequency of occurrence in different tourmaline species as well as the petrologic significance of their occurrence is currently lacking. In this work over 50 different tourmaline samples are investigated using a combination of ^{11}B and ^{27}Al Magic-Angle-Spinning Nuclear Magnetic Resonance (MAS NMR) spectroscopy, and Electron MicroProbe Analysis (EMPA). The structures of several samples with $^{[4]}$B are also refined by Site-scattering REFinement (SREF). Furthermore, although ^{11}B MAS NMR has been shown to be effective in detecting $^{[4]}$B (Tagg *et al.* 1999; Marler & Ertl 2002; Marler *et al.* 2002), the use of ^{27}Al MAS NMR to detect $^{[4]}$Al has not yet been reported in the literature, although it should be amenable to the task. Thus, this work will also concentrate on developing this method.

1.7.3 Compositional zoning in tourmalines from granitic pegmatites

Four types of tourmaline from granitic pegmatites are characterised in detail throughout this work; each having a unique composition and/or morphologic feature: (1) a crystal from Black Rapids Glacier, Alaska, showing a central pink zone that is mantled by a thin rim of green tourmaline; the composition was found to range from elbaite in the centre to liddicoatite at the outermost edge; (2) a large slab (~25 cm across) of Madagascar liddicoatite cut along (001) showing complex patterns of oscillatory zoning in pyramidal {201} and prismatic {110} sectors. (3) Wheatsheaf and (4) mushroom (2 samples) elbaites from Mogok, Myanmar; both samples show extensive bifurcation (*i.e.*, splitting) of fibrous crystals originating from a central core region, as well as pronounced colour zoning. In one mushroom, a rind of pink material mantles a central region of white fibres with a black core; in the other mushroom, a rind of purple material mantles a region of grayish-purple fibres with a dark-purple-to-black core.

For each of these samples, the chemical variation is characterised in detail using EMPA. For samples (2) to (4), ^{11}B and ^{27}Al MAS NMR spectroscopy, Mössbauer spectroscopy, Site-scattering REFinement (SREF) and EMPA data were acquired to fully characterise the crystal chemistry and crystal structure, as well as the substitution mechanisms responsible for the compositional variation. Finally, these data sets are integrated in order to constrain aspects of the crystal growth histories. It is of particular interest to determine which features of

compositional zoning and crystal morphology may result from externally-forced parameters, such as variations in melt properties, as opposed to internally-forced parameters, such as development of non-equilibrium conditions and the crystal-melt interface and coupled feedback mechanisms.

1.7.4 Note about publications

Many of the data presented and discussed in this work have been the published in separate papers (Lussier *et al*. 2008a,b, 2009, 2011a,b,c; Lussier & Hawthorne 2011). The format of the current work integrates the data from all these studies, allowing the reader to compare and contrast the results.

CHAPTER 2

THE CRYSTAL CHEMISTRY OF TOURMALINE

2.1 INTRODUCTION

As given in Chapter 1, the general formula of tourmaline is as follows:

$$X\,Y_3\,Z_6\,[BO_3]_3\,[T_6O_{18}]\,V_3\,W$$

where

X = Ca, Na, K, □, (vacancy), Pb, Ag (syn.)

Y = Li, Mg, Fe^{2+}, Mn^{2+}, Al, Cr^{3+}, V^{3+}, Fe^{3+}, Ti, Ni, Zn, (□)

Z = Mg, Al, Fe^{3+}, V^{3+}, Cr^{3+}, Fe^{2+}

T = Si, Al, B, (Be)

B = B, (□)

V = OH, O^{2-} [≡O(3)]

W = OH, F, O^{2-} [≡O(1)]

where the species in parentheses have not yet been proven to occur at these sites. By writing the formula this way, we can easily see some of the more important challenges that must be overcome in order to fully characterise any tourmaline: (1) up to three light lithophile elements (H, Li, B) may be present that cannot be analysed easily by common instrumental techniques; (2) Fe can occur as Fe^{2+} and Fe^{3+}; (3) most divalent and trivalent cations can occur at both the *Y*- and *Z*-sites, making site assignment difficult; and (4) multiple substitution mechanisms are possible such that tourmaline crystals may be heavily zoned, making bulk analytical techniques ineffective. Over the past ~20 years, the number of fully characterised tourmaline structures in the published literature has

increased from ~25 to ~200, and as a result, our understanding of certain aspects of these issues has improved. In this chapter, some of the more significant developments in our understanding of tourmaline crystal chemistry are also presented. In addition, the compositions and structures of the 188 tourmalines listed in Table 2.1 are compared to determine if the tourmaline structure is compatible with linear bondlength *vs*. aggregate radius models.

2.2 SITE POPULATIONS AND POLYHEDRON GEOMETRY

A fundamental step toward a complete understanding of tourmaline crystal chemistry is being able to accurately write the complete chemical formula. This requires complete determination of the abundances of chemical species and their correct assignment to sites in the structure. This may be done by crystal-structure refinement coupled with electron- and ion-microprobe analysis. Site populations may then be assigned by comparing site-scattering values and chemical composition along with any known relations between mean bondlengths and constituent cation radii at various sites in the structure. This may be done manually (*e.g.*, Grice & Ercit 1993; Burns *et al.* 1994; MacDonald & Hawthorne 1995a,b) or by automated optimization routine (*e.g.*, Wright *et al.* 2000; Lavina *et al.* 2002). In the latter, site-assignments are made iteratively until agreement between observed and ideal parameters (*e.g.*, site-scattering, composition, incident bond valence sums, bondlengths) is maximized.

2.2.1 THE *Z*-SITE

The *Z*-site is surrounded by six anions in an octahedral arrangement; five of these anions are O^{2-} and the sixth (the *V* position in the general formula and the O(3)-site in the structure) is commonly (OH) but may also be O^{2-}. Hawthorne *et al.* (1993) showed that Al and Mg can be partly disordered between the *Y*- and *Z*-sites. MacDonald & Hawthorne (1995a) showed that Mg may occur at the *Z*-site in uvite (ideal formula Ca $^{Y}Mg_3$ $^{Z}(Al_5Mg)$ Si_6O_{18} $(BO_3)_3$ $(OH)_3(OH)$; Hawthorne & Henry 1999). Trivalent Cr (*e.g.*, Bosi *et al.* 2004a) and Fe (*e.g.*, Grice & Ercit, Bosi *et al.* 2004b, 2005) may be disordered between the *Y*- and *Z*-sites. Taylor *et al.* (1995) showed that incorporation of O^{2-} at the O(1)-site can drive disorder of divalent and trivalent cations over the *Y*- and *Z*-sites. Thus it has been established that Al, Fe^{3+}, Cr^{3+} and Mg can occur at the *Z*-site.

The situation for Fe^{2+} is more controversial. Hawthorne *et al.* (1993) originally considered the disorder of Mg and Al over the *Y*- and *Z*-sites. The decision to restrict disorder to Mg and Al (only) was not based on crystal-chemical reasons; they stated that it was done this way because there was no information available on site-scattering apart from the fact that previous refinements had been done with $Z = Al_6$ *apfu*. For tourmalines of the schorl-dravite series, Bloodaxe *et al.* (1999) stated that their refined site-scattering values for the *Z*-site lie in the range 12-13 e (although they did not give the specific values, and did not state what type of scattering factors they used to refine their structures). Accordingly, they assigned only Mg and Al to the *Z*-site for these structures. Conversely, for tourmalines of the schorl-dravite series,

TABLE 2.1 LIST OF 188 PUBLISHED TOURMALINE STRUCTURES

REFERENCE		SAMPLE NAME
Barton 1969		Buergerite
Bloodaxe *et al.* 1999	*	108749, Dlux1, LCW2356, HP 2-1, O-T16-92, SmFalls, Ru-T17-92, Tu-T18-92, No. 32008
Bosi 2008	*	Uto
Bosi & Lucchesi 2004		TM507c, TM507e, TM235a, TM235b, TM112a, TM112c, TM233g, TM501e, TM84a, TM60e, TH65e, TH504c, TMI2ap, TMI2al, TMI3l, TMI4aa, TM9840c, TM9840f, TM9914b
Bosi *et al.* 2004	*	TMt3b, TMt6b, TMt3c, TMpr79f, TM1p43e
Bosi *et al.* 2005	*	Elb2rim, Tsl2y, Tsl2z, Tsl2w, Tsl2x, Tsl2m, Tsl2g
Bosi *et al.* 2005	*	66c, 61Rda, 60fc, 62ha, 64gh, L4e, 61Vbh, L4c, L3h, L4b, L4d, L1v, L1z
Bosi *et al.* 2010	*	SA, DT, SKT, ST
Burns *et al.* 1994	*	NP1, NP2, NP3, T10, T11, T12, T15, SD
Cámara *et al.* 2002	*	gfj, gde, gen
Cempírek *et al.* 2006	*	Kutna Hora
Clark *et al.* 2011	*	F-dravite
Ertl & Hughes 2002	*	Koralpe schorl
Ertl *et al.* 1997	*	Koralpe
Ertl *et al.* 2003a	*	Gos1, Gos2
Ertl *et al.* 2003b	*	BT, P6
Ertl *et al.* 2004a	*	T2
Ertl *et al.* 2004b	*	OLG
Ertl *et al.* 2005	*	REDT1, REDT2
Ertl *et al.* 2006a	*	LID3NEW, LID6A1, LID52 ,LC1
Ertl *et al.* 2006b	*	GRAS1
Ertl *et al.* 2007	*	Mushroom
Ertl *et al.* 2010a	*	HIM1, HIM2, HIM3, HIM4, HIM5, HMGC1, SS4
Foit 1989		"Alkali-deficient schorl"
Francis *et al.* 1999		"Foitite"
Grice & Ercit 1993	*	Pov. 144478,Schorl 2672, Schorl 49356, Schorl CROSS, Buergerite – 43293, Feruvite 53776, Dravite-43167, Dravite-32008, Dravite-43873, Dravite-43230, Uvite-52210, Elbaite-55224
Grice *et al.* 1993		Povondraite
Grice & Robinson 1989		Feruvite
Hawthorne *et al.* 1993		Dravite
Hughes *et al.* 2000	*	Olenite
Hughes *et al.* 2004	*	T1, T2, T3, T4, T5
Hughes *et al.* 2011	*	Dravite
London *et al.* 2006		Ag-elbaite
Lussier *et al.* 2008	*	SHM1, SHM2, SHM3, SHM3a, SHM3e, SHM5, SHP1, SHP2, SHP3
Lussier *et al.* 2011a	*	L1, L2, L4, L5, L6, L7, L11, L12, L13, L15, L16, L17, L18, L19, L20, L21, L22, L23, L24, L25, L26, L27, L28
Lussier *et al.* 2011b	*	SHW1, SHW2, SHW3, SHW4, SHW5, SHW6, SHW7, SHW8
MacDonald & Hawthorne 1995a	*	T72, T73, T74, T75, T76, T77, T78, T79, T80
MacDonald & Hawthorne 1995b		T54, T55
MacDonald *et al.* 1993		Foitite
Marler *et al.* 2002		Sample1, Sample2
Marschall *et al.* 2004		Dravite

TABLE 2.1 (CON'T)

REFERENCE		SAMPLE NAME
Nuber & Schmetzer 1981		Lid
Pertlik *et al.* 2003		Dravite
Prowatke *et al.* 2003		Fe-olenite
Rozhdestvenskaya *et al.* 2008		Sangilen
Rozhdestvenskaya *et al.* 2005		T17, T14, T7
Rozhdestvenskaya *et al.* 2007		Li-uvite
Schreyer *et al.* 2002b	*	Olenite
Selway *et al.* 1998		Rossmanite
Taylor *et al.* 1995		OH-deficient uvite
Tippe & Hamilton 1971		Buergerite

* denotes data used in Figure 6.19.

Bosi & Lucchesi (2004) reported refined *Z*-site scattering values in the range 12.87(5)-13.48(7) *e* and assigned small amounts of Fe^{2+} to the *Z*-site in some (but not all) structures of this series. Finally, Bosi (2008) and Andreozzi *et al.* (2008) put forward a persuasive case for partial disorder of Fe^{2+} over the *Y*- and *Z*-sites in some tourmalines of the schorl-dravite series. What is certain from the above discussion is that other cations in addition to Al can occur at the *Z*-site in the tourmaline structure.

2.2.1.1 Variation in <Y,Z-Φ>

Hawthorne *et al.* (1993) showed it advantageous to consider the variation in grand mean bondlength at the *Y*- and *Z*-sites as a function of constituent-cation radius, as this avoids problems associated with erroneous assignment of cations between the two sites. Errors in the assignment of site populations will result in nonlinear plots for individual sites, but may still give linear plots for the aggregate-site relation.

Hawthorne *et al.* (1993) drew a line of best fit through 12 data points spanning the range 0.57 < <*r*[*Y*,*Z*]> < 0.63 Å (where <r[*Y*,*Z*]> = [3<*r*[*Y*]> + 6<*r*[*Z*]>] / 9); the line of best fit corresponds to: <*Y*,*Z*-*Φ*> = 0.55<r[*Y*,*Z*]> + 1.64 (where *Φ* is an unspecified anion). Grice & Ercit (1993) also report a well-defined linear relation for 12 (different) data points that span the slightly broader range of 0.58 < <*r*[*Y*,*Z*]> < 0.66 Å; they give the regression equation: <*Y,Z*-*Φ*> = 0.83<r[*Y*,*Z*]> + 1.46. In both cases the slope differs significantly from the ideal hard-sphere relation, where the slope is unity and the intercept on the bondlength

axis corresponds to the mean radius of the coordinating anions. The significant difference between these two regression curves signifies that although a linear model seems correct, the true relation between bondlengths and constituent-cation-radii has not yet been well characterised.

Figure 2.1 plots the variation in $\langle Y,Z\text{-}\Phi \rangle$ against $\langle r[Y,Z] \rangle$ for the 188 tourmaline structures listed in Table 2.1; different species are represented by different colours (see caption). Inclusion of the more recent data increases the range of the abscissa to $0.54 < \langle r[Y,Z] \rangle < 0.67$ Å and clearly defines a linear relation with no significant outliers. There is reasonable agreement with the trend given by Grice & Ercit (dashed grey line in Figure 2.1), but less agreement with the trend given by Hawthorne *et al.* (solid grey line in Figure 2.1). Least-squares linear regression of all 188 structures results in the curve: $\langle Y,Z\text{-}\Phi \rangle = 0.790(1)\langle r[Y,Z] \rangle + 1.490(8)$ [$R^2 = 0.952(3)$] (dotted grey line in Figure 2.1) with the standard error of estimate, s^*, of 0.003 Å. Note: the results of all regressions are summarized in Table 2.2.

2.2.1.2 Variation in <Z-Φ>

The average $\langle Z\text{-}\Phi \rangle$ values range between ~1.904 to ~1.910 for tourmalines where Z = Al_6, ~1.920-1.945 Å for tourmalines where Z = $(Al,Mg)_6$, and may be > 2 Å in some tourmalines with large (*i.e.*, > 3 *apfu*) amounts of $^{Z}Fe^{3+}$ (*e.g.*, povondraite, Grice & Ercit 1993; Grice *et al.* 1993). Figure 2.2a shows the variation in $\langle Z\text{-}\Phi \rangle$ as a function of the constituent ionic radius of the *Z*-cations,

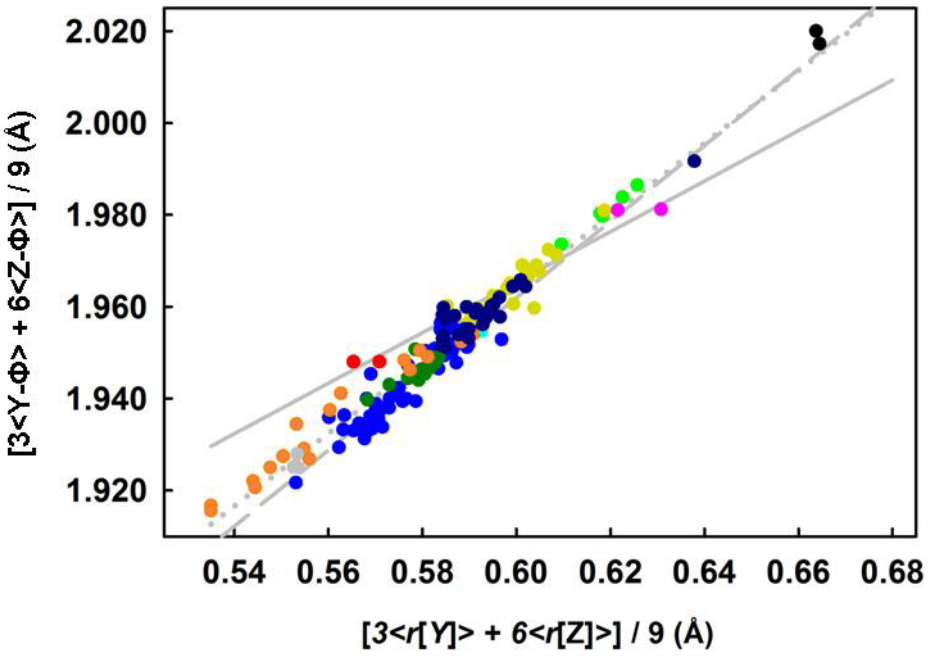

Figure 2.1. Grand mean bondlengths as a function of mean constituent cation radii averaged over the *Y*- and *Z*-octahedra for the 188 tourmaline structures listed in Table 2.1. Data points are coloured by species: buergerite (red); dravite (dark yellow); chromdravite (green); elbaite (blue); uvite/feruvite (pink); foitite (cyan); liddicoatite (dark green); olenite (orange); povondraite (black); rossmanite/oxyrossmanite (grey); schorl/F-schorl/oxy-schorl (dark blue). Grey lines are linear regression curves; dashed line from Grice & Ercit (1993); solid line from Hawthorne *et al.* (1993); dotted line from this work. Note: typical error in ordinate value is 0.002-0.003 Å.

TABLE 2.2 BIVARIATE REGRESSION RESULTS FOR POLYHEDRAL BONDLENGTHS IN TOURMALINES BASED ON 188 STRUCTURES LISTED IN TABLE 2.1.

Dependent (Å)	*Independent* (Å)	*Constant* (Å)	a_o	*R*	*s** (Å)
<*Y,Z*-*Φ*>	<*r*[*Y*,*Z*]>	1.486	0.79(1)	0.974(3)	0.003
<*Y*-*Φ*>	<*r*[*Y*]>	1.61(1)	0.62(2)	0.936(9)	0.009
<*Z*-*Φ*>	<*r*[Z]>	1.50(2)	0.78(3)	0.990(5)	0.005
<*X*-*Φ*>	<*r*[*X*]>	1.39(5)	1.04(4)	0.88(1)	0.011
<*Y*-*Φ*>	$<r[Y]>_{OPT}$	1.54(1)	0.73(2)	0.960(7)	0.003
<*Z*-*Φ*>	$<r[Z]>_{OPT}$	1.46(6)	0.82(1)	0.982(3)	0.003
<*Y*-*Φ*>	<*r*[YΦ_6]>	0.75(4)	1.26(4)	0.936(9)	0.009

*s**, standard error of estimate.

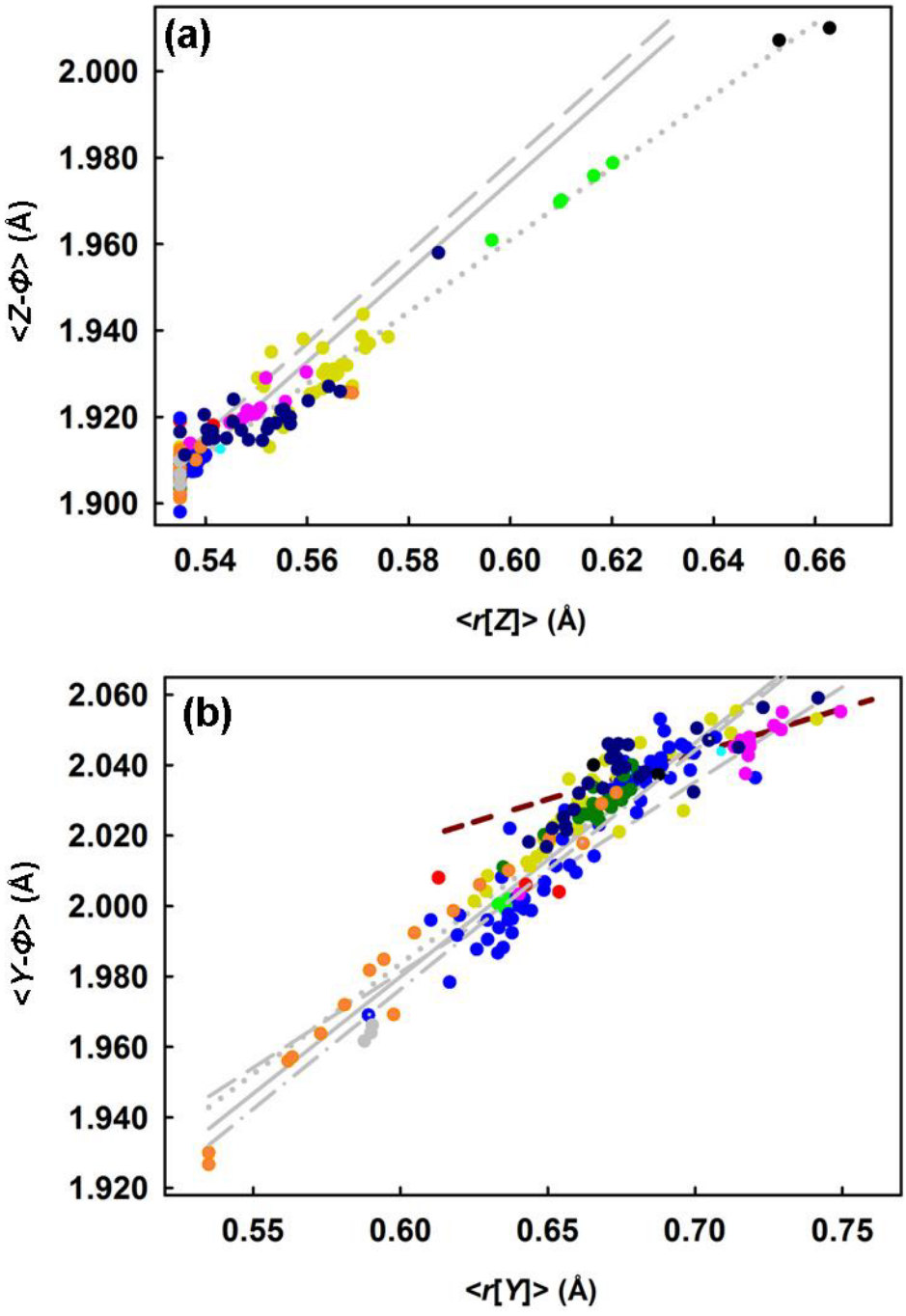

Figure 2.2 Observed bondlength as a function of constituent cation radius for all 188 tourmaline structures shown in Table 2.1: (a) <*Z*-*Φ*> vs. <*r*[*Z*]>; and (b) <*Y*-*Φ*> vs. <*r*[*Y*]>. Dashed red line shows deviation of <*r*[*Y*]> data > 0.67 Å. Symbols and lines as in Figure 2.1; dash-dotted lines; Burns *et al.* (1994). Note: typical error in ordinate value is 0.002-0.003 Å.

<r[Z]>, for the structures given in Table 2.1. Both Hawthorne *et al.* (1993) and Grice & Ercit (1993) give very similar curves for this relation: <Z-Φ> = 1.05<r[Z]> + 1.347 and <Z-Φ> = 1.05<r[Z]> + 1.349, respectively. The curve of Hawthorne *et al.* (1993) (solid grey line) is in slightly better agreement with the current data than is that of Grice & Ercit (1993) (dashed grey line); however neither adequately represent the data with higher values of <r[Z]>. Linear regression on all the current data yields the curve: <Z-Φ> = 0.78(3)<r[Z]> + 1.50(2) [R^2 = 0.980(2)]. It is important to note that the data in Figure 2.2a are not evenly distributed over the observed range of <r[Z]>, and hence the small number of data points at high <r[Z]> are disproportionally significant to the regression calculation.

It should be noted that although Grice & Ercit (1993) refined a povondraite crystal with <r[Z]> ~0.66 Å, the authors chose not to consider it in the determination of their regression curve as it disagreed with the linear trend established by their other data points and also was a less-than-satisfactory refinement. It has been included in the current calculations, as the recent data from dravite-chromdravite tourmaline reported in Bosi *et al.* (2004) fill the gap 0.58 < <r[Z]> < 0.64 Å, and show good linear agreement with the povondraite data.

2.2.2 THE *Y*-SITE

The *Y*-site is surrounded by six anions in an octahedral arrangement; four of these anions are always O^{2-} and the others are O(1) = [F, (OH), O^{2-}] and O(3)

= [O, OH]; three edge-sharing octahedra form a trimer centred on the 3-fold axis. The <*Y*-*Φ*> distance varies within the range 1.96 Å, where *Y* is predominantly occupied by Al (olenite, Ertl *et al.* 1997), and 2.06 Å, where *Y* is predominantly Fe^{2+} (schorl, Grice & Ercit 1993). For each structure in Table 2.1, the *Y*-octahedron is larger than the *Z*-octahedron, and typically shows the more complex site-occupancy (as reflected in the general formula). Each *Y*-octahedron shares two edges with two other *Y*-octahedra and two edges with two Z-octahedra (Figures 1.1 and 1.2).

2.2.2.1 Variation in <Y-Φ>

Burns *et al.* (1994), Grice & Ercit (1993) and Hawthorne *et al.* (1993) each developed a linear relation between the <*Y*-*Φ*> distance and the aggregate *Y*-cation radius. These are shown in Figure 2.2b, along with the 188 data points from structures listed in Table 2.1. The plot shows a linear variation in <*Y*-*Φ*> as a function of <*r*[*Y*]> over the range 0.55 < <*r*[*Y*]> < 0.70 Å, and a deviation from this linear trend at <*r*[*Y*]> > ~0.70 Å. Compared with Figure 2.1, there is significant scatter in the data, making it difficult to determine which of the previously-developed curves is most representative. Linear regression of the current data gives: <*Y*-*Φ*> = 0.62(2)<*r*[*Y*]> + 1.61(1) [R^2 = 0.936(9)]. The standard error of estimate, s*, is 0.009 Å, which is considerably higher than for the other regressions calculated here (Table 2.2).

The O(1)-site is occupied by [(OH), F, O^{2-}], and these anions have different radii [$^{[3]}r$(OH) = 1.34 (Ribbe & Gibbs 1971); $^{[3]}r$(O) = 1.36; and $^{[3]}r$(F) =

1.30 Å Shannon (1976)] that may affect <*Y*-*Φ*>. Figure 2.2b does not account for these differences. Calculating the grand mean constituent ion radius for all ions in the *Y*-site octahedron by:

$$< r_{[Y\varphi_6]} > = [\ [<r[O(1)]> + <r[O(3)]> + 2<r[O(2)]> + 2<r[O(6)]>] + <r[Y]>\ ]/2$$

$$= [\ <r[^{Y}\Phi]> + <r[Y]>\ ] / 2$$

(where *Φ* represents all anions in the *Y*-octahedron) and plotting $< r_{[Y\varphi_6]} >$ against <*Y*-*Φ*> should remove the component of scatter in Figure 2.2b resulting from variation in anion species. This is shown in Figure 2.3a. The amount of scatter is visually comparable to the amount observed in Figure 2.2b, and *s** is 0.009 Å, hence no improvement. Several possibilities may account for this: (1) incorrect determination of ^{W}F-content; (2) inductive strain at the *Y*-octahedron; and (3) incorrect partitioning of cations between the *Y*- and *Z*-sites. With regards to (1) the determination of F in tourmaline by EMPA is relatively straightforward and hence not likely to be the issue. With regards to (2), Bosi & Lucchesi (2007) show that the *Y*-octahedron is subject to progressive extensional strain as a function of Li content. This does not appear to be a significant contributor to the scatter in Figures 2.2b and 2.3a either, as the data points corresponding to the most Li-rich tourmalines (liddicoatite - green dots; uvite - pink dots) do not deviate from the main trend. It seems likely that <*Y*-*Φ*> may be inductively affected by variations at the adjacent *Y*-, *Z*-, and *T*-sites.

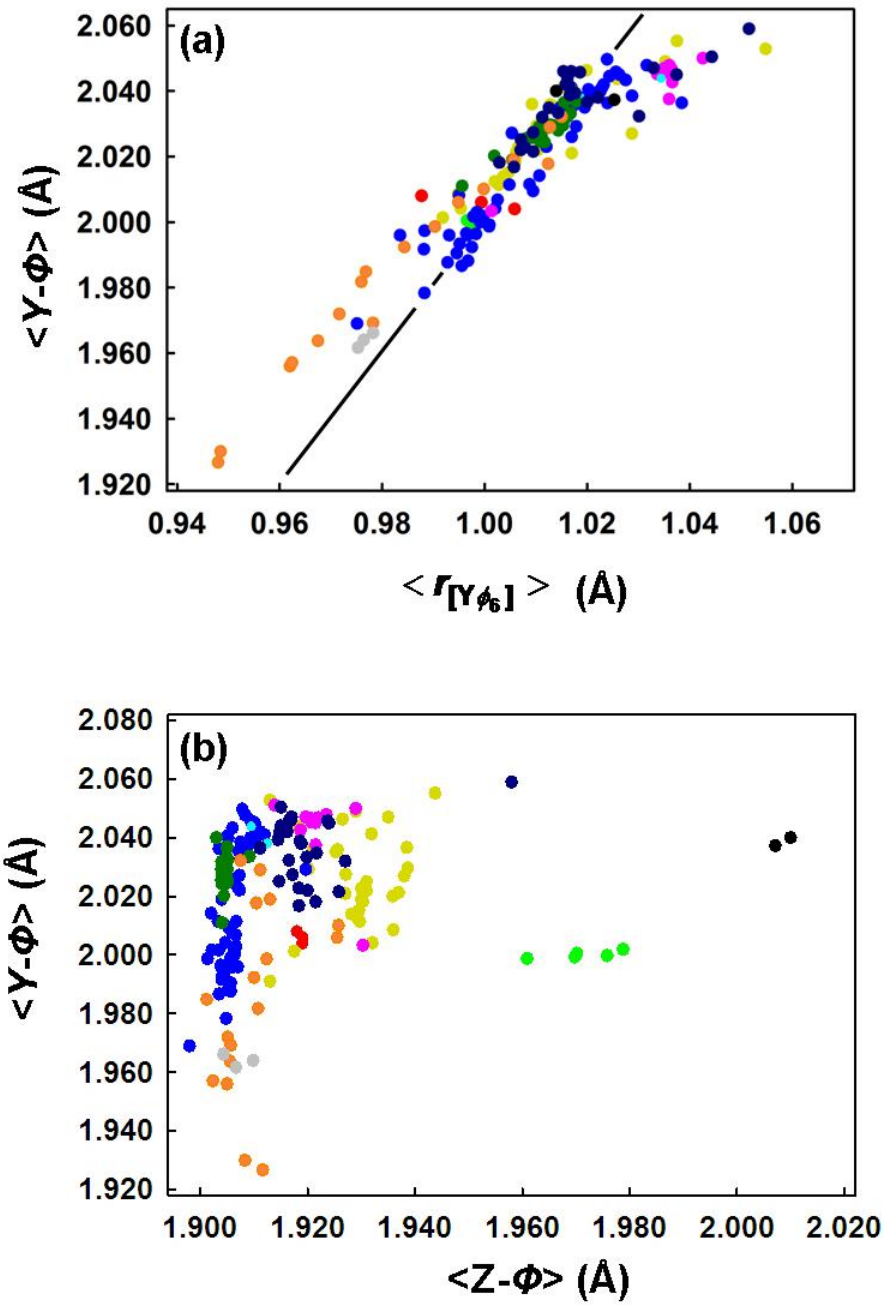

Figure 2.3 Variation in observed <*Y*-*Φ*> as a function of: (a) aggregate ion radii for all constituents of the [$Y\Phi_6$] octahedron; and (b) <Z-*Φ*> for all 188 structures listed in Table 2.1; symbols as in Figure 2.1. Note: typical error in ordinate value is 0.002-0.003 Å; and (c) *Z*-shift *vs.*<*Y*-site charge>.

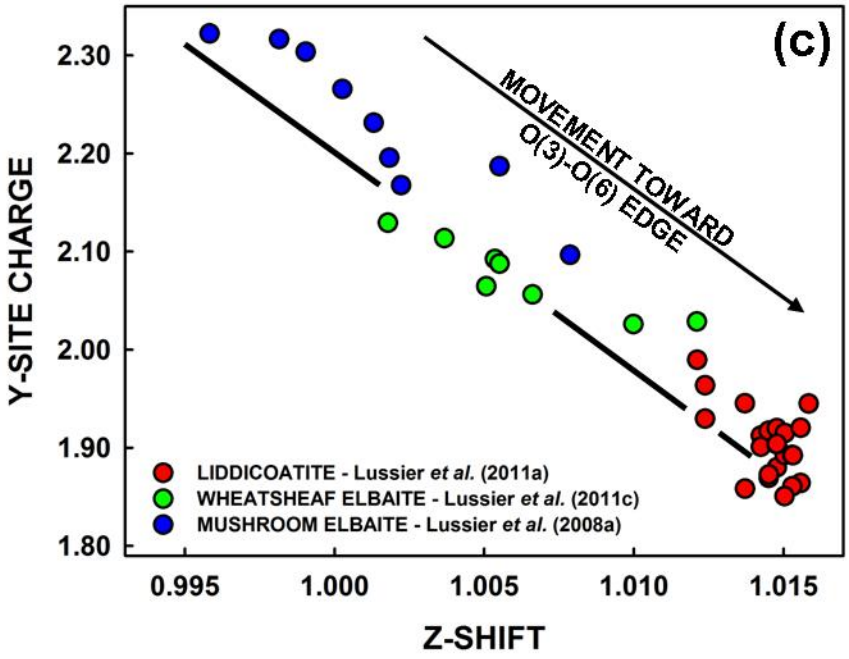

Figure 2.3 (con't)

Figure 2.3b plots <*Y*-*Φ*> *vs*. <*Z*-*Φ*> in order to assess if any obvious inductive relation exists between *Y*- and *Z*-octahedra; however, there is almost no correlation between the two. There is a large amount of data corresponding to tourmalines with Z = Al_6 (elbaite - blue dots; liddicoatite - green dots; olenite - orange dots; rossmanite - grey dots), with <*Z*-*Φ*> values constantly plotting at ~1.905 Å, the expected mean bondlength for full occupancy of *Z* by Al (Bosi & Lucchesi 2007; Bosi 2008), despite a relatively large variation in <*Y*-*Φ*>.

Although <Z-*Φ*> remains constant in these tourmalines with Z = Al_6, there is a change in the geometry of the *Z*-octahedra. Z-cation shift [=(Z-O7D + Z-O7E) / (Z-O3 + Z-O6)]; Foit, 1989) reflects the extent to which the Z-cation moves away from the O(3)-O(6) edge, which is shared by *Y*- and *Z*-octahedra. For the 40 elbaite-liddicoatite (with Z = Al_6 *apfu*) tourmalines of Lussier *et al*. (2008; 2011a,c) (see Chapter 6), Figure 2.3c shows that with increasing aggregate ionic charge at *Y*, the Z-cations shift away from the shared edge; consistent with Bosi & Lucchesi (2007). Hence, the nature of the relation between *Y*- and *Z*-octahedra in tourmaline is not completely reflected in the mean bondlengths.

Hawthorne & Oberti (2007) show that for amphiboles, the significance of inductive effects is large enough to be detectable by stepwise linear regression techniques. However, attempts at identifying significant variables in the tourmalines discussed here by stepwise linear regression were not successful (results not shown), possibly due, in part, to phenomena invisible to the mean bondlengths that were used as independent variables, such as that illustrated in Figure 2.3c.

With regards to (3), comparing linear relations between Figures 2.1 and 2.2 shows that the relation <*Y*,*Z* - O> - <*r*[*Y*,Z]> has much less scatter, suggesting that cations may be incorrectly partitioned between *Y* and *Z* (and perhaps *T*).

2.2.2.2 Cation disorder between Y- and Z-octahedra

More recent studies have shown that in tourmalines such as dravite (Hawthorne *et al.* 1993; Grice & Ercit 1993), chromdravite (Bosi *et al.* 2004), schorl (Bosi 2008), uvite (MacDonald & Hawthorne 1995a), feruvite (Grice & Ercit 1993), Mn-elbaites (Bosi *et al.* 2005a,b), schorl (Bloodaxe *et al.* 1999; Bosi & Lucchesi 2004; Bosi *et al.* 2005b, 2009), and fluor-dravite (Clark *et al.* 2011), cation disorder between the *Y*- and *Z*-octahedra may be significant.

In Figure 2.2b, data points corresponding to <*r*[*Y*]> > 0.70 Å show the most significant disagreement with the linear trends: the dark red dotted line is meant as a guide to the eye and shows the approximate trend defined if only data with <*r*[*Y*]> > 0.67 Å are considered. These larger values of <*r*[*Y*]> also correspond to tourmalines with higher amounts of ^{Y}Mg (*e.g.*, uvites - MacDonald & Hawthorne 1995a; dravites - Grice & Ercit 1993) and Fe^{2+} (Grice & Ercit 1993; Ertl *et al.* 2006) assigned to the *Y*-site. These compositions are potentially those that are the most susceptible to *Y*-*Z* disorder.

Grice & Ercit (1993) developed curves relating [^{Z}Mg/(^{Z}Al+^{Z}Mg)] to cell volume and Fe/(Fe+Mg) to ^{Y}Mg and used these as the basis for making site assignments. MacDonald & Hawthorne (1995a) did not allow Al to disorder

between *Y*- and *Z*-sites in the uvites; they assigned all Al to *Z* (and *T*) and noted very good agreement with the <*Y*-*Φ*> *vs*. <*r*[*Y*]> curve of Grice & Ercit (1993). However, the majority of recent studies account for *Y*-*Z* disorder by using the optimization algorithms of Lavina *et al.* 2002 or Wright *et al.* 2000, with the latter becoming the more-commonly used. The site-occupancies of several of the structures showing the greatest disagreement with the linear trend in Figure 2.2b (MacDonald *et al.* 1993; Hawthorne *et al.* 1993; Grice & Ercit 1993; MacDonald & Hawthorne 1995a; Taylor *et al.* 1995; Cámara *et al.* 2002) were optimized by the OCCQP routine of Wright *et al.* (2000) and results are shown in Appendix A.4.3. The results show a greater degree of cation disordering between the *Y*- and *Z*-sites, as compared to the site-assignments initially made by the authors. For example, optimizing the uvites of MacDonald & Hawthorne (1995a) results in Al at *both Y* and *Z*, with $0.18 < {}^{Y}\mathrm{Al} < 0.68$ *apfu*. Figure 2.4 again shows the curves for <*Y*-*Φ*> *vs*. <*r*[*Y*]> and <*Z*-*Φ*> *vs*. <*r*[*Z*]> using all structures from Table 2.1, but with optimized site assignments for the above-listed structures. Here, the optimized data are in good agreement with the trend established by the non-optimized data, and least-squares regression gives the curves: <*Y*-*Φ*> = 0.73(2)<*r*[*Y*]> + 1.54(1) [R^2 = 0.921(7)] and <*Z*-*Φ*> = 0.82(1)<*r*[*Z*]> + 1.466(6) [R^2 = 0.966(3)], with slightly improved standard errors of estimate of 0.007 and 0.003 Å, respectively. It should be emphasized that it is not the intention of this exercise to suggest that the optimized site occupancies are more accurate than those made by the original authors, merely it shows that the average change in <*r*[*Y*]> and <*r*[*Z*]> corresponding to a disordered model may account for some of the

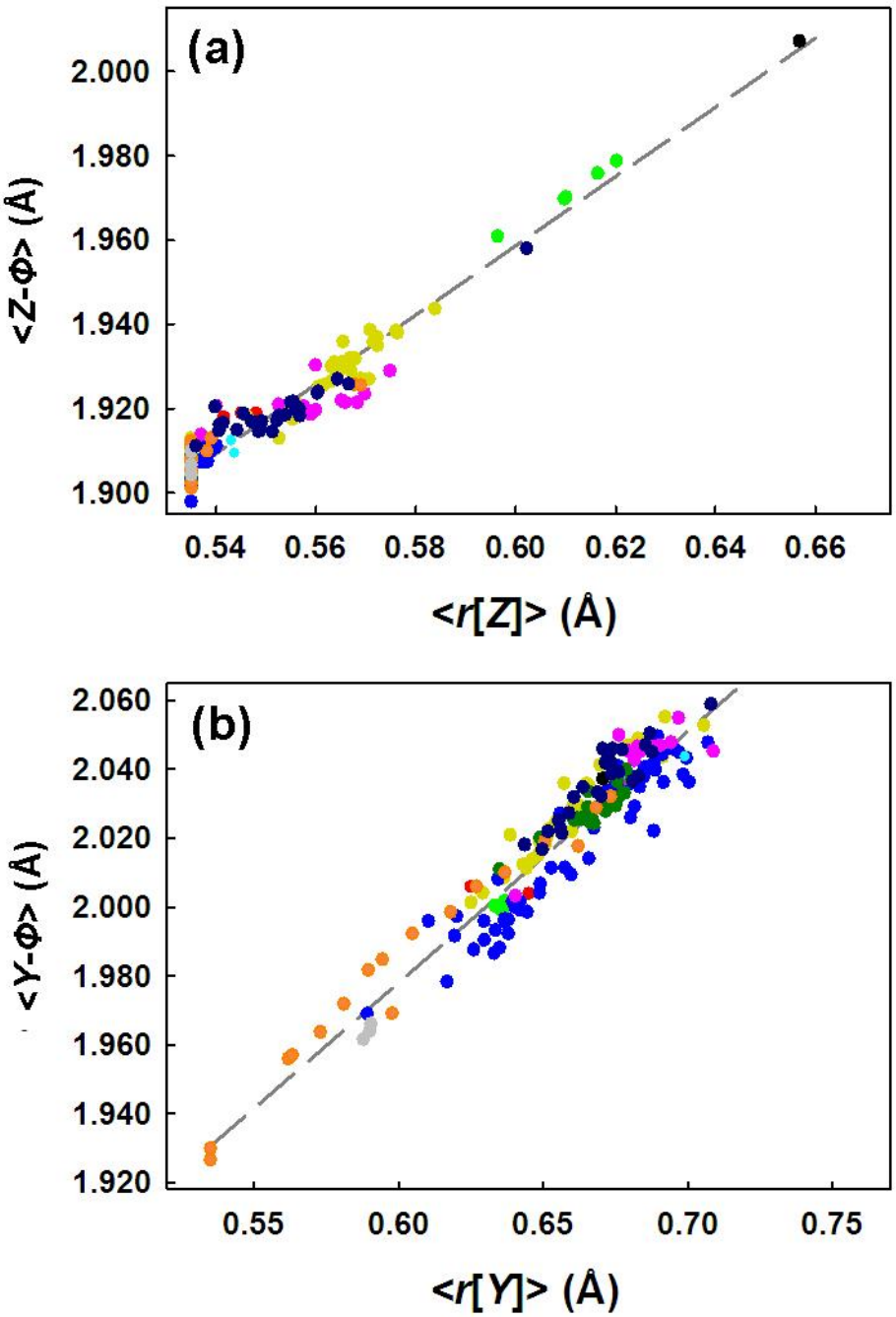

Figure 2.4 Variation in (a) <*Y*-*Φ*> and (b) <*Z*-*Φ*> as a function of constituent ion radii for structures in Table 2.1. For structures with potential *Y*-*Z* disorder (see text for details), site assignments were optimized using OCCQP routine of Wright *et al.* (2000) and used to calculated aggregate radii. Symbols as in Figure 2.1; dashed lines calculated by bivariate linear regression. Note: typical error in ordinate value is 0.002-0.003 Å.

observed disagreement in Figure 2.2b. The OccQP routine relies heavily on optimizing the incident bond valences in the structure, and thus fails to account for any imperfection in the estimate of bond-valence parameters. Furthermore, the occurrence of short-range order in *YYY* trimers, which Taylor *et al*. (1995) show to affect the calculations of *average* incident bond valence sums at O(1), is not accounted for.

2.2.2.3 Y-site vacancies

Burt (1989) initially suggested that vacancies at the *Y*-site in tourmaline may occur *via*: $^{Y}\square + {}^{Y}Al_2 \leftrightarrow {}^{Y}Mg_3$. In more recent studies, *Y*-site vacancies up to 0.27 *pfu* (Ertl *et al*. 2006) have been reported where complete characterization of light elements (by ion-microprobe) has shown deficiencies in species typically assigned to the *Y*-site (*e.g*., Ertl *et al.* 1997, 2003a,b, 2004, 2006a,b; 2007, 2010; Hughes *et al.* 2000, 2004, 2011; Schreyer *et al.* 2002a).

Bosi (2011a) carefully investigated this issue using bond-valence theory and determined that it was possible for octahedral vacancies to occur at the *Y*-site (but less likely at the *Z*-site) in local configurations of $[{}^{Y}R^{3+}\,{}^{Y}R^{3+}\,{}^{Y}\square]$-^{W}(OH) and $[{}^{Z}R^{3+}\,{}^{Z}R^{3+}\,{}^{Y}\square]$-^{V}(OH). However, tourmalines where $^{Y}\square$ is reported typically contain Li, and distinguishing between small amounts of $^{Y}\square$ and Li may be difficult. If Li analysis is not done, it is common practice to calculate its abundance as Li = 3 - $\sum Y$. If Li analysis is done (by ion-microprobe), any observed deficiency at *Y* is assigned to $^{Y}\square$ (*i.e*., $^{Y}\square = 3 - \sum Y$). However, the determination of Li by ion-microprobe may be very sensitive to matrix-effects

related to the presence of Fe and Mn and possibly sample orientation (see Ottolini & Hawthorne 1999; Dyar *et al.* 2001; Ottolini *et al.* 2002) and a closely matrix-matched standard is not always available. Calculating $^{Y}\square$ to fill the *Y*-sites is also sensitive to any mistake in characterizing the Al-disorder between *Y*- and *T*-sites. Hence, the presence of vacancies at the *Y*-site appears to remain controversial.

2.2.3 THE *T*-SITE

The *T*-site is surrounded by four anions, which are always O^{2-}, in a tetrahedral arrangement. The site is occupied predominantly by Si; however, in many tourmalines, the amount of Si is less than 6 *apfu* and it has been shown by SREF and compositional analysis (*e.g.*, Ertl *et al.* 2004, 2005, 2006, 2007; Hughes *et al.* 2000; Lussier *et al.* 2008, 2011b) and ^{11}B and ^{27}Al MAS NMR studies (Tagg et al. 1999; Lussier et al. 2009) that B and Al may also occur. The <*T*-O> distance varies in the range 1.604 Å, where significant $^{[4]}$B occurs (*e.g.*, olenite, Ert *et al.* 2007) to 1.628 Å, where significant $^{[4]}$Al occurs (uvite, MacDonald & Hawthorne 1995a) Å in natural samples, and has a mean value of 1.620 Å where T = Si_6. The *T*-site occupancy remains one of the more difficult aspects of tourmaline crystal chemistry to characterise because B is not often analysed and Al may disorder between *Z*, *Y* and *T*. Also, when B is analysed, the accuracy of analysis is not generally sufficient to detect it, as precision and accuracy are low, and the amount of $^{[4]}$B is a very small fraction of the total B.

2.2.3.1 Variation in <T-O>

The ionic radius for [4]-coordinate Si is 0.26 Å, and the ionic radii for [4]-coordinate Al and B are 0.39 and 0.11 Å, respectively (Shannon 1976), Hence, these differences are sufficiently large that any B ↔ Si *or* Al ↔ Si substitution should be reflected in a predictable decrease and increase in the <*T*-O> distance, respectively.

Foit (1989) reviewed available data from the literature and showed that the <*T*-O> distance in tourmaline increases with increasing $^{[4]}$Al content. However, he found the correlation between <*T*-O> and $^{[4]}$Al to be poor, probably because of inaccurate compositional data for the tourmaline crystals used for structure refinement. MacDonald & Hawthorne (1995a) re-examined this issue by investigating nine uvites where T = $(Si,Al)_6$ and found a linear relation between <*T*-O> and the aggregate cation radius, approximating hard-sphere behaviour.

Figure 2.5a shows the relation for B ↔ Si *or* Al ↔ Si for all tourmalines in Table 2.1 where T = $(Al,Si)_6$ and T = $(B,Si)_6$ (*i.e.*, *not* T = $(B, Al, Si)_6$ or T = Si_6); the black lines represent ideal hard-sphere behaviour. It is clear that the incorporation of: (1) Al at *T* does increase <*T*-O>, and the observed variation shows approximate agreement with hard-sphere predictions; and (2) B at *T* does decrease <*T*-O> , but there is significant scatter in the data.

Figure 2.5b shows the relation between <*T*-O> and <*r*[*T*]> for all tourmalines in Table 2.1. A linear relation is expected, in accord with those observed between <*Y*-*Φ*> *vs*. <*r*[*Y*]> and <*Z*-*Φ*> *vs*. <*r*[*Z*]>. If this relation were reasonably well-established, it would be possible to calculate with structural data,

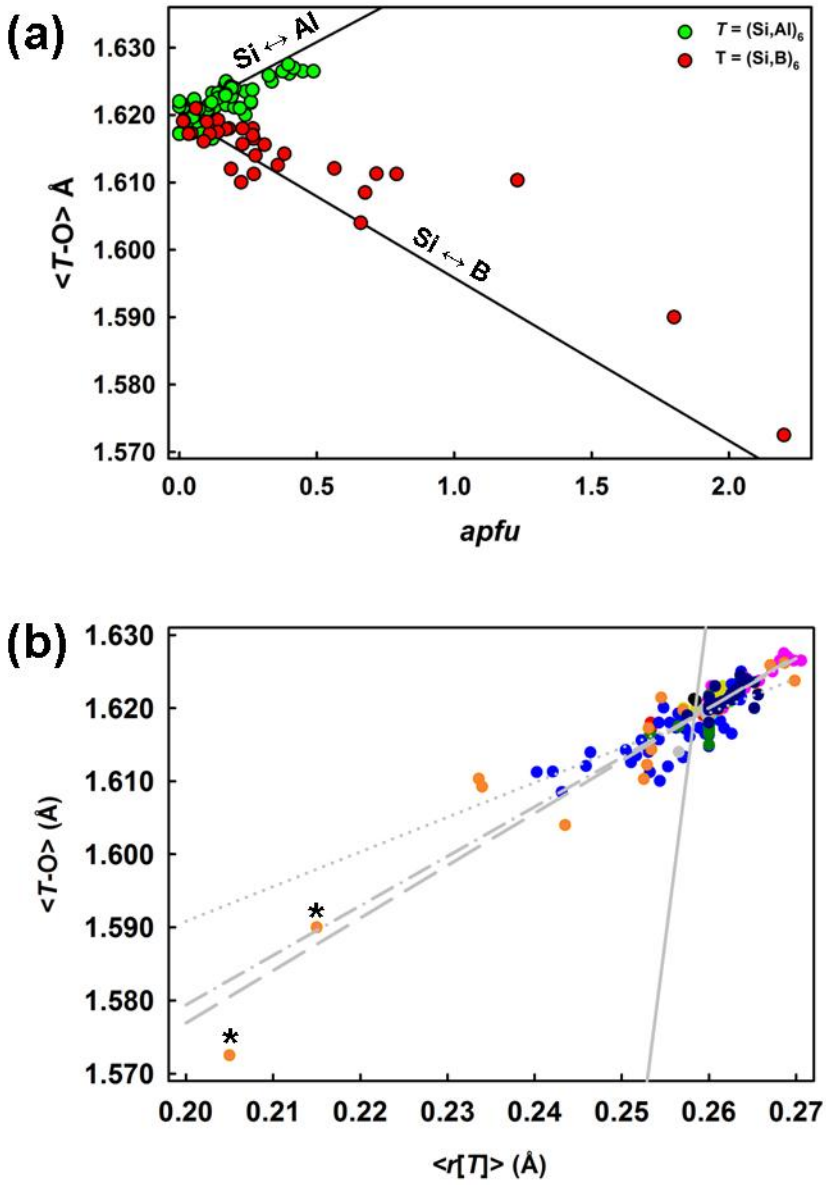

Figure 2.5 Variation in <*T*-O> as a function of (a) [4]B and [4]Al for all structures in Table 2.1 with T = (Al, Si)$_6$ and *T* = (Al,B)$_6$; and (b) aggregate *T*-site cation radius for all 188 structures Table 2.1. Symbols as in Figure 2.1; dotted line – Ertl *et al.* 2006; dashed line – MacDonald & Hawthorne 1995a; solid line – Hughes *et al.* 2004; dash-dot – regression line, this work.(* denote synthetic tourmalines; Marler *et al.* 2002). Note: typical error in ordinate value is 0.002-0.003 Å.

abundances of $^{[4]}$B and $^{[4]}$Al (*e.g.*, Cooper *et al.* 2009). However, Figure 2.5b shows a high degree of scatter in the relation between <*T*-O> and <*r*[*T*]>, indicating that: (1) the relations are not sufficiently well-characterised at the present time; (2) <*T*-O> is highly influenced by inductive effects from variations at other sites; or (3) both. The recent work Bosi & Lucchesi (2007) suggest that (2) is unlikely the problem. These authors show that the configuration of the *entire* tetrahedral ring adjusts to accommodate variation at other parts of the tourmaline structure, either by tetrahedral rotation (Foit 1989), crimping (Gorskaya *et al.* 1982), and ditrigonality (Barton 1969), and that <*T*-O> is *relatively* unaffected. In fact, in 127 different tourmaline structures, Bosi & Lucchesi (2007) showed that the tetrahedra remain nearly holosymmetric, with quadratic distortions (Robinson *et al.* 1971) varying only slightly ($1.0005 < \lambda_T < 1.0050$) and mostly as a function of the aggregate charge of *X*-site cations.

2.2.3.2 Fe^{3+} and the T-site

Mössbauer spectra of tourmaline have been shown to include Fe^{3+} doublets with very low isomer shift (δ) values of ~0.2 mm/s, which are in a range typically assigned to [4]-coordinate Fe^{3+}. On this basis, Dyar *et al.* (1998) and Ertl *et al.* (2004) assigned Fe^{3+} at the *T*-site. Andreozzi *et al.* (2008) examined this issue in detail and concluded that the low-δ Fe^{3+} doublet could not correspond to $^{[4]}Fe^{3+}$ as there were no commensurate changes in the observed <*T*-O> distance. Instead, the authors concluded that the low-δ doublets correspond to $^{Y}Fe^{3+}$.

Thus, to date, there is no conclusive evidence for the presence of Fe^{3+} at the *T*-site in tourmaline.

2.2.4 THE *X*-SITE

The *X*-site is surrounded by nine anions, which are always O^{2-}. (Figure 1.2). The <*X*-O> distance is in the range 2.625 Å (liddicoatite – Lussier *et al.* 2011) to 2.771 Å (elbaite – Lussier *et al.* 2008) and SREF shows this site to be occupied predominantly by □ (vacancy), Na and Ca with (occasionally) small amounts of K and (rarely) Pb. Grice & Ercit 1993 refined a povondraite sample with K = 0.26 *apfu*, proving that the dimensions of the *X*-site are sufficiently flexible to allow the incorporation of significant amounts of larger cations, although the authors report a <*X*-O> distance of only 2.74(1) Å.

2.2.4.1 Variation in <X-O>

Foit & Rosenberg (1979) note that no observable trend exists between observed <*X*-O> and the effective ionic radius of *X*-site constituents; however, the data available to them at the time were very limited. Grice & Ercit (1993) show that for 12 tourmaline crystals of different compositions, there is a clear increase in <*X*-O> as a function of <*r*[*X*]>, and they suggest that the relatively high degree of scatter is likely due to the fact that the effect of ^{X}□ on <*r*[*X*]> cannot be accounted for. Several studies have noted a positive correlation between <*X*-O> and the abundance of ^{X}□ (Foit 1989; Bosi *et al.* 2005a,b). Figure 2.6a plots the variation in <*X*-O> with ^{X}□ *pfu* for all structures in Table 2.1;

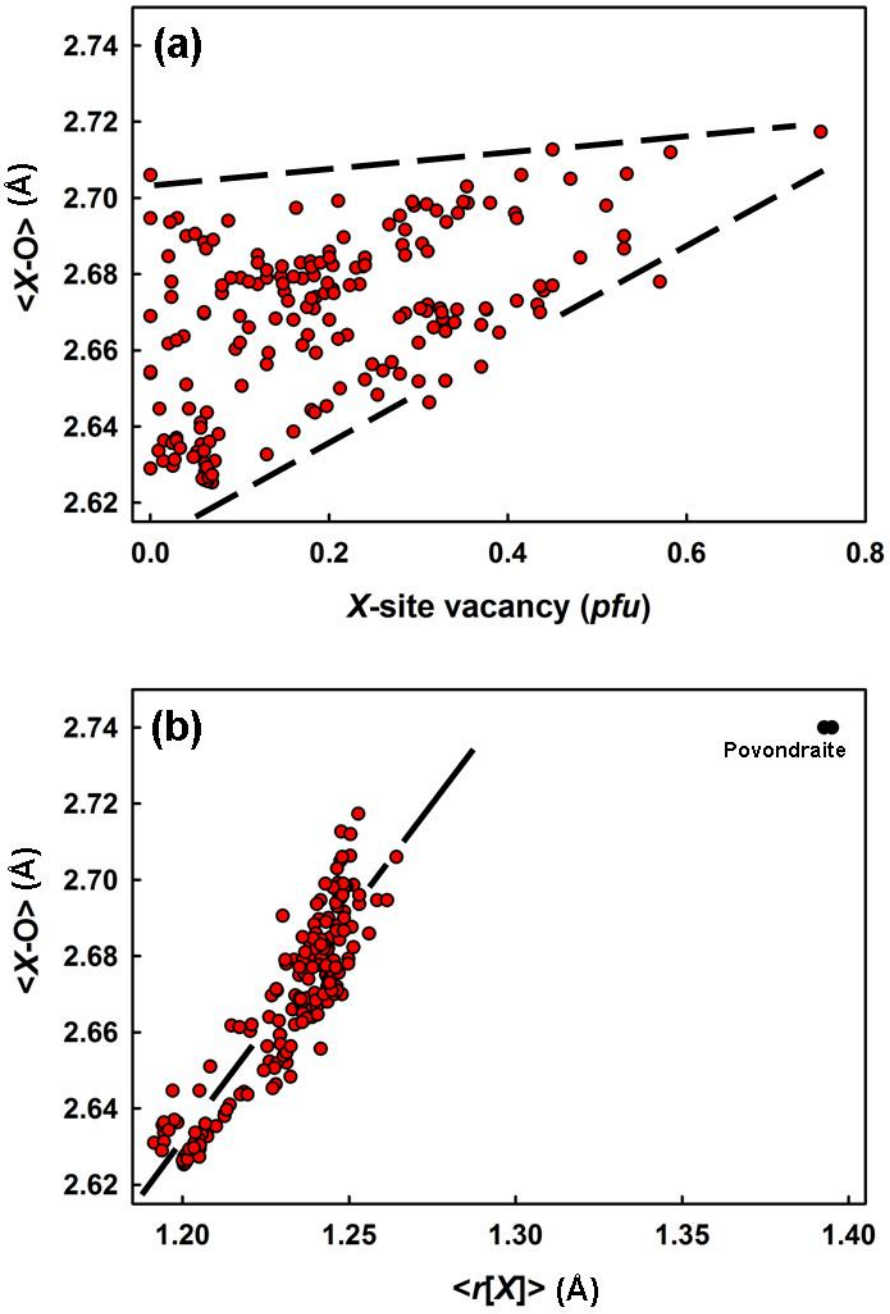

Figure 2.6 Variation in observed <*X*-O> for all structures listed in Table 2.1 plotted as a function of: (a) *X*-site vacancy; dashed lines drawn as guides to the eye; and (b) aggregate *X*-site cation radius, calculated with $r[^{X}\square]$ = 1.26 Å. Note: typical error in ordinate value is 0.002-0.003 Å.

despite significant scatter, there is a general tendency for <*X*-O> to increase with $^{X}\square$ *pfu*.

In accord with the linear relations observed between mean bondlength and aggregate constituent radius at other sites, a linear relation between <*X*-O> and <*r*[*X*]> might be expected if the average size of $^{X}\square$ were *relatively* consistent between tourmalines. There are sufficient amounts of high-quality data currently available to test this.

Using the ionic radii of Shannon (1976), the aggregate cation radius at the *X*-site is given by:

$$\langle r[X]\rangle = {}^{[9]}r[\mathrm{Ca}]a_{\mathrm{Ca}} + {}^{[9]}r[\mathrm{Na}]a_{\mathrm{Na}} + r[{}^{X}\square]a_{\square} + {}^{[9]}r[\mathrm{K}]a_{\mathrm{K}}$$

$$= 1.18a_{\mathrm{Ca}} + 1.24a_{\mathrm{Na}} + r[{}^{X}\square]a_{\square} + 1.55a_{K}.$$

Presuming the relation between <*X*-O> and <*r*[*X*]> is reasonably linear, a value of $r[^{X}\square]$ could be approximated by iteration until the relation between <*r*[*X*]> and <*X*-O> becomes linear, and the coefficient of determination (R^2) for the <*r*[*X*]>-<*X*-O> linear regression, is maximized.

For all the structures in Table 2.1, this maximal linearity occurs with $r[^{X}\square]$ = ~1.26 ± 0.02 Å and R^2 = 0.79 (Figure 2.6b). The K-povondraite crystals of Grice & Ercit (1993) and Grice *et al*. (1993) fall off this linear trend; hence they were not included in the calculations. The '*radius*' of $^{X}\square$ is greater than of the other dominant *X*-site constituents in tourmaline, in agreement with the positive effect of $^{X}\square$ on <*X*-O> previously noted by the other authors. When the X-site is vacant, anions normally bonded to an X-site cation must move closer to the *Y*-, *Z*-, *T*- and *B*-site cations in order to compensate for the lack of bond valence

normally received from the X-site cation. Hence, the *X*-site may also be compatible with linear models, and the presence of vacancy at *X* has a similar *average* effect on all tourmalines. However, Bosi & Lucchesi (2007) show a greater range of strain (from ~0.1 to 0.5 Å) observed in the *X*-site than at any other cation site in tourmaline, and hence $r[^{X}\square]$ = ~1.26 ± 0.02 Å can *at best* be considered as a loosely constrained average.

2.2.5 THE *B*-SITE

The *B*-site is surrounded by three anions (which are always O^{2-}) in a triangular arrangement (Figure 1.1) with a <*B*-O> distance of ~1.37 Å. Observed *X*-ray scattering and the lack of significant variation in the mean bondlength indicate that this site is occupied predominantly-to-completely by B (*i.e.*, B_3 *apfu*). To date, no tourmaline crystal with B < 3 *apfu* has been documented, although Hawthorne (1996) suggested what must happen in the structure if B were < 3 *apfu*: the coordinating O(2) and O(8) anions would have to become protonated (*i.e.*, by the mechanism $^{B}B + ^{H(2)}\square + ^{H(8)}\square_2 \leftrightarrow ^{B}\square + ^{H(2)}H + ^{H(8)}H_2$), to satisfy bond-valence requirements of the anions.

2.2.6 THE O(1)-SITE

The O(1)-site is located on the 3-fold axis passing though the origin of the unit cell, and is surrounded by three *Y*-sites (Figures 1.1 and 1.2), such that the *Y*-O(1) bonds are crystallographically (*i.e.*, long-range) equivalent. The O(1)-site is usually occupied by (OH), but may also be occupied by F (*e.g.*, fluor-uvite and fluor-liddicoatite) and O^{2-} (*e.g.*, olenite and povondraite)

2.2.6.1 The occurrence of F at O(1)

Grice & Ercit (1993) showed by bond-valence arguments that F orders at the O(1)-site in a wide variety of tourmaline structures, and MacDonald & Hawthorne (1995a) showed by direct site-scattering refinement that F orders at the O(1)-site in a series of nine uvites. Further, no published chemical analysis of any tourmalines shows F > 1 *apfu*, which would stoichiometrically force it to occur elsewhere in the structure. Thus, it seems well-established that F orders exclusively at the O(1)-site in tourmaline.

It has been suggested (Robert *et al.* 1997; Henry & Dutrow 2011) that crystal-chemical factors impose certain constraints on the F-content of tourmaline. A recent study by Henry & Dutrow (2011) examined >8800 F-bearing tourmalines (harvested from the literature) originating from diverse petrologic environments and suggest that both crystal-chemical and petrogenetic factors influence the F-content. They show that a threshold F-content correlates with the aggregate charge of the *Y*-site and the aggregate charge (and chemistry) of the *X*-site (see Figure 8.1). However, the exact crystal-chemical mechanism(s)

responsible for controlling F abundance remain(s) poorly understood. Henry & Dutrow (2011) also show that local petrogenetic factors may also influence the abundance of F in tourmaline; this will be discussed in greater detail in Section 8.2.1.

2.2.7 THE O(3)-SITE

The O(3)-site is coordinated by two *Z*-site cations and one *Y*-site cation (Figures 1.1 and 1.2). In most tourmaline species, the O(3)-site is occupied by $(OH)^-$, and the sum of the incident bond-valences is close to 1.1 *vu* if the associated H atom is excluded (*e.g.*, Grice & Ercit 1993; Lussier et al. 2011a). As given in the ideal end-member formulae of Henry *et al.* (2011), the O(3)-site may also be occupied by O^{2-} in species such as buergerite (Tippe & Hamilton 1971), povondraite (Grice & Ercit 1993), oxy-rossmanite (Ertl *et al.* 2005), olenite (Cempírek *et al.* 2006).

2.3 IMPLICATIONS OF SHORT-RANGE ORDER AROUND THE O(1)-SITE

It is established that the O(1)-site can be (at least) partly occupied by O^{2-} (*e.g.*, Grice & Ercit 1993; Taylor *et al.* 1995). This has important implications concerning several aspects of tourmaline structure and composition: (1) calculation of the chemical formula; (2) bond-valence requirements at the O(1)-site; and (3) short-range order around the O(1)-site. A discussion of (1) is beyond the scope of this review and readers are instead referred to discussions in Clark

(2002, 2007) and Henry *et al.* (2011). Points (2) and (3) are key to our understanding of the crystal chemistry of tourmaline, and are thus considered in more detail.

2.3.1 Bond-valence requirements at the O(1)-site

The valence-sum rule (Brown 1981) requires that the sum of the bond-valences incident at the O(1)-site match the formal valence of the anion(s) at O(1). Thus in those *short-range* configurations that have O^{2-} at O(1), the sum of the bond valences incident at O(1) must be ~2 *vu*; in those short-range configurations that have (OH) or F at O(1), the sum of the incident bond-valences at O(1) must be ~1 *vu*. Taylor *et al.* (1995) first showed this to be important in a (OH)-deficient uvite where bond-valence calculations showed that $^{W}O^{2-}$ and $^{O(1)}$(OH) had to be locally bonded to clusters of ^{Y}[AlAlMg] and ^{Y}[MgMgMg], respectively. Subsequently, the ability of the formal charge at the O(1)-site to drive short-range order in locally-bonded [*YYY*] clusters has been shown to be of significant importance in controlling the structural stability of tourmalines (Bosi & Lucchesi 2007) and is discussed below.

2.3.2 The stability of short-range clusters

Using the bond-valence curves of Brown & Altermatt (1985), the bondlengths corresponding to any particular arrangement of bond valences may be calculated to check whether or not the resulting bondlengths fall within the range observed for that specific cation-anion pair. In this way, the relative

stability, and thus probability of occurrence, of all short range [*YYY*] clusters incident to a particular anion at O(1) may be assessed. This was initially done for tourmalines with *Y*-sites dominated by Al-Mg-Li (Hawthorne 2002). Bosi (2011) re-examined the stability of Mg-Al clusters and quantified cluster stability based on the discrepancy between bondlengths calculated by the bond valence method and by ionic radii given in Shannon (1976). As these results are in good agreement with Hawthorne (1996), he uses the same approach to assess the stability of $^{Y}Fe^{2+}$-$^{Y}Fe^{3+}$ analogues. The results of these two studies are summarized in Table 2.3 and show that in general, the most stable short range cluster types have the forms: $^{Y}[R^{3+}R^{3+}R^{3+}]$ - $^{W}O^{2-}$, $^{Y}[R^{3+}R^{3+}R^{2+}]$ - $^{W}O^{2-}$, $^{Y}[R^{2+}R^{2+}R^{2+}]$ - $^{W}(OH, F)^{-}$ and $^{Y}[R^{2+}R^{2+}R^{3+}]$ - $^{W}(OH, F)^{-}$

2.3.3 O^{2-} at the W-site: a cause of Y-Z disorder in tourmaline

Significant disorder may occur between the *Y*- and *Z*-octahedra in tourmalines *via* the mechanism

$$2^{Y}R^{2+} + {}^{Z}R^{3+} + {}^{W}(OH)^{-} \leftrightarrow 2^{Y}R^{3+} + {}^{Z}R^{2+} + {}^{W}O^{2-}$$

which Bosi (2011b) shows to be a valid generalization of the substitution $2^{Y}Mg + {}^{Z}Al + OH \leftrightarrow 2^{Y}Al + {}^{Z}Mg + O^{2-}$, originally given by Hawthorne (1996). This type of substitution mechanism has been shown to drive the disordering of heterovalent ion couples between the *Y- and Z*-sites in tourmaline, including; Al-Mg (Hawthorne *et al.* 1993; Bosi *et al.* 2004; Bosi *et al.* 2010), Fe^{2+}-Fe^{3+} (Bosi 2008; Andreozzi *et al.* 2008; Bosi *et al.* 2005, 2010), Al-Mn^{2+} (Bosi *et al.* 2005), and Cr^{3+}-Mg (Bosi *et al.* 2004). The operation of this mechanism has the overall effect

of minimizing the difference between <*Y*-*Φ*> and <*Z*-*Φ*>, which promotes a better fit between the *Y*- and *Z*-octahedra. Bosi & Lucchesi (2007) showed that the tourmaline structure may exert limits on its composition by constraining the size difference between <*Y*-*Φ*> and <*Z*-*Φ*> to < 0.15 Å, as this is the maximum size difference they observed.

2.4 SHORT-RANGE ORDER AROUND THE O(3)-SITE

The compositional constraints on short range clusters local to the O(3)-site (*i.e.*, ZZY) resulting from local bond-valence requirements have also been assessed using the analogous method presented above for the [*YYY*]-*W* clusters (Hawthorne 1996; Bosi 2011). Table 2.3 presents a summary of stable clusters. In general, the occurrence of (OH) at the *V*-site is far less compositionally restrictive, with all possible combinations of Li-Al-Mg and Fe^{2+}-Fe^{3+} being possible, with the exception of ${}^{Y}Li\,{}^{Z}[MgMg] - {}^{V}(OH)$. Conversely, the occurrence of O^{2-} at the *V*-site can *only* be associated with clusters of the type: ${}^{Y}R^{2+}\,{}^{Z}[R^{3+}R^{3+}] - {}^{V}O^{2-}$ (and ${}^{Y}R^{3+}\,{}^{Z}[R^{2+}R^{3+}] - {}^{V}O^{2-}$) and ${}^{Y}R^{3+}\,{}^{Z}[R^{3+}R^{3+}] - {}^{V}O^{2-}$. which may account for why $V = O^{2-}$ is relatively rarely observed in natural tourmalines.

TABLE 2.3 STABILITY OF SHORT RANGE CLUSTERS LOCAL TO O(1)- AND O(3)-SITES IN TOURMALINE; COMPILED FROM HAWTHORNE (2002) AND BOSI (2011b).

YYY		O(1)	Stable?
MgMgMg	$Fe^{2+}Fe^{2+}Fe^{2+}$	F, (OH)	Yes
AlAlAl	$Fe^{3+}Fe^{3+}Fe^{3+}$	F, (OH)	No
MgMgAl	$Fe^{2+}Fe^{2+}Fe^{3+}$	F, (OH)	Yes
AlAlMg	$Fe^{2+}Fe^{3+}Fe^{3+}$	F, (OH)	No
LiLiLi	---	F, (OH)	No
AlAlLi	---	F, (OH)	Yes
AlLiLi	---	F, (OH)	Yes
MgMgMg	$Fe^{2+}Fe^{2+}Fe^{2+}$	O^{2-}	No
AlAlAl	$Fe^{3+}Fe^{3+}Fe^{3+}$	O^{2-}	Yes
MgMgAl	$Fe^{2+}Fe^{2+}Fe^{3+}$	O^{2-}	No
AlAlMg	$Fe^{2+}Fe^{3+}Fe^{3+}$	O^{2-}	Yes
LiLiLi	---	O^{2-}	No
AlAlLi	---	O^{2-}	No
AlLiLi	---	O^{2-}	No
Y + [ZZ]		O(3)	Stable?
Li + [AlAl]	---	F, (OH)	No
Mg + [AlAl]	Fe^{2+} + $[Fe^{3+}Fe^{3+}]$	F, (OH)	Yes
Al + [AlAl]	Fe^{3+} + $[Fe^{3+}Fe^{3+}]$	F, (OH)	Yes
Al + [MgAl]	Fe^{3+} + $[Fe^{2+}Fe^{3+}]$	F, (OH)	Yes
Al + [MgMg]	Fe^{3+} + $[Fe^{2+}Fe^{2+}]$	F, (OH)	Yes
Mg + [MgAl]	Fe^{2+} + $[Fe^{2+}Fe^{3+}]$	F, (OH)	Yes
Li + [MgAl]	---	F, (OH)	Yes
Li + [MgMg]	---	F, (OH)	No
Li + [AlAl]	---	O^{2-}	No
Mg + [AlAl]	Fe^{2+} + $[Fe^{3+}Fe^{3+}]$	O^{2-}	No
Al + [AlAl]	Fe^{3+} + $[Fe^{3+}Fe^{3+}]$	O^{2-}	Yes
Al + [MgAl]	Fe^{3+} + $[Fe^{2+}Fe^{3+}]$	O^{2-}	No

CHAPTER 3

PHYSICAL DESCRIPTIONS OF TOURMALINE SAMPLES OF THIS WORK

3.1 INTRODUCTION

Over 50 different tourmalines samples were used in this work, and five of these were characterised in significant detail. Samples were selected for intensive study if they displayed unusual and/or complex morphological features, had rare compositions, or showed complex colour variations. The physical characteristics and geological provenances of these samples are described next.

3.2 OSCILLATORY ZONED LIDDICOATITE FROM THE ANJANABONOINA PEGMATITE, MADAGASCAR

3.2.1 Sample description

The liddicoatite specimen used here is a ~5 mm thick crystal slice (Figure 3.1), cut perpendicular to the *c*-axis through a much larger crystal (the dimensions of which are unknown). A drawing of a typical oscillatory zoned crystal of fluor-liddicoatite is shown in Figure 3.2, together with the approximate position of the slice used in the present work; the details in this drawing are composite from a large number of images of crystals given by Benesch (2000).

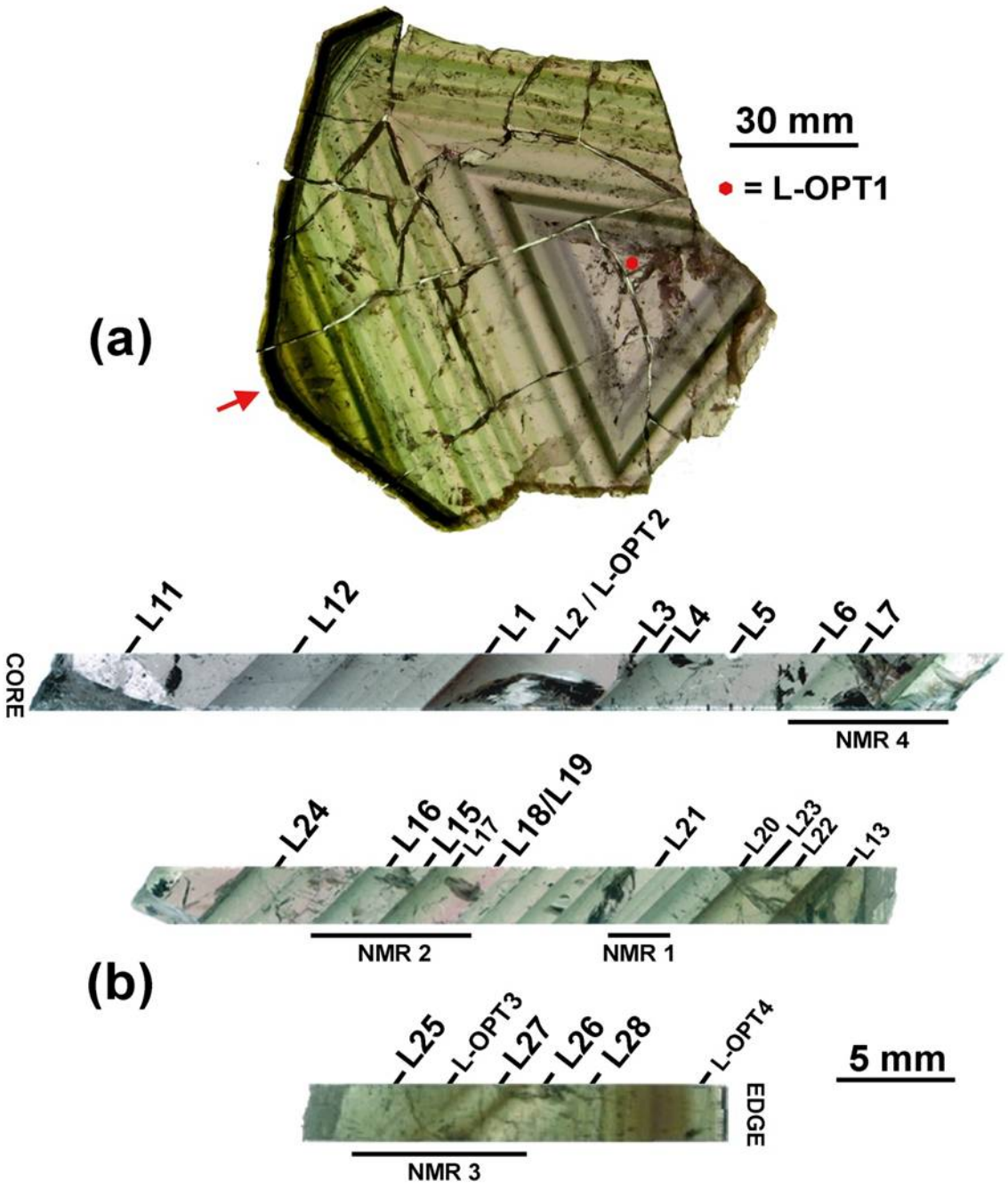

Figure 3.1 The liddicoatite crystal investigated in this work: (a) slice perpendicular to the *c*-axis showing oscillatory colour zoning; (b) a thin strip of material extracted at the location indicated by the red arrow in (a), polished and photographed is transmitted light. L*X*, L-OPT*X*, and NMR*X* labels correspond to locations where material was removed for single-crystal, X-ray diffraction/electron microprobe, optical, and MAS NMR spectroscopy analysis, respectively.

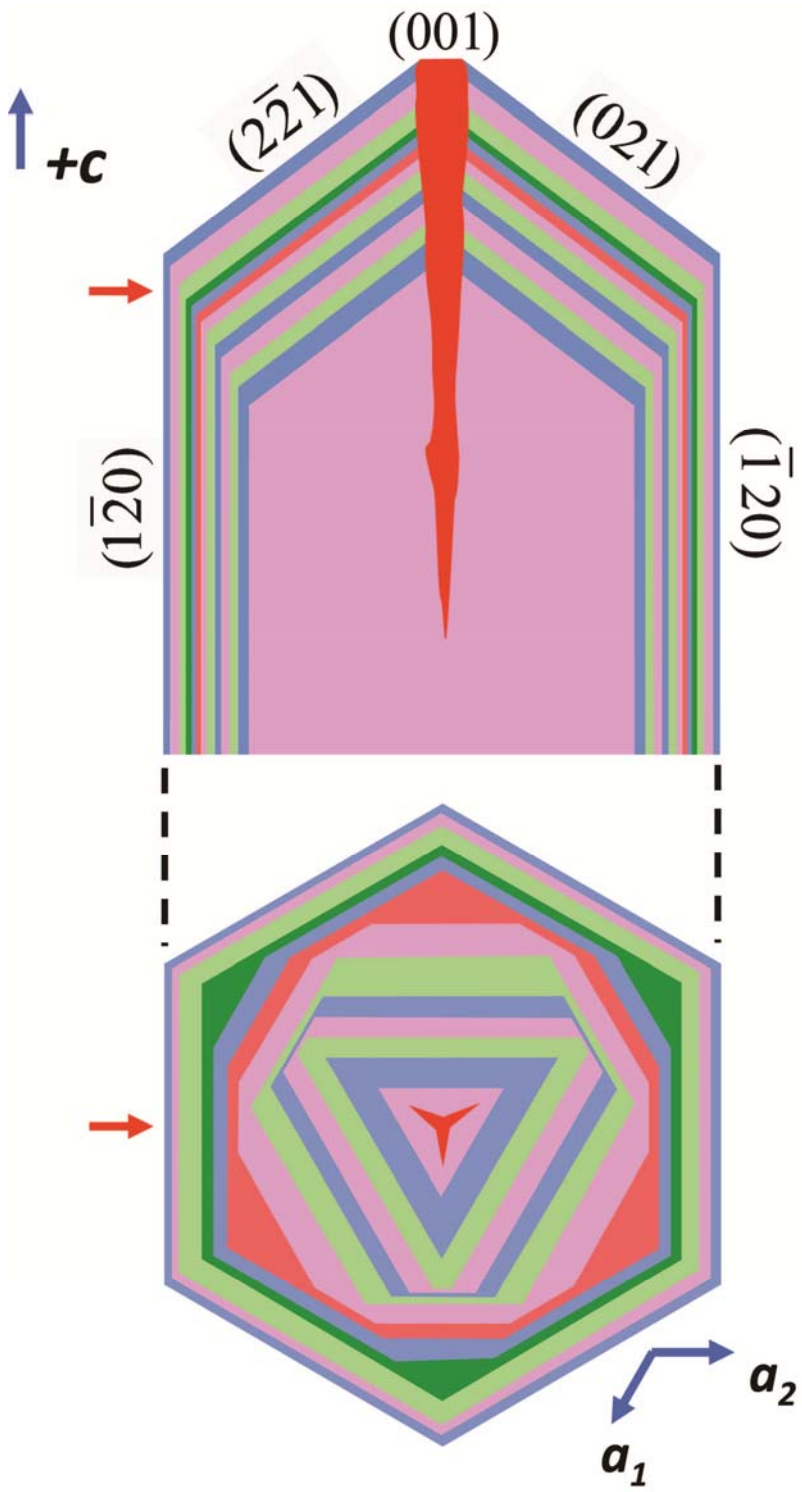

Figure 3.2 A drawing of a crystal of oscillatory-zoned fluor-liddicoatite sliced in (a) (100) and (b) (001) orientations. The measured crystallographic orientation is given. The red arrows denote the line of intersection between the two images as well as the approximate position where the (001) slice (Figure 3.1), on which the current work was done, was removed.

The liddicoatite slice examined here shows strong sector zoning on (001), {201} and {110}, and exhibits three types of oscillatory zones: (1) at the centre of the (001) slice is a small fairly (optically and compositionally) uniform zone that corresponds to growth on the (001) surface parallel to the +*c*-direction; (2) toward the crystal centre, zones are relatively thick (> 0.5 mm), are trigonal pyramidal in form, and the pyramid apices are directed along the +*c* direction; these zones may or may not show diffuse colour intensity across each zone; (3) toward the crystal edge, zones are typically narrower (<0.5 mm) and are prismatic parallel to {110}. The crystallographic details were derived by removing oriented fragments from the slice and determining their orientation on a *P*4 single-crystal X-ray diffractometer (see Chapter 4).

Within the (001) and {201} zones, there are four major colour regions (from core to edge): (1) purple (~5 cm wide); (2) pale green (~5 cm wide), (3) dark green (~2 cm wide), and (4) dark green-black (~0.7 cm wide). Each of these regions is divided into a number of smaller zones (Figure 3.1) which are distinguished by the oscillatory repetition of diffuse colour variation, and are bordered by sharp, grayish-green-to-black boundaries, each of which is inclined at ~45° to the (001) plane. Near the crystal edge, the sample is dark green-to-black; the form of the zones is prismatic, they have sharp boundaries and are <1 mm wide.

3.2.2 Provenance

The pegmatites of Central Madagascar were emplaced about 490 million years ago during late-stage granitic plutonism related to the Pan-African event, which occurred from 570 to 455 million years ago (Paquette & Nédélec 1998). These pegmatites are hosted by gneisses, marbles and quartzites of the Itremo Group, which overlies the crystalline basement of the Mozambique Orogenic Belt (Malisa & Muhongo 1990, Ashwal & Tucker 1999, Dissanayake & Chandrajith 1999, Collins & Windley 2002, Dirlam *et al.* 2002).

Although the crystal examined here is known to be from Central Madagascar, its exact locality is not known; however, the Anjanabonoina Pegmatite, located about 55 km west-southwest of the city of Antsirabe in Antannanarivo Province, is famous for producing such crystals. In support of this provenance, the tourmaline section examined here (Figure 3.1) bears a very strong resemblance to the tourmaline from Anjanabonoina illustrated in Lacroix (1922, Figure 329). According to the classification scheme of Černý (1982), this pegmatite is intermediate between the LCT and NYF families of the rare-element and miarolitic classes. The Anjanabonoina pegmatite is enriched in Na and Li, and has pronounced structural and mineralogical internal zoning; it contains large miarolitic cavities, up to ~5 m in dimension, heavily kaolinized by the action of late-stage hydrothermal fluids and consisting of assemblages of quartz, feldspar, beryl, hambergite, danburite, phenakite and scapolite. Pezzotta (1996) reported the most geologically significant characteristics of the Anjanabonoina deposit to be (1) extremely high content of B, resulting in an abundance of tourmaline and

primary danburite, and (2) the widespread presence of Ca, leading to the abundance of liddicoatite, danburite and diopside.

3.3 MUSHROOM AND WHEATSHEAF TOURMALINES FROM MOGOK, MYANMAR

3.3.1 Mushroom tourmaline: sample description

Mushroom tourmalines consist of acicular crystals that radiate from a blocky base, giving the overall appearance of a mushroom (Figure 3.3). Two samples of mushroom tourmaline, referred to as SHM and SHP, were investigated; both having similar morphologic characteristics, but differing significantly in colour. In hand specimen, SHM (Figure 3.3a) consists of a black base (a single crystal) that grades into a greyish-white aggregate of sub-parallel acicular crystals, bounded by a thin band of black acicular tourmaline that is mantled by a thick cap of aggregates of fibrous, pink acicular crystals. SHP (Figure 3.3b) consists of a blackish-purple base that grades into a dark-purple aggregate of sub-parallel acicular crystals, bounded by a thin band of black acicular tourmaline that is mantled by aggregates of fibrous, dark-purple acicular crystals.

Thick sections cut through the centres of the SHM and SHP mushrooms (Figure 3.4) in the *c*-direction show that each sample has three morphologically distinct regions. The first region consists of an optically continuous base formed from a single crystal. In reflected light (Figure 3.4a, f), the base grades from black

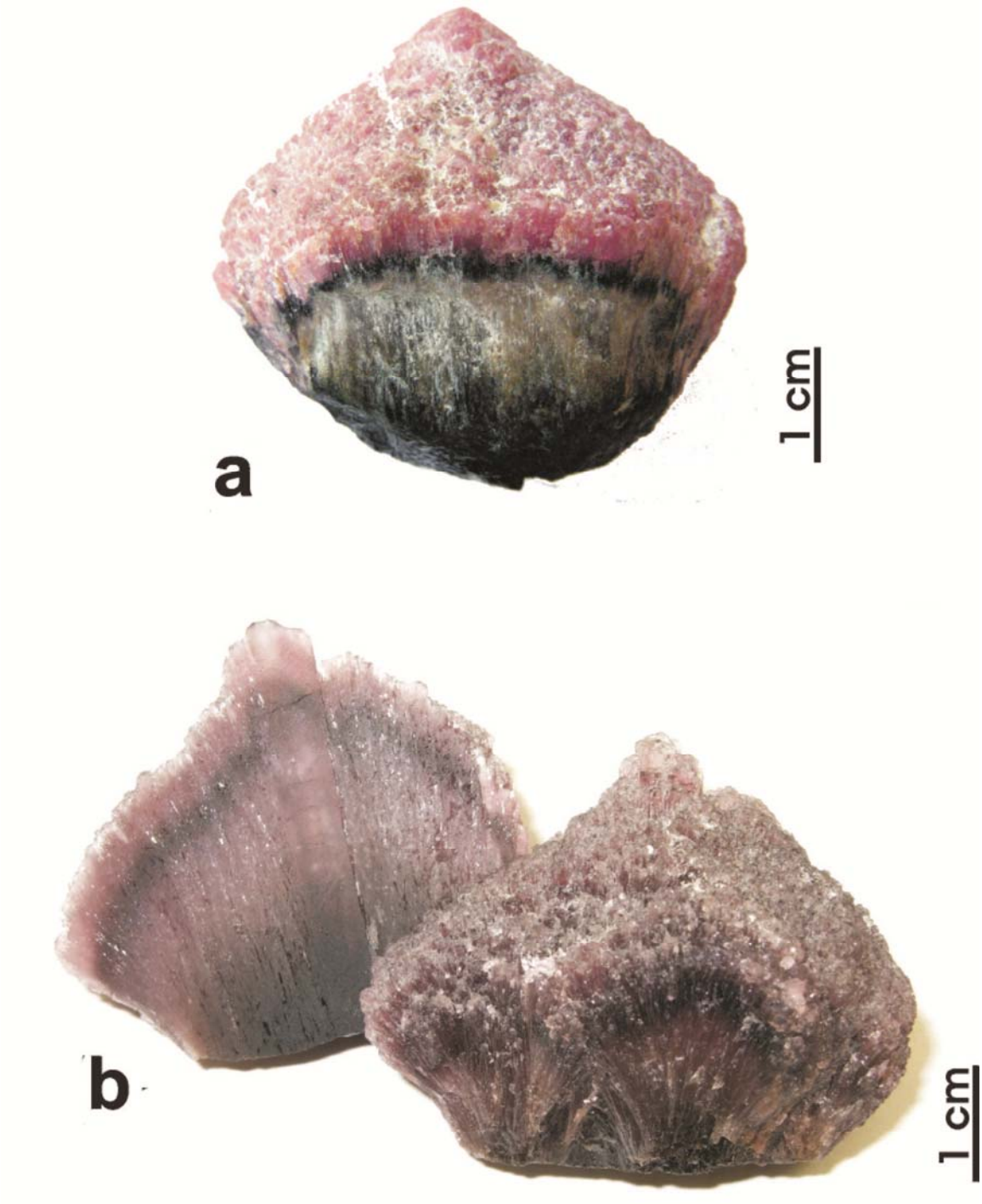

Figure 3.3 Mushroom tourmalines from Mogok, Myanmar: (a) pink-white-black Mogok mushroom tourmaline (SHM); (b) purple-black 'mushroom' tourmaline (SHP).

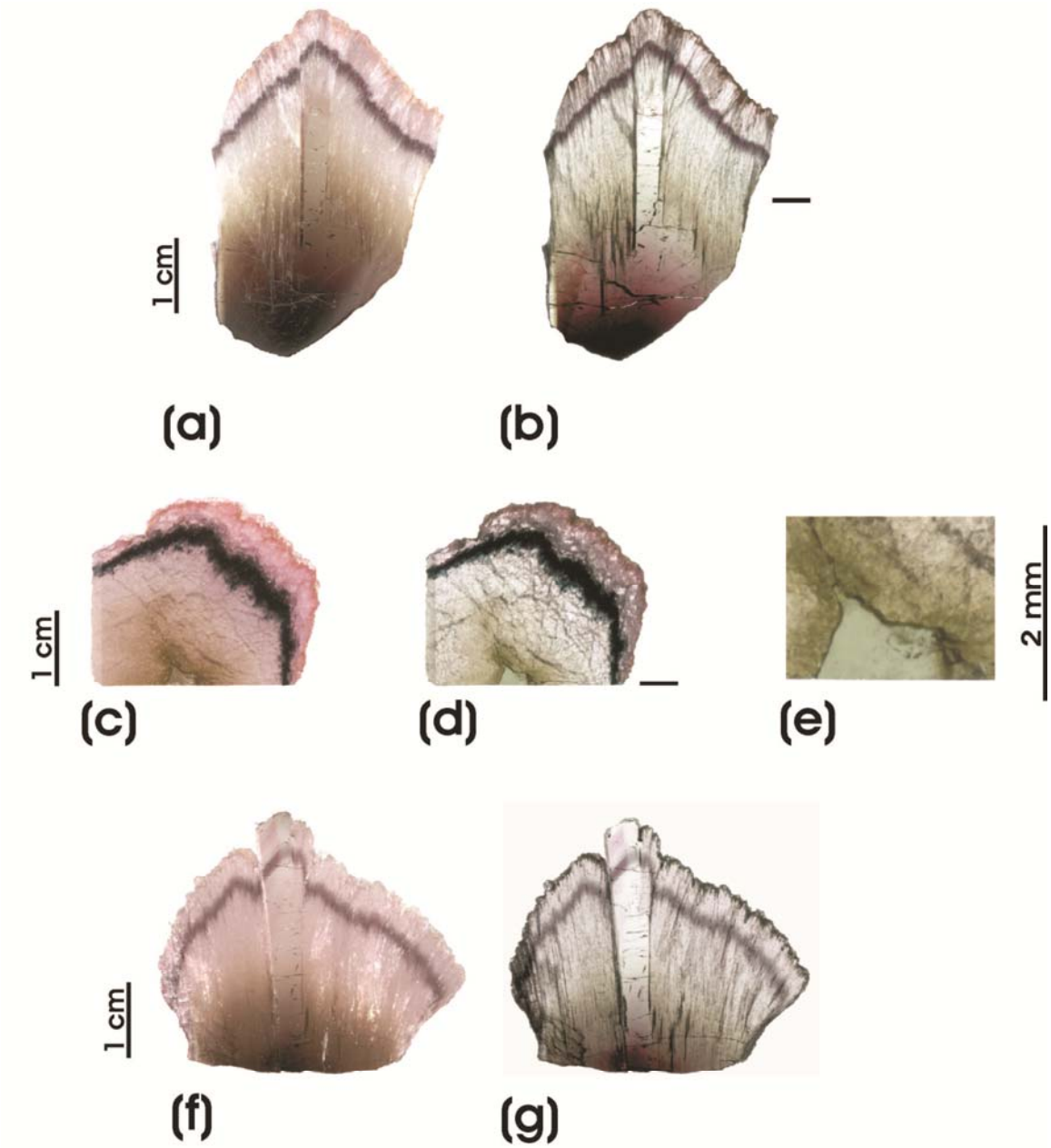

Figure 3.4 Doubly-polished sections (~1 mm thick) of the mushroom tourmalines from Mogok. Myanmar in both reflected (a, c, f) and transmitted (b, d, e, g) light; (a, b) SHM cut parallel to the c axis; (c, d, e) SHM cut orthogonal to c axis; (e) is an enlargement of the central prismatic crystal; (f, g) SHP cut parallel to the c axis. Note, the symbol (–) in (b) and (d) denotes the line of intersection of the two SHM sections.

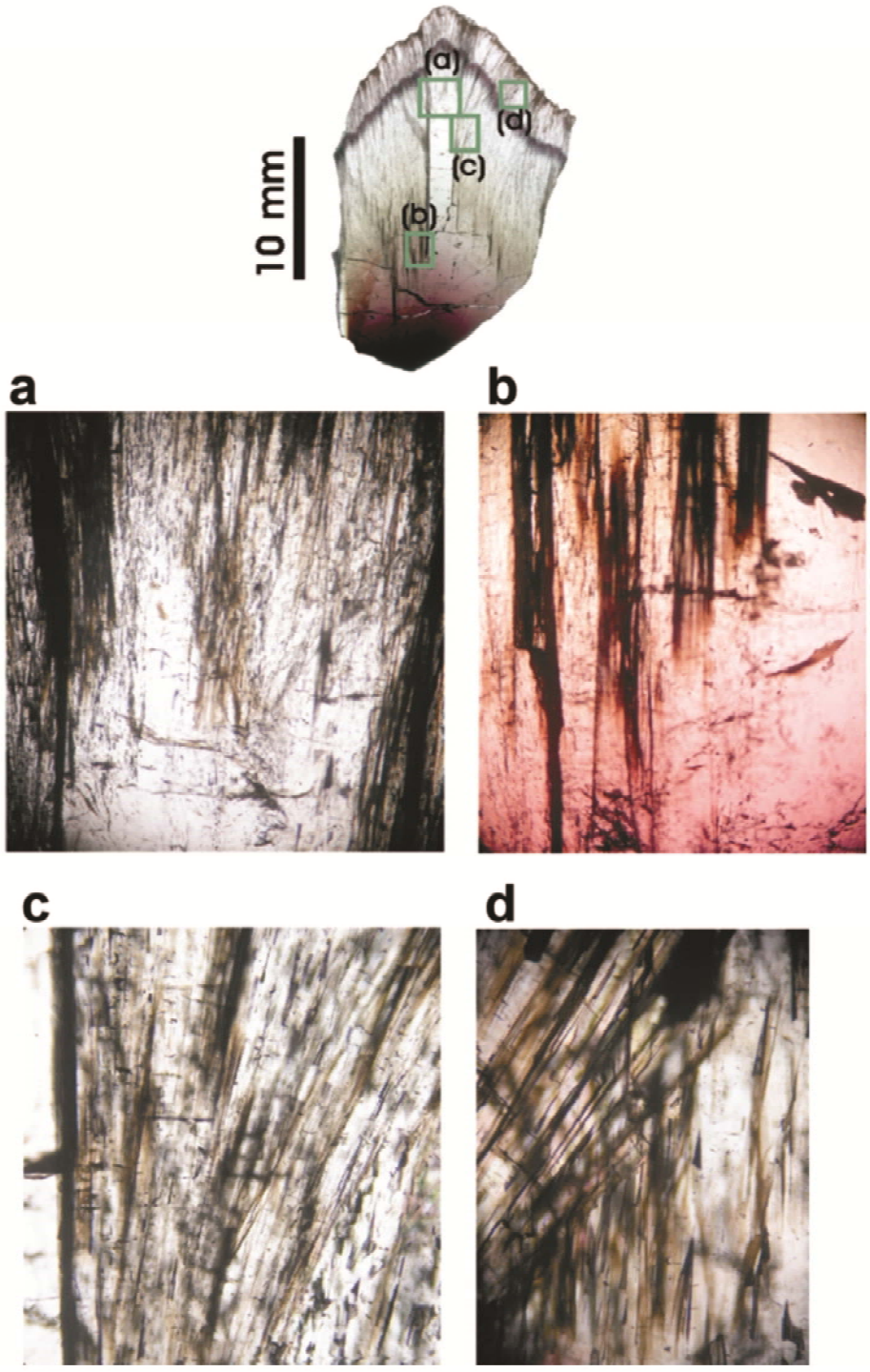

Figure 3.5 High-magnification photographs of mushroom tourmaline (SHM) in plane-polarized light, showing the character of the grain boundaries: (a) transition of the central prismatic crystal to numerous acicular crystals; (b) transition of the core region from a single crystal to numerous acicular crystals; (c) the divergence of acicular crystals from the central prismatic crystal visible at the extreme left of the photograph; (d) interpenetration of acicular crystals of different orientation.

to grayish-brown, whereas in transmitted light (Figure 3.4*b*,*f*) it grades from black to bluish-purple to purple-grey in both SHP and SHM samples.

The second region consists of a prismatic, optically continuous crystal (~3 cm long and ~0.3 cm across) that extends from the centre of the base through the core of the sample. In reflected light, it is a greyish-brown (SHM; Figure 3.4a) and pale pinkish-purple (SHP; Figure 3.4f), whereas in transmitted light it is nearly light-grey to colourless (SHM and SHP; Figure 3.4b,g). In both samples, the single core crystal splits (*i*.*e*., bifurcates) into multiple fibrous crystals toward the thin black rind. This is most clearly visible in high-magnification photographs of SHM (Figure 3.5a) where the fibrous crystals diverge, broadening the central crystal at the top and making a small protrusion at the apex of the sample. In the core crystal of SHP, however, this splitting is less pronounced and nearly half of the core remains one optically continuous crystal (Figure 3.4f-g).

The third region consists of highly-elongated, fibrous crystals. In both samples, these extend from the dark base crystal (Figure 3.5b) and surround the core crystal. In reflected light the fibres grade from dark brown to white to black to light pink (SHM) and dark-brown to light pinkish-purple to black to light pinkish-purple (SHP), whereas in transmitted light they grade from pale brown to colourless to grayish-black to pale pink (SHM) and pale brown to colourless to grayish-black to pale purple (SHP). Toward the base, the *c*-axes of the acicular crystals are parallel to the *c*-axis of the central prismatic crystal (Figures 3.4a-b, f-g, 3.5b), whereas further along the prismatic crystal, they diverge from the central prismatic crystal, and the core crystal splits into numerous acicular

crystals on either side (Figure. 3.5c). The acicular crystals pass through the black and pink parts of the sample and impart an irregular rounded aspect to the surface, somewhat resembling the surface of a cauliflower. In the outer part of the rind, the acicular crystals can interweave, giving a mottled appearance in cross-polarized light (Figure 3.5d).

A thick section cut orthogonal to the *c*-axes of SHM (Figures 3-4c-e) shows the central prismatic crystal surrounded by microcrystals (cross-sections of acicular crystals). The central prismatic crystal is irregular in outline (only half the cross-section is visible, and is best seen in Figure 3-4e).

3.3.2 Wheatsheaf tourmaline: sample description

Wheatsheaf tourmalines consists of an aggregate of euhedral crystals that diverge from base to termination (Figure 3.6a) in a manner resembling a sheaf of wheat. In hand specimen, the top 2-5 mm of the sample is dark opaque reddish-purple, and the rest of the sample is a translucent reddish-brown. Cross sections parallel and perpendicular to the average direction of the *c*-axes of the crystals (Figure 3.6b-c) show the sample to consist of many crystals between 1 and 3 mm across. These crystals can be traced throughout the length of the sample and display well-formed terminations. Several longitudinal zones can be distinguished on the basis of colour and composition.

High magnification photographs of several regions of the SHW sample are shown in Figure 3.7a-b.Toward the base of the crystal is a dark red core that shows intense pleochroism from red to greenish-grey. This core increases in size

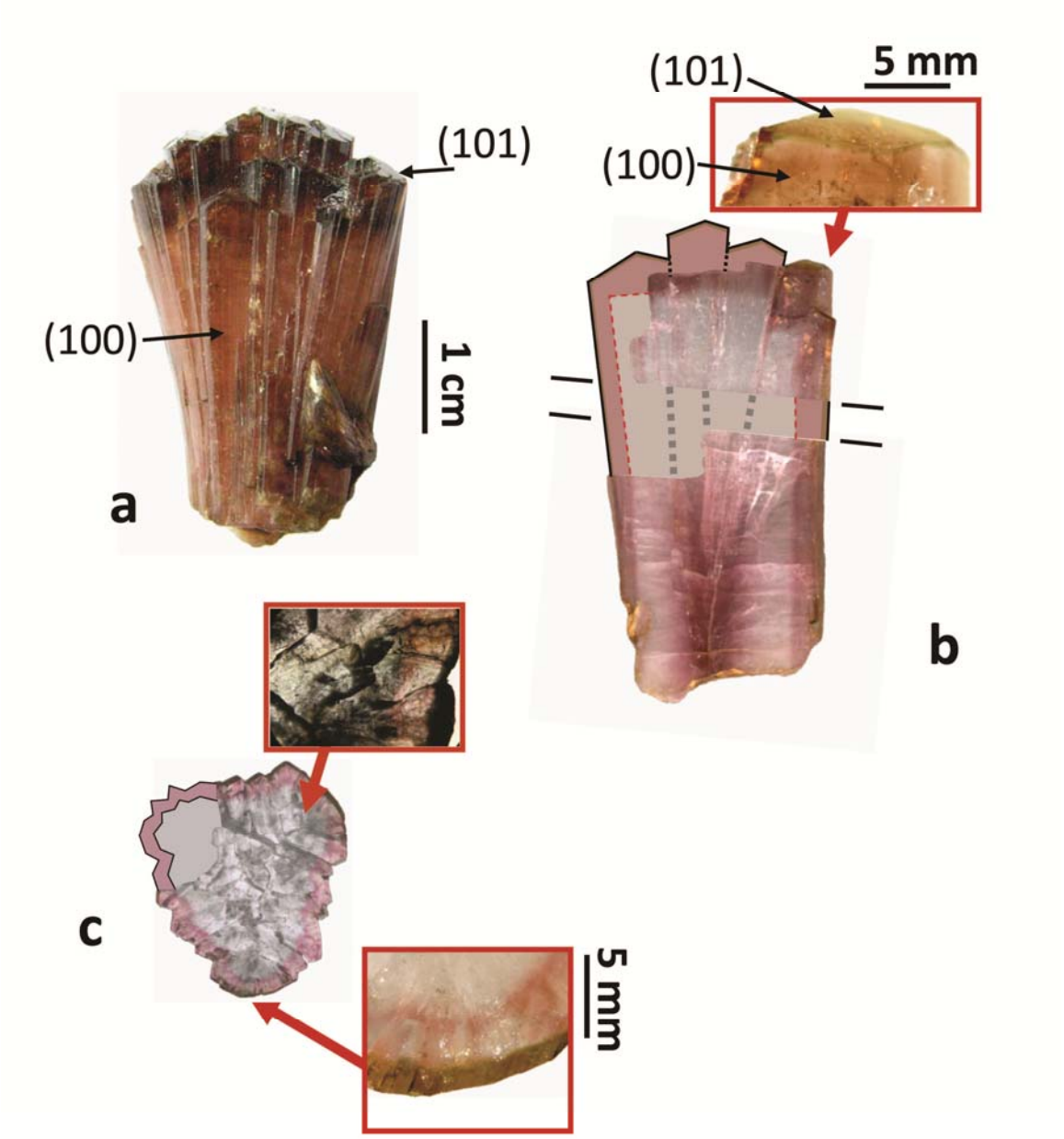

Figure 3.6. Photograph of wheatsheaf tourmaline from Mogok Myanmar: (a) hand sample; (b) doubly-polished cross-section cut parallel to *c*-axis shown in reflected light; the green layer on the end of crystal is shown enlarged in the red box (the section of the crystal removed for examination prior to photography has been drawn in schematically in uniform grey); (c) doubly-polished section cut perpendicular to *c*-axis and shown in transmitted light; the green rim is shown enlarged in one of the red boxes.

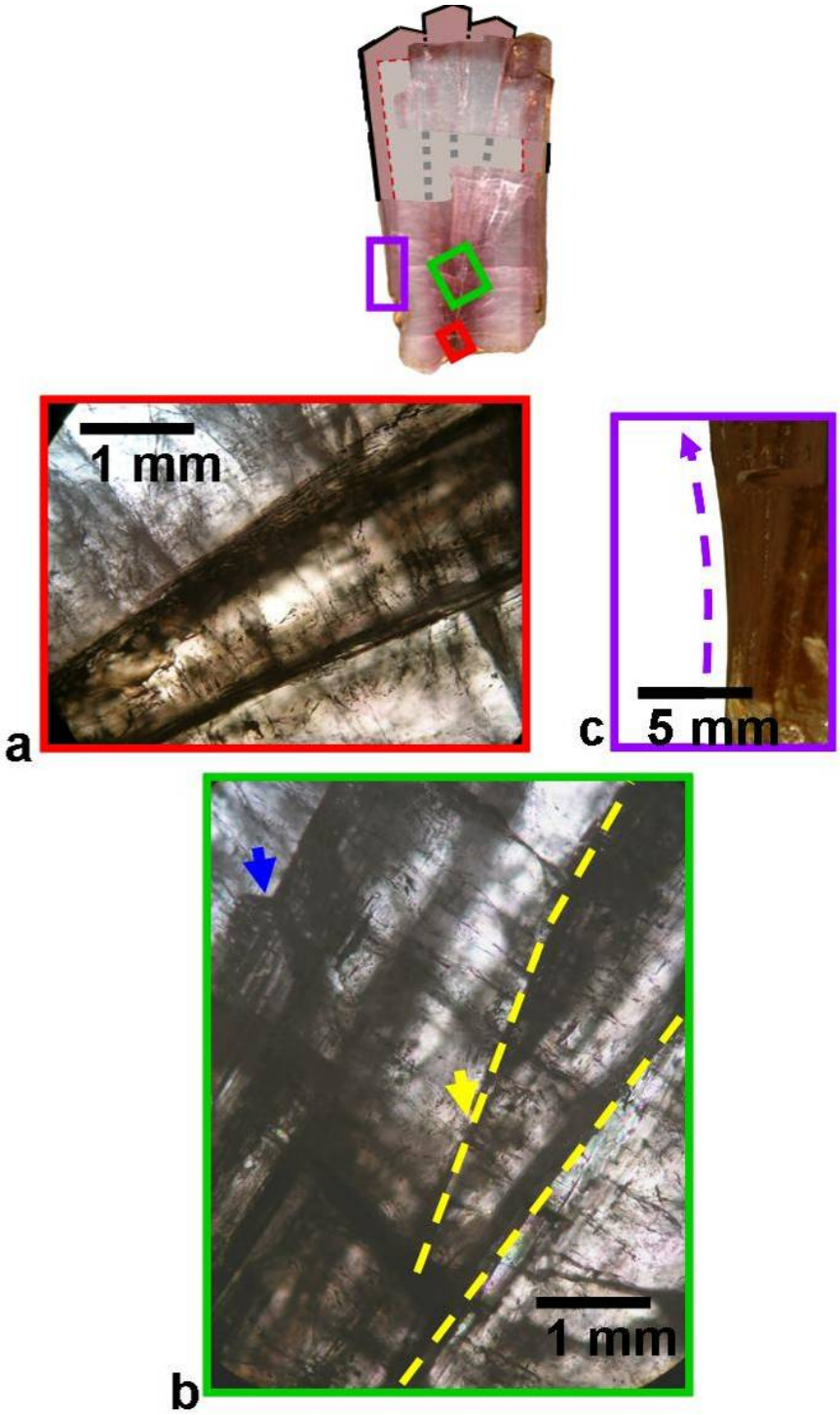

Figure 3.7. High-magnification photographs of wheatsheaf tourmaline (from a doubly-polished section) in plane-polarized light and showing (a) the central core zone at the base of the sample, (b) the central section of the sample where splitting of the initial core occurs, and (c) the edge of the sample showing the bent edge of a crystal.

along the *c*-axis (Figure 3.7*a*) until it changes gradationally into a white-to-colourless region that forms the bulk of the sample. A sharp boundary separates this white zone from a dark reddish-pink rind, 2 to 3 mm thick, that surrounds the entire sample (Figures 3.7b,c). The outer edge of the sample consists of a very thin light- to dark-green rind, ranging in thickness from < 0.5 to ~1 mm (Figure 3.6b,c). This layer is discontinuous along the prism faces but is uniform on the pyramid faces.

3.3.3 Provenance

The area around Mogok is the main gem-producing region of Mandalay Division, Myanmar. Mogok is in north central Myanmar and is well known for being the source of some of the world's finest rubies (Keller 1983). Tourmalines with both mushroom and wheatsheaf habits are known to originate from the granitic pegmatites in the region of Momeik, north-east of Mogok and north-west of Sakangyi. The granitic pegmatites occur within a central belt of evolved tin-tungsten granites and associated topaz-bearing pegmatites that stretches north-south. The pegmatites occur as veins and dikes cutting granitoid, migmatite, gneiss and schist, and range from 2 to 5 metres wide and 30 to 150 metres long (Zaw 1998; Hia *et al.* 2005; Themelis 2007). They contain quartz, orthoclase, albite, microcline microperthite and muscovite, with accessory minerals that include biotite, tourmaline, beryl, garnet, topaz, lepidolite, magnetite, wolframite, cassiterite and rare columbite (Themelis 2007). The pegmatites are commonly zoned; where tourmaline is present, it is usually confined to the outer zone.

3.4 ELBAITE-LIDDICOATITE FROM BLACK RAPIDS GLACIER, ALASKA

3.4.1 Sample description

The bulk sample consists of several euhedral, prismatic crystals ranging from 0.5-1.5 wide to 1.0-5.0 cm long (Figure 3.8a). These were set in quartz, and all are heavily fractured. No terminal forms are present. All crystals show two pronounced colour zones: (1) pale pink, which makes up the interior of the crystal; and (2) green, which makes up the outer 3-5 mm (Figure 3.8b).

3.4.1 Provenance

The tourmaline crystal examined here was retrieved from the surface of the Black Rapids Glacier in the Alaska Range, Alaska. No further information regarding sample provenance is known.

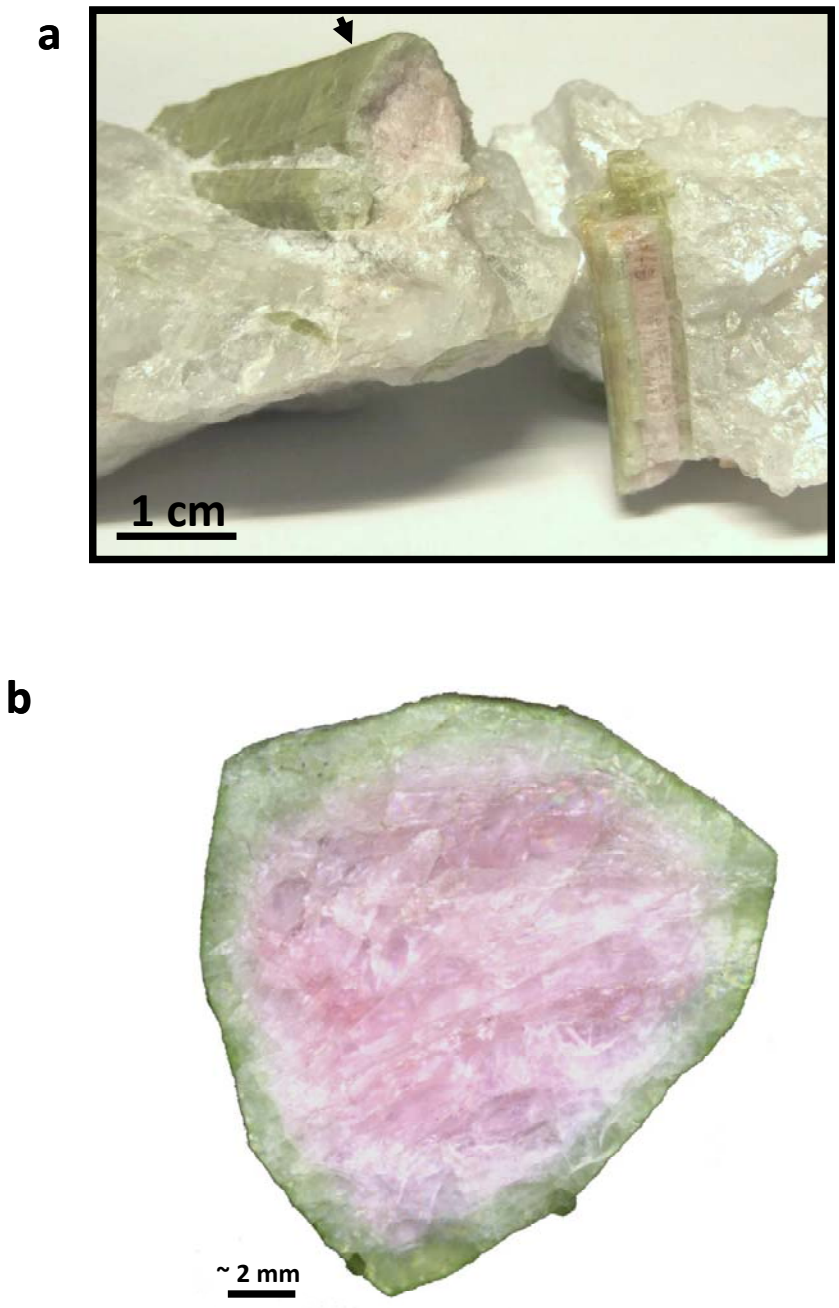

Figure 3.8 Sample of pink-green tourmaline retrieved from the surface of the Black Rapids Glacier, Alaska: (a) the crystals embedded in quartz (arrow indicates approximate location of slice taken for analysis); (b) analysed cross section.

CHAPTER 4

EXPERIMENTAL METHODS

4.1 SINGLE-CRYSTAL X-RAY DIFFRACTION

4.1.1 Collection of X-ray intensity data using a serial detector

All *X*-ray intensity data for Anjanabonoina liddicoatite (23 crystals) and for mushroom tourmaline (crystals: SHM1, SHM2, SHM3, SHP1, SHP2, and SHP3) and wheatsheaf tourmaline (crystals:SHW1 and SHW2) were acquired with a Bruker *P*3 automated four-circle single-crystal diffractometer equipped with a serial detector and a graphite-monochromated Mo*Kα* X-radiation source. Crystals were extracted from the bulk samples, ground to (approximate) spheres and mounted on glass fibres prior to data acquisition. Cell dimensions were derived from the setting angles of thirteen automatically aligned reflections by least-squares refinement. A total of ~1110 symmetry-independent reflections was measured for each crystal over the interval $4° < 2\theta < 60°$, with index ranges $0 < h < 23$, $0 < k < 23$, $-11 < l < 11$. A standard reflection was collected every 50 measurements to monitor instrument stability; no significant change was noted during any of the data collections. Psi-scan intensity data were collected, a psi-scan absorption correction was applied to each crystal, together with the usual geometrical corrections, and the data were reduced to structure factors.

4.1.2 Collection of X-ray intensity data using a CCD area detector

For all other crystals (SHM3a, SHM3e, SHM4, SHW3-SHW8), *X*-ray intensity data were collected using a Bruker *P*4 automated four-circle single-crystal diffractometer equipped with a CCD detector and a MoKα *X*-ray source. Selected crystals were ground to approximate spheres and mounted on thin tapered glass fibres prior to analysis. Several crystals were not ground due to their small size or acicular nature.

Reflections were measured out to 60° 2θ with a frame width of 0.2^{o} and a frame time consistent with crystal size. In excess of a hemisphere of data was collected in all cases. Prior to further data processing, all spots were checked to ensure that they were circular and uniform with no significant streaking. Unit-cell dimensions were determined on all reflections with $|I| > 10\sigma I$. Absorption corrections were done using the program SADABS (Sheldrick 1998). The data were then corrected for Lorentz, polarization and background effects, averaged and reduced to structure factors. Miscellaneous details of the data collection for all crystals are given in Appendix A.1.

4.2 CRYSTAL STRUCTURE REFINEMENT

Crystal-structure refinement was done on a total of 40 crystals extracted from larger specimens using the SHELXTL PLUS© (PC version) software package. All structures were refined in the space group *R*3*m.* The *Z*- and *B*-sites were refined with full occupancy of Al and B, respectively, as unlocking the occupancies of these sites showed no appreciable deviation from full occupancy.

The refined occupancies of the *Y*- and *T*-sites were typically fixed to Al + Li = 3 *apfu* and Si + B = 6 *apfu* (unless MAS NMR showed that T = Si_6).

All structures were refined twice: first, with the O(1) and *O*(*2*) anions constrained to lie on the 3-fold axis (0, 0, *z*) and mirror planes (*x*, 2*x*, *z*), respectively; and second, with the O(1) and O(2) anions on the mirror planes (*x*, ½*x*, *z*) and general positions (*x*, *y*, *z*), following the findings of Burns *et al.* (1994), who showed the positional disordering of these anions in elbaitic tourmalines. Between ordered and disordered refinements, only O(1) and O(2) positional parameters showed differences exceeding error. Final refinement was done with fully anisotropic-displacement factors for all positions (except for O(1) and O(2) in the disordered model). Neutral scattering factors were used for all species except O for which a fully ionized scattering factor was used (this procedure will be discussed in detail in Chapter 5). Each specimen was tested for absolute orientation and transformed as appropriate, ensuring that the apices of the tetrahedra point in the direction of -*c* (Barton 1969; Dietrich 1985). For each refinement, the effect of an isotropic extinction correction of the form $k[1 + 0.001x F_c^2 \lambda^3 / \sin 2\theta]^{-1/4}$ was tested. For data acquired using the serial detector, values of *x* were found to be in the range 0.0005(2) to 0.0060(3); however, for data acquired using the APEX II CCD camera, the extinction correction was typically found to refine to 0, and was hence removed from the instruction file. Final R_1 and wR_2 indices and other refinement details are given in Appendix A.1.

Atom coordinates and selected interatomic distances of all samples are given in Appendices A.2 and A.3, respectively; refined site-scattering values (Hawthorne *et al.* 1995) are given in Appendix A.5.

4.3 ELECTRON MICROPROBE ANALYSIS

All tourmaline specimens were analysed using a Cameca SX-100 electron microprobe at the University of Manitoba, operating in wavelength-dispersion mode with an accelerating voltage of 20 kV, a specimen current of 15 nA, and a beam diameter of 10 μm. The following analysing crystals and standards were used: TAP: albite (Na); andalusite (Al); diopside (Si); LPET: orthoclase (K); diopside (Ca); LTAP: fluororiebeckite (F); forsterite (Mg); LLiF: fayalite (Fe); spessartine (Mn); titanite (Ti); VPO_4 (V), chromite (Cr), ghanite (Zn), PbTe (Pb). The data were reduced and corrected by the PAP method of Pouchou & Pichoir (1985).

4.3.1 EMP analysis of crystals used in X-ray diffraction experiments

Crystals used for *X*-ray data collection were removed from the glass fibres and mounted in Petropoxy 154® on one-inch diameter Perspex® discs. They were then ground to a flat surface, polished on a lapidary to a final grit-size of 0.05 μm, and carbon-coated prior to analysis. Backscattered-electron images of each crystal were examined to check for compositional zoning, and ten points on each crystal were analysed. Chemical compositions for all crystals are listed in Appendix A.4.1.

4.3.2 EMP analysis of NMR samples

In cases where compositional data were required to match samples on which MAS NMR or Mössbauer spectroscopy data were acquired, samples were ground to an average crystallite grain size of ~15 μm and set in Petropoxy 154® on one-inch diameter Perspex® discs. The material was then ground to expose flat crystallite surfaces, polished on a lapidary to a final grit-size of 0.05 μm, and carbon-coated prior to analysis. The composition of 5 to 10 individual crystallites were averaged.

4.3.3 Compositional variation as a function of distance

For crystals showing complex colour zoning, such as Madagascar fluor-liddicoatite, wheatsheaf elbaite and mushroom elbaite, the compositional variation as a function of distance was characterised by collecting electron-microprobe traverses. The specimens were cut into thick sections (~1-2 mm) along the desired orientation using a Buhler® Microsaw and the resulting flat surface was polished on a lapidary down to a grit size of 0.05 μm before the sample was mounted on a glass slide and carbon-coated (Madagascar liddicoatite: Figure 3.1b; wheatsheaf: Figure 3.6b; mushroom: Figure 3.4a; Black Rapids; Figure 3.8b). For each traverse, the spacing between electron microprobe points was kept as even as possible, and ranged from 30-250 μm between traverses in accord with the size of the compositional feature being resolved.

4.4 ^{27}Al AND ^{11}B MAGIC-ANGLE-SPINNING NUCLEAR MAGNETIC RESONANCE SPECTROSCOPY

^{11}B (ν_L = 194.4 MHz) and ^{27}Al (ν_L = 156.3 MHz) Magic-Angle-Spinning Nuclear Magnetic Resonance (MAS NMR) spectroscopy was used to probe the presence of [4]-coordinate Al and B in various samples. Data were acquired using a Varian ^{UNITY}Inova 600 (14.1T) spectrometer with an Oxford magnet. All samples were ground to a fine powder (~10-30 μm crystallites) using a mortar and pestle. For those samples showing complex optical and compositional zoning (see Chapters 3, 6 and 7), sub-samples were extracted at specific locations, whereas all other samples were typically optically homogeneous and crushed in bulk.

For each sample, a weighed amount (~10-30 mg) of powdered sample was placed in a 3.2 mm (22 uL capacity) zirconia rotor and spun at speeds of 18-24 kHz in a double-resonance probe. The optimized recycle delay was determined independently for each sample; averages were 7 and 5 s for ^{27}Al and ^{11}B, respectively. The final spectra are composites of 512-3072 averaged scans. Spectra were referenced to 0.1 M H_3BO_3 as a secondary reference (= +19.6 ppm with respect to $BF_3(CH_3CH_2)_2O$), and 1.1 M $Al(NO_3)_3$. Pulse widths were selected to coincide approximately with a 15-20° tip angle at an rf nutation frequency of 42 kHz (^{11}B) and 52 kHz (^{27}Al). Spectra were periodically collected on empty rotors prior to rule out cross-contamination and spectral interference from rotor materials. For each tourmaline sample, the ^{11}B and ^{27}Al MAS NMR spectra are shown in Appendix A.6.

4.4.1 High-field ^{11}B and ^{27}Al MAS NMR spectra

An Avance II 900 spectrometer (21.1 T) using a 2.5 double-resonance Bruker probe at sample-spinning rates of 30 kHz was used to acquire ^{11}B MAS NMR (v_L = 288.8 MHz) spectra on sections of wheatsheaf tourmaline at ultra-high field. Due to a strong ^{11}B background signal from BN in the probe, single-pulse (Bloch-decay) spectra were unusable. Instead, rotor-synchronized Hahn-echo spectra were collected with v_{rf} = 62.5 kHz, recycle delays of 1 s, and 175 co-added transients. This approach yielded reliable peak positions, but compromised the precision of the relative peak intensities.

Further, the ^{27}Al (v_L = 234.4 MHz) MAS NMR spectrum of sample NMR2 (Madagascar liddicoatite; Figure 3.1) was also acquired at ultra-high field. A 1.3 mm ZrO_2 rotor was spun at 62.000 ± 0.002 kHz, and acquired with a 12° tip angle (v_{rf} = 73 kHz), a recycle delay of 5 s and 1024 co-added transients. This spectrum added no new information, and is therefore not shown.

4.5 MÖSSBAUER SPECTROSCOPY

For samples with adequate amounts of $\sum FeO_x$ (> 1.0 wt%), Mössbauer spectroscopy was used to determine the proportions of ferrous to ferric iron. An adequate amount of material (> 4 mg) was extracted from the bulk sample, mixed with sucrose, and carefully ground under acetone. For all samples, care was taken to remove a minimum amount of material required from the region of interest in order to minimize any possible sample heterogeneity. The mixture was then loaded into a Pb ring (2 mm inner diameter) and covered by tape on both

sides. Mössbauer spectra were acquired in transmission geometry using a ^{57}Co(Rh) point source. The spectrometer was calibrated with the room-temperature spectrum of α-Fe. Using the RECOIL® software package, the spectra were analysed by a Voigt-function-based quadrupole-splitting distribution (mushroom and wheatsheaf elbaites) and by Lorentzian doublets (Madagascar fluor-liddicoatite), as these were found to give the best fit in each case.

4.6 CALCULATION OF STRUCTURAL FORMULAE

All structural formulae were calculated on the basis of 31 anions. The ratio of Fe^{3+}/Fe^{2+} was set to equal that determined by Mössbauer spectroscopy. Light elements (*i.e.*, H_2O, Li_2O, B_2O_3) were not determined by EMP analysis, and hence were calculated on the basis of stoichiometric constraints: Li (*apfu*) = 9 = $\sum(Y + Z)$ and (OH) + F = 4 *apfu*. The amount of B *apfu* was calculated in conjunction with the results of ^{11}B and ^{27}Al MAS NMR spectroscopy and SREF: B = 3 *apfu*, where no $^{[4]}$B or $^{[4]}$Al was found to be present (*e.g.*, Madagascar liddicoatite), B = 9 – Si *apfu*, where only $^{[4]}$B was found to be present (mushroom elbaite); and $^{[4]}$B + $^{[4]}$Al = 9 – Si *apfu*, where both $^{[4]}$B and $^{[4]}$Al were found to be present (wheatsheaf elbaite). The composition was iterated to self-consistency. Further, all Mn was assumed to be divalent as Mössbauer spectroscopy consistently showed that not all Fe was trivalent. The calculation of unit formulae is discussed in greater detail in Chapter 6.

4.7 TRANSMISSION ELECTRON MICROSCOPY

A section of the mushroom ebaite sample was examined using a JEOL JEM-2010F field-emission electron microscope operating at 200 keV. Prior to analysis, a small section of the sample was ground to a thickness of ~80 μm and then doubly-polished to a grit size of 1 μm. A Gatan Model 691 Precision Ion Polishing System (PIPS™) operating in double ion beam modulation mode (beam energy, 4.5 keV; beam current, 12 nA) was used to bore a hole in the centre of the sample so that the thinnest part of the edge could be analysed by TEM. The incident ion angle was systematically decreased from ~12° to 3° over the course of the ~3 h.

4.8 OPTICAL MINERALOGY

Optical images (Chapter 3) were required for the Madagascar liddicoatite, mushroom and wheatsheaf elbaite samples. These samples were cut into thick sections (2-4 mm) using a Buhler IsoMet® Precision Saw with a 7” diameter Buhler Diamond Waffering Blade and doubly-polished to a grit-size of 0.05 μm. Photographs were taken with an Epson® flatbed scanner in either reflected or transmitted (using transparency adapter) light at the highest resolution possible (1200-3000 dpi). For wheatsheaf and mushroom elbaite samples, high-magnification optical photographs were acquired for textural descriptions. These

photographs were taken in either transmitted or reflected light on a Nikon Eclipse E600W POL polarizing microscope at 10 to 20 times magnification. Furthermore, where optical data (such as 2*V*) were required, crystal fragments were mounted on a Supper® Spindle Stage, and observed measurements were processed using the program Excalibr II (Bartelmehs *et al.* 1992).

CHAPTER 5

TETRAHEDRALLY COORDINATED Al AND B IN TOURMALINE

5.1 INTRODUCTION

Silicon is the most abundant constituent of the *T*-site in tourmaline, and all currently-recognized species have a nominal T = Si_6 (Tables 1.2 to 1.4; Henry *et al.* 2011). Until relatively recently, it was thought that only Al (Povondra 1981; Grice & Ercit 1993; MacDonald & Hawthorne 1995a) could substitute for Si in the tourmaline structure, but it has since been shown directly that B may also substitute for Si (Tagg *et al.* 1999; Schreyer *et al.* 2000; Marler & Ertl 2002), However, several questions surrounding the occurrence of tetrahedrally coordinated Al ($^{[4]}$Al) and B ($^{[4]}$B) remain, for instance: (1) are they common constituents in natural tourmalines?; (2) are they restricted to certain tourmaline species?; and (3) do they occur only in tourmalines from certain geologic environments?

Here, ^{11}B and ^{27}Al MAS NMR (Magic-Angle-Spinning Nuclear Magnetic Resonance) spectroscopy is used to investigate the occurrence of tetrahedrally coordinated constituents in a large suite of low-(Fe, Mn) tourmalines of various compositions. Previous ^{11}B MAS NMR work has examined elbaite or olenite, and many of the tourmalines examined in the present study are the same species because elbaite or olenite can be sufficiently low in paramagnetic constituents to obtain good-quality MAS NMR spectra. Some samples from the present work correspond to other compositions (magnesio-foitite, “fluor-elbaite”, liddicoatite,

uvite), but it is difficult to find samples sufficiently low in paramagnetic species for MAS NMR spectroscopy. Furthermore, the limits of detection of $^{[4]}$B and $^{[4]}$Al in tourmaline by ^{27}Al and ^{11}B MAS NMR are also assessed by spectral simulation, and the sensitivity of SREF to small amounts of $^{[4]}$B is assessed by comparing the use of ionized and neutral scattering factors during least-squares structure refinement.

5.2 DETECTION OF $^{[4]}$B AND $^{[4]}$Al IN TOURMALINE BY CONVENTIONAL ANALYSIS

5.2.1 Electron microprobe

Electron microprobe analysis (EMPA) is the most common method of determining tourmaline composition. Unit formulae are typically calculated on the basis of a 31 anion normalization scheme, and hence, the presence of tetrahedral constituents other than Si would result in Si < 6 *apfu* in the final formula calculations. This is true where *significant* amounts of $^{[4]}$Al + $^{[4]}$B (*e.g.*, > ~0.75 *apfu*) are present, however, if the amounts of $^{[4]}$B + $^{[4]}$Al are small (~0.1 *apfu*), analytical errors may not be sufficiently small to confidently identify crystals where Si < 6 *apfu*. This may arise because: (1) standards of different phases may be used for EMPA calibration, and hence will be imperfectly matrix-matched; and/or (2) the chemistry of tourmaline may be complex, and the total analytical error, being the sum of individual errors of all components, is potentially significant.

Furthermore, it is still usual to calculate tourmaline formulae by setting B = 3 *apfu* (*i.e.*, only $^{[3]}$B is assumed to be present) and $^{[4]}$Al = 6 – Si *apfu*. Any error introduced into the unit formula by this approach is typically obscured by the fact that the light elements (*i.e.*, Li_2O, B_2O_3 and H_2O) are usually calculated using stoichiometric constraints, such as Li = 9 – ∑(*Y* + *Z) apfu* and (OH) = 4 - F *apfu.* Neither of these constraints is necessarily accurate as O^{2-} may also occur at O(1)- and O(3)-sites, and Fe^{3+} contents are commonly estimated by electroneutrality and stoichiometry assumptions, or assumed to be zero. Kalt *et al.* (2001) and Ertl *et al.* (2005) report the occurrence of Al and B (as well as Si) at the *T*-site in Li-rich tourmalines based on direct analysis of B, but this type of site assignment is rather imprecise as it relies on the accurate analysis of B, and uncertainties in the determination of B is ~10% relative.

5.2.2 Site-scattering REFinement (SREF)

The SREF technique calculates the mean atomic number of elements present at a given crystallographic site in units of electrons per formula unit (*epfu*), and hence may be a sensitive indicator of site-composition. Therefore, it is appropriate to consider if SREF can determine if either $^{[4]}$Al or $^{[4]}$B (or both) are present (along with Si) at the *T*-site in tourmaline. Furthermore, the substitution of ions with different radii at a given crystallographic site may also be detectable by systematic variations in the refined bond lengths.

First, consider the case where T = (Si_5B). There is a significant difference in atomic scattering power between Si (*Z* = 14) and B (*Z* = 5). Where the *T*-site is

fully-occupied by Si, the site-scattering for the *T*-site will refine, within standard error, to a value of 1.00. However, if T = (Si_5B), the average site-scattering value at the *T*-site should refine to 0.89 (= [14 x 5.0 + 5 x1.0] / 84). Additionally, the grand mean <*T*-O> for full Si occupancy in tourmaline is ~1.620 Å (MacDonald & Hawthorne 1995a), whereas the grand mean $<^{[4]}$B-O> in borate minerals is 1.476 Å (Hawthorne *et al.* 1996). Hence for T = (Si_5B) the refined <*T*-O> would be [5/6 x 1.620] + [1/6 x 1.476] = 1.596 Å, assuming a linear change in <*T*-O> with along the ^{T}B ↔ Si substitution. As errors on bondlengths determined by SREF are typically 0.001-0.003 Å, 1.596 Å would be easily resolved from 1.620 Å.

Second, consider the case where T = (Si_5Al). Between the scattering power of Si and Al (Z = 13), there is only a difference of 1 electron, which results in an aggregate site-scattering value of 0.99 which cannot be reliably resolved from 1.00. However, the average bondlength for $^{[4]}$Al-O is ~1.75 [= $^{[4]}r$(Al) + *r*(O) = 0.39 + 1.36] and a linear model predicts an observed <*T*-O> of 1.642 Å for T = (Si_5Al), which could also be easily resolvable from 1.620 Å.

Figure 2.5 shows the relationship between <*T*-O> and <*r*[*T*]> for the 9 uvite crystals of McDonald & Hawthorne (1995) as well as data from more recently published crystals were Si < 6 *apfu*. As noted in Chapter 2, tourmalines where T = $(Si,Al)_6$ are in reasonable agreement with the initially-proposed curve of McDonald & Hawthorne (1995). However, data corresponding to crystals with T = $(Si, B, Al)_6$ show significant scatter, and it is not possible to determine the nature of the relation between <*T*-O> and <r[*T*]>. Hence the use of bond lengths to assign T-site constituents in tourmaline is currently not possible. However, if

the relation between <*T*-O> was well-characterised, bondlengths and average site-scattering data derived from SREF could be used to determine the proportions of both, as has been shown possible in the kornerupine-prismatine series (Cooper *et al*. 2009).

5.3 PREVIOUS WORK BY MAS NMR

MAS NMR spectroscopy is a powerful method for determining coordination numbers of specific isotopes in solids. As discussed above, B (^{11}B) and Al (^{27}Al) are of particular interest with regard to tourmaline. $^{[3]}$B and $^{[4]}$B have chemical shifts of 12 to 19 ppm and -4 to 2 ppm in oxides, respectively (Bray *et al.* 1961; Turner *et al.* 1986), and $^{[4]}$Al and $^{[6]}$Al have chemical shifts of 50 to 80 ppm and -10 to 15 ppm in oxides, respectively (Kirkpatrick 1988, Kirkpatrick *et al.* 1985, 1986). Thus, coordination numbers, and hence site assignments, can be determined, provided the structure does not contain sufficient paramagnetic species (particularly transition metals) to attenuate the signal. ^{11}B MAS NMR has been used for the detection of $^{[4]}$B in tourmaline. Tagg *et al.* (1999) reported small amounts (0.1 - 0.2 apfu) of $^{[4]}$B in elbaite, showing that at low field (7.05 T), there is overlap between the peaks for $^{[3]}$B and $^{[4]}$B, whereas at higher field (11.74 T), the peaks are well-resolved. Schreyer *et al.* (2000) and Marler & Ertl (2002) reported low-field ^{11}B MAS NMR spectra of a synthetic olenite with a nominal *T*-site content of Si_3B_3, and a $^{[4]}$B-bearing olenite from a granitic pegmatite. Ertl *et al.* (1997) and Hughes *et al.* (2000, 2001) have shown that <*T*-O> distances in the tourmaline examined by Marler & Ertl (2002) are in accord with the presence

of $^{[4]}$B. Similar stereochemical results have been reported by Hughes *et al.* (2004), Kalt *et al.* (2001), Marler *et al.* (2002), and Ertl *et al.* (2005, 2006, 2007) indicating the presence of $^{[4]}$B in Li-bearing tourmaline.

To date, MAS NMR has not been applied to the investigation of $^{[4]}$Al (tetrahedrally coordinated Al) in tourmaline, despite the fact that it is suitable for this purpose as both [4]- and [6]-coordinated Al differ sufficiently in resonance frequency (50 to 80 and -10 to 15 ppm, respectively) to provide good resolution at the moderately high field of 14.1 T used here.

5.4 SAMPLES

A total of 50 tourmaline crystals from various localities (Table 5.1) was assembled for MAS NMR spectroscopy. Investigation by MAS NMR requires that the samples be as free of transition metals as possible, due to the fact that paramagnetic species can induce very fast relaxation of the nuclear spins, broadening the resonance signal. This limitation restricts this investigation to Li-Al tourmalines: liddicoatite, elbaite (“fluor-elbaite”), rossmanite and olenite, and low-Fe dravite, uvite and magnesio-foitite. The samples examined here are summarized in Figure 5.1. Each sample was examined very carefully for inclusions and any grains that had optically visible solid inclusions or extraneous material adhering to grain boundaries was discarded. A complete catalogue of ^{11}B and ^{27}Al MAS NMR spectra collected is given in Appendix A.6.

TABLE 5.1 LIST OF TOURMALINE SAMPLES INVESTIGATED BY ^{11}B AND ^{27}Al MAS NMR, COLORS, LOCALITIES, AND T-SITE OCCUPANCIES

Sample	Species	Locality	Colour		Sample No.
		$^{[4]}B$, $^{[4]}Al$, and Si present			
AT06	Elbaite	Black Rapids Glacier, Alaska	Light pink	a	BRP
AT07	Liddicoatite	Black Rapids Glacier, Alaska	Light green	a	BRG
AT09	"Fluor-elbaite"	Moravia, Czech Republic	Pale pink	a	LA 7-1 CR
AT10	Elbaite	Pesrig, Saxony, Germany	Pink/purple	b	T48 / M6101
AT14	Olenite	Köralpe, Austria	Colorless / pale green	g	---
AT16	Liddicoatite	Namibia	Dark pink to colorless	a	NT3
AT18	Fluor-liddicoatite	Namibia	Light pink	a	NT5
AT19	Fluor-liddicoatite	Namibia	Light pink/green/orange	a	NT6
AT20	Fluor-liddicoatite	Namibia	Pink	a	NT7
AT21	Fluor-liddicoatite	Namibia	Pink	a	NT8
AT28	"Fluor-elbaite"	Pala, California	Light pink	a	---
AT50	Olenite	Belo Horizonte, California	Colorless	a	---
AT51	Olenite	Nina La Verda, Brazil	Colorless	a	---
AT52	Elbaite	Sverdlouskoblast, Ural Mts., USSR	Pink	e	T15
AT54	Elbaite	Tanco Pegmatite, Manitoba	Pink	f	T34
AT73	Elbaite	Mogok, Myanmar	Pink	a	SHM1
AT73	Elbaite	Mogok, Myanmar	Colorless	a	SHM2
AT75	Elbaite	Mogok, Myanmar	Purple / colorless	a	SHW2
		$^{[4]}Al$ and Si present			
AT13	Dravite	Brandu Valley, Pakistan	Honey brown	a	---
AT53	Uvite	Laxton Twp, Ontario	Pink	b	T23 / M20414
AT55	Dravite	Karsten, Germany	Golden brown	b	T42 / M19631
AT57	Uvite	Franklin, New Jersey	Green	c	T59 / C80699
AT58	Dravite	Darau Stazh, SW Pamirs	Colorless	h	T69 / DC080813
AT59	Uvite	East Africa	Green	a	T73
AT60	Uvite	East Africa	Green	a	T75
AT61	Uvite	East Africa	Green	a	T79
AT63	Dravite	Tanzania	Green	d	T85 / 143901
AT67	Uvite	Burma	Dark green	a	133839
AT68	Uvite	East Africa	Green	a	T78
AT70	Mg-foitite	Kyonosawa, Japan	Pale grey / colorless	a	---
AT72	Dravite	Morogoro, Tanzania	Pale brown / colourless	a	---

TABLE 1 (CON'T)

Sample	Species	Locality	Colour		Sample No.
		$^{[4]}$B and Si present			
AT47	Fluor-liddicoatite	Namibia	Dark green to colorless	a	NT13
AT56	Elbaite	Elba, Italy	Colorless	b	T47 / E1454
AT75	Elbaite	Mogok, Myanmar	Pinkish purple	a	SHW1
		$^{[4]}$Si present			
AT11	Elbaite	Minas Gerais, Brazil	Light green	b	T50 / M31184
AT48	Fluor-liddicoatite	Namibia	Green	a	NT14
AT49	Elbaite	Namibia	Pale green	a	NT15
AT65	Elbaite	Brazil	Pink	a	T96
AT66	Fluor-liddicoatite	Madagascar	Colourless	d	T98 / T98m / 165836
AT71	Fluor-liddicoatite	Anjanbonoina Pegmatite-Madagascar	Light green	i	NMR1
AT71	Fluor-liddicoatite	Anjanbonoina Pegmatite-Madagascar	Light purple	i	NMR7
AT71	Fluor-liddicoatite	Anjanbonoina Pegmatite-Madagascar	Dark purple	i	NMR9
AT71	Elbaite	Anjanbonoina Pegmatite-Madagascar	Dark purple	i	NMR10
		Unresolvable			
AT17	Fluor-liddicoatite	Namibia	Dark pink	a	NT4
AT23	Fluor-liddicoatite	Namibia	Light pink/colorless	a	NT10
AT25	"Fluor-elbaite"	Namibia	Light pink/colorless	a	NT12
AT62	"Fluor-elbaite"	Brazil	Green	a	T83
AT64	"Fluor-elbaite"	San Diego County, California	Pale yellow/green	j	T94 / T94m
AT73	Elbaite	Mogok, Myanmar	Black	a	SHM3
AT76	Elbaite	Astor, Pakistan	Pale green	a	MT16

*Sources: a: Frank C. Hawthorne, University of Manitoba; b: Royal Ontario Museum, Ottawa, Canada; c: American Museum of Natural History; d: Smithsonian Institute, Washington; e: National Museum of Natural Sciences; f: Mark Cooper, University of Manitoba; g: Andreas Ertl; h: Edward S. Grew; I: Carl Francis, Harvard University; j: Dalhousie University.

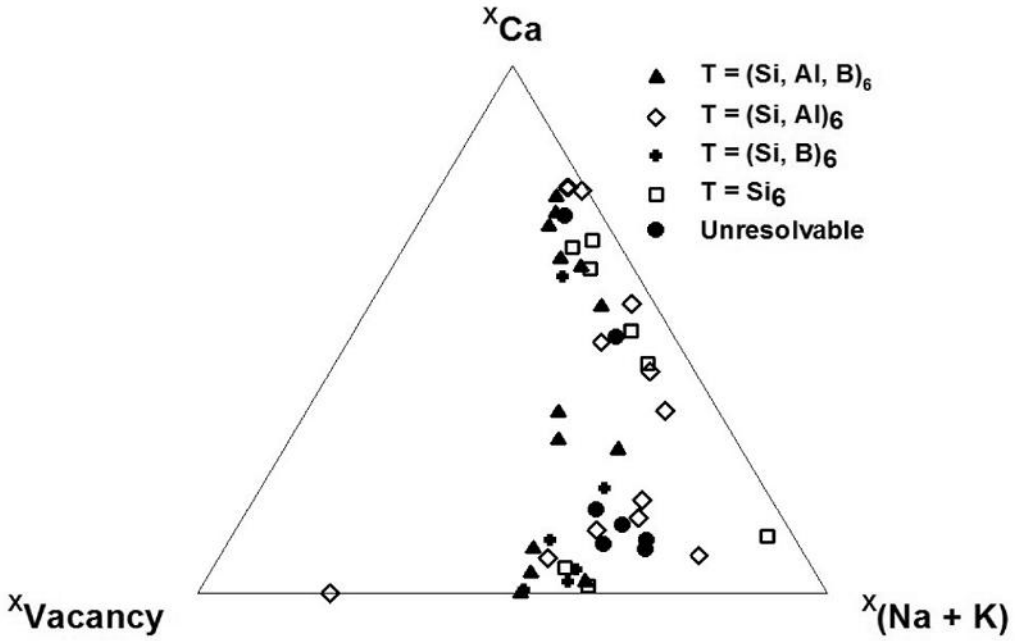

Figure 5.1 Variation in occupancy of the *X*-site in the tourmalines of this study; the symbols indicate the type of *T*-site occupancy.

5.5 ^{11}B MAS NMR

Selected ^{11}B MAS NMR spectra are shown in Figure 5.2 and clearly illustrate the ability of MAS NMR to resolve [3]- and [4]-coordinated B at higher field (14.1 T), in accord with Tagg *et al.* (1999). The peak for B in triangular coordination has a characteristic quadrupolar lineshape with δ_{iso} ~18 - 20 ppm, whereas the peaks for B in tetrahedral coordination are significantly narrower and occur at δ_{iso} ~0 ppm (Bray 1999, Bray *et al.* 1961; Turner *et al.* 1986; Kroeker *et al.* 2001, Kroeker & Stebbins 2001).

^{11}B MAS NMR spectra were calculated using the time-domain density-matrix calculation program, STARS (Skibsted *et al.* 1991), as implemented in the spectrometer software. Isotropic chemical shifts, quadrupole coupling constants and quadrupolar asymmetry parameters were obtained, as appropriate, for the different boron environments by manual adjustment of these NMR parameters for all transitions, in addition to the relative amplitude and line-broadening functions. The ^{27}Al MAS NMR spectra lack the well-defined lineshapes required to obtain NMR parameters, but could be faithfully modeled by asymmetric Lorentzian-Gaussian peakshapes, from which the integrated intensities could be reliably determined. In both cases, fits were evaluated by visual comparison between experimental and calculated spectra, and uncertainties assessed by altering given parameters to the threshold of reasonable agreement. Errors are estimated as ±0.05 *apfu* for B and ±0.08 *apfu* for Al as site populations. An example of spectral simulation for Köralpe olenite (AT14) is shown in Figure 5.3. Values for quadrupolar NMR parameters (*i.e.*, C_q and η) and δ_{iso} were determined for each

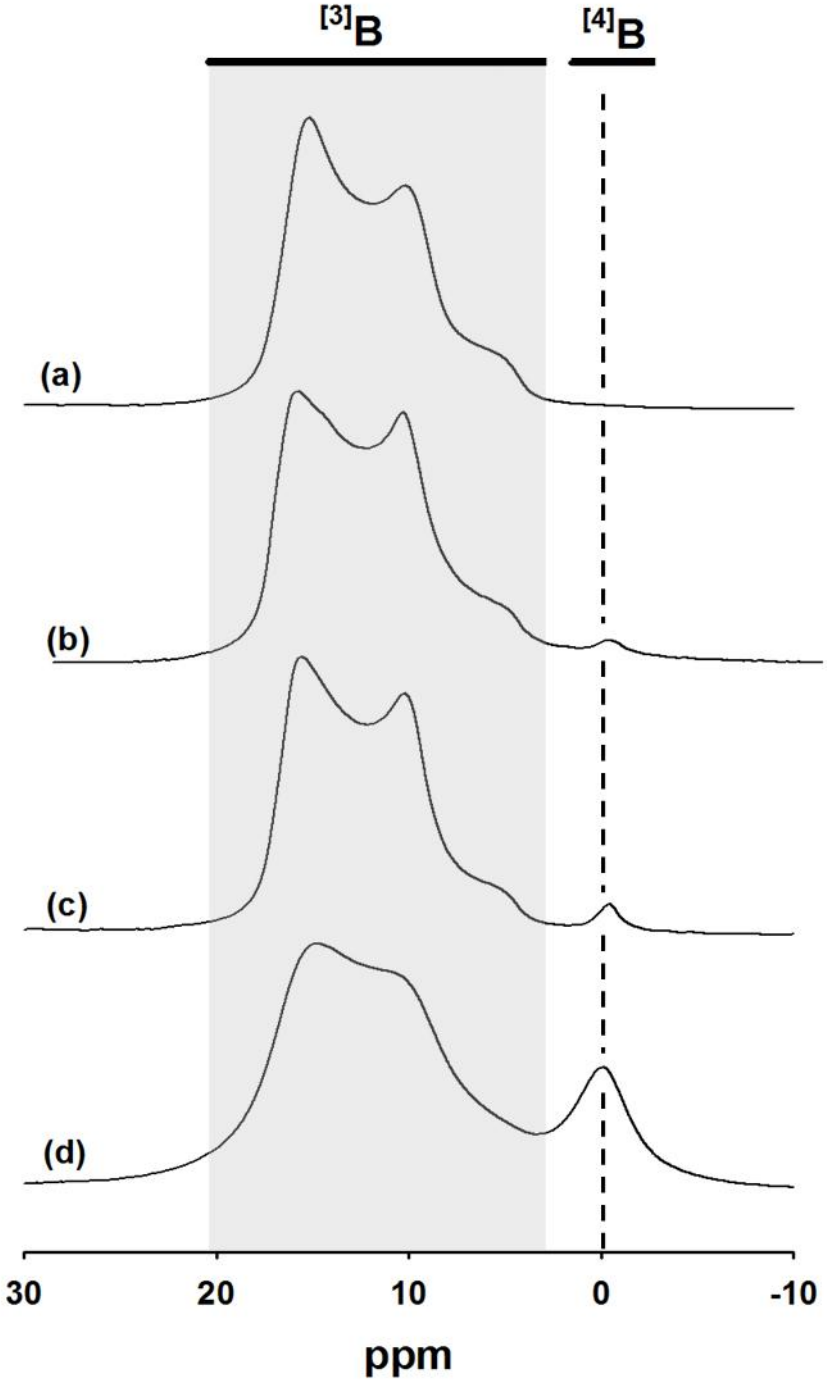

Figure 5.2 Selected ^{11}B MAS NMR spectra of tourmaline ranging from 0.0 - 0.5 *apfu* $^{[4]}B$ (as determined by spectral simulation): (a) Mg-foitite (AT70), (b) uvite (AT59), (c) dravite (AT72), (d) liddicoatite (AT20), (e) elbaite (AT52), (f) olenite (AT14). All spectra are scaled to the same height to facilitate comparison.

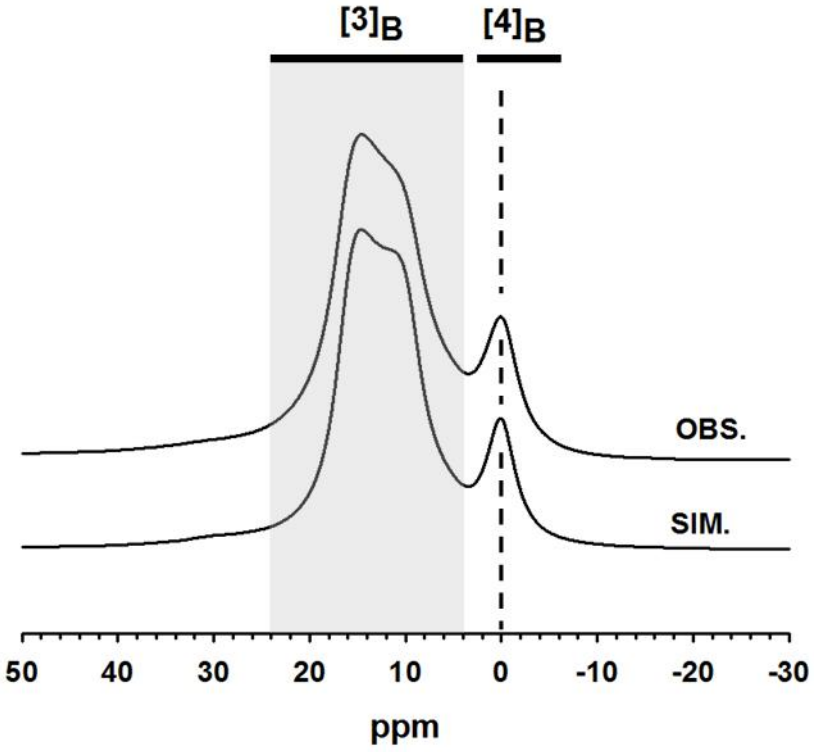

Figure 5.3 Example of an ^{11}B spectral simulation for Koralpe olenite. Final NMR parameters are as follows: BO_3, δ_{iso} = 18.1 ppm, C_q = 2.89 MHz, η = 0.15; BO_4, δ_{iso} = -0.1 ppm, C_q = 0.2 MHz, η = 0.8.

sample by optimization, beginning with the values given for elbaite and dravite by Tagg *et al.* (1999). Chemical-shift anisotropy (CSA) was ignored, following the findings of Tagg *et al.* (1999) and Marler & Ertl (2002) that this parameter does not significantly affect the lineshape of the central $^{[3]}$B transition. Lorentzian line-broadening (100 - 400 Hz) was added in order to improve agreement between the observed and simulated spectra and obtain reliable integrated intensities representing relative site populations. Intensities are converted into site populations as follows. (1) Boron: $^{[4]}B/(^{[3]}B + ^{[4]}B) = ^{[4]}I^{B} / (^{[3]}I^{B} + ^{[4]}I^{B})$ where $^{[4]}I^{B}$ is the absolute intensity of the MAS NMR peak for $^{[4]}$B; the amount of $^{[3]}$B is fixed stoichiometrically at 3.0 apfu, and hence the above equation may be rearranged to give:

$$^{[4]}B = 3 \times ^{[4]}I^{B} / ^{[3]}I^{B} \ apfu \qquad \text{(Eq. 5.1)}$$

(2) Aluminum:

$$^{[4]}Al / (^{[4]}Al + ^{[6]}Al) = ^{[4]}I^{Al} / (^{[4]}I^{Al} + ^{[6]}I^{Al}) \ apfu \qquad \text{(Eq. 5.2)}$$

where $^{[4]}I^{Al}$ is the absolute intensity of the MAS NMR peak for $^{[4]}$Al; the total amount of Al, $(^{[4]}Al + ^{[6]}Al) = Al^{total}$, is determined by normalization of the electron microprobe analysis to give the chemical formula, and hence the above equation may be rearranged to give $^{[4]}Al = Al^{total} \times ^{[4]}I^{Al} / (^{[4]}I^{Al} + ^{[6]}I^{Al})$ *apfu*. The results are given in Table 5.2.

Ultrahigh field (21.1 T) spectra collected on a tourmaline with $^{[4]}$B (wheatsheaf, SHW) show the expected narrowing of the $^{[3]}$B signal and accompanying shift of the centre-of-gravity to higher frequency (*i.e.*, nearer the isotropic chemical shift; Figure 5.4). This results in enhanced resolution of the $^{[3]}$B

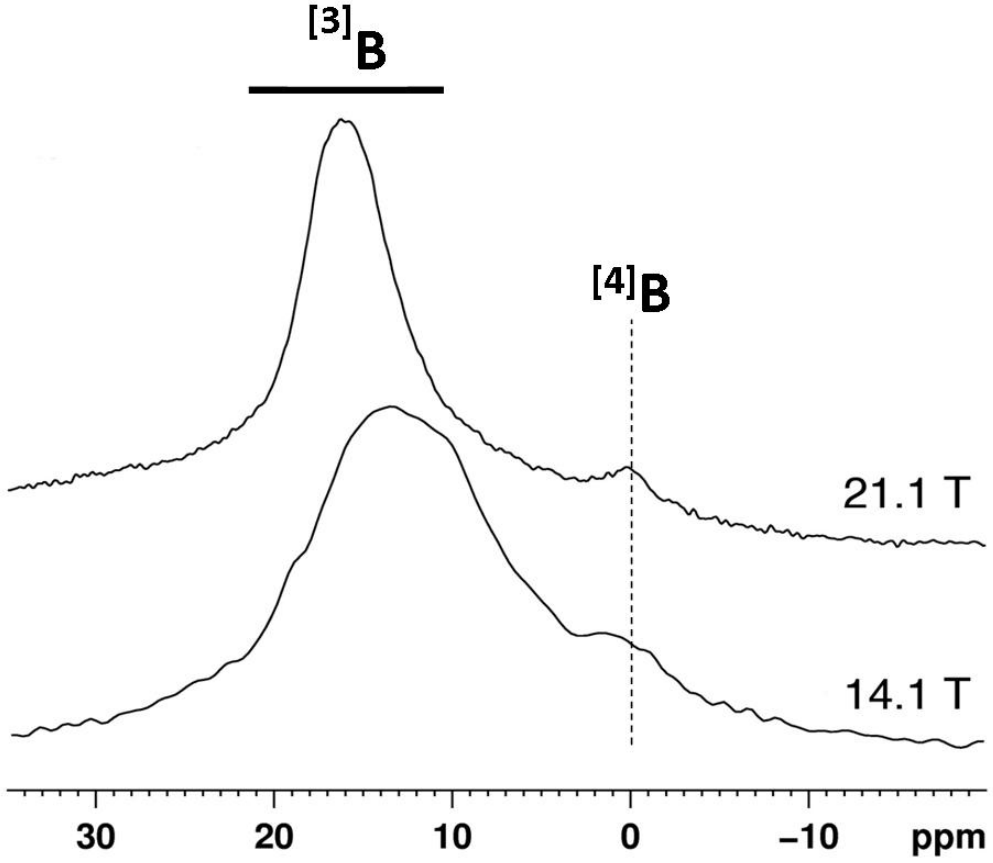

Figure 5.4 Comparison of ^{11}B MAS NMR spectra of wheatsheaf tourmaline (sample similar to SHW-NMR2, Figure 6.4b) collected at high field (14.1 T) and ultra-high (21 T) field.

TABLE 5.2 CALCULATED PERCENTAGES OF TETRAHEDRAL OCCUPANTS

	Species	$^{[4]}$B (*apfu*)*	$^{[4]}$Al (*apfu*)†
AT6	Elbaite	<0.03	<0.08
AT7	Liddicoatite	<0.03	<0.07
AT9	"Fluor-elbaite"	0.06	0.20
AT10	Elbaite	0.03	0.10
AT13	Dravite	–	0.10
AT14	Olenite	0.45	0.26
AT16	Liddicoatite	0.06	<0.07
AT18	Liddicoatite	0.05	<0.07
AT19	Liddicoatite	0.05	<0.07
AT20	Liddicoatite	<0.03	<0.07
AT21	Liddicoatite	<0.03	tr
AT28	Elbaite	0.12	0.08
AT47	Liddicoatite	0.05	–
AT50	Olenite	0.30	0.13
AT51	Olenite	0.39	0.11
AT52	Elbaite	0.06	0.15
AT53	Uvite	–	0.11
AT54	Elbaite	<0.03	0.18
AT55	Dravite	–	0.09
AT56	Elbaite	0.12	–
AT57	Uvite	–	tr
AT58	Dravite	–	<0.06
AT59	Uvite	–	0.28
AT60	Uvite	–	0.45
AT61	Uvite	–	0.18
AT63	Dravite	–	0.19
AT65	Elbaite	–	tr
AT67	Uvite	–	0.11
AT68	Uvite	–	0.25
AT70	Mg-foitite	–	<0.07
AT72	Dravite	–	0.07
AT73(SHM1)	Elbaite	0.13	<0.08
AT73(SHM2)	Elbaite	0.13	<0.08
AT75(SHW1)	Elbaite	0.19	–
AT75(SHW2)	Elbaite	0.23	0.34

* simulation using STARS;
† peak-fitting.

and $^{[4]}$B signals. However, overlap with an intense broad signal arising from boron-nitride components in the probe reduced the accuracy of the quantities obtained.

5.6 ^{27}Al MAS NMR

Typical examples of ^{27}Al MAS NMR spectra of tourmalines with very low paramagnetic constituents are shown in Figure 5.5. All spectra show a very strong peak close to 0 ppm, characteristic of $^{[6]}$Al, as expected given that Al completely occupies the [6]-coordinated *Z*-site in all tourmalines in Figure 5.5. Most spectra show a weak peak at ~65 - 80 ppm, characteristic of $^{[4]}$Al, whereas the spectrum of a liddicoatite (Figure 5.5d) shows no such signal, indicating that there is no $^{[4]}$Al present in this tourmaline.

5.7 $^{[4]}$Al IN TOURMALINE

The spectral range of signals from $^{[4]}$Al in several samples is shown enlarged in Figure 5.6. It is apparent that there is significant variation in peak shape and position. In the tourmaline structure, the *T*-tetrahedron shares corners with one *Y*-octahedron and two *Z*-octahedra, and the two additional anions link to the *X*-cation (Figure 5.7). As ^{27}Al MAS NMR is sensitive to small differences in local atomic arrangement (Klinowski *et al.* 1987), it should be possible to detect the difference between $^{[4]}$Al in dravite and uvite, in which the *Z*-site is occupied by Al and Mg and the *Y*-site is occupied by Mg, and elbaite and liddicoatite, in which the *Z*-site is occupied only by Al, and the *Y*-site is occupied by Al and Li. This is

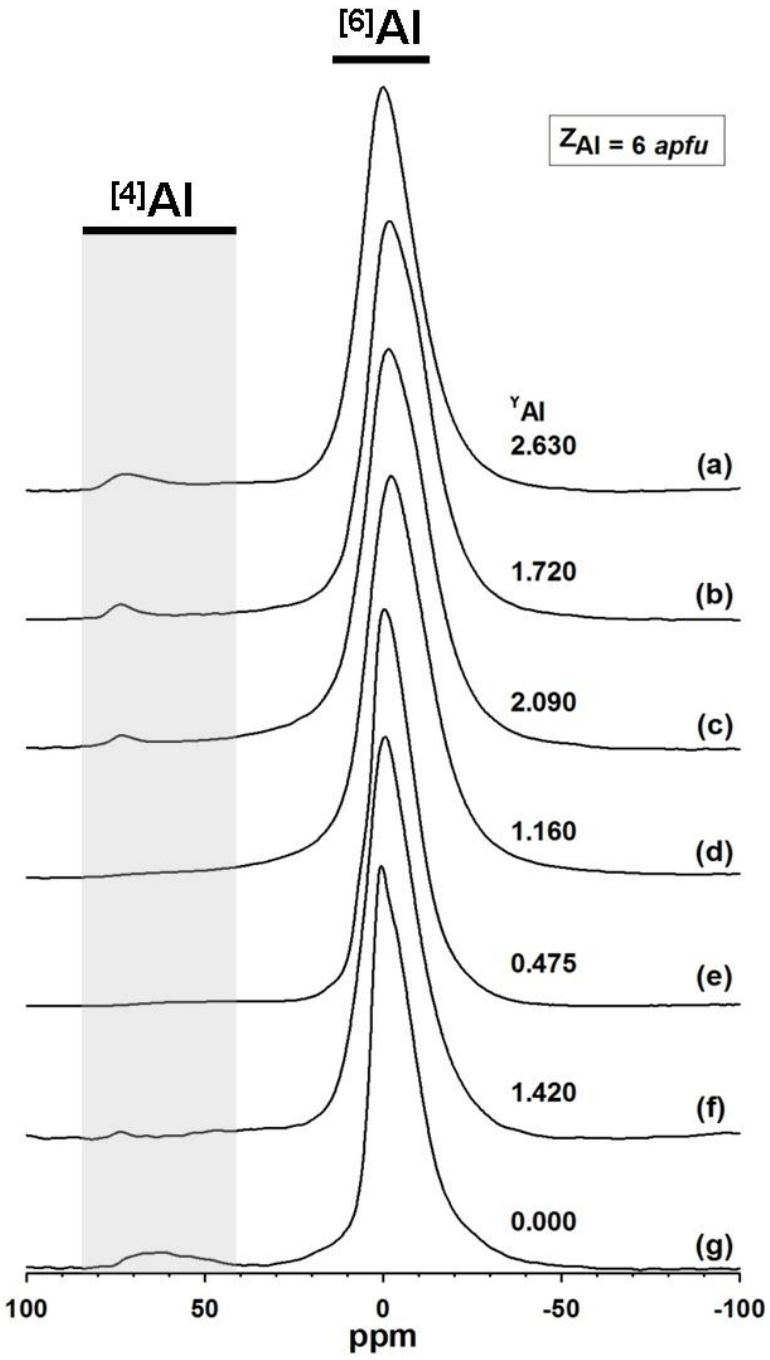

Figure 5.5 Selected ^{27}Al MAS NMR spectra: (a) olenite (AT14), (b) “fluor-elbaite” (AT9), (c) elbaite (AT10), (d) liddicoatite (AT20), (e) dravite (AT72), (f) magnesiofoitite (AT70), (g) uvite (AT61); the regions characteristic of $^{[4]}$Al and $^{[6]}$Al are marked. All spectra are scaled to the same height to facilitate comparison. Note: for (g), Z = ($Al_{5.5}Mg_{0.5}$).

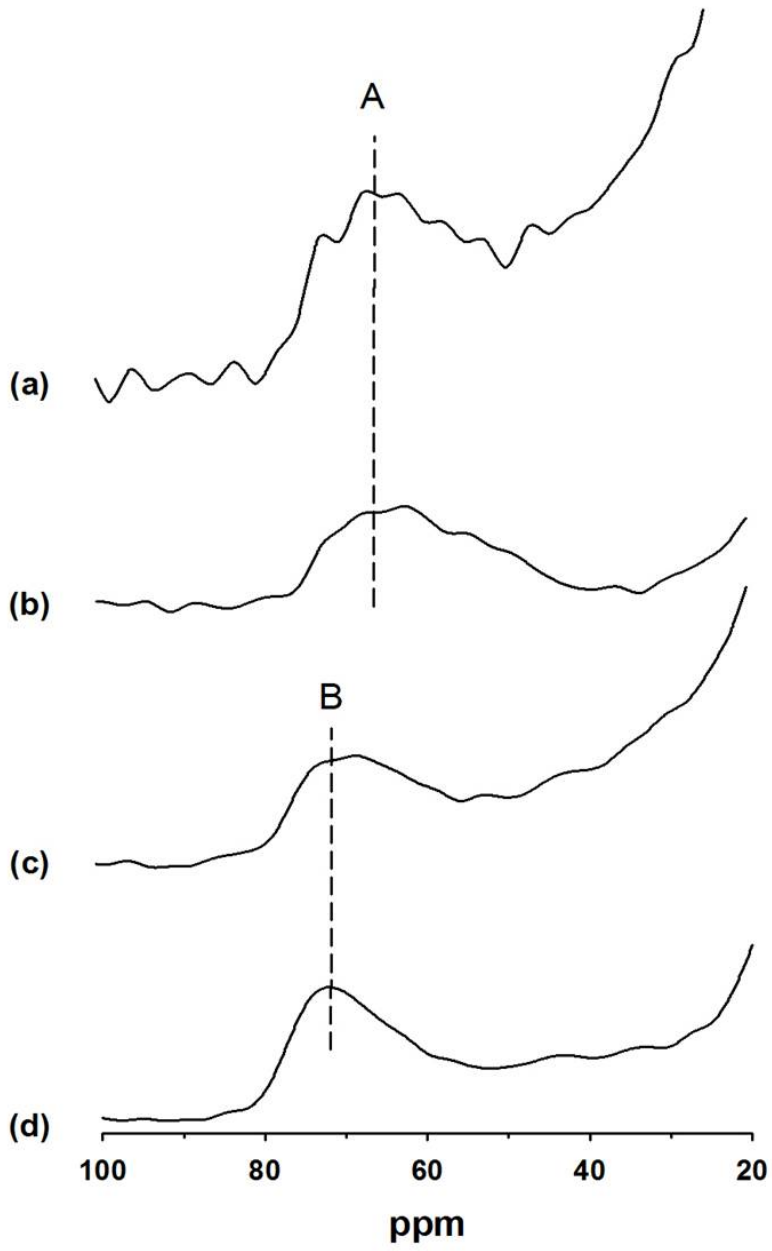

Figure 5.6 ^{27}Al MAS NMR spectra showing the $^{[4]}$Al region in (a) uvite (AT57), (b) uvite (AT60), (c) elbaite (AT54), and (d) olenite (AT14). The lines A and B are drawn to emphasize the difference in position of the peaks in the spectra.

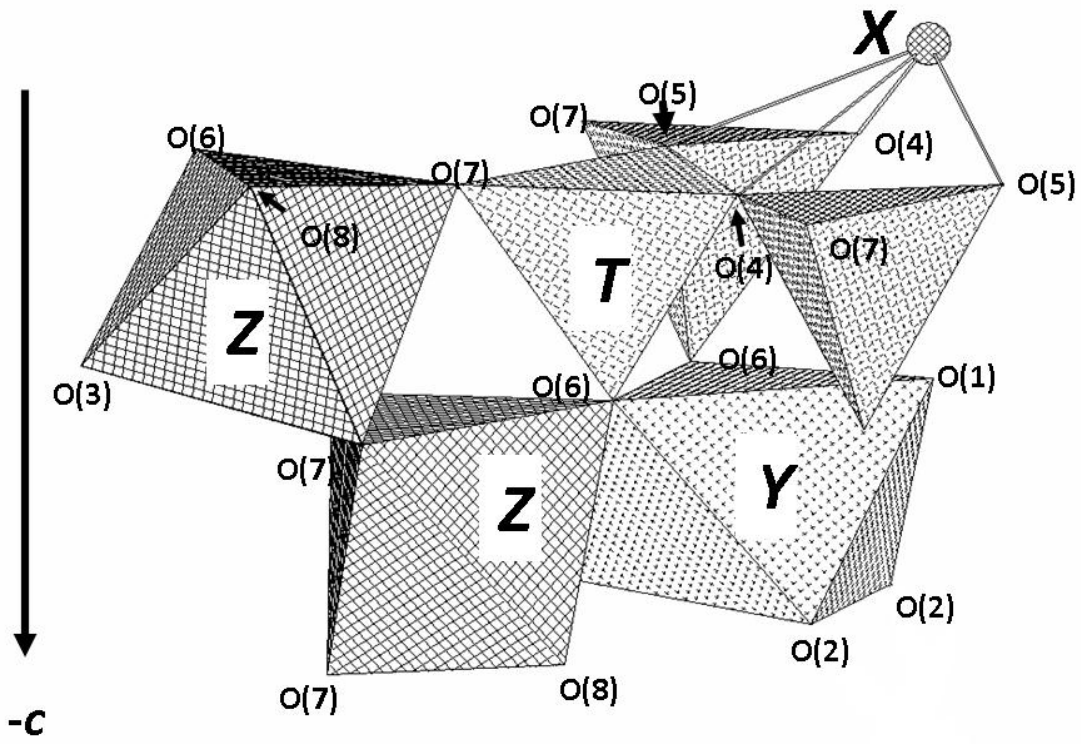

Figure 5.7 Local environment around the *T*-site in tourmaline; *Z*-octahedron = orthogonal cross-hatched pattern, *Y*-octahedron = crosses, and *T*-tetrahedra = decorated square net.

indeed the case: for tourmaline in which $Y_3 = Mg_3$, the $^{[4]}$Al peak is in the range 62 - 64 ppm, whereas for tourmaline in which $Y = (Al, Li)_3$, the $^{[4]}$Al peak occurs in the range 65 - 70 ppm (Figure 5.6).

5.8 $^{[6]}$Al IN TOURMALINE

In tourmaline, we expect signals for $^{[6]}$Al from ^{Y}Al and ^{Z}Al. The ^{27}Al MAS NMR spectrum of transition-metal-free uvite (AT61) is shown in Figure 5.5g. MacDonald & Hawthorne (1995a) investigated this sample, as well as several other uvite samples, by crystal-structure refinement and electron-microprobe analysis. Site assignments are in accord with the variation in bond lengths, indicating that $^{[6]}$Al occurs only at the *Z*-site, and Mg occupies both the *Y*-site and the *Z*-site. Given that Al is minimally disordered in this structure, only a single prominent $^{[6]}$Al peak should be observed in the ^{27}Al MAS NMR spectrum, and in accord with this pattern of order, AT61 shows the smallest peakwidth of all the spectra in Figure 5.5.

The spectra in Figure 5.5 show a subtle variation in the profile of the envelope centered at 0 ppm. Some peaks (such as g) are narrow and asymmetric, whereas other peaks are broader and symmetric. To the right of each spectrum is shown the amount of ^{Y}Al in that particular tourmaline; values range from 0.00 to 2.63 *apfu*. As the *Z*-site is completely filled with Al in all the tourmalines involved in Figure 5.5 [with the expection of g, which contains a small amount of ^{Z}Mg, $Z = (Al_{5.5}Mg_{0.5})$], we must conclude that the width of the peak centered on 0 ppm increases with increasing Al content of the *Y*-site. There

are two possible causes for this: (1) the envelope centered on 0 ppm contains two discrete peaks with slightly different values of chemical shift; (2) there is increasing quadrupolar broadening with increasing Al content of the *Y*-site. It is not possible to distinguish between these two possibilities here, but it is probable that both contribute to the increasing peak width in Figure 5.5.

5.9 THE EFFECT OF PARAMAGNETIC CONSTITUENTS

Figure 5.8 compares the ^{27}Al and ^{11}B MAS NMR spectra of elbaite-liddicoatite with different contents of paramagnetic constituents (*i.e.*, Fe^{2+} + Mn^{2+} = 0.01 - 0.30 *apfu*; Appendix A.4.2). Cursory inspection of these spectra indicates that increasing amounts of paramagnetic constituents result in dramatic changes to the spectral intensity. The integrated peak intensities of the spectra (which were all collected under identical experimental conditions on weighed amounts of sample) diminish dramatically with the incorporation of paramagnetic components in the tourmaline. Inspection of Figure 5.9 suggests that the response of the ^{27}Al and ^{11}B spectra to paramagnetic broadening is the same, and this is confirmed by comparison of the relative intensities of the different spectra in each sample (Figure 5.9); the data scatter closely about the 1:1 line.

5.10 OCCURRENCE OF TETRAHEDRALLY COORDINATED CONSTITUENTS IN TOURMALINE

The quantitative results of spectral integrations (for $^{[4]}$Al) and simulations (for $^{[4]}$B) are summarized in Table 5.2. In Table 5.1, the tourmalines are

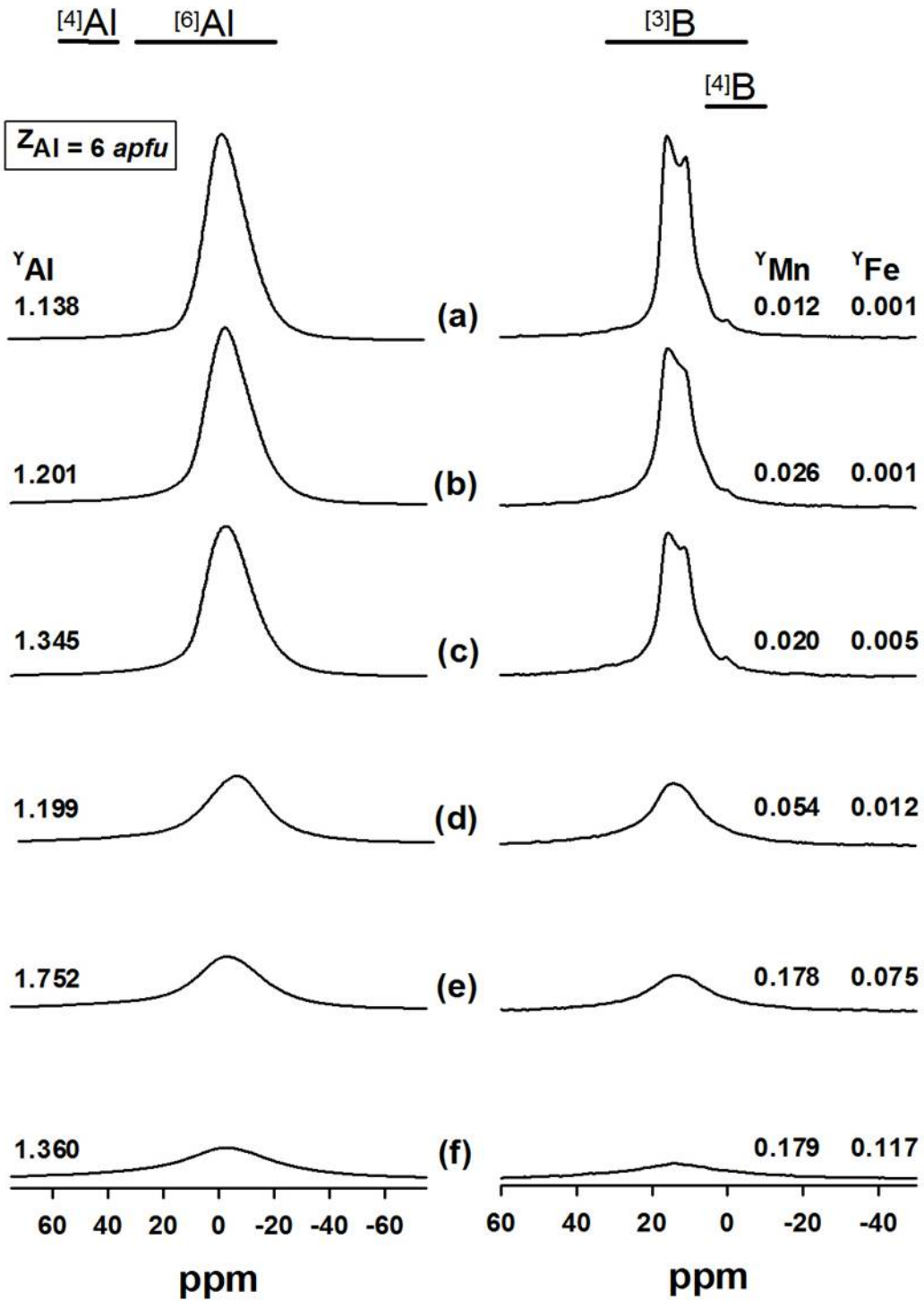

Figure 5.8 ^{27}Al and ^{11}B MAS NMR spectra of elbaite-liddicoatite with differing contents of paramagnetic constituents; (a) AT21; (b) AT18; (c) AT16; (d) AT23; (e) AT48; (f) AT17. All spectra are on the same vertical scale. All values have units of *apfu*.

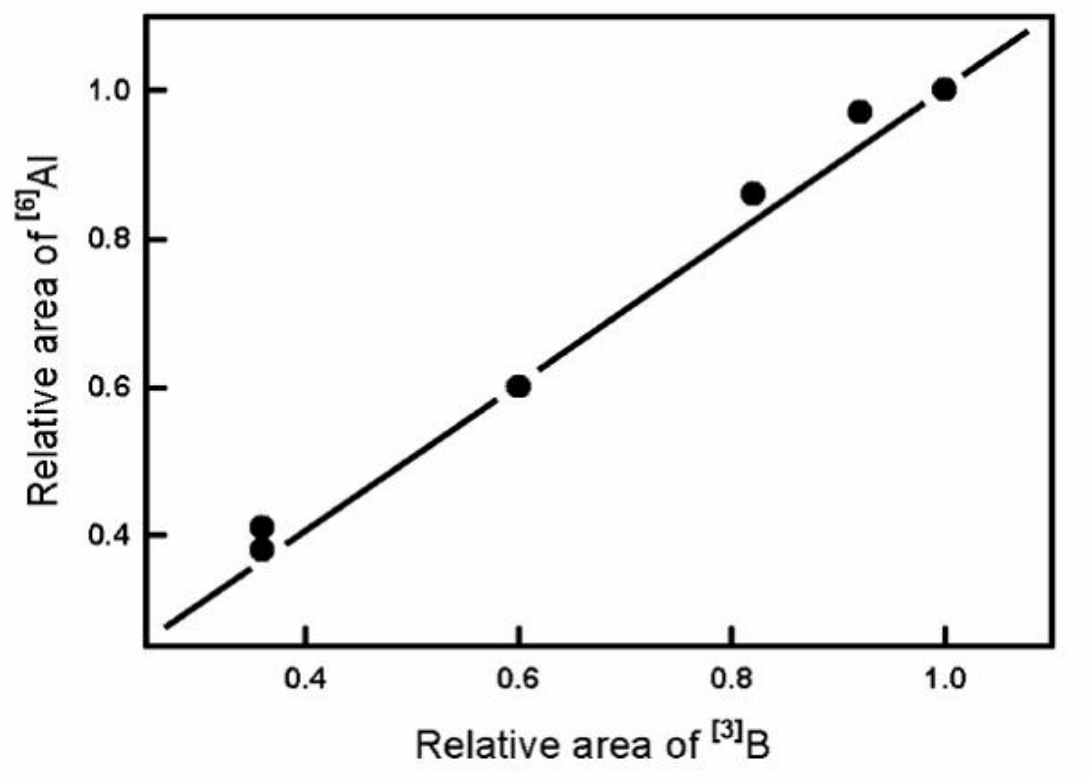

Figure 5.9 Comparison of the relative areas of the ^{27}Al and ^{11}B MAS spectra of elbaite-liddicoatite shown in Figure 5.8. The data scatter about the 1:1 line, indicating that they are equally affected by paramagnetic quenching.

separated into four groups on the basis of the *T*-site species present: (1) T = Si_6 *apfu*; (2) T = $(Si + B)_6$ *apfu*; (3) T = $(Si + Al)_6$ *apfu*; (4) T = $(Si + B + Al)_6$ *apfu*. Upon inspection of Table 5.1, it is immediately apparent that the tetrahedrally coordinated constituents of tourmaline are more variable than was previously realized. Of the 50 individual samples investigated, 8 have T = Si_6 *apfu*, 3 have T = $(Si + B)_6$ *apfu*; 14 have T = $(Si + Al)_6$ *apfu*; 18 have T = $(Si + B + Al)_6$ *apfu*; and seven had too high a content of paramagnetic species (and hence rather degraded spectra) to reliably detect minor Al and/or B (Table 5.1).

There is no clear-cut correspondence between the species of tourmaline and whether $^{[4]}B$ or $^{[4]}Al$ are present in the structure. Of course, sufficient samples for some compositions are lacking (*e.g.*, magnesiofoitite) to state definitively that no pattern exists. Only in species where the *Y*-site is dominated by Mg (*i.e.*, dravite, uvite and magnesiofoitite), is $^{[4]}Al$ consistently present and $^{[4]}B$ consistently absent (and this is only for 3 samples). Within the elbaite-liddicoatite series, there seems to be no method of predicting the type of *T*-site occupancy, which is quite variable: T = $(Si, B)_6$, or T = $(Si, Al, B)_6$, but not T = $(Si, Al)_6$ *apfu*.

5.11 LIMITS OF DETECTION OF $^{[4]}B$ AND $^{[4]}Al$ BY MAS NMR

MAS NMR is clearly very sensitive to the presence of small amounts of $^{[4]}B$ and $^{[4]}Al$ in tourmalines. The degradation of the spectral quality resulting from the presence of paramagnetic elements, however, has an adverse effect on the limits of detection for [4]-coordinate species. MAS NMR spectra collected on the Madagascar liddicoatite (Figure 3.1) show no evidence for the presence of

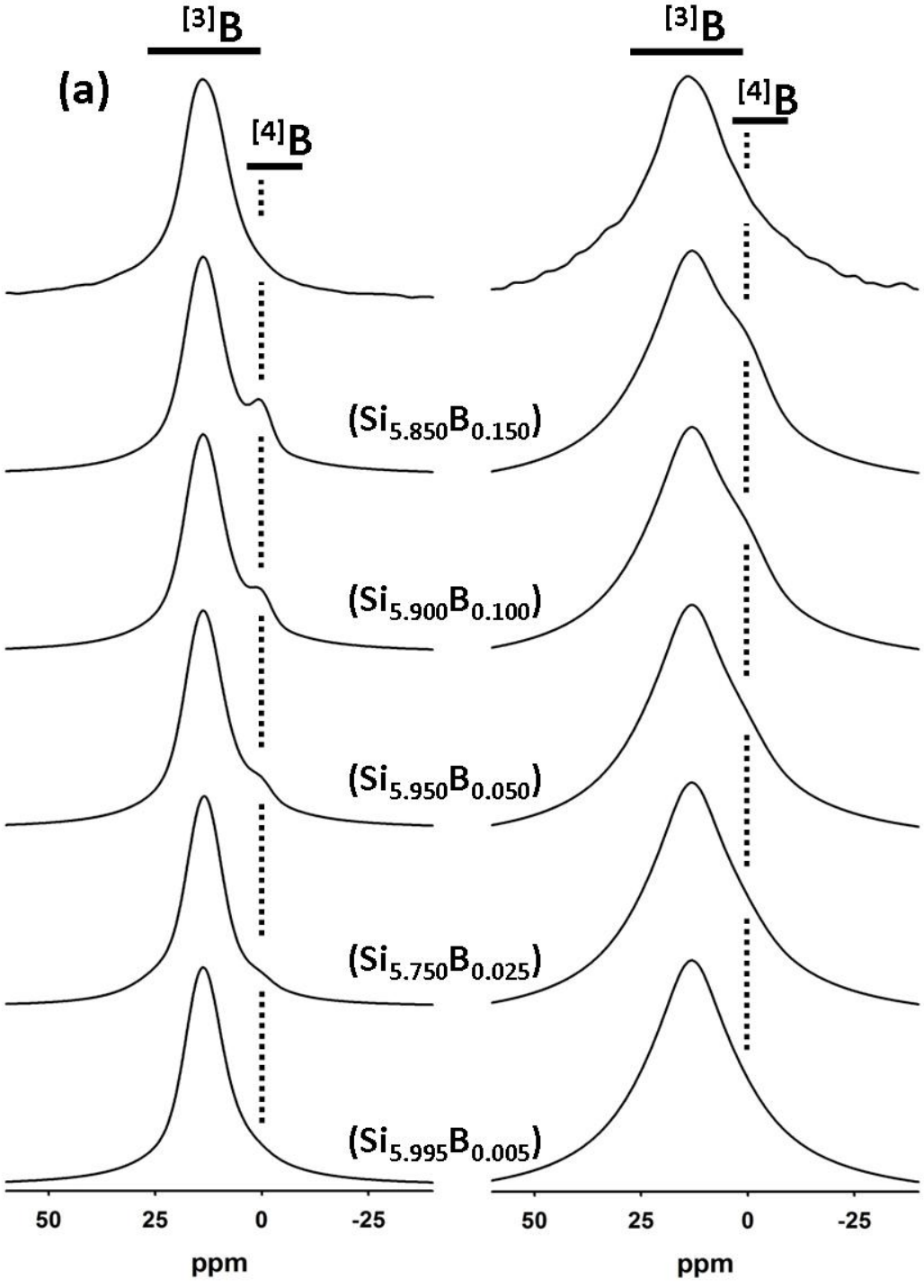

Figure 5.10 ^{11}B and ^{27}Al MAS NMR spectra (top) of Madagascar liddicoatite samples NMR1 and NMR4 (see Figures 4.1, 6.3 and 6.7) with five additional simulated peaks added at the positions for (a) $^{[4]}B$ (~0 ppm) and (b) $^{[4]}Al$ (~70 ppm) for various contents of $^{[4]}B$ and $^{[4]}Al$ in *apfu* (indicated on the figure).

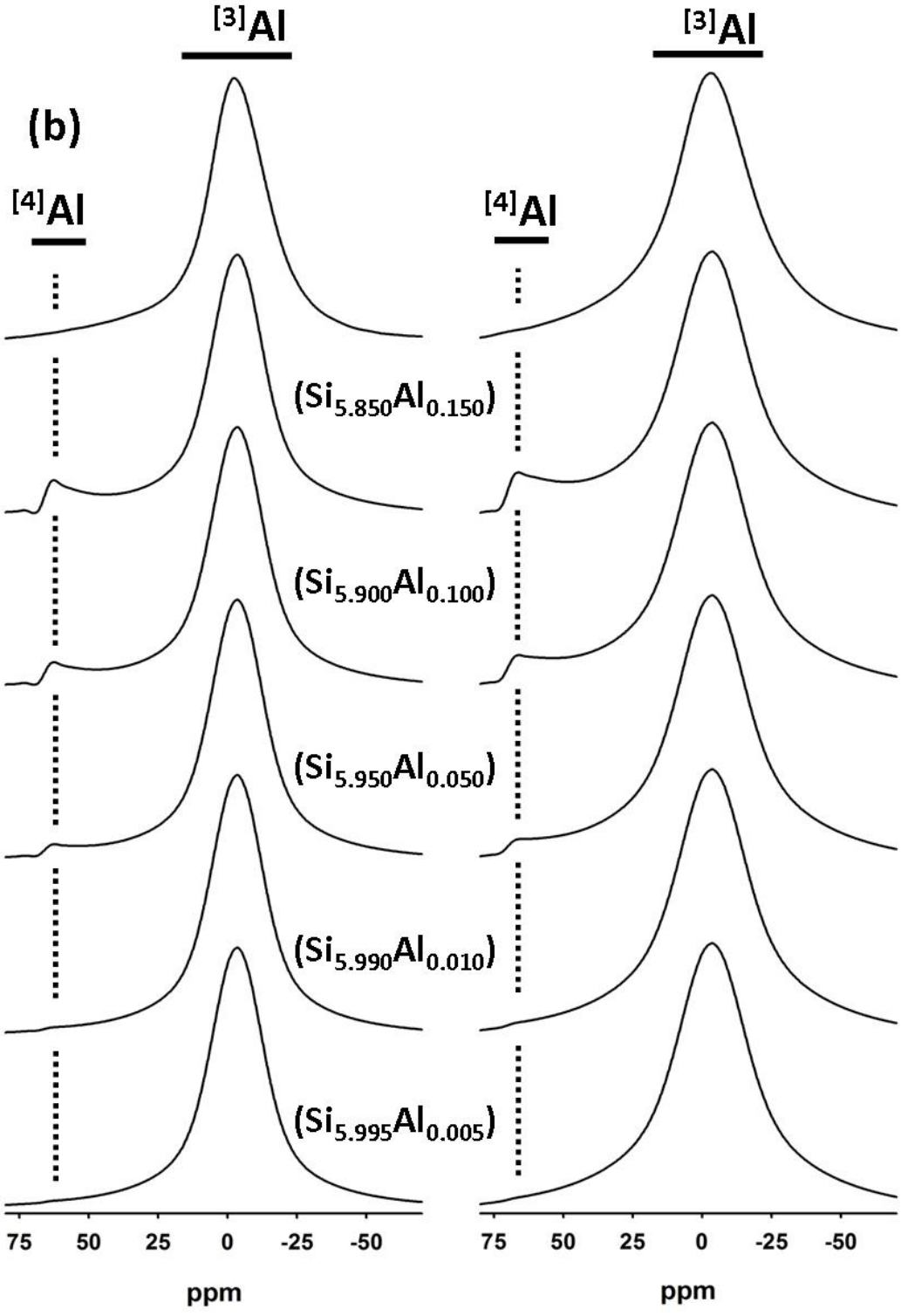
(b)
[3]Al
[4]Al
[3]Al
[4]Al
(Si5.850Al0.150)
(Si5.900Al0.100)
(Si5.950Al0.050)
(Si5.990Al0.010)
(Si5.995Al0.005)
75
50
25
0
-25
-50
ppm
75
50
25
0
-25
-50
ppm

tetrahedrally-coordinated Al or B (Figure 6.3, 6.7 and 5.10), however, extensive EMPA data collected throughout the sample (nearly 500 data points; see discussion in Chapter 7) show that <Si> = 5.950 *apfu*, suggesting the possible presence of $^{[4]}$Al or $^{[4]}$B in quantities not exceeding the limits of detection by MAS NMR.

This prompted an investigation into the limits of detectibility of [4]-coordinated B and Al in tourmaline by ^{11}B and ^{27}Al MAS NMR by simulation. The two spectra with the least and greatest widths collected on the Madagascar liddicoatite were selected (in order to accommodate the peak broadening resulting from the different amounts of paramagnetic constituents) and component peaks at 0 and 70 ppm corresponding to [4]-coordinated B and Al in tourmaline were added with relative intensities corresponding to a range of amounts of [4]-coordinated B and Al from 0.150 to 0.005 *apfu*. The widths of the inserted peaks were calculated in the following manner. The ratios of the widths of the $^{[3]}$B and $^{[4]}$B peaks and the $^{[4]}$Al and $^{[6]}$Al peaks observed in spectra shown in Appendix A.6 were used to calculate the widths of the $^{[4]}$B and $^{[4]}$Al peaks in the simulated spectra. The results are shown in Figure 5.10; peaks corresponding to [4]-coordinated B and Al are discernable down to $^{[4]}$B and $^{[4]}$Al contents of 0.02 and 0.01 *apfu*, respectively, for low contents of paramagnetic ions (<0.04 *apfu*) and 0.08 and 0.01 *apfu*, respectively, for slightly higher contents (~0.12 *apfu*). From this exercise, we may conclude that the limits of detection of $^{[4]}$B is less than 0.02 and $^{[4]}$Al is less than 0.01 *apfu* in the samples examined here.

5.12 REFINEMENT OF *T*-SITE SCATTERING IN TOURMALINE

SREF data were collected on 23 crystals extracted from the Madagascar liddicoatite sample. The electron microprobe analyses on the 23 crystals (Appendix A.4) consistently show 5.90 < Si < 5.97 *apfu* despite the fact that the MAS NMR data conclusively show that Si > 5.98 *apfu* throughout the regions of the crystals sampled by MAS NMR. The *T*-site scattering was refined by considering the *T*-site as occupied by Si and B with the sum of their occupancies constrained to 1. A key issue in such a procedure is the type of scattering factors used for the refinement. In least-squares refinement of a crystal structure, the magnitudes of the calculated structure-factors are scaled to the magnitudes of the observed structure-factors by the scale factor, and there is a relatively strong correlation between the scale factor and the refined site-scattering factors. If all site-scattering factors in a crystal structure are considered as variable, the shift matrix becomes singular and refinement fails. It is necessary that the scattering for some of the atoms in the structure be fixed such that the refined site-scattering values are correctly scaled, and the atoms thus fixed should constitute a significant fraction of the total scattering (preferably significantly greater than 50%) in order that the scaling be reasonably accurate. This scaling is affected by the type of scattering factors used for the atoms (*i.e.*, ionized or neutral). The total scattering for an ionized species is less than that for a neutral species for cations, and the inverse for anions. Hence the type of scattering factors used will affect the total refined site-scattering both directly through the scattering factors of the refined species (usually cations), and indirectly through the scattering

factors of the nonrefined species (commonly anions). This issue was investigated in detail by Cooper *et al.* (2009) for the structure of kornerupine, $XM_9T_5O_{21}$(OH,F) where X = □, Fe^{2+}, Mg; M = Al, Mg, Fe^{2+}, Fe^{3+}; T = Si, Al, B in which the three tetrahedrally coordinated *T*-sites are occupied by Si, Al and B. Using ionized scattering factors, the scattering at the *M*-sites is ~1 *epfu* larger using an ionized scattering factor rather than a neutral scattering factor for oxygen (Figure 5.11a). The site-scattering at the partly occupied *X*-site is in accord with that determined by EMPA and SIMS for refinement with an ionized scattering factor for oxygen (Figure 5.11b), whereas the values determined using a neutral scattering factor for oxygen deviate from the values determined by EMPA-SIMS by ~1.1 *epfu*. These results suggest that the refined values of B at the *T*-site in tourmaline should be sensitive to the type of scattering factors used. Here, the effects of the use of different scattering curves on the refinement of site-scattering values in tourmaline are investigated, focusing on the occurrence of B at the *T*-site.

All structures of liddicoatite were refined in four different ways under the constraint that Si + $^{[4]}$B = 6 *apfu*, and different values were obtained for the *T*-site occupancy of $^{[4]}$B for each different set of scattering factors used. The results are summarized in Figure 5.12. Refinement with ionized scattering-curves for O and Si failed because refinement converged toward negative occupancy values for $^{[4]}$B. In this case, the occupancy of the *T*-site is set to Si only and the occupancy is refined, producing values > 1. The cations as Si and B were then calculated under the constraint that Si + B = 1, arriving at small negative occupancy values for $^{[4]}$B. The grand mean $^{[4]}$B content of the *T*-site varies from -0.04 *apfu* for

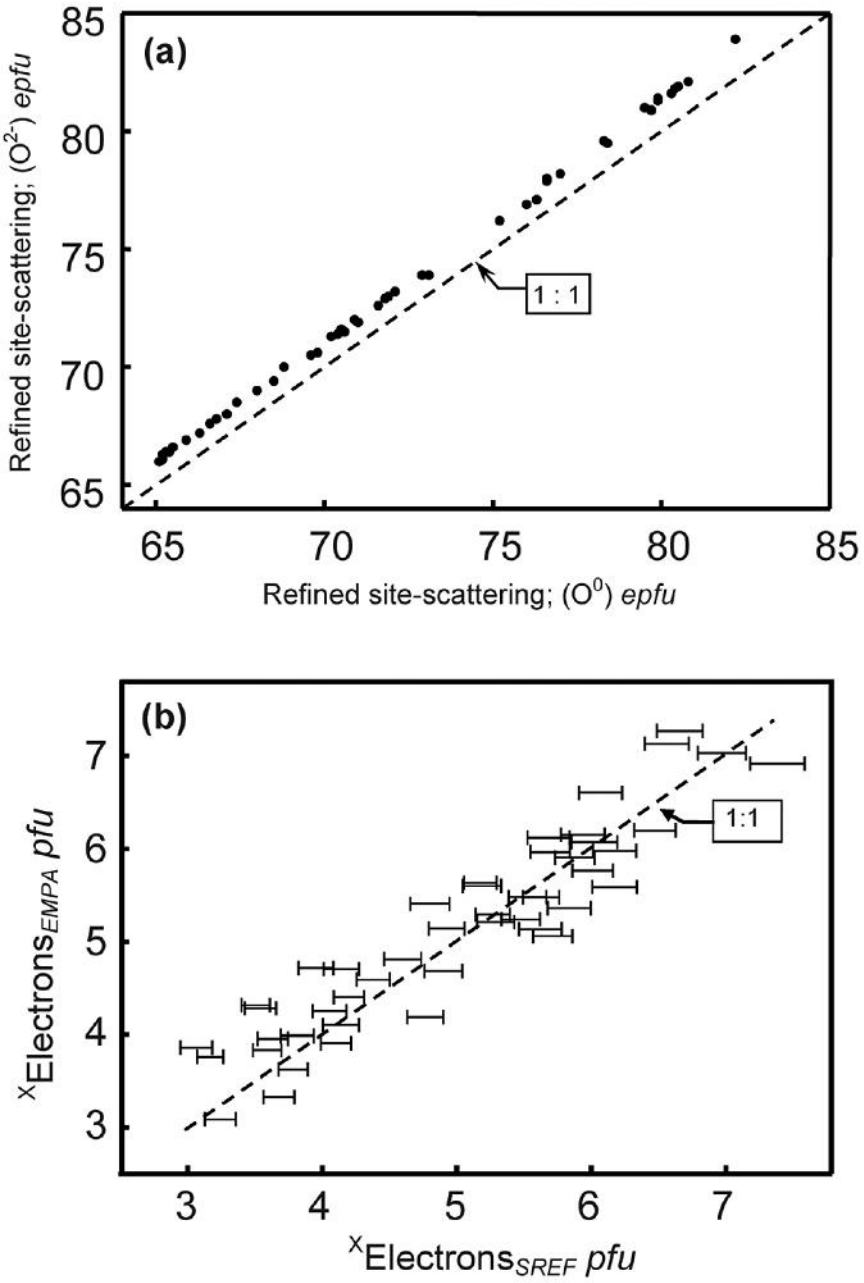

Figure 5.11 Results for kornerupine; (a) comparison of the site-scattering at the [*X* + *M*(1,2,4)] sites refined using ionized (O^{2-}) and neutral (O^{o}) X-ray scattering factors; (b) comparison of the *X*-site scattering derived by crystal-structure refinement (SREF) using an ionized scattering-factor for oxygen and the effective scattering calculated from the unit formula derived from the electron-microprobe analysis; the dashed line indicates the 1:1 relation, and the lines through the data points represent ±1 standard deviation in this and the following figures. Modified from Cooper *et al.* (2009).

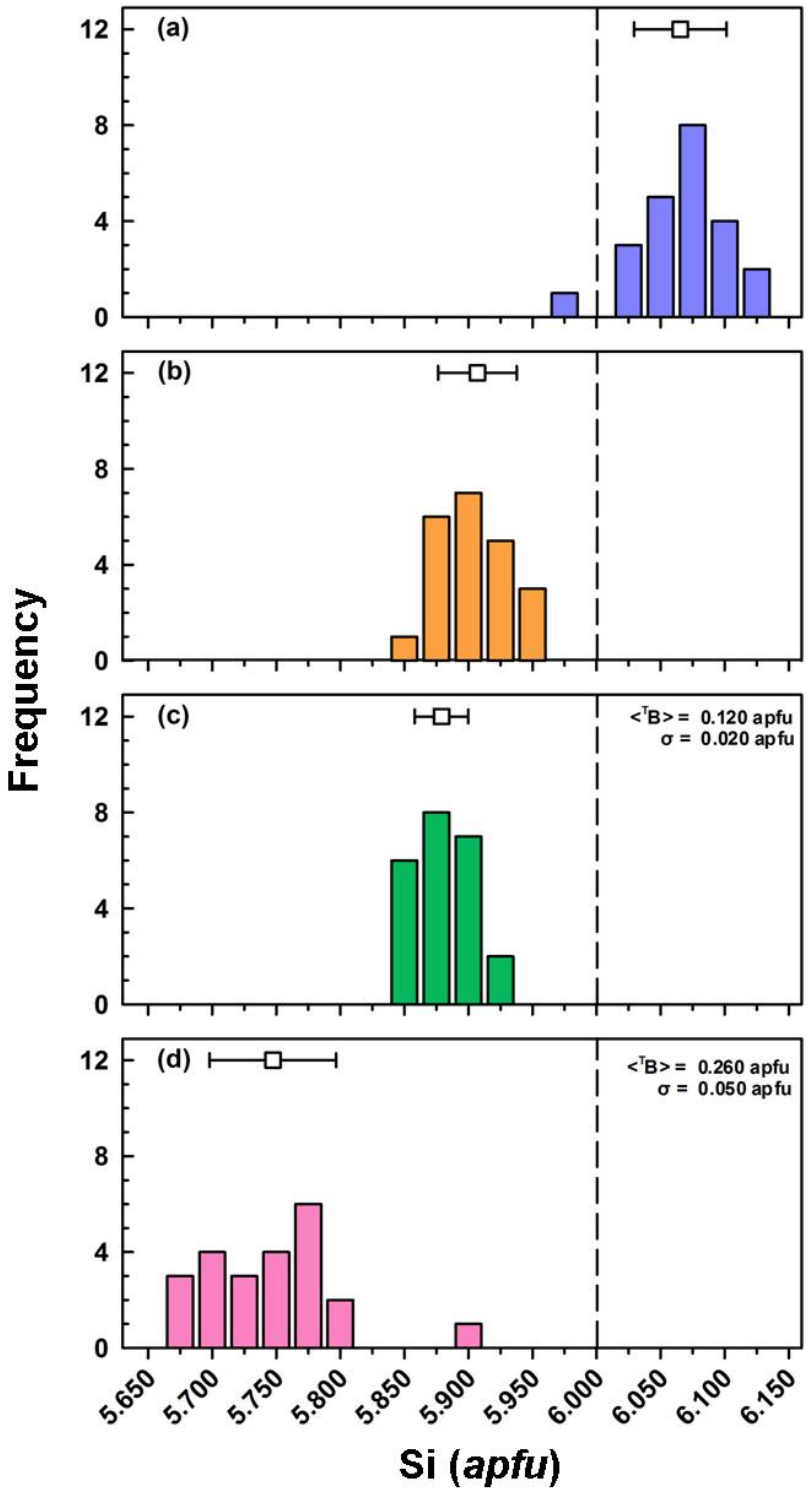

Figure 5.12 Variation in refined site-population for the *T*-site in the liddicoatite fragments of this work using the following scattering factors: (a) Si^{4+} and O^{2-}; (b) Si^{4+} and O^{0}; (c) Si^{0} and O^{2-}; (d) Si^{0} and O^{0}.

ionized scattering-curves for O and Si to 0.25 *apfu* for neutral scattering-curves for O and Si. No $^{[4]}$B was detected in the Madagascar liddicoatite samples examined here by ^{11}B MAS NMR, and the simulation results of Figure 5.10 suggests limits of detection of the order of 0.02 *apfu*. This result is in accord with our refinement results using ionized scattering-curves for O or Si (but not both together), suggesting that use of these curves is giving more accurate results for *T*-site populations than refinement with neutral scattering factors. Moreover, our refinements using neutral scattering factors for O and Si gave $^{[4]}$B *T*-site populations of ~0.25 *apfu*, values which should easily be observed by ^{11}B MAS NMR.

5.13 GENERAL SUMMARY ON *T*-SITE CHARACTERIZATION

The presence of small amounts (*i.e.*, < 0.1 *apfu* each) of $^{[4]}$Al and $^{[4]}$B appears to be a relatively common feature in natural tourmalines, and the above discussion illustrates that ^{11}B and ^{27}Al MAS NMR can definitively detect (and distinguish between) the two. Site-scattering refinement appears to be potentially sensitive to small amounts of $^{[4]}$B at the *T*-site, but the choice of scattering curve must be carefully considered. Although the limits of detection of $^{[4]}$B and $^{[4]}$Al by MAS NMR in tourmalines with low contents of paramagnetic elements are on the order of 0.01 - 0.03 *apfu*, the presence of even small amounts (Fe + Mn) ~0.1 - 0.15 *apfu* results in severe signal degradation, precluding its use on many natural tourmalines, as the occurrence of Fe (and Mn) is very common.

CHAPTER 6

CRYSTAL CHEMISTRY AND CRYSTAL STRUCTURE

6.1 INTRODUCTION

Forty crystals were extracted from Madagascar liddicoatite (23), wheatsheaf elbaite (8), and mushroom elbaite (9); the approximate locations on each sample are shown in Figure 3.1, for Madagascar liddicoatite, and described in Appendix A.1, for wheatsheaf and mushroom elbaite. The structure and composition of each crystal is fully characterised by 4-circle *X*-ray diffraction and electron-microprobe analysis, respectively. Site occupancies are determined by comparison of site-scattering values (in electrons per formula unit) derived from Site-scattering REFinment (SREF) and the analogous values calculated from the chemical formula derived from electron-microprobe analysis. Extensive ^{11}B and ^{27}Al MAS NMR spectra are collected on material removed from several regions of each sample to identify the presence of $^{[4]}$B and $^{[4]}$Al at the *T*-site. Material was also extracted from regions of the samples with $\sum FeO_x$ > ~1 wt. %, for determination of Fe^{3+}/Fe^{2+} by Mössbauer spectroscopy. Spectroscopic results are used to modify formula calculations and site-scattering-refinement protocols. The data presented in the following three chapters have been discussed in several publications (Lussier *et al.* 2008a,b, 2011a,b,c), each dealing with an individual tourmaline sample. However, the following chapter compares and contrasts crystal-chemical parameters such as site-occupancies and bondlength variations of all 40 structures examined.

6.2 BIAXIAL OPTICS AND SPACE GROUP DETERMINATION

For Madagascar liddicoatite, samples were extracted from the main crystal at four different positions (L-OPT1 to L-OPT4; Figure 3.1) and the 2*V* angles were measured with a spindle stage and the program Excalibr II (Bartelmehs *et al.* 1992). Sample L-OPT1, taken from the purple centre of the crystal, has uniaxial optics (2*V* = 0.0°); samples L-OPT2 and L-OPT3 from the pyramidal zone have 2*V* values of 8(3)° and 18.9(5)°, respectively, and L-OPT4 from the prism zone has a 2*V* value of 20.5(9)°.

X-ray intensity data were collected on L-OPT1-4 (with 2*V* values corresponding to those given above) using an APEX CCD detector. In excess of a hemisphere of data was collected for each crystal in order to test for their diffraction symmetry. The calculated *R*(int) values for L-OPT1-3 with trigonal Laue symmetry are 1.73, 2.41 and 1.99%, respectively, and with monoclinic symmetry are 1.38, 1.88 and 1.67% , an insignificant difference. Shtukenberg *et al*. (2007) found that cation order at the three edge-sharing *Y*-octahedra resulted in poor *R*(int) values about two of the three mirror planes. This issue is tested for L-OPT1-4 crystals: *R*(int) values for groups of reflections directly related by each of the three mirror planes at (*x 2x z*), (*2x x z*) and (*x -x z)* were calculated. The results (Table 6.1) indicate no difference in merge quality for any particular mirror, and all values of *R*(int) for each crystal are < 1% of each other. These results provide no evidence of lower symmetry *in the diffraction data*, and hence all Madagascar liddicoatite structures were refined with *R*3*m* symmetry. Similarly,

TABLE 6.1 CALCULATED R_{int} VALUES* FOR LIDDICOATITE ACROSS *R*3*m* MIRROR PLANES

		x, 2*x*, *z*	2*x*, *x*, *z*	*x*, –*x*, *z*
L-OPT1	R_{int} * (%)	2.57	2.54	2.45
	N	2138	2167	2078
L-OPT2	R_{int}	4.53	4.43	4.51
	N	1991	2076	2006
L-OPT3	R_{int}	3.22	3.08	3.08
	N	2107	2138	2094
L-OPT4	R_{int}	4.32	4.39	4.51
	N	2245	2165	2116
	N	2245	2165	2116

* averages calculated using $\Sigma|F_o^2 - \langle F_o^2 \rangle| / \Sigma |F_o^2|$ on *N* pairs of reflections.

the calculated R(int) values for wheatsheaf and mushroom crystals with trigonal Laue symmetry (where data were collected using the APEX CCD detector) were consistently < 2.75 %, and hence these crystals were also refined with *R*3*m* symmetry.

6.3 DISORDER AT THE O(1)- AND O(2)-SITES

In a totally ordered tourmaline structure described in space group *R*3*m*, the O(1) and O(2) anion sites are located on the 3-fold axis and mirror planes: at crystallographic positions (0, 0, *z*) and (*x*, 2*x*, *z*), respectively. Burns *et al.* (1994) showed that in elbaitic tourmalines, where the *Y*-site is dominated by Mn, Li and Al, the difference in ionic radii ($^{[6]}r$[Mn] = 0.83 Å, $^{[6]}r$[Li] = 0.76 Å, and $^{[6]}r$[Al] = 0.535 Å; Shannon 1976) drives the disordering of the O(1)- and O(2)- sites such that they lie at mirror (*x*, 2*x*, *z*) and general (*x*, *y*, *z*) positions, respectively.

Refining these 40 crystals with O(1) and O(2) constrained to the highest symmetry positions results in equivalent isotropic-displacement factors, U_{eq}, for these anion sites that are larger than those observed for all other anion sites. For all 40 crystals, $<^{O(1)}U_{eq}>$ = 0.0444(4) Å^2 (σ = 0.0124 Å^2; where σ indicates standard deviation calculated from all 40 crystals) and $<^{O(2)}U_{eq}>$ = 0.0165(4) Å^2 (σ = 0.0010 Å^2), whereas the average for all other anions is $<^{O(3\text{-}8)}U_{eq}>$ = 0.0089(3) Å^2 (σ = 0.0019 Å^2), suggestive of positional disorder at these sites.

Difference-Fourier maps were calculated using the XP program in the SHELX 7.1 software package (PC version) for three representative crystals (SHM1, SHW6 and LID7) are shown taken through the O(1)- (Figure 6.1) and

O(2)- (Figure 6.2) sites projected on (001). These were calculated while omitting scattering species from the site of interest, as this minimizes errors due to series termination. Around the O(1) position, the disorder is observed as a delocalization of electron density in the (001) plane, forming a 3-lobed structure along the mirror planes. Around the O(2) position disorder forms an oval structure as the anion displaces from the mirror in the direction of one of the bonding *Y* cations. Figure 6.1 shows that all lobes extend in the direction [*x*, ½*x*], such that the resulting arrangement of *Y*-O(1) bonds is always 2 long and 1 short.

Figures 6.1 and 6.2 show that the amount of disorder at both O(1) and O(2) positions increases proportionally with the abundance of larger cations (Li, Fe, Mn) at the *Y*-site, with SHM1 [Y = $Al_{1.81}Li_{1.12}Mn_{0.07}$] showing virtually no disorder (that can be resolved with MoKα radiation), and LID7 [Y = $Al_{1.22}Li_{1.59}Mn_{0.13}Fe^{2+}_{0.04}$] showing considerable disorder, and SHW6 [Y = $Al_{1.7}Li_{1.3}$] showing intermediate disorder. Refining each crystal a second time, allowing for positional disorder results in lower $<U_{eq}>$ values for O(1) and O(2) of 0.0141(11) Å^2 (σ = 0.0034 Å^2) and 0.0117(7) Å^2 (σ = 0.0125 Å^2), respectively. For all crystals, only values of atom coordinates and $<U_{eq}>$ for O(1) and O(2) positions differed between ordered and disordered refinements. All atom coordinates and mean bondlengths are listed in Appendices A.2 and A.3, respectively. Moreover, Appendix A.1 shows that the disordered models consistently result in a slight lowering of both R_1 and wR_2 values (by an average of 0.2%).

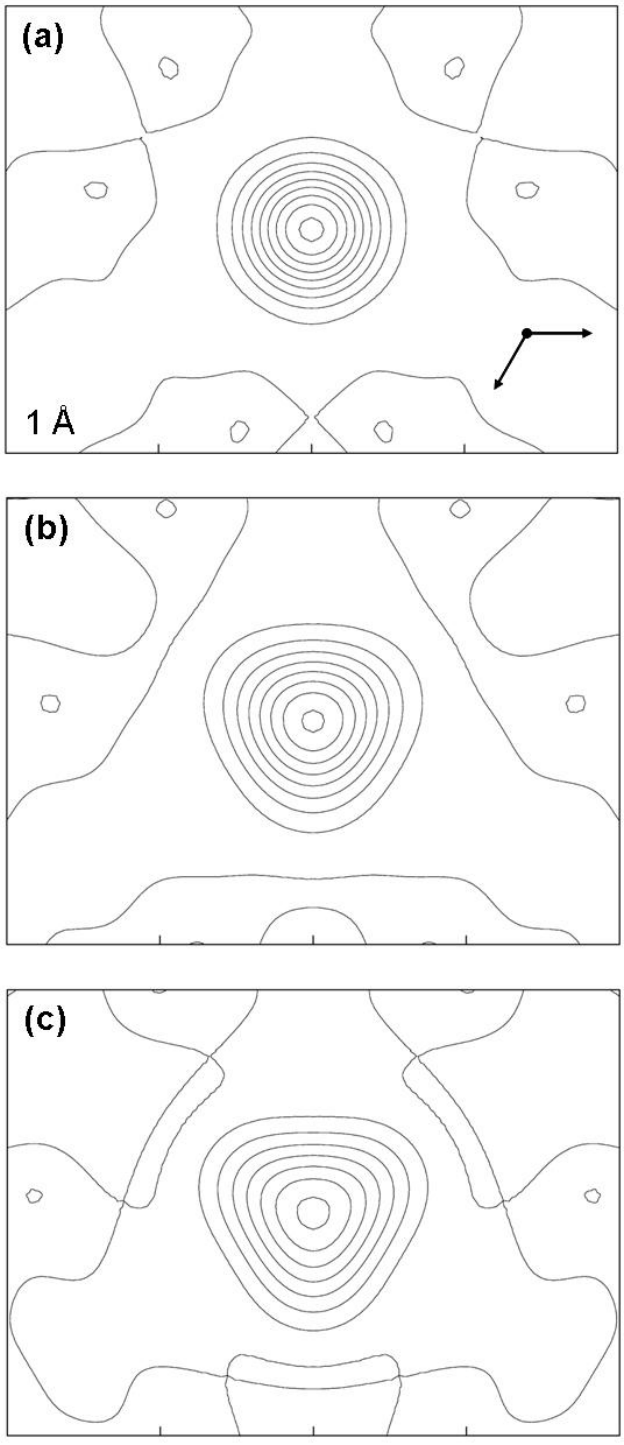

Figure 6.1 Difference-Fourier electron-density maps showing positional disorder of the O(1)-site projected on (001) in samples: (1) SHM1; (b) SHW6; and (c) LID7. Contour interval = 1 *e*/Å3.

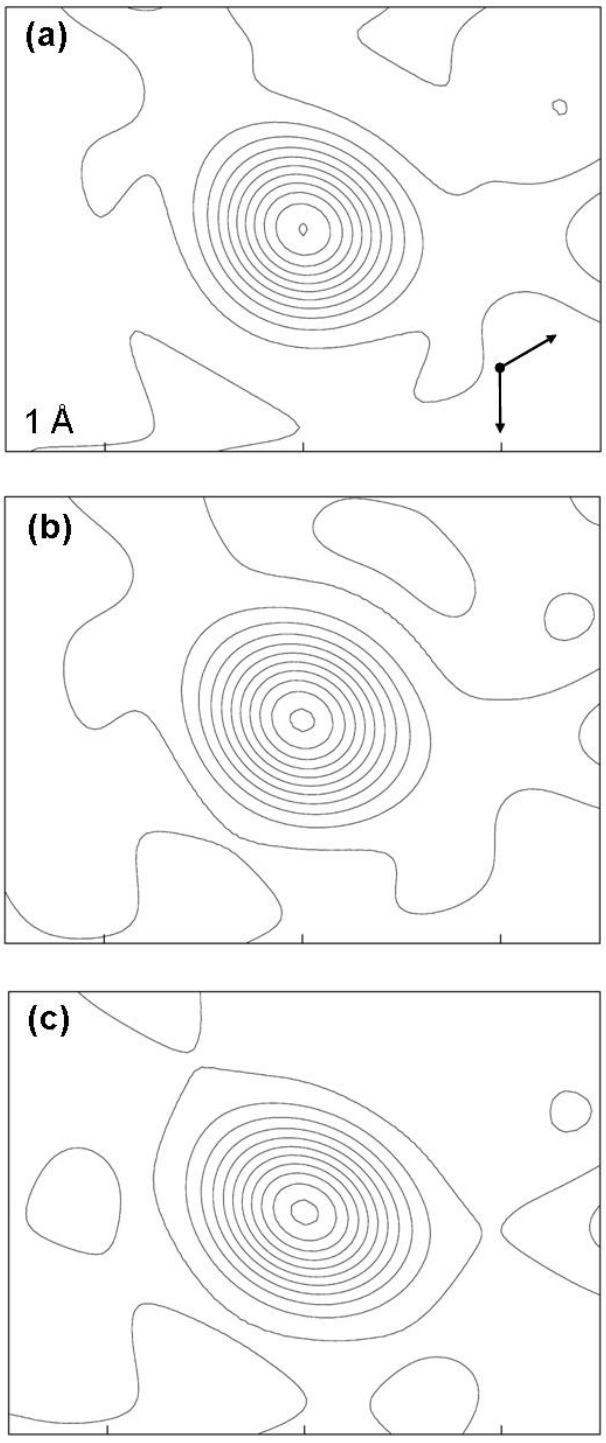

Figure 6.2 Difference-Fourier electron-density maps showing positional disorder of the O(2)-site projected on (001)in samples: (1) SHM1; (b) SHW6; and (c) LID7. Contour interval = 1 *e*/Å3.

6.4 DETERMINATION OF *T*-SITE OCCUPANCY BY MAS NMR

As shown in detail in Chapter 5, ^{11}B and ^{27}Al MAS NMR spectroscopy can identify $^{[4]}$B and $^{[4]}$Al in tourmaline with sufficiently low amounts of paramagnetic elements. For all tourmalines discussed here, regions of the bulk sample, representative of the approximate locations of single crystals, were selected for ^{11}B and ^{27}Al MAS NMR spectroscopy. Pertinent methodological details were discussed in Chapters 4 and 5, and thus the spectral results are presented here.

6.4.1 ^{11}B MAS NMR

The ^{11}B MAS NMR spectra are presented in Figures 6.3 to 6.6. Each spectrum shows a strong peak centered at ~14 ppm and corresponding to $^{[3]}$B (Kroeker & Stebbins 2001). In the four spectra collected on Madagascar liddicoatite (Figure 6.3), only the [3]-coordinate peak is present, and the spectra lack any observable intensity in the regions characteristic of $^{[4]}$B, although there is the suggestion of a shoulder at ~0 ppm in Figure 6.3, which could correspond to ~0.01-0.02 *apfu* $^{[4]}$B, based on the limits of detection calculated in Chapter 5.

The four ^{11}B spectra collected on wheatsheaf tourmaline (Figure 6.4) show a prominent, sharp peak at ~0 ppm, corresponding to $^{[4]}$B. Of the three spectra collected on mushroom elbaite (SHM) (Figure 6.5), two (SHM1 and SHM2) show strong peaks indicating the presence of $^{[4]}$B. The third spectrum (SHM3) has a quantity of paramagnetic elements (Fe + Mn > 1 *apfu*) sufficient to quench any signal from ^{11}B. The spectra in Figure 6.5 are plotted on the same vertical scale

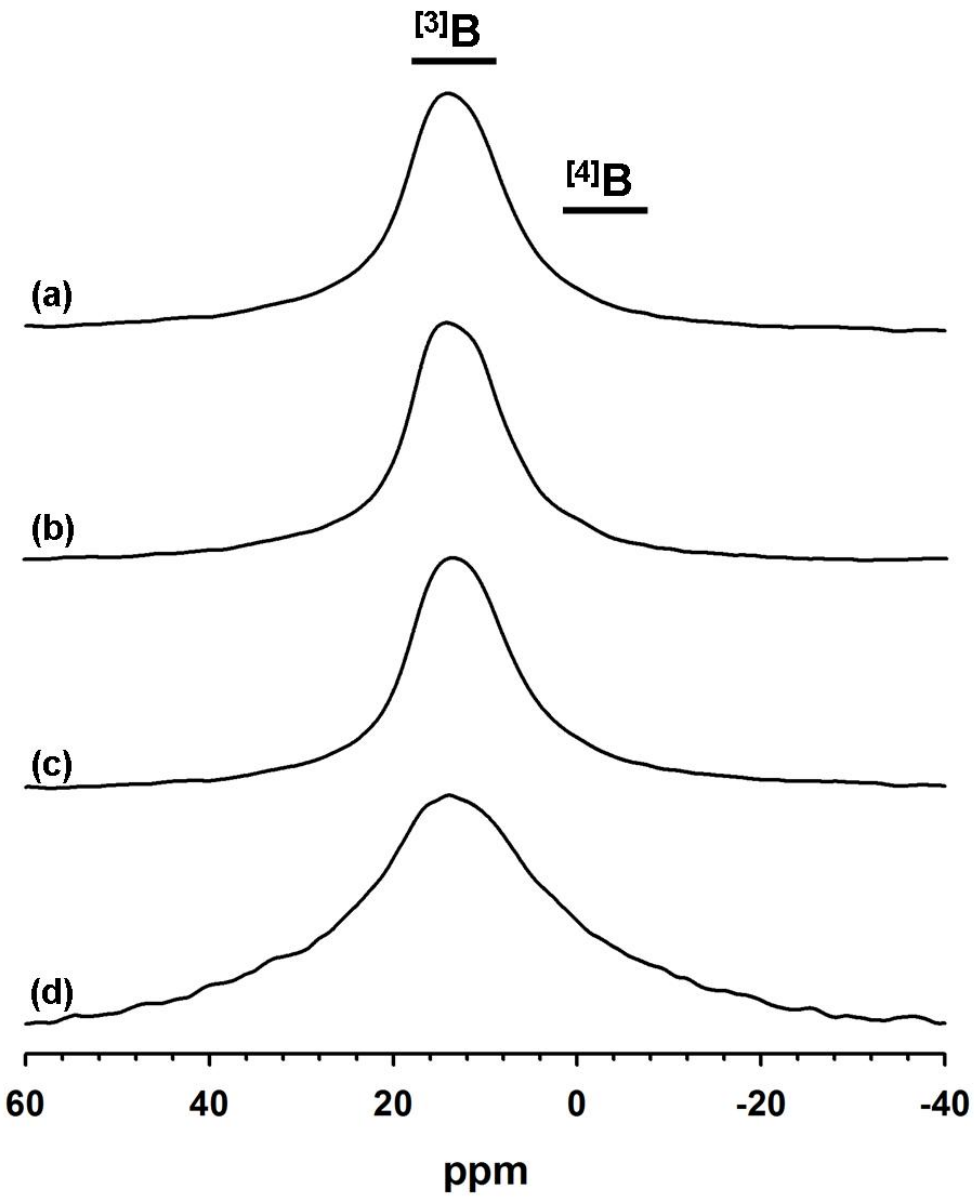

Figure 6.3 ^{11}B MAS NMR spectra of liddicoatite: (a) NMR1; (b) NMR2; (c) NMR3; (d) NMR4 (see Figure 3.1b) .

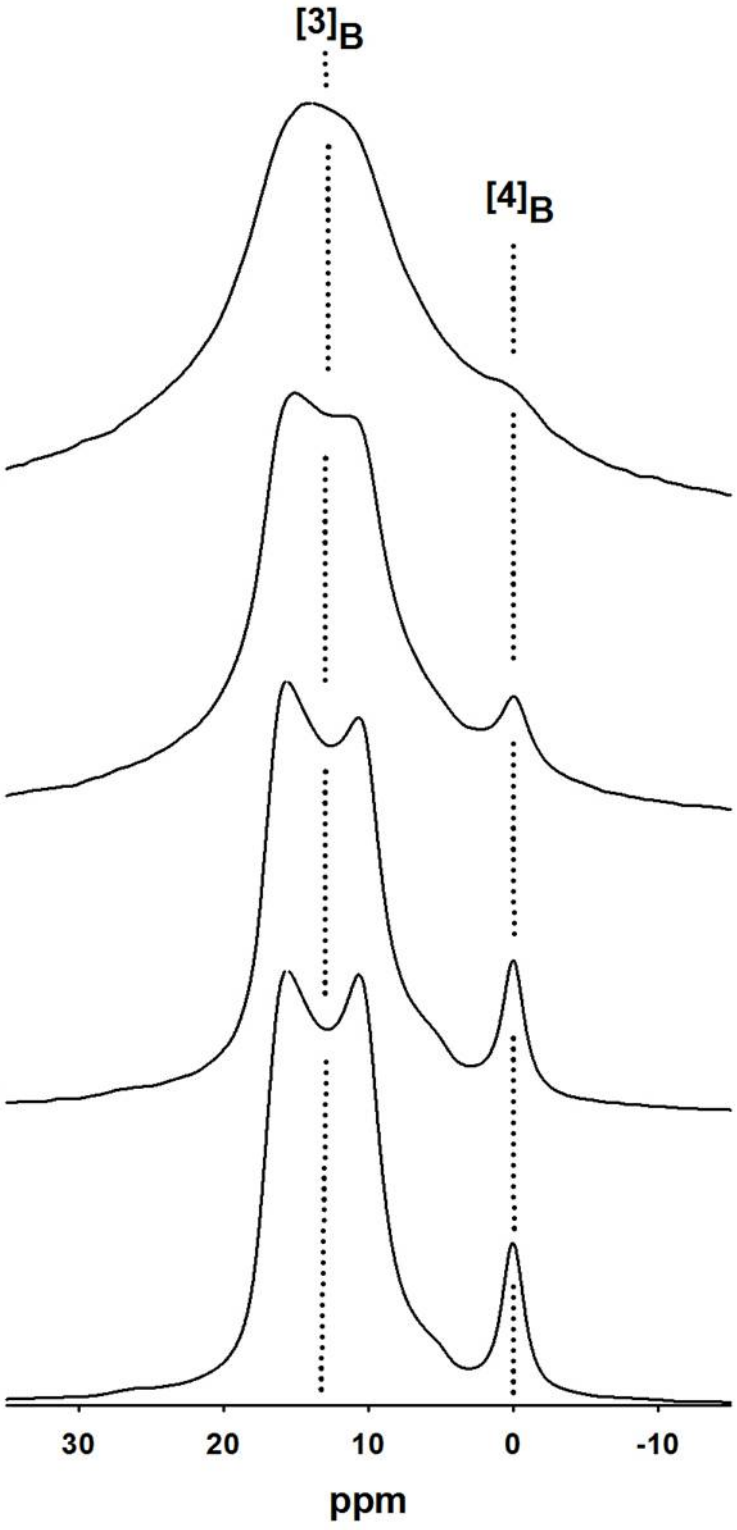

Figure 6.4 ^{11}B MAS NMR spectra of wheatsheaf tourmaline: (a) SHW-NMR1 (purple tip); (b) SHW-NMR2 (purple brown); (c) SHW-NMR3 (white centre); and (d) SHW-NMR4 (red core).

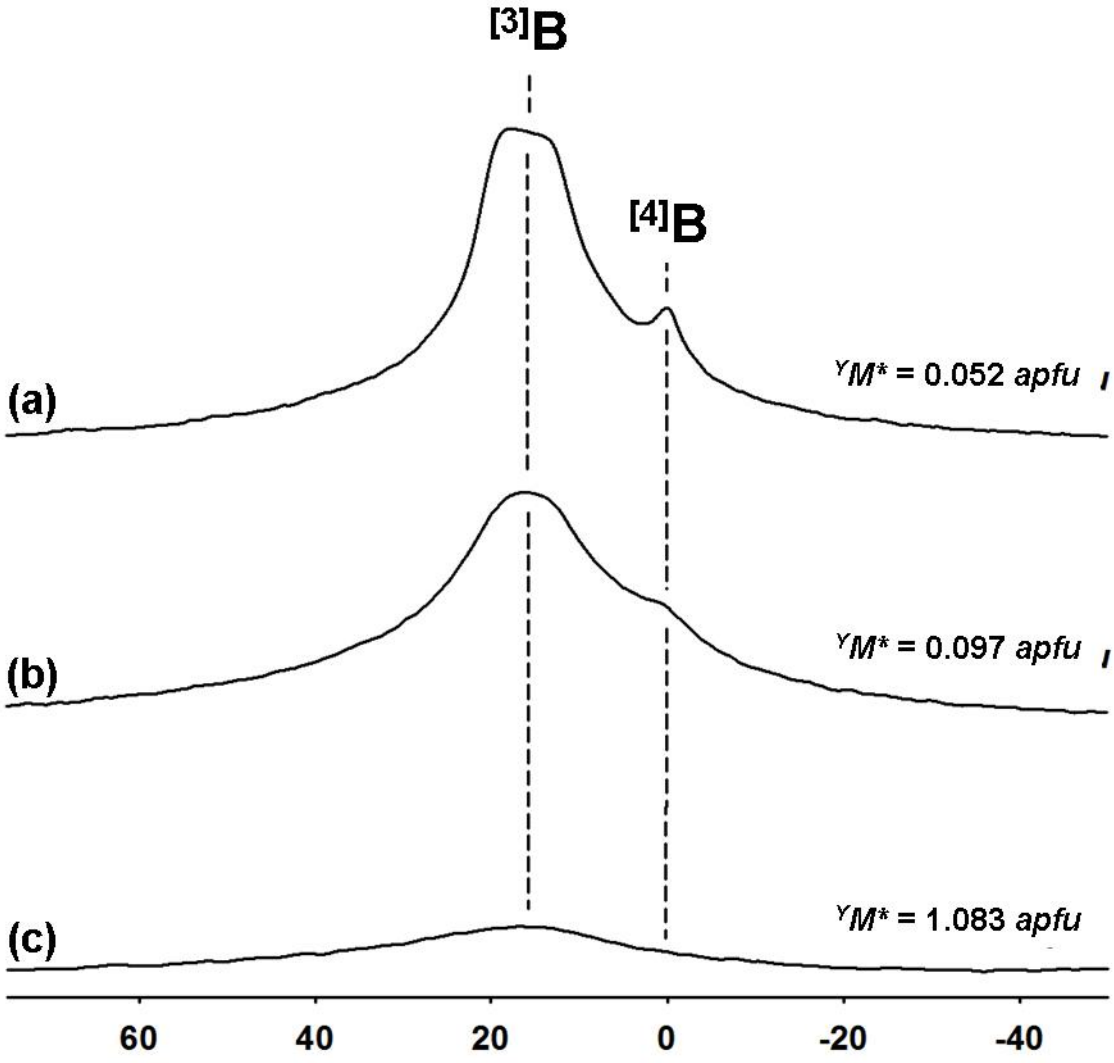

Figure 6.5 ^{11}B MAS NMR spectra of mushroom tourmaline: (a) SHM1; (b) SHM2; and (c) SHM3. The positions of the peaks corresponding to [3]-coordinate B and [4]-coordinate B are marked; *M** = sum of transition metals assigned to the *Y*-site.

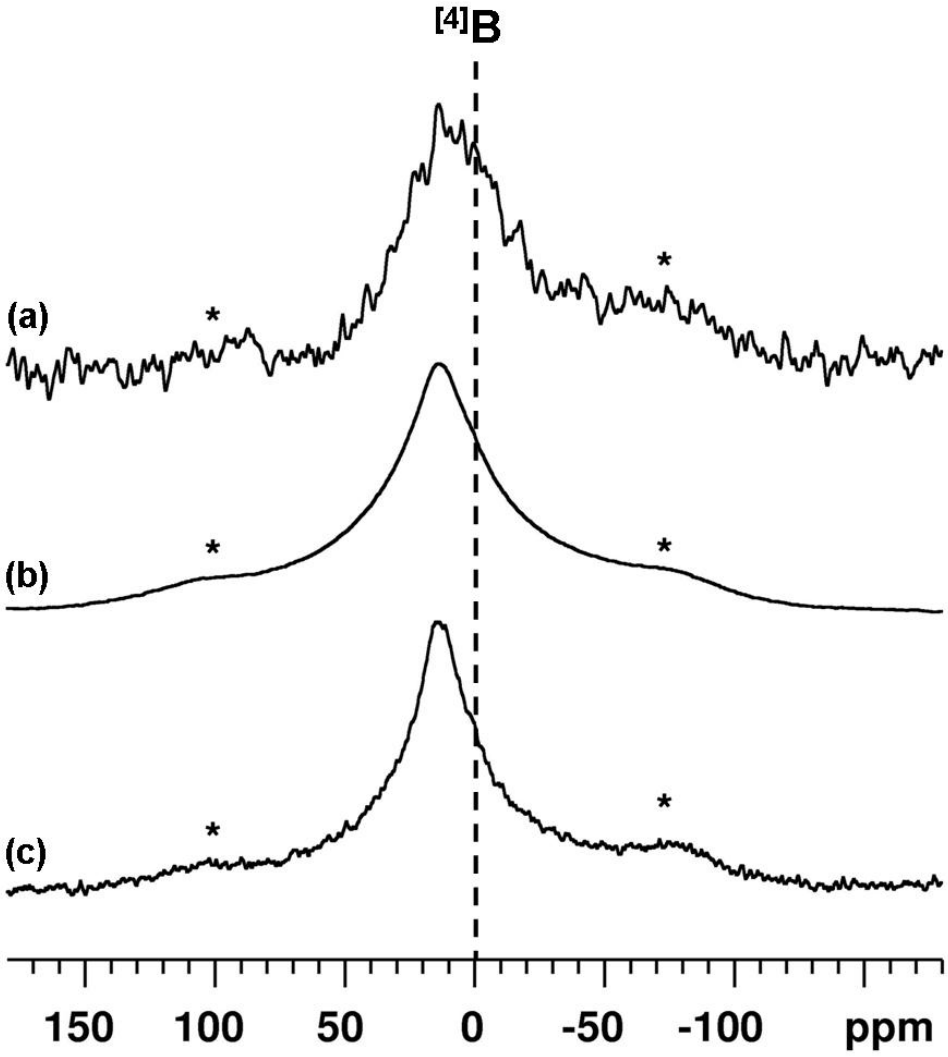

Figure 6.6 ^{11}B MAS NMR spectra acquired on material coincident with single-crystals (a) SHP1 (b) SHP2 and (c) SHP3 acquired at 14.1 T. These spectra are much broader than those from the SHM tourmaline. Spinning sidebands are denoted by asterisks, and the position of the peak corresponding to $^{[4]}$B is marked by the dashed line.

in order to illustrate the signal degradation that increases with increasing paramagnetic-element content.

The three spectra collected on mushroom tourmaline SHP (Figure 6.6) show significant line-broadening due to the presence of paramagnetic elements (Appendix A.4.1), relative to spectra of the SHM tourmaline, and the resolution is significantly decreased as the $^{[3]}$B peak extends well into the region where $^{[4]}$B signals might be expected. This very broad $^{[3]}$B signal is likely obscuring small signals arising from possible minor $^{[4]}$B in these samples, which is consistent with the observed <*T*-O> distances of 1.612 to 1.614 Å. Simulated ^{11}B MAS NMR parameters and values of $^{[4]}$B in both wheatsheaf and mushroom tourmalines are shown in Table 6.2; both tourmalines show an average of 0.3 *apfu* $^{[4]}$B.

6.4.2 ^{27}Al MAS NMR

The ^{27}Al MAS NMR spectra are shown in Figures 6.7 to 6.9. Each spectrum shows a large peak centered at ~0 ppm, corresponding to $^{[6]}$Al. The four ^{27}Al spectra collected on Madagascar liddicoatite (Figure 6.7) and the three spectra collected on mushroom SHM (Figure 6.9) show no intensity in the region characteristic of $^{[4]}$Al. There is a hint of intensity in Figure 6.9a (SHM2) and 6.9b (SHM2), and the simulated spectra of Figure 5.10 show that this would correspond to <~0.01 *apfu*. Moreover, high-field NMR (21.1 T) and ultra-fast MAS (62 kHz) were used in conjunction on one sample of Madagascar liddicoatite to reduce second-order quadrupolar broadening and minimize any paramagnetic interactions. The $^{[6]}$Al peak narrowed by a factor of 2 in ppm

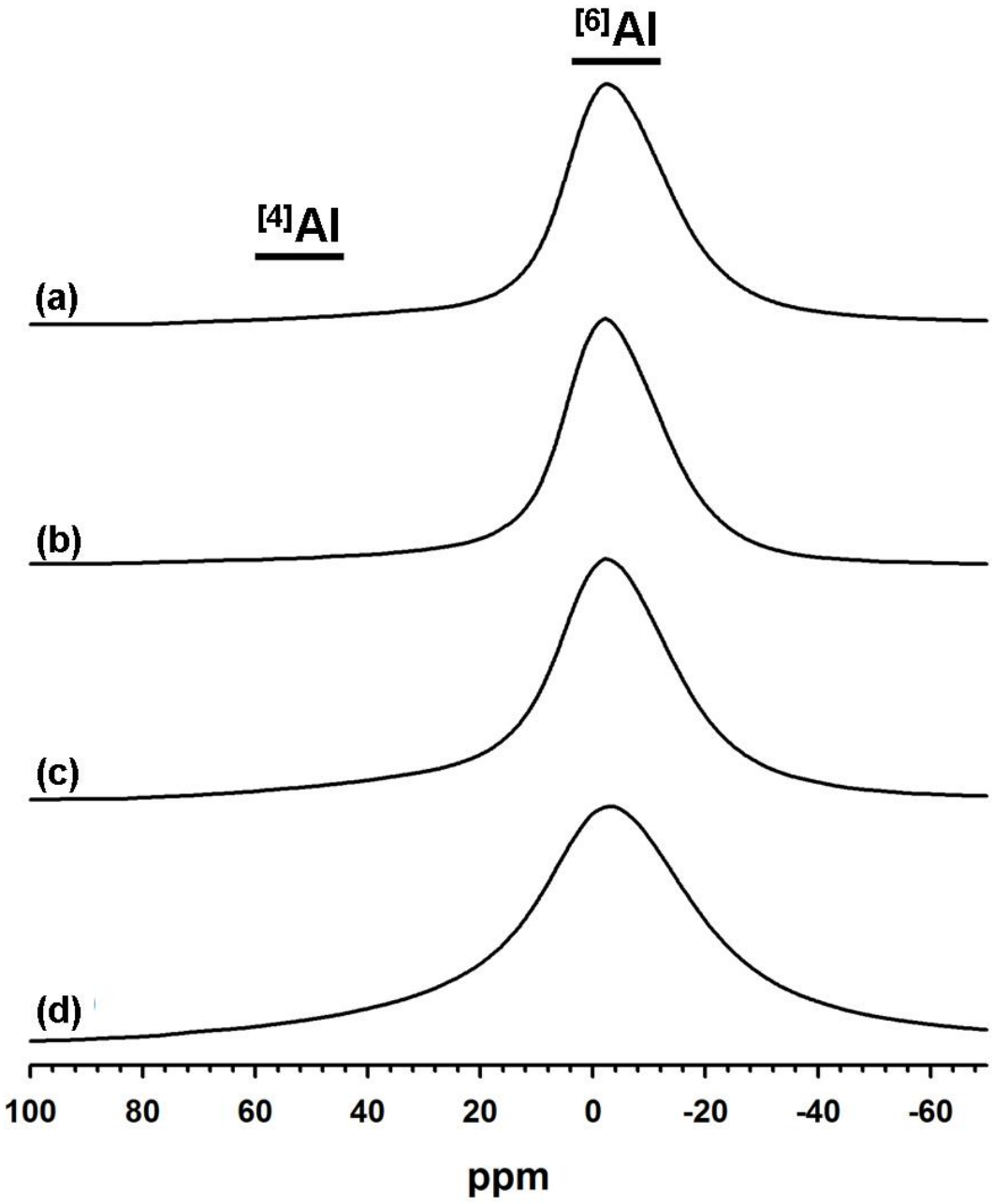

Figure 6.7 ^{27}Al MAS NMR spectra of liddicoatite: (a) NMR1; (b) NMR2; (c) NMR3; (d) NMR4 (see Figure 3.1b).

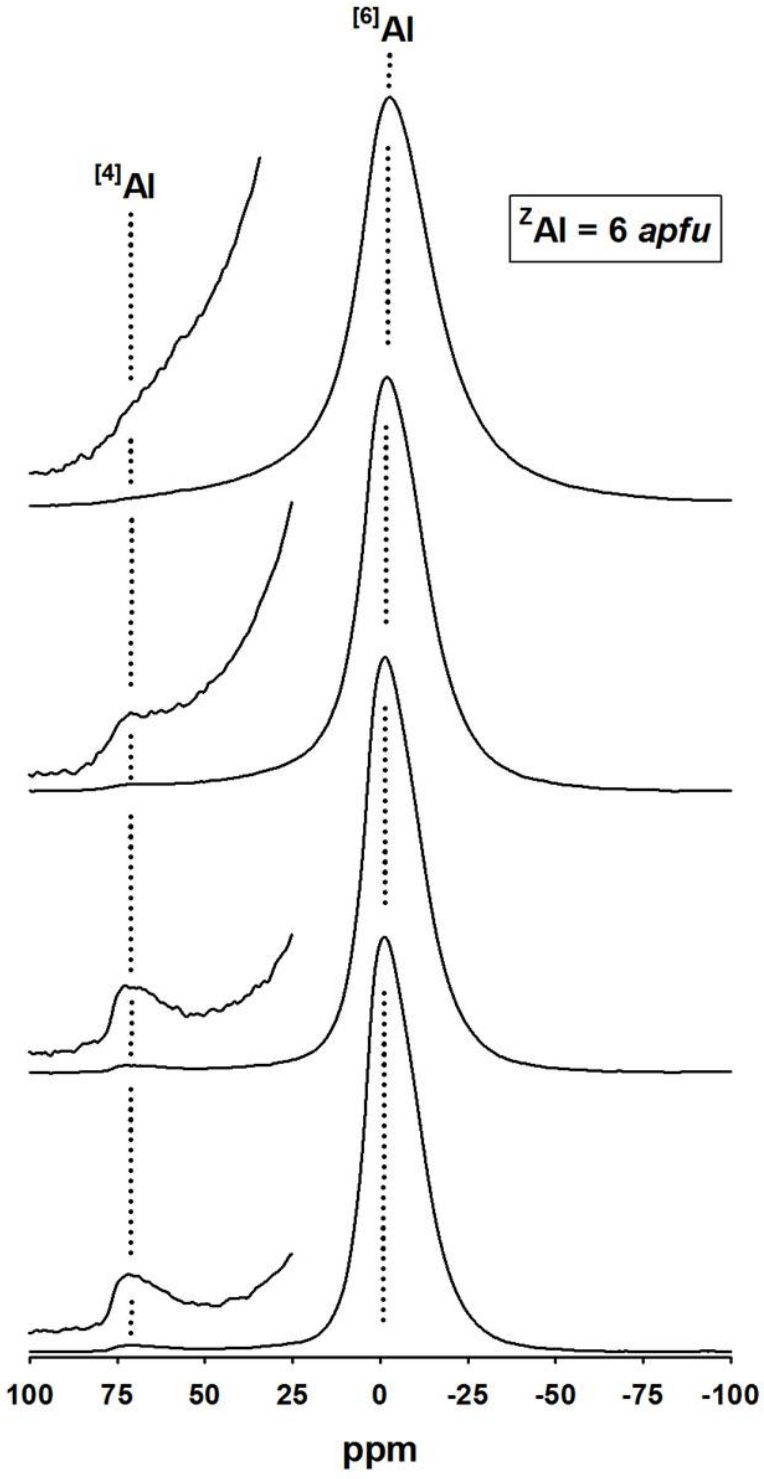

Figure 6.8 ^{27}Al MAS NMR spectra of wheatsheaf tourmaline: (a) SHW-NMR1 (purple tip); (b) SHW-NMR2 (purple brown); (c) SHW-NMR3 (white centre); and (d) SHW-NMR4 (red core). Spectra are shown with an increased intensity scale in the vicinity of signals assigned to $^{[4]}$Al.

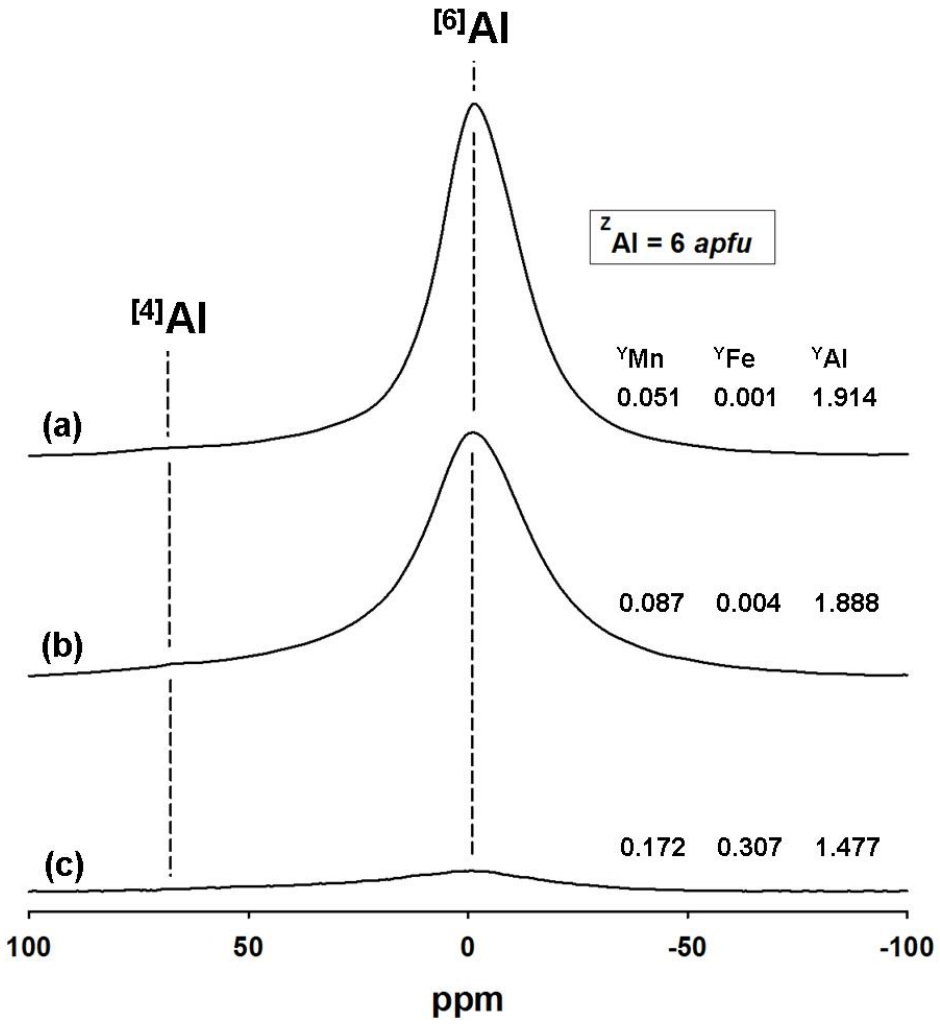

Figure 6.9 ^{27}Al MAS NMR spectra of mushroom tourmaline (SHM) acquired on material coincident with: (a) SHM1 –pink rind; (b) SHM2 – white fibres; and (c) SHM3 – dark core. The positions of the signals corresponding to $^{[4]}$Al and $^{[6]}$Al are marked. All values have units of *apfu*.

relative to the 14.1 T data, thereby increasing the spectral resolution and verifying that no $^{[4]}$Al signal is observed (data not shown). All four spectra collected on wheatsheaf elbaite show a peak centered at ~70 ppm, corresponding to $^{[4]}$Al. The results of fitting the ^{27}Al MAS NMR spectra are presented in Table 6.2 and indicate that < 2 % of the total Al is [4]-coordinated. For the average wheatsheaf tourmaline composition (Appendix A.4.1), this corresponds to < 0.12 *apfu*.

The MAS NMR data thus indicate that in Madagascar liddicoatite, wheatsheaf elbaite and mushroom elbaite, the average *T*-site occupancies in the bulk samples are T = $Si_{>5.98}$, T = ($Si_{5.7}B_{0.3}$), and T = ($Si_{5.6}B_{0.3}Al_{0.1}$), respectively.

6.5 FORMULA CALCULATION

For the 40 crystals investigated here, analysis for H, Li, and B was not done, and some assumptions concerning their presence in the structure are required when calculating the chemical formula. If $^{[4]}$B is known to be absent, the constraints (OH + F) = 4 *apfu*, B = 3 *apfu*, and ^{Y}Li = 15 - Σ (*Y* + *Z* + *T*) *apfu* are used, and the formula is calculated on the basis of 31 anions with these constraints. Where Mössbauer spectra show $Fe^{3+}/Fe^{2+} > 0$, the ratio of Fe_2O_3/FeO was iterated until the ratio of Fe^{3+}/Fe^{2+} *apfu* was in agreement with spectroscopic results. This procedure will calculate the total amount of Al in the structure, which may then be separated into $^{[4]}$Al and $^{[6]}$Al. For Madagascar liddicoatite, both MAS NMR and SREF data show that T = Si_6, within statistical error (see discussion in Section 6.2.2.), yet the above procedure consistently

TABLE 6.2 ^{11}B AND ^{27}Al MAS NMR SAMPLE LOCATIONS AND PARAMETERS FOR WHEATSHEAF AND MUSHROOM TOURMALINES

Sample	Location / Colour	Site	δ_{iso} (ppm)	C_q (MHz)	η	Peak intensity (rel.%)	$^{[4]}B$. (*apfu*)	$\%^{[4]}Al$	$^{[4]}Al$ (*apfu*)
Wheatsheaf elbaite									
SHW11	Purple tip	$^{[3]}B$	18.7 ± 1	2.9 ± 0.3	0.2 ± 0.2	91 ± 4	0.30 ± 0.14	<<1	---
		$^{[4]}B$	0 ± 1	0.3[a]	1[a]	9 ± 4			
SHW2	Purple brown	$^{[3]}B$	18.5 ± 1	2.9 ± 0.2	0.1 ± 0.1	92 ± 2	0.26 ± 0.07	1.1(9)	0.08(7)
		$^{[4]}B$	0 ± 0.5	0.3[a]	1[a]	8 ± 2			
SHW3	White centre	$^{[3]}B$	18.5 ± 0.5	2.88 ± 0.1	0.1 ± 0.1	91 ± 1	0.30 ± 0.03	2(1)	0.12(8)
		$^{[4]}B$	0.1 ± 0.5	0.3[a]	1[a]	9 ± 1			
SHW4	Red core	$^{[3]}B$	18.5 ± 0.5	2.9 ± 0.1	0.1 ± 0.1	90 ± 1	0.33 ± 0.05	1.7(6)	0.12(4)
		$^{[4]}B$	0 ± 0.5	0.3[a]	1[a]	10 ± 1			
Mushroom elbaite									
SHM1	Pink rind	$^{[3]}B$	18 ± 1	2.75 ± 0.1	0.1 ± 0.1	90 ± 3	0.33 ± 0.05	---	---
		$^{[4]}B$	–0.1 ± 1	0.3[a]	1.0[a]	10 ± 3		---	---
SHM2	White centre	$^{[3]}B$	18 ± 1	2.75 ± 0.1	0.1 ± 0.1	91 ± 3	0.30 ± 0.03	---	---
		$^{[4]}B$	0.1 ± 1	0.3[a]	1.0[a]	9 ± 3		---	---
SHM3	Dark grey core	$^{[3]}B$	12 ± 2[b]	---	---	---	---	---	---
		$^{[4]}B$	---	---	---	---	---	---	---
SHP1	Purple rind		13 ± 2	---	---	---	---	---	---
SHP2	Purple-grey		13 ± 2	---	---	---	---	---	---
SHP3	Dark purple		14 ± 2	---	---	---	---	---	---

[a] Values fixed for simulation. [b] Due to broadening, centre of mass taken in place of isotropic shift.

showed Si < 6 *apfu*. The above constraint was therefore changed to ^{Y}Li = 9 - Σ (*Y* + *Z*) *apfu* and the occupancy of the *T*-site is reported as incomplete in Appendix A.4.1.

In crystals where MAS NMR show $^{[4]}$B to be present, such as wheatsheaf and mushroom elbaite, additional constrains are required. For mushroom crystals, where MAS NMR showed that T = (Si_{6-x}, B_x), the formulae were normalized to 31 anions with (OH + F) = 4 *apfu* and ^{Y}Li = 9 – Σ (*Y* + *Z*) *apfu*, and $^{[4]}$B was incorporated into the calculation by setting Si + $^{[3+4]}$B = 9 *apfu*. In the case of wheatsheaf crystals, where MAS NMR showed that T = (Si_{6-x-y},B_x,Al_y), the formulae were again normalized to 31 anions with (OH + F) = 4 *apfu* and Li = 9 – Σ (*Y* + *Z*) *apfu*, and $^{[4]}$B was incorporated into the calculation by setting Si + $^{[4]}$Al + $^{[4]}$B = 6 *apfu*. Here, the value of either $^{[4]}$Al (Eq. 5.2) or $^{[4]}$B (Eq. 5.1) is required from MAS NMR spectra. The former was chosen, as spectral quantification (Table 6.2) consistently shows $^{[4]}$Al < $^{[4]}$B apfu, which is in accord with the observation that <*T*-O> < 1.620 Å. Thus substituting the value of $^{[4]}$Al determined by MAS NMR spectroscopy minimizes the propagation of error due to misfitting of the spectra. For crystals SHW3 and SHW4, the larger amounts of paramagnetic elements precluded MAS NMR spectroscopy. However, the <*T*-O> distances of 1.619 Å (Appendix A.3) indicate approximately equal amounts of $^{[4]}$B and $^{[4]}$Al, and the formulae were calculated accordingly.

The resulting formulae for all 40 tourmaline crystals are listed in Appendix A.4.1 and are classified on the basis of *X*-site occupancy in Figure 6.10. Of the 23 crystals extracted from the Madagascar liddicoatite, the compositions of 22

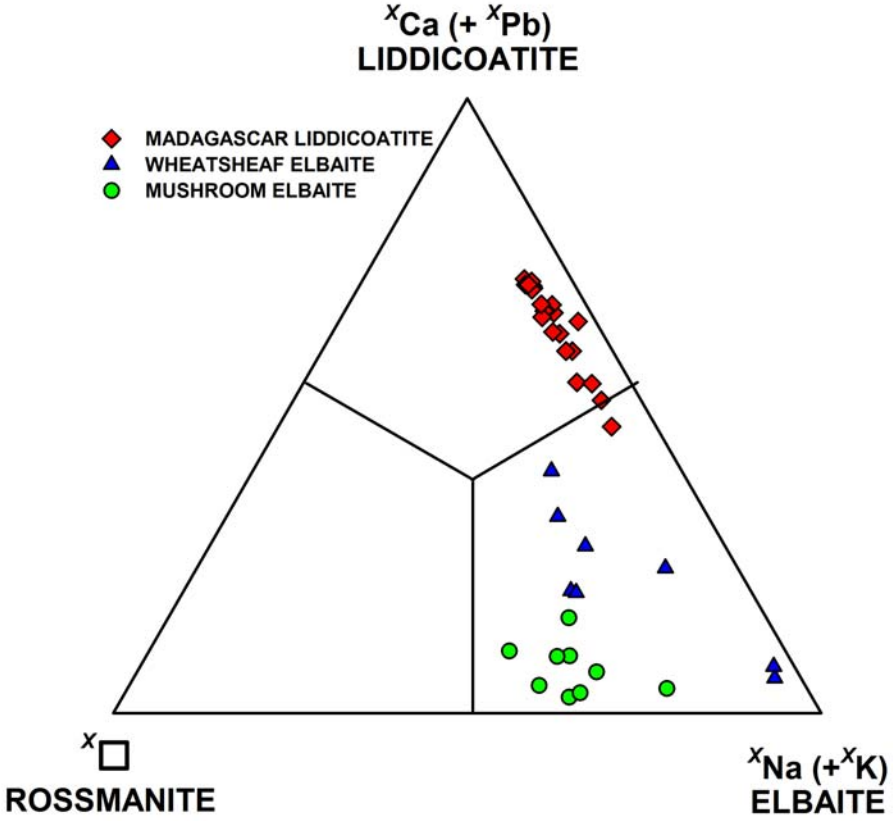

Figure 6.10 Ternary plot showing *X*-site occupancy for the 40 single crystals characterised in this study.

correspond to fluor-liddicoatite according to the classification methodology of Henry *et al*. (2011). Of the remaining 17 crystals extracted from the wheatsheaf and mushroom tourmalines, all correspond to elbaite, expect for SHW3, SHW4, SHW7 and SHW8 that correspond to 'fluor'-elbaite[1].

6.6 SITE POPULATIONS

Unit-formula calculations provide the amounts of atomic constituents in the crystal, and site populations are assigned on the basis of (1) refined site-scattering values (Appendix A.5), (2) the unit formulae calculated from the electron-microprobe analyses (Appendix A.4.1), (3) the results of MAS NMR (Table 6.2; Appendix A.6) and Mössbauer spectroscopies (Table 6.3), and (4) mean bondlengths (Appendix A.3). In the following text, the sites are discussed in the order which the populations are assigned.

6.6.1 The T-site

The occupancy of the *T*-site is calculated and refined in accord with the results of ^{11}B and ^{27}Al MAS NMR spectroscopy: Madagascar liddocatite crystals are refined with full occupancy of the *T*-site by Si, whereas wheatsheaf and mushroom elbaites are constrained to Si + B = 6 *apfu* during final least-squares cycles. *T*-site-scattering values in *epfu* (electrons per formula unit) calculated by site-scattering refinement and electron-microprobe analysis are in reasonable accord (Appendix A.5) for all crystals, with a mean deviation of 1.3 *e*.

[1] Although correctly fluor-liddicoatite and fluor-elbaite according to Henry *et al*. (2011), these are referred to as simply liddicoatite and elbaite in this work, for the sake of brevity.

6.6.2 Site-occupancy and <T-O> in Madagascar liddicoatite

In all MAS NMR spectra, there is no evidence of $^{[4]}$B or $^{[4]}$Al in this crystal (Figures 6.3 and 6.7). These results are in accord with the observed <*T*-O> bondlengths (Appendix A.3), which range from 1.616 to 1.619 Å with a grand mean of 1.6174 Å, (σ = 0.0007 Å). Hence, we conclude that for this crystal, there are 6 Si *apfu* at the *T*-site. Formula normalization of the results of all the chemical analyses done on this crystal results in values with the range 5.90 < Si < 5.97 *apfu* with a mean value of 5.93 (σ = 0.02 *apfu*). In Chapter 5, it was concluded from simulation of ^{11}B and ^{27}Al MAS NMR spectra that $^{[4]}$B is less than 0.02 *apfu* and $^{[4]}$Al is less than 0.01 *apfu* in this crystal of liddicoatite, indicating the Si should be greater than 5.97 *apfu* in these crystals. The difference between the mean observed Si content of 5.93(2) *apfu* and the value of 5.97 *apfu* is 0.04(2) *apfu*, a value that is not significantly different from zero at the 99% confidence limit. If we assume a Si value of 6.00 *apfu* in these crystals, the difference between the average observed value and our assumed value is 0.07(2) *apfu*, a value that is marginally significant at the 99% confidence limit. Incorporation of such small amounts of $^{[4]}$B or $^{[4]}$Al at the *T*-sites would change the <*T*-O> distances by approximately 0.002 Å, of the same order of magnitude as the standard deviations on the distances, and hence provide no evidence of deviation from 6.00 Si *apfu*. The observed <*T*-O> distances measured by SREF are in the range 1.616-1.619 Å, statistically identical to the ideal <^{T}Si-O> distances (in the tourmaline structure) optimized by Bosi & Lucchesi (2007) which range from ~1.615 to ~1.630 Å. Thus it appears that there is a small but

systematic error (that could not be found) in the electron-microprobe data and the *T*-site occupancies are assigned as 6.00 Si *apfu*.

Ertl *et al.* (2006) reported structure and chemical data on four crystal fragments of liddicoatite from Anjanabonoina, Madagascar. They analysed B by SIMS and reported 0.14-0.57 *apfu* $^{[4]}$B. This amount of $^{[4]}$B would easily be detected by ^{11}B MAS NMR, and hence the two samples of liddicoatite must differ significantly in their *T*-site contents.

6.6.3 The Z-site

For all 40 crystals in this study, when allowed to vary during refinement, the *Z*-site refined to complete Al occupancy within error, and it was fixed as such in the final stages of refinement. Equivalent isotropic-displacement parameters are in accord with equal scattering at the *Z*-site in all of the structures refined here [U_{eq} = 0.0068(10)]. A grand mean <*Z*-O> distance of 1.905 (σ = 0.004 Å) is observed with no significant variation of <*Z*-O> in any of these structures, typical of tourmalines where Z = Al_6.

By examining 127 published tourmaline structures, Bosi & Lucchesi (2007) showed a linear dependence between the length of the shared O(7)-O(8) edge of adjacent *Z*-octahedra and <Z-O> in tourmalines with $^{Z}R^{2+}$ > 0.4 *apfu*. However, in structures they investigated with $^{Z}R^{2+}$ < 0.4 *apfu* (*i.e.*, Z ~ Al_6) the electrostatic repulsion between adjacent *Z*-cations is sufficiently strong that <*Z*-O> values below ~1.905 Å may not occur (Figure 6.11a), although the length of the

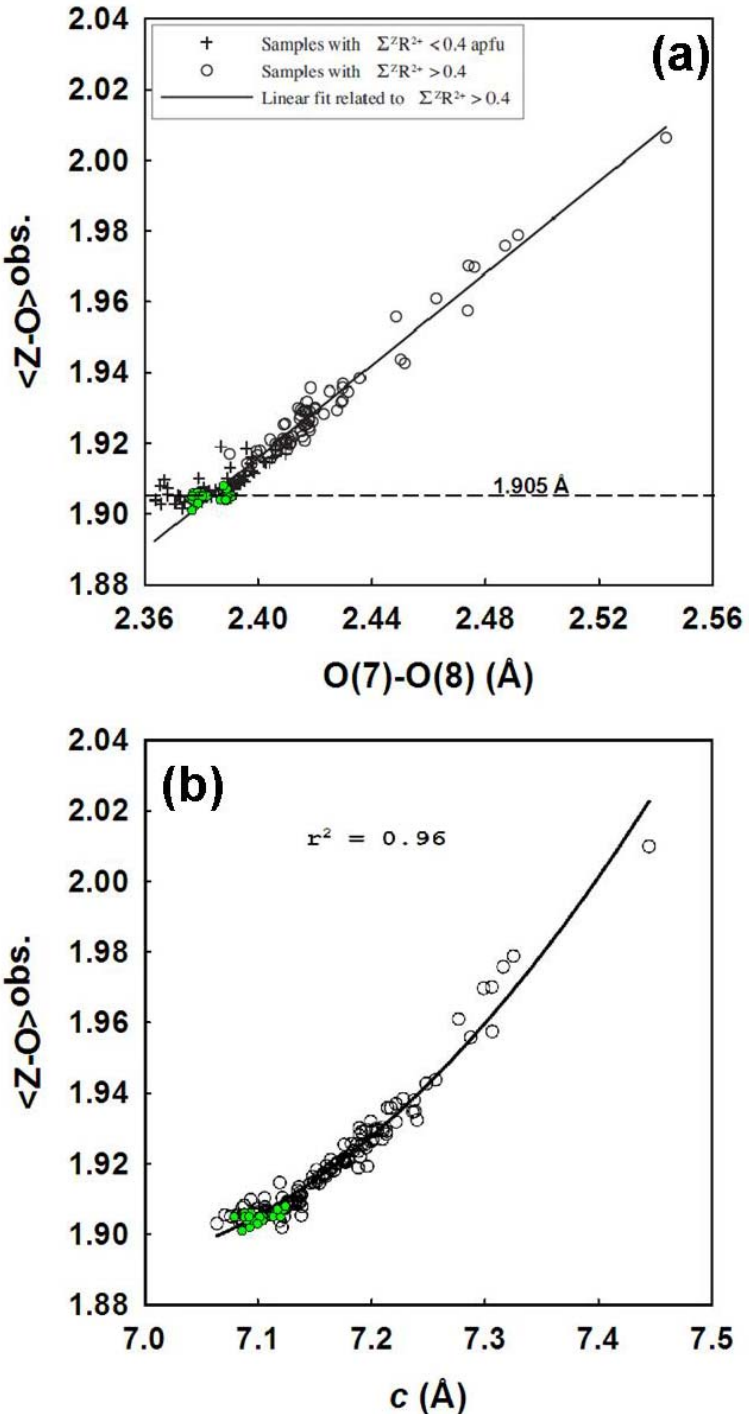

Figure 6.11 Figures modified from (a) Bosi & Lucchesi (2007) showing relation between lengths of <*Z*-O> and O(7)-O(8) edge (shared by adjacent *Z*-octahedra); and (b) Bosi (2008) showing dependence of <*Z*-O> on length of *c*-parameter. The 40 tourmaline structures from current study are plotted in green circles and in both cases are in good agreement with the published curves.

O(7)-O(8) may change over the region where <Z-O> ≈ 1.905 Å. Thus, 1.905 Å appears to be the lowest <Z-O> distance possible in tourmaline and corresponds to Z = Al_6. Moreover, the grand <*Z*-O> distance of 1.905 Å and the mean *c*-parameter (~7.11 Å, Appendix A.1) are in close accord with the corresponding curve of Bosi (2008), who showed a strong, nonlinear dependence between these two parameters for 129 structures of different species (Figure 6.11b). The 40 crystals examined here plot in the region of Figure 6.11a where the contraction of <*Z*-O> is forbidden, and in the region of Figure 6.11b where both <*Z*-O> and *c*-parameters are consistent with the *Z*-site being completely occupied by Al.

6.6.4 The B-site

The $<^{[3]}$B-O> distances vary over the narrow range of 1.371(2) to 1.379(2) Å with a grand mean value of 1.376(2) Å (σ = 0.002 Å). These values are close to the grand $<^{[3]}$B-O> distance in borate minerals of 1.370 Å given by Hawthorne *et al.* (1996), indicating complete occupancy of the *B* site by B.

6.6.5 The X-site

The formulae derived from the chemical compositions (Appendix A.4.1.) have Na, Ca (and Pb for Madagascar liddicoatite) assigned to the *X*-site. In general, the elbaite tourmalines (SHW and SHM) have a significant proportion of the *X*-site vacant, with a mean value of 0.241 □ *pfu*. A large range is observed, however, with a maximum value of 0.390 □ *pfu* (SHM2) and a minimum value of

0.029 □ *pfu* (SHW4). In contrast, the liddicoatite tourmalines consistently show nearly complete *X*-site occupancy, with a mean value of 0.061 □ *pfu*, and a range of 0.025 to 0.076 □ *pfu*.

6.6.6 The Y-Site

Comparison of compositional and structural data confirms that the *Y*-site is occupied by Li, Al, Fe^{2+}, Fe^{3+}, and Mn^{2+}, with minor-to-trace amounts of Ti^{4+}, Zn, and Mg. For all 40 crystals characterised, the grand mean absolute deviation between the refined site-scattering values and the analogous values derived from the unit formulae is small (0.7 e/site; Appendix A.5). Further, the strong linear relation between <*r*[*Y*]> and <*Y*-*Φ*> also suggests that *Y*-site constituents have been correctly assigned (Figure 6.15).

6.6.7 The oxidation state of ^{Y}Fe and InterValence Charge Transfer

In regions of the specimens where sufficient Fe (> ~1 wt% FeO_x) was determined by EMPA to be present, ^{57}Fe Mössbauer spectra were collected to determine the oxidation state of Fe. Throughout the Madagascar liddicoatite, the Fe content of this crystal is quite low, averaging less than 1 wt% FeO, and is quite variable over very short distances in the crystal (Figure 7.10). As a result, Mössbauer spectra could not be measured for individual colour zones, and instead, spectra were acquired on aggregate samples taken in the most Fe-rich regions of the pyramidal (Figure 6.12a) and prismatic (Figure 6.12b) sectors. In wheatsheaf elbaite, only the green rim was sufficiently Fe-rich (with ~4.0 wt%

FeO) for Mössbauer spectroscopy (Figure 6.13). The dark core region of the mushroom tourmalines contains up to ~7 wt% FeO, and on the SHM sample, Mössbauer spectra (Figure 6.14) were collected on three areas of the black core. The locations marked (a), (b) and (c) in Figure 6.14 correspond approximately with locations of crystals SHM3a, SHM3e and SHM5.

All Mössbauer spectra show the presence of both Fe^{2+} and Fe^{3+} (Figures 6.12 to 6.14), with the former consistently being the dominant species. The results of spectral-fitting are given in Table 6.3. The amount of Fe^{3+} varies from ~5 % in Madagascar liddicoatite up to ~32% in the most Fe-rich part of mushroom elbaite. Each spectrum is fitted with a multi-site model, using the doublet assignments of Andreozzi *et al.* (2008) as starting parameters.

It has been shown that Mössbauer spectroscopy is sensitive to Fe^{2+} and Fe^{3+} in different short-range arrangements in tourmaline (Dyar *et al.* 1998; Andreozzi *et al*. 2008; Bosi 2008), although correlating doublets to specific arrangements is complicated. Mössbauer spectroscopy can also identify the presence of Fe^{2+}-Fe^{3+} clusters where there is electron delocalization (Hawthorne 1988; Ferrow 1994; Dyar *et al.* 1998; De Oliveira *et al.* 2002; Eeckhout *et al.* 2004). There are at least two doublets assigned to Fe^{2+} in octahedral coordination in all spectra, with the exception of that of wheatsheaf elbaite in which there is only one. For each spectrum, Mössbauer hyperfine parameters are in accord with the doublets Y1, Y2 or Y3 of Andreozzi *et al.* (2008) that are assigned to Fe^{2+} at *Y* in different next-nearest-neighbour arrangements.

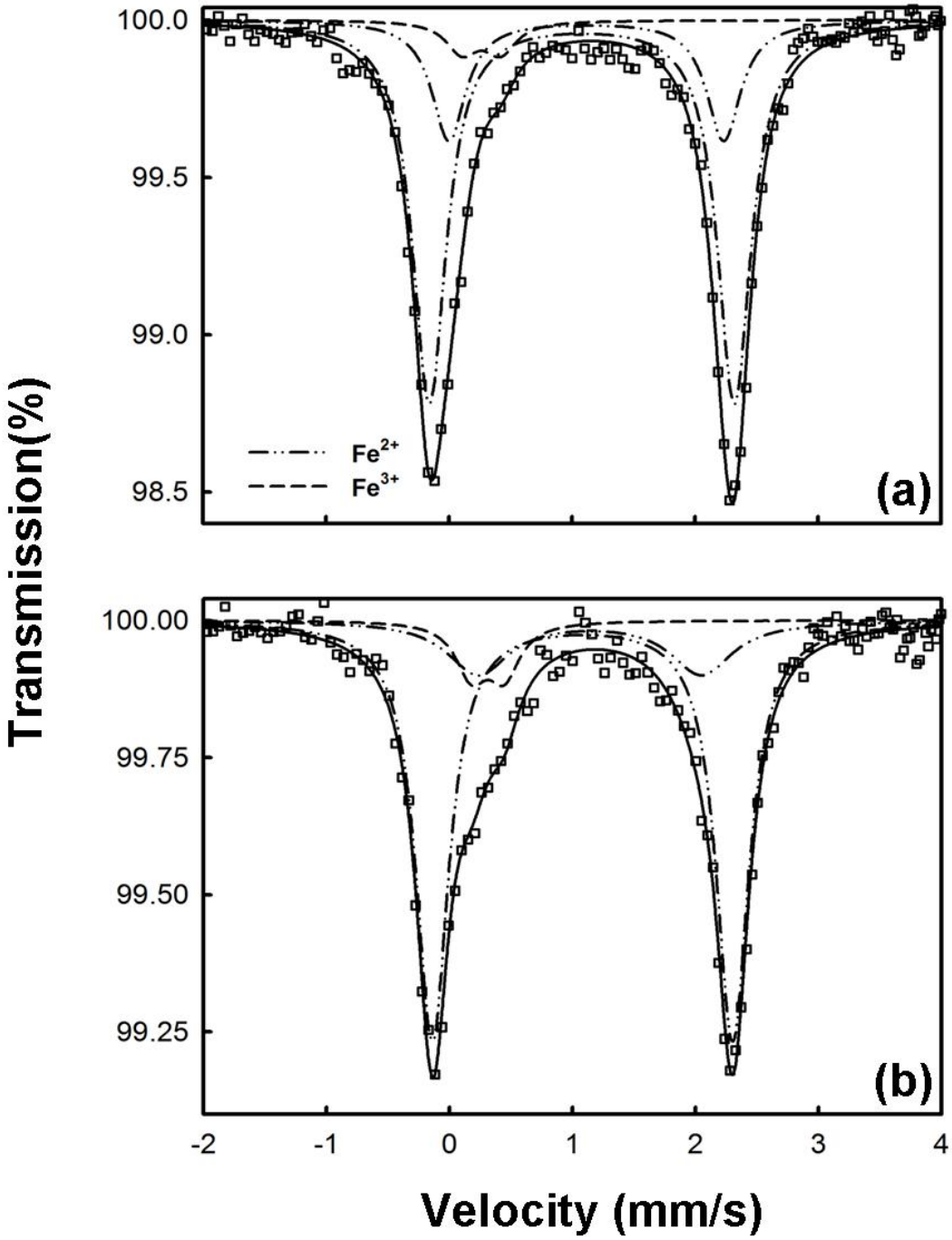

Figure 6.12 Mössbauer spectra for Madagascar liddicoatite averaging zones from: (a) prism sector; (b) pyramid sector.

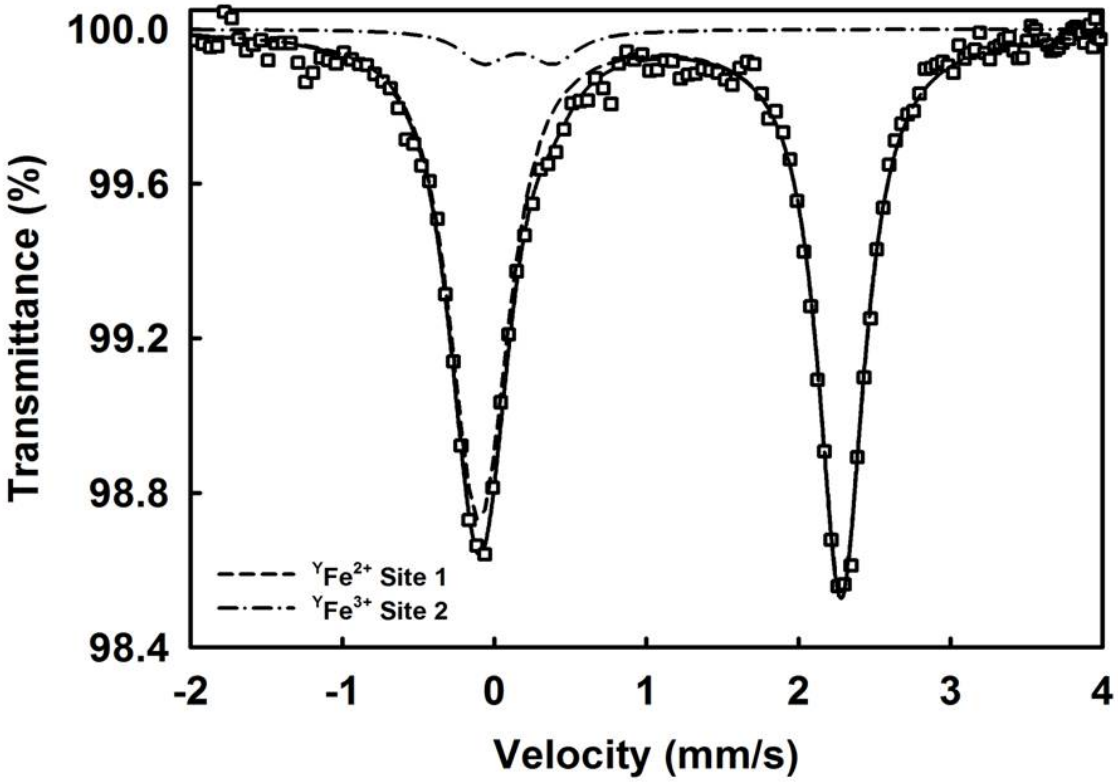

Figure 6.13 Mössbauer spectrum of the thin 'green-cap' layer of wheatsheaf tourmaline.

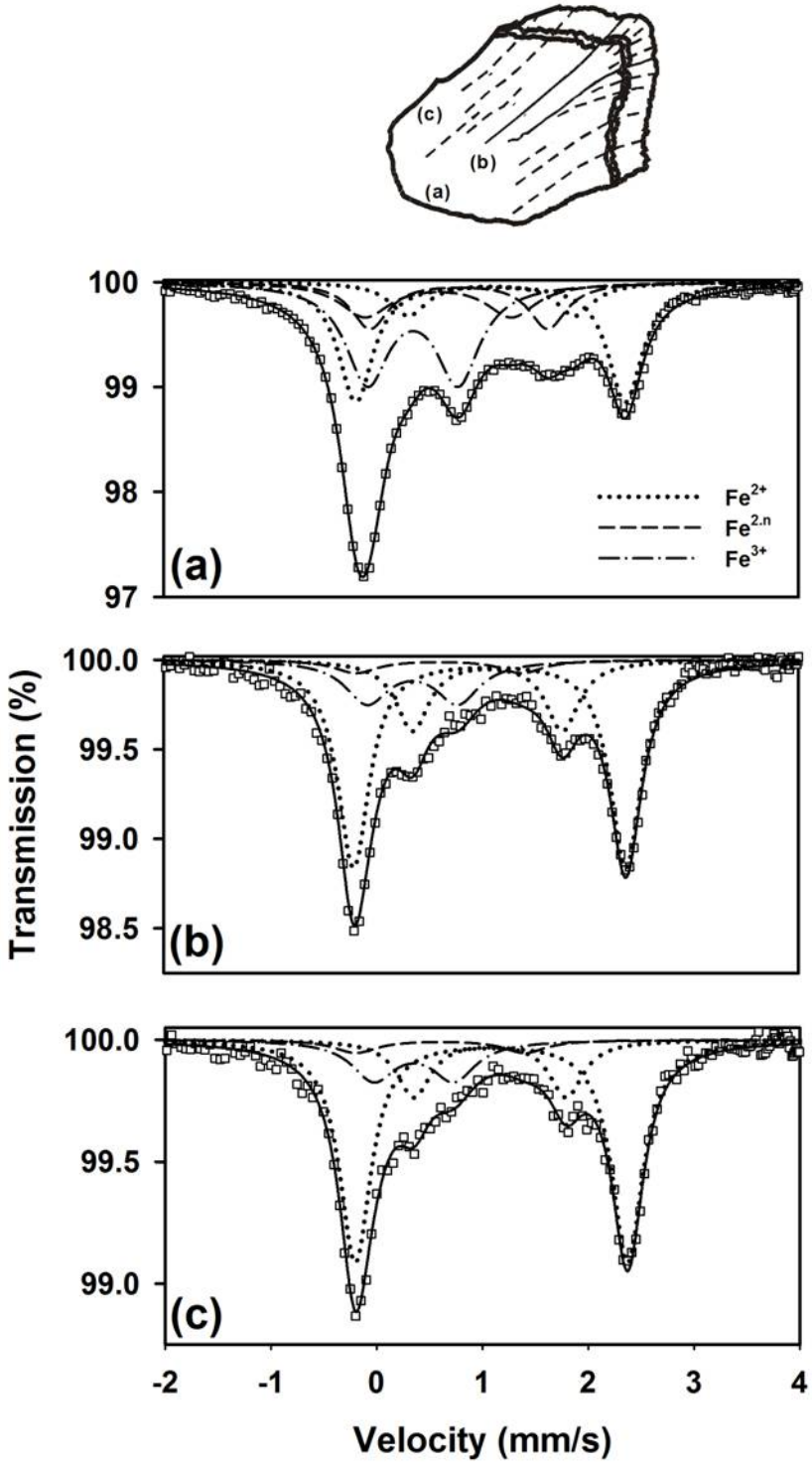

Figure 6.14 The Mössbauer spectra of mushroom tourmaline SHM: the positions of the material examined are shown on the sketch of the mushroom (compare with Figure 3.4a,b) and are identified as (a), (b) and (c), corresponding approximately to crystals SHM3a, SHM3e, and SHM5.

TABLE 6.3 MÖSSBAUER PARAMETERS MEASURED ON MADAGASCAR LIDDICOATITE, WHEATSHEAF ELBAITE AND MUSHROOM ELBAITE

	δ (mm/s)	Δ (mm/s)	Γ (mm/s)	Rel. area (%)
Madagascar liddicoatite				
		(x^2 = 0.62) Prism		
Fe^{2+}	1.080(12)	2.48(5)	0.30(2)	72(34)
Fe^{2+}	1.12(4)	2.23(17)	0.30(8)	23(35)
Fe^{3+}	0.26(11)	0.31(18)	0.28*	5(2)
		(x^2 = 0.54) Pyramid		
Fe^{2+}	1.081(8)	2.44(2)	0.29(2)	74(14)
Fe^{2+}	1.14(13)	1.81(45)	0.43(19)	18(18)
Fe^{3+}	0.31(12)	0.27(15)	0.28(12)	8(4)
Wheatsheaf elbaite				
Fe^{2+}	1.09	2.38	---	95(2)
Fe^{3+}	0.16	0.46	---	5(2)
Mushroom elbaite				
		SHM3a		
Fe^{2+}	1.09(2)	2.55(5)	---	32(2)
Fe^{2+}	1.10(6)	1.57(5)	---	10(9)
$Fe^{2.n+}$	0.8(2)	1.7(5)	---	13(11)
$Fe^{2.n+}$	0.6(4)	1.4(7)	---	13(13)
Fe^{3+}	0.4(2)	0.9(4)	---	32(5)
		SHM3e		
Fe^{2+}	1.08(1)	2.57(1)	---	58(3)
Fe^{2+}	1.06(2)	1.41(3)	---	21(3)
$Fe^{2.n+}$	0.6*	1.6(3)	---	6(3)
Fe^{3+}	0.35*	0.86(8)	---	16(2)
		SHM5		
$^{Y}Fe^{2+}$	1.08(1)	2.57(2)	---	63(4)
$^{Y}Fe^{2+}$	1.07(3)	1.44(6)	---	17(5)
$^{Y}Fe^{2.n}$	0.6*	1.6(4)	---	5(4)
$^{Y}Fe^{3+}$	0.35*	0.8(1)	---	15(3)

* constrained

The three spectra measured on mushroom SHM sample also show doublets with hyperfine parameters indicative of electron delocalization between edge-sharing $^{Y}Fe^{3+}$-$^{Y}Fe^{2+}$, labeled $Fe^{2.n}$. InterValence Charge-Transfer (IVCT) can occur in minerals where adjacent sites of similar stereochemistry are occupied by transition elements of different valence state, such that on absorption of an incident photon, an electron moves from one cation to another (for a more detailed explanation, see Burns 1981; Hawthorne 1988). The absorption of visible-light photons during the charge-transfer process will often result in colouration that is more intense than would normally be expected for *d-d* transitions. In mushroom tourmaline (SHM) tourmaline, the compositional analysis and black coloration of the core region of the sample indicates the possibility of both heteronuclear and homonuclear IVCT. In SHM1 and SHM2, Mn is the only transition-element present (~0.1 *apfu*) whereas SHM3 contains a similar amount of Mn and significant Fe (~0.5 - 1.0.*apfu*), and hence the black colour of SHM3 suggests an IVCT process involving Fe. This is confirmed by the occurrence of the $Fe^{2.n}$ doublets observed in Mössbauer spectra of SHM3 (Figure 6.14), which have hyperfine parameters in between those of Fe^{2+} and Fe^{3+}.

6.6.8 Short-range order/disorder involving Fe^{2+} and Fe^{3+} in mushroom elbaite

Short-range order in minerals is the occurrence of clusters of species that occur with frequencies greater (or lesser) than those predicted by a random distribution. With respect to Fe^{2+} and Fe^{3+} cations in mushroom tourmaline, Mössbauer spectra may be used to test for the occurrence of short-range order.

In the spectra of Figure 6.14 isomer shift and quadrupole-splitting parameters coincide with $^{Y1}Fe^{2+}$, $^{Y3}Fe^{2+}$, $^{Y/Z}Fe^{3+}$, and Fe^{2+}–Fe^{3+}. However, on the basis of structure-refinement data, it has been shown that no appreciable amount of Fe^{3+} is present at the *Z*-site (which is occupied exclusively by Al), precluding the possibility of any Y ↔ Z charge transfer; thus all Fe^{2+} and Fe^{3+} occurs at the *Y* site (Appendix A.4.1.). For SHM3a, The relative intensities of the peaks in the Mössbauer spectra give the amounts of isolated Fe^{2+}, isolated Fe^{3+} and adjacent Fe^{2+}–Fe^{3+} (Table 6.3): *e.g*. Figure 6.14a: 42% (0.394 apfu), 32% (0.300 apfu) and 26% (0.244 apfu), respectively. Splitting the adjacent Fe^{2+}–Fe^{3+} pairs into their component cations gives Fe^{2+} = 0.516 and Fe^{3+} = 0.422 apfu. The probability of Fe^{3+} occurring adjacent to Fe^{2+} for a random short-range distribution is 1 x 0.422/3 = 0.141. As this cluster contains two Fe atoms, the total amount of Fe occurring as Fe^{2+}–Fe^{3+} pairs for a random short-range distribution is 0.282 apfu, in close accord with the observed amount of Fe involved in Fe^{2+}-Fe^{3+}: 0.244 apfu. Thus, there is no short-range order involving Fe^{2+} and Fe^{3+} in mushroom tourmaline.

6.6.9 The O(1)- and O(3)- sites

For any tourmaline, the occupancy of the *W*-position [≡ O(1)-site] in the general formula is $[(OH)_x F_y O_{1-x-y}]$, where $0 \le x, y \le 1$ (and $x + y \le 1$), and the occupancy of the *V*-position [≡ O(3)-site] is $[(OH)_x O_{3-x}]$ where $0 \le x \le 3$. The occurrence of F at *V* has not been detected (*e.g*., Henry & Dutrow 2011). For all 40 tourmaline crystals analysed here, the structural formulae (Appendix A.4.1.)

are calculated on the initial assumption that ^{W}(OH) + ^{W}F = 1 *apfu* and ^{V}(OH) = 3 *apfu*, and hence (OH) + F = 4 *apfu*. By calculating the average sums of bond valences at the O(1)- and O(3)-sites for each crystal, the validity of these assumptions can be assessed.

Consider first the occupancy of the O(1)-site, which is bonded to three *Y*-site cations (Figures 1.1 and 1.2). For a tourmaline where ^{W}F = 1 *apfu* or $^{W}O^{2-}$ = 1 *apfu*, the sum of bond valences incident from the *Y*-site cations must be ~1.0 and ~2.0 *vu*, respectively. Where ^{W}(OH) = 1.00 *apfu*, the sum of bond valences on the oxygen ion is ~1.2 *vu*, with the remaining ~0.8 *vu* incident from the H ion. If the assumption that ^{W}(OH) + ^{W}F = 1 *apfu* is correct, the *average* sum of bond valences at O(1) is expected to be between 1.00 and 1.20 *vu.* For example, Appendix A.4.1 shows that for all the analysed crystals of Madagascar liddicoatite, the average occupancy of the *W*-site is $[F_{0.671}(OH)_{0.329}]$, with relatively little variance (σ = 0.062 *apfu*). The expected bond-valence sum is the linear combination of these two values: this gives a value of ~1.06 *vu* [= 0.671 x 1.00 + 0.329 x 1.2]. The same approach gives average values of 1.08 *vu* for wheatsheaf elbaite, and 1.18 *vu* for mushroom elbaite. Table 6.4 shows valence sums at the O(1) site for each crystal, calculated using the curves of Brown & Altermatt (1985) and the observed bondlengths for the *disordered* O(1) position are listed in Appendix A.3. Here, the calculation is weighted assuming a random distribution of *Y*-$^{O(1)}$F and *Y*-$^{O(1)}$(OH) bonds in each sample. Cations with smaller radii (such as $^{[6]}r$[Al] = 0.535 Å) are assigned to the shorter *Y*-O(1) bond, whereas cations with larger radii (such as $^{[6]}r$[Li] = 0.76, $^{[6]}r$[Fe^{2+}] = 0.78 and $^{[6]}r$[Mn^{2+}] =

TABLE 6.4 BOND-VALENCE SUMS AT O(1) AND O(3) SITES IN TOURMALINE CRYSTALS

Madagascar liddicoatite			*Wheatsheaf elbaite*			*Mushroom elbaite*		
	$\Sigma s_{O(1)}$	$\Sigma s_{O(3)}$		$\Sigma s_{O(1)}$	$\Sigma s_{O(3)}$		$\Sigma s_{O(1)}$	$\Sigma s_{O(3)}$
Sample	(*vu*)		*Sample*	(*vu*)		*Sample*	(*vu*)	
L1	1.00	1.11	SHW1	1.24	1.11	SHM1	1.20	1.09
L2	0.98	1.11	SHW2	1.23	1.11	SHM2	1.31	1.10
L4	1.02	1.11	SHW3	0.98	1.11	SHM3	1.28	1.09
L5	0.97	1.11	SHW4	0.97	1.12	SHM3a	1.18	1.08
L6	0.97	1.10	SHW5	1.11	1.12	SHM3e	1.29	1.09
L7	0.98	1.11	SHW6	1.24	1.10	SHM5	1.22	1.10
L11	0.98	1.11	SHW7	1.18	1.09	SHP1	1.09	1.09
L12	0.96	1.11	SHW8	1.23	1.10	SHP2	1.12	1.09
L13	1.02	1.11				SHP3	1.13	1.10
L15	1.01	1.10						
L16	1.01	1.10						
L17	1.03	1.10						
L18	1.01	1.10						
L19	1.02	1.10						
L20	1.03	1.10						
L21	1.02	1.10						
L22	1.02	1.10						
L23	1.02	1.11						
L24	1.01	1.10						
L25	0.97	1.10						
L26	1.05	1.10						
L27	1.05	1.11						
L28	0.98	1.11						
$\langle s \rangle_{calc.}$	1.01(2)	1.10(1)		1.15(1)	1.11(1)		1.20(8)	1.09(1)
$\langle s \rangle_{theo.}$[a]	1.06	1.20		1.08	1.20		1.18	1.20

a, average expected valences for each tourmaline sample calculated as: 1.2(OH) + 1.0F (*apfu*)

0.83 Å) are assigned to the longer *Y*-O(1) bonds. Calculated average values are 1.01 *vu* (Madagascar liddicoatite), 1.15(1) *vu*,(wheatsheaf elbaite), and 1.20(8) *vu*, (mushroom elbaite). These values are in reasonable accord with the predicted values, validating the assumption that ^{W}(OH) + ^{W}F = 1 *apfu*.

Similarly, for the O(3) site, incident bond-valence sums are also listed in Table 6.4. In all 40 crystals, the calculated values show very little variance, with all values ranging between 1.08 and 1.12 *vu*, and an average value of 1.10 *vu*, in reasonable accord with the theoretical value of 1.20 *vu* for ^{V}(OH) = 3 *apfu*.

6.7 BONDLENGTH VARIATIONS

6.7.1 Variation in <Y-Φ>

The variation in <*Y*-*Φ*> distances with the aggregate radius of the constituent *Y*-site cations is shown for all 40 crystals in Figure 6.15. Although the general trend is linear with no significant deviations, data from Madagascar liddicoatite consistently lie on a different trend than do data from wheatsheaf and mushroom elbaites, such that a regression line through the complete data set is not warranted. When considered separately, the data from wheatsheaf and mushroom tourmalines correspond to the regression line shown in solid black (<*Y*-*Φ*> = 0.731<*Y*[*r*]> + 1.530, R^2 = 0.978), whereas the data from the Madagascar liddicoatite correspond to the regression line shown in dotted black <*Y*-*Φ*> = 0.608<*Y*[*r*]> + 1.622, R^2 = 0.828). The poorer agreement, and the apparently different slope observed in the liddicoatite data are likely attributable to the relatively narrow range of <*Y*-*Φ*> and <*r*[*Y*]> over which the data spread.

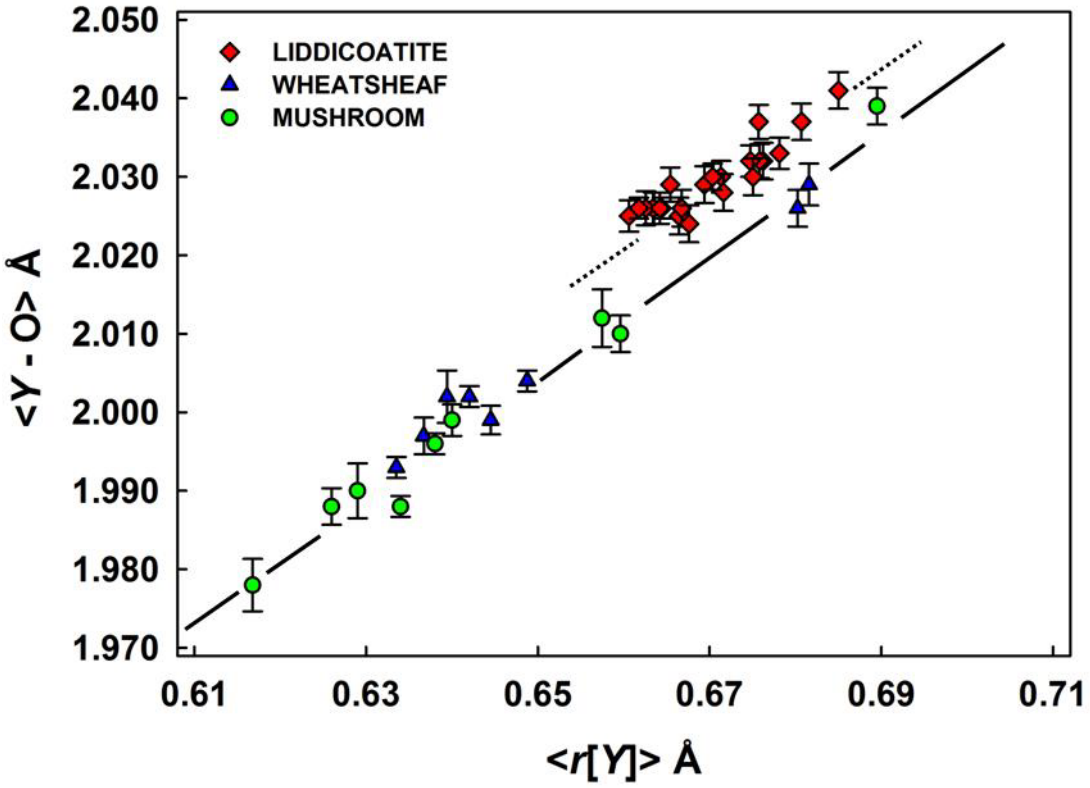

Figure 6.15 The variation in <*Y*-*Φ*> as a function of mean aggregate radius of *Y*-site cations for all 40 crystals.

6.7.2 $^{O(1)}F$ and <*Y*-Φ>

The histogram in Figure 6.16 shows that in the 40 tourmaline crystals characterised here, there is considerable variation in the F content, ranging from 0.000 *apfu* (SHP3) to 0.809 *apfu* (SHW4). Bond-valence calculations have shown that the O(1)-site is occupied solely by (OH) and F; these anions have radii of 1.34 Å (Ribbe & Gibbs 1971) and 1.30 Å (Shannon 1976), respectively, hence the presence of F should have an effect on <*Y*-Φ>. Using ionic radii of Shannon (1976), the ideal hard-sphere relation between <*Y*-Φ>, <*r*[*Y*]> and ^{W}F in tourmaline where W = [(OH),F] and V = $(OH)_3$ is given by: <*Y*-Φ> = <*r*[*Y*]> - $0.007^{W}F$ + 1.360, which shows that the presence of F should have a *negative* effect on <*Y*-Φ> distances. As errors in determining bondlengths in tourmaline from SREF are commonly on the order of 0.001 to 0.003 Å (see Appendix A.3), the effect of F should be detectable. As the F-content is consistently greater in Madagascar liddicoatite [<F> = 0.671 *apfu*] than in wheatsheaf [<F> = 0.584 *apfu*] and mushroom [<F> = 0. 095 *apfu*] elbaite crystals, it is expected that $< Y - \Phi >_{obs.}^{lid.} > < Y - \Phi >_{obs.}^{wheat+mush}$; however, the *opposite* is observed in Figure 6.15.

The configuration of amphiboles is similar to tourmalines in this regard: three edge-sharing octahedra *M*(*1*)*M*(*1*)*M*(*3*) are linked to a common anion [O(3)] that is occupied by [$(OH)_x$, O_y, F_{3-x-y}]. Stepwise linear regression on over more than a hundred data points by Hawthorne & Oberti (2007) shows the expected negative relation between <*M*-O> and F content at the O(3) site (Hawthorne & Oberti 2007). The discussion in Section 2.2.1.1 suggested that attempts at multivariate regression on <*Y*-Φ> were thwarted by misassignment of cations

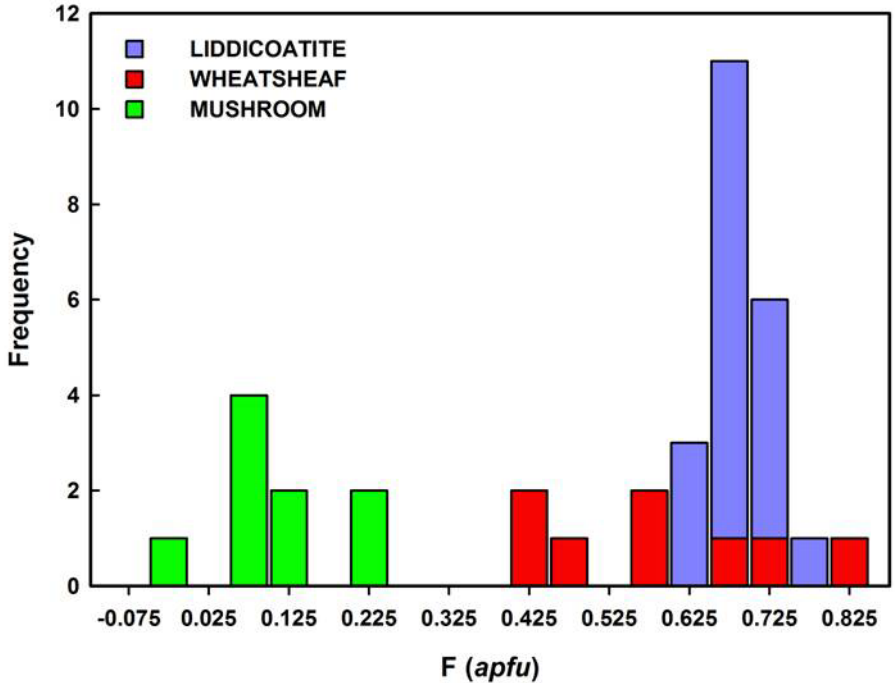

Figure 6.16 Histogram of F values in the 40 single tourmaline crystals investigated in this work.

between *Y*- and *Z*-sites. However, in the 40 tourmaline crystals considered here, it has been shown that Z = Al_6 and therefore there is virtually no possibility for such partitioning errors, and multivariate regression techniques may be more successful. However, this was not found to be the case, and stepwise linear regression approaches yielded ambiguous results, for example, regressing <*Y*-*Φ*> on <*r*[*Y*]> and F *apfu* yields the following relation: <*Y*-*Φ*> = 0.192(3)F + 0.85(4)<*r*[*Y*]>, R^2 = 0.976(4): note the *positive* coefficient for the independent variable F. Expanding the list of possible independent variations to <*r*[*Y*]>, F, <*Z*-O>, and <*T*-O> and <*X*-O>, the regression equation for <*Y*-*Φ*> becomes: <*Y*-*Φ*> = -0.22(3)<*X*-O> + 0.1(3)<*T*-O> + 0.76(4)<*r*[*Y*]>, R^2 = 0.991(2): note that F is *rejected* from the model.

Examining the relation between the *Y*-O(1) bondlength and F in greater detail may assist our understanding of this issue, as this distance is the most sensitive to the presence of F at O(1). A positive linear relation is expected between *Y*-O(1)$^{obs.}$ *vs*. *Y*-O(1)$^{calc.}$ [=<*r*[*Y*]> + <*r*[*Φ*]>, based on the hard-sphere model]. Figure 6.17a shows that such a linear trend is observed for liddicoatite and wheatsheaf crystals but *not* for mushroom crystals, where data points appear mostly as scatter. Figure 6.17b plots the difference between the calculated hard-sphere and the observed *Y*-O(1) distances, $\Delta_{Y\text{-}O(1)}$, against the aggregate anion radii at O(1), as doing so removes the component of bondlength variation resulting purely from varying abundances of species with difference ionic radii. At low values of <*r*[O(1)]>, *Y*-O(1)$^{obs.}$ is *longer* than the calculated value, and at high values of <r[O(1)]>, *Y*-O(1)$^{obs.}$ is *shorter* than the hard-sphere

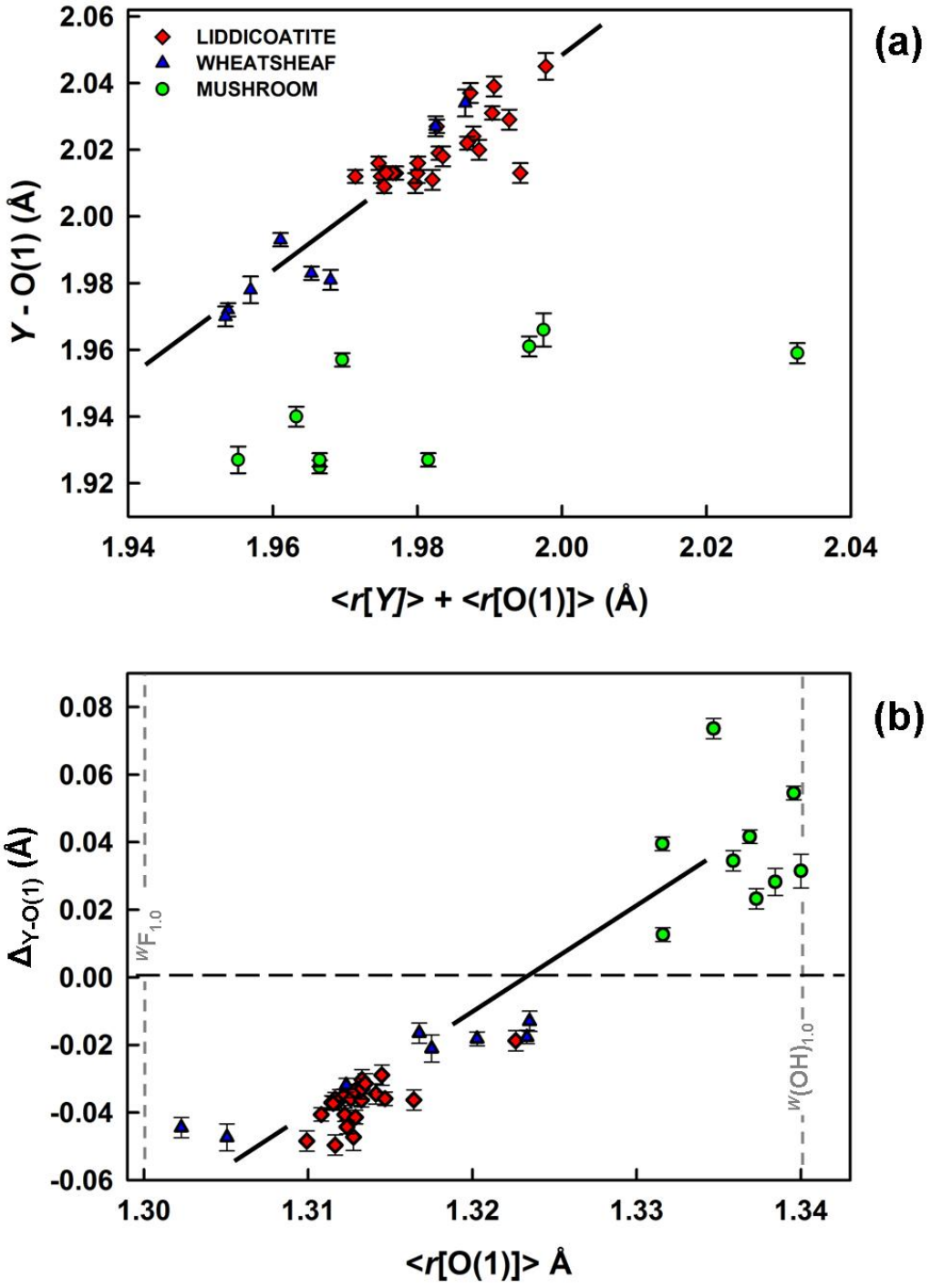

Figure 6.17 Variation, in *Y*-O(1) bondlength as a function (a) *Y*-O(1) calculated by hard-sphere radii; and (b) variation in $\Delta_{Y\text{-}O(1)}$.as a function of <*r*[O(1)]> (see text for details).

calculation. This shows that the expected increase in *Y*-O(1) due to the incorporation of larger anions at the O(1)-site is systematically offset, most likely by other crystal chemical interactions. Therefore, the presence of F is not visible to the multivariate regressions discussed above. The mechanism responsible for this currently unclear; however, what is clear is that Y-O(1) and thus <*Y*-*Φ*> is affected by factors other than just constituent ionic radii.

6.7.3 Variation in <T-O> along the Si ↔ B substitution

In all mushroom elbaite crystals, MAS NMR spectra show that there is significant $^{[4]}$B present and no $^{[4]}$Al *apfu* present. Thus, the *T*-site is occupied by Si and B, and we expect a negative correlation between <*T*-O> and the amount of $^{[4]}$B at the *T*-site as indicated from the formula calculations. The line in Figure 6.18 was drawn through the expected distance for complete Si occupancy of the *T*-site (1.620 Å, MacDonald & Hawthorne 1995a) and the grand <$^{[4]}$B–O> distance of 1.475 Å given by Hawthorne *et al.* (1996) for borate minerals. The average <T-O> observed in all 23 Madagascar liddicoatite crystals with T = Si_6 is plotted (red diamond). The data are in accord with this ideal line in that no point deviates from it by > 2.7 standard deviations.

6.7.4 <T-O> versus site occupancy

Figure 2.5b compares the variation in <*T*-O> as a function of the aggregate radius at the *T*-site for each structure listed in Table 2.1, which includes the 40 crystals discussed here. Visual inspection of this figure shows

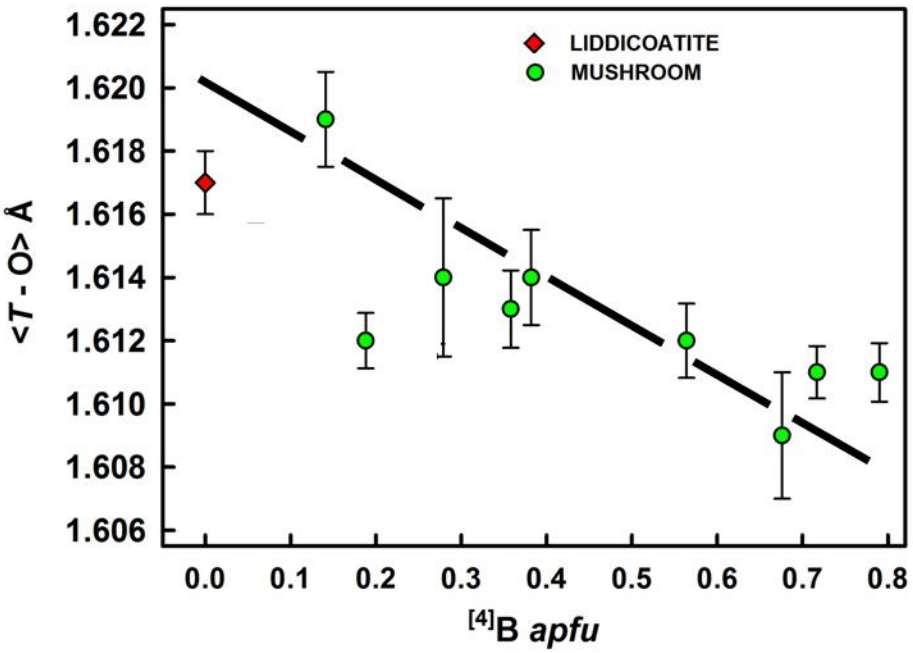

Figure 6.18 Variation in <*T*-O> as a function of [4]B *apfu* in Madagascar liddicoatite and mushroom elbaite.

data from this study to be in good general agreement with data of previous authors (*i.e.*, do not appear as outliers). However, there is significant scatter in the data, such that the true nature of the general trend is not readily discernable, and least-squares regression is not warranted. Figure 6.19 shows the region of Figure 2.5b spanning <*r*[*T*]> ~0.23 to ~0.27 Å enlarged for clarity. Here, symbols have been changed to represent reported *T*-site occupancy: T = $(Al,Si)_6$, squares; T = $(Si,B)_6$, circles; T = $(Si,B,Al)_6$, triangles; note, the data from the 40 crystals discussed here are shown with larger symbols.

In the current literature, three relations between <*T*-O> and *T*-site populations have been proposed: (1) <*T*-O> versus $^{[4]}$Al for a series of uvite samples (MacDonald & Hawthorne 1995a), (2) <*T*-O> versus $^{[4]}$B (refined) for a series of olenite samples (Hughes *et al.* 2004); and (3) <*T*-O> versus $^{[4]}$B for a series of Madagascar elbaite-liddicoatite samples (Ertl *et al.* 2006). These are shown as numbered, dark grey lines in the Figure 6.19. It is immediately apparent that the proposed curves are not all mutually compatible, and neither represents a general trend supported by all the observed data. In particular, the significant scatter in the data at low aggregate radii (high $^{[4]}$B values) precludes selecting between any of these trends. This emphasises the need for more reliable data for high-$^{[4]}$B tourmalines in order to tie down the lower end of the trend.

The vertical arrow at <*r*[*T*]> = 0.26 Å (Figure 6.19) shows where crystals with T = Si_6 or T = $(Si, Al \approx B)_6$ are expected to plot, and tourmalines with $0 \leq {}^{[4]}Al < {}^{[4]}B$ and $0 \leq {}^{[4]}B < {}^{[4]}Al$ *apfu* plot in the space to the left and right of the vertical

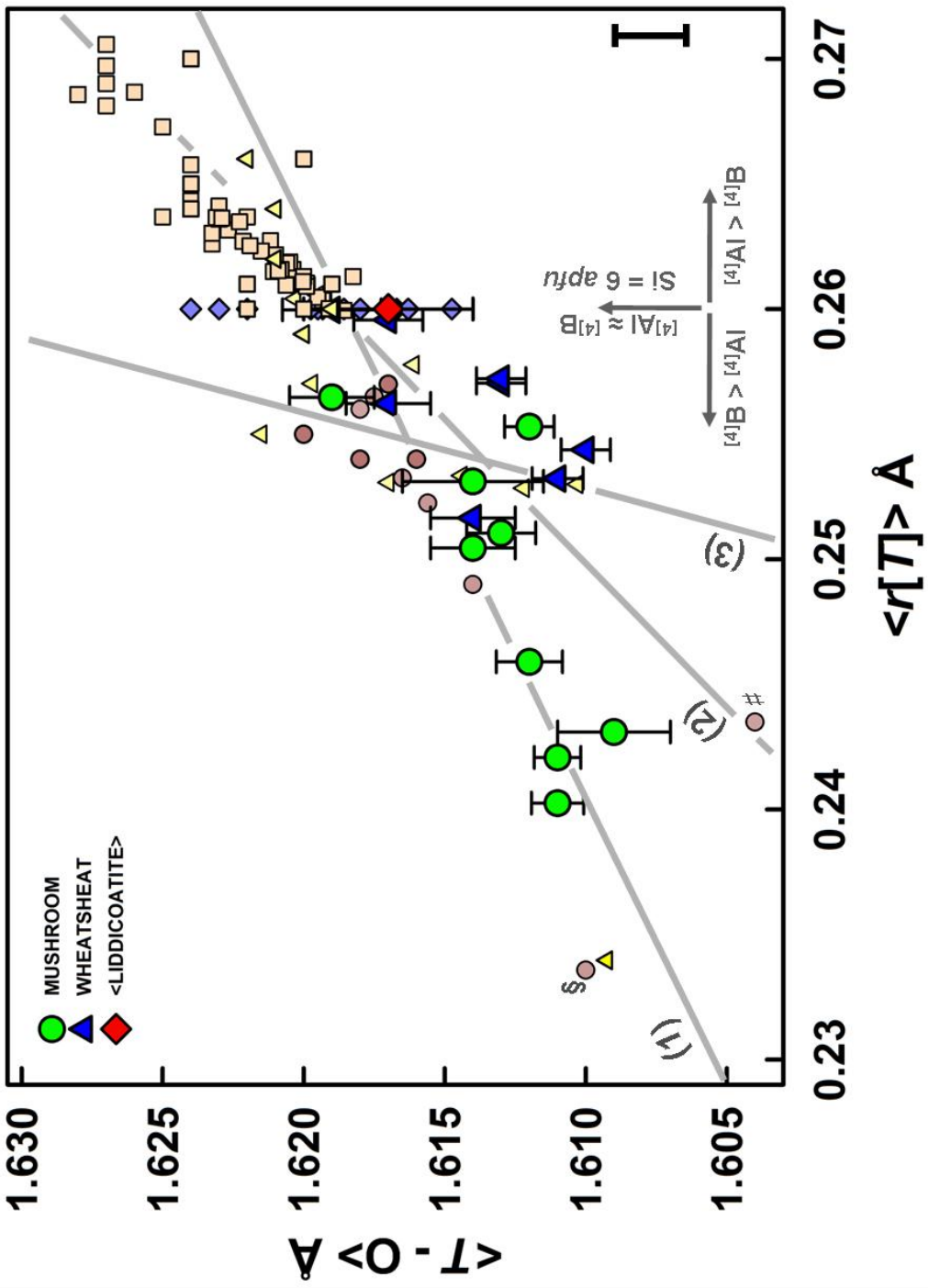

Figure 6.19 Enlargement of Figure 2.5b showing different trends reported for <*T*-O> vs <*r*[*T*]> in the literature: (1) Hughes *et al*. (2004); (2) MacDonald & Hawthorne (1995a); and (3) Ertl *et al*. (2006). § next to data point of Ertl *et al* (1997); # next to data point of Ertl *et al* (2007). Shapes correspond to *T*-site occupancies: O: T = $(Si,B)_6$; □ : T = $(Si,Al)_6$; Δ: T = $(Si,Al,B)_6$; ◇: T = Si_6. The error bar represents the average error observed in bond lengths calculated by SREF.

line, respectively. Nearly all crystals with T = (Al_xSi_{6-x}) show good linear agreement, and are in accord with, line (2) proposed by MacDonald & Hawthorne (1995a). Conversely, the scatter observed in the crystals reported to have 0 ≤ $^{[4]}$Al < $^{[4]}$B *apfu*, does not permit selecting between any of the proposed relations, although clearly that of Hughes *et al*. (2004) is unreasonable. It may be concluded that the problem is likely due to inaccuracies surrounding the determination of $^{[4]}$B in tourmalines.

6.7.5 The reliability of current T-site data

Closer consideration of Figure 6.19 reveals that the site-populations given for several structures are not compatible with the observed mean bondlengths. For example, the olenite of Ertl *et al.* (1997) (with $^{[4]}$B = 1.225 *apfu*; marked by §) has a much larger $^{[4]}$B content than the olenite of Ertl *et al.* (2007) (with $^{[4]}$B= 0.660 *apfu*; marked by ♯) and yet has a considerably longer mean bondlength: 1.610 *vs* 1.604 Å. Ertl *et al.* (2007) updated the *T*-site population of the olenite reported by Ertl *et al.* (1997) from ($Si_{4.775}B_{1.225}$) to ($Si_{4.89}B_{0.83}Al_{0.27}Be_{0.01}$) but this is difficult to evaluate as no new chemical analysis or structural results are given to justify this reassignment. Marler *et al.* (2002) report two synthetic tourmalines with $^{[4]}$B calculated by Rietveld refinement to be ~1.8 and ~2.2 *apfu*; however, compositional data are only available for the former crystal and B_2O_3 was calculated as B_2O_3 (wt. %) = 100 - ∑(oxides), with a final structural formula that gives the impossible summation of $^{[4]}$B + Si = 6.58 *apfu*. These points are shown in Figure 2.5b (marked by *).

Hughes *et al.* (2004) expressed <*T*-O> solely as a function of refined $^{[4]}$B where the assigned *T*-site populations also contain $^{[4]}$Al and $^{[4]}$Be, and so the status of this relation is not clear. MacDonald & Hawthorne (1995a) did not consider the possible presence of $^{[4]}$B in their uvite samples, but three of the samples (T73, T75, and T79) from their study were tested for the presence of $^{[4]}$B by ^{11}B MAS NMR and in none of these was it observed (Tables 5.1 and 5.2; Appendix A.6).

Ertl *et al.* (2006) refined the occupancies of the *T*-site B in four crystals of elbaite-liddicoatite from Madagascar and presented a relation between the optimized $^{[4]}$B content and the corresponding <*T*-O> values (Figure 6.20a). The correlation coefficient given for the relation shown in Figure 6.20a is 0.984 and the standard error of estimate is 0.001 Å. In considering the agreement between observed data and a model, the deviations of the data from their ideal values of that model should follow a normal distribution. We may examine the deviations between the measurements and their ideal values using half-normal probability-plot analysis (Abrahams 1972, 1974, Abrahams & Keve 1971). If the weighted deviations from the ideal values are drawn from a normal distribution, the ranked weighted observed differences, $\Delta/\sigma\Delta$, should be linear with the expected normal distribution (defined for small samples by Hamilton & Abrahams 1972), and have a slope of unity and an intercept of zero. Figure 6.20b shows the resulting relation for the data of Figure 6.20a; the data are linear but the slope of the relation is 0.28, a factor of ~4 less than the correct value of 1.0. The origin of the error in this type of plot may come from (1) erroneous assignment of standard

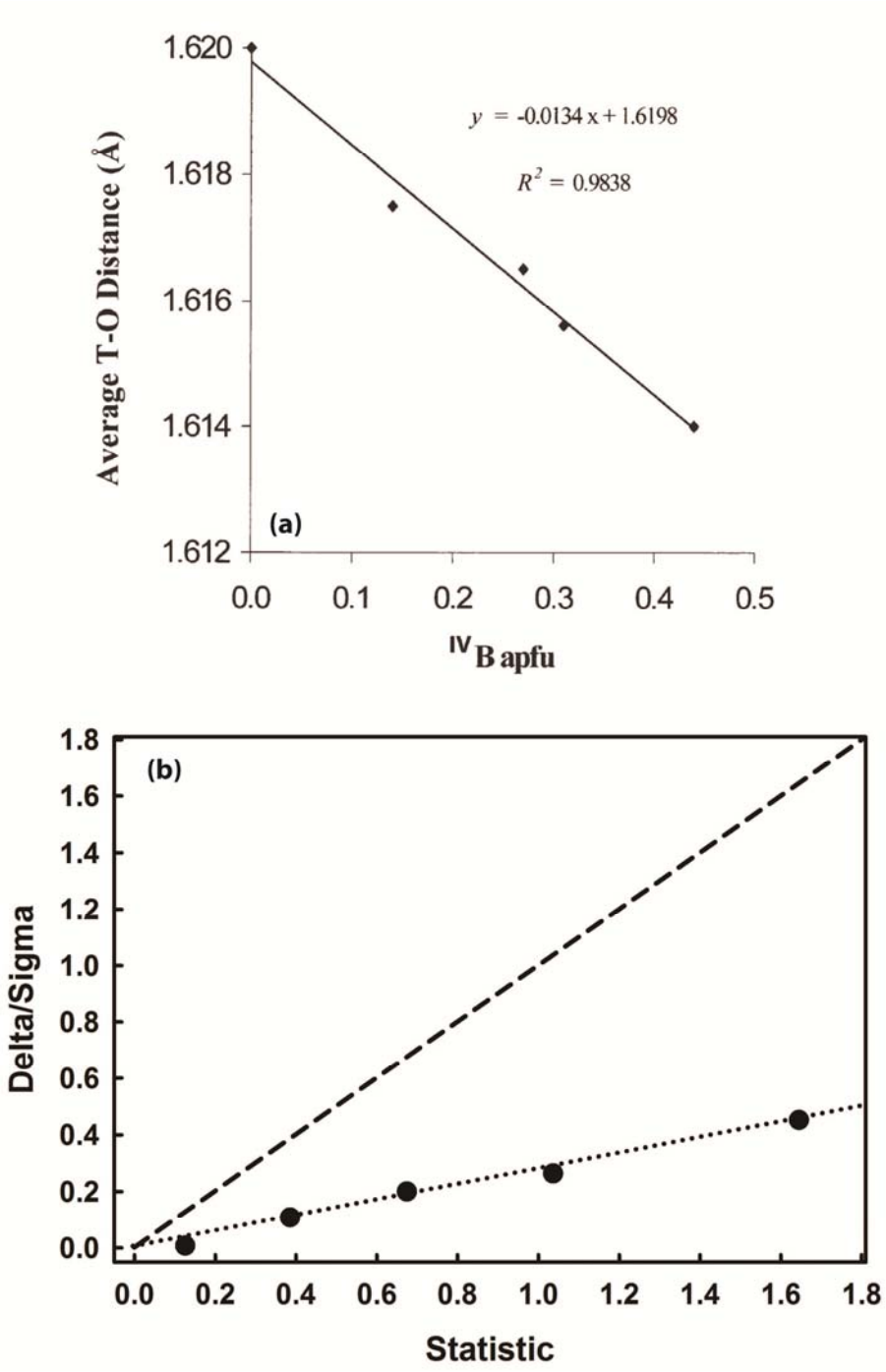

Figure 6.20 (a) The relation between <*T*-O> and [4]B content from Ertl *et al*. (2006); (b) half-normal probability plot for the data of Figure 6.20a; the broken line shows the correct relation, and the dotted line shows a least-squares fit to the data.

deviations; (2) some systematic bias in the data. The origin of this bias is not clear. However, what is clear is that this relation between <*T*-O> and $^{[4]}$B content cannot be considered as firmly established.

6.7.6 <Y-Φ> versus <T-O>

Figure 6.21 shows that a positive correlation exists between <*Y*-*Φ*> and <*T*-O> in the 40 tourmaline crystals discussed here. This is consistent with the substitution mechanisms operating to allow $^{[4]}$B at the *T*-sites. In Chapter 7, it will be shown that the main substitutions involving $^{[4]}$B are: (1) ^{Y}Al + $^{[4]}$B $\leftrightarrow$ ^{Y}(Fe, Mn)$^{2+}$ + Si; and (2) ^{Y}Al + $^{[4]}B_2$ $\leftrightarrow$ ^{Y}Li + Si_2. The ionic radii from Shannon (1976) for these atoms are $^{[6]}r$[Al]= 0.535, $^{[6]}r$ [Fe] = 0.72, $^{[4]}r$[Si] = 0.26, and $^{[4]}r$[B] = 0.11 Å. Thus, in both substitutions, larger ions at the *Y*- and *T*-sites are substituted for the smaller ions, in accord with the positive correlation in between <*Y*-*Φ*> and <*T*-O>.

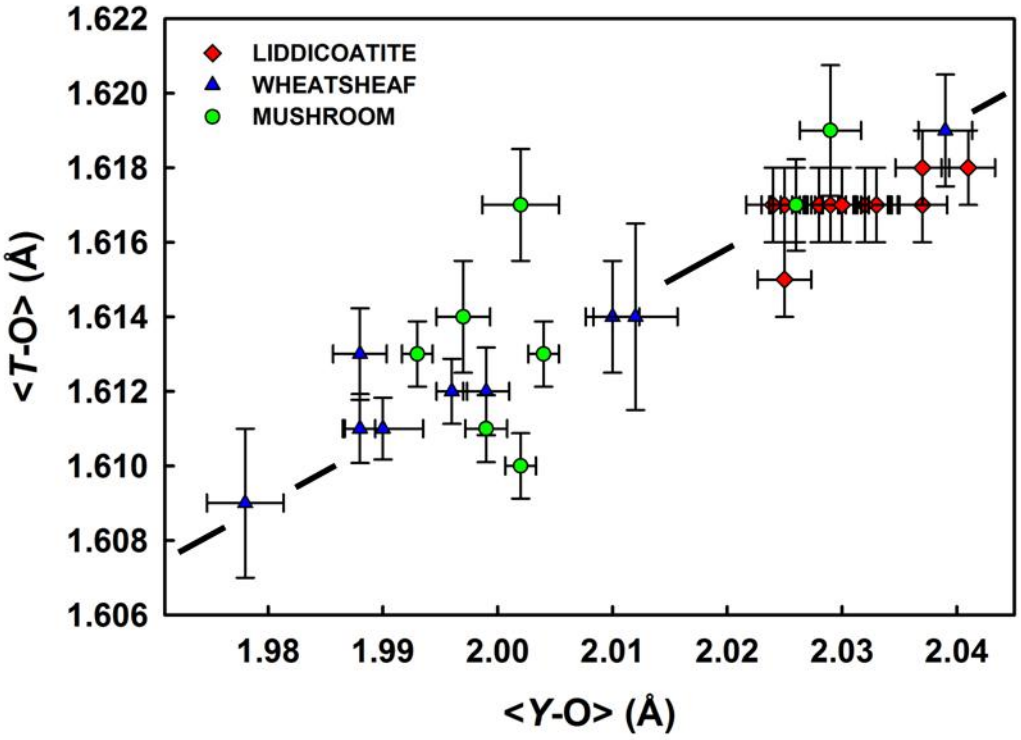

Figure 6.21 Relation between <*Y*-*Φ*> and <*T*-O> for the 40 single crystals of tourmaline discussed in this work.

CHAPTER 7

COMPOSITIONAL VARIATION AND ZONING IN TOURMALINE

7.1 INTRODUCTION

It has been shown that compositional variation in even a single crystal of tourmaline may provide comprehensive records of the evolution of magmatic and hydrothermal fluids (*e.g.*, Dutrow & Henry 2000; Henry et al. 1999; van Hinsberg & Schumacher 2007b; van Hinsberg *et al*. 2006). The four tourmaline samples described in detail in Chapters 3 and 6 differ dramatically in colour and crystal habit. Optically, each specimen shows a unique pattern of colour zonation, implying that composition also varies. In this chapter, extensive suites of compositional data, collected along traverses using an electron microprobe, are used to characterise the variation in chemical composition throughout each of the crystals.

7.2 ZONING IN COMPLEX CRYSTALS

Compositional variation in a crystal may be described in either the spatial or the compositional domain, and both require consideration as they may contain different types of information pertaining to crystal growth history. In the spatial domain, composition is plotted as a function of position on the crystal (*e.g.*, from core to edge). If the relation between distance and growth or distance and growth rate is well-understood, spatial data may yield information on progressive changes in the physical and chemical properties of the nascent melt or fluid. By

contrast, in the compositional domain, variations in the abundance of elements are plotted as a function of the abundance of other elements. Compositional domain data may be used to identify the site-specific substitution mechanisms which may contain information on element-selective processes and how the growing crystal faces interact with the solidifying melt.

7.2.1 Example system

Consider a hypothetical mineral with two different cations sites and the general formula $XY_3[O_2F]$, where X = Ca, Na, □ (vacancy), and Y = Al, Li. The composition of a growing crystal is free to vary as a linear mixture of the compositions: (I) $Na(Al_{1½}Li_{1½})[O_3F]$; (II) $Ca(AlLi_2)[O_3F]$; and (III) $□(Al_2Li)[O_3F]$ (Figure 7.1a). Now, three fictitious crystals (A, B and C) grow in three separate pegmatite melts, but the composition of each is constrained to lie on the A-A' join in Figure 7.1a.

An electron microprobe traverse is collected on each crystal, and the profiles in Figure 7.2a-c result. As a function of position, the composition of crystal A changes linearly (Figure 7.2a), the composition of crystal B *appears* to change randomly (Figure 7.2b), and the composition of crystal C, changes nonlinearly (Figure 7.2c; with an oscillatory pattern). On the basis of these observations, details of melt evolution could be determined. The most straightforward interpretations of these profiles is that as the mineral crystallized, the nascent fluids underwent different changes in physical and chemical properties. However, Figure 7.2d shows that the data from all three crystals

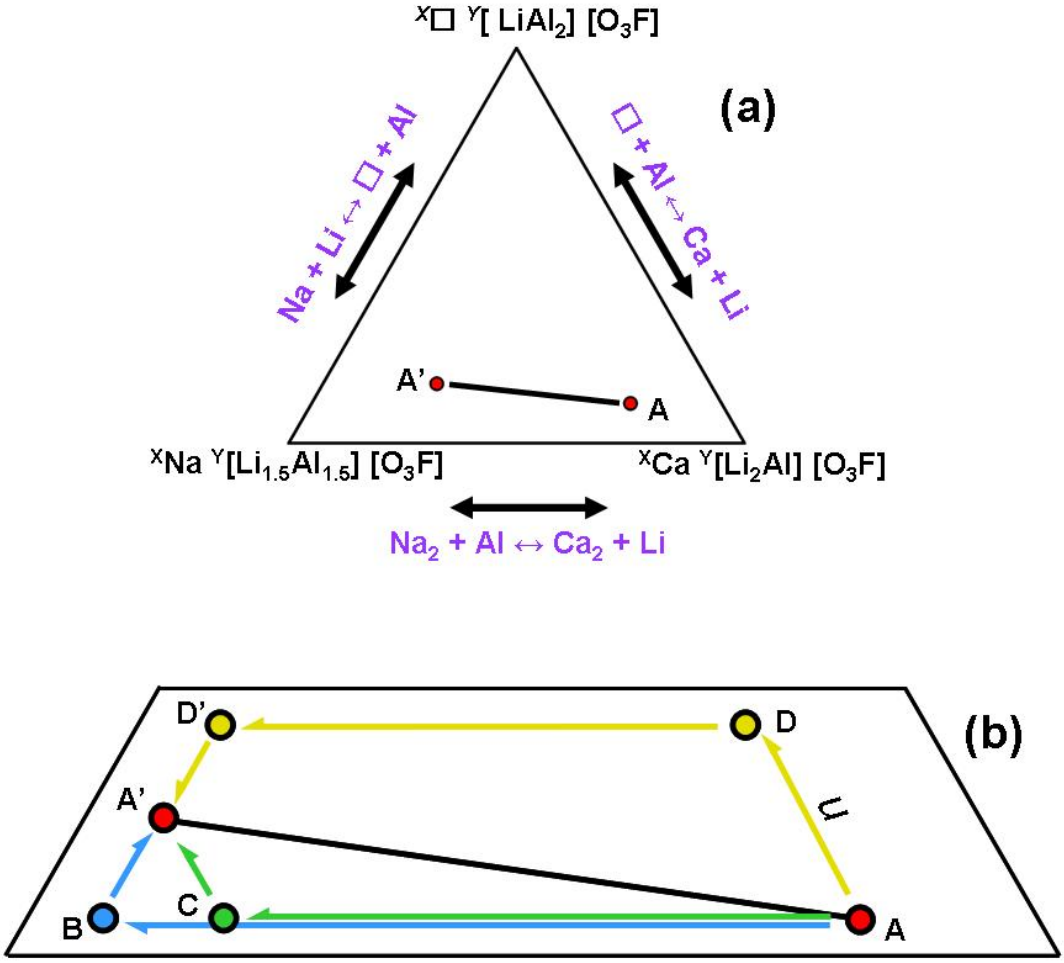

Figure 7.1 Hypothetical mineral system defined by end-members (I) $^{X}\square^{Y}(LiAl_2)[O_2F]$, (II) $^{X}Ca^{Y}(Li_2Al)[O_2F]$, (III) $^{X}Na^{Y}(Li_{1.5}Al_{1.5})[O_2F]$; (a) ternary diagram; (b) enlarged section of the ternary system showing three possible paths joining compositions A and A'.

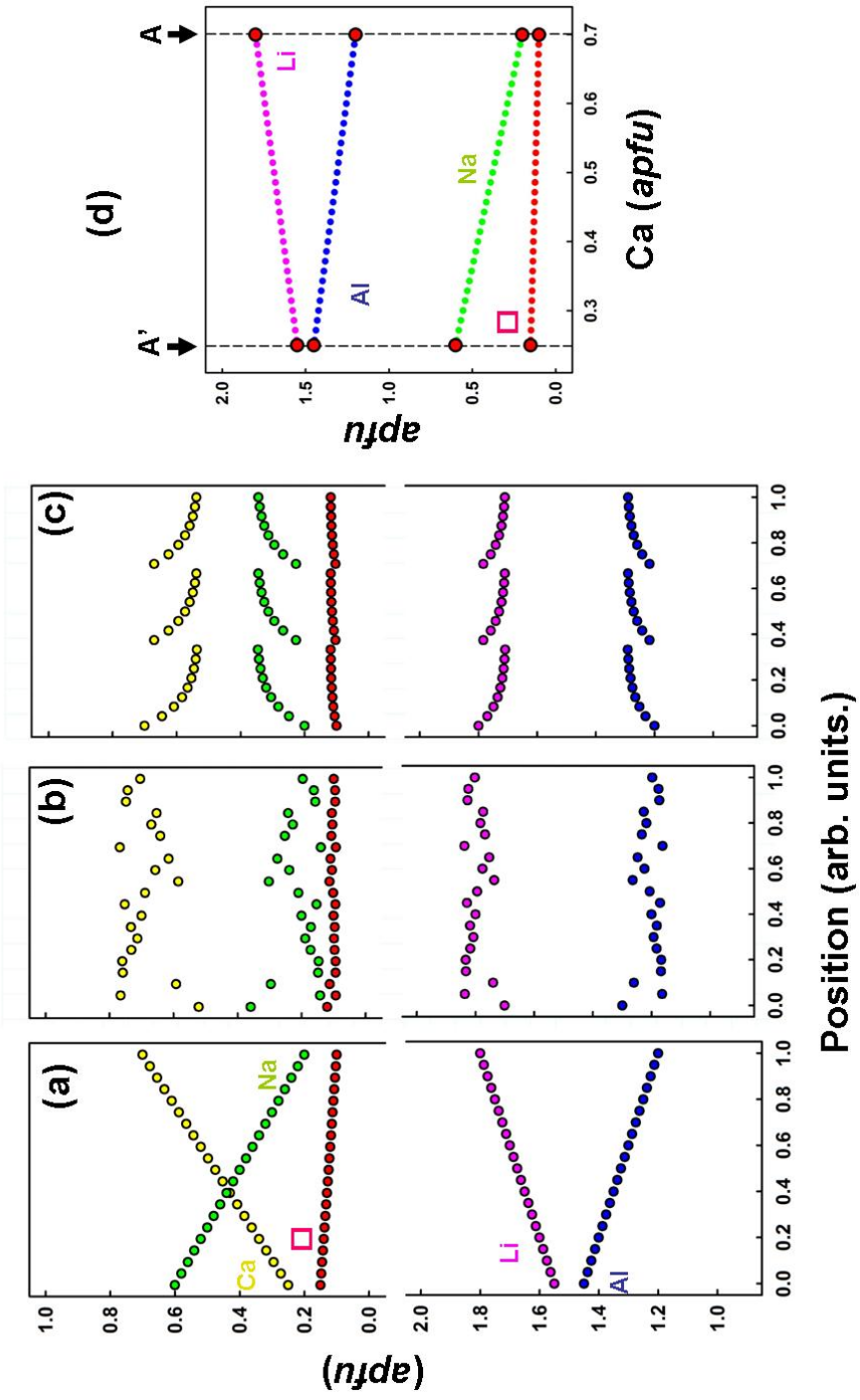

Figure 7.2 Hypothetical analytical traverses compositionally-constrained to A-A' in Figure 7.1a. Spatial domain profiles in which the compositions of successive points are: (a) linear, (b) random, and (c) nonlinear; (d) corresponding compositional domain profile for (a-c).

correspond to the same composition domain profile, indicating the same site-specific substitution mechanisms may have been in operation. For the ternary system in Figure 7.1a, the simplest substitutions are those relating compositions I, II and III:

(1) $^{X}Na_2 + {}^{Y}Al \leftrightarrow {}^{X}Ca_2 + {}^{Y}Li$,

(2) $^{X}Na_2 + {}^{Y}Li \leftrightarrow {}^{X}\square_2 + {}^{Y}Al$,

(3) $^{X}Ca + {}^{Y}Li \leftrightarrow {}^{X}\square + {}^{Y}Al$.

and when given magnitudes (in *apfu*), these correspond to vectors in Figure 7.1a oriented parallel to the ternary axes. From a strictly arithmetic perspective, it is clear that any two compositions in Figure 7.1a, may be related by some combination of the three vectors.

To relate compositions A to A', and generate the composition domain profile of Figure 7.2d, there are three choices of vectors:

Option A (green arrows in Figure 7.1b):

(1) $^{X}Ca_2 + {}^{Y}Li \rightarrow {}^{X}Na_2 + {}^{Y}Al$ (0.40 *apfu*)

(3) $^{X}Ca + {}^{Y}Li \rightarrow {}^{X}\square + {}^{Y}Al$ (0.05 *apfu*)

Option B (blue arrows in Figure 7.1b):

(1) $^{X}Ca_2 + {}^{Y}Li \leftrightarrow {}^{X}Na_2 + {}^{Y}Al$ (0.45 *apfu*)

(2) $^{X}Na_2 + {}^{Y}Li \leftrightarrow {}^{X}\square_2 + {}^{Y}Al$ (0.05 *apfu*)

Option C (yellow arrows in Figure 7.1b):

(1) $^{X}Ca_2 + {}^{Y}Li \rightarrow {}^{X}Na_2 + {}^{Y}Al$, ($u$ - $\square_A$ apfu)

(2) $^{X}\square_2 + {}^{Y}Al \rightarrow {}^{X}Na_2 + {}^{Y}Li$ (Ca_A - $Ca_{A'}$ + u *apfu*)

(3) $^{X}\square + {}^{Y}Al \rightarrow {}^{X}Ca + {}^{Y}Li$ (u - $\square_{A'}$ *apfu*)

where *u* is an arbitrary value . The direction of the arrows in each substitution is significant. For example, the arrow in (1) [in Option A] is right-pointing and shows that Ca and Li are replacing Na and Al as a function of distance in the spatial profile, whereas the arrow (1) [in Option B] is bidirectional and shows that because of the scattered spatial profile, the sense of replacement cannot be determined.

In this system, it is not necessarily possible to state which of the options (A, B, or C) is correct, however, Option A makes the most crystal chemical sense, as Options B and C both show antithetical behaviour of at least one element (*e.g.*, Na decrease *and* increases in Option B). As will be seen in the following discussions, the number of possible substitution mechanisms in tourmaline is constrained by the complex relations observed in compositional domain plots.

7.3 COMPOSITIONAL ZONING IN BLACK RAPIDS TOURMALINE

7.3.1 Spatial variation in chemical composition

Figure 7.3a shows the location of the analytical traverse across the prism of the Black Rapids Glacier sample, and Figure 7.4 summarizes the variation in all major constituents as a function of position along the traverse. In the central pink region, between 0.0 and ~9.2 mm, the average sum of the transition metals, *M** (= Fe^{2+} + Mn^{2+} + Ti^{4+} + Zn^{2+} + Mg) is extremely low (~0.01 *apfu*). However, (Ti^{4+} + Zn^{2+} + Mg) is close to 0.0 *apfu*, and the Mn^{2+} content (~0.01 *apfu*, Table 7.1), in the absence of any other interfering transition-element, gives rise to the

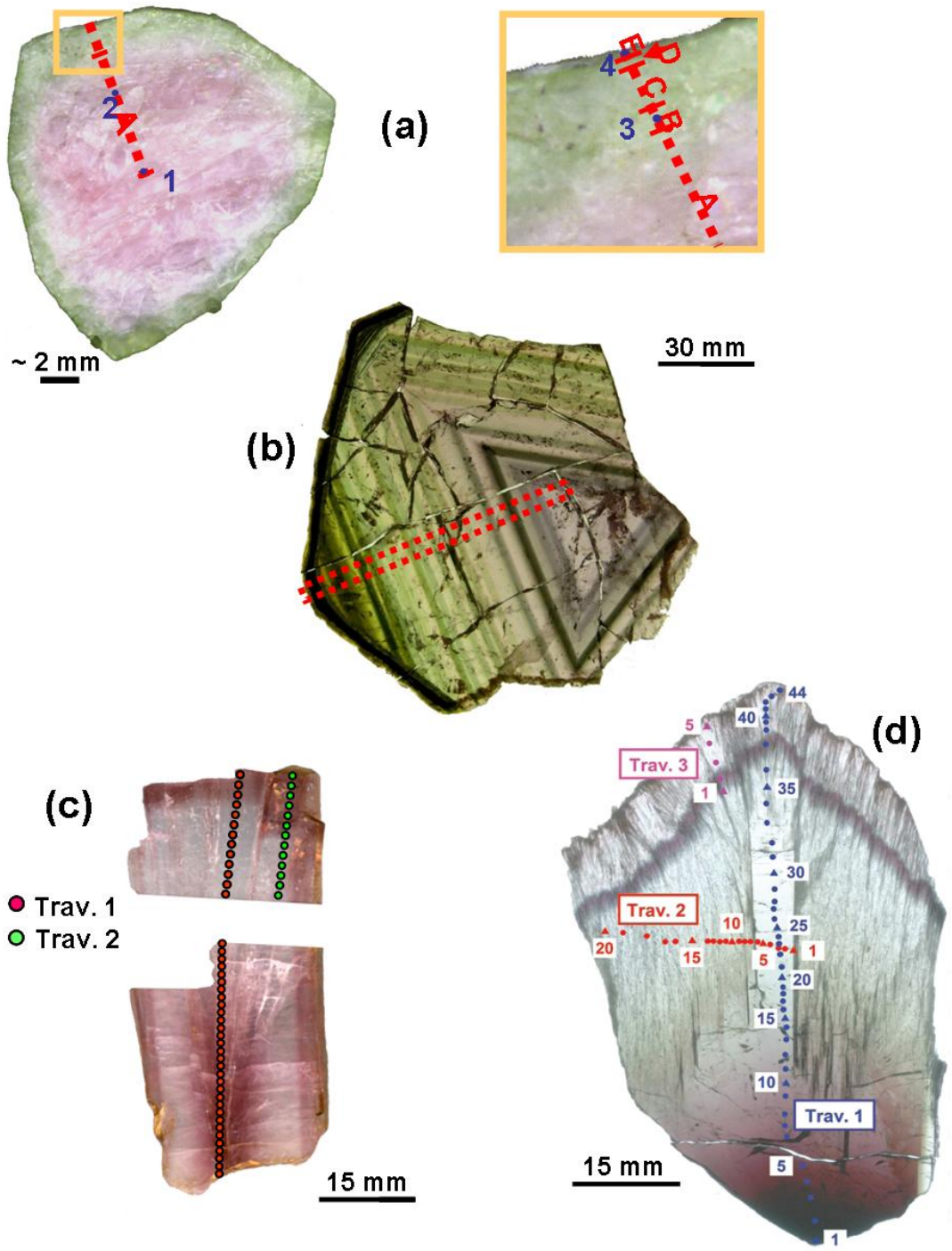

Figure 7.3 Cross sections of samples used for electron-microprobe analysis. The dotted lines indicate the locations of the analytical traverses on: (a) Black Rapids Glacier tourmaline; (b) Madagascar liddicoatite; (c) wheatsheaf tourmaline (SHW); and (d) mushroom tourmaline (SHM). Compare with Figures 3.1, 3.3, 3.6 and 3.8.

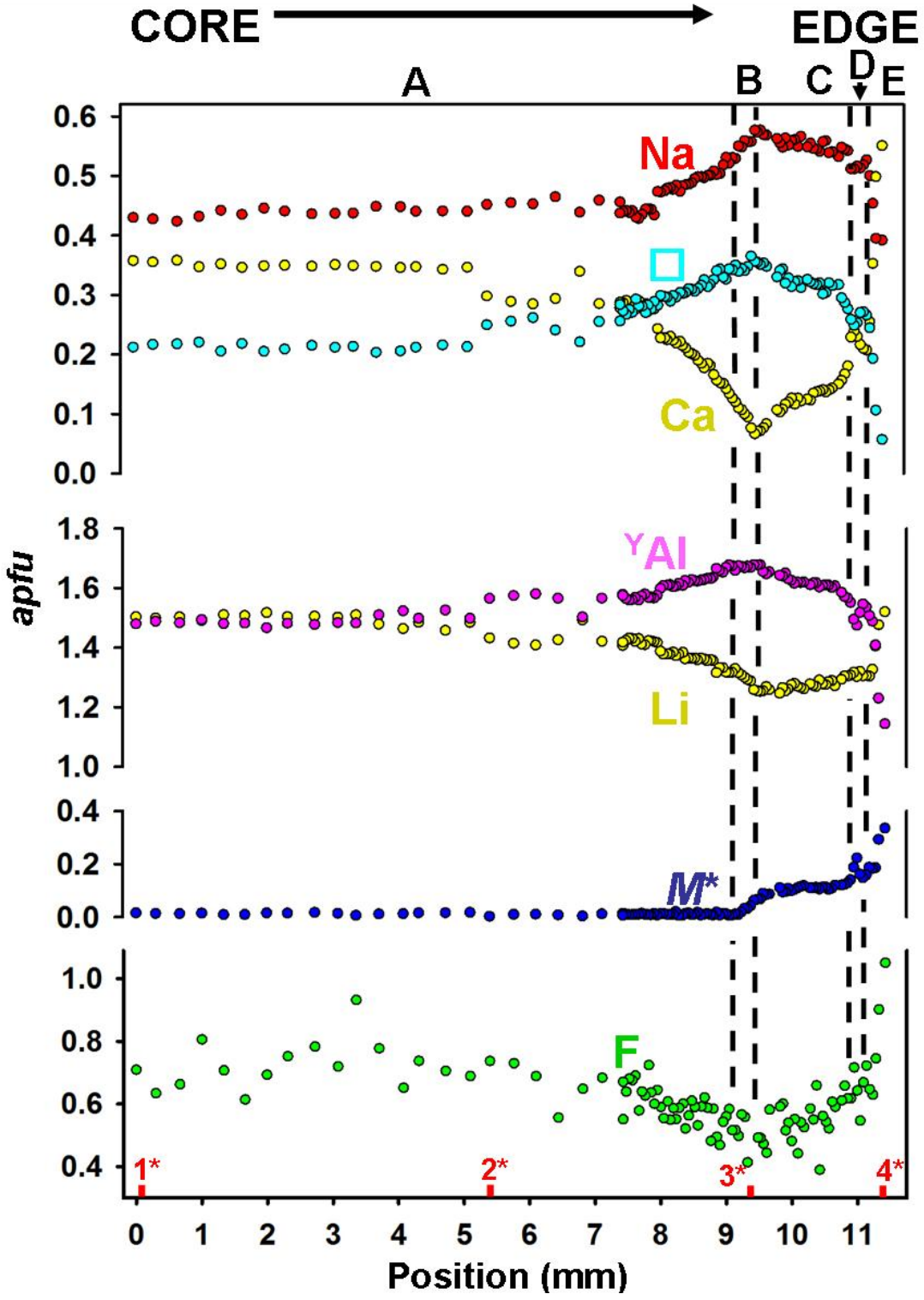

Figure 7.4 Variation in chemical composition of Black Rapids Glacier tourmaline as a function of position along the traverse shown in Figure 7.3a. The letters A-D correspond to regions of distinct substitution behaviour. The red marks and associated numbers at the bottom of the figure indicate the location of the compositions in Table 7.1.

TABLE 7.1 THE EXTREME LIDDICOATITE AND ELBAITE CHEMICAL COMPOSITIONS (wt%) AND FORMULAE (*apfu*) FOR BLACK RAPIDS GLACIER TOURMALINE.

	1**	2	3	4
SiO_2	37.87	37.41	37.65	37.46
TiO_2	0.00	0.00	0.01	0.04
B_2O_3*	11.38	11.61	11.24	11.19
Al_2O_3	41.21	41.99	42.19	39.02
MgO	0.00	0.01	0.00	0.04
CaO	2.15	1.71	0.40	3.29
MnO	0.09	0.06	0.15	0.54
FeO	0.00	0.01	0.32	1.89
ZnO	0.04	0.00	0.04	0.03
Li_2O*	2.32	2.08	1.84	2.26
Na_2O	1.43	1.51	1.91	1.30
K_2O	0.01	0.02	0.02	0.02
H_2O*	3.18	3.19	3.36	2.79
F	1.44	1.40	1.00	2.16
O = F	-0.61	-0.59	-0.42	-0.91
Σ	100.65	100.41	99.71	101.12
Si	5.877	5.811	5.889	5.891
B	0.048	0.113	0.035	0.037
Al	0.075	0.076	0.077	0.072
Σ*T*	6.000	6.000	6.000	6.000
B	3.000	3.000	3.000	3.000
Al	6.000	6.000	6.000	6.000
Al	1.536	1.688	1.777	1.233
Ti^{4+}	0.000	0.000	0.001	0.005
Mg	0.000	0.003	0.000	0.009
Fe^{2+}	0.000	0.001	0.042	0.249
Mn^{2+}	0.012	0.007	0.020	0.072
Zn^{2+}	0.005	0.000	0.005	0.003
Li	1.448	1.301	1.156	1.430
Σ*Y*	3.000	3.000	3.000	3.000
Na	0.430	0.454	0.579	0.396
Ca	0.357	0.285	0.067	0.554
K	0.002	0.004	0.004	0.004
□	0.211	0.257	0.350	0.045
Σ*X*	1.000	1.000	1.000	1.000
OH	3.291	3.310	3.506	2.926
F	0.709	0.690	0.495	1.074
Σ(*V* + *W*)	4.000	4.000	4.000	4.000

* Calculated by stoichiometry;
** Numbers correspond to locations marked on Figure 7.4

pink colour of the core. For most of the pink core, the composition is essentially invariant. There is a minor discontinuity between ~5.1 and ~8.0 mm, where $^{X}\square$ and ^{Y}Al increase abruptly and ^{X}Ca and ^{Y}Al decrease abruptly by ~0.1 *apfu*, but Na and *M** are unaffected by this change in the other constituents.

The green rind shows a far more dramatic variation in composition. Between ~8.0 and ~9.5 mm, the Na, □, and ^{Y}Al contents increase monotonically, whereas Ca, Li and F decrease monotonically. At ~9.2 mm, just before Ca is at a minimum, *M** abruptly begins to increase. Figure 7.5 shows the variation of *M** and its dominant constituent species Fe^{2+} and Mn^{2+} as a function of position in the outer region of the crystal. In this outer region, the Fe^{2+} content becomes greater than the Mn^{2+} content, accounting for the green colour of the rim. At 9.3 mm, the Na, □, and ^{Y}Al contents begin to decrease (Figure 7.4) whereas Ca, Li and F begin to increase monotonically. At ~10.8 cm, the Na, □, and ^{Y}Al contents begin to decrease more rapidly whereas Ca, Li and F begin to increase more rapidly. In the outer 0.4 mm of the crystal (~11.1 to ~11.5 mm), Ca, *M** and F increase significantly, from ~0.20 to ~0.57, 0.15 to 0.35, and 0.7 to 1.0 *apfu*, respectively. Thus the Black Rapids Glacier tourmaline is elbaite with a thin (≤ 0.2 mm) rind of fluor-liddicoatite. On the basis of spatial chemical variation, we may divide the crystal into five distinct regions, marked A-E in Figure 7.3a, 7.4 and 7.5.

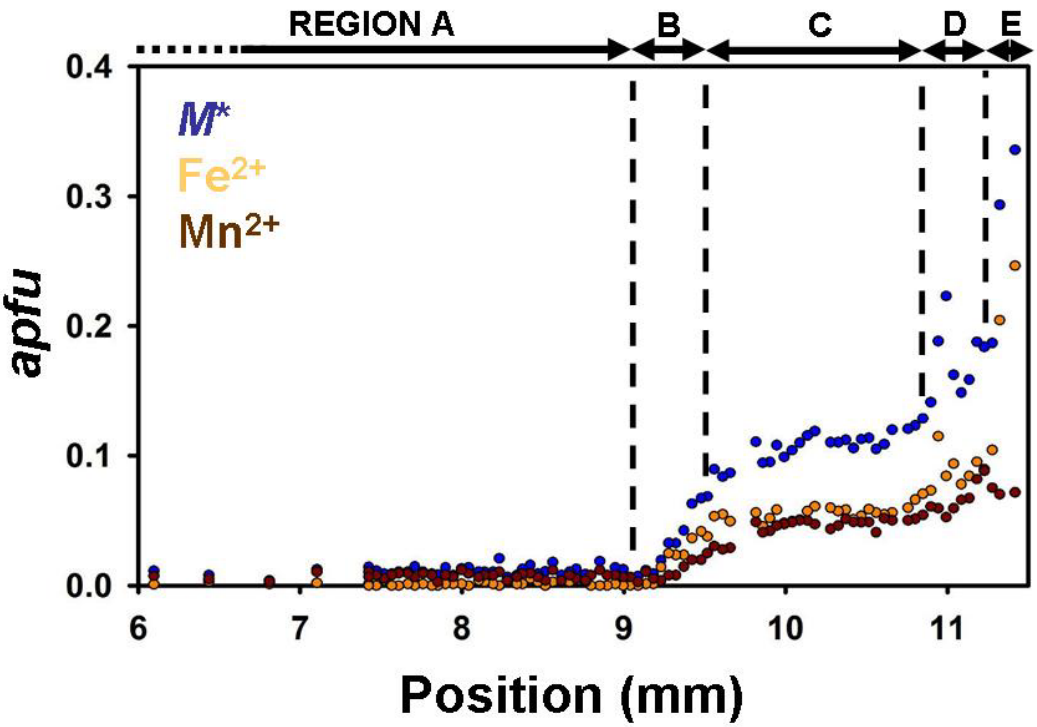

Figure 7.5 Variation in transition metals, *M**, in the outer 6 mm of the traverse; *M** is also separated into its Fe^{2+} and Mn^{2+} constituents

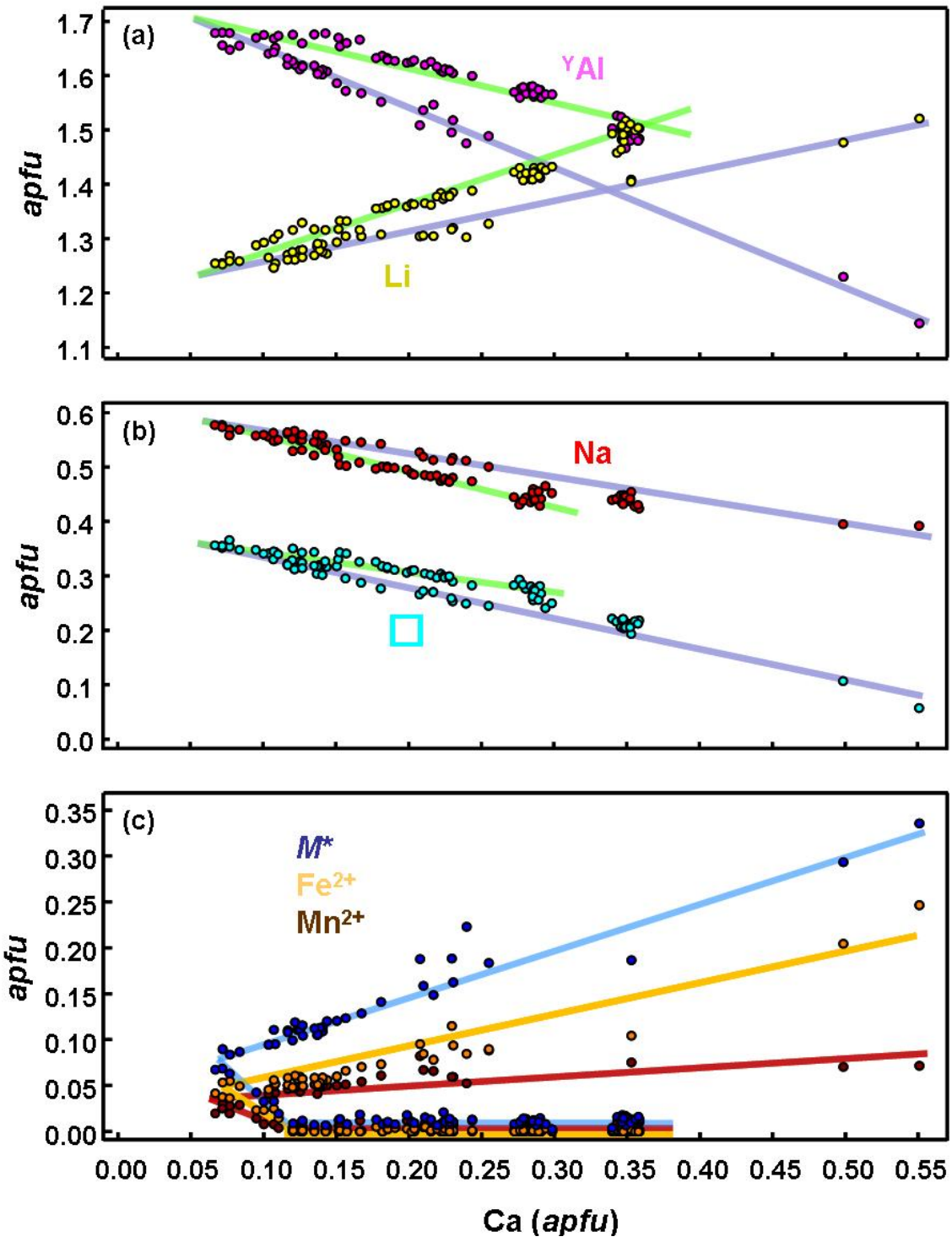

Figure 7.6 Variation in chemical composition of Black Rapids Glacier tourmaline: (a) Al and Li as a function of Ca; (b) Na and □ as a function of Ca; (c) *M**, Fe^{2+} and Mn^{2+} as a function of Ca. The coloured lines are drawn as guides to the eye.

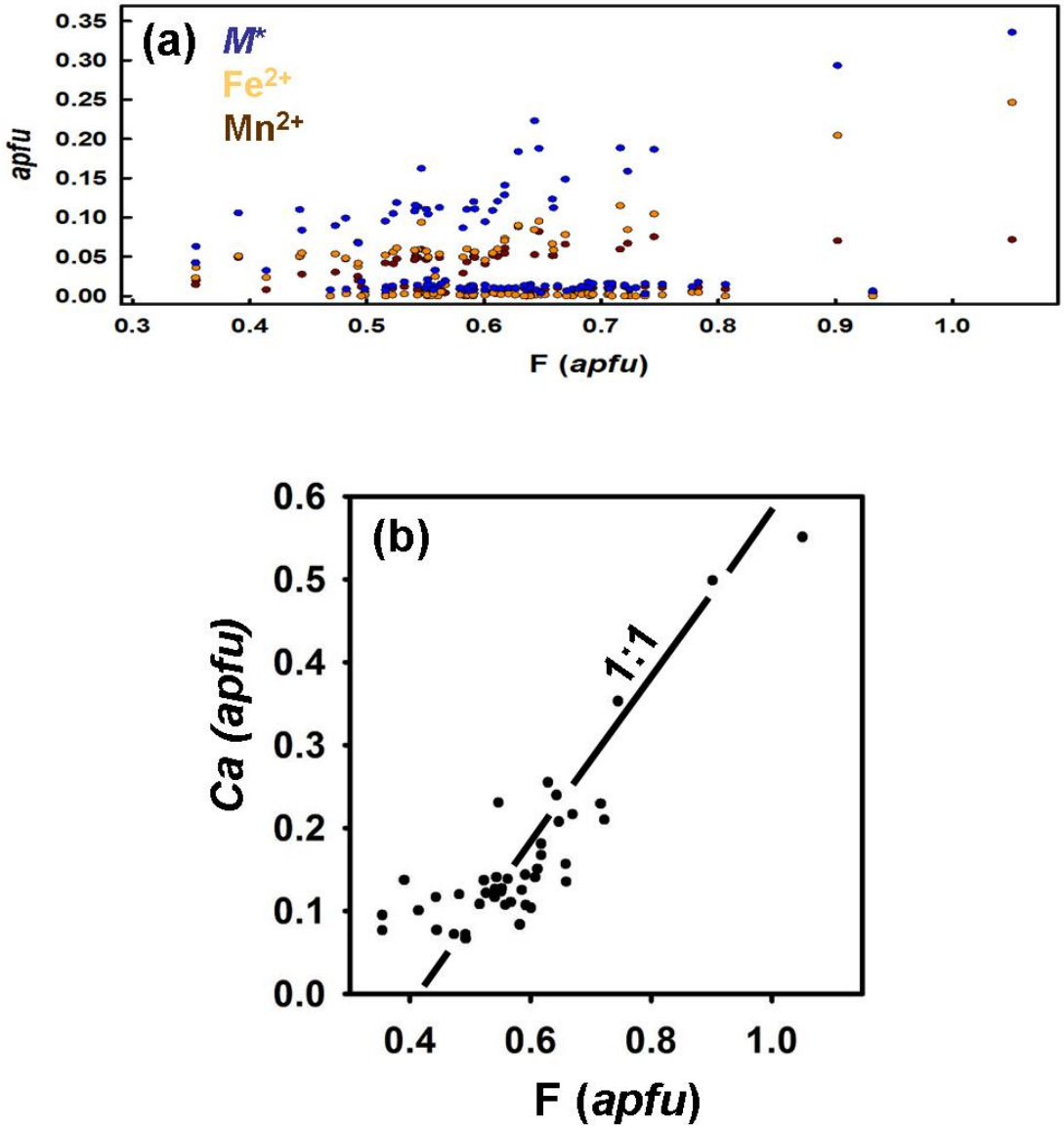

Figure 7.7 Variation in chemical composition of Black Rapids Glacier tourmaline as a function of F: (a) *M**, Fe^{2+} and Mn^{2+}; (b) Ca. The slope of the line in Figure 7.7b is unity.

7.3.2 Bulk chemical variation: from elbaite to liddicoatite

The total chemical variation in the crystal is shown in Figure 7.6 as a function of Ca content, and ranges from elbaite, $Na_{0.58}Ca_{0.07}\square_{0.35}$ $[Li_{1.27}Al_{1.66}M^*_{0.07}]$ Al_6 $[Si_{5.89}B_{0.03}Al_{0.08}]$ O_{18} $(BO_3)_3$ $(OH)_{3.53}F_{0.47}$, to fluor-liddicoatite, $Na_{0.39}Ca_{0.55}\square_{0.06}$ $[Li_{1.52}Al_{1.14}M^*_{0.34}]$ Al_6 $[Si_{5.89}B_{0.03}Al_{0.08}]$ O_{18} $(BO_3)_3$ $(OH)_{2.95}F_{1.05}$. There are two distinct trends in Figure 7.6 that we can understand from inspection of Figure 7.4. In Region A of the crystal, the amount of the *M** component is ~0.01 *apfu*, whereas in Regions B-E, the amount of *M** increases toward the edge of the crystal. Thus in Regions B-E, the greater amount of *M** results in a lower content of ^{Y}(Al + Li), resulting in the compositional trend indicated by the purple lines in Figure 7.6a,b. In Region A, the lower content of *M** results in the compositional trend with higher amounts of Al and Li indicated by the green lines in Figure 7.6a,b. The presence of two trends and the role of *M** is confirmed by the variation of *M** (and its various constituents) as a function of Ca (Figure 7.6c). It must be emphasized that Figure 7.6 gives only the chemical variations in the tourmaline and contains no information concerning the spatial aspects of zoning. However, the presence of two distinct trends in compositional change indicates that crystallization has not proceeded to completion by simple crystallization from an initial melt or fluid. There has been a hiatus in crystallization, and the presence of two distinct trends suggests that the crystallizing melt or fluid has been contaminated by an external fluid of distinctly different composition.

Variation as a function of F content is shown in Figure 7.7a. There is (a lot of) scatter in these trends because of the scatter in the F values due to the imprecision of the F analysis due to low count-rates; nevertheless, two important issues are apparent. First, the variation in *M**, Fe^{2+} and Mn^{2+} shows two distinct trends (Figure 7.7a), one with *M**, Fe^{2+} and Mn^{2+} close to 0 *apfu* (and corresponding to Region A of the crystal), and one with *M**, Fe^{2+} and Mn^{2+} increasing with increasing Ca in Regions B-E. There is also a strong 1:1 correlation between Ca and F (except for the lowest values of F, Figure 7.7b), and inspection of Figure 7.4 shows that Ca and F track each other through some fairly dramatic changes as a function of position in the crystal. The F content reaches a maximum of 1 *apfu* at the edge of the crystal, corresponding to the highest fluor-liddicoatite content of the crystal.

7.3.3 Substitution mechanisms in Black Rapids tourmaline

For the entire central pink region of the crystal (from 0 to 9.1 mm; Region A, Figure 7.4), the observed substitutions are as follows (Figure 7.8a):

$$(1_{BR}) \quad {}^{X}\square + {}^{Y}Al \rightarrow {}^{X}Ca + {}^{Y}Li \qquad (0.13)$$

$$(2_{BR}) \quad {}^{X}Ca_2 + {}^{Y}Li \rightarrow {}^{X}Na_2 + {}^{Y}Al \qquad (0.06)$$

where numbers in brackets are in units of *apfu*, and the arrows indicate replacement of (1) ${}^{X}Ca$ and ${}^{Y}Li$ by ${}^{X}\square$ and ${}^{Y}Al$, and (2) ${}^{X}Na$ and ${}^{Y}Al$ by by ${}^{X}Ca$ and ${}^{Y}Li$ with increasing distance from the centre of the crystal[2] from 0 to 9.1 mm. Substitution (1) describes the compositional change along the rossmanite-

[2] Note: For all substitution mechanisms: numeral refers to order in which it is observed along traverse; subscript denotes sample; BR = Black Rapids; ML = Madagascar liddicoatite, WS = wheatsheaf, MS = mushroom.

liddicoatite join, and substitution (2) describes the compositional change along the elbaite-liddicoatite join. The straight lines in Figure 7.8a show the aggregate variations represented by these substitutions. From the onset of enrichment in *M** (9.2 mm; Region B; Figure 7.4) until the minimum Ca value (9.5 mm; Region B; Figure 7.4), the Al content of the crystal is invariant, and the substitution mechanisms in operation are as follows (Figure 7.8b):

$$(3_{BR}) \quad {}^{X}Na + {}^{Y}M^{*} \rightarrow {}^{X}Ca + {}^{Y}Li \qquad (0.04)$$

$$(4_{BR}) \quad {}^{X}\square + {}^{Y}M^{*}_{2} \rightarrow {}^{X}Ca + {}^{Y}Li_{2} \qquad (0.01)$$

At 9.2 to 9.4 mm along the traverse, the compositional profile shows a prominent change where the trends of all constituents reverse (Figure 7.4, 7.5, 7.8). From 9.4 to ~10.9 mm (Figure 7.8b, Region C), the inverse of substitution (1_{BR}) becomes active, and the remaining chemical variation occurs *via* substitution (5_{BR}):

$$(-1_{BR}) \quad {}^{X}Ca + {}^{Y}Li \rightarrow {}^{X}\square + {}^{Y}Al \qquad (0.08)$$

$$(5_{BR}) \quad {}^{X}Ca + {}^{Y}M^{*} \rightarrow {}^{X}Na + {}^{Y}Al \qquad (0.08)$$

$$(6_{BR}) \quad {}^{X}Ca + {}^{Y}M^{*}_{2} \rightarrow {}^{X}\square + {}^{Y}Al_{2} \qquad (0.01)$$

At ~10.9 mm (until ~11.1 mm, Figure 7.4, 7.5, and 7.8c, Region D), there is another reversal of compositional trends involving the following substitutions (Figure 7.8c; note the reversed *M** scale):

$$(7_{BR}) \quad {}^{X}\square + {}^{Y}Al_{2} \rightarrow {}^{X}Ca + {}^{Y}M^{*}_{2} \qquad (0.05)$$

In the last ~0.2 mm of the crystal (Figure 7.4, 7.5, 7.8d; Region E), the trend of increasing Ca resumes and substitutions (5) and (-1) again become active, together with substitution (-7_{BR}):

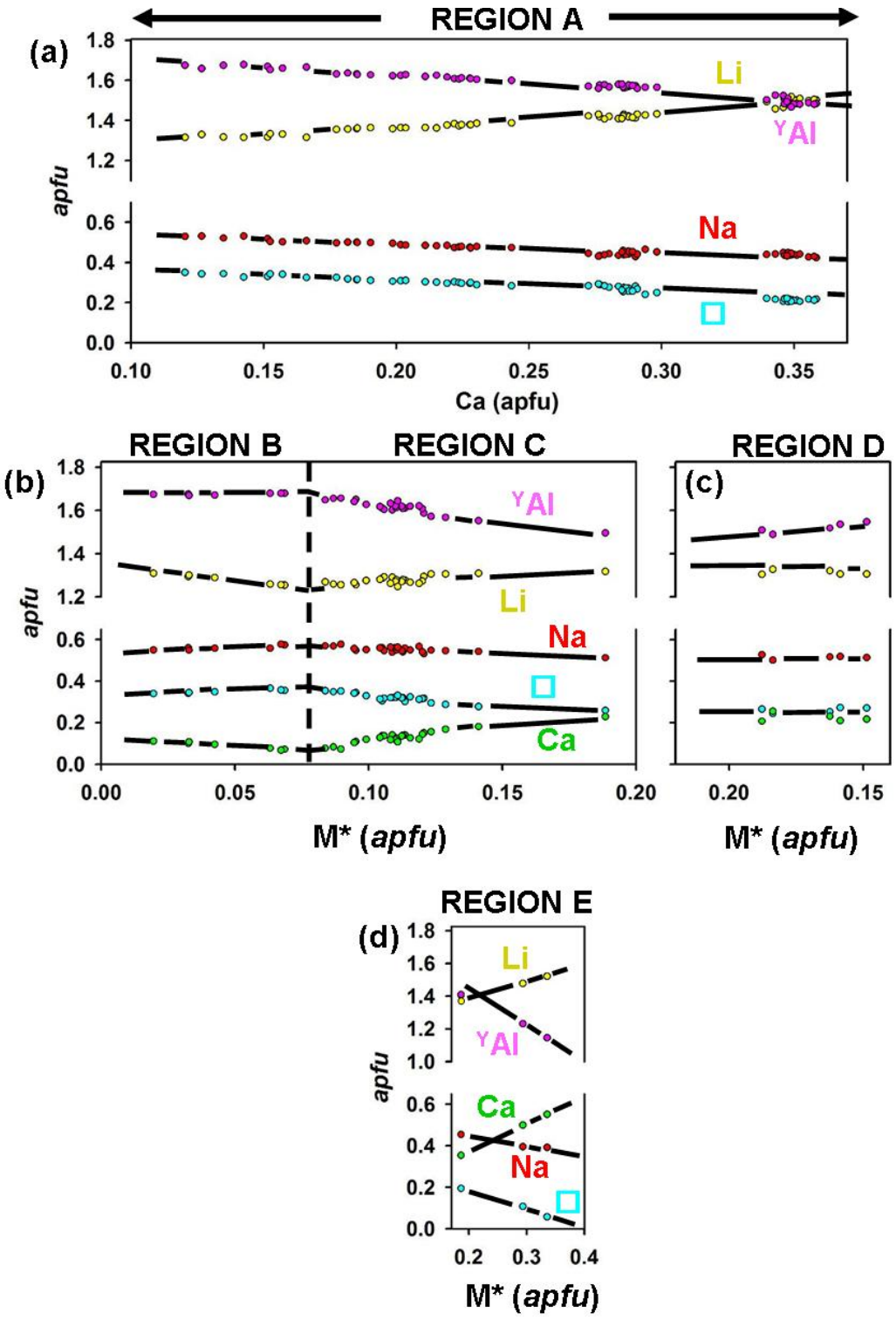

Figure 7.8 Variation in composition of Black Rapids Glacier tourmaline: (a) Al, Li, Na, and □ versus Ca for Region A; (b-d) Li, ^{Y}Al, Na, Ca and □ versus M* for Regions B, C, D and E. The lines are drawn as guides to the eye.

(-1_{BR}) $^{X}Ca + {}^{Y}Li \rightarrow {}^{X}\square + {}^{Y}Al$ (0.12)

(5_{BR}) $^{X}Ca + {}^{Y}M^{*} \rightarrow {}^{X}Na + {}^{Y}Al$ (0.08)

(7_{BR}) $^{X}Ca + {}^{Y}M^{*}_{2} \rightarrow {}^{X}\square + {}^{Y}Al_{2}$ (0.05)

The elbaite-liddicoatite substitution (4_{BR}) is relatively minor, occurring only in Region B, whereas the liddicoatite-rossmanite substitution (1_{BR}) accounts for the majority of the chemical variability observed. The substitution mechanisms of the total Black Rapids Glacier tourmaline sample are summarized in Table 7.2.

Possible variations in the small amount of tetrahedrally-coordinated Al and B in this sample have been disregarded (see samples AT06 (pink core) and AT07 (green rim), Table 5.2; Appendix A.6). The overall low amounts ($^{[4]}B + {}^{[4]}Al << 0.11$ *apfu*) observed by MAS NMR in all regions of the crystal indicate that although substitution mechanisms accommodating the exchange of these constituents may be active, they are not responsible for a significant part of the compositional variation observed throughout the sample. Kalt et al. (2000) showed that for olenite tourmalines where significant amounts of $^{[4]}B$ are present, $^{T}B + {}^{Y}Al \rightarrow Si + {}^{Y}M^{*}$ is the principal substitution This is also observed in wheatsheaf and mushroom elbaite. Given the composition of the Black Rapids Glacier sample, it is probable that this mechanism is in operation, although its magnitude is likely much less than 0.11 *apfu* throughout the crystal.

7.4 COMPOSITIONAL ZONING IN MADAGASCAR LIDDICOATITE

7.4.1 Spatial variation in chemical composition and oscillatory zoning

The relative variation in *X*-site composition is shown in Figure 7.9, with the different zones and the general direction of compositional evolution indicated. In the core, (Na + K) is dominant at the *X*-site, the corresponding *Y*-site composition is dominant in (Li + Al) (Figure 7.10), and the core is elbaite out to ~15 mm on the traverse shown in Figures 7.10 and 7.11. At ~15 mm along the traverse, the composition becomes liddicoatite, and (Ca + Pb) gradually rises (with some oscillatory fluctuations) to ~0.75 (Ca + Pb) *apfu* at ~38 mm (Figures 7.9 and 7.11). Here, the (Ca + Pb) content levels out and the variation in the rest of the pyramidal zones is due primarily to oscillatory variation (Figure 7.11). At the junction with the prismatic zones close to the edge of the crystal, Ca decreases rapidly and the composition again becomes elbaitic (*i.e.*, Na > Ca *apfu*).

7.4.2 Core

The purple core of the liddicoatite crystal (0-8 mm along the profile, Figure 7.3b, 4.1b) does not show any pronounced oscillatory zoning. This region is relatively homogenous with a composition of approximately $^{X}(Na_{0.5}Ca_{0.4}\square_{0.08}Pb_{0.02})\ ^{Y}(Li_{1.5}Al_{1.0}Mn_{0.5})\ ^{Z}Al_6\,(BO_3)_3\,(Si_6O_{18})\ (OH_{3.2}F_{0.8})$.

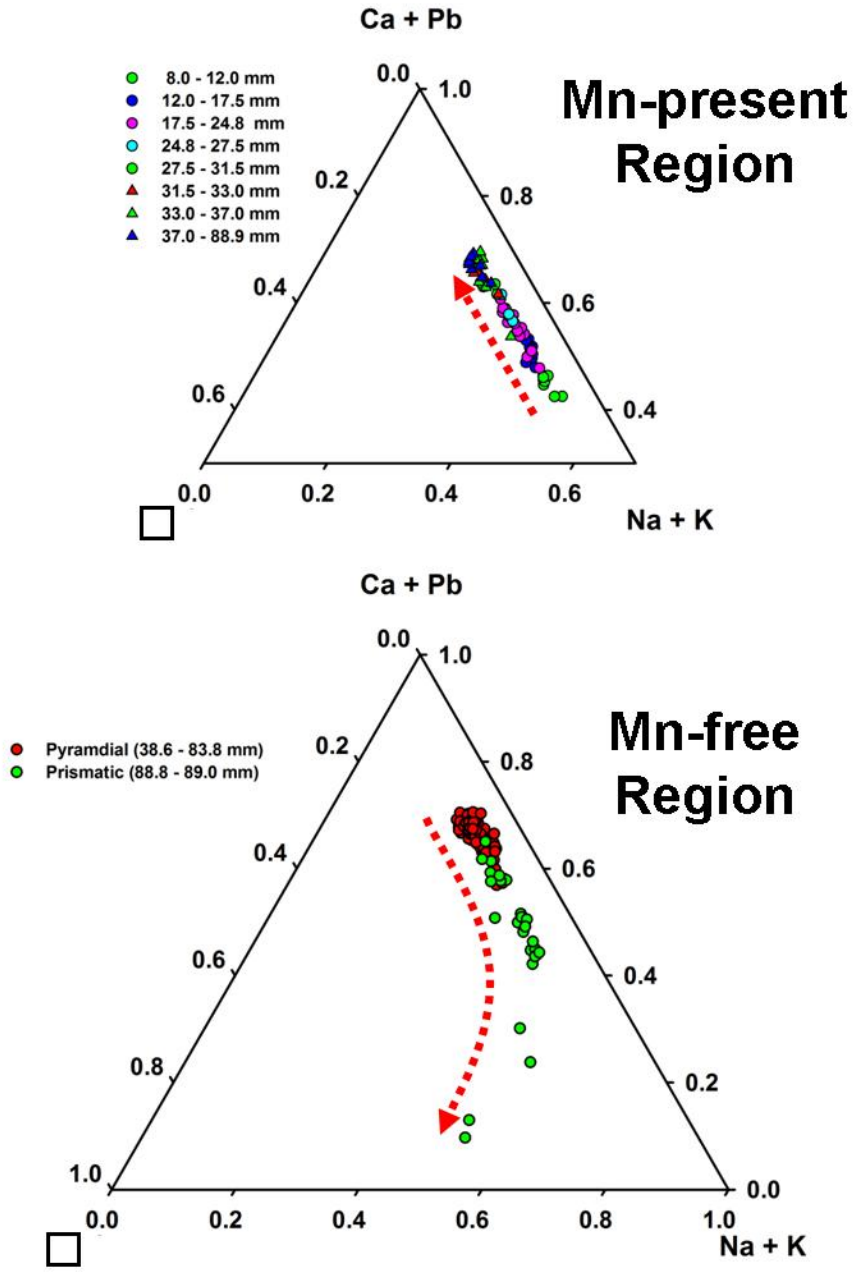

Figure 7.9. Variation in *X*-site cation abundance in Madagascar liddicoatite (Figure 7.3b). □ = vacancy. Distances correspond to traverses in Figures 7.10 and 7.11. Red arrows indicate trend from crystal core to crystal edge.

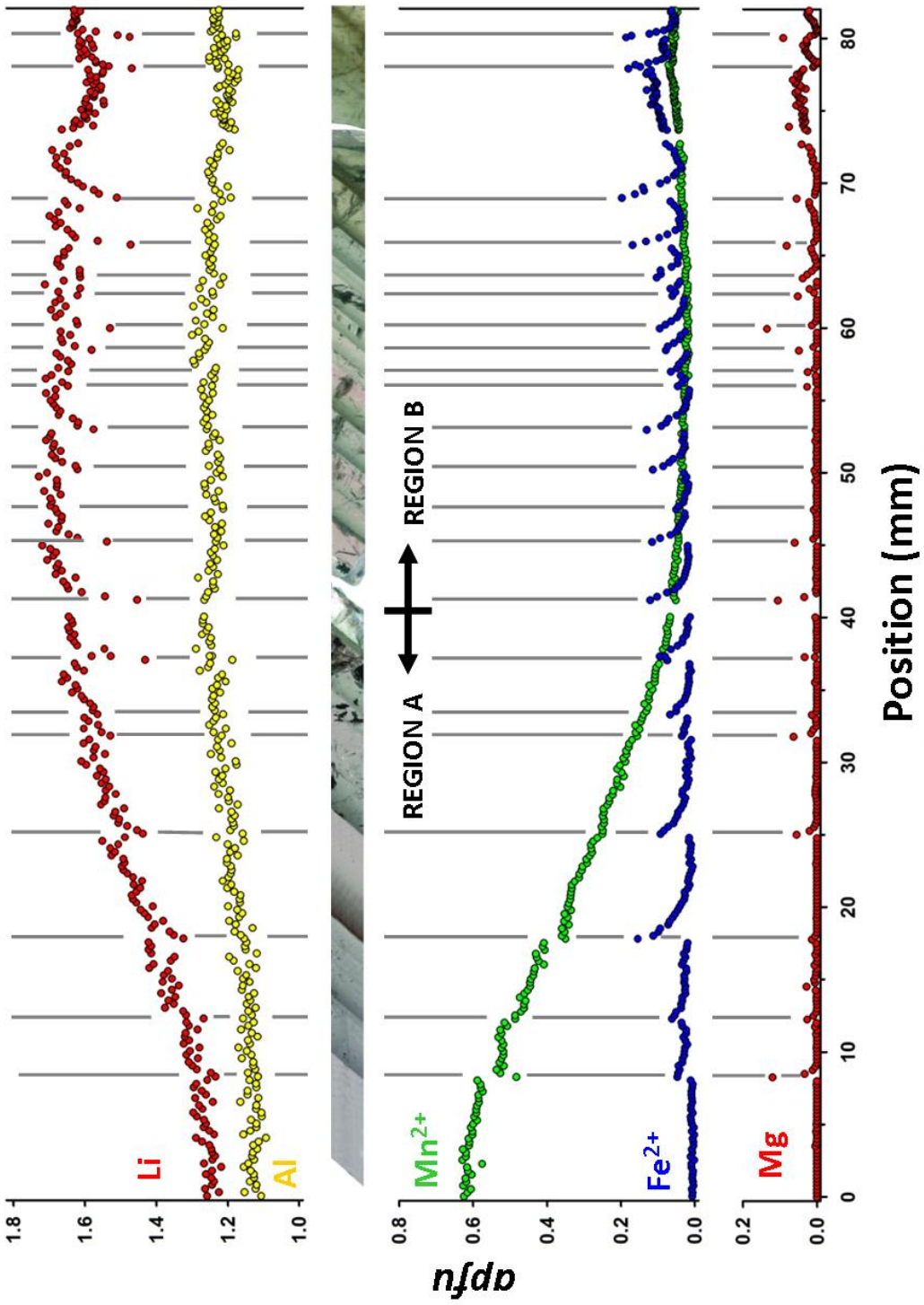

Figure 7.10 Variation in *Y*-site cation abundance from core to edge as a function of position along slice taken from Madagascar liddicoatite at location indicated in Figure 7.3b (step size 300 μm). Vertical lines denote boundaries between individual oscillatory zones.

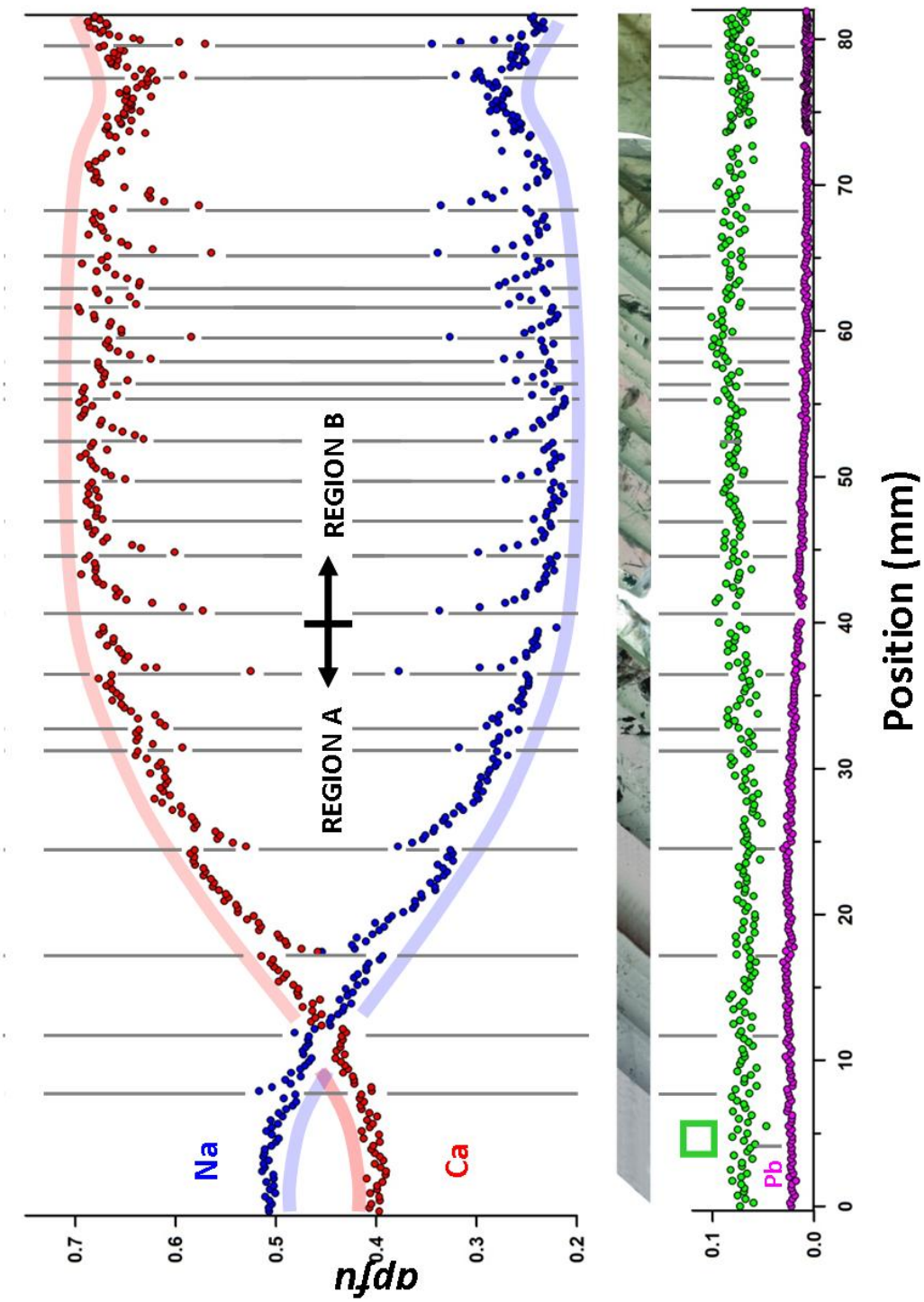

Figure 7.11 Variation in *X*-site cation abundance from core to edge as a function of position along slice taken from Madagascar liddicoatite at location indicated in Figure 7.3b (step size 300 μm). Vertical lines denote boundaries between individual oscillatory zones. Pink an blue lines show non-period variation in composition. ☐ = vacancy.

7.4.3 Pyramidal zones

The pyramidal sector can be separated into two zones on the basis of Mn content (Figure 7.10): Region A: 0-40 mm, Mn > 0.05 apfu; Region B: 40-82 mm, Mn < 0.05 apfu. Throughout most of Region A, Mn is the most abundant transition-metal present and the <*Y*-*Φ*> distances (Section 6.7.1.) indicate that all Mn is in the divalent state, in agreement with Mössbauer spectra, which show that not all Fe in Fe^{3+}. The average Mn content declines more or less monotonically from 0.70 to ~0.05 *apfu* between 0 and 40 mm, corresponding with a decrease in the intensity of the purple colour of the crystal. In Region B, where Mn is absent, Fe is the most abundant transition metal in each zone, giving rise to the green colour.

Figures 7.10 and 7.11 show two types of chemical variation as a function of distance from the core of the crystal: (1) a smooth variation in constituents, as shown by the solid red and blue lines (slightly displaced from the upper and lower limits of variation for these constituents for clarity) in Figure 7.11; (2) oscillatory variations superimposed on those smooth curves (indicated by the broken vertical lines in Figures 7.10 and 7.11). Thus in the pyramidal region, the upper bound of Ca increases smoothly, then levels out, and finally decreases slightly, and oscillatory decreases in Ca are superimposed on this upper bound, whereas Na shows the inverse behaviour. $^{X}\square$ and ^{X}Pb are each almost constant across the crystal and show little or no correlation with the oscillatory zoning so prominent in Ca and Na.

The behaviour of both Fe and Mg is also unusual. The bounding values for both these constituents is 0.00 *apfu* (Figure 7.10) for much of the traverse (although the minimum bound for Fe does rise from 0.00 at the core to ~0.02 *apfu* in the outer dark-green part of the pyramidal zone. However, there are oscillatory variations in the amount of Fe (up to 0.20 *apfu*) and Mg (up to 0.12 *apfu*) superimposed on this background count of ~0.0 *apfu*. It must be significant that two of the most prominent constituents associated with the oscillatory zoning have limiting contents of 0.0 *apfu*.

Throughout the entire crystal, the dark colour at the onset of each new zone (Figure 3.1b) is coincident with a discontinuous increase in both Fe and Mg at the *Y*-site, followed by a continuous exponential decrease in both of these constituents (Figure 7.10). The magnitude of the discontinuous increase that marks the beginning of each zone varies from ~0.04 to 0.22 *apfu* Fe and 0.03 to 0.16 *apfu* Mg. Where both constituents decrease exponentially, the Mg content consistently drops at a greater rate than Fe over the same interval. Moreover, there are several zones where the corresponding Mg spike is either absent or very minor (*e.g.*, between 50 and 60 mm). The abundance of Li decreases discontinuously at the onset of each zone and then increases with decrease in Fe and Mg. At the *X*-site (Figure 7.11), there is a discontinuous decrease in Ca and increase in Na at the beginning of each new zone. Conversely, the abundances of Mn, ^{Y}Al, and $^{X}\square$ are less sensitive to the occurrence of oscillatory zoning. Where the crystal contains >0.02 Mn *apfu*, the onset of a new (optically recognizable) zone is characterised by small decreases (~<0.03> *apfu*) in both

Mn and ^{Y}Al (Figure 7.10) at the vertical broken lines. Where Mn ≤ 0.02 *apfu*, the onset of new oscillatory zones is sometimes (but not always) marked by a small decrease in ^{Y}Al but there is no change in Mn.

In Region A, the discontinuities in (Fe + Mg) content are completely abrupt; there is no observable increase in either Fe or Mg prior to the onset of a new zone. Each zone continues past the point at which Fe ~0 *apfu*, becoming very pale or colourless (Figures 3.1 and 7.10). In Region B, the beginning of each zone is marked by a green discontinuity, which fades to nearly colourless within each zone as the Fe content decreases to less than 0.05 *apfu* (Figures 3.1 and 7.10). Although the oscillatory zoning in Region A continues into Region B, there are several features (in addition to the absence of Mn) that clearly distinguish the zones of Region B from those of Region A: (1) the zoning pattern adopts a more uniform and repetitive character with less observed variation in zone width, and nearly all zones are 2-3 mm wide; (2) in some of the zones in Region B, there are increases in Fe (and Mg) contents prior to the onset of a new zone. This behaviour is most clearly seen between 60 and 75 mm in Figure 7.10; (3) zones do not continue past the point where Fe = 0 *apfu*, unlike in Region A.

7.4.4 Prismatic zones

In the region of prismatic zoning (83-92 mm, Figure 7.12), close to the crystal edge, the oscillatory zones become very narrow (< 0.1 mm) and are oriented parallel to the prism faces. Together, these zones form a dark band in which there is a significant increase in the abundance of Mg and Fe (0.2 *apfu*

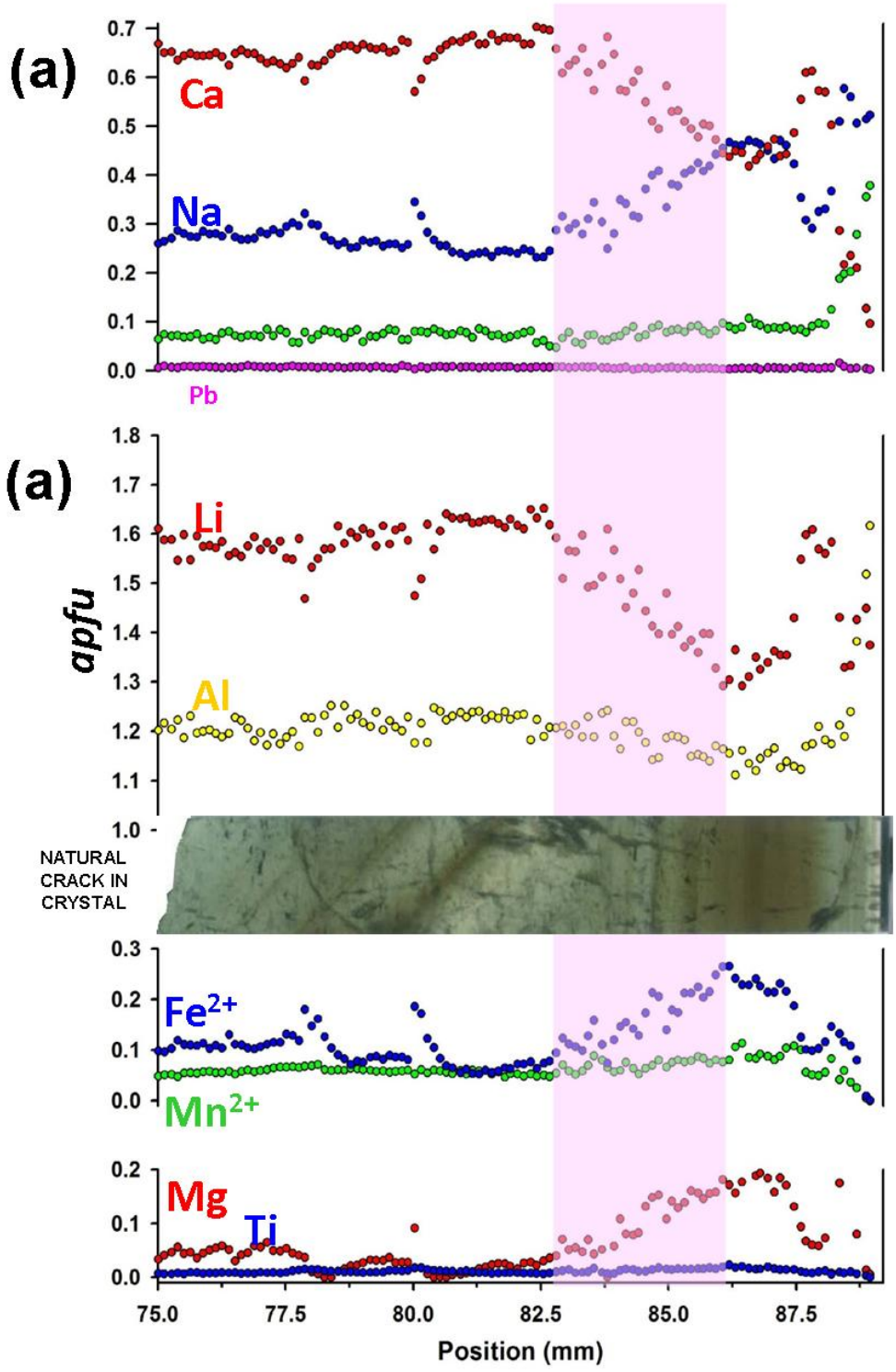

Figure 7.12 (a) Variation in *X*-site and (b) *Y*-site cation abundances adjacent to the rim of the liddicoatite shown in Figures 7.3b and 3.1b (step size equal 125 μm). Shaded pink area shows region of detail traverse in Figure 7.13.

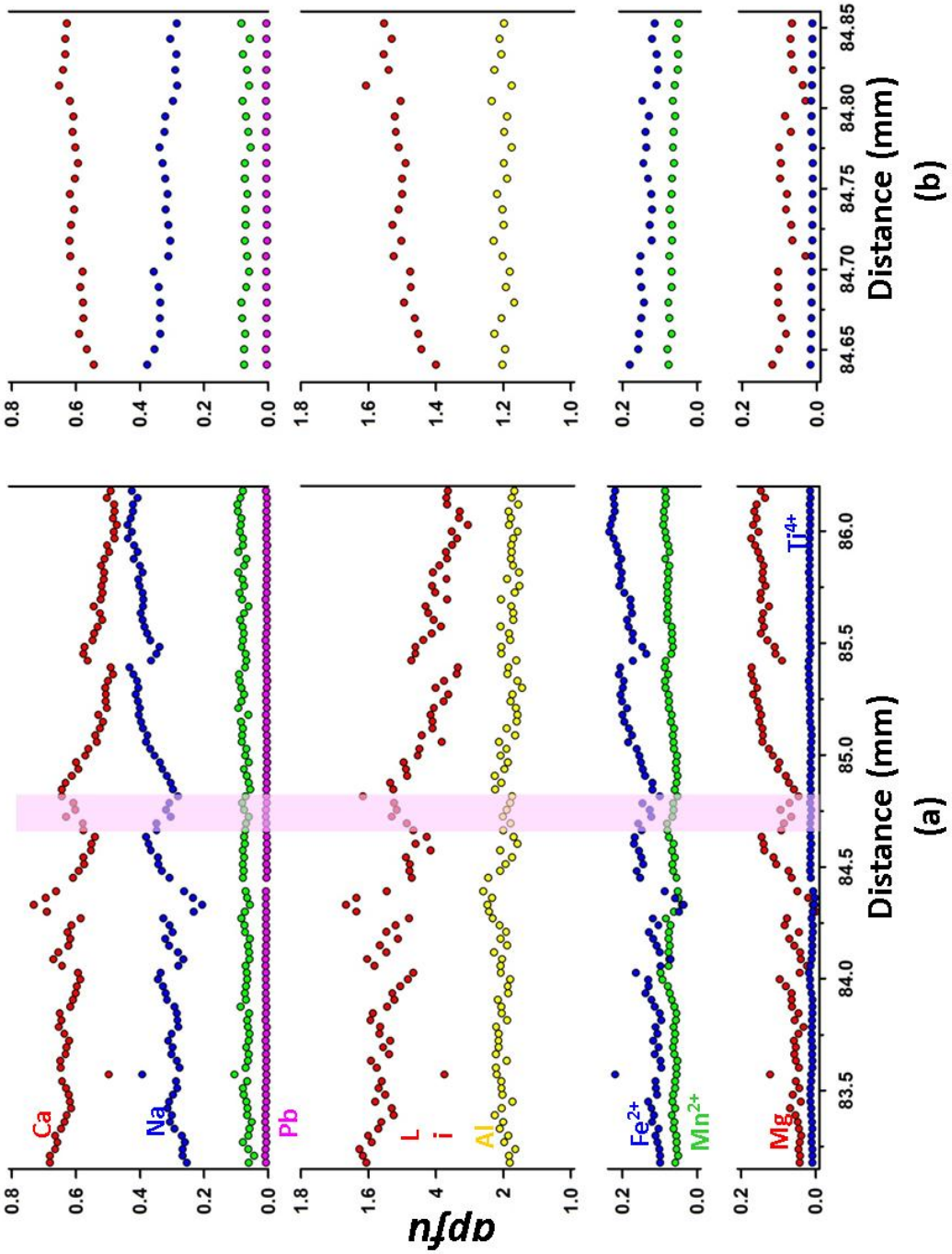

Figure 7.13 Compositional profiles taken with reduced step sizes across the region denoted by the pink boxes in: (a) Figure 7.12 , step size equals 30 μm; and (b) Figure 7.13a, step size equals 10 μm.

each) and a smaller increase in Mn (0.05 *apfu*) and Ti^{4+} (~0.01 *apfu*). Also, there is a major decrease in Ca from ~0.7 to 0.2 *apfu* (Figure 7.12), with a change from liddicoatite to elbaite.

The chemical character of the oscillatory zoning in this zone is *radically* different from that in the pyramidal zone when examined at larger scale (Figure 7.13). We cannot correlate corresponding zones in the pyramidal and prism sectors as the two-dimensional nature of the slice does not allow this to be done (Figures 3.1 and 3.2). However, the character of the zoning is consistent in each sector, and to emphasize the difference between the two sectors, we compare similar zones in Figure 7.14. In the pyramid sector, a zone begins with sharp spikes in Fe and Mg, followed by continuous exponential decrease in both, whereas in the prism sector, a zone begins with Fe and Mg at 0.00 *apfu* and slowly increases across the zone to reach a maximum at the end of the zone, followed by an abrupt decrease in both Fe and Mg.

7.4.5 Substitution mechanisms in zoned liddicoatite

Figure 7.15 shows the compositional variation at the *X*- and *Y*-sites for the whole crystal as a function of $^{Y}M^{*}$ content. All occupants show a linear variation with *M**, and because ^{11}B and ^{27}Al MAS NMR data and <*Z*-O> distances (Section 6.4) show that Si = 6 *apfu* and ^{Z}Al = 6 *apfu* throughout the crystal, the major substitution mechanisms can only involve the *X*- and *Y*-sites. Over the bulk crystal, the compositional variation corresponds to the two substitutions

(1_{ML}) $Ca + Li \rightarrow Na + M^{*}$

(2_{ML}) $Li + {}^{Y}Al \rightarrow M^{*} + M^{*}$

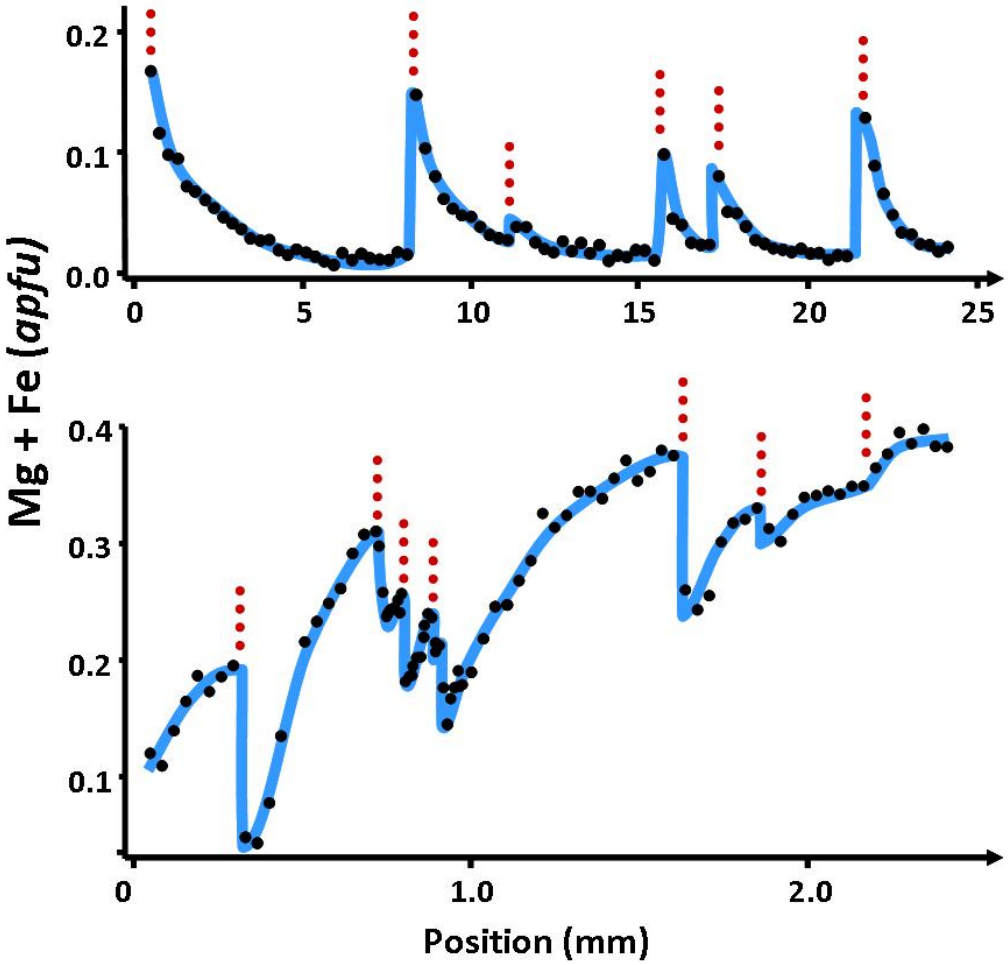

Figure 7.14 Comparison of the variations in Fe and Mg with position across several zones in the pyramidal sector (above) and in the prism sector of Madagascar liddicoatite (below); note that the horizontal scales in the two figures are different in order to aid comparison.

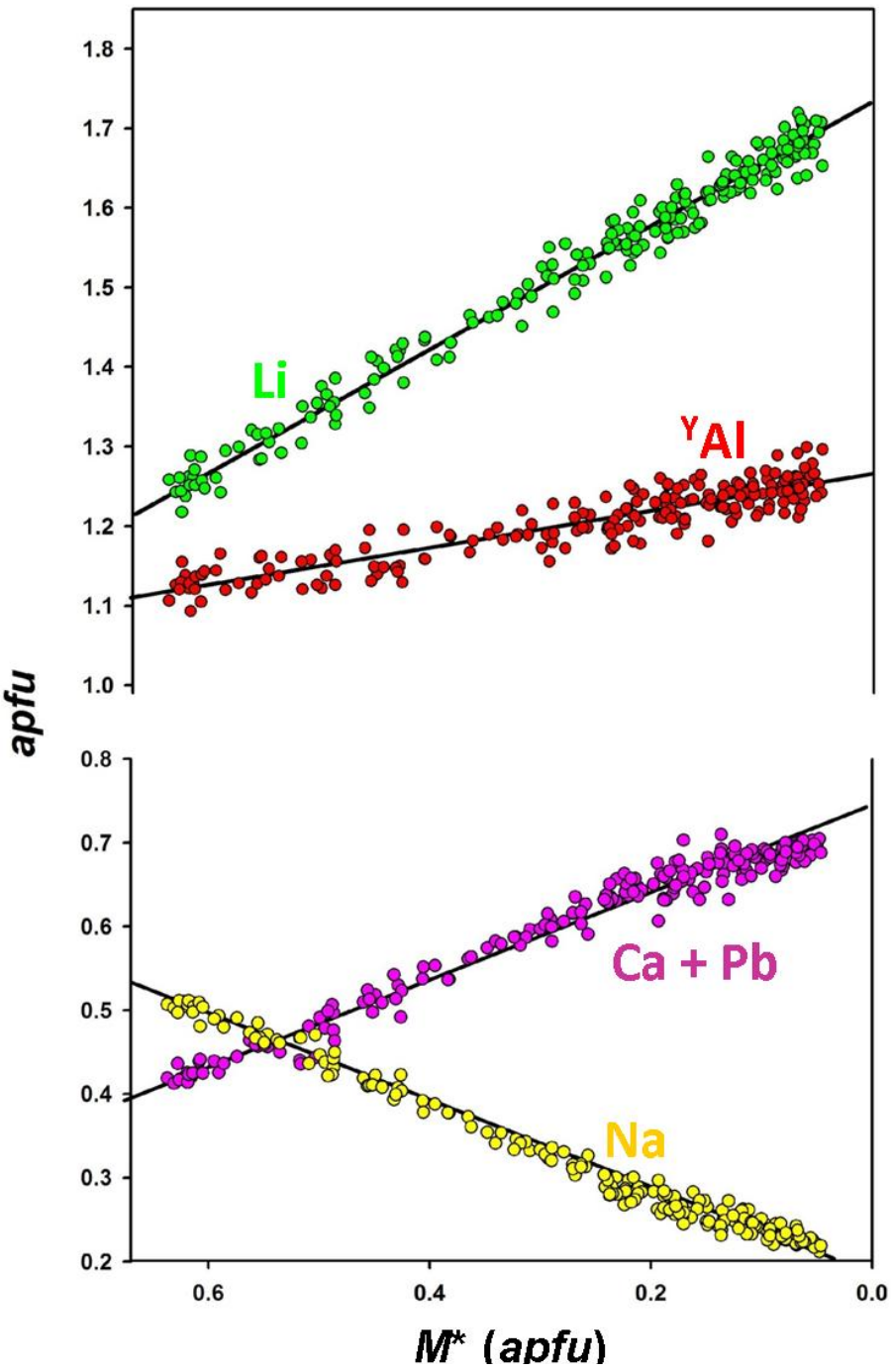

Figure 7.15 Variation in major constituents of *X*- and *Y*-sites in Madagascar liddicoatite as a function of *M** (=Fe + Mn + Mg).

However, this representation of compositional variation does not adequately describe the substitutions active within individual zones; to do so requires *M** to be separated into its constituent parts. Consider the compositional variation in the large zone 17.8-25.0 mm along the traverse in Figures 7.10 and 7.11. At 17.8 mm, the beginning of the zone is clearly marked by a strong increase in Fe and a small increase in Mg, both of which then decrease smoothly. Mg reaches zero after ~0.10 mm whereas Fe reaches zero after ~4.7 mm (at 22.5 mm), and inspection of Figure 7.10 shows that in general, Mg decreases more rapidly than Fe away from the beginning of each zone. In the 17.8-25.0 mm zone, Fe + Mg reachs zero at ~22.5 mm; however, as the zone does not terminate at this point, there must be a corresponding change in substitution behaviour.

7.4.6 *Region A: Individual zones*

Figure 7.16 shows the variation of (Fe + Mg) and Mn as a function of Ca, Li and Na across the 17.8-25.0 mm zone. Close to the beginning of the zone, where (Fe + Mg) > 0.0 *apfu*, the variation in composition corresponds to the following three substitutions:

(3_{ML}) $Ca + Li \rightarrow Na + (Fe, Mg)^{2+}$

(4_{ML}) $Li + {}^{Y}Al \rightarrow (Fe, Mg)^{2+} + (Fe, Mg)^{2+}$

(5_{ML}) $Ca + {}^{Y}Li \rightarrow Na + Mn^{2+}$

Where the ${}^{Y}(Fe + Mg)^{2+}$ content of the zone approaches 0.0 *apfu*, substitutions (3_{ML}) and (4_{ML}) cease operating, and the Mn^{2+} content of the crystal then varies according to substitution (5_{ML}) and (6_{ML}) where:

(6_{ML}) $^{Y}Li + {}^{Y}Al \rightarrow {}^{Y}Mn^{2+} + {}^{Y}Mn^{2+}$

Presumably the strong change in slope of the decrease in Mn^{2+} at the point where Fe^{2+} ceases to vary (Figure 7.16a) registers the beginning of substitution (6). This pattern of variation is repeated in the oscillatory zones of Region A, albeit with less variation in the Fe^{2+} content.

7.4.7 Region B: Individual zones

Figure 7.17 shows the variation of (Fe + Mg) and Mn as a function of Ca, Li and Na across the 52.9-55.9 mm zone. The major difference from the zones of Region A is that Fe decreases continuously across the zone to reach a minimum at the boundary with the adjacent zone; there is no continued crystallization once Fe reaches ~0.01 *apfu* (*i.e.*, close to zero). There are no breaks in the behaviour of Li, Na and Ca, again in contrast to the zoning in Region A. As noted above, the substitution mechanisms active in the second part of each zone in Region A are (5) $Ca + Li \rightarrow Na + Mn^{2+}$ and (6) $Li + {}^{Y}Al \rightarrow Mn^{2+} + Mn^{2+}$; these mechanisms are suppressed in Region B by the absence of Mn^{2+}, preventing the crystallization of a second part of each zone (as happened in Region A).

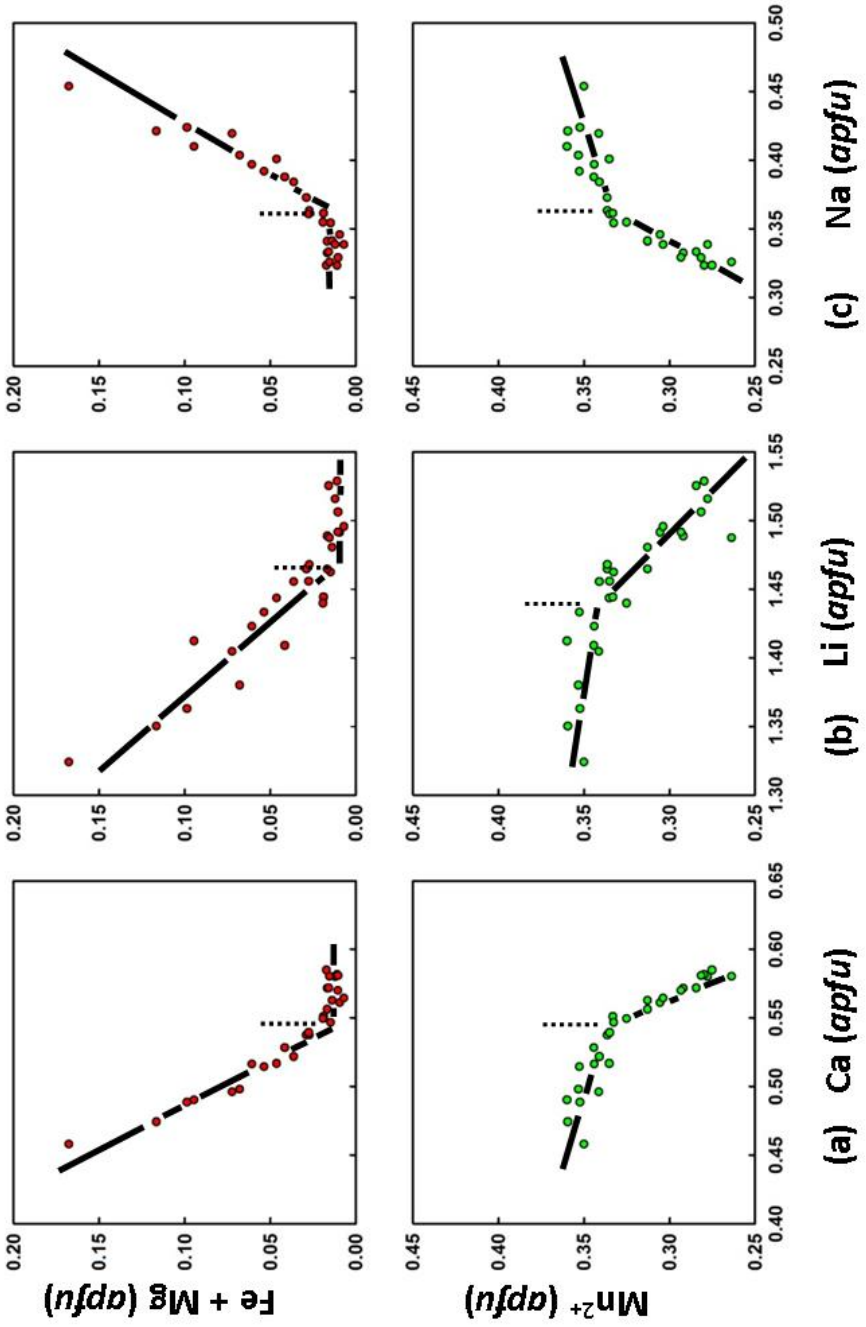

Figure 7.16 Compositional variation across zone 17.8-25.0 mm in Region A of Madagascar liddicoatite (Figures 7.10 and 7.11), showing the variation of (Fe + Mg) and Mn as function of (a) Ca, (b) Li and (c) Na; the dotted lines mark where (Fe + Mg) approaches zero *apfu* (~0.01 *apfu*).

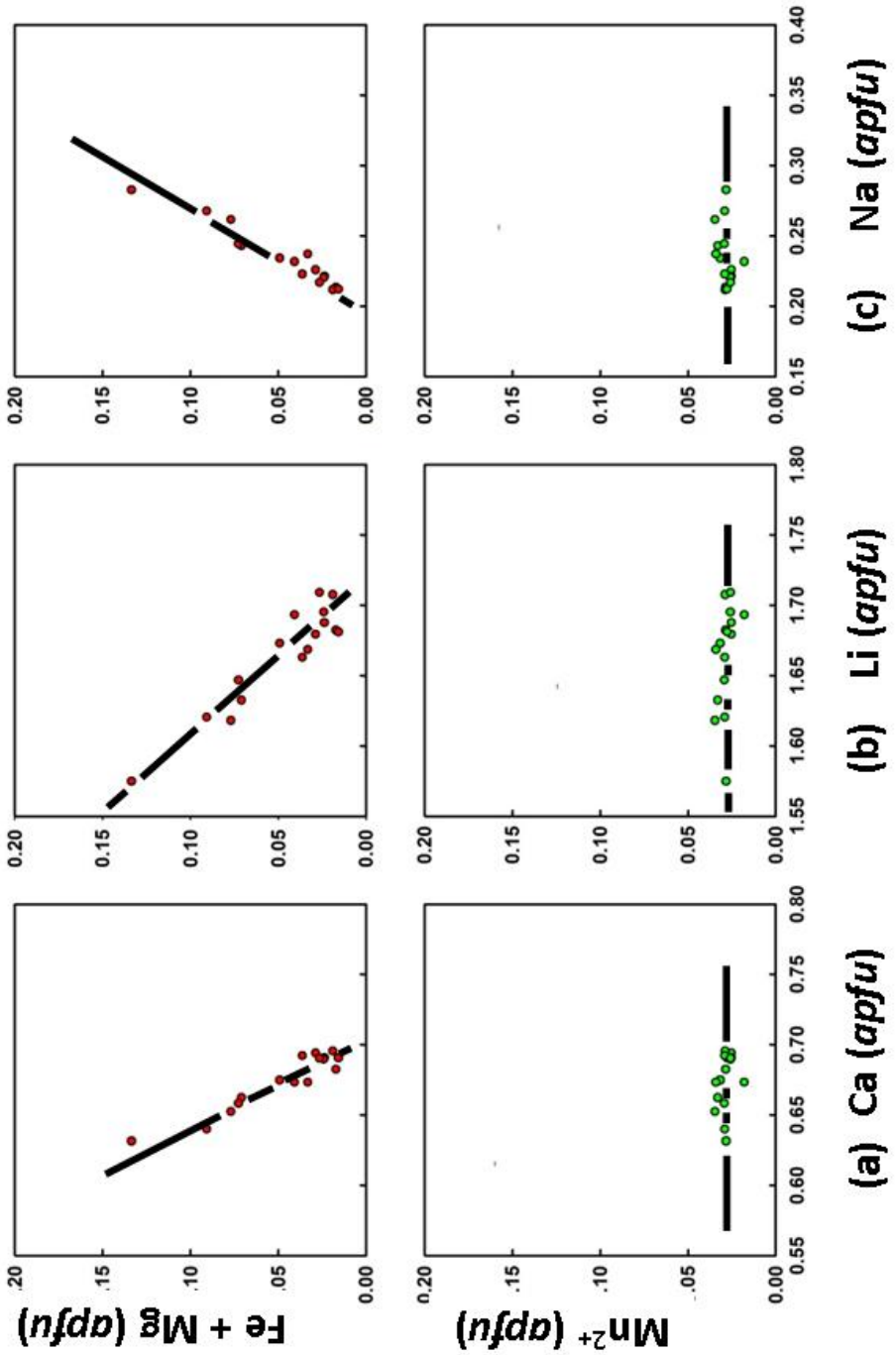

Figure 7.17 Compositional variation across zone 52.9-55.9 mm in Region B of Madagascar liddicoatite (Figures 7.10 and 7.11), showing the variation of (Fe + Mg) and Mn as function of (a) Ca, (b) Li and (c) Na.

7.5 COMPOSITIONAL ZONING IN WHEATSHEAF TOURMALINE

7.5.1 Spatial variation in chemical composition

Two traverses of compositional data were collected along the profiles shown in Figure 7.3c: Traverse 1 (red dots) across the central region of the crystal, and Traverse 2 (green dots) at the edge of the sample. Figures 7.18 and 19 summarize the cation variation with increasing distance from the start of each traverse. The abundance of transition metals correlates strongly with the red colour of the crystal (Figures 3.6, 7.18 and 7.19), the white regions having less than ~0.02 *apfu* transition metals. Inspection of Figures 7.18 and 7.19 shows that variation in $^{[4]}$B content plays a major role in chemical variation throughout this crystal. From the start of Traverse 1, $^{[4]}$B rises abruptly from 0.4 to 0.6 *apfu*. and ^{Y}Al rises from 1.5 to 1.7 *apfu* while *M** falls from 0.15 to 0.04 *apfu* and Li falls from 1.4 to 1.2 *apfu*. Along the traverse, $^{[4]}$B declines to ~0.20 *apfu* at the rim of the crystal *via* a series of discontinuous changes that show analogous variations in ^{Y}Al, Li and, to a lesser extent, *M**. These discontinuous changes in *T*- and *Y*-site occupancies are accompanied by little or no change in the *X*-site occupancies in the first half of the traverse. At the base of the crystal, Ca is slightly less than Na (both close to 0.4 *apfu*.) and the two converge halfway along the traverse, with the vacancy content, $^{X}\square$, constant at 0.2 *pfu.* Close to the

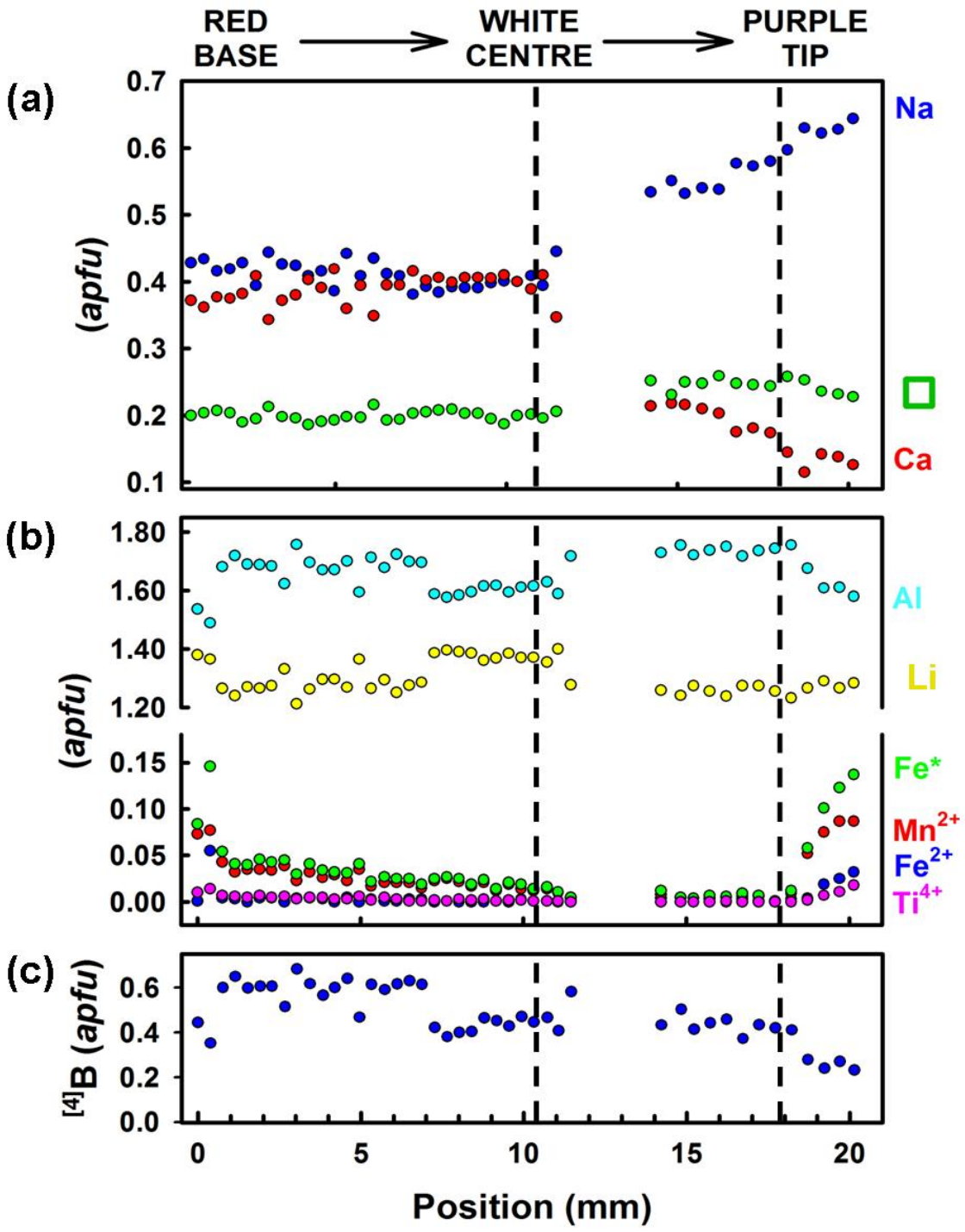

Figure 7.18 Variation in chemical composition of wheatsheaf tourmaline along Traverse 1 (see Figure 7.3c): (a) *X*-site; (b) *Y*-site; and (c) $^{[4]}$B at *T*-site. □ = vacancy.

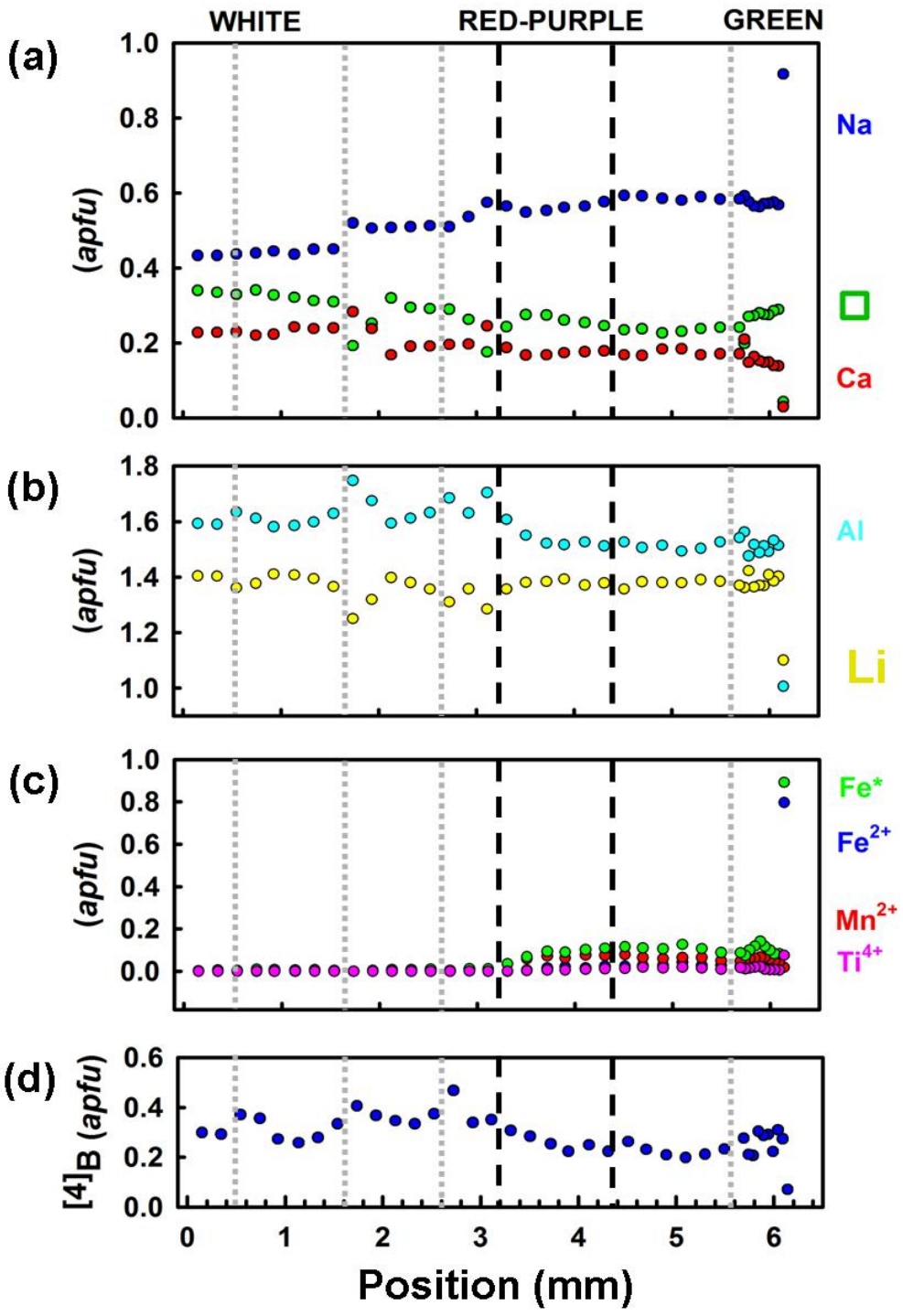

Figure 7.19 Variation in chemical composition of wheatsheaf tourmaline along Traverse 2 (see Figure 7.3c): (a) *X*-site; (b) Al and Li at *Y*-site; (c) transition metals at *Y*-site; and (d) $^{[4]}$B at *T*-site.

middle of the traverse (the broken line marked WHITE CENTRE in Figure 7.18), Ca begins to decrease sharply and Na begins to increase sharply, reaching 0.12 and 0.66 *apfu*, respectively, at the edge of the crystal. These changes in Na and Ca are smooth and show no abrupt change that correlates with the sharp rise in *M** and drop in ^{Y}Al and $^{[4]}$B close to the edge of the crystal (at the second broken line in Figure 7.18).

Traverse 2 shows a similar picture. Discontinuities in $^{[4]}$B correlate with similar changes in Al and Li, but not *M** (see dotted lines in Figure 7.19). There is one analytical point in the green rim, and this shows a major compositional discontinuity with the rest of the crystal. Ca and $^{X}\square$ fall close to zero and Na exceeds 0.9 *apfu*. *M** rises sharply from <0.1 *apfu* to 0.9 *apfu*, both Al and Li fall to close to 1 *apfu* and $^{[4]}$B drops from ~0.3 to <0.1 *apfu*.

7.5.2 Substitution mechanisms in wheatsheaf tourmaline

Inspection of Figures 7.18 and 7.19 shows what initially seems to be scatter in the variation of $^{[4]}$B as a function of distance. Plotting major constituents as a function of either $^{[4]}$B or Li (Figures 7.20 and 7.21) shows that this is not the case: major constituents vary in a linear manner such that this compositional change involving $^{[4]}$B may be described by series of coupled substitutions. Prior to determining which substitutions are operative, the spatial profiles must be divided into regions with coherent substitution character; this is shown in Figures 7.20 and 7.21. Six substitutions are required to explain the variation observed in Figures 7.18 and 7.20, although not all of these operate simultaneously. For each

region, the relevant substitutions, the amounts of each substitution *pfu*, and the corresponding distances along the spatial profiles, are summarized in Table 7.4.

All regions of the crystal show well-developed, linear relations for ^{Y}Al, Li, and $^{Y}M^{*}$ as a function of $^{[4]}$B, such that the principal substitutions accommodating the variation in *T*-site constituents are:

(1_{WS}) $^{T}B_2 + {}^{Y}Al \rightarrow Si_2 + Li$

(2_{WS}) $^{T}B + {}^{Y}Al \rightarrow Si + M^{*}$

In nearly every region, (1) and (2) couple with additional substitutions to accommodate compositional variation at the *X*-site.

Figure 7.20a,b show the compositional variation for the red core of the sample, from 0.0 to 3.0 mm along the profile in Figure 7.18. Here, substitutions (1_{WS}) and (2_{WS}) proceed for 0.10 and 0.05 *pfu*, respectively (Figure 7.20a). Additionally, Figure 7.20b shows that the *X*-site constituents also vary linearly with ^{Y}Li along the following substitutions (note bidirectional arrows):

(3_{WS}) $\square + {}^{Y}Al \leftrightarrow Ca + Li$ (0.04)

(4_{WS}) $Na_2 + {}^{Y}Al \leftrightarrow Ca_2 + Li$ (0.03)

In the white central region of the wheatsheaf crystal, from 3.2 to 6.9 mm in Figure 7.18, substitutions (1_{WS}) and (2_{WS}) remain active (Figure 7.20c,d) with amounts of 0.07 and 0.01 *pfu*, respectively. Additional substitutions are required to maintain the compositional balance that must involve the *X*- and *Y*-site constituents. In contrast to the red core, here the trends relating the variation in *X*- and *Y*-site

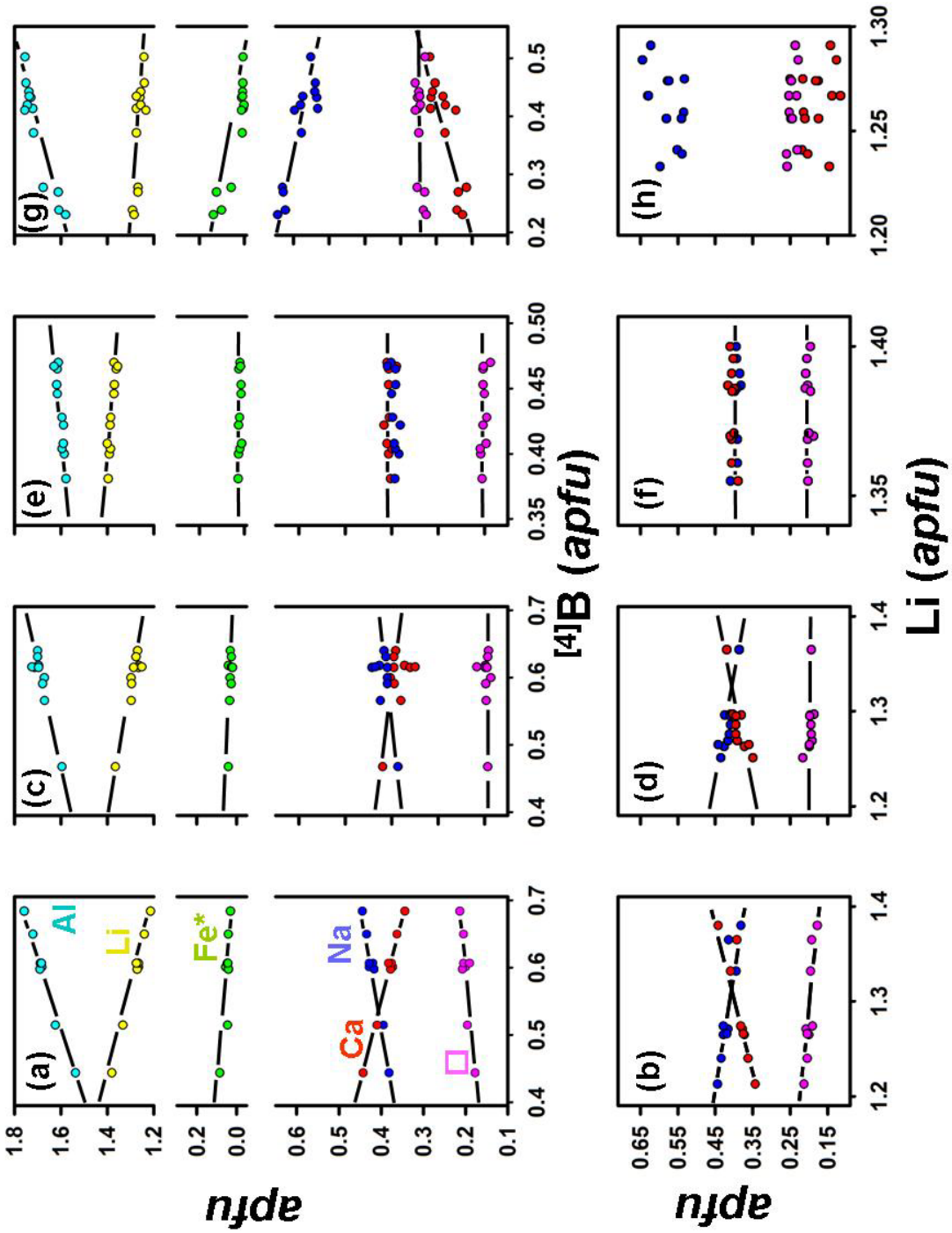

Figure 7.20 Variation in major *X*-site and *Y*-site constituents as a function of $^{[4]}$B and ^{Y}Li along Traverse 1 of wheatsheaf tourmaline (red dots in Figure 7.3c, see also Figure 7.18): (a, b) 0.0 to 3.2 mm; (c, d) 3.2 to 6.9 mm; (e, f) 6.9 to 11.1 mm: (g, h) 14.2 to 20.2 mm.

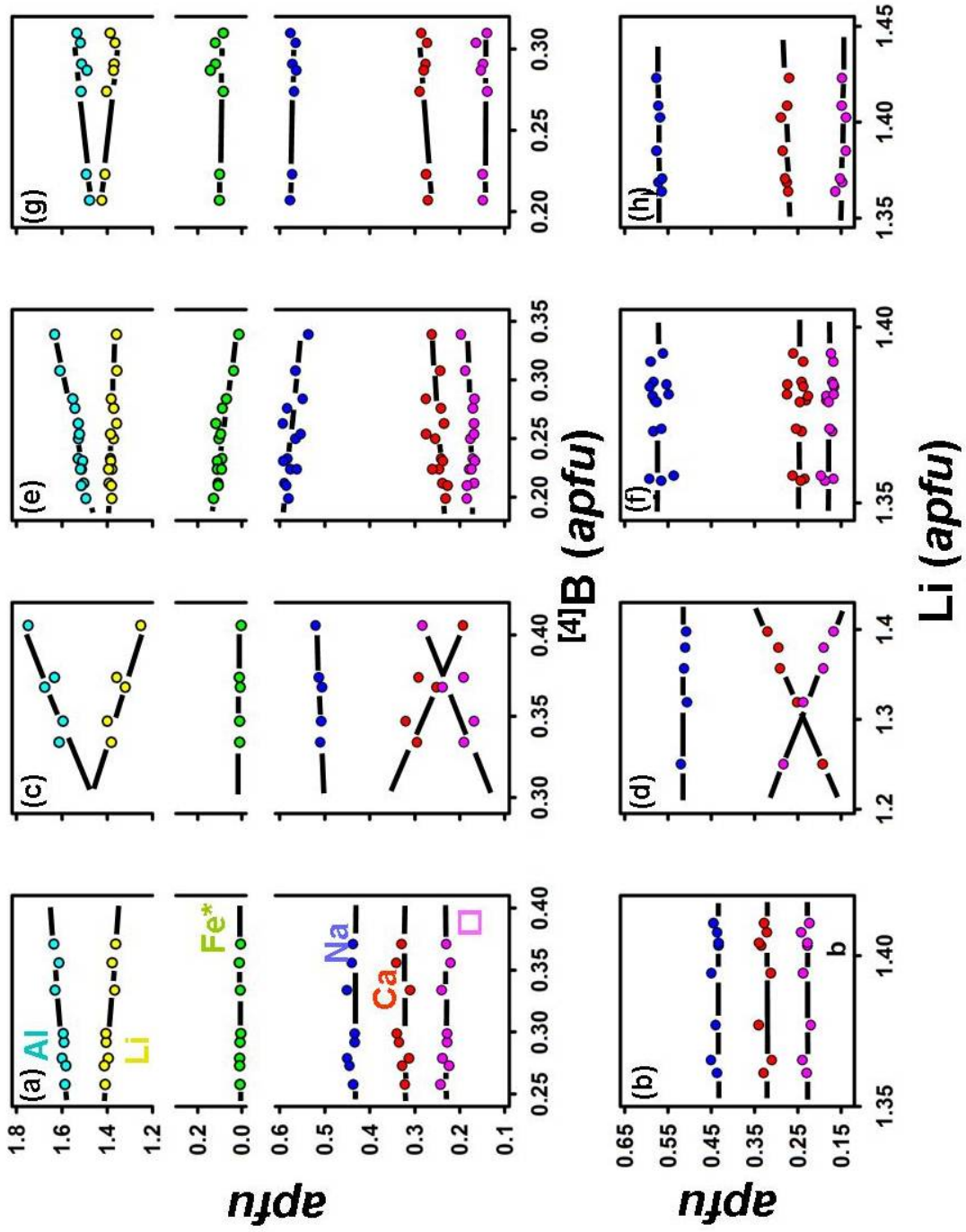

Figure 7.21 Variation in major *X*-site and *Y*-site constituents as a function of $^{[4]}$B and Li along Traverse 2 of wheatsheaf tourmaline (green dots in Figure 7.3b): (a,) 0.0 to 1.5 mm; (c,) 1.5 to 2.5 mm; (e,) 2.5 to 5.7 mm: and (g, h) 5.7 to 6.1 mm.

constituents to *T*- and/or *Y*-site constituents are less obvious, given the amount of scatter about the ideal lines shown in Figures 7.20c,d; the substitution may only be approximated as:

(5_{WS}) $Na + {}^{Y}Al + {}^{T}B \leftrightarrow Ca + Li + Si$ (0.03)

Between 6.9 and 11.1 mm in Figure 7.18, which is still in the white region of the sample, there is no appreciable change in *X*-site composition and *M** is ~0 *apfu* throughout the region (Figures 7.20e, f). Hence only substitution (-1_{WS}) [note reversed direction] is operative, with an amount of 0.05 *pfu.*

Toward the darker edge of the wheatsheaf sample (Figures 7.20g, h), between 14.2 and 20.2 mm on the traverse shown in Figure 7.18, there is considerable scatter in the data, and Figure 7.20h shows no discernable relation between the *Y*- and *X*-site constituents; hence only the variations in *X*- and *T*-site constituents are coupled. In this region, the variation in Na changes sign with respect to $^{[4]}B$ when compared to the other regions of the wheatsheaf sample and the composition varies according to the following three substitutions:

(-1_{WS}) $Si_2 + Li \rightarrow {}^{T}B_2 + {}^{Y}Al,$ (0.07)

(-2_{WS}) $Si + M^{*} \rightarrow {}^{T}B + {}^{Y}Al$ (0.01)

(6_{WS}) $Na + Si \rightarrow Ca + {}^{T}B$ (0.02)

Figure 7.21a-h show the compositional variation along Traverse 2 (shown in Figure 7.19), which ends at a crystal face. From 0.0 to 1.5 mm, there is no variation in *X*-site constituents (Figures 7.21a, b), and substitution (1_{WS}) (0.05 *pfu*) accounts for all the observed variation.

Between 1.5 and 2.5 mm (Figure 7.21c), substitution (1_{WS}) remains active

(0.03 *pfu*). In addition, a well-developed linear relation between *X*- and *Y*-site constituents (Figure 7.21c) indicates that substitutions (3_{WS}) and (5_{WS}) are active,

(3_{WS}) $Ca + Li \rightarrow \square + {}^{Y}Al$ (0.10)

(5_{WS}) $Na + {}^{Y}Al + {}^{T}B \rightarrow Ca + Li + Si$ (0.01)

Between 2.5 and 5.7 mm (Figures 7.21e, f), substitution (1_{WS}) is active (0.01 *pfu*) and substitution (2_{WS}), which accounts for the entire variation in *M**, is active (0.12 *pfu*). There is no correlation between *Y*- and *X*-site constituents. As observed in Figure 7.21g, there is a decrease in Na as a function of $^{[4]}B$, corresponding to

(6_{WS}) $Ca + {}^{T}B \rightarrow Na + Si$ (0.02).

Between 5.7 to 6.1 mm (Figures 7.21g, h), there is effectively no change in *X*-site constituents, and the composition varies according to substitutions (-1_{WS}) (0.04 *apfu*) and (-2_{WS}) (0.02 *pfu*).

7.6 COMPOSITIONAL ZONING IN MUSHROOM TOURMALINE

7.6.1 Spatial variation in chemical composition

Figure 7.3d shows the locations of analytical traverses across mushroom tourmaline. Figure 7.22 summarizes the variation in cations as a function of position along a traverse (Figure 7.3d) across the black core at the base of the crystal (points 1-10), the central prismatic crystal (points 11-36), the black zone (point 37), and the pink rim (points 38-45). The sum of the transition metals is ~1.30 *apfu* at the base of the core (Figure 7.22*a*), it falls rapidly to ~0.50 *apfu* at the junction between the core and the central prismatic crystal, then decreases.

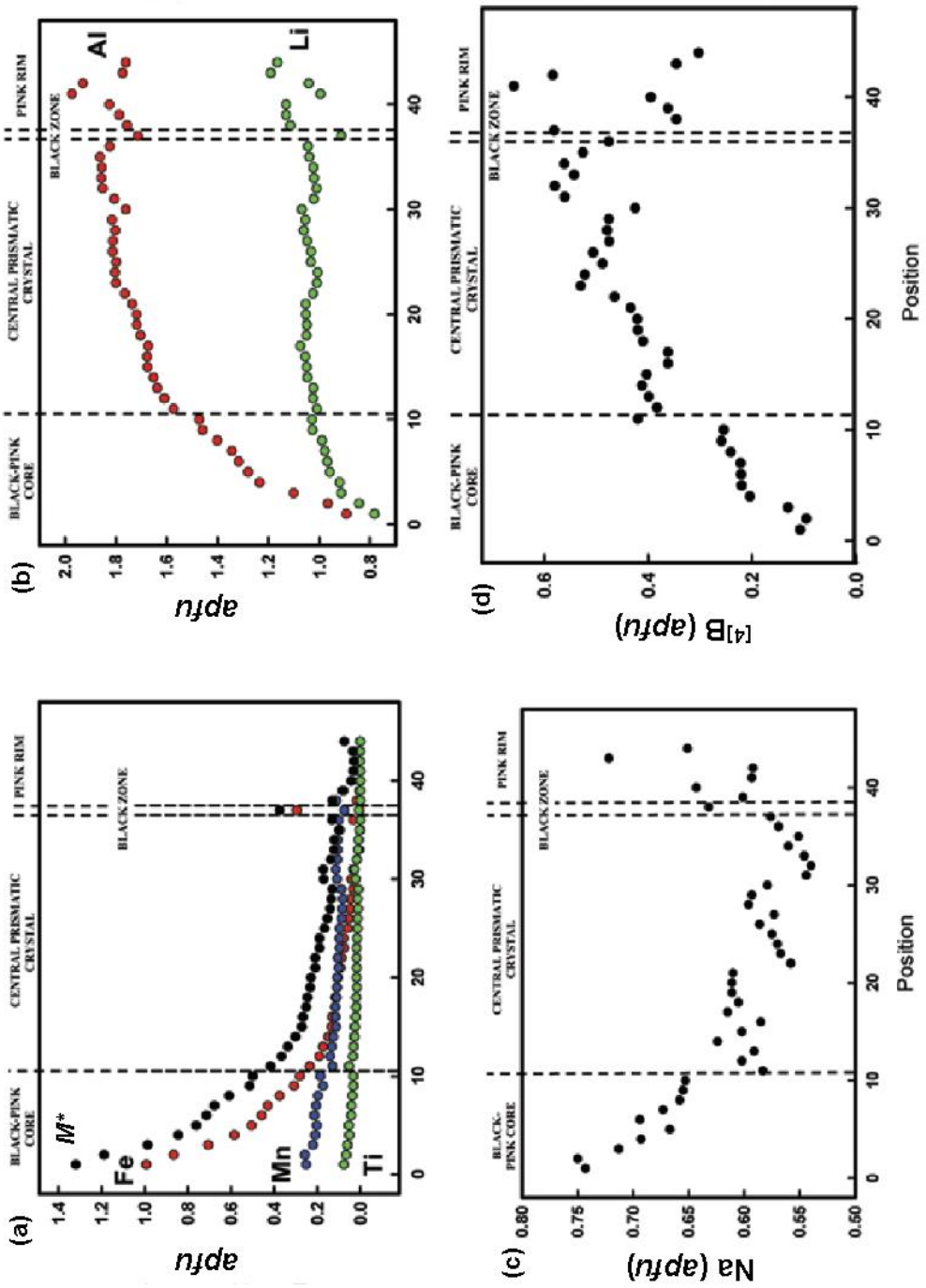

Figure 7.22 Variation in chemical composition of mushroom tourmaline (SHM) as a function of position along traverse 1, Figure 7.3d : (a) Total transition metals (*M**) black; Fe red; Mn blue; Ti green; (b) ^{Y}Al (red) and Li (green); (c) $^{[4]}$B; (d) Na

slowly with distance along the crystal, gradually approaching 0.00 *apfu* at the edge of the pink rim. Figure 7.22 summarizes the variation in cations as a function of position along the central crystal. The narrow black zone that is a very prominent feature of this sample (Figure 7.3d) shows a sharp rise in total transition metals. Individual transition metals follow a similar trend (Figure 7.22a), except that the Fe content falls below the Mn content halfway along the central prismatic crystal, only to increase strongly in the black zone (where the Mn content does not rise at all). Both Li and ^{Y}Al increase strongly from the base to the edge of the core; the Li content flattens out along the length of the central prismatic crystal, whereas ^{Y}Al continues to increase. At the boundary between the core and the base of the prismatic crystal, there are small but distinct discontinuities in Li and ^{Y}Al (Figure 7.22b). There are also discontinuities in the black zone, the contents of both Li and ^{Y}Al dropping by 0.10–0.20 *apfu*. In the pink rim, the variations in Li and ^{Y}Al become more irregular.

The variation in Na at the *X*-site also shows strong discontinuities at the boundary between the core and the base of the prismatic crystal, and at the black zone (Figure 7.22c). Na decreases strongly through the black core, decreases less strongly along the central prismatic crystal, increases strongly in the black zone, and then decreases strongly in the pink rim. The calculated $^{[4]}$B increases continuously from the base of the core to the boundary with the central prismatic crystal where there is a jump in $^{[4]}$B, followed by a steady increase

along the length of the central crystal. In the pink rim, the variation in $^{[4]}$B at first seems very irregular, but in fact shows a strong correlation with the variation in ^{Y}Al and Li (see below).

7.6.2 Substitution mechanisms in mushroom tourmaline

Figure 7.22 indicates a major discontinuity in chemical variation at the boundary between the core and the base of the prismatic crystal, and another major discontinuity at the black zone close to the margin of the sample. Figure 7.23 shows the variation in cations as a function of *M** content in the black core and the prismatic crystal. In the black core (Figure 7.23a), all cations show linear variation as a function of *M** content. The substitutions operating throughout the entire sample are summarized in Table 7.5. For the black core, these substitutions are given below:

$$(1_{MS}) \quad {}^{Y}\text{Li} + {}^{Y}\text{Al} \rightarrow {}^{Y}M^{*} + {}^{Y}M^{*} \qquad (0.25)$$

$$(2_{MS}) \quad {}^{T}\text{B} + {}^{Y}\text{Al} \rightarrow \text{Si} + {}^{Y}M^{*} \qquad (0.15)$$

$$(3_{MS}) \quad {}^{X}\square + {}^{Y}\text{Al} \rightarrow \text{Na} + {}^{Y}M^{*} \qquad (0.09)$$

$$(4_{MS}) \quad {}^{Y}\text{Al} \rightarrow {}^{Y}\text{Fe}^{3+} \qquad (0.09)$$

and the straight lines in Figure 7.24a show the aggregate variations represented by these substitutions.

The same variations are shown for the central prismatic crystal in Figure 7.23b. As is apparent in Figure 7.22a, there is a slight discontinuity halfway along the crystal, where the slopes of the variations in ^{Y}Al and $^{[4]}$B increase (by the same amount) and the slopes of the variations in Li and Na decrease (again by

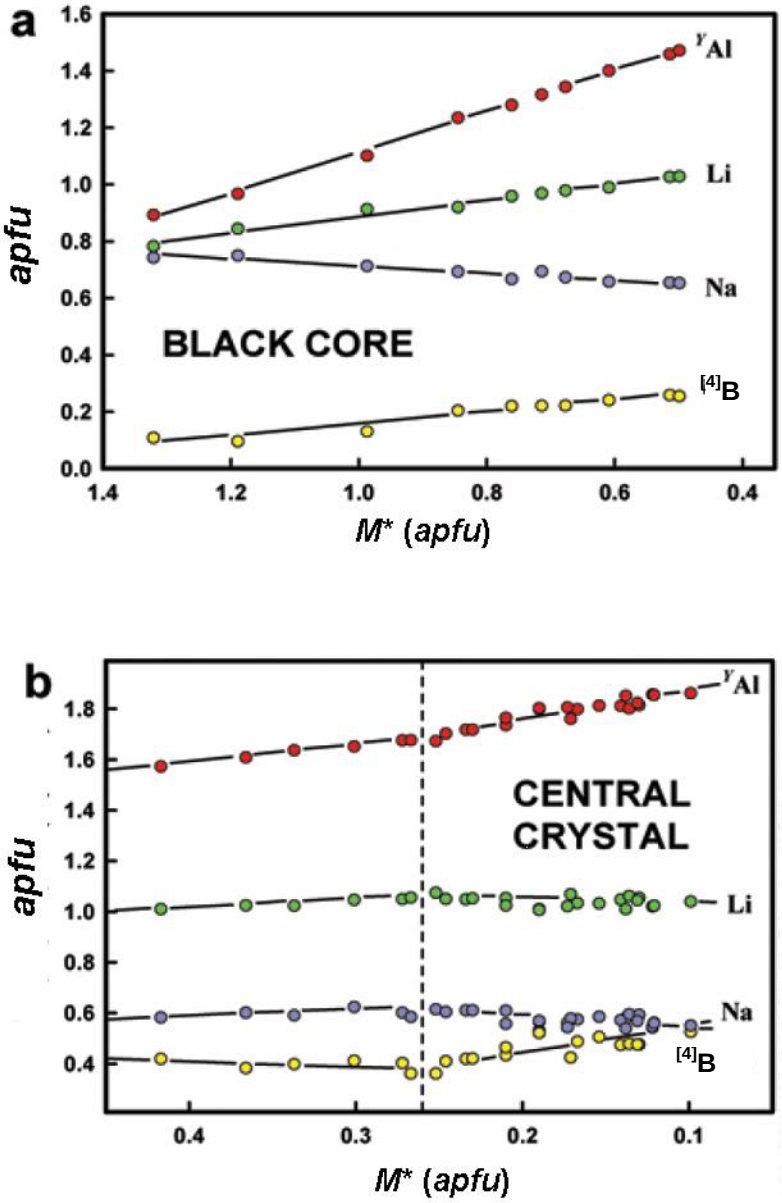

Figure 7.23 Variation in chemical composition of mushroom tourmaline (SHM) as a function of total transition-metals along traverse 1, Figure 7.3d: (a) black core; (b) central prismatic crystal.

approximately the same amount) (Figure 7.23b). In the first half of the crystal, the following changes occur: ^{Y}Al (+0.11), Li (+0.05), *M** (–0.15), B(–0.06) and Ca (-0.04 apfu); thus Li and ^{Y}Al continue to increase and *M** decreases, and hence substitution (1_{MS}) continues, increasing Li and ^{Y}Al by 0.06 *apfu* and decreasing *M** by 0.12 *apfu*. The remaining changes relate to substitution (5_{MS}) below, and thus the compositional changes in the first part of the crystal are summarized as follows:

$$(1_{MS}) \quad {}^{Y}\mathrm{Li} + {}^{Y}\mathrm{Al} \rightarrow {}^{Y}M^{*} + {}^{Y}M^{*} \qquad (0.06)$$

$$(5_{MS}) \quad \square + {}^{Y}\mathrm{Al} + \mathrm{Si} \rightarrow \mathrm{Ca} + {}^{Y}M^{*} + {}^{T}\mathrm{B} \qquad (0.06)$$

At the boundary shown by the dashed line in Figure 7.23b, there is a break in each constituent, but Li and $^{[4]}$B are particularly important as their variation changes sign, denoting a significant change in the substitutions at this point. As the variations in Li and ^{Y}Al are no longer sympathetic, substitution (1_{MS}) is no longer active. $^{[4]}$B begins to increase again *via* substitution (2_{MS}), and the remaining changes are accounted for by substitution (6_{MS}):

$$(2_{MS}) \quad {}^{T}\mathrm{B} + {}^{Y}\mathrm{Al} \rightarrow \mathrm{Si} + M^{*} \qquad (0.12)$$

$$(6_{MS}) \quad 2\square + {}^{Y}\mathrm{Al} \rightarrow \mathrm{Na_2} + \mathrm{Li} \qquad (0.02)$$

At the black zone, there is a sudden increase in Fe and decrease in Mn (Figure 7.22a) that reverses on the other side of the black zone. Both Li and ^{Y}Al drop sharply at the black zone (Figure 7.22a), indicating that this zone corresponds to sudden activity of substitution (1_{MS}).

In the outer pink zone, $^{[4]}$B decreases sharply from ~0.80 to >0.30 *apfu* (Traverse 3, Figure 7.3d; Figure 7.24a), accompanied by significant increases in

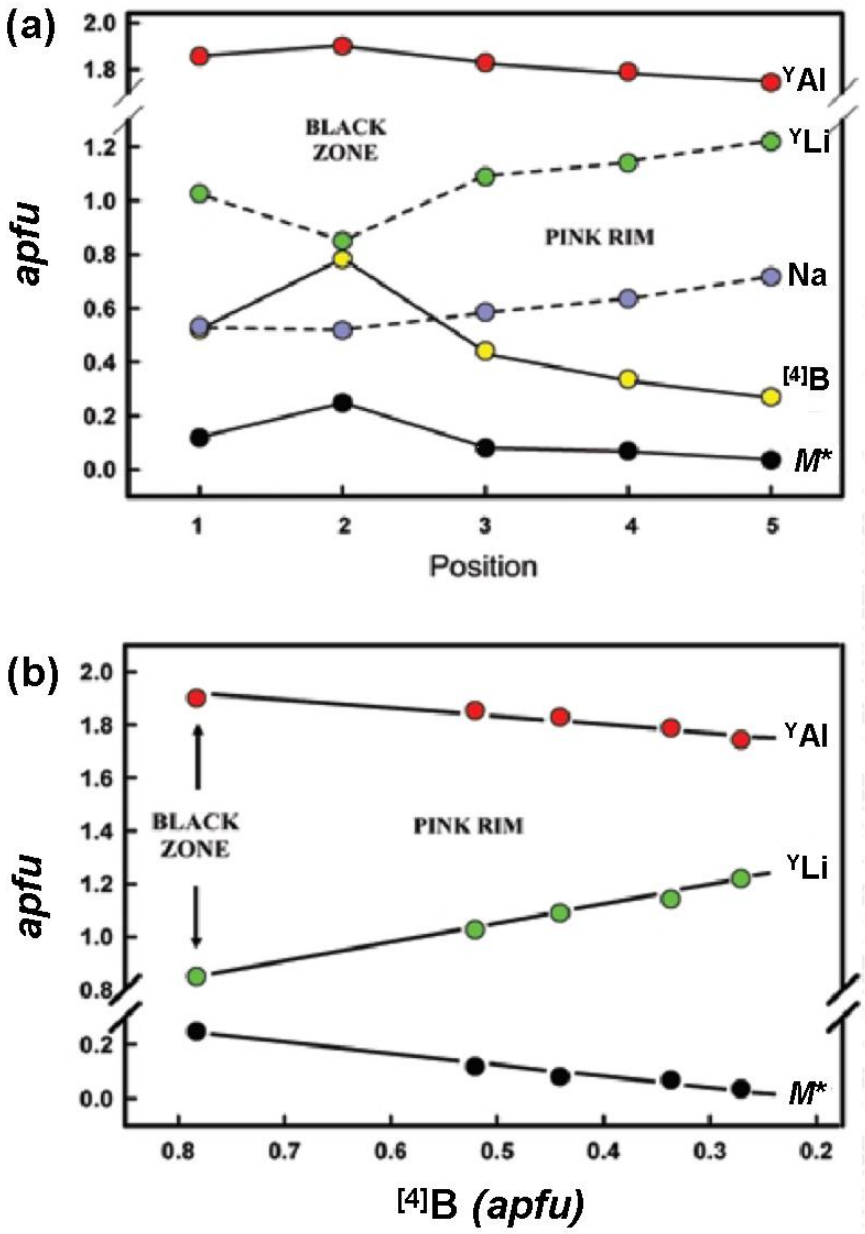

Figure 7.24 Variation in chemical composition of mushroom tourmaline (SHM) along traverse 3, Figure 7.3d: (a) composition as a function of position; (b) ^{Y}Al, Li and Fe* (= Fe + Mn + Ti) as a function of $^{[4]}$B content.

Li and Na, and decreases in ^{Y}Al and *M**. Figure 7.24b shows the chemical variations in the pink zone, not as a function of *M** (as this is now extremely low) but of $^{[4]}$B. Again, there is a very coherent variation in chemical constituents, and the operating substitutions are (7_{MS}) and (8_{MS}):

(7_{MS}) $\quad Li + Si \rightarrow Fe + {}^{T}B \qquad (0.20)$

(8_{MS}) $\quad Li + Si_2 \rightarrow {}^{Y}Al + {}^{T}B_2 \qquad (0.16)$

Kalt *et al.* (2001) proposed substitution (2_{MS}) for the incorporation of $^{[4]}$B into olenite-schorl tourmalines, and this is also a major substitution accounting for the variation in $^{[4]}$B in mushroom and wheatsheaf tourmaline, although it is not the only major substitution that involves ^{T}B in these samples.

In order to assess the relative timing of the growth of the different zones of the mushroom, we also examined the variation in composition across crystal SHM (Traverse 2, Figures 7.3d and 7.25). There are four distinct zones that correspond to the texturally different regions of the crystal. In the central prismatic zone, the transition metals decrease slightly toward the edge (Figure 7.25a), ^{Y}Al increases slightly and Li decreases slightly (Figure 7.25b), $^{[4]}$B increases slightly (Figure 7.25c) and the *X*-site constituents are fairly constant. At the boundary with the region where there is the transition from a coherent single crystal to acicular crystals, there is a sharp increase in all of the transition metals (Figure 7.25a) and a drop in ^{Y}Al (Figure 7.25b). All other constituents show no discontinuity at this boundary, although their variation within the transition region is much more irregular than in the central prismatic crystal. At the boundary between the transition region and the acicular crystals, again there is an increase

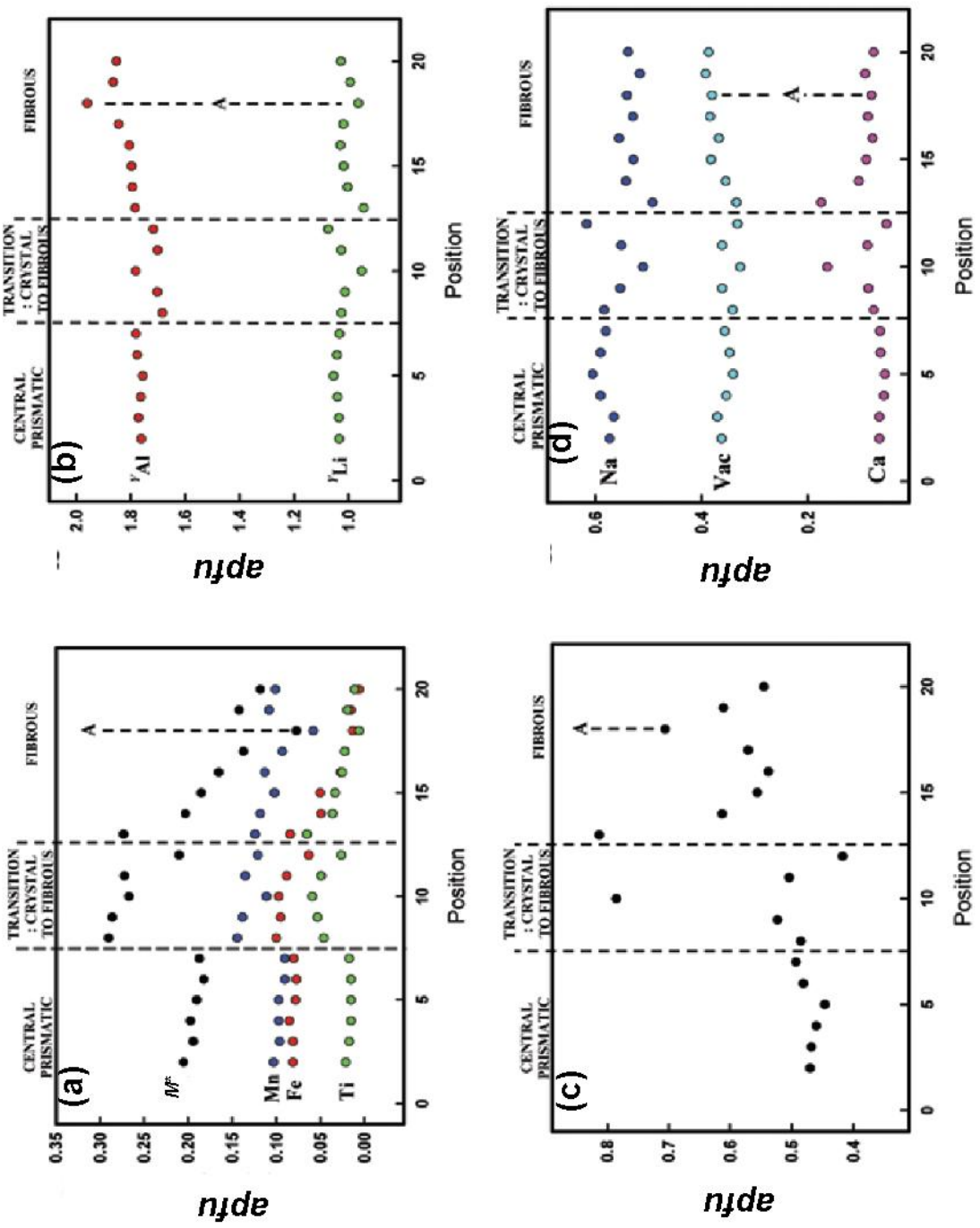

Figure 7.25 Variation in chemical composition of SHM as a function of position along traverse 2, Figure 7.3b: (a) transition metals; (b) ^{Y}Al and Li; (c) $^{[4]}$B; (d) Na, Ca and X♦. Line A is referred to in the text.

in the transition metals (Figure 7.25a), small discontinuities in ^{Y}Al and Li (Figure 7.25b), a very large discontinuity in $^{[4]}$B (Figure 7.25c), and discontinuities in Na and Ca but not in $^{X}\square$ (Figure 7.25d). In addition, Figure 7.25 also shows a specific point within the acicular region (marked A in Figure 7.25) that shows a strong compositional difference with the adjacent regions.

The variation in composition as a function of transition-metal content along the same section is shown in Figure 7.26. The data for the central prismatic crystal and the acicular region show continuous linear variations in ^{Y}Al, Li, $^{[4]}$B and Na that are similar to the variations shown in Figure 7.23b, whereas the transition zone (Figure 7.26) shows more extreme variations with $^{[4]}$B being rather irregular.

7.7 GENERAL REMARKS

Detailed analytical traverses collected on the four tourmaline specimens presented in Chapter 3 show well-developed compositional zoning that coincides with prominent colour zoning. Although these crystals have dramatically different compositional profiles when plotted in the spatial domain, the corresponding compositional domain profiles can all be described as a series of linear-substitution mechanisms (summarized in Tables 7.2 to 7.5). Compositionally distinct zones in the Black Rapids Glacier, wheatsheaf, and mushroom tourmalines are distinguished by discontinuous changes in chemical composition which correspond with abrupt changes in the operating substitution mechanisms. In contrast, successive oscillatory zones, in either the pyramidal or the prismatic

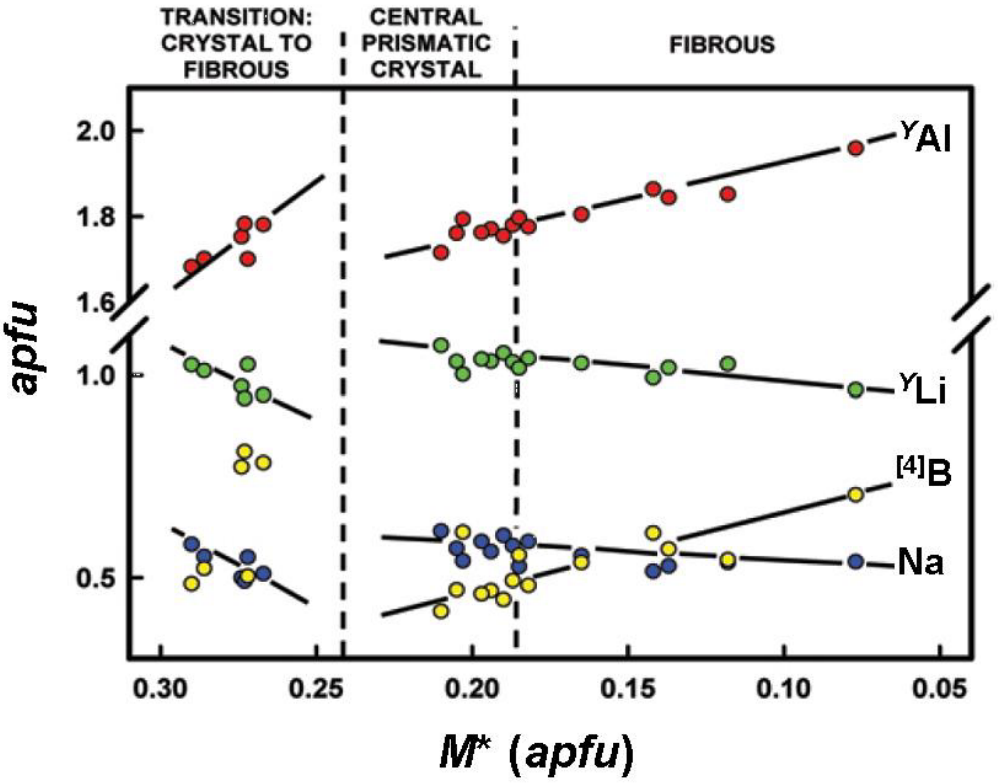

Figure 7.26 Variation in chemical composition of SHM as a function of total transition-metals along traverse 2, Figure 7.3d.

sectors, of the Madagascar liddicoatite repeat similar spatial patterns and the compositional variation is constrained by only two substitution mechanisms.

Furthermore, in the crystals where the abundance of $^{[4]}$B varies significantly (*i.e.*, wheatsheaf and mushroom tourmalines), three substitutions account for this compositional change: (1) $^{[4]}B + {}^{Y}Al \rightarrow Si + {}^{Y}M^*$ where transition metals are present: (2) $^{[4]}B_2 + {}^{Y}Al \rightarrow Si_2 + {}^{Y}Li$ where transition metals are not present; and (3) occasionally $^{[4]}B_2 + {}^{Y}M^* \rightarrow Si + {}^{Y}Li$ is also observed. These consistently couple with other substitutions (Tables 7.4 and 7.5). The former has also been observed in B-rich olenite-schorl tourmalines (Kalt *et al*. 2001), and hence seems to be one of the more common ways of incorporating $^{[4]}$B into Al-rich tourmaline. Variation in $^{[4]}$B is clearly a significant contributor to zoning in tourmalines where Si < 6 *apfu*, reaffirming that full characterization of the *T*-site occupancy is essential to tourmaline research.

TABLE 7.2 SUBSTITUTION MECHANISMS AND AMOUNTS (in *apfu*) FOR BLACK RAPIDS GLACIER TOURMALINE

Region A (0 to 9.1 mm in Figure 7.6)		
(1_{BR})	$\square + {}^{Y}Al \rightarrow Ca + Li$	0.13
(2_{BR})	$2Ca + Li \rightarrow 2Na + {}^{Y}Al$	0.06
Region B (9.2 to 9.4 mm in Figure 7.6)		
(3_{BR})	$Na + M^* \rightarrow Ca + Li$	0.06
(4_{BR})	$\square + 2M^* \rightarrow Ca + 2Li$	0.06
Region C (9.4 to 10.9 mm in Figure 7.6)		
(-1_{BR})	$Ca + Li \rightarrow \square + {}^{Y}Al$	0.08
(5_{BR})	$Ca + M^* \rightarrow Na + {}^{Y}Al$	0.08
(6_{BR})	$Ca + 2M^* \rightarrow \square + 2{}^{Y}Al$	0.01
Region D (10.9 to 11.1 mm in Figure 7.6)		
(7_{BR})	$\square + 2{}^{Y}Al \rightarrow Ca + 2M^*$	0.05
Region E (11.1 to 11.3 mm in Figure 7.6)		
(-1_{BR})	$Ca + Li \rightarrow \square + {}^{Y}Al$	0.12
(5_{BR})	$Ca + M^* \rightarrow Na + {}^{Y}Al$	0.08
(7_{BR})	$Ca + 2M^* \rightarrow \square + 2{}^{Y}Al$	0.05

TABLE 7.3 SUBSTITUTION MECHANISMS AND AMOUNTS (in *apfu*) FOR MADAGASCAR LIDDICOATITE.

Whole crystal	
(1_{ML})	$Ca + Li \rightarrow Na + M^*$
(2_{ML})	$Li + {}^{Y}Al \rightarrow M^* + M^*$
Pyramidal zones – Region A (Mn > 0 apfu)	
(3_{ML})	$Ca + Li \rightarrow Na + (Fe, Mg)^{2}$
(4_{ML})	$Li + {}^{Y}Al \rightarrow (Fe, Mg)^{2+} + (Fe, Mg)^{2+}$
(5_{ML})	$Ca + {}^{Y}Li \rightarrow Na + Mn^{2+}$
(6_{ML})	${}^{Y}Li + {}^{Y}Al. \rightarrow {}^{Y}Mn^{2+} + {}^{Y}Mn^{2+}$
Pyramidal zones - Region B (Mn ~ 0* apfu*)	
(3_{ML})	$Ca + Li \rightarrow Na + (Fe, Mg)^{2}$
(4_{ML})	$Li + {}^{Y}Al \rightarrow (Fe, Mg)^{2+} + (Fe, Mg)^{2+}$

TABLE 7.4 SUBSTITUTION MECHANISMS AND AMOUNTS (in *apfu*) FOR WHEATSHEAF ELBAITE

Red Base (0.0 to 3.2 mm in Figure 7.20)		
(1_{WS})	$^{T}B_2 + {}^{Y}Al \leftrightarrow Si_2 + Li$	0.10
(2_{WS})	$^{T}B + {}^{Y}Al \leftrightarrow Si + M^*$	0.05
(3_{WS})	$\square + {}^{Y}Al \leftrightarrow Ca + {}^{Y}Li$	0.04
(4_{WS})	$Na_2 + {}^{Y}Al \leftrightarrow Ca_2 + Li$	0.03
White Core (3.2 to 6.9 mm in Figure 7.20)		
(1_{WS})	$^{Y}Al + {}^{T}B_2 \rightarrow Li + Si_2$	0.07
(2_{WS})	$^{Y}Al + {}^{T}B \rightarrow M^* + Si$	0.01
(5_{WS})	$Na + {}^{Y}Al + {}^{T}B \rightarrow Ca + Li + Si$	0.03
White Core (6.9 to 11.1 mm in Figure 7.20)		
(1_{WS})	$^{Y}Al + 2{}^{T}B \rightarrow Li + 2Si$	0.07
Dark Edge (14.2 to 20.2 mm in Figure 7.20)		
(-1_{WS})	$Si_2 + Li \rightarrow {}^{T}B_2 + {}^{Y}Al$	0.07
(-2_{WS})	$Si + M^* \rightarrow {}^{T}B + {}^{Y}Al$	0.01
(6_{WS})	$Na + Si \rightarrow Ca + {}^{T}B$	0.02
End (0.0 to 1.5 mm in Figure 7.21)		
(1_{WS})	$^{Y}Al + 2{}^{T}B \rightarrow Li + Si$	0.05
End (1.5 to 2.5 mm in Figure 7.21)		
(1_{WS})	$^{Y}Al + 2{}^{I}B \rightarrow Li + 2{}^{I}Si$	0.03
(3_{WS})	$Ca + Li \rightarrow \square + {}^{Y}Al$	0.10
(5_{WS})	$Na + {}^{Y}Al + {}^{T}B \leftrightarrow Ca + Li + {}^{T}Si$	0.01
End (2.5 to 5.7 mm in Figure 7.21)		
(1_{WS})	$^{Y}Al + 2{}^{T}B \rightarrow Li + 2Si$	0.01
(2_{WS})	$^{Y}Al + B \rightarrow Fe + Si$	0.12
(6_{WS})	$Ca + {}^{T}B \rightarrow Na + Si$	0.02
End (5.7 to 6.1 mm in Figure 7.21)		
(-1_{WS})	$Si_2 + Li \rightarrow {}^{T}B_2 + {}^{Y}Al$	0.04
(-2_{WS})	$Si + M^* \rightarrow {}^{T}B + {}^{Y}Al$	0.02

TABLE 7.5 SUBSTITUTION MECHANISMS AND AMOUNTS (in *apfu*) FOR MUSHROOM ELBAITE

Black Base (pos. 0 to 10 in Figure 7.24)		
(1_{MS})	$Li + {}^{Y}Al \rightarrow M^{*} + M^{*}$	0.25
(2_{MS})	$B + {}^{Y}Al \rightarrow Si + M^{*}$	0.15
(3_{MS})	$\square + {}^{Y}Al \rightarrow Na + M^{*}$	0.09
(4_{MS})	${}^{Y}Al \rightarrow Fe^{3+}$	0.09
Grey Central Prism (pos. 11 to 22 in Figure 7.24)		
(1_{MS})	$Li + {}^{Y}Al \rightarrow M^{*} + M^{*}$	0.06
(5_{MS})	$\square + {}^{Y}Al + Si \rightarrow Ca + M^{*} + {}^{I}B$	0.06
White Central Prism (pos. 23 to 37 in Figure 7.24)		
(2_{MS})	${}^{T}B + {}^{Y}Al \rightarrow Si + M^{*}$	0.12
(6_{MS})	$2\square + {}^{Y}Al \rightarrow 2Na + Li$	0.02
Blank Zone (pos. 28 in Figure 7.24)		
(1_{MS})	$Li + {}^{Y}Al \rightarrow M^{*} + M^{*}$	
Pink Rind (pos. 39 to 26 in Figure 7.24)		
(7_{MS})	$Li + Si \rightarrow {}^{Y}Fe^{2+} + {}^{T}B$	0.20
(8_{MS})	$Li + 2Si \rightarrow {}^{Y}Al + 2{}^{T}B$	0.16

CHAPTER 8

GROWTH CONSIDERATIONS

8.1 INTRODUCTION

The samples characterised in detail in Chapters 4, 6 and 7 all originate from granitic pegmatites, and each has characteristics making it dramatically different from the others. Black Rapids Glacier tourmaline has a massive, prismatic habit and shows discrete zoning in cross section (Figure 3.8), with a mostly heterogeneous core of elbaite and a thin rim of Fe-rich fluor-liddicoatite. Madagascar liddicoatite also has a massive prismatic habit and shows a complex pattern of oscillatory zoning (Figures 3.1, 7.10, 7.11, 7.13). Both wheatsheaf and mushroom elbaites contain significant amounts of [4]-coordinate B and extensive splitting (or bifurcation) of crystals (Figures 3.5 and 3.7), with bifurcation being far more prominent in mushroom than in wheatsheaf. Considering these differences, it stands to reason that the crystallization and growth histories of each of these tourmalines are likely very different.

For each sample, relatively little is known about the specific locality. In the case of Madagascar liddicoatite and Myanmar elbaite, this is because the pegmatites of Anjanabonoina and Momeik remain relatively poorly studied. In the case of Black Rapids Glacier tourmaline, it is because the crystal was glacially-transported. Despite these setbacks, the detailed structural, compositional and morphological characterizations presented in this work may be used to constrain

aspects of the conditions and mechanisms that potentially led to the development of these unusual tourmalines.

8.2 LIDDICOATITE FROM THE ANJANABONOINA PEGMATITE, SOUTH-CENTRAL MADAGASCAR

8.2.1 Causes of oscillatory zoning

Zoning in minerals is caused by variations in the composition (X), temperature (T) and (possibly) pressure (P) of the crystallizing (or solidifying) liquid. Variations in X, T and P are of two sorts, depending on their origin: (1) those that are externally imposed (external forcing) on the crystallizing system as a result of open-system processes (*e.g.*, input of new fluid at different temperature or pressure); (2) those that are internally induced and due to non-equilibrium processes such as diffusion. Measurement of the fractal dimension of the zoning pattern (Halden & Hawthorne 1993) indicates that the distribution of zones is non-random, suggesting that type (1) processes are unlikely to have caused the observed zoning patterns. Thus we consider models of type (2). These models invoke the basic crystal-growth equation (*e.g.*, Lasaga 1982)

$$\frac{\partial c(x,t)}{\partial t} = D_i \frac{\partial^2 c(x,t)}{\partial x^2} + V \frac{\partial c(x,t)}{\partial x}$$

where $c(x, t)$ is the concentration of species i at position x in the melt at time t, D_i is the diffusion coefficient of species i in the melt, and V is the growth velocity of the crystal surface (for simplicity, the system is assumed to be closed, although this is not a requirement of the general model). L'Heureux (1993) described a non-linear dynamical model for the formation of oscillatory zoning in crystals

based on constitutional undercooling involving diffusion and growth kinetics in the crystal-melt or fluid system, and L'Heureux & Fowler (1994, 1996) applied this model to the growth of plagioclase feldspar. The basic idea is that under isothermal conditions in multiply saturated systems, the concentration of species at the growing face of a crystal may be different from the bulk value in the system owing to diffusion, thus inducing an effective undercooling in the fluid close to the face (Sibley *et al*. 1976, L'Heureux & Fowler 1996). The boundary condition at the crystal face requires a relation between the concentration of a species in the crystal and in the melt, and Lasaga (1982) introduced a partition coefficient $K = c_s/c_m$ where c_s and c_m are the concentrations of a component in the solid (s) and liquid (m), respectively. The growth rate, V, is expressed in terms of various growth-kinetic parameters (L'Heureux 1993, see also L'Heureux & Fowler 1996) and provides the non-linear feedback required for oscillatory behaviour of the system. Lasaga (1982) examined the case where $K > 1$ and did not find any oscillatory solutions to the growth equation. L'Heureux (1993) showed that where $K > 1$, a steady state is stable, whereas where $K < 1$, oscillatory solutions occur for some ranges of values of the variable parameters. Figure 8.1a shows one example of a solution found for the concentration of An (anorthite component) at the growing face of a plagioclase crystal as a function of distance from the centre of the crystal. In particular, note the asymmetric compositional variation within individual zones.

Sibley *et al.* (1976) originally introduced the isothermal undercooling model and invoked differential surface roughness as a factor affecting variations

in growth rate. Tsune & Toramaru (2007) developed this model in more detail, particularly the effect of surface roughness on growth rate, and show that oscillatory solutions are obtained for K > 1. Figure 8.1b shows one example of a solution for the concentration of An (anorthite component) at the growing face of a plagioclase crystal as a function of distance from the centre of the crystal. Again, note the asymmetric compositional variation within individual zones.

8.2.2 Application to tourmaline

All of the models discussed above are essentially one-component systems, and all contain the constraint that the variable components are *x* and 1-*x* (*e.g.*, L'Heureux & Fowler 1994, 1996). This is obviously not the case for tourmaline, in which there are several algebraically independent components. It is not even possible to simplify the problem by assuming crystal-chemically coherent cations, as it is apparent from Figures 7.10 and 7.16 that Mn behaves differently from Fe and Mg. Even in plagioclase feldspar, although there is one algebraically independent component, this component is not a single chemical species and there is no requirement for it to behave physically as a single component (*e.g.*, the diffusion rates of Ca and Al are unlikely to be identical).

As shown in Chapter 7, the oscillatory zoning profiles in liddicoatite are distinctly different in the pyramidal and prismatic sectors (Figure 7.14), indicating that the zoning profiles are dependent on the surface properties of the growing

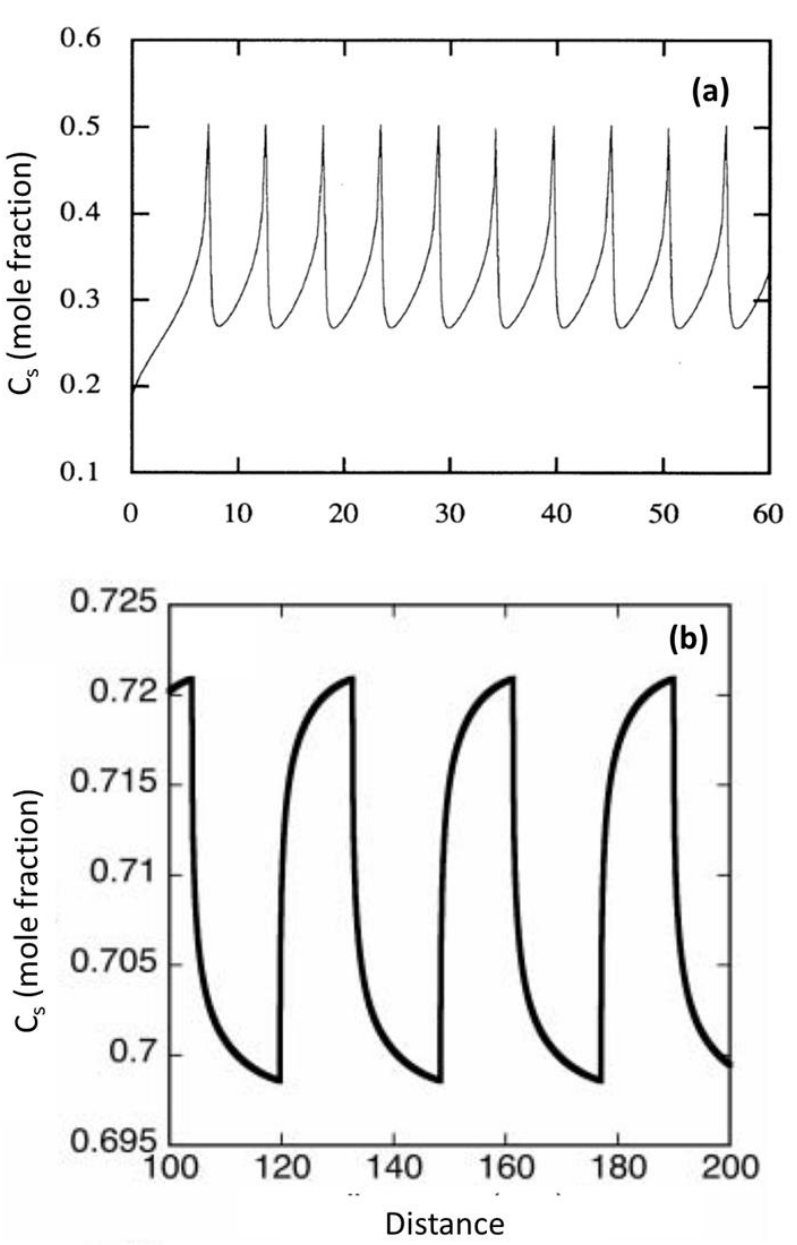

Figure 8.1 Concentrations of constituents at the growing face of a crystal as a function of distance (arbitrary units) from the centre of the crystal, calculated from various growth models. An (anorthite component) at the growing face of a plagioclase from (a) L'Heureux & Fowler (1994, Figure 5a) and (b) Tsune & Toramaru (2007, Figure 5a).

crystal as well as the physical parameters of the liquid. In this regard, the surface-roughness model of Tsune & Toramaru (2007) may contain some features of a model appropriate for tourmaline.

8.2.3 Liddicoatite crystal growth

The general zoning features of a typical Madagascar liddicoatite are illustrated in Figure 3.2. The cross-section taken parallel to the *c*-axis (Figure 3.2a) suggests that the prismatic and pyramidal oscillatory zones are continuous and crystallize simultaneously. However, the cross-section taken perpendicular to the *c*-axis (Figure 3.2b) shows oscillatory zone boundaries that are parallel to several different crystal forms which appear to truncate each other, indicating a more complex crystallization history than that suggested by the section taken parallel to *c*. Figures 3.1, 3.2 and 8.2 show the spatial relations of oscillatory zones in typical Madagascar liddicoatites, and on the basis of these relations, we may reconstruct a plausible growth history model for these crystals.

Figure 8.2 shows two illustrations of Madagascar liddicoatite crystals. These illustrations integrate many of the zoning details commonly observed in the photographs found in Benesch (2000) and Rustemeyer (2003). In Figure 8.2a, a key observation can be made by examining the large yellow-green triangular zone (outlined in yellow and marked [1]) parallel to the {201} form. The apices of the triangle are clearly missing, and cursory inspection of Figure 8.2a suggests that the yellow-green zone is truncated by the dark black/brown zone (at the blue arrow marked [A]; Figure 8.2b). However, the enlarged image

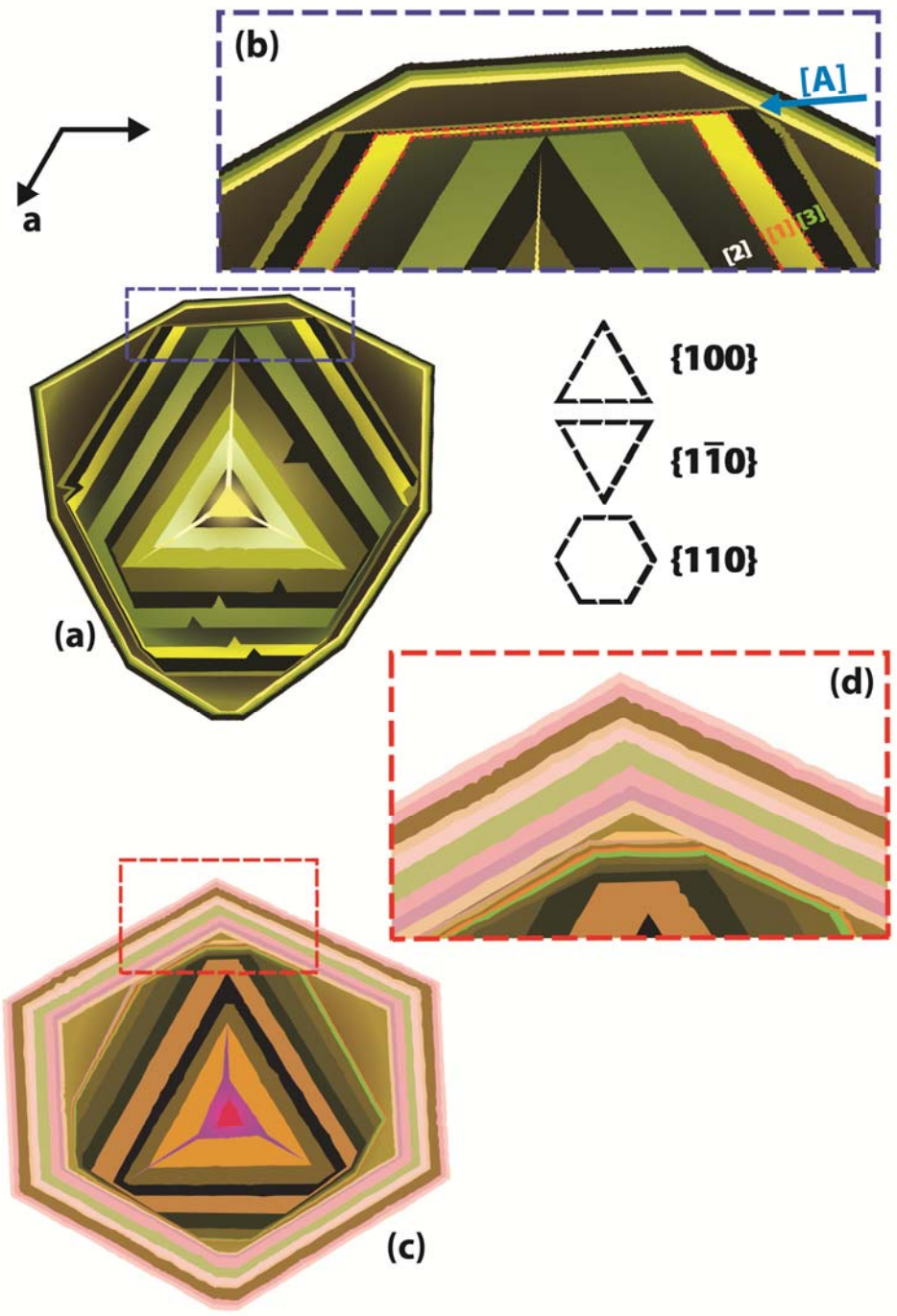

Figure 8.2 Schematic illustrations of Madagascar liddicoatite crystals with features observed in various photographs in Benesch (2000) and Rustemeyer (2003) showing (a) crystal with nonagonal cross-section and (b) enlargement; (c) crystal with hexagonal cross-section and (d) enlargement (see text for discussion). Oriented cross-sectional outlines of {100}, {1-10}, and {110} prisms are shown for reference.

shows this yellow-green zone to be *continuous*, *i.e.*, present on *both* pyramidal (concentric triangles on {201}) and prismatic faces $\{1\,\bar{1}\,0\}$. This is also true of the green [1] and black [2] zones. The continuity of zones is a commonly-observed feature in liddicoatite crystals (*e.g.*, note the fine-scale zoning in the red box of Figure 8.2b). From this observation, we may conclude that the crystallization of the whole liddicoatite crystal is a continuous process, occurring without hiatus or resorption of material.

In addition to zones parallel to the {201} pyramid and {110} prism documented in Chapter 7, Figure 8.2 also shows that zones also occur parallel to $\{1\,\bar{1}\,0\}$ and {100} triangular prisms, although zones on the later face are consistently not well-developed in the images. The apparent thickness of the yellow-green zone on the {201} face is significantly greater than the thickness of the corresponding zone on the $\{1\,\bar{1}\,0\}$ face. Although we lack an absolute timescale for growth of the yellow zone, the marked differences in thicknesses suggests that the growth velocity, V, of these faces differs significantly, with $V_{\{201\}} > V_{\{1\text{-}10\}}$. Comparison of the thicknesses of zones parallel to $\{1\,\bar{1}\,0\}$ and {110} also shows a difference in average thicknesses, with $\{1\,\bar{1}\,0\}$ zones being (slightly) thicker than {110} zones (Figure 8.2a,c). Applying the same logic results in the relation: $V_{\{201\}} >> V_{\{1\text{-}10\}} \geq V_{\{110\}}$. By applying this relation to a growing crystal of liddicoatite, the complex spatial distribution of oscillatory zones observed in Figures 3.1, 3.2 and 8.3 may be reconstructed.

Growth Phase I: The crystal may grow as a {100} prism terminated by a {201} pyramid, a {001} pedion, and possibly a $\{10\bar{1}\}$ pyramid (Figure 8.3a). As $V_{\{201\}} > V_{\{100\}}$, the crystal elongates in the direction of the *c*-axis. A cross-section taken through such a crystal, at approximately the location of the red tick-mark, would appear similar to that shown in Figure 8.3a, with the concentric triangles of the {201} zones being the dominantly visible features.

Growth Phase II: At some point during growth, the faces of the trigonal $\{1\bar{1}0\}$ prism begin to grow (Figure 8.3b), although it is not clear what causes this to occur. With continued growth, a crystal with the six-sided cross-section shown in Figure 8.3b results, where the original {100} prism faces progressively yield to the slower $\{1\bar{1}0\}$ prism faces.

Growth Phase III: The faces of the {110} hexagonal prism begin to develop (Figure 8.3c). As these faces have the lowest growth velocity, they grow at the expense of those of the triangular prisms. If still present, the {100} faces ultimately disappear (Figure 8.3d).

The cross-section of the liddicoatite crystals in Figure 8.2a and Figure 8.2b are very different. The former has a nonagonal (9-sided) cross-section, and the later has a hexagonal cross-section. These differences can be accounted for by considering the relative velocities of the faces in the $\{1\bar{1}0\}$ and {110} forms.

Growth Phase IVa: In the scenario where the velocities of the $\{1\bar{1}0\}$ and {110} forms are approximately the same (*i.e.*, $V_{\{1\text{-}10\}} \approx V_{\{110\}}$), both forms will persist and the crystal develops a nonagonal cross-section such as that shown in Figure 8.3e. The pyramidal oscillatory zones are mantled by a rim of prismatic zones parallel to both $\{1\bar{1}0\}$ and {110} prisms, and this is the cross-sectional form observed in the photograph of Figure 8.2a.

Growth Phase IVb: In the scenario where the velocity of {110} form remains significantly less than the velocity of the $\{1\bar{1}0\}$ form (*i.e.*, $V_{\{110\}} > V_{\{1\text{-}10\}}$). In this case, the $\{1\bar{1}0\}$ prism disappears and the hexagonal prism comes to dominate, resulting in a cross-section similar to that shown in Figure 8.3f. This cross-section resembles that observed in Figure 8.2b, and also to the particular Madagascar liddicoatite specimen investigated throughout this work (see Figure 3.1a).

8.3 THE OCCURRENCE OF LIDDICOATITE IN GRANITIC PEGMATITES

The scarcity of liddicoatite in granitic pegmatites is related to the unusual conditions required to concentrate substantial amounts of Ca *and* Li in the same consolidating melt. In the typical crystallization sequence observed in granitic pegmatites, the bulk of Ca enters early-stage minerals, and occurs in the endocontact and border- and wall-zone assemblages (*e.g.*, feldspar, fluorapatite). In contrast, Li is concentrated in relatively late-crystallizing phases such as Li-aluminosilicates (spodumene or petalite) and lepidolite (*e.g.*, Černý 1991; London 1992). Two mechanisms have been invoked to explain the

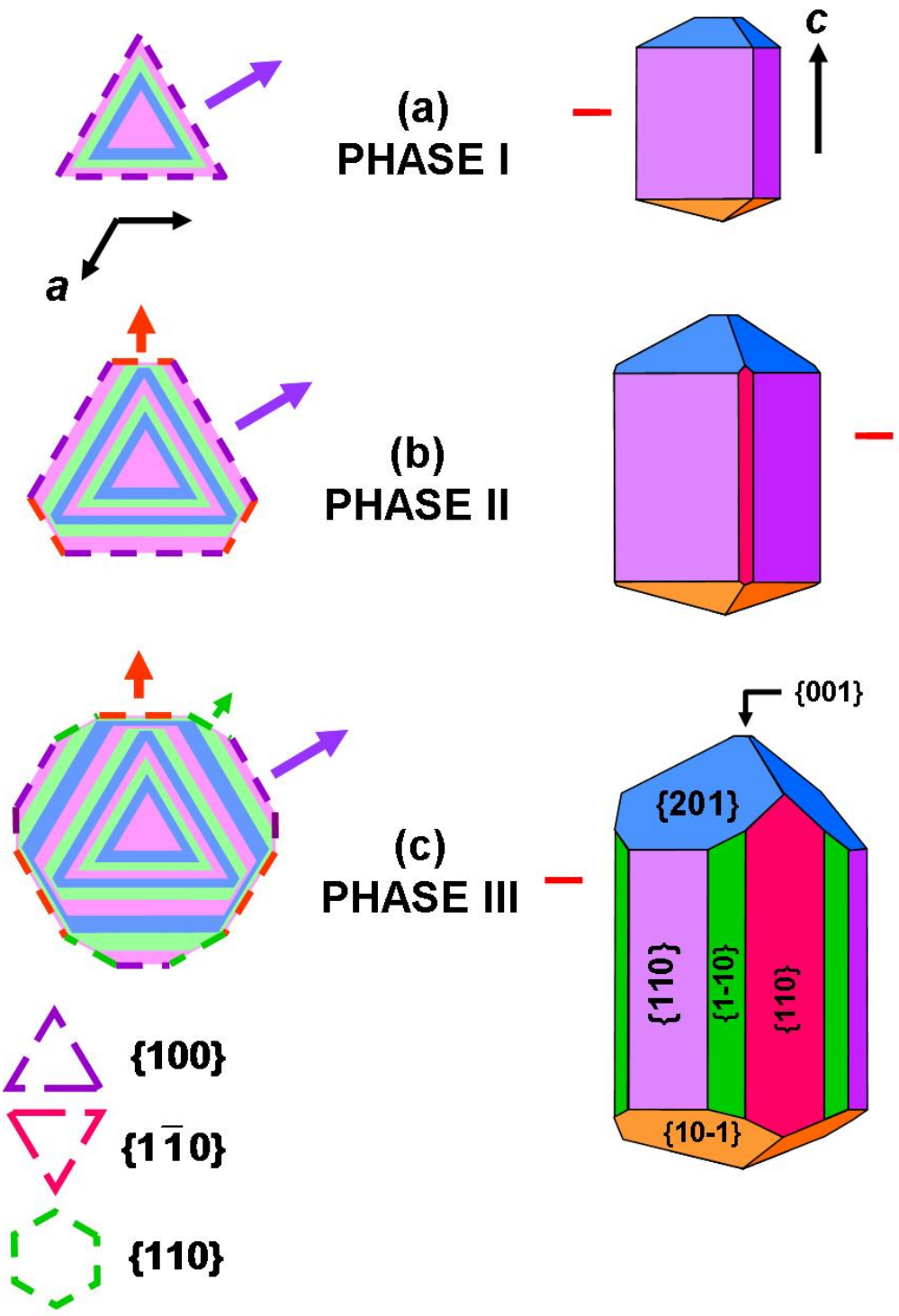

Figure. 8.3 Schematic model of a Madagascar liddicoatite crystal growth (see text for details). Oriented cross-sectional outlines of {100}, {1-10}, and {110} prisms are shown for reference.

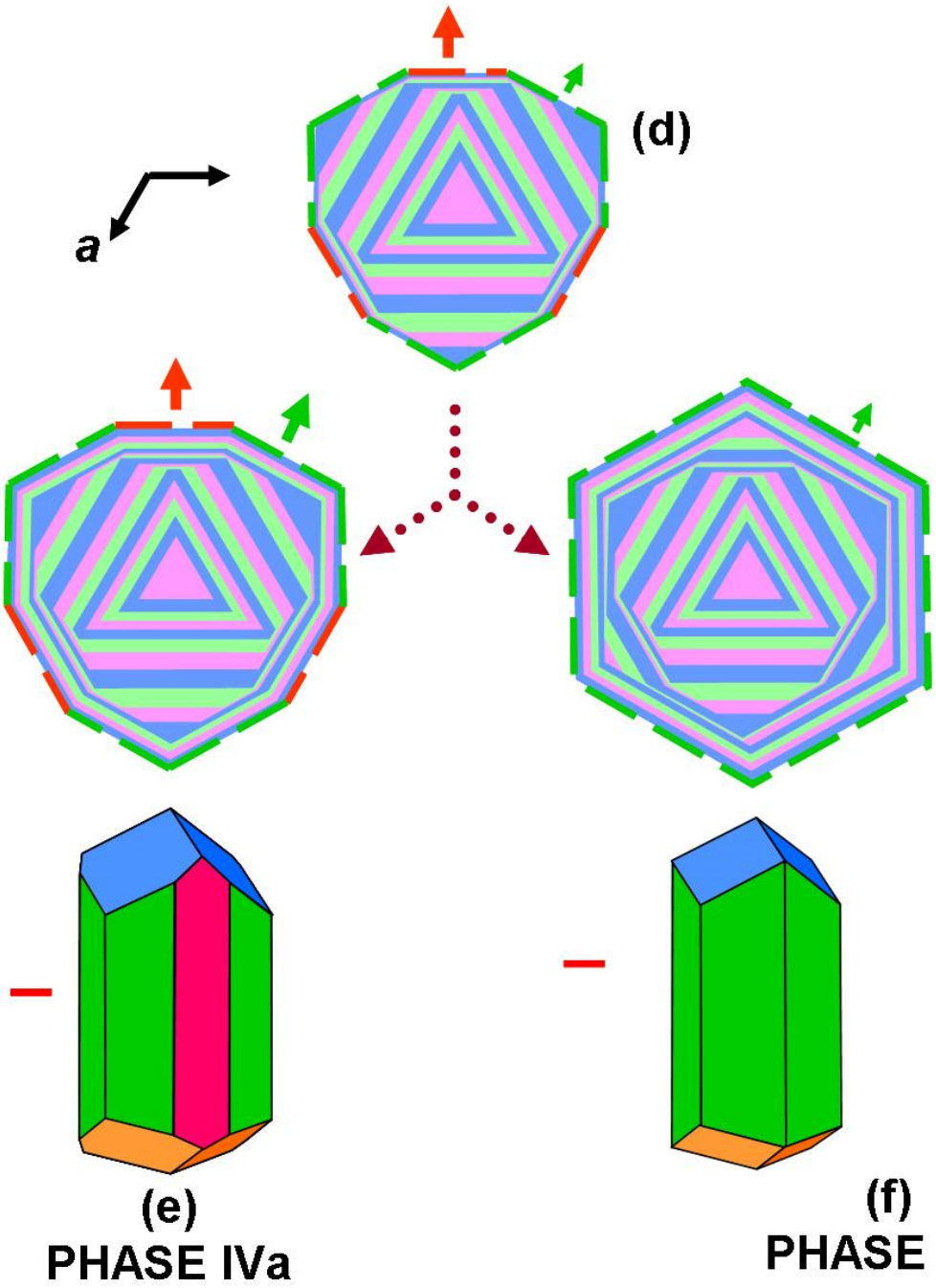
a
(d)
(e)
PHASE IVa
(f)
PHASE IVb

presence of Ca in late-stage minerals in granitic pegmatites. (1) Weidner & Martin (1987) proposed that F in a granitic melt may complex with Ca, and as a result, Ca can remain in the melt until late in the fractionation process. This suggestion has been adopted by several authors in the past 10 years. Selway *et al*. (2000a, 2002) suggested this mechanism for the crystallization of Ca-rich tourmaline as a late-stage mineral in the Tanco and Nyköpingsgruvan granitic pegmatites. The occurrence of liddicoatite in the elbaite-subtype Bližná pegmatite in the Czech Republic (Novák *et al*. 1999) was considered to have resulted from the crystallization of a (Na, Al, Li, B)-rich melt wherein Ca was conserved throughout fractionation of a melt of unique composition. A similar argument is put forth to explain the occurrence of tourmaline crystals with an elbaite (Ca ~ 0.15 *apfu*) core and a liddicoatite (Ca ~ 0.50 *apfu*) rim in the High Grade Dike, eastern Manitoba, Canada. Here, Teertstra *et al*. (1999) observed no evidence of a potential secondary source of Ca. In both of these occurrences, F- and Ca-contents are positively correlated in the tourmaline, consistent with the development of Ca-F complexes that delay the onset of Ca precipitation. (2) Calcium may be introduced into the pegmatite melt at any stage as a contaminant. Thus in the McCombe pegmatite of northwestern Ontario, Canada (Tindle *et al*. 2005), the precipitation of Ca-rich elbaite is argued to be the result of assimilation and leaching of Ca, Mg, and Ti from the host rock and introduction into the late-stage pegmatite melt or fluid. With this particular mechanism, one does not expect just an increase of Ca and F, but a change in other constituents that were involved in the contamination process.

8.3.1 Elbaite-liddicoatite from Black Rapids Glacier, Alaska

In Black Rapids Glacier tourmaline, the lack of transition metals in the central core (Zone A; Figure 7.4) indicates that, when crystallization of tourmaline began, the pegmatite melt had fractionated sufficiently to remove all transition metals from the melt. This situation is in accord with the occurrence of this tourmaline in massive quartz that is presumably part of the quartz core of the parent pegmatite. Despite this indication of a highly fractionated parent melt, the core of the tourmaline has approximately 0.35 *apfu* Ca and 0.75 *apfu* F which is uniform across ~7 mm of the pink core. So what is the source of this Ca and F? The only other constituents of the core of the tourmaline are H, Li, B, Na, Al and Si, all common constituents of a highly fractionated granitic melt. The “foreign constituents” are Ca and F, suggesting either (1) they have come from a Ca-F fluid introduced in a contamination event, or (2) the Ca and F come from primary Ca-F complexes in the granitic melt. Toward the edge of the pink core, both Ca and F increase sharply, suggesting that both are being depleted in the nascent melt/fluid relative to the other constituents.

At the margin between the pink core and the green rim (Region B, Figures 3.8, 7.4), there is a sharp change in composition: Ca, F, Li and transition metals increase, and Na and Al decrease. The Ca-F association continues, but is accompanied by the increase in Fe and Mn. It is difficult to see this as anything but a contamination event with the introduction of Ca, Fe, Mn and F, presumably the result of low-temperature hydrothermal fluids that have reacted with host-rock ferromagnesian minerals. However, Ca, Fe, Mn and F continue to rise from the

junction of the pink core and green rim continuously to the edge of the crystal while Na and Al continue to fall. This change does not accord with the usual depletion of Fe and Mn with continued crystallization of tourmaline, such as that observed in wheatsheaf and mushroom tourmalines (Figures 7.18 and 7.22), suggesting that the contamination event may have been a continuing process until cessation of crystallization of the tourmaline.

Figure 8.4 plots the variation in F against mean charge at the *X*- and *Y*-sites. Henry & Dutrow (2011) showed that for >8800 tourmalines there is a well-defined "*Region of No F*" in site-charge *vs*. F-content space, which they interpret to be the result of a crystal-chemical-control on F incorporation. The blue arrow in Figure 8.4a shows the trend observed during crystallization in both the McCombe Pegmatite and in a fibrous tourmaline sample from the Cruzeiro Mine, Brazil (Dutrow & Henry, 2000) and has a slope of +1. In contrast to the fluid contamination events attributed to the McCombe Pegmatite, the trend of increasing F in the Cruzeiro Mine tourmaline is attributed to progressive fluid fractionation resulting in an increase in F activity. Data from Black Rapids Glacier tourmaline plot very close to the blue line and Figures 7.4 and 7.7b show that Ca and F track very closely. Hence, it seems that correlations between F and Na (*e*.*g*., Selway *et al*. 1999, 2000a), Ca (*e*.*g*., Novak *et al*. 1999) and perhaps Li (*e*.*g*., Tindle *et al*. 2005) in tourmalines are likely to be affected by both petrogenetic origins and interactions (*i*.*e*., fractionation *vs*. contamination *vs*. complexing) between these cations and the stereochemistry of the *X*- and

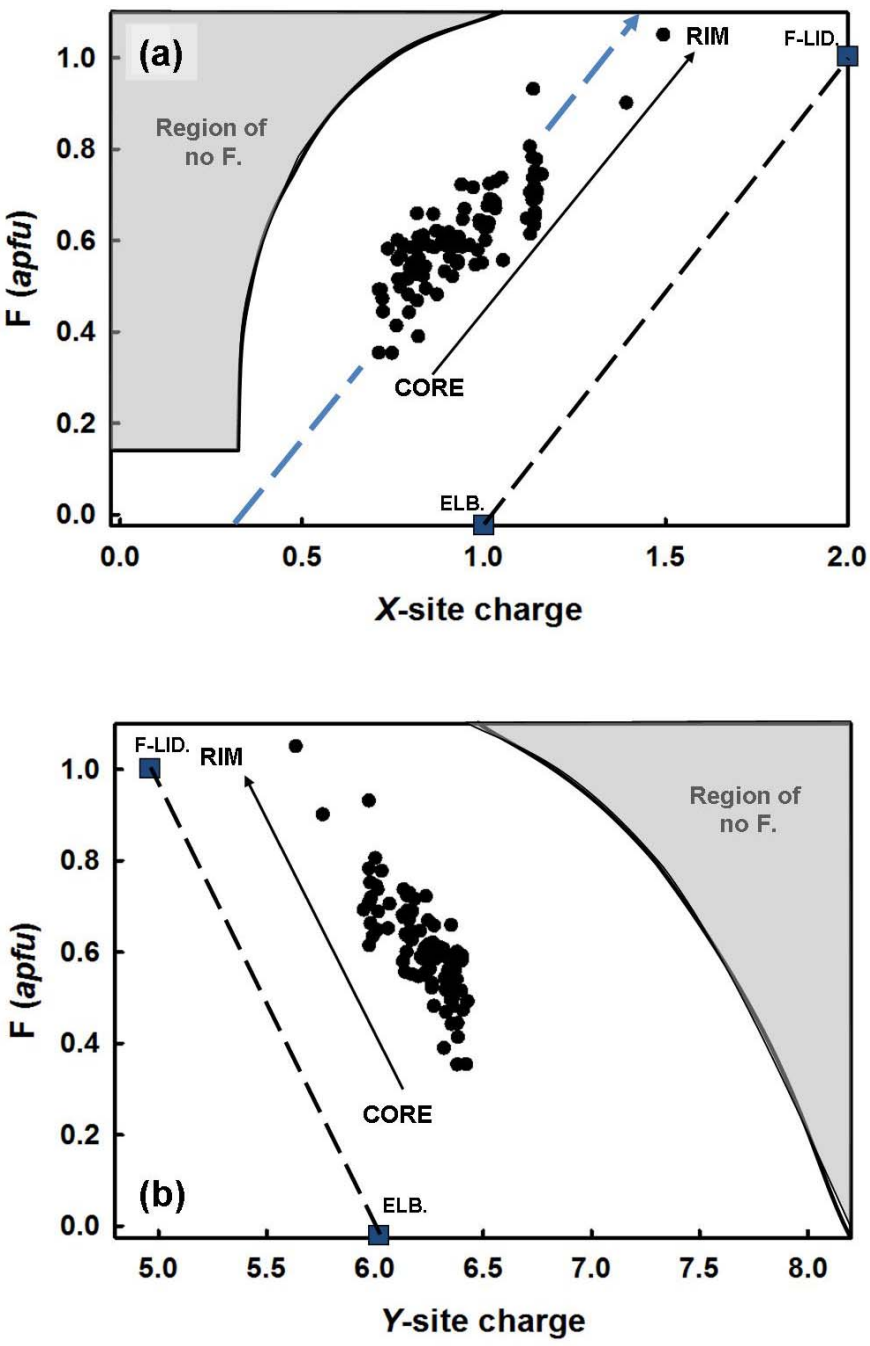

Figure 8.4 Data for Black Rapids Glacier tourmaline plotted in (a) X-site charge and (b) Y-site charge vs. F-content space. Region of no F defined by Henry & Dutrow (2011) Blue line in (a) shows trends observed in the McCombe Pegmatite and fibrous tourmaline from Cruziero Mine, Brazil and is in good agreement with current data. Squares correspond to "ideal" elbaite and fluor-liddicoatite composition given in Tables 1.3 and 1.4.

(perhaps *Y*-) site cation(s) and the anion at the O(1)-site (*i.e.*, OH vs F vs O^{2-}). These issues still remain to be clarified in detail.

8.3.2 The origin of Madagascar liddicoatite

Liddicoatite crystals displaying extensive oscillatory zoning such as the one investigated here are known to occur only in the Anjanabonoina Pegmatite of south-central Madagascar. Unlike Black Rapids Glacier tourmaline, the compositional profiles presented in Chapter 7 as well as the proposed growth model do not suggest that any significant episode of melt contamination occurred during crystallization.

As briefly presented in Chapter 3, the pegmatites of Central Madagascar were emplaced about 490 million years ago during late-stage granitic plutonism related to the Pan-African event, which occurred from 570 to 455 million years ago (Paquette & Nédélec 1998). These pegmatites are hosted by gneisses, marbles and quartzites of the Itremo Group, which overlies the crystalline basement of the Mozambique Orogenic Belt (Malisa & Muhongo 1990, Ashwal & Tucker 1999, Dissanayake & Chandrajith 1999, Collins & Windley 2002, Dirlam *et al*. 2002).

According to the classification scheme of Černý (1982), this pegmatite is intermediate between the LCT (Li-Cs-Ta) and NYF (Nb-*Y*-F) families of rare-element and miarolitic classes. The early stages of crystallization have an NYF signature, whereas the pocket assemblages are indicative of LCT association. Martin & De Vito (2005) consider NYF and LCT pegmatites to be associated with

anogorenic and orogenic settings, respectively. This is consistent with the interpretation of Pezzotta (1996, 2005), who suggests that in southern Madagascar, the NYF-pegmatite-forming melts were derived from anorogenic plutons of syenitic to granitic composition. These were emplaced in the younger sedimentary package, not yet exposed to metamorphism. The *P-T* regime was consistent with metamorphism up to amphibolite facies and resulted in the liberation of B-rich fluids with LCT character, as well as Ca and Mg from the sedimentary package; this enrichment led to a melt rich in Ca-Li-B, resulting in the crystallization of elbaite-liddicaotite tourmaline.

8.4 GROWTH OF FIBROUS WHEATSHEAF AND MUSHROOM TOURMALINES

8.4.1 Growth conditions of wheatsheaf and mushroom tourmalines

The general transition from *M**-bearing to *M**-absent (*M** = Fe + Mn + Ti + Mg) tourmaline along the growth profiles of wheatsheaf and mushroom samples, with exception of the pink (mushroom) and dark red (wheatsheaf) outer regions, is consistent with a typical evolutionary trend of tourmaline composition in granites and pegmatites during fractionation (*e.g.* Jolliff *et al.* 1986).

The stability field for elbaite remains poorly defined and constraining T- and P-conditions is therefore difficult. London (2011) notes that attempts to constrain the stability field of Li-Al tourmaline (*i.e.*, elbaite, rossmanite and liddicoatite) by experimental synthesis has largely yielded unsatisfactory results, with material > 50% elbaite (of liddicoatite or rossmanite) never having been

(confidently) synthesized. London goes on to suggest that because elbaite is commonly associated with spodumene, and both phases contain [6]-coordinated Li, they may have similar stability fields. The experiments of London (1984) show spodumene to be stable over a wide range of *P*- and *T*-conditions, from 1-6 kbar and 200-700 °C, making it difficult to bracket the *P*-*T* conditions of the mushroom growth. However, London (1986), based on petrologic observations, suggested that the development of tourmaline-rich pockets in rare-element pegmatites occurs in the range 425-475 °C and 240-280 MPa.

Ertl *et al*. (2007) investigated another elbaitic tourmaline from the Mogok Mineral Track in Myanmar, with the structural formula, $^{X}(Na_{0.55}Ca_{0.08}Pb_{0.01}\square_{0.36})$ $^{Y}(Al_{2.13}Li_{0.75}Mn^{2+}_{0.01}\square_{0.11})$ $^{Z}Al_6$ $(BO_3)_3$ $(Si_{5.34}B_{0.66}O_{18})$ $^{V}(OH)_3$ $^{W}[(OH)_{0.50}O_{0.26}F_{0.24})$, which resembles the average composition of the elbaites investigated here (Appendix A.4.1). Using the Li-aluminosilicate phase diagram of London (1984) and the observed association of this tourmaline with petalite, these authors constrain the *P*- and *T* conditions to ~550 °C and ~250 MPa, in approximate agreement with London (1986). These temperature estimates are higher than those suggested by the fluid-inclusion work of Zaw (1998), which puts the formation temperature of some pegmatites in Myanmar between 210 and 410 °C.

In the mushroom tourmaline, the textural and optical continuity from the base of the mushroom to the tips of the pink fibres (Figures 3.4 to 3.7) suggests that there was no dissolution of previously-precipitated tourmaline. The nucleation of secondary crystals on the sides of those already present is in accord with the solution being consistently supersaturated with respect to the

tourmaline being precipitated. The fact that secondary crystals are not observed in the wheatsheaf tourmaline may suggest a lesser degree of silica-supersaturation.

In both tourmalines, the overall compositional change from core to rim is consistent with depletion of the nascent fluid in transition metals. However, there are significant abrupt compositional discontinuities. These occur in wheatsheaf tourmaline at 0.5, ~7 and ~11 mm (Figure 7.18), and in mushroom tourmaline at positions 11, 21 and 30 (Figures 7.22). In both specimens, these compositional discontinuities are concurrent with changing substitution mechanisms, as shown in Chapter 7. Compositional discontinuities not corresponding to definite colour changes (*e.g.*, in wheatsheaf elbaite at ~7 mm in Figure 7.18 and in mushroom elbaite at positions 20 and 30 in Figure 7.22) are often more pronounced in some constituents (*e.g.* Na and B) than in others (*e.g.* Li and Al). Hence it is difficult to state whether or not these discontinuities result from the influx of new fluids, or to saturation and subsequent crystallization of other minerals proximal to the growing mushroom, which may affect only certain elements. The major compositional discontinuities at position 37 (Figure 7.22) in mushroom tourmaline and at 18.5 mm (Figure 7.18) in wheatsheaf tourmaline are strongly suggestive of pocket rupture, with the introduction of a more mafic fluid, likely due to influxing of *M** from fluid interaction with mafic wallrocks (*e.g.*, London & Manning 1985; Foord *et al.* 1986; London 1999).

8.4.2 Bifurcation as a process in the growth of tourmaline

A feature of particular interest in the study of wheatsheaf and mushroom samples is the role of crystal bifurcation in tourmaline growth and its role in affecting crystal habit. Specifically, *bifurcation* is the splitting of a larger (parent) crystal into two (or possibly more) thinner, fibrous (daughter) crystals. Mushroom tourmaline from Mogok shows extensive crystallite bifurcation and the unusual mushroom habit is the macroscopic expression of the underlying bifurcated microstructure. Wheatsheaf tourmaline shows a lesser amount of bifurcation that gives rise to the wheatsheaf habit at the macroscopic level. It is important to note that divergent crystal aggregates are common in elbaitic tourmalines from pegmatites, and suggest that crystal bifurcation is the common mechanism by which such habits form.

Crystal bifurcation occurs such that the crystal structures of the parent crystal and daughter fibre are: (1) continuous and in exactly the same orientation - this is *crystallographic bifurcation* and may be recognized by optical continuity and simultaneous extinction when under crossed-polars; or (2) are discontinuous and form separate crystals - this is *non-crystallographic bifurcation*. Both (1) and (2) are observed in the tourmalines here. The descriptive growth models presented below integrate compositional and morphologic observations of previous chapters as well as constrain the type and occurrence of bifurcation episodes during crystal growth. Possible mechanisms causing bifurcation are discussed in later sections.

8.4.3 Growth of mushroom tourmaline

Both texturally and compositionally, four different zones in mushroom tourmaline can be distinguished: (1) the dark-black-to-grey base crystal; (2) the central prismatic crystal; (3) the acicular grey-to-white-to-colourless fibres; and (4) the acicular zone, which includes the thin black zone toward the edge of the mushroom. On the basis of the textural and compositional data, the following growth model for the mushroom tourmaline is proposed.

Phase I: Growth began with nucleation and initial growth of a single crystal, and this phase progressed to produce a stout (likely euhedral) crystal that now forms the core of the mushroom (Figure 8.5a). Crystallization rapidly depleted the environment in transition metals (Figure 7.22) and Na, with a concomitant increase in both ^{Y}Al and Li (Figure 7.22b) and $^{[4]}$B (Figure 7.22d).

Phase II: A central prismatic crystal began to grow from the black core (Figure 8.5b), and smaller, thinner prismatic crystals grow on each side (Figures 8.5b); this represents the first instance of crystal bifurcation and fibrous growth and the relation between parent and daughter matieral is clearly crystallographic (Figure 3.5b). There are marked discontinuities in Na (Figure 7.22c), $^{[4]}$B (Figure 7.22d), ^{Y}Al and Li (Figure 7.22b), and small discontinuities in Mn and Ti but not

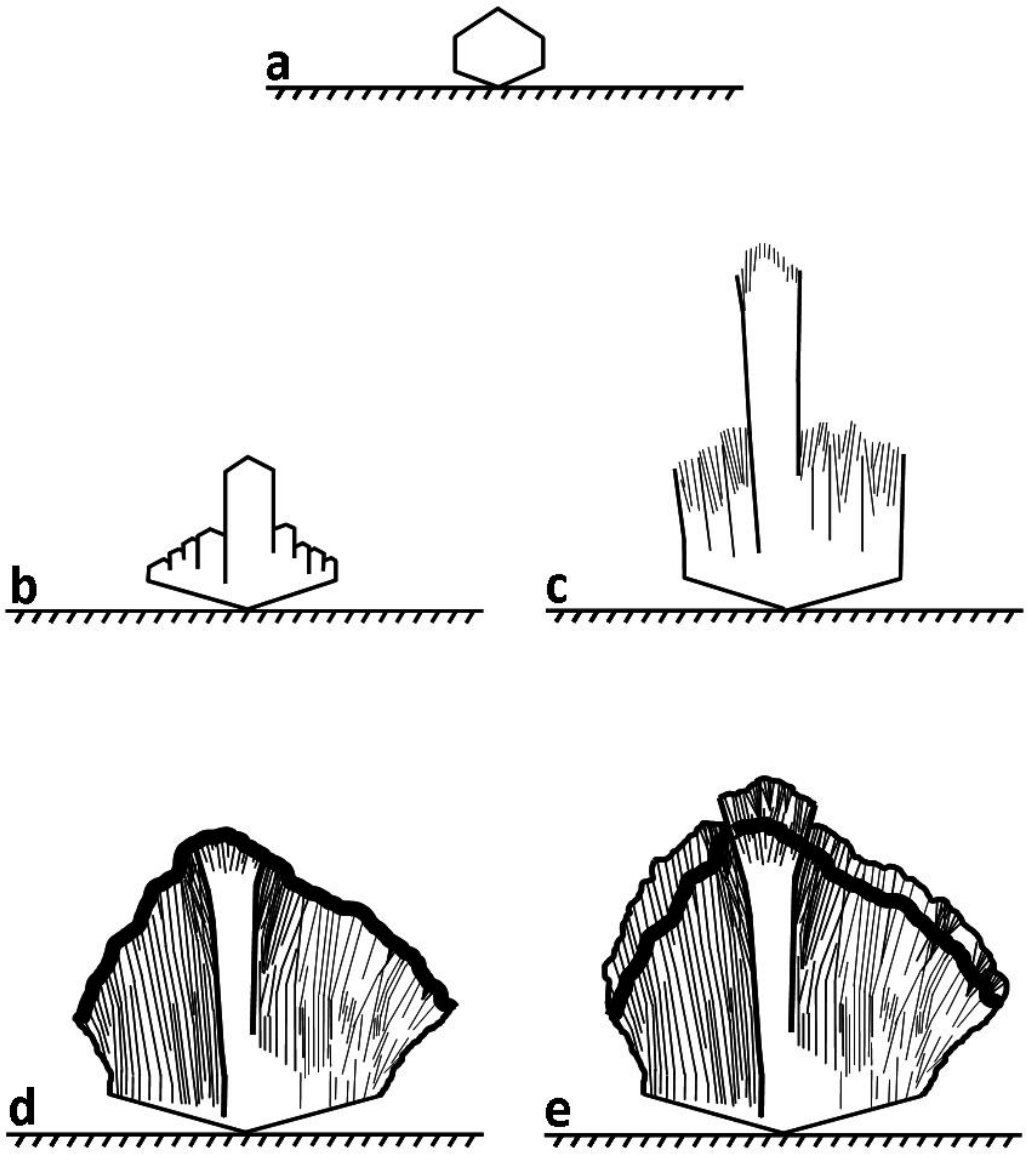

Figure. 8.5 Model of the growth process in mushroom tourmaline: (a) nucleation and growth of the single-crystal black core; (b) growth of central prismatic crystal; (c) initiation of fibre growth; (d) growth of black band during fibre growth; (e) growth of the final dense intergrowth of fibres at the surface.

Fe (Figure 7.22a), where bifurcated growth began. The central prismatic crystal continued to grow with further decrease in transition metals and Na, and increase in ^{Y}Al, Li and $^{[4]}$B.

Phase III: Very acicular crystals began to grow from the end of the central prismatic crystal further from the core (Figure 8.5c), with similar growth from the smaller subsidiary crystals to either side of the main prismatic crystal; this represents a second instance of crystal bifurcation and has a non-crystallographic character. At this stage, there are significant discontinuities in composition of the crystallizing tourmaline, with small increases in transition metals (Figure 7.22a), a drop in Na (Figure 7.22c), and decreases in ^{Y}Al, Li and $^{[4]}$B (Figures 7.22b,d). The narrow black band that occurs toward the edge of the mushroom provides a constraint on growth of the acicular tourmaline: compositional changes indicate that growth of acicular crystals began contemporaneously at all places in the mushroom. As a result, growth must have been much more rapid in the peripheral parts of the mushroom than at the end of the central prismatic crystal. This is in accord with the strong compositional discontinuity between the central crystal and the adjacent transition regions in traverse 2 (Figure 7.25). These acicular crystals tend to curve away from the central axis of the mushroom (Figure 3.5c), and there may be nucleation and growth of new crystals on the sides of pre-existing crystals.

Phase IV: The black band (Figures 3.3, 3.4 and 8.5d) is characterised by a strong increase in transition metals (Figure 7.22a) and Na (Figure 7.22c) and a decrease in the other constituents. This presumably reflects a pulse of fluid rich in transition metals. Unfortunately, there is no information on the local environment of the mushroom tourmalines within their parent pegmatites. However, the unusual habit suggests growth within a miarolitic cavity in which the tourmaline could grow unimpeded by other minerals. This being the case, the black band may mark cavity rupture, with a resulting drop in P_{H2O}. The spike in transition metals may result from the sudden change in P_{H2O} or an influx of fluid of different composition. Certainly the sharp increase in Na and Li and the decrease in $^{[4]}$B and Al at and outside the black band (Figures 7.22 and 7.25) suggest influx of a more alkali-rich fluid.

Phase V: During this final stage of growth, acicular crystals continued to develop, forming dense and elaborate intergrowths (Figure 8.5e). This may represent another instance of bifurcation and is clearly non-crystallographic (Figure 3.5 a,c,d).

8.4.4 Growth of wheatsheaf tourmaline

A similar model may be developed for the growth of wheatsheaf tourmaline. At the base of the sample in the reddish region visible in Figure 3.6b, there is a single crystal flanked by lighter coloured material to either side (Figures 3.6 and 8.6a). The width of this crystal increases in the *c*-direction, and a high-

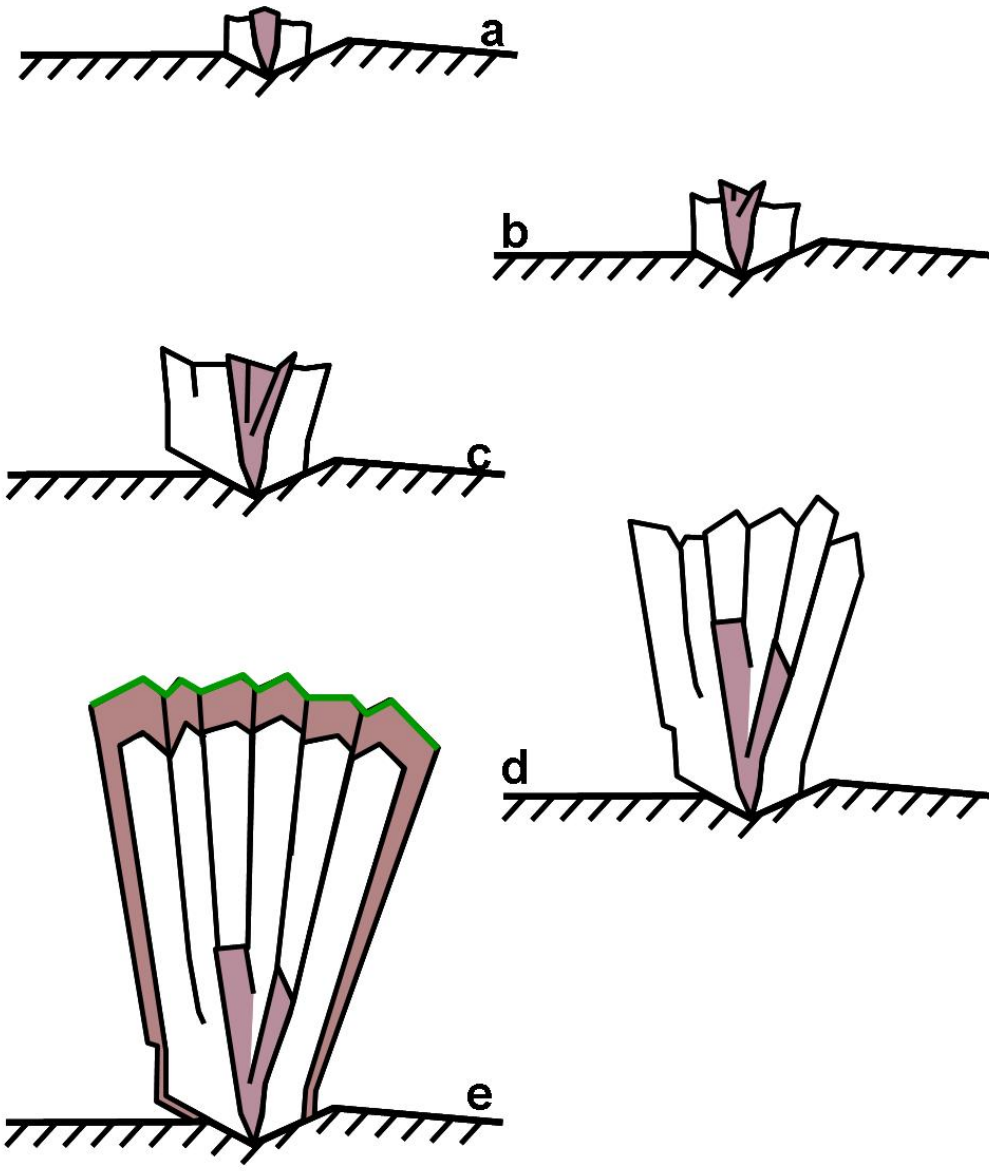

Figure. 8.6 Model of the growth process in wheatsheaf tourmaline (see text for details).

magnification image (Figures 3.7b) shows that the central core crystal splits into multiple crystals which again bifurcate non-crystallographically and increase in width (Figure 8.6b,c). Continued bifurcation and growth has imparted a non-planar aspect to the outer surface of the crystal aggregate (Figures 3.7c) which results in the overall 'wheatsheaf' shape that is observed (Figure 3.6a). After this, major episodes of bifurcation are not observed and growth of the relatively thick (~1 mm) fibres continues, ultimately ending with the euhedral crystal terminations observed in Figure 3.6b.

The red core and surrounding colourless crystals that constitute the bulk of the aggregate (Figure 3.6b,c) show a gradual decrease in *M** to <0.02 *apfu* in the direction of growth parallel to *c*, suggesting crystallization from a continuously-differentiating parent fluid without any abrupt change in composition of the latter. The purplish-red rind toward the edge of the crystal aggregate (Figure 3.6b,c) shows a gradual increase in *M** in the direction of growth. This compositional change is rather unusual, as *M** contents of elbaitic tourmaline tend to decrease with progressive crystallization (*e.g.*, as in the central regions of this crystal, and in the mushroom tourmaline). It seems reasonable to suggest that an external *M**-rich fluid began to leak into the miarolitic cavity and the gross fluid composition began to evolve toward a more *M**-rich composition with the crystallizing tourmaline becoming more *M**-rich as the fluid composition evolved. This period terminated with breaching of the cavity and a sudden increase in Fe in the fluid, with crystallization of the green cap of Fe-rich elbaite (Figures 7.19c and 8.6e) in which the *M** content reaches ~0.90 *apfu*.

8.4.5 Growth surface instability as a cause for crystal bifurcation

Given that both wheatsheaf and mushroom tourmalines originate from the same geologic region, have similar compositions, and share similar morphologic features, we may conjecture that the mechanism resulting in the observed crystal bifurcation is the same in both samples, despite the differences detailed in the above growth history models.

No models have been explicitly developed to explain bifurcation in compositionally-complex crystals such as tourmaline. However, the fibrous crystal habits encountered here resemble those observed in dendrites and spherulites, which may originate from the crystallization of viscous melts where the melt at the growth face becomes constitutionally undercooled. In general, dendrites exhibit crystallographic bifurcation, whereas spherulites exhibit non-crystallographic bifurcation. Models describing the dendrite- and spherulite-forming mechanisms are discussed in detail in such publications as Keith & Padden 1963, 1964a,b; Langer 1981; Magill 2000); a general overview of these, as they may pertain to fibrous tourmaline growth is presented here.

As an illustrative example, consider a two-component melt of A_{melt} and B_{melt} in which a crystal of pure A_{xl} is growing. As the growing face of A_{xl} advances, it preferentially incorporates A_{melt} and excludes B_{melt}, such that the concentration of B_{melt} increases at the growth surface. Here B_{melt} is an impurity, hindering further growth of A_{xl}, and the growth rate of the A_{xl} face is thus controlled by the rate at which B_{melt} impurity diffuses away from the growth face. The following steady-state results (Keith & Padden 1963):

$$C(x) = C_{(0,\mathrm{B_{melt}})}\exp\left[\frac{-x}{\delta}\right] + C_{(\infty,\mathrm{B_{melt}})}, \qquad \text{(Eq. 8.1)}$$

$$\delta = \frac{D_{B_{melt}}}{V} \qquad \text{(Eq. 8.2)}$$

In these equations, x is the distance from the crystal-melt interface (x = 0) into the melt, C_∞ is the mean impurity concentration in the bulk melt, $C_{(0.\mathrm{B\text{-}melt})}$ is the impurity concentration at the crystal-melt interface, $D_{\mathrm{B\text{-}melt}}$ is the diffusion coefficient of the B-impurity in the melt, V is the velocity of the growing face of A_{xl}, and δ defines the thickness of the 'impurity-rich layer' in the melt. A schematic profile is shown in Figure 8.7.

The presence of B_{melt} depresses the liquidus temperature of A_{xl} in the melt immediately near the growth surface, and although the temperature gradient may be positive (dT/dX > 0), the temperature of the liquid proximal to the interface is below the liquidus: this is the condition of *constitutional undercooleding* (purple shading Figure 8.7a). The degree of undercooling, ΔT, given by $T_{melt}(x) - T_L(x)$, can be observed to increase (*i.e.*, dΔT/dx > 0) for a distance from the growth surface. In this situation, the growth of a flat crystal surface is unstable, as any small perturbation on the otherwise flat crystal growth surface will project into a region of the melt that is progressively *more undercooled*, promoting further growth of the perturbation tip.

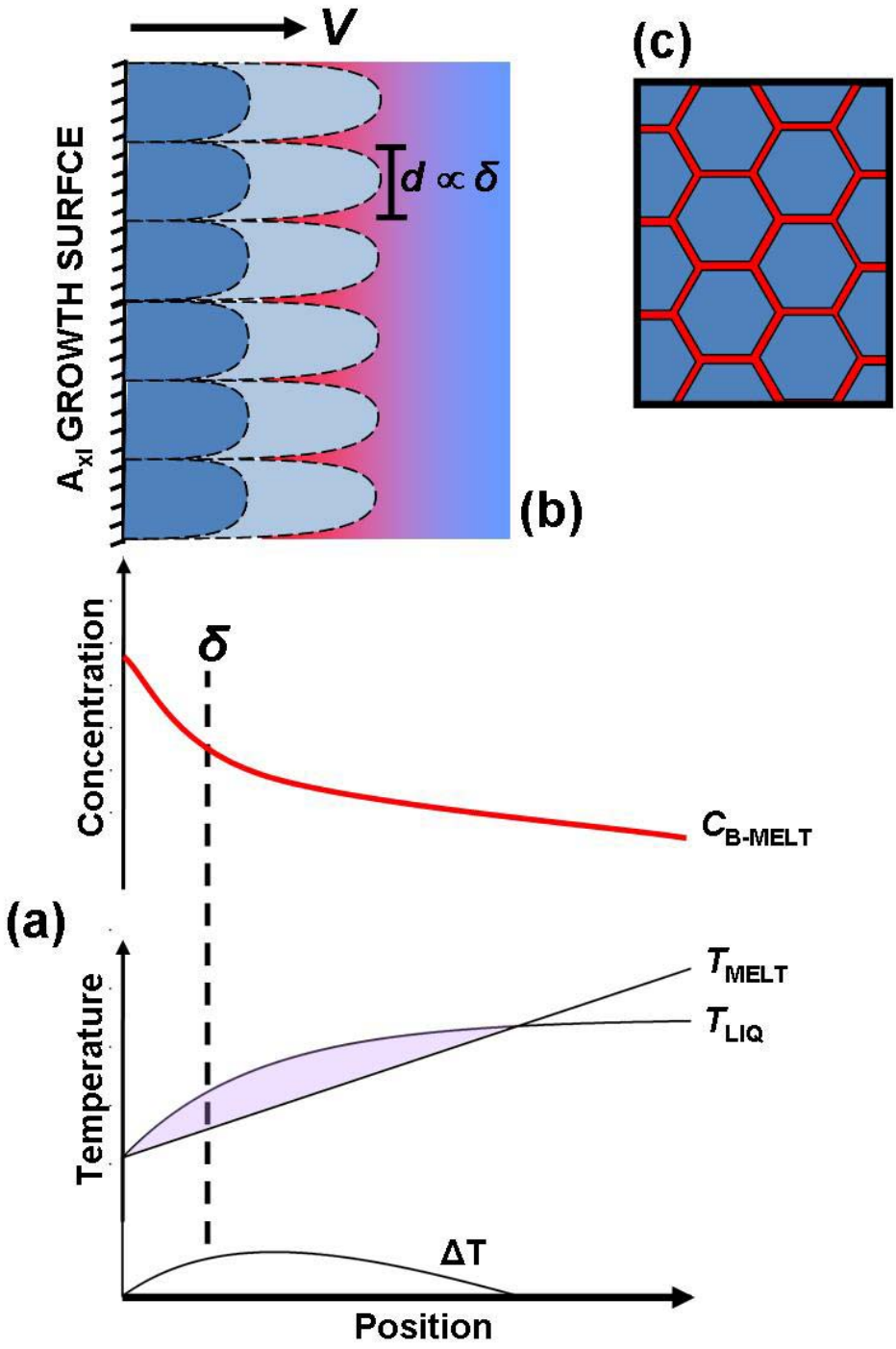

Figure 8.7 Schematic representation growth of A_{xl} (blue) in presence of B_{melt} impurity (red). Development of surface instability resulting from constitutional undercooling; (a) temperature and impurity-concentration profiles at crystal growth surface; (b) development of fibrous protrusions that project into region of increasing undercooling with dimensions $\delta \sim d$; and (c) initial development of 2-dimensional cells on an unstable growth surface, hexagonal outlines represent crystallographic control of parent crystal material (see text for details).

According to Keith & Padden (1963), the initial destabilizing of the flat surface may develop 2-dimensional cells on the surface (Figure 8.7c), where impurity-rich melt is segregated between them. This impurity-rich melt tends not solidify, due to further depression of the liquidus, and the cells persist, continuing to grow into the melt, eventually developing into fibres protruding from the surface.

Spherulite-forming-melts are characterised by high viscosities with low values of D_i and δ, thus resulting in a higher degree of constitution undercooling. Keith & Padden (1963a,b) showed experimentally, and Mullins & Serkera (1963, 1964) show theoretically, that that the width of growing fibres, *d*, tends to scale such that d ~ δ. This occurs because perturbations significantly larger than δ break up to form smaller fibres, and perturbations significantly smaller than δ are overcome by the natural microscopic roughouness of the crystal surface. A consequence of this is that, melts of lower viscosity (larger δ) promote the growth of thicker daughter fibres in crystallographic continuity with the parent crystal, whereas melts of higher viscosity (smaller δ) will promote the growth of thinner non-crystallographic fibres. Non-crystallographic bifurcations occur because the small perturbations that are consistent with small values of δ, have a higher probability of being structurally misaligned.

8.4.5.1 Application to wheatsheaf and mushroom tourmaline

This model of constitutional undercooling appears to be consistent with several of the observations made in wheatsheaf and mushroom tourmalines.

First, the irregular shapes of the bases of the samples indicate that the tourmalines were likely attached to a wall in a pegmatite vug. As the wall was likely cooler than the crystallizing melt, the necessary temperature gradient for constitutional undercooling would have developed (see Figure 8.7a).

Secondly, in mushroom tourmaline, both crystallographic and non-crystallographic bifurcations are observed. Towards the base of the sample, crystallographic bifurcation occurs (growth stage in Figure 8.5b), and parent and daughter crystals show optical continuity and simultaneous extinction under cross-polars (Figure 3.5b). Here, the daughter fibres are relatively thick (0.5 - 1.0 mm). Toward the pink rind, non-crystallographic bifurcation is observed (growth stage in Figure 8.5d,e), resulting in splays of relatively thin (<< ~0.2 mm) crystals (Figure 3.5a,c,d). The onset of these two episodes is approximately coincident with positions 11 and 38 along the traverse of Figure 7.22, at which abrupt changes in composition and substitution behaviour are observed (Table 7.5). In wheatsheaf tourmaline, there is apparently only one major episode of bifurcation, resulting in fibres that are considerably thicker (~ 1 mm) that diverge non-crystallographically. Non-crystallographic bifurcation may also originate from the poisoning of growth surfaces by incompatible phases, which promote growth of branching fibres. García-Ruiz *et al*. (2010) experimentally show the occurrence of non-crystallographic bifurcation forming wheatsheaf and “cauliflower” structures in witherite ($BaCO_3$) growing in the presence of ‘poisoning’ amorphous silica. However, these experiments consistently produce very thin (order of μm) fibres, in contrast to the relatively thick tourmaline fibres observed here. Furthermore,

the model of Garcia-Ruiz (2010) also produces fibres with consistent widths, in contrast to the differences in fibre widths between the mushroom and wheatsheaf samples, and between different sections of the mushroom sample. This is more consistent with progressive changes in melt properties, which result in the observed compositional discontinuities, having also resulted in dramatic changes in δ (Eq. 8.2), promoting the onset of bifurcation.

Furthermore, Transmission Electron Microscope (TEM) images (Figure 8.8) in the white fibrous region (Figure 3.5) of the mushroom tourmaline show fibres where the crystal structure is continuous between parent and daughter crystals (*i.e.*, bifurcation is crystallographic): the high-magnification image shown in Figure 8.8c, shows the presence of only one rhombohedral structure. Although these fibres are on the order of nanometers in size, and hence much smaller than the mm-to-sub-mm-scale fibres observed in hand sample and under the petrographic microscope, they are consistent with fibre development on an unstable crystal surface. Further, the nanoparticle, 'poisoning-impurity' phase required by the model of Garcia-Ruiz *et al*. (2010) is clearly not visible at the interface of parent-daughter crystals at any magnification.

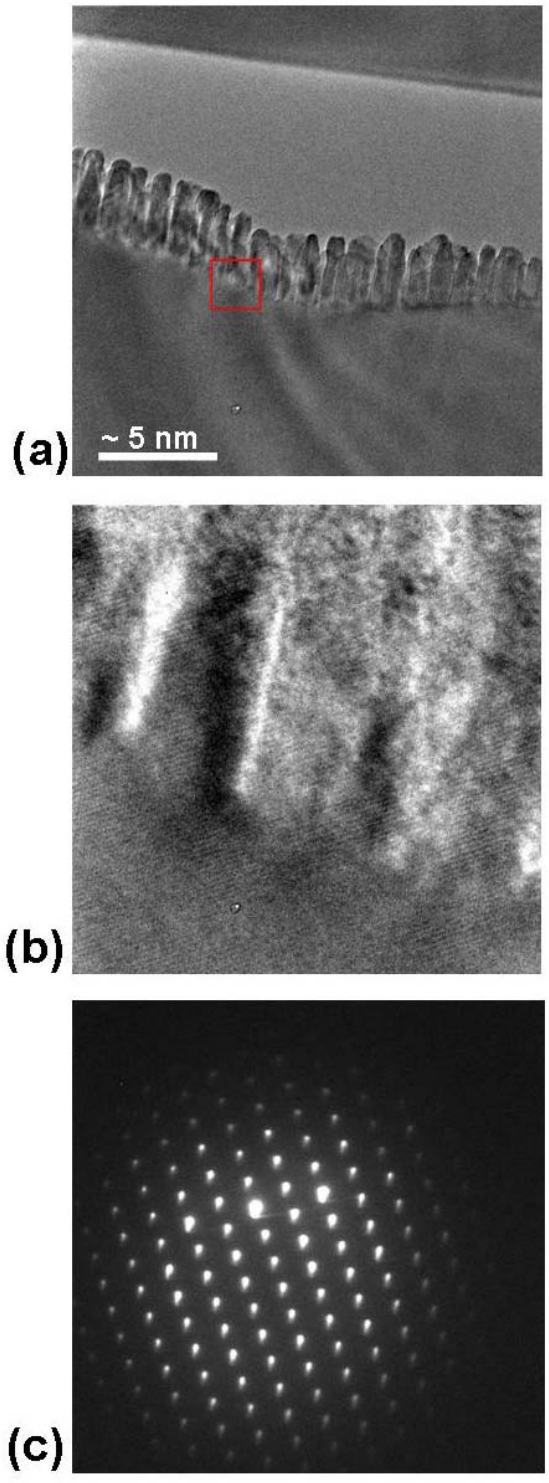

Figure 8.8 Transmission electron microscope images taken on the fibrous region of mushroom tourmaline, showing fibres: (a) interface between parent and daughter crystals; (b) enlargement of red box in (a) to show structural continuity; and (c) high-magnification image on interface region showing the presence of a single rhombohedral diffraction pattern.

It should be noted that there is a major potential setback in applying the above model to pegmatite systems: the requirement for high melt viscosity. Highly-evolved granitic melts typically have high quantities of network-modifying volatile elements (*e*.*g*., H_2O, F BO_3^{3-}), which tend to decrease viscosity and dramatically increase diffusion coefficients. These would tend to increase δ (Eq. 8.2), 'flatten out' $C(x)$ (Eq. 8.1), and thus reduce undercooling (ΔT). However, as it is the ratio, D/V, that controls the system, the growth rate of the tourmaline fibres in the $+c$ direction may be sufficiently rapid to maintain the required disequilibrium condition. As δ scales to d, the tendency for δ to increase at lower viscosities may also correspond to the fact that the widths of fibres in the tourmalines (<< 1 mm) are considerably wider than those observed in typical spherulites (<< 0.1 mm). Another potential problem is that, there is no evidence for any of the 'impurity' required to depress the solidus at the growth front of the tourmaline, however, such evidence need not necessarily be preserved in the crystal.

CHAPTER 9

SUMMARY & FUTURE RESEARCH

9.1 STEREOCHEMICAL CONSIDERATIONS

Comparing mean bondlengths and aggregate ionic radii of 188 published tourmaline structures (including the 40 structures presented in Chapter 6), spanning nearly all tourmaline species, shows:

[1] A strong linear relation between grand mean octahedral bondlength, <*Y*,*Z*-*Φ*> (where *Φ* is an unspecified anion), and constituent cation radius, <*r*[*Y*,*Z*]>. Linear correlations are also observed between the mean bondlength of individual octahedra and constituent cation radius (*i.e.*, <*Y*-*Φ*> *vs*. <*r*[*Y*]> and <*Z*-*Φ*> *vs*. <*r*[*Z*]>); however, there is significantly more scatter about the linear trend. This could suggest that cations are frequently incorrectly assigned to the *Y*- and *Z*-sites. In support of this, tourmalines with significant amounts of Mg (dravite, uvite) and Fe^{2+}-Fe^{3+} (schorl, povondraite, buergerite), which have the greatest potential for disorder between *Y* and *Z*, tend to show the greatest disagreement from the main linear trend.

[2] The occurrence of $^{[4]}$Al and $^{[4]}$B at the *T*-site *increases* and *decreases* the mean <*T*-O> bondlength, respectively, from the mean value of 1.620 Å corresponding to T = Si_6. However, the relation between <*T*-O> *vs*.<r[*T*]> for all tourmalines is poorly-constrained, particularly in the region of low <*r*[*T*]> (i.e.,

high abundance of $^{[4]}$B. This suggests that inaccuracies persist in the determination of B-content.

[3] A consistent positive relation between <*X*-O> and $^{X}\square$ *pfu* is observed in tourmaline, such that <*X*-O> is a linear function of <*r*[*X*]> where the size of the vacancy at the *X*-site is set to 1.26 ± 0.02 Å.

[4] In tourmaline, W = [(OH, F, O^{2-}], and as these anions have different radii, they should influence the observed <*Y*-*Φ*>. However, the relation between O(1) site-occupancy and <*Y*-*Φ*> remains difficult to assess. The detailed study of the 40 tourmalines where Z = Al_6 showed that the <*Y*-*Φ*> bond is systematically larger than expected in tourmaline where W = F. It seems clear that crystal-chemical factors exerting influence on bondlengths and polyhedron geometry in tourmaline are subtle and not yet completely understood.

9.2 THE OCCURRENCE AND DETECTION OF TETRAHEDRALLY COORDINATED Al AND B IN TOURMALINE

A detailed ^{11}B and ^{27}Al MAS NMR investigation into the occurrence of $^{[4]}$B and $^{[4]}$Al in 50 tourmalines of various compositions shows:

[1] MAS NMR is an effective method to identify the presence of small (~0.1 *apfu*) quantities of $^{[4]}$Al and $^{[4]}$B in tourmalines where the abundance of paramagnetic species (Fe + Mn) is sufficiently low to prevent quenching of the NMR signal.

[2] The occurrence of small quantities (*i.e.*, < ~0.15 *apfu*) of $^{[4]}$Al and $^{[4]}$B seems to be more frequent in natural tourmaline than previously suspected, with all possible *T*-site occupancies occurring: T = Si_6, T=$(Si,Al)_6$, T = $(Si,B)_6$ and T = $(Si,Al,B)_6$. The link between tourmaline species and *T*-site occupancy remains unclear as the number of different samples corresponding to each species is not statistically representative. However, certain trends emerge, and investigating several samples of the same species showed that: (1) uvites and dravites consistently have T = $(Si,Al)_6$; (2) elbaites and liddicoatites are variable, but are *never* observed to have T = $(Si,Al)_6$; and (3) olenites seem to consistently have T = $(Si, Al, B)_6$.

[3] The small amounts of $^{[4]}$B and $^{[4]}$Al observed in the samples investigated are virtually invisible to more conventional methods (*e.g.*, EMPA, SREF and SIMS), and MAS NMR is currently the best method for identifying their presence in tourmaline.

[4] The occurrence of even small amounts of paramagnetic elements degrades ^{27}Al and ^{11}B MAS NMR spectra severely, and by the same degree. This makes the derivation of quantitative results difficult, because: (1) in ^{27}Al MAS NMR spectra, spectral bands are subject to severe broadening; and (2) in ^{11}B MAS NMR spectra, the $^{[4]}$B peak becomes unresolvable from the $^{[3]}$B peak.

With increasing paramagnetic content, there is a corresponding increase in the limit of detection of both $^{[4]}$Al and $^{[4]}$B in the MAS NMR spectra. Visually assessing the limits of detection by spectral simulation shows that an increase in paramagnetic elements from 0.05 to 0.1 *apfu* (Fe + Mn) increases the limit of

detection of $^{[4]}$B from ~0.02 to ~0.08 for $^{[4]}$B, yet the limit of detection of $^{[4]}$Al remains at ~0.01-0.2 *apfu*. This is problematic with respect to tourmaline research, as the occurrence of $^{[4]}$B seems to be common, and the occurrence of significant amounts of Fe (and Mn) in natural tourmalines is even more so.

9.3 ZONED TOURMALINES FROM GRANITIC PEGMATITES

Extensive analytical traverses were collected by electron microprobe on four zoned tourmalines with different crystal habits, originating from granitic pegmatites: (1) prismatic liddicoatite tourmaline from Madagascar; (2) mushroom tourmaline from Mogok, Myanmar; (3) prismatic tourmaline from Black Rapids Glacier, Alaska; and (4) wheatsheaf tourmaline from Mogok, Myanmar. Samples (2) to (4) showed discontinuous colour zoning, whereas sample (1) showed oscillatory zoning. Analysing compositional change across these crystals yields information about crystal-growth mechanisms and/or melt evolution during solidification of the host pegmatite. Furthermore, the compositional variation in each crystal may be described by a series of site-specific linear-substitution mechanisms. For each crystal, significant results are summarized below.

9.3.1 Elbaite-liddicoatite from Black Rapids Glacier, Alaska

[1] Examination of the compositional change in Black Rapids tourmaline from crystal centre to crystal edge shows an increase in the abundance of transition elements, and enrichment of Ca (and F) toward the crystal edge. Both observations are contrary to the typical evolution of a fractionating, solidifying

melt and strongly indicate melt contamination during crystal growth. This crystal is thus an excellent example of the ability of tourmaline to record changes in composition (as well as possibly temperature and pressure, although this is not explored here) of the crystallizing melt, even though detailed information of provenance and mineral associations may be absent.

[2] Ca and F are observed to track each other closely through major changes. The F-content of the tourmaline is approximately a linear function of the mean change at the *X*- and *Y*-sites, suggesting that crystal-chemical factors, in addition to petrological factors, act to control the incorporation of F in tourmaline.

9.3.2 Oscillatory zoning in Madagascar liddicoatite:

[1] Throughout the crystal, the oscillatory zoning is superimposed on a smooth monotonic variation in the principal constituents. Fe and Mg show prominent oscillatory behaviour, but are superimposed on background values of ~0 *apfu*.

[2] Oscillatory zoning was observed to occur in both the pyramidal {201} and prismatic {110} sectors of the crystal, and the spatial relations observed between these, in this and other Madagascar liddicoatite crystals, show that these sectors crystallize simultaneously and without hiatus. The patterns differ significantly between these two sectors. In the pyramidal sector, each zone starts with a *discontinuous increase* in Fe and Mg (0.1 - 0.2 *apfu*), which then monotonically decreases to zero across the zone, and this pattern is repeated across the series of zones. In the prism sector, each zone starts with a *gradual increase* from zero

in Fe^{2+} and Mg, which reach maximum values at the end of each zone and then drop sharply to zero; this pattern is repeated across the series of zones.

[3] Structural and compositional data show that the occupancies of the *T*- and *Z*-sites are invariant, and over the bulk crystal, the compositional variation corresponds to only two substitutions:

(1) $^{X}Ca + {}^{Y}Li \rightarrow {}^{X}Na + {}^{Y}M$ and

(2) $^{Y}Li + {}^{Y}Al \rightarrow {}^{Y}M^{*} + {}^{Y}M^{*}$

(where M^{*} = Fe + Mg + Mn + << Ti). It is possible to decompose M^{*} into its constituents parts as Fe (+ Mg) and Mn behave very differently throughout the crystal. Substitutions where $M^{*} = (Fe^{2+} + Mg)$ occur preferentially to those where $M^{*} = Mn^{2+}$, which become increasingly active only where $(Fe^{2+} + Mg) \sim 0$ *apfu*.

[4] The element-selective nature of the compositional pattern, as well as the observed differences between the {110} and {021} sectors, is strongly suggestive of the operation of an internally-controlled mechanism where the physical nature of the growth surface exerts a strong control on the oscillatory mechanism. The diffusion of elements in the melt to the growth surface must also be considered as it appears that the depletion of certain elements in the proximal melt (*i.e.*, Fe + Mg going to 0 *apfu* marking the end of each zone) has a major influence on zone development. Although models describing these types of phenomena have been proposed to explain oscillations in chemically simple minerals (*e.g.*, plagioclase), they are not applicable to the multi-dimensional nature of the problem that defines oscillatory zoning in tourmaline, nor do they account of the diffusion of individual elements to the growth surface.

9.3.3 Wheatsheaf and mushroom elbaite

[1] Morphologically, the wheatsheaf and mushroom elbaites are characterised by extensive bifurcation (splitting) of crystals originating from a central core region. In mushroom elbaite, the crystal core is far more pronounced and the bifurcations are more extensive, resulting in elaborate intergrowths and splays of fibrous crystals with mean thicknesses << 1 mm. In wheatsheaf elbaite, bifurcation is more subtle, resulting in thicker crystal fibres (~1 mm) that have euhedral terminations.

[2] Wheatsheaf and mushroom samples show two types of compositional change. The first is a decrease in transition metals starting at the base of the sample, consistent with typical evolutionary trends of tourmaline composition in granites and pegmatites during melt fractionation. The second is an abrupt increase in transition metals toward the outer edges of the samples. In mushroom tourmaline, there is an *M**-rich black shell that gives way to a pink rind in which Mn is the dominant transition metal. In wheatsheaf tourmaline, there is a burgundy-red rind on the prismatic faces of the sample exterior and on the terminations of the crystal prisms toward the sample top were *M** increases rapidly. The very top of the crystal terminations are also covered by a thick film of dark-green Fe-rich tourmaline.

In the absence of detailed field relations, it is difficult to state whether or not these compositional discontinuities result from the influx of new fluids, or from the saturation and subsequent crystallization of other minerals proximal to the growing tourmalines. However, the major compositional discontinuity at the black

rim of the mushroom and sudden onset of red crystal material in wheatsheaf strongly suggest pocket rupture, with the introduction of a more mafic fluid, likely due to influxing of *M** from fluid interactions with mafic wallrocks.

[3] In wheatsheaf and mushroom elbaite, there are a total of 6 and 8 distinct site-specific substitution mechanisms involved in chemical variation, respectively, and in several instances, these are observed to switch direction with crystal growth. In both samples, boundaries between colour zones correlate which discontinuous breaks in composition where new substitution mechanisms become operative, and these may correlate with the onset of crystal bifurcation.

[4] The variation of $^{[4]}B$ in both mushroom and wheatsheaf samples is significant, and the substitutions that involve variation in $^{[4]}B$ account for much of the observed chemical variation. These are:

(1) $^{T}B + {}^{Y}Al \rightarrow Si + M^*$,

(2) $Li + Si \rightarrow M^* + B$, and

(3) $Li + Si_2 \rightarrow {}^{Y}Al + {}^{T}B_2$.

In general, (1) operates when *M** is present, (3) operates *only* when *M** is absent; and (2) is relatively minor.

[5] Two types of crystal bifurcation are observed in mushroom tourmaline: (1) crystallographic bifurcation, in which emerging fibres maintain crystallographic continuity with the initial crystals; this results in relatively thick (~1 mm) fibres toward the *M**-rich base of the sample; and (2) non-crystallographic bifurcation, in which emerging fibres grow divergently from the initial crystal, resulting in

relatively thin (<< 1 mm) fibres toward the end of white fibrous core and into the pink rind.

These two types of bifurcation seem to be consistent with models wherein the condition of constitutional undercooling develops in the melt proximal to the crystal growth surface, and the otherwise flat crystal growth surface becomes unstable with respect to crystal bifurcation and fibre growth.

9.4 SUGGESTIONS FOR FUTURE RESEARCH

9.4.1 Tetrahedral Al and B in tourmaline

The current work shows that tetrahedrally coordinated Al and B in tourmaline: (1) occur (either separately or together) more commonly than hitherto realized in crystals where the total amount of paramagnetic elements (*i.e*, Fe + Mn) does not exceed ~0.1 *apfu*; (2) occur frequently in very small amounts (*i.e*., $^{[4]}$Al, $^{[4]}$B < 0.1 *apfu*); and (3) may play an important role in the compositional variation of tourmaline by participating in substitution mechanisms. Hence, accurately determining the *T*-site occupancy is a crucial step to fully characterizing any tourmaline. Although the results clearly show that MAS NMR spectroscopy is an effective method for determining the *T*-site occupancy in paramagnetic-free samples, it cannot be used in samples with appreciable Fe and Mn. Tourmalines sufficiently low in these elements for MAS NMR studies are relatively unusual in Nature, and the development of a method capable of determining the *T*-site occupancy in paramagnetic-bearing samples is needed.

It has been shown that *X*-ray absorption spectroscopy, particularly Extended X-ray Fine Structure (EXAFS) and X-ray Absorption Near-Edge Spectroscopy (XANES), is a successful method for differentiating between tetrahedrally- and triangularly-coordinated B (*e.g.*, Fleet & Mathupari 1999; Fleet & Lui 2001) and Al (*e.g.*, Weigel *et al* 2008) in both silicate glasses and crystalline silicates, and these techniques have the advantages of being very sensitive and unhindered by bulk-sample composition. Hence, it is possible that XAS may be effective in determining *T*-site populations in (Fe, Mn)-bearing tourmalines.

9.4.2 Modeling oscillatory zoning in tourmaline

The extensive suite of compositional and structural data collected on oscillatory zones that occur parallel to the {100} and {110} sectors of the Madagascar liddicoatite shows: (1) an element-specific behaviour in major chemical constituents, *e.g.*, Mn^{2+} behaves differently than Fe^{2+} whereas Mg^{2+} behaves similarly to Fe^{2+}; and (2) that the observed zoning patterns differ significantly between the two sectors. This work suggests that zone development originates from non-equilibrium processes maintained by an interplay between the structure of the growing crystal surface and the coupled diffusion of nutrients in the melt next to the growth surface. However, the exact mechanism by which these two processes operate is not yet understood, prohibiting development of a comprehensive mathematical model to explain the occurrence of oscillatory zones in liddicoatite. Future research is therefore required to determine: (1) how

the structure of the growing surface differentiates between different, yet geochemically very similar, elements; and (2) the physical and chemical properties of the melt required to maintain the condition of non-equilibrium necessary for oscillatory-zone development.

Images of growth features on tourmaline surfaces taken by Atomic Force Microscopy (AFM) show the development of difference growth structures on different crystal faces (*e.g.*, Rustemeyer 2003). Paquette & Reeder (1995) initially examined the composition of symmetrically distinct faces of growth features on the (104) face of calcite crystals and showed how the structure of the surface actively selects ions of different size, leading to sector zoning. A similar approach may yield information on how the tourmaline sector faces selectively incorporate elements during growth.

Furthermore, given that such prominent oscillatory zoning is observed in crystals from only one place on Earth, it is likely that the physical and chemical properties of the Anjanabonoina pegmatite melt are very unusual. For instance, a quiescent, low-temperature silicate gel may be required to slow element diffusion sufficiently in order to maintain non-equilibrium at the growth surface. However, our current understanding of what the properties of the crystallizing melt may have been is greatly hindered by the fact that very little is known about the geology of the Anjanabonoina area (*e.g.*, Pezzotta 2006). In this regard, it would be of great use to acquire a more extensive suite of geologic field data from the pegmatites of central Madagascar, such as a detailed account of mineral assemblages and crystallization sequences to determine the composition, origin,

and evolution (geochemistry, temperature and pressure) of the crystallizing melt. The collection of stable isotope data on various mineral suites throughout the pegmatite may also help to constrain the geologic history of the area.

In addition, examination of photographs of Madagascar liddicoatite in Benesch (2000), Rustemeyer (2003) and Dirlam *et al*. (2002) shows that the colours (and hence compositions) of oscillatory zones are extremely varied. As no other Madagascar liddicoatite crystal has been as extensively studied as the one presented here (largely owing to the expense in acquiring such material), it is impossible to determine if the observed element patterns are common to all liddicoatites. If this information was known, however, it could better constrain the parameters of any future model.

9.4.3 Bifurcation of fibrous tourmalines

The thorough characterization of the mushroom and wheatsheaf elbaites presented here shows that, in addition to tracking compositional changes with growth, changes in tourmaline habit may also yield valuable petrologic data by providing information on the evolution of melt properties during crystallization. Bifurcation seems to be a common process during tourmaline growth, but the conditions required for its occurrence are not currently known. This work suggests that a model evoking a region of constitutional undercooling in the melt at the growth front, similar to that used to explain the growth of spherulites and dendrites, may serve as a reasonable analogue on which to base future research. The small amount of TEM data presented here clarified *some* aspects

of the nature of the parent-daughter fibre interface, but was not sufficiently extensive to confirm if the constitutional undercooling model is appropriate. In future, more extensive TEM work on tourmalines with fibrous habits may yield information capable of further clarifying the bifurcation mechanism.

Ultimately, experimental synthesis of fibrous tourmalines would best constrain the conditions necessary for bifurcation. However, in general, the synthesis of tourmalines with elbaitic compositions seems to be currently beyond us (see London 2011, and references therein). Thus, future research should work to ameliorate this situation so that it could be applied to (amongst many other aspects of tourmaline research) fibrous tourmaline growth.

9.4.4 The significance of site-specific substitution mechanisms

Combinations of linear, site-specific substitutions efficiently describe the compositional variations observed in all four of the zoned tourmalines investigated in this work (Tables 7.2 to 7.5); however, the petrologic significance of these substitutions and their relation to crystal growth is unclear and thus deserving of future consideration. In particular, it is not known what factors control why a particular substitution mechanism operates in preference to another.

In the compositionally-complex tourmalines investigated here, there often seems to be a clear selection of one substitution over another. For example, in Madagascar liddicoatite, there is a preference for the substitutions Na + (Fe, $Mg)^{2+} \leftrightarrow$ Ca + Li and 2(Fe, $Mg)^{2+} \leftrightarrow$ Li + Al to operate over the analogous

substitutions with Mn^{2+}, despite the fact that Mn > Fe in certain regions of the crystal (and thus presumably the melt). Similarly, in wheatsheaf and mushroom elbaite, the operation of substitution Fe + Si $\leftrightarrow$ ^{T}B + Al is favoured over Li + Si_2 $\leftrightarrow$ ^{Y}Al + B_2 where Fe is present, and these substitutions are rarely observed to operate together. Determining what factors influence why certain substitutions operate in preference to others may yield detailed information about how the crystal growth surface interacts with the melt.

REFERENCES

Abrahams, S.C. (1972) Systematic error differences between two refined sets of position coordinates for $Na_3PO_3CO_2.6H_2O$. *Acta Crystallographica*, **B28**, 2886-2887.

Abrahams, S.C. (1974) The reliability of crystallographic structural information. *Acta Crystallographica*, **B30**, 261-268.

Abrahams, S.C. & Keve, E.T. (1971) Normal probability plot analysis of error in measured and derived quantities and their standard deviations. *Acta Crystallographica*, **A27**, 157-165.

Agrosi, G., Bosi, F., Lucchesi, S., Melchiorre, G. & Scandale, E. (2006) Mn-tourmaline crystals from island of Elba (Italy) growth history and growth marks. *American Mineralogist,* **91**, 944-952.

Akizuki, M. & Sunagawa, I. (1978) Study of the sector structure in adularia by means of optical microscopy, infra-red absorption, and electron microscopy. *Mineralogical Magazine,* **42**, 453-462.

Akizuki, M. & Terada, T. (1998) Origin of abnormal optical property of apophyllite. *Neues Jarb. Mineral,* **42**, 234-240.

Akizuki, M., Hampar, M.S. & Zussman, J. (1979) An explanation of anomalous optical properties in topaz. *Mineralogical Magazine,* **43**, 237-241.

Akizuki, M., Kuribayashi, T., Nagase, T. & Kitakaze, A. (2001) Triclinic liddicoatite and elbaite in growth sectors of tourmaline from Madagascar. *American Mineralogist,* **86**, 364-369.

Andreozzi, G.B., Bosi, F. & Longo, M. (2008) Linking Mössbauer and structural parameters in elbaite-schorl-dravite tourmalines. *American Mineralogist*, **93**, 658-666.

Ashwal, L.D. & Tucker, R.D. (1999) Geology of Madagascar: a brief outline. *Gondwana Research,* **2**, 335-339.

Aurisicchio, C., Ottolini, L., and Pezzotta, F. (1999) Electron- and ion-microprobe analyses, and genetic inferences of tourmalines of the foitite-schorl solid solution. *European Journal of Mineralogy*, **11**, 217-225.

Bartelmehs, K.L., Bloss, F.D., Downs, R.T. & Birch, J.B. (1992) Excalibr II. *Zeitschrift für Kristallographie*, **199**, 185-196.

Barton 1969. Refinement of the crystal structure of buergerite and the absolute orientation of tourmalines. *Acta Crystallographica*, **B25**, 1524-1533.

Benesch, F. (2000) *Der Tourmaline Eine Monographie*. Urachhaus, Stuttgart, Germany.

Bloodaxe, E.S., Hughes, J.M., Dyar, M.D., Grew, E.S. & Guidotti, C.V. (1999) Linking structure and chemistry in the schorl-dravite series. *American Mineralogist*, **84**, 922-928.

Bosi, F. (2008) Disordering of Fe^{2+} over octahedrally coordinated sites of tourmaline. *American Mineralogist*, **93**, 1647-1653.

Bosi, F. (2011a) Octahedrally-coordinated vacancies in tourmaline: a theoretical approach. *Mineralogical Magazine*, **74**, 1037-1044.

Bosi, F. (2011b) Stereochemical constraints in tourmaline: from a short-range to a long-range structure. Canadian Mineralogist, **49**, 17-27.

Bosi, F. & Lucchesi, S. (2004) Crystal chemistry of the schorl-dravite series. *European Journal of Mineralogy,* **16**, 335-344.

Bosi, F. & Lucchesi, S. (2007) Crystal chemistry in the tourmaline group: structural constraints on chemical variability. *American Mineralogist*, **92**, 1054-1063.

Bosi, F., Lucchesi, S. & Reznitskii L. (2004) Crystal chemistry of the dravite-chromdravite series. *European Journal of Mineralogy,* **16**, 345-352.

Bosi, F., Agrosi, G., Lucchesi, S., Melchiorre, G. & Scandale, E. (2005a) Mn-tourmaline from island of Elba (Italy) crystal chemistry. *American Mineralogist*, **90**, 1661-1668.

Bosi, F., Andreozzi, G.B., Federico, M., Graziani, G. & Lucchesi, S. (2005b) Crystal chemistry of the elbaite-schorl series. *American Mineralogist*, **90**, 1784-1792.

Bosi, F., Balić-Žinić, T., Surour, A.A. (2010) Crystal structure analyses of four tourmaline specimens from the Cleopatra's Mines (Egypt) and Jabal Zalm (Saudi Arabia), and the role of Al in the tourmaline group. *American Mineralogist, **95***, 510-518**.**

Braun, R. (1891) Optischen Anomalien der Krystalle. Bey S. Hirzel, Leipzig.

Bray, P.J. (1999) NMR and NQR studies of boron in vitreous and crystalline borates. *Inorganica Chimica Acta*, **289**, 158-173.

Bray, P.J., Edwards, J.O., O'Keefe, J.G., Ross, V.F. & Tatsuzaki, I. (1961) Nuclear magnetic resonance studies of B^{11} in crystalline borates. *Journal of Chemical Physics,* **35**, 435-442.

Burns, R.G. (1981) Intervalence transitions in mixed-valence minerals of iron and titanium. *Annual Review of Earth and Planetary Sciences*, **9**, 345-383.

Burns, P.C., Macdonald, D.J. & Hawthorne, F.C. (1994) The crystal chemistry of manganese-bearing elbaite. *Canadian Mineralogist,* **32**, 31-41.

Burt, D.M. (1989) Vector representation of tourmaline compositions. *American Mineralogist,* **74**, 826-839.

Cámara, F., Ottolini, L. & Hawthorne, F.C. (2002) Crystal chemistry of three tourmalines by SREF, EMPA, and SIMS. *American Mineralogist*, **87**, 1437-1442.

Cempírek,J., Novák, M., Ertl, A., Hughes, J.M., Rossman, G.R. & Dyar, M.D. (2006) Fe-bearing olenite with tetrahedrally coordinated Al from an abyssal pegmatite at Kutná Hora, Czech Republic: structure, crystal chemistry, optical and XANES spectra. *Canadian Mineralogist*, **44**, 23-30.

Černý, P. (1982) Anatomy and classification of granitic pegmatites. Pp. 1-39 in: *Mineralogical Association of Canada: Short Course in Granitic Pegmatites in Science and Industry* (P. Černý, editor). Winnipeg, Manitoba, Canada.

Černý P. (1991) Rare-element granitic pegmatites, I. Anatomy and internal evolution of pegmatite deposits. *Geoscience Canada*, **18**, 49-67.

Clark, C.M., Hawthorne, F.C., & Ottolini, L. (2011) Fluor-dravite, $NaMg_3Al_6Si_6O_{18}(BO_3)_3(OH)_3F$, a new mineral species of the tourmaline group from the Crabtree Emerald Mine, Mitchell County, North Carolina: description and crystal structure. *Canadian Mineralogist*, **49**, 57-62.

Clark McCracken, C.M. (2002) *Aspects of the crystal chemistry of the tourmaline-group minerals*. unpublished thesis (Ph.D.), University of Manitoba

Collins, A.S. & Windley, B.F. (2002) The tectonic evolution of central and northern Madagascar and its place in the final assembly of Gondwana. *Journal of Geology,* **110**, 325-339.

Cooper, M.A, Hawthorne, F.C. & Grew, E.S. (2009) The crystal chemistry of the kornerupine-prismatine series. I. crystal structure and site populations. *Canadian Mineralogist*, **47**, 233-262.

De Oliveira, E.F., Castaneda, C., Eeckhout, S.G., Gilmar, M.M., Kwitko, RR., De Grave, E. & Botelho, N.F. (2002) Infrared and Mössbauer study of Brazilian tourmalines from different geological environments. *American Mineralogist*, **87**, 1154-1163.

Deer, W.A., Howie, R.A., & Zussman, J. (1992) *An Introduction to the Rock-Forming Minerals* (*2nd Ed.*) Longman, China.

Dirlam, D.M., Laurs, B.M., Pezzotta, R. & Simmons, W.B. (2002) Liddicoatite tourmaline from Anjanabonoina, Madagascar. *Gems & Gemmology,* **38**, 28-53.

Dissanayake, C.B. & Chandrajith, R. (1999) Sri Lanka-Madagascar Gondwana linkage: evidence for a Pan-African mineral belt. *Journal of Geology,* **107**, 223-235.

Dunn, P.J., Appleman, D.E. & Nelen, J. (1977) Liddicoatite, a new calcium end-member of the tourmaline group. *American Mineralogist*, **62**, 1121-1124.

Dunn, P.J., Nelen, J.A. & Appleman, D.E. (1978) Liddicoatite, a new gem tourmaline species from Madagascar. *Journal of Gemmology*, **16**, 172-176.

Dutrow, B.L. & Henry, D.J. (2000) Complexly zoned fibrous tourmaline, Cruzeiro Mine, Minas Gerais, Brazil: a record of evolving magmatic and hydrothermal fluids. *Canadian Mineralogist*, **38**, 131-143.

Dyar, M.D., Taylor, M.E., Lutz, T.M., Francis, C.A., Robertson, J.D., Cross, L.M., Guidotti, C.V. & Wise, M. (1998) Inclusive chemical characterization of tourmaline: Mössbauer study of Fe valence and site occupancy. *American Mineralogist,* **83**, 848-864.

Dyar, M. D., Wiedenbeck. M., Robertson, D., Cross, L.R., Delaney, J.S., Ferguson, K., Francis, C.A., Grew, E.S., Guidotti, C.V., Hervig, R.L., Hughes, J.M., Husler, J., Leeman, W.P., McGuire, A.V., Dieter, R., Rothe, H., Paul, R.L., Richards, I. & Yates, M. (2001) Reference minerals for the microanalysis of light elements. *Geostandards Newsletter*, **25**, 446-463.

Eeckhout, S.G., Corteel, C., Van Coster, E. De Grave, E. & De Paepe, P. (2004) Crystal-chemical characterization of tourmalines from the English Lake District: electron-microprobe analyses and Mössbauer spectroscopy. *American Mineralogist*, **89**, 1743-1751.

Ertl, A. & Hughes, J.M. (2002) The crystal structure of an aluminum-rich schorl overgrown by boron-rich olenite from Koralpe, Styria, Austria. *Mineralogy and Petrology*, **75**, 69-78.

Ertl, A., Pertlik, F. & Bernhardt, H.-J. (1997) Investigations on olenite with excess boron from the Koralpe, Styria, Austria. *Österreichische Akademie der Wissenschaften, Mathematisch-Naturwissenschaftliche Klasse, Abteilung I, Anzeiger,* **134**, 3-10.

Ertl, A., Hughes, J.M., Brandstätter, F., Dyar, M.D. & Prasad, P.S.R. (2003a) Disordered Mg-bearing olenite from a granitic pegmatite from Goslarn, Austria: a chemical, structural, and infrared spectroscopic study. *Canadian Mineralogist,* **41**, 1363-1370.

Ertl, A., Hughes, J.M., Prowatke, S., Rossman, G.R., London, D. & Fritz, E.A. (2003b) Mn-rich tourmaline from Austria: structure, chemistry, optical spectra, and relations to synthetic solid solutions. *American Mineralogist,* **88**, 1369-1376.

Ertl, A., Pertlik, F., Dyar, M.D., Prowatke, S., Hughes, J.M., Ludwig, T. & Bernhardt, H.-J. (2004) Fe-rich Olenite with tetrahedrally coordinated Fe^{3+} from Eibenstein, Austria: structural, chemical, and Mössbauer data. *Canadian Mineralogist,* **42**, 1057-1063.

Ertl, A., Schuster, R., Prowatke, S., Brandstaetter, F., Ludwig, T., Bernhardt, H., Koller, F. & Hughes, J.M. (2004b). Mn-rich tourmaline and fluorapatite in a variscan pegmatite from Eibenstein an der Thaya, Bohemian Massif, Lower Austria. *European Journal of Mineralogy,* **16**, 551-560.

Ertl, A., Rossman, G., R., Hughes, J.M., Prowatke, S. & Ludwig, T. (2005) Mn-bearing "oxy-rossmanite" with tetrahedrally coordinated Al and B from Austria: structure, chemistry, and infrared and optical spectroscopy. *American Mineralogist*, **90**, 481-487.

Ertl, A., Hughes, J.M., Prowatke, S., Ludwig, T., Prasad, P.S.R., Brandstätter, F., Körner, W., Schuster, R., Pertlik, F. & Marschall, H. (2006a) Tetrahedrally coordinated boron in tourmalines from the liddicoatite-elbaite series from Madagascar: structure, chemistry, and infrared spectroscopic studies. *American Mineralogist*, **91**, 1847-1856.

Ertl, A., Kolitsch, U., Prowatke, S., Dyar, M. D. & Henry, D. J. (2006b). The F-analogue of schorl from grasstein, trentino-south tyrol, italy; crystal structure and chemistry. *European Journal of Mineralogy,* **18**, 583-588.

Ertl, A., Hughes, J.M., Prowatke, S., Ludwig, T., Brandstatter, F., Korner, W. & Dyar, M.D. (2007) Tetrahedrally coordinated boron in Li-bearing olenite from “Mushroom” tourmaline from Momeik, Myanmar. *Canadian Mineralogist*, **45**, 891-899.

Ertl, A., Tillmans, E., Ntaflos, T., Francis, C., Giester, G., Körner, W., Hughes, J.M., Lengauer, C. & Prem, M. (2008) Tetrahedrally coordinated boron in Al-rich tourmaline and its relationship to the pressure-temperature conditions of formation. *European Journal of Mineralogy*, **20**, 881-888.

Ertl A, Rossman, G.R., Hughes J.M., London D., Wang Y., O'Leary J.A., Dyar M.D., Prowatke S., Ludwig T. & Tillmanns E. (2010) Tourmaline of the elbaite-schorl series from the Himalaya mine, Mesa Grande, California; a detailed investigation. American Mineralogist, **95,** 24-40.

Ertl, A., Mali, H., Schuster, R., Körner, Hughes, J.M., Brandstätter, F. & Tilmanns, E. (2010) LI-bearing, disordered Mg-rich tourmaline from a pegmatite-marlbe contact in the Austroalpine basement units (Styria, Austria). *Mineralogy and Petrology*, **99**, 89-104.

Faye, G.H., Manning, P.G., Gosselin, J.R. & Tremblay, R.J. (1974) The optical absorption spectra of tourmaline: importance of charge-transfer processes. *Canadian Mineralogist*, **12**, 370-380.

Ferrow, E.A. (1994) Mössbauer effect study of the crystal chemistry of tourmaline. *Hyperfine Interactions*, **91**, 689-695.

Fleet, M.E. & Liu, X. (2001) Boron K-edge XANES of boron oxides: tetrahedral B-O distances and near-surface alteration. *Physics and Chemistry of Materials*, **28**, 421-427.

Fleet, M.E. & Mathupari, S. (1999) Coordination of boron in alkali borosilicate glasses using XANES. *Journal of Non-Crystalline Solids*, **255**, 233-241.

Foit., F.F. Jr. (1989) Crystal chemistry of alkali deficient schorl and tourmaline structural relationships. *American Mineralogist*, **74**, 422-431.

Foit, F.F. Jr. & Rosenberg, P.E. (1979) The structure of vanadium-bearing tourmaline and its implication regarding tourmaline solid solution. *American Mineralogist*, **64**, 788-798.

Foord, E.E. & Cunningham, C.G. (1978) Thermal transformation of anomalously biaxial dimetric crystals. *American Mineralogist* **63**, 747-749.

Foord, E.E. & Mills, B.A. (1978) Biaxiality in ‘isometric’ and ‘dimetric’ crystals. *American Mineralogist*, **63**, 316-325.

Foord , E.E., Starkey, H.C. & Taggert, J.E. Jr. (1986) Mineralogy and paragenesis of “pocket’ clays and associated minerals in complex granitic pegmatites, San Diego County, California. *American Mineralogist*, **71**, 428-439.

Francis, C.A., Dyar, M.D., Williams, M.L. & Hughes, J.M. (1999) The occurrence and crystal structure of foitite from a tungsten-bearing vein at Copper Mountain, Taos County, New Mexico. *Canadian Mineralogist,* **37**, 1431-1438.

Furbish, W.J. (1968) Tourmaline of acicular and filiform morphology from pyrophyllite deposits of North Carolina. *Rocks and Minerals*, **43**, 584-586.

García-Ruiz, J.M., Melero-García, E. & Hyde, S.T. (2010) Morphogenesis of Self-Assembled Nanocrystalline Materials of Barium Carbonate and Silica. *Science,* **323***, 362-365.*

Gorskaya, M.G., Frank-Kamenetskaya, O.V., Rozhdest-Venskaya, I.V. & Frank-Kamenetskii, V.I. (1982) Refinement of the crystal structure of Al-rich elbaite and some aspects of the crystal chemistry of tourmalines. *Sov. Phys. Crystallogr.* **27**, 63-66.

Grice, J.D. & Ercit, T.S. (1993) Ordering of Fe and Mg in the tourmaline crystal structure: the correct formula. *Neues Jahrbuch für Mineralogie Abhandlungen*, **165**, 245-266.

Grice, J.E. & Robinson, G.W. (1989) Feruvite, a new member of the tourmaline group and its crystal structure, *Canadian Mineralogist*, ***27***, 199-203.

Grice J.D., Ercit, T.S. & Hawthorne, F.C. *(*1993*)* Povondraite, a redefinition of the tourmaline ferridravite, *American Mineralogist*, **78**, 433.436.

Halden, N.M. & Hawthorne, F.C. (1993) The fractal geometry of oscillatory zoning in crystals : application to zircon. *American Mineralogist*, **78**, 1113-1116.

Hamilton, W.C. & Abrahams, S.C. (1972) Normal probability plot analysis for small samples. *Acta Crystallographica*, **A28**, 215-218.

Hawthorne , F.C. (1988) Mössbauer Spectroscopy In Spectroscopic Methods. *Reviews in Mineralogy*, **18**, 255-340.

Hawthorne, F.C. (1996) Structural mechanisms for light-element variations in tourmaline. *Canadian Mineralogist,* **34**, 123-132.

Hawthorne, F.C. (2002) Bond-valence constraints on the chemical composition of tourmaline. *Canadian Mineralogist,* **40**, 789-798.

Hawthorne F.C. & Henry D.J. (1999) Classification of minerals of the tourmaline group. *European Journal of Mineralogy*, **11**, 201-215.

Hawthorne, F.C. & Oberti, R. (2007) Amphiboles: crystal chemistry. *Reviews in Mineralogy & Geochemistry*, **67**, 1-51.

Hawthorne, F.C., Macdonald, D.J. & Burns, P.C. (1993) Reassignment of cation site occupancies in tourmaline: Al-Mg disorder in the crystal structure of dravite. *American Mineralogist,* **78**, 265-270.

Hawthorne, F.C., Ungaretti, L. & Oberti, R. (1995) Site populations in minerals: terminology and presentation of results of crystal-structure refinement. *Canadian Mineralogist*, **33***,* 907-911.

Hawthorne, F.C., Burns, P.B., & Grice, J.D. (1996) The crystal chemistry of boron. *Reviews in Mineralogy*, **33**, 41-110.

Hawthorne, F.C., Selway, J.B., Kato, A., Matsubara, S., Shimizu, M., Grice, J.D., and Vajdak, J. (1999) Magnesiofoitite, □ (Mg_2Al) Al_6 (Si_6O_{18}) (BO_3)$_3$ $(OH)_4$, a new alkali-deficient tourmaline. *Canadian Mineralogist*, **37**, 1439-1443.

Henry, D.J. & Dutrow, B.L. (1992) Tourmaline in low-grade clastic sedimentary rocks: an example of the petrogenetic potential of tourmaline. *Contributions to Mineralogy and Petrology*, **112**, 203-218.

Henry D.J. & Dutrow, B.L. (1996) Metamorphic tourmaline and its petrogenetic applications. In Boron: Mineralogy Petrology, and Geochemistry (Grew E. & Anovitz L.M., Eds.), *Reviews in Mineralogy*, **33**, Mineralogical Society of America, Washington DC, 503-557.

Henry, D.J. & Dutrow, B.L. (2011) The incorporation of fluorine in tourmaline: internal crystallographic controls or external environmental influence? *Canadian Mineralogist*, **49**, 41-56.

Henry, D.J. & Guidotti, C.V. (1985) Tourmaline as a petrogenetic indicator mineral: an example from the staurolite-grade metapelites of NW Maine. *American Mineralogist*, **70**, 1-15.

Henry, D.J., Novak, M., Hawthorne, F.C., Ertl, A., Dutrow, B., Uher, P. & Pezzotta, F. (2011) Nomenclature of the tourmaline-supergroup minerals. *American Mineralogist*, **96**, 895-913.

Hughes, J.M., Ertl, A., Dyar, M.D., Grew, E.S., Shearer, C.K., Yates, M.G. & Guidotti, C.V. (2000) Tetrahedrally coordinated boron in a tourmaline: boron-rich olenite from Stoffhütte, Koralpe, Austria. *Canadian Mineralogist*, **38**, 861-868.

Hughes, K.-A., Hughes, J.M. & Dyar, M.D. (2001) Chemical and structural evidence for $^{[4]}B \leftrightarrow {}^{[4]}Si$ substitution in natural tourmalines. *European Journal of Mineralogy,* **13**, 743-747.

Hughes, J.M., Ertl, A., Dyar, M.D., Grew, E.S., Wiedenbeck, M. & Brandstätter F. (2004) Structural and chemical response to varying $^{[4]}B$ content in zoned Fe-bearing olenite from Koralpe, Austria. *American Mineralogist*, **89**, 447-454.

Hughes, J.M., Rakovan, J., Ertl, E., Rossman, G.P., Baksheev, I., & Bernhardt (2011) Dissymmetrization in tourmaline: the atomic arrangement of sectorally zoned triclinic Ni-bearing dravite. *Canadian Mineralogist*, **49**, 29-40.

Jolliff, B.L., Papike, J.J. & Shearer, C.K. (1986) Tourmaline as a recorder of pegmatite evolution: Bob Ingersoll pegmatite, Black Hills, South Dakota. *American Mineralogist*, **71**, 472-500.

Kalt, A., Schreyer, W., Ludwig, T., Prowatke, S., Berhardt, H.-J.& Ertl, A. (2001) Complete solid solution between magnesian schorl and lithian excess-boron olenite in a pegmatite from the Koralpe (eastern Alps, Austria). *European Journal of Mineralogy*, **13**, 1191-1205.

Keith, H.D. & Padden, F.J. (1963) A phenomenological theory of spherulitic crystallization, *Journal of Applied Physics*, **34**, 2409 – 2421

Keith, H. D. & Padden, F. J. (1964a) Spherulitic crystallization from the melt. I. Fractionation and impurity segregation and their Influence on Crystalline Morphology, *Journal of Applied Physics*, **35**, 1270-1285.

Keith, H. D. & Padden, F. J. (1964b) Spherulitic crystallization from the melt II. Influence of Fractionation and Impurity Segregation on the Kinetics of Crystallization, *Journal of Applied Physics*, **35**, 1286 - 1296

Keller, P.C. (1983) The rubies of Burma: A review of the Mogok stone tract. *Gems & Gemology*, **6**, 209-219.

Kirkpatrick, R.J. (1988) MAS NMR spectroscopy of minerals and glasses. *Reviews in Mineralogy*, **18**, 341-403.

Kirkpatrick, R.J., Smith, K.A., Schramm, S., Turner, G. & Yang, W.-H. (1985) Solid-state nuclear magnetic resonance spectroscopy of minerals. *Annual Reviews in Earth and Planetary Sciences.* **13**, 29-47.

Kirkpatrick, R.J., Oestrike, R., Weiss, C.A.Jr., Smith, K.A. & Oldfield, E. (1986) High-resolution ^{27}Al and ^{29}Si NMR spectroscopy of glasses and crystals along the join $CaMgSi_2O_6$-$CaAl_2SiO_6$. *American Mineralogist*, **71**, 705-711.

Klein, C. and Dutrow B. (2008) *Manual of Mineral Sciences (23rd Ed.)* John Wiley & Sons. New York. pp. 641.

Klinowski, J., Carr, S., W., Tarling, S., E., & Barnes, P. (1987) Magic-angle-spinning NMR shows the aluminosilicate framework of ultramarine to be disordered. *Nature*, **330(5)**, 56-58.

Kroeker, S. & Stebbins, J.F. (2001) Three-Coordinated Boron-11 Chemical Shifts in Borates. *Inorganic Chemistry*, **40**, 6239-6246.

Kroeker, S., Neuhoff, P.S. & Stebbins, J.F. (2001) Enhanced resolution and quantitation from 'ultrahigh' field NMR spectroscopy of glasses. *Journal of Non-Crystalline Solids*, 293-295, 440-445.

Lacroix, A. (1922) *Minéralogie de Madagascar, I.* Libraire Maritime et Coloniale, Paris.Lager, J.S. (1980) Instabilities and pattern formation in crystal growth. *Reviews in Modern Physics*, **52**, 1-28.

Lasaga, A.C. (1982) Toward a master equation in crystal growth. *American Journal of Science*, **282**, 1264-1288.

Lavina, B., Salviulo, G. & Della Giusta, A. (2002) Cation distribution and structure modelling of spinel solid solutions. *Physics and Chemistry of Minerals*, **29**, 10-18.

Laurs, B.M., Zwaan, J.C., Breeding, C.M., Simmon, W.B., Beaton, D., Rijsdijk, K.F., Befi, R. & Falster, A.U. (2008) Copper-bearing (Paraíba-type) Tourmaline from Mozambique. *Gems & Gemology*, **44**, 4-30.

L'Heureux, I. (1993) Oscillatory zoning in crystal growth: a constitutional undercooling mechanism. *Physical Review E*, **48**, 4460-4469.

L'Heureux, I. & Fowler, A.D. (1994) A nonlinear dynamical model of oscillatory zoning in plagioclase. *American Mineralogist*, **79**, 885-891.

L'Heureux, I. & Fowler, A.D. (1996) Isothermal constitutive undercooling as a model for oscillatory zoning in plagioclase. *Canadian Mineralogist*, **34**, 1137-1147.

London, D. (1984) Experimental phase equilibria in the system LiAlSiO4-SiO2-H2O: a petrogenetic grid for lithium-rich pegmatites. American Mineralogist, **69**, 995-1004.

London, D. (1986) Formation of tourmaline-rich gem pockets in miarolitic pegmatites. *American Mineralogist*, **71**, 396-405.

London D. (1992) The application of experimental petrology to the genesis and crystallization of granitic pegmatites. *Canadian Mineralogist*, **30**, 499-540.

London, D. (1999) Stability of tourmaline in peraluminous granite systems: the boron cycle from anatexis to hydrothermal aureoles. *European Journal of Mineralogy*, **11**, 253-262.

London, D. (2011) Experimental synthesis and stability of tourmaline: a historical overview. *Canadian Mineralogist*, **49**, 117-136.

London, D. & Manning, D.A.C. (1995) Chemical variation and significance of tourmaline from Southwest England. *Economic Geology*, **90**, 495-519.

London, D., Ertl, A., Hughes, J.M., Morgan, G.B., VI, Fritz, E.A. & Harms, B.S. (2006) Synthetic Ag-rich tourmaline: structure and chemistry, *American Mineralogist*, **91**, 680-684.

Lussier, A.J, & Hawthorne, F.C. (2011) Oscillatory zoned elbaite-liddicoatite from central Madagascar II: compositional variation and mechanisms of substitution. *Canadian Mineralogist*, **49**, 89-104.

Lussier, A.J., Aguiar, P.M., Michaelis, V.K., Kroeker, S., Herwig, S., Abdu, Y. & Hawthorne, F.C. (2008a) Mushroom elbaite from the Kat Chay mine, Momeik, near Mogok, Myanmar: I. crystal chemistry by SREF, EMPA, MAS NMR and Mössbauer spectroscopy. *Mineraogical Magazine,* **72**, 747-761.

Lussier, A.J., Hawthorne, F.C., Herwig, S., Abdu, Y., Aguiar, P.M., Michaelis, V.K. & Kroeker, S. (2008b) Mushroom elbaite from the Kat Chay mine, Momeik, near Mogok, Myanmar: II. zoning and crystal growth. *Mineralogical Magazine,* **72**, 999-1010.

Lussier, A.J., Aguiar, P.M., Michaelis, V.K., Kroeker, S. & Hawthorne, F.C. (2009) The occurrence of tetrahedrally coordinated Al and B in tourmaline; an ^{11}B and ^{27}Al MAS NMR study. *American Mineralogist*, **94**, 785-792.

Lussier, A.J, Abdu, Y., Hawthorne, F.C., Michaelis, V., Aguiar, P.M. & Kroeker, S. (2011a) Oscillatory zoned elbaite-liddicoatite from central Madagascar I: crystal chemistry and structure by SREF and ^{11}B and ^{27}Al MAS NMR spectroscopy. *Canadian. Mineralogist,* **49**, 63-88.

Lussier, A.J., Hawthorne, F.C., Abdu, Y., Herwig, S., Michaelis, V.K., Aguiar, P.M. & Kroeker, S. (2011b) The crystal chemistry of `wheatsheaf' tourmaline from Mogok, Myanmar. *Mineralogical Magazine*, **72**, 999-1010.

Lussier, A.J., Hawthorne, F.C., Michaelis, V.K., Aguiar, P.M. & Kroeker, S. (2011c) Elbaite-liddicoatite from Black Rapids glacier, Alaska. *Periodico di Mineralogia*, **80**, 57-73.

Lyckberg, P. (1997). Giant tourmaline crystals in granitic pegmatites. Paper presented at the *International symposium on Tourmaline. Abs. Vol.*, 120.

Macdonald, D.J. & Hawthorne, F.C. (1995a) The crystal chemistry of Si-Al substitution in tourmaline. *Canadian Mineralogist,* **33**, 849-858.

Macdonald, D.J. & Hawthorne, F.C. (1995b) Cu-Bearing Tourmaline from Paraiba, Brazil, *Acta Crystallographica*, **C51**, 555-557.

Macdonald, D.J., Hawthorne, F.C. & Grice, J.D. (1993) Foitite, $\square[Fe^{2+}_2(Al,Fe^{3+})]Al_6Si_6O_{18}(BO3)_3(OH)_4$, a new alkali deficient tourmaline: description and crystal structure. *American Mineralogist*, **78**, 1299-1303.

Madelung, A. (1883) *Beobachtungen mit Brethaupt's Polarisationmikroskop, Zeitschrift für Kristallographie,* **7**, 73-76.

Magill, J.H. (2000) Spherulites: a personal perspective. *Journal of Material Science*, *36*, 3143-3164.

Malisa, E. & Muhongo, S. (1990) Tectonic setting of gemstone mineralization in the Proterozoic metamorphic terrane of the Mozambique Belt in Tanzania. *Precambrian Research,* **46**, 167-176.

Marler, B. & Ertl, A. (2002) Nuclear magnetic resonance and infrared spectroscopic study of excess-boron olenite from Koralpe, Styria, Austria. *American Mineralogist*, **87**, 364-367.

Marler, B., Borowski, M., Wodara, U. & Schreyer, W. (2002) Synthetic tourmaline (olenite) with excess boron replacing silicon in the tetrahedral site: II. Structure analysis. *European Journal of Mineralogy*, **14**, 763-771.

Martin, R.F. & De Vito, C. (2005) The patterns of enrichment in felsic pegmatites ultmately depend on tectonic setting. *Canadian Mineralogist*, **43**, 2027-2048.

Massiot, D., Bessada, C., Coutures, J. P. & Taulelle, F. (1990) A quantitative study of ^{27}Al MAS NMR in crystalline YAG. *Journal of Magnetic Resonance*, **90**, 231-242.

Mattson, S.M. & Rossman, G.R. (1984) Ferric iron in tourmaline. *Physics and Chemistry of Minerals*, **11**, 225-234.

Mattson, S.M. & Rossman, G.R. (1987) Fe^{2+}-Fe^{3+} interactions in tourmaline. *Physics and Chemistry of Minerals*, **14**, 163-171.

Mills, S.J., Hatert, F., Nickel, E.H. & Ferraris, G. (2009) The standardization of mineral group hierarchies: application to recent nomenclature proposals. *European Journal of Mineralogy*, 21, 1073–1080.

Mullins, W.W. & Sekerka, R.F. (1964) Stability of planar interface during solidification of dilute binary alloy. *Journal of Applied Physics*, **35**, 444-451.

Mullins, W.W. & Sekerka, R.F. (1963) Morphological stability of a particle growing by diffusion or heat flow. *Journal of Applied Physics*, **34**, 323-329.

Neiva, A.M.R., Manuela, M., Silva, V.G. & Gomes, M.E. (2007) Crystal chemistry of tourmaline from Variscan granites, associated tin-tungsten- and gold deposits, and associated metamorphic and metasomatic rocks from northern Portugal. *Neues Jahrbuch für Mineralogie Abhandlungen*, **184**, 45-76.

Novák, M. & Povondra, P. (1995) Elbaite pegmatites in the Moldanubicum: a new subtype of the rare-element class. *Mineralogy and Petrology*, **55**, 159-176.

Novák, M., Selway, J., Černý, P., Hawthorne, F.C. & Ottolini, L. (1999) Tourmaline of the elbaite-dravite series from an elbaite-subtype pegmatite at Bliñná, southern Bohemia, Czech Republic. *European Journal of Mineralogy,* **11**, 557-568.

Nuber, V.B. & Schmetzer, K. (1981) Structurverfeinerung von liddicoatite, *Neues Jahrbuch für Mineralogie* Monatshefte, **1981**, 215-219.

Ottolini, R. & Hawthorne, F.C. (1999) An investigation of SIMS matrix effects on H, Li and B ionization in tourmaline. *European Journal of Mineralogy*, **11**, 679-690.

Ottolini, L., Camara, F., Hawthorne, F.C. & Stirling, J. (2002) SIMS matrix effects in the analysis of light element in silicate minerals: comparison with SREF and EMPA data. *American Mineralogist*, **87**, 1477-1485.

Paquette, J. & Reeder, R.J. (1995) Relationship between surface structure, growth mechanism, and trace element incorporation in calcite. *Geochimica et Cosmochimica Acta*, 59, 735-749.

Paquette, J.L. & Nédélec, A. (1998) A new insight into Pan-African tectonics in the East–West Gondwana collision zone by U–Pb zircon dating of granites from central Madagascar. *Earth and Planetary Science Lett*ers, **155**, 45-56.

Pertlik, F., Ertl, A., Körner, W., Brandstätter, F. & Schuster, R. (2003) Na-rich dravite in the marbles from Friesach, Carinthia, Austria: chemistry and crystal structure. *Neues Jahrbuch für Mineralogie. Monatshefte*, **2003**, 277-288.

Pezzotta, F. (1996) Preliminary data on the physical-chemical evolution of the gem-bearing Anjanabonoina Pegmatite, Central Madagascar (Abstr.). Programs with Abstracts, Geological Association of Canada-Mineralogical Association of Canada, Winnipeg, Manitoba, May 27-29, p. A-75.

Pezzotta, F. (2005) First attempt to the petrogenesis and the classification of granitic pegmatites of the Itremo Region (central Madagascar). Crystallization processes in granitic pegmatites. *International Meeting (Elba) Abst. Vol.*

Pouchou, J.L. & Pichoir, F. (1985) 'PAP' φ(ρZ) procedure for improved quantitative microanalysis. Pp. 104-106 in: *Microbeam Analysis* (J.T.Armstrong, editor). San Francisco Press, San Francisco, California, USA.

Povondra, P. (1981) The crystal chemistry of tourmalines of the schorl-dravite series. *Acta Universitatis Carolinae Geologica*, **3**, 223-264.

Povondra, P. & Novák, M. (1986) Tourmalines in metamorphosed carbonate rocks from western Moravia, Czechoslovakia. *Neues Jahrbuch für Mineralogie - Monatshefte*, **1986,** 273-282.

Prowatke, S., Ertl, A., and Hughes, J.M. (2003) Tetrahedrally-coordinated Al in Mn-rich, Li- and Fe-bearing olenite from Eibenstein an der Thaya, Lower Austria: a chemical and structural investigation. *Neues Jahrbuch für Mineralogie - Monatshefte*, **2003**, 385-395.

Ribbe, P.H. & Gibbs, G.V. (1971) Crystal structures of the humite minerals: III. Mg/Fe ordering in humites and its relation to other ferromagnesian silicates. *American Mineralogist*, **56**, 1155-1173.

Robert, J.-L., Gourdant, J.-P., Linnen, R.L., Rouer, O. & Benoist, P. (1997): Crystal-chemical relationships between OH, F and Na in tourmaline. *Tourmaline 1997, International. Symposium. on Tourmaline* (*Nové Město na Moravě*), *Abstract Volum*, 84-85.

Robinson, K., Gibbs, G.V. & Ribbe, P.H. (1971) Quadratic elongation: a quantitative measure of distortion in coordination polyhera. *Science*, **172**, 567-570.

Rossman, G.R. & Mattson, S.M. (1986) Yellow, Mn-rich elbaite with Mn-Ti intervalence charge transfer. *American Mineralogist*, **71**, 599-602.

Rozhdestvenskaya, I., Frank-Kamenetskaya, O., Zolotarev, A., Bronzova, Yu. & Bannova, I. (2005) Refinement of the crystal structures of three fluorine-bearing elbaites. *Crystallography Reports*, **50**, 907-913.

Rozhdestvenskaya, I., Frank-Kamenetskaya, O., Kuznetsova, L., Bannova, I., Bronzova, Yu. (2007) Refinement of the crystal structure of lithium-bearing uvite, *Crystallography Reports*, **52**, 203-207.

Rozhdestvenskaya, I., Bronzova, Yu., Frank-Kamenetskaya, O.,Zolotarev, A.,Kuznetsova, L. & Bannova, I. (2008) Refinement of the crystal structure of calcium-lithium-aluminum tourmaline from the pegmatite vein in the Sangilen Upland (Tuva Republic), *Crystallography Reports*, **53**, 223-227.

Rowley, E.B. (1942) Huge tourmaline crystals discovered. *The Mineralogist*, **10**, 47-48.

Rustemeyer, P. (2003) *Faszination Turmalin. Formen, Farben, Strukture*. Spektrum Akademischer Verlag, Heidelberg, Germany.

Schreyer, W., Hughes, J.M., Bernhardt, H.-J., Kalt, A., Prowatke, S. & Ertl, A. (2002a) Reexamination of olenite from the type locality: detection of boron in tetrahedral coordination. *European Journal of Mineralogy*, **14**, 935-942.

Schreyer, W., Wodara, U., Marler, B., Van Aken, P.A., Seifert, F. & Robert, J.-L. (2002b) Synthetic tourmaline (olenite) with excess boron replacing silicon in the tetrahedral site: I. synthesis conditions, chemical and spectroscopic evidence. *European Journal of Mineralogy*, **12**, 529-541.

Selway, J., Černý, P. & Hawthorne, F.C. (1998) Feruvite from lepidolite pegmatites at Red Cross Lake, Manitoba. *Canadian Mineralogist,* **36**, 433-439.

Selway, J.B., Novák, M. Černý, P. & Hawthorne, F.C. (1999) Compositional evolution of tourmaline in lepidolite-subtype pegmatites. *European Journal of Mineralogy,* **11**, 569-584.

Selway, J.B., Novák, M., Černý, P. & Hawthorne, F.C. (2000a) The Tanco pegmatite at Bernic Lake, Manitoba. XIII. Exocontact tourmaline. *Canadian Mineralogist,* **38**, 869-976.

Selway, J.B., Černý, P., Hawthorne, F.C. & Novák, M. (2000b) The Tanco pegmatite at Bernic Lake, Manitoba. XIV. Internal tourmaline. *Canadian Mineralogist,* **38**, 877-891.

Selway, J.B., Smeds, S-A., Černý, P. & Hawthorne, F.C. (2002) Compositional evolution of tourmaline in the petalite-subtype Nyköpingsgruvan pegmatites, Utö, Stockholm Archipelago, Sweden. *GFF*, **124**, 93-102.

Shannon, R.D. (1976) Revised effective ionic radii and systematic studies of interatomic distances in halides and chalcogenides. *Acta Crystallographica*, **A32**, 751-767.

Sheldrick, G.M. (1998) *SADABS* User Guide, University of Göttingen, Germany.

Shtukenberg, A., Rozhdestvenskaya, I., Frank-Kamenetskaya, O., Bronzova, J., Euler, H., Kirfel, A., Bannova, I. & Zolotarev, A. (2007) Symmetry and crystal structure of biaxial elbaite-liddicoatite tourmaline from the Transbaikalia region, Russia. *American Mineralogist*, **92**, 675-686.

Sibley, D.F., Vogel, T.A., Walker, B.M. & Byerly, G. (1976) The origin of oscillatory zoning in plagioclase: a diffusion and growth controlled model. *American Journal of Science*, **276**, 275-284.

Skibsted, J., Nielsen, N.C., Bildsøe, H. & Jakobsen, H.J. (1991) Satellite transitions in MAS NMR spectra of quadrupolar nuclei. *Journal of Magnetic Resonance*, **95**, 88–117.

Smith, G. (1978a) A reassessment of the role of iron in the 5000 – 30,000 cm^{-1} range of the electronic absorption spectra of tourmaline. *Physics and Chemistry of Minerals*, **3**, 343-373.

Smith, G. (1978b) Evidence for absorption by exchange-coupled Fe^{2+}-Fe^{3+} pairs in the near infrared spectra of minerals. *Physics and Chemistry of Minerals*, **3**, 375-383.

Smith, G. & Strens, R.G. (1976) Intervalence transfer absorption in some silicate, oxides, and phosphate minerals. Pp. 583-612 in: *The Physics and Chemistry of Minerals and Rocks* (R.G.J. Strens, editor). Wiley, New York.

Tagg, S.L., Cho, H., Dyar, M.D. & Grew, E.S. (1999) Tetrahedral boron in naturally occurring tourmaline. *American Mineralogist,* **84**, 1451-1455.

Taran, M.N., Lebedev, A.S. & Platonov, A.N. (1993) Optical absorption spectroscopy of synthetic tourmalines. *Physics and Chemistry of Minerals*, **20**, 209-220.

Taylor, M.C., Cooper, M.A. & Hawthorne, F.C. (1995) Local charge-compensation in hydroxy-deficient uvite. *Canadian Mineralogist*, **33**, 1215-1221.

Teertstra, D.K., Cerny, P. & Ottolini, L. (1999) Stranger in paradise; liddicoatite from the High Grade Dike pegmatite, southeastern Manitoba, Canada. *European Journal of Mineralogy*, **11**, 227-235.

Themelis, T. (2007) *Gems and Mines of Mogok: The Forbidden Land.* A & T Press, Bangkok, Thailand.

Tindle A.G., Breaks F.W. & Selway J.B. (2002) Tourmaline in petalite-subtype granitic pegmatites: evidence of fractionation and contamination from the Pakeagama Lake and Separation Lake areas of Northwestern Ontario, Canada. *Canadian Mineralogist*, **40**, 753-788.

Tindle A.G., Selway J.B. & Breaks F. (2005) Liddicoatite and associated species from the McCombe spodumene-subtype rare-element granitic pegmatite, northwestern Ontario, Canada. *Canadian Mineralogist*, **43**, 769-793.

Tippe, A., & Hamilton, W.C. (1971) A neutron-diffraction study of the ferric tourmaline, buergerite, *American Mineralogist*, **56**, 101-113

Tsune, A. & Toramaru, A. (2007) A simple model of oscillatory zoning in magmatic plagioclase: development of an isothermal undercooling model. *American Mineralogist*, **92**, 1071-1079.

Turner, G.L., Smith, K.A., Kirkpatrick, R.J. & Oldfield, E. (1986) Boron-11 nuclear magnetic resonance spectroscopic study of borate and borosilicate minerals and a borosilicate glass. *Journal of Magnetic Resonance*, **67**, 544-550.

van Hinsberg, ,VJ, & Schumacher, J. C. (2007a) Using estimated thermodynamic properties to model accessory phases: The case of tourmaline. *Journal of Metamorphic Geology,* **25**, 769-779.

van Hinsberg, V.,J., & Schumacher, J. C. (2007b). Intersector element partitioning in tourmaline; a potentially powerful single-crystal thermometer. *Contributions to Mineralogy and Petrology,* **153**, 289-301.

van Hinsberg, V.,J., Henry, D. J. & Marschall, H. R. (2011) Tourmaline; an ideal indicator of its host environment. *The Canadian Mineralogist,* **49**, 1-16.

van Hinsberg, V.,J., Schumacher, J. C., Kearns, S., Mason, P. R. D. & Franz, G. (2006) Hourglass sector zoning in metamorphic tourmaline and resultant major and trace-element fractionation. *American Mineralogist,* **91**, 717-728.

von Goerne, V., Franz, G. & Wirth, R. (1999) Hydrothermal synthesis of large dravite crystals by the chamber method. *European Journal of Mineralogy*, *11*, 1061-1077.

Weidner J.R. & Martin R.F. (1987) Phase equilibria of a fluorine-rich leucogranite from the St. Austell pluton, Cornwall. *Geochimica et Cosmochimica Acta*, **51**, 1591-1597.

Weigel, C., Calas, G., Cormier, L., Galoisy, L. & Henderson G. (2008) High-resolution Al L2,3-edge x-ray absorption near edge structure spectra of Al-containing crystals and glasses: coordination number and bonding information from edge components. *Journal of Physics – Condensed Matter*, **20**, 1-8.

Yavuz, F., Çelik, M. & Karakaya, N. (1999) Fibrous foitite from Şebínkarahísar, Gíresun Pb-Zn-Cu-(U) mineralized area, Northern Turkey. *Canadian Mineralogist*, **37**, 155-161.

Zaw, K. (1998) Geological evolution of selected granitic pegmatites in Myanmar (Burma) constraints from regional setting, lithology, and fluid-inclusion studies. *International Geology Review*, **40**, 647-662

APPENDIX A.1

MISCELLANEOUS DATA COLLECTION
&
STRUCTURE REFINEMENT INFORMATION

APPENDIX A.1. MISCELLANEOUS DATA COLLECTION AND STRUCTURE REFINEMENT INFORMATION

	L1	L2	L4	L5
a (Å)	15.8636(16)	15.8529(13)	15.8548(14)	15.8456(12)
c (Å)	7.1119(9)	7.1101(8)	7.1099(8)	7.1066(7)
V (Å^3)	1551.2(4)	1547.4(3)	1547.9(3)	1545.2(3)
Space group	*R*3*m*	*R*3*m*	*R*3*m*	*R*3*m*
Colour	Dark Pink	Pink	Pink	Pink
Location on	Pyramidal	Pyramidal	Pyramidal	Pyramidal
Sample	Zone	Zone	Zone	Zone
Crystal Size[a]	sphere	sphere	sphere	sphere
Rad/Mon	MoKα/Gr	MoKα/Gr	MoKα/Gr	MoKα/Gr
Unique	1111	1111	1111	1111
Z	3	3	3	3
No. Refs. > 10 σI	---	---	---	---
$\lvert F_o \rvert > 4\sigma$	1087	1092	1087	1088
$R_1^{\text{Dis.}}$ (%)[b]	1.77	1.66	1.8	1.7
$wR_2^{\text{Dis.}}$ (%)[b]	4.43	4.32	4.45	4.27
GOOF[d]	1.072	1.072	1.052	1.085
EXTI[e]	0.0042(3)	0.0025(2)	0.0028(2)	0.0037(3)
$R_1^{\text{Ord.}}$ (%)	1.90	1.85	1.94	1.73
$wR_2^{\text{Ord.}}$ (%)	4.75	4.71	4.66	4.29

a, All crystals of Madagascar Liddicoatite (L1-L28) were ~150–200 ìm ground spheres.

b, $R_1 = \sum \left| |F_O| - |F_C| \right| / \sum |F_O|$

c, $wR_2 = \left\{ \sum \left[w\left(F_O^2 - F_C^2\right)^2 \right] / \sum \left[w\left(F_O^2\right)^2 \right] \right\}^{1/2}$

d, $GooF = \left\{ \sum \left[w\left(F_O^2 - F_C^2\right)^2 \right] / (n - p) \right\}^{1/2}$

e, $k\left[1 + 0.001 x F_C^2 \lambda^3 / \sin(2\theta s)\right]^{-1/4}$, where x is the refined extinction parameter.

APPENDIX A.1. (CON'T)

	L6	L7	L11	L12
a (Å)	15.8418(17)	15.8363(15)	15.8675(13)	15.853(7)
c (Å)	7.1044(10)	7.1040(9)	7.1135(8)	7.120(4)
V (Å^3)	1544.0(4)	1543.0(3)	1551.1(3)	1549(1)
Space group	*R*3*m*	*R*3*m*	*R*3*m*	*R*3*m*
Colour	Pink	Pink	Pink	Pink
Location on Sample	Pyramidal Zone	Pyramidal Zone	Pyramidal Zone	Pyramidal Zone
Crystal Size[a]	sphere	sphere	sphere	sphere
Rad/Mon	MoKα/Gr	MoKα/Gr	MoKα/Gr	MoKα/Gr
Unique	1111	1111	1111	1111
Z	3	3	3	3
No. Refs. > 10 σI	---	---	---	---
$\|F_o\| > 4\sigma$	1090	1096	1102	1095
$R_1^{Dis.}$ (%)[b]	1.71	1.64	1.73	1.73
$wR_2^{Dis.}$ (%)[b]	4.29	4.11	4.41	4.27
GOOF[d]	1.083	1.103	1.073	1.065
EXTI[e]	0.0026(2)	0.0037(3)	0.0020(2)	0.0046(3)
$R_1^{Ord.}$ (%)	1.80	1.75	1.94	1.92
$wR_2^{Ord.}$ (%)	4.43	4.30	4.80	4.77

	L13	L15	L16	L17
a (Å)	15.8449(15)	15.8248(16)	15.8307(10)	15.8337(12)
c (Å)	7.1053(9)	7.0993(9)	7.1013(6)	7.1023(7)
V (Å^3)	1544.9(3)	1539.6(4)	1541.3(2)	1541.9(3)
Space group	*R*3*m*	*R*3*m*	*R*3*m*	*R*3*m*
Colour	Green	Green	Green	Green
Location on Sample	Pyramidal Zone	Pyramidal Zone	Pyramidal Zone	Pyramidal Zone
Crystal Size[a]	sphere	sphere	sphere	sphere
Rad/Mon	MoKα/Gr	MoKα/Gr	MoKα/Gr	MoKα/Gr
Unique	1111	1109	1109	1109
Z	3	3	3	3
No. Refs. > 10 σI	---	---	---	---
$\|F_o\| > 4\sigma$	1099	1097	1099	1088
$R_1^{Dis.}$ (%)[b]	1.96	2.23	1.44	1.62
$wR_2^{Dis.}$ (%)[b]	4.84	5.89	3.75	4.03
GOOF[d]	1.099	1.108	1.117	1.071
EXTI[e]	0.0026(2)	0.0039(4)	0.0052(3)	0.0034(2)
$R_1^{Ord.}$ (%)	2.05	2.32	1.51 / 3.78	1.67
$wR_2^{Ord.}$ (%)	5.03	6.11	3.78	4.00

APPENDIX A.1. (CON'T)

	L18	L19	L20	L21
a (Å)	15.8293(11)	15.8343(11)	15.8303(11)	15.8399(11)
c (Å)	7.1003(6)	7.1012(7)	7.1017(6)	7.1030(6)
V (Å^3)	1540.7(3)	1541.8(3)	1541.2(3)	1543.5(5)
Space group	*R*3*m*	*R*3*m*	*R*3*m*	*R*3*m*
Colour	Green	Green	Green	Dark green
Location on Sample	Pyramidal Zone	Pyramidal Zone	Pyramidal Zone	Pyramidal Zone
Crystal Size[a]	sphere	sphere	sphere	sphere
Rad/Mon	MoKα/Gr	MoKα/Gr	MoKα/Gr	MoKα/Gr
Unique	1109	1109	1109	1111
Z	3	3	3	3
No. Refs. > 10 *σI*	---	---	---	---
$\|F_o\| > 4\sigma$	1094	1094	1091	1104
$R_1^{Dis.}$ (%)[b]	1.61	1.69	1.7	1.68
$wR_2^{Dis.}$ (%)[b]	4.09	4.29	4.1	6.03
GOOF[d]	1.111	1.103	1.104	1.574
EXTI[e]	0.0034(3)	0.0061(3)	0.0034(2)	0.0036(3)
$R_1^{Ord.}$ (%)	1.72	1.77	1.80	1.87
$wR_2^{Ord.}$ (%)	4.31	4.46	4.28	5.05

	L22	L23	L24	L25
a (Å)	15.8306(16)	15.8299(13)	15.8286(14)	15.8438(14)
c (Å)	7.0999(9)	7.1009(7)	7.1012(8)	7.1043(8)
V (Å^3)	1540.9(4)	1540.9(3)	1540.9(3)	1544.4(3)
Space group	*R*3*m*	*R*3*m*	*R*3*m*	*R*3*m*
Colour	Green	Green	Green	Dark green
Location on Sample	Pyramidal Zone	Pyramidal Zone	Pyramidal Zone	Pyramidal Zone
Crystal Size[a]	sphere	sphere	sphere	sphere
Rad/Mon	MoKα/Gr	MoKα/Gr	MoKα/Gr	MoKα/Gr
Unique	1109	1109	1109	1111
Z	3	3	3	3
No. Refs. > 10 *σI*	---	---	---	---
$\|F_o\| > 4\sigma$	1087	1098	1089	1096
$R_1^{Dis.}$ (%)[b]	2.95	1.51	1.58	1.83
$wR_2^{Dis.}$ (%)[b]	7.16	3.96	4.05	4.88
GOOF[d]	1.07	1.125	1.079	1.096
EXTI[e]	0.0047(6)	0.0061(3)	0.0400(3)	0.0015(3)
$R_1^{Ord.}$ (%)	2.95	1.64	1.68	1.98
$wR_2^{Ord.}$ (%)	7.32	4.27	4.18	5.17

APPENDIX A.1. (CON'T)

	L26	L27	L28	SHW1
a (Å)	15.8368(11)	15.8333(14)	15.8404(13)	15.7791(16)
c (Å)	7.1014(6)	7.1025(8)	7.1039(7)	7.0928(12)
V (Å^3)	1542.4(2)	1541.8(3)	1543.6(3)	1529.37
Space group	*R*3*m*	*R*3*m*	*R*3*m*	*R3m*
Colour	Dark green	Dark green	Dark Green	purple-brown
Location on Sample	Pyramidal Zone	Pyramidal Zone	Pyramidal Zone	near surface, dark tip
Crystal Size[a]	sphere	sphere	sphere	sphere
Rad/Mon	Mo*K*α/Gr	Mo*K*α/Gr	Mo*K*α/Gr	Mo*K*α/Gr
Unique	1109	1109	1111	1107
Z	3	3	3	3
No. Refs. > 10 σI	---	---	---	---
$\|F_o\| > 4\sigma$	1078	1086	1092	1098
$R_1^{Dis.}$ (%)[b]	1.81	1.71	1.54	1.69
$wR_2^{Dis.}$ (%)[b]	4.62	4.37	3.93	4.34
GOOF[d]	1.046	1.081	1.092	1.073
EXTI[e]	0.0013(2)	0.0007(2)	0.0054(3)	0.0012(2)
$R_1^{Ord.}$ (%)	1.88	1.83	1.69	1.70
$wR_2^{Ord.}$ (%)	4.60	4.56	4.24	4.40

	SHW2	SHW3	SHW4	SHW5
a (Å)	15.7841(17)	15.8779(4)	15.8673(7)	15.8126(4)
c (Å)	7.0859(13)	7.1223(2)	7.1172(2)	7.1010(2)
V (Å^3)	1528.85	1555.0(1)	1551.84(15)	1537.6(1)
Space group	*R3m*	*R3m*	*R3m*	*R3m*
Colour	light pink	green	dark green	red-purple
Location on Sample	near surface, light base	green cap, end	green cap, end	near surface, light base
Crystal Size	0.2 mm	0.15 mm	0.1 mm	0.1 mm
Rad/Mon	Mo*K*α/Gr	Mo*K*α/Gr	Mo*K*α/Gr	Mo*K*α/Gr
Unique	974	1111	1090	1103
Z	3	3	3	3
No. Refs. > 10 σI	---	6612	6988	7146
$\|F_o\| > 4\sigma$	970	1109	1090	1102
$R_1^{Dis.}$ (%)[b]	1.73	3.18	2.22	1.75
$wR_2^{Dis.}$ (%)[b]	4.38	7.26	5.36	4.48
GOOF[d]	1.136	1.251	1.218	1.146
EXTI[e]	0.0010(2)	---	----	---
$R_1^{Ord.}$ (%)	1.72	3.26	2.39	1.75
$wR_2^{Ord.}$ (%)	4.37	7.51	5.83	4.48

APPENDIX A.1. (CON'T)

	SHW6	SHW7	SHW8	SHM1
a (Å)	15.7982(4)	15.8160(5)	15.7949(4)	15.799(1)
c (Å)	7.0904(2)	7.0953(2)	7.0902(2)	7.094(1)
V (Å^3)	1532.6(1)	1537.1(1)	1531.88(12)	1533.49
Space group	*R3m*	*R3m*	*R3m*	*R3m*
Colour	colourless	light pink /	light pink /	pink
Location on Sample	white interior,	red core, base	red core, middle	surface, top
Crystal Size	0.12 mm	0.08 mm	0.1 mm	0.2 mm
Rad/Mon	Mo*K*α/Gr	Mo*K*α/Gr	Mo*K*α/Gr	MoKa/Gr
Unique	1097	1102	1095	1107
Z	3	3	3	3
No. Refs. > 10 σ*I*	7056	5559	7143	---
$\|F_o\| > 4\sigma$				1056
$R_1^{Dis.}$ (%)[b]	1.94	3.26	2.55	2.09
$wR_2^{Dis.}$ (%)[b]	4.63	7.1	5.89	4.98
GOOF[d]	1.139	1.258	1.21	1.058
EXTI[e]	---	---	---	0.0009(2)
$R_1^{Ord.}$ (%)	1.86	3.26	2.55	2.08
$wR_2^{Ord.}$ (%)	4.63	7.10	5.89	4.97

	SHM2	SHM3	SHM3a	SHM3e
a (Å)	15.774(1)	15.818(1)	15.9005(5)	15.8034(4)
c (Å)	7.079(1)	7.094(1)	7.1241(2)	7.0880(2)
V (Å^3)	1525.41	1537.18	1559.84	1533.3(1)
Space group	*R3m*	*R3m*	*R3m*	*R3m*
Colour	colourless	black	black	black
Location on Sample	surface, mid.	Surface, base	interior, near base	interior, near base
Crystal Size	0.05 mm	0.2 mm	0.1 mm	0.12 mm
Rad/Mon	MoKa/Gr	MoKa/Gr	MoKa/Gr	MoKa/Gr
Unique	1097	1109	1109	1094
Z	3	3	3	3
No. Refs. > 10 σ*I*	---	---	5991	7352
$\|F_o\| > 4\sigma$	1075	1104	1108	1094
$R_1^{Dis.}$ (%)[b]	3.85	1.73	2.15	1.66
$wR_2^{Dis.}$ (%)[b]	9.73	4.6	5.06	4.29
GOOF[d]	1.089	1.178	1.148	1.151
EXTI[e]	---	0.0030(2)	---	---
$R_1^{Ord.}$ (%)	3.82	1.69	2.15	1.60
$wR_2^{Ord.}$ (%)	9.66	4.55	5.00	4.19

APPENDIX A.1. (CON'T)

	SHM5	SHP1	SHP2	SHP3
a (Å)	15.7972(4)	15.8063(16)	15.8402(16)	15.8375(18)
c (Å)	7.0883(2)	7.0923(7)	7.1015(13)	7.0996(10)
V (Å^3)	1531.9(1)	1534.5(5)	1543.1(6)	1542.2(6)
Space group	*R3m*	*R3m*	*R3m*	*R3m*
Colour	very dark	Light purple-	purple	black
Location on Sample	interior, near middle	0.2 mm equant		
Crystal Size	0.15 mm	0.2 mm	0.2 mm	0.09 mm
Rad/Mon	MoKa/Gr	MoKa/Gr	MoKa/Gr	MoKa/Gr
Unique	1096	1110	1109	1109
Z	3	3	3	3
No. Refs. > 10 σI	8048	---	---	---
$\|F_o\| > 4\sigma$	1096	1100	1092	942
$R_1^{Dis.}$ (%)[b]	1.82	1.65	3.09	3.2
$wR_2^{Dis.}$ (%)[b]	4.64	4.54	7.85	6.87
GOOF[d]	1.176	1.154	1.059	0.955
EXTI[e]	---	0.0006(2)	0.005(4)	0.0014(3)
$R_1^{Ord.}$ (%)	1.87	1.63	3.05	3.20
$wR_2^{Ord.}$ (%)	4.51	4.53	7.73	6.85

APPENDIX A.2.1

FINAL ATOM POSITIONS* AND EQUIVALENT ISOTROPIC-DISPLACEMENT PARAMETERS ($Å^2$)

APPENDIX A.2.1. FINAL ATOM POSITIONS* AND EQUIVALENT ISOTROPIC-DISPLACEMENT PARAMETERS[a] (Å^2)

		L1	L2	L4	L5	L6
X	*x*	0	0	0	0	0
	y	0	0	0	0	0
	z	0.23899(17)	0.23972(14)	0.23940(17)	0.23989(15)	0.23972(15)
	U_{eq}	0.0175(3)	0.0157(3)	0.0165(3)	0.0143(3)	0.0145(3)
Y	*x*	0.12384(7)	0.12384(8)	0.12383(8)	0.12383(9)	0.12377(9)
	y	½*x*	½*x*	½*x*	½*x*	½*x*
	z	0.63094(15)	0.63186(15)	0.63187(16)	0.63327(17)	0.63404(18)
	U_{eq}	0.0113(3)	0.0117(3)	0.0114(3)	0.0117(4)	0.0124(4)
Z	*x*	0.29717(4)	0.29700(3)	0.29703(4)	0.29691(3)	0.29686(3)
	y	0.26015(4)	0.25992(3)	0.26002(4)	0.25977(4)	0.25972(4)
	z	0.61207(10)	0.61218(9)	0.61216(10)	0.61209(9)	0.61199(9)
	U_{eq}	0.00617(11)	0.00640(10)	0.00647(11)	0.00637(11)	0.00633(11)
T	*x*	0.19213(3)	0.19215(3)	0.19210(3)	0.19215(3)	0.19212(3)
	y	0.19025(3)	0.19020(3)	0.19018(3)	0.19025(3)	0.19023(3)
	z	0	0	0	0	0
	U_{eq}	0.00496(10)	0.00507(9)	0.00515(10)	0.00511(9)	0.00500(9)
B	*x*	0.10916(10)	0.10911(9)	0.10899(10)	0.10901(10)	0.10896(10)
	y	2*x*	2*x*	2*x*	2*x*	2*x*
	z	0.4552(3)	0.4549(3)	0.4552(4)	0.4554(3)	0.4553(3)
	U_{eq}	0.0064(4)	0.0068(4)	0.0072(4)	0.0075(4)	0.0068(4)
O(*1*)[d]	*x*	0.0231(3)	0.0230(3)	0.0227(3)	0.0227(3)	0.0226(3)
	y	½*x*	½*x*	½*x*	½*x*	½*x*
	z	0.7885(5)	0.7882(5)	0.7875(5)	0.7881(5)	0.7886(5)
	U_{eq}	0.0149(11)	0.014(1)	0.0144(11)	0.0151(11)	0.0145(11)
O(*1*)[o]	*x*	0	0	0	0	0
	y	0	0	0	0	0
	z	0.78830(6)	0.7880(5)	0.7874(5)	0.7879(5)	0.7885(5)
	U_{eq}	0.0566(14)	0.0554(13)	0.0537(13)	0.0551(13)	0.0540(13)
O(2)[d]	*x*	0.0508(2)	0.0505(2)	0.0511(2)	0.0509(2)	0.0509(2)
	y	0.1206(2)	0.1201(2)	0.1203(2)	0.1204(2)	0.1203(2)
	z	0.4800(3)	0.4803(3)	0.4805(3)	0.4804(3)	0.4804(3)
	U_{eq}	0.0087(5)	0.0102(5)	0.0088(5)	0.0088(5)	0.0092(5)
O(*2*)[o]	*x*	0.06026(7)	0.06002(7)	0.06017(7)	0.06014(7)	0.06010(7)
	y	2*x*	2*x*	2*x*	2*x*	2*x*
	z	0.4798(4)	0.4801(3)	0.4803(3)	0.4802(3)	0.4802(3)
	U_{eq}	0.0171(5)	0.0183(5)	0.0162(5)	0.0167(4)	0.0171(4)
O(*3*)	*x*	0.26967(14)	0.26977(14)	0.26956(15)	0.26957(14)	0.26987(14)
	y	½*x*	½*x*	½*x*	½*x*	½*x*
	z	0.5103(2)	0.5107(2)	0.5105(2)	0.5105(2)	0.5101(2)
	U_{eq}	0.0100(3)	0.0102(3)	0.0101(4)	0.0104(3)	0.0103(3)

a, $exp\left(-2\pi^2\left[h^2(a^*)^2U_{11} + k^2(b^*)^2U_{22} + ... + 2hka^*b^*U_{12}\right]\right)$

APPENDIX A.2.1. (CON'T)

		L1	L2	L4	L5	L6
O(*4*)	*x*	0.09229(7)	0.09227(6)	0.09227(7)	0.09219(7)	0.09220(6)
	y	2*x*	2*x*	2*x*	2*x*	2*x*
	z	0.0731(2)	0.0737(2)	0.0735(2)	0.0745(2)	0.0744(2)
	U_{eq}	0.0080(3)	0.0081(3)	0.0082(3)	0.0087(3)	0.0084(3)
O(*5*)	*x*	0.18468(14)	0.18425(13)	0.18452(14)	0.18433(13)	0.18419(13)
	y	½*x*	½*x*	½*x*	½*x*	½*x*
	z	0.0946(2)	0.0953(2)	0.0952(2)	0.0959(2)	0.0958(2)
	U_{eq}	0.0082(3)	0.0086(3)	0.0090(3)	0.0082(3)	0.0085(3)
O(*6*)	*x*	0.19640(8)	0.19624(8)	0.19616(8)	0.19590(8)	0.19597(8)
	y	0.18672(8)	0.18644(8)	0.18634(8)	0.18640(8)	0.18632(8)
	z	0.77639(17)	0.77642(16)	0.77642(18)	0.77651(17)	0.77635(17)
	U_{eq}	0.0074(2)	0.0074(2)	0.0074(2)	0.0071(2)	0.0071(2)
O(*7*)	x	0.28578(8)	0.28581(8)	0.28588(8)	0.28589(8)	0.28596(8)
	y	0.28551(8)	0.28547(7)	0.28554(8)	0.28537(8)	0.28534(8)
	z	0.08158(16)	0.08180(15)	0.08146(16)	0.08172(16)	0.08163(16)
	U_{eq}	0.0063(2)	0.0063(2)	0.0064(2)	0.0064(2)	0.0064(2)
O(*8*)	*x*	0.20968(9)	0.20953(8)	0.20964(9)	0.20972(9)	0.20969(9)
	y	0.27012(9)	0.27016(8)	0.27019(9)	0.27004(9)	0.27000(9)
	z	0.44216(17)	0.44229(16)	0.44233(17)	0.44228(16)	0.44206(17)
	U_{eq}	0.0075(2)	0.0077(2)	0.0076(2)	0.0075(2)	0.0076(2)
H(*3*)	*x*	0.268(2)	0.264(2)	0.260(2)	0.264(2)	0.261(2)
	y	½*x*	½*x*	½*x*	½*x*	½*x*
	z	0.376(3)	0.3744(13)	0.375(3)	0.377(3)	0.378(3)
	U_{eq}	0.015*	0.015*	0.015*	0.015*	0.015*

APPENDIX A.2.1. (CON'T)

		L7	L11	L12	L13	L15
X	*x*	0	0	0	0	0
	y	0	0	0	0	0
	z	0.23943(14)	0.23962(16)	0.23985(15)	0.23769(19)	0.23867(17)
	U_{eq}	0.0144(3)	0.0173(3)	0.0160(3)	0.0161(4)	0.0134(3)
Y	*x*	0.12370(8)	0.12399(7)	0.12383(7)	0.12391(9)	0.12365(11)
	y	½*x*	½*x*	½*x*	½*x*	½*x*
	z	0.63425(16)	0.62964(14)	0.63060(15)	0.63410(19)	0.6363(2)
	U_{eq}	0.0113(3)	0.0108(3)	0.0115(3)	0.0110(4)	0.0113(5)
Z	*x*	0.29683(3)	0.29728(3)	0.29709(3)	0.29699(4)	0.29670(4)
	y	0.25973(3)	0.26026(4)	0.26009(4)	0.25978(4)	0.25956(4)
	z	0.61199(9)	0.61243(9)	0.61226(9)	0.61182(11)	0.61166(11)
	U_{eq}	0.00640(10)	0.00609(11)	0.00653(10)	0.00631(12)	0.00608(13)
T	*x*	0.19210(3)	0.19214(3)	0.19212(2)	0.19212(3)	0.19210(3)
	y	0.19017(3)	0.19021(3)	0.19020(3)	0.19019(4)	0.19020(3)
	z	0	0	0	0	0
	U_{eq}	0.00518(9)	0.00493(9)	0.00518(9)	0.00539(11)	0.00509(12)
B	*x*	0.10885(9)	0.10933(10)	0.10904(9)	0.10918(11)	0.10889(11)
	y	2*x*	2*x*	2*x*	2*x*	2*x*
	z	0.4556(3)	0.4549(3)	0.4546(3)	0.4550(4)	0.4554(4)
	U_{eq}	0.0069(4)	0.0069(4)	0.0069(4)	0.0073(5)	0.0067(5)
O(*1*)[d]	*x*	0.0222(3)	0.0243(3)	0.0233(3)	0.0223(4)	0.0218(3)
	y	½*x*	½*x*	½*x*	½*x*	½*x*
	z	0.7883(5)	0.7888(5)	0.7889(5)	0.7872(6)	0.7886(6)
	U_{eq}	0.014(1)	0.014(1)	0.012(1)	0.0158(12)	0.0148(12)
O(*1*)[o]	*x*	0	0	0	0	0
	y	0	0	0	0	0
	z	0.7882(5)	0.7886(6)	0.7887(6)	0.7870(6)	0.7884(7)
	U_{eq}	0.0522(12)	0.0612(16)	0.0549(14)	0.0546(15)	0.0522(15)
O(2)[d]	*x*	0.0510(2)	0.0507(2)	0.0505(2)	0.0511(3)	0.0506(2)
	y	0.1201(2)	0.1209(2)	0.1205(2)	0.1205(3)	0.11999(2)
	z	0.4803(2)	0.4793(3)	0.4798(3)	0.4810(3)	0.4812(3)
	U_{eq}	0.0095(4)	0.0090(5)	0.0088(4)	0.0090(5)	0.0082(5)
O(*2*)[o]	*x*	0.05999(7)	0.06040(7)	0.06021(7)	0.06020(8)	0.05993(8)
	y	2*x*	2*x*	2*x*	2*x*	2*x*
	z	0.4801(3)	0.4791(3)	0.4797(3)	0.4809(4)	0.4812(4)
	U_{eq}	0.0169(4)	0.0180(5)	0.0176(5)	0.0167(5)	0.0164(5)
O(*3*)	*x*	0.26967(13)	0.27007(14)	0.26985(14)	0.26915(16)	0.26930(17)
	y	½*x*	½*x*	½*x*	½*x*	½*x*
	z	0.5104(2)	0.5106(2)	0.5106(2)	0.5100(3)	0.5098(3)
	U_{eq}	0.0104(3)	0.0091(3)	0.0102(3)	0.0100(4)	0.0105(4)

APPENDIX A.2.1. (CON'T)

		L7	L11	L12	L13	L15
O(*4*)	*x*	0.09214(6)	0.09245(6)	0.09233(6)	0.09235(7)	0.09215(8)
	y	2*x*	2*x*	2*x*	2*x*	2*x*
	z	0.0743(2)	0.0732(2)	0.0732(2)	0.0745(3)	0.0752(3)
	U_{eq}	0.0085(3)	0.0078(3)	0.0085(3)	0.0085(4)	0.0084(4)
O(*5*)	*x*	0.18407(12)	0.18489(13)	0.18454(13)	0.18438(15)	0.18385(15)
	y	½*x*	½*x*	½*x*	½*x*	½*x*
	z	0.0958(2)	0.0947(2)	0.0949(2)	0.0957(3)	0.0958(3)
	U_{eq}	0.0084(3)	0.0081(3)	0.0088(3)	0.0085(3)	0.0079(3)
O(*6*)	*x*	0.19593(8)	0.19657(8)	0.19646(8)	0.19593(9)	0.19537(9)
	y	0.18607(8)	0.18694(8)	0.18674(8)	0.18640(10)	0.18579(10)
	z	0.77643(16)	0.77645(17)	0.77646(16)	0.77619(19)	0.7767(2)
	U_{eq}	0.0071(2)	0.0073(2)	0.0073(2)	0.0073(2)	0.0072(3)
O(*7*)	x	0.28596(8)	0.28565(8)	0.28579(8)	0.28582(9)	0.28582(9)
	y	0.28541(7)	0.28546(8)	0.28551(7)	0.28531(9)	0.28522(9)
	z	0.08169(15)	0.08189(16)	0.08176(15)	0.08145(18)	0.08144(18)
	U_{eq}	0.0065(2)	0.0062(2)	0.0064(2)	0.0063(2)	0.0063(2)
O(*8*)	*x*	0.20947(8)	0.20974(8)	0.20967(8)	0.20974(10)	0.20955(10)
	y	0.26996(8)	0.27017(9)	0.27016(9)	0.27008(10)	0.26990(10)
	z	0.44221(15)	0.44251(17)	0.44228(16)	0.4417(19)	0.4419(19)
	U_{eq}	0.0074(2)	0.0076(2)	0.0082(2)	0.0076(3)	0.0076(3)
H(*3*)	*x*	0.256(2)	0.264(2)	0.262(2)	0.266(3)	0.277(3)
	y	½*x*	½*x*	½*x*	½*x*	½*x*
	z	0.380(3)	0.377(3)	0.376(3)	0.375(3)	0.375(3)
	U_{eq}	0.015*	0.015*	0.015*	0.015*	0.015*

APPENDIX A.2.1. (CON'T)

		L16	L17	L18	L19	L20
X	*x*	0	0	0	0	0
	y	0	0	0	0	0
	z	0.23879(12)	0.23833(14)	0.23882(14)	0.23858(14)	0.23839(15)
	U_{eq}	0.0142(2)	0.0148(3)	0.0140(3)	0.0141(3)	0.0136(3)
Y	*x*	0.12367(8)	0.12366(8)	0.12363(9)	0.12372(9)	0.12350(10)
	y	½*x*	½*x*	½*x*	½*x*	½*x*
	z	0.63563(16)	0.63542(17)	0.63634(18)	0.63604(18)	0.63606(19)
	U_{eq}	0.0103(3)	0.0110(3)	0.0110(4)	0.0110(4)	0.0103(4)
Z	*x*	0.29671(3)	0.29678(3)	0.29670(3)	0.29672(3)	0.29668(3)
	y	0.25959(3)	0.25965(3)	0.25957(3)	0.25958(3)	0.25959(4)
	z	0.61175(8)	0.61179(9)	0.61179(9)	0.61181(9)	0.61173(9)
	U_{eq}	0.00608(9)	0.00616(10)	0.00626(10)	0.00609(10)	0.00590(10)
T	*x*	0.19206(2)	0.19211(3)	0.19211(3)	0.19210(3)	0.19207(3)
	y	0.19018(3)	0.19020(3)	0.19018(3)	0.19019(3)	0.19017(3)
	z	0	0	0	0	0
	U_{eq}	0.00493(8)	0.00530(9)	0.00528(9)	0.00509(9)	0.00471(9)
B	*x*	0.10874(8)	0.10880(9)	0.10877(9)	0.10894(9)	0.10865(10)
	y	2*x*	2*x*	2*x*	2*x*	2*x*
	z	0.4553(3)	0.4556(3)	0.4556(3)	0.4553(3)	0.4552(3)
	U_{eq}	0.0068(3)	0.0071(4)	0.0069(4)	0.0069(4)	0.0070(4)
O(*1*)[d]	*x*	0.0217(2)	0.0222(3)	0.0215(3)	0.0219(3)	0.0216(3)
	y	½*x*	½*x*	½*x*	½*x*	½*x*
	z	0.7885(4)	0.7880(5)	0.7892(4)	0.7886(5)	0.7886(5)
	U_{eq}	0.0131(9)	0.015(1)	0.013(1)	0.014(1)	0.0138(11)
O(*1*)[o]	*x*	0	0	0	0	0
	y	0	0	0	0	0
	z	0.7883(5)	0.7879(5)	0.7890(5)	0.7885(5)	0.7883(5)
	U_{eq}	0.0492(10)	0.0521(12)	0.0482(11)	0.0518(12)	0.0491(12)
O(2)[d]	*x*	0.05097(19)	0.0511(2)	0.0511(2)	0.0510(2)	0.0510(2)
	y	0.11970(19)	0.1200(2)	0.1198(2)	0.1199(2)	0.1196(2)
	z	0.4806(2)	0.4813(2)	0.4809(2)	0.4810(2)	0.4809(3)
	U_{eq}	0.0093(4)	0.0091(4)	0.0092(4)	0.0089(4)	0.0086(5)
O(*2*)[o]	*x*	0.05980(6)	0.05994(7)	0.05985(7)	0.05990(7)	0.05975(7)
	y	2*x*	2*x*	2*x*	2*x*	2*x*
	z	0.4803(3)	0.4811(3)	0.4807(3)	0.4810(3)	0.4807(3)
	U_{eq}	0.0164(4)	0.0162(4)	0.0161(4)	0.0162(4)	0.0157(4)
O(*3*)	*x*	0.26924(12)	0.26922(13)	0.26897(13)	0.26910(13)	0.26939(14)
	y	½*x*	½*x*	½*x*	½*x*	½*x*
	z	0.51005(19)	0.5101(2)	0.5101(2)	0.5101(2)	0.5098(2)
	U_{eq}	0.0107(3)	0.0106(3)	0.0111(3)	0.0105(3)	0.0104(3)

APPENDIX A.2.1. (CON'T)

		L16	L17	L18	L19	L20
O(*4*)	*x*	0.09209(5)	0.09215(6)	0.09209(6)	0.09207(6)	0.09208(6)
	y	2*x*	2*x*	2*x*	2*x*	2*x*
	z	0.07478(19)	0.0747(2)	0.0748(2)	0.0752(2)	0.0748(2)
	U_{eq}	0.0084(3)	0.0084(3)	0.0083(3)	0.0081(3)	0.0077(3)
O(*5*)	*x*	0.18396(11)	0.18399(12)	0.18395(12)	0.18413(12)	0.18389(13)
	y	½*x*	½*x*	½*x*	½*x*	½*x*
	z	0.09614(19)	0.0961(2)	0.0963(2)	0.0960(2)	0.0963(2)
	U_{eq}	0.0083(3)	0.0088(3)	0.0085(3)	0.0083(3)	0.0078(3)
O(*6*)	*x*	0.19569(7)	0.19576(8)	0.19565(7)	0.19554(8)	0.19565(8)
	y	0.18587(7)	0.18605(8)	0.18598(8)	0.18595(8)	0.18585(8)
	z	0.77642(14)	0.77632(16)	0.77627(16)	0.77643(16)	0.77649(17)
	U_{eq}	0.00718(18)	0.0072(2)	0.0075(2)	0.0070(2)	0.0068(2)
O(*7*)	x	0.28599(7)	0.28594(7)	0.28610(7)	0.28589(7)	0.28601(8)
	y	0.28539(6)	0.28538(7)	0.28547(7)	0.28524(7)	0.28545(8)
	z	0.08161(13)	0.08161(14)	0.08153(14)	0.08172(15)	0.08152(15)
	U_{eq}	0.00602(17)	0.00614(19)	0.00617(19)	0.00618(19)	0.0059(2)
O(*8*)	*x*	0.20948(7)	0.20952(8)	0.20950(8)	0.20964(8)	0.20944(8)
	y	0.26990(7)	0.26986(8)	0.26992(8)	0.26999(8)	0.26981(9)
	z	0.44185(14)	0.44204(15)	0.44195(15)	0.44183(15)	0.44194(16)
	U_{eq}	0.00735(19)	0.0074(2)	0.0074(2)	0.0072(2)	0.0069(2)
H(*3*)	*x*	0.264(2)	0.264(2)	0.259(2)	0.263(2)	0.259(2)
	y	½*x*	½*x*	½*x*	½*x*	½*x*
	z	0.376(2)	0.378(2)	0.376(3)	0.377(3)	0.376(3)
	U_{eq}	0.015*	0.015*	0.015*	0.015*	0.015*

APPENDIX A.2.1. (CON'T)

		L21	L22	L23	L24	L25
X	*x*	0	0	0	0	0
	y	0	0	0	0	0
	z	0.23793(15)	0.2387(2)	0.23857(13)	0.23913(14)	0.23843(16)
	U_{eq}	0.0147(3)	0.0135(4)	0.0141(3)	0.0137(3)	0.0144(3)
Y	*x*	0.12366(8)	0.12360(13)	0.12389(8)	0.12373(9)	0.12392(9)
	y	½*x*	½*x*	½*x*	½*x*	½*x*
	z	0.63523(17)	0.6356(3)	0.63558(16)	0.63569(18)	0.63449(18)
	U_{eq}	0.0105(4)	0.0093(6)	0.0104(4)	0.0110(4)	0.0098(4)
Z	*x*	0.29684(3)	0.29673(5)	0.29670(3)	0.29673(3)	0.29684(4)
	y	0.25969(3)	0.25963(5)	0.25958(3)	0.25962(3)	0.25973(4)
	z	0.61171(9)	0.61189(13)	0.61181(8)	0.61177(9)	0.61194(10)
	U_{eq}	0.00592(10)	0.00570(16)	0.00602(9)	0.00610(10)	0.00601(11)
T	*x*	0.19212(3)	0.19212(4)	0.19212(2)	0.19209(3)	0.19211(3)
	y	0.19020(3)	0.19025(4)	0.19019(3)	0.19019(3)	0.19018(3)
	z	0	0	0	0	0
	U_{eq}	0.00494(9)	0.00454(15)	0.00503(8)	0.00501(9)	0.00480(10)
B	*x*	0.10891(10)	0.10872(13)	0.10883(8)	0.10881(9)	0.10897(10)
	y	2*x*	2*x*	2*x*	2*x*	2*x*
	z	0.4551(3)	0.4543(5)	0.4553(3)	0.4547(3)	0.4553(3)
	U_{eq}	0.0068(4)	0.0066(6)	0.0068(4)	0.0066(4)	0.0065(4)
O(*1*)[d]	*x*	0.0220(3)	0.0217(4)	0.0217(3)	0.0217(3)	0.0226(3)
	y	½*x*	½*x*	½*x*	½*x*	½*x*
	z	0.7881(5)	0.7881(7)	0.7886(4)	0.7884(5)	0.7881(5)
	U_{eq}	0.0152(11)	0.0129(14)	0.0140(9)	0.0136(10)	0.0125(10)
O(*1*)[o]	*x*	0	0	0	0	0
	y	0	0	0	0	0
	z	0.7877(7)	0.7879(7)	0.7884(5)	0.7882(5)	0.7879(6)
	U_{eq}	0.0535(15)	0.0494(17)	0.0500(11)	0.0498(11)	0.0526(14)
O(2)[d]	*x*	0.0509(2)	0.0515(4)	0.05087(19)	0.0510(2)	0.0509(2)
	y	0.1202(2)	0.1198(3)	0.11970(19)	0.1200(2)	0.1201(2)
	z	0.4810(3)	0.4804(4)	0.4805(2)	0.4808(2)	0.4806(3)
	U_{eq}	0.0089(5)	0.0103(7)	0.0088(4)	0.0086(4)	0.0079(5)
O(*2*)[o]	*x*	0.05992(8)	0.05984(9)	0.05980(6)	0.05992(6)	0.05997(8)
	y	2*x*	2*x*	2*x*	2*x*	2*x*
	z	0.4805(3)	0.4802(4)	0.4803(3)	0.4805(3)	0.4804(3)
	U_{eq}	0.0168(5)	0.0167(6)	0.0162(4)	0.0160(4)	0.0157(5)
O(*3*)	*x*	0.26908(14)	0.2689(2)	0.26923(12)	0.26930(13)	0.26949(15)
	y	½*x*	½*x*	½*x*	½*x*	½*x*
	z	0.5100(2)	0.5103(3)	0.5102(2)	0.5100(2)	0.5100(2)
	U_{eq}	0.0102(3)	0.0100(5)	0.0104(3)	0.0103(3)	0.0098(3)

APPENDIX A.2.1. (CON'T)

		L21	L22	L23	L24	L25
O(*4*)	*x*	0.09218(6)	0.09211(9)	0.09222(6)	0.09214(6)	0.09215(7)
	y	2*x*	2*x*	2*x*	2*x*	2*x*
	z	0.0743(2)	0.0749(2)	0.0749(2)	0.0748(2)	0.0745(2)
	U_{eq}	0.0080(3)	0.0075(4)	0.0082(3)	0.0081(3)	0.0080(3)
O(*5*)	*x*	0.18407(13)	0.18402(19)	0.18394(11)	0.18382(12)	0.18405(14)
	y	½*x*	½*x*	½*x*	½*x*	½*x*
	z	0.0959(2)	0.0963(3)	0.09653(19)	0.0964(2)	0.0960(2)
	U_{eq}	0.0086(3)	0.0084(4)	0.0083(3)	0.0084(3)	0.0079(3)
O(*6*)	*x*	0.19579(8)	0.19559(11)	0.19565(7)	0.19570(8)	0.19593(9)
	y	0.18617(8)	0.18584(12)	0.18598(7)	0.18601(8)	0.18627(9)
	z	0.7762(17)	0.7762(3)	0.77637(15)	0.77615(16)	0.77638(18)
	U_{eq}	0.0071(2)	0.0066(3)	0.00692(19)	0.0074(2)	0.0068(2)
O(*7*)	x	0.28596(8)	0.28610(11)	0.28597(7)	0.28595(8)	0.28590(8)
	y	0.28527(8)	0.28535(11)	0.28533(7)	0.28541(7)	0.28533(8)
	z	0.08137(15)	0.0817(2)	0.08164(14)	0.08163(15)	0.08165(17)
	U_{eq}	0.0061(2)	0.0061(3)	0.00607(18)	0.0062(2)	0.0062(2)
O(*8*)	*x*	0.20969(9)	0.20946(12)	0.20957(7)	0.20947(8)	0.20966(9)
	y	0.27006(9)	0.26992(12)	0.26995(7)	0.26994(8)	0.27008(9)
	z	0.44169(16)	0.4418(2)	0.4421(14)	0.44205(16)	0.44209(18)
	U_{eq}	0.0074(2)	0.0072(3)	0.00736(19)	0.0074(2)	0.0075(2)
H(*3*)	*x*	0.270(2)	0.261(4)	0.262(2)	0.266(2)	0.263(3)
	y	½*x*	½*x*	½*x*	½*x*	½*x*
	z	0.374(3)	0.375(3)	0.378(2)	0.377(2)	0.377(3)
	U_{eq}	0.015*	0.015*	0.015*	0.015*	0.015*

APPENDIX A.2.1. (CON'T)

		L26	L27	L28	SHW1	SHW2
X	*x*	0	0	0	0	0
	y	0	0	0	0	0
	z	0.23833(16)	0.23849(14)	0.23867(14)	0.2313(3)	0.2314(3)
	U_{eq}	0.0146(3)	0.0147(3)	0.0153(3)	0.0183(5)	0.0170(5)
Y	*x*	0.12362(9)	0.12366(9)	0.12420(8)	0.12326(7)	0.12352(8)
	y	½*x*	½*x*	½*x*	½*x*	½*x*
	z	0.63527(19)	0.63470(18)	0.63337(16)	0.63487(15)	0.63598(19)
	U_{eq}	0.0117(4)	0.0112(4)	0.0104(3)	0.0102(3)	0.0104(4)
Z	*x*	0.29686(4)	0.29677(3)	0.29691(3)	0.29696(3)	0.29695(3)
	y	0.25973(4)	0.25964(4)	0.25975(3)	0.26017(3)	0.26011(3)
	z	0.61199(10)	0.61189(9)	0.61201(8)	0.61030(9)	0.61035(10)
	U_{eq}	0.00606(11)	0.00613(10)	0.00619(10)	0.00660(11)	0.00727(12)
T	*x*	0.19207(3)	0.19214(3)	0.19212(3)	0.19168(3)	0.19173(3)
	y	0.19014(3)	0.19022(3)	0.19019(3)	0.18976(3)	0.18975(3)
	z	0	0	0	0	0
	U_{eq}	0.00490(10)	0.00500(9)	0.00504(9)	0.00540(14)	0.00598(15)
B	*x*	0.10871(10)	0.10877(10)	0.10899(9)	0.10896(9)	0.10889(9)
	y	2*x*	2*x*	2*x*	2*x*	2*x*
	z	0.4556(3)	0.4550(3)	0.4552(3)	0.4552(3)	0.4551(4)
	U_{eq}	0.0061(4)	0.0067(4)	0.0067(4)	0.0070(4)	0.0081(4)
O(*1*)[d]	*x*	0.0215(3)	0.0220(3)	0.0225(3)	0.0178(4)	0.0175(4)
	y	½*x*	½*x*	½*x*	½*x*	½*x*
	z	0.7883(5)	0.7881(5)	0.7880(5)	0.7826(5)	0.7822(6)
	U_{eq}	0.0037(11)	0.0131(10)	0.0144(9)	0.0084(10)	0.0095(12)
O(*1*)[o]	*x*	0	0	0	0	0
	y	0	0	0	0	0
	z	0.7880(5)	0.7882(5)	0.7878(5)	0.7825(5)	0.7821(6)
	U_{eq}	0.0533(13)	0.0501(12)	0.0534(12)	0.0311(9)	0.0315(9)
O(2)[d]	*x*	0.0513(3)	0.0507(2)	0.0510(2)	0.0527(3)	0.0525(3)
	y	0.1201(2)	0.1200(2)	0.1201(2)	0.12040(3)	0.1200(3)
	z	0.4808(3)	0.4802(3)	0.4802(2)	0.4868(2)	0.4867(3)
	U_{eq}	0.0092(5)	0.0080(5)	0.0086(4)	0.0108(5)	0.0110(5)
O(*2*)[o]	*x*	0.05997(7)	0.05997(7)	0.06000(7)	0.06015(6)	0.05995(7)
	y	2*x*	2*x*	2*x*	2*x*	2*x*
	z	0.4801(3)	0.4802	0.4801(3)	0.4866(3)	0.4866(3)
	U_{eq}	0.0160(4)	0.0159(4)	0.0160(4)	0.0158(4)	0.0164(4)
O(*3*)	*x*	0.26945(15)	0.26968(14)	0.26946(13)	0.26611(14)	0.26600(15)
	y	½*x*	½*x*	½*x*	½*x*	½*x*
	z	0.5097(3)	0.5101(2)	0.5103(2)	0.5085(2)	0.5088(3)
	U_{eq}	0.0098(4)	0.0103(3)	0.0102(3)	0.0121(3)	0.0125(3)

APPENDIX A.2.1. (CON'T)

		L26	L27	L28	SHW1	SHW2
O(*4*)	*x*	0.09216(7)	0.09206(6)	0.09212(6)	0.09303(6)	0.09302(6)
	y	2*x*	2*x*	2*x*	2*x*	2*x*
	z	0.0746(2)	0.0745(2)	0.0743(2)	0.0735(2)	0.0743(3)
	U_{eq}	0.0081(3)	0.0083(3)	0.0084(3)	0.0092(3)	0.0104(3)
O(*5*)	*x*	0.18399(14)	0.18399(13)	0.18411(12)	0.18581(13)	0.18566(13)
	y	½*x*	½*x*	½*x*	½*x*	½*x*
	z	0.0960(2)	0.0959(2)	0.0956(2)	0.0951(2)	0.0952(3)
	U_{eq}	0.0085(3)	0.0087(3)	0.0082(3)	0.0094(3)	0.0105(3)
O(*6*)	*x*	0.19589(9)	0.19576(8)	0.19591(7)	0.19537(8)	0.19515(8)
	y	0.18617(9)	0.18609(8)	0.18633(7)	0.18540(8)	0.18514(8)
	z	0.77657(18)	0.77640(17)	0.77636(15)	0.77569(17)	0.77550(18)
	U_{eq}	0.0071(2)	0.0068(2)	0.0071(2)	0.0079(2)	0.0083(2)
O(*7*)	x	0.28601(8)	0.28590(8)	0.28587(7)	0.28587(8)	0.28600(8)
	y	0.28545(8)	0.28528(8)	0.28542(7)	0.28560(7)	0.28558(8)
	z	0.08163(17)	0.08175(16)	0.08159(14)	0.07885(15)	0.07905(17)
	U_{eq}	0.0061(2)	0.0063(2)	0.00608(19)	0.00699(19)	0.0076(2)
O(*8*)	*x*	0.20961(9)	0.20960(8)	0.20957(8)	0.20956(8)	0.20965(8)
	y	0.26993(9)	0.26999(9)	0.26994(8)	0.26992(8)	0.26990(9)
	z	0.44217(17)	0.44202(16)	0.44218(15)	0.43964(16)	0.43979(19)
	U_{eq}	0.0073(2)	0.0073(2)	0.0076(2)	0.0077(2)	0.0082(2)
H(*3*)	*x*	0.254(3)	0.262(2)	0.268(2)	0.257(2)	0.249(3)
	y	½*x*	½*x*	½*x*	½*x*	½*x*
	z	0.382(3)	0.378(3)	0.375(2)	0.374(3)	0.378(3)
	U_{eq}	0.015*	0.015*	0.015*	0.015*	0.015*

APPENDIX A.2.1. (CON'T)

		SHW3	SHW4	SHW5	SHW6	SHW7
X	*x*	0	0	0	0	0
	y	0	0	0	0	0
	z	0.2342(5)	0.2323(4)	0.2294(2)	0.2317(3)	0.2332(4)
	U_{eq}	0.0236(10)	0.0242(7)	0.0208(5)	0.0197(7)	0.015(1)
Y	*x*	0.12382(11)	0.12377(8)	0.12383(8)	0.12312(8)	0.12300(15)
	y	½*x*	½*x*	½*x*	½*x*	½*x*
	z	0.6306(2)	0.63092(17)	0.63562(16)	0.63673(17)	0.6368(3)
	U_{eq}	0.0131(4)	0.0129(3)	0.0129(3)	0.0101(3)	0.0104(6)
Z	*x*	0.29732(6)	0.29737(5)	0.29701(3)	0.29680(4)	0.29681(6)
	y	0.26024(7)	0.26033(5)	0.26003(3)	0.26016(4)	0.26003(6)
	z	0.61167(17)	0.61159(12)	0.61059(9)	0.60965(10)	0.61017(17)
	U_{eq}	0.00824(19)	0.00867(13)	0.00929(10)	0.00850(11)	0.00717(18)
T	*x*	0.19190(5)	0.19185(4)	0.19171(3)	0.19156(3)	0.19179(5)
	y	0.19001(6)	0.19001(4)	0.18983(3)	0.18961(3)	0.18979(6)
	z	0	0	0	0	0
	U_{eq}	0.0057(2)	0.00670(17)	0.00722(13)	0.00692(14)	0.0057(2)
B	*x*	0.10934(19)	0.10936(13)	0.10911(9)	0.10902(10)	0.10898(18)
	y	2*x*	2*x*	2*x*	2*x*	2*x*
	z	0.4557(6)	0.4555(5)	0.4556(3)	0.4541(4)	0.4538(6)
	U_{eq}	0.0104(8)	0.0105(6)	0.0104(4)	0.0094(4)	0.0093(8)
O(*1*)[d]	*x*	0.0231(5)	0.0225(4)	0.0183(4)	0.0160(5)	0.0166(9)
	y	½*x*	½*x*	½*x*	½*x*	½*x*
	z	0.7873(9)	0.7864(7)	0.7833(5)	0.7816(5)	0.7830(9)
	U_{eq}	0.0165(19)	0.0170(14)	0.0217(11)	0.0097(12)	0.023(2)
O(*1*)[o]	*x*	0	0	0	0	0
	y	0	0	0	0	0
	z	0.787(1)	0.7860(7)	0.7831(5)	0.7814(5)	0.7829(9)
	U_{eq}	0.058(2)	0.0560(16)	0.0459(9)	0.0273(8)	0.0426(16)
O(2)[d]	*x*	0.0511(4)	0.0515(3)	0.0521(2)	0.0531(3)	0.0520(5)
	y	0.1211(4)	0.1211(3)	0.1200(2)	0.1202(3)	0.1201(5)
	z	0.4846(5)	0.4848(3)	0.4867(2)	0.4881(3)	0.4859(5)
	U_{eq}	0.0102(8)	0.0109(6)	0.0125(5)	0.0122(5)	0.0105(9)
O(*2*)[o]	*x*	0.06053(12)	0.06050(9)	0.05999(6)	0.06004(7)	0.06001(12)
	y	2*x*	2*x*	2*x*	2*x*	2*x*
	z	0.4844(5)	0.4846(4)	0.4865(3)	0.4880(3)	0.4858(5)
	U_{eq}	0.0188(8)	0.0187(6)	0.0181(4)	0.0166(4)	0.0164(7)
O(*3*)	*x*	0.2687(3)	0.26835(18)	0.26625(14)	0.26466(15)	0.2660(3)
	y	½*x*	½*x*	½*x*	½*x*	½*x*
	z	0.5109(4)	0.5108(3)	0.5100(2)	0.5079(2)	0.5088(4)
	U_{eq}	0.0113(6)	0.0124(4)	0.0146(3)	0.0137(4)	0.0130(6)

APPENDIX A.2.1. (CON'T)

		SHW3	SHW4	SHW5	SHW6	SHW7
O(*4*)	*x*	0.09283(12)	0.09295(8)	0.09297(6)	0.09336(7)	0.09304(12)
	y	2*x*	2*x*	2*x*	2*x*	2*x*
	z	0.0722(4)	0.0725(3)	0.0741(2)	0.0736(3)	0.0742(4)
	U_{eq}	0.0113(6)	0.0114(4)	0.0123(3)	0.0120(3)	0.0114(6)
O(*5*)	*x*	0.1860(2)	0.18597(17)	0.18569(13)	0.18644(14)	0.1860(2)
	y	½*x*	½*x*	½*x*	½*x*	½*x*
	z	0.0944(4)	0.0943(3)	0.0952(2)	0.0960(2)	0.0964(4)
	U_{eq}	0.0111(6)	0.0117(4)	0.0127(3)	0.0123(3)	0.0110(6)
O(*6*)	*x*	0.19662(15)	0.19639(10)	0.19521(8)	0.19499(8)	0.19513(15)
	y	0.18653(15)	0.18640(10)	0.18522(8)	0.18452(8)	0.18473(15)
	z	0.7755(3)	0.7760(2)	0.77589(17)	0.77494(18)	0.7745(3)
	U_{eq}	0.0094(4)	0.0098(3)	0.0104(2)	0.0094(2)	0.0092(4)
O(*7*)	x	0.28553(14)	0.28550(10)	0.28585(8)	0.28613(8)	0.28617(14)
	y	0.28567(14)	0.28562(10)	0.28557(7)	0.28578(8)	0.28580(14)
	z	0.0803(3)	0.0804(2)	0.07927(15)	0.07811(17)	0.0789(3)
	U_{eq}	0.0076(4)	0.0085(3)	0.0091(2)	0.0086(2)	0.0076(4)
O(*8*)	*x*	0.20987(16)	0.20980(11)	0.20963(8)	0.20963(9)	0.20974(15)
	y	0.27044(16)	0.27037(11)	0.26995(8)	0.26992(9)	0.26991(16)
	z	0.4413(3)	0.4414(2)	0.44037(16)	0.43866(18)	0.4394(3)
	U_{eq}	0.0103(4)	0.0104(3)	0.0099(2)	0.0095(2)	0.0087(4)
H(*3*)	*x*	0.271(4)	0.270(3)	0.256(2)	0.255(2)	0.255(4)
	y	½*x*	½*x*	½*x*	½*x*	½*x*
	z	0.375(3)	0.376(3)	0.377(3)	0.376(3)	0.376(3)
	U_{eq}	0.015*	0.015*	0.015*	0.015*	0.015*

APPENDIX A.2.1. (CON'T)

		SHW8	SHM1	SHM2	SHM3	SHM3a
X	*x*	0	0	0	0	0
	y	0	0	0	0	0
	z	0.2307(3)	0.2278(5)	0.2234(8)	0.2244(4)	0.2278(5)
	U_{eq}	0.0151(7)	0.0230(11)	0.0258(18)	0.0233(9)	0.027(1)
Y	*x*	0.12314(11)	0.12127(9)	0.12124(13)	0.12012(6)	0.11911(6)
	y	½*x*	½*x*	½*x*	½*x*	½*x*
	z	0.6380(2)	0.63748(19)	0.6384(3)	0.63785(13)	0.63589(13)
	U_{eq}	0.0105(5)	0.0109(3)	0.0102(5)	0.0115(3)	0.0120(2)
Z	*x*	0.29689(5)	0.29681(4)	0.29684(7)	0.29699(4)	0.29730(4)
	y	0.26010(5)	0.26013(4)	0.26038(7)	0.26033(4)	0.26043(4)
	z	0.61008(14)	0.60871(12)	0.60810(19)	0.60879(10)	0.61038(13)
	U_{eq}	0.00826(15)	0.00718(13)	0.0075(2)	0.00757(12)	0.00694(13)
T	*x*	0.19161(4)	0.19161(4)	0.19130(6)	0.19157(3)	0.19188(4)
	y	0.18971(5)	0.18958(4)	0.18949(6)	0.18968(3)	0.19002(4)
	z	0	0	0	0	0
	U_{eq}	0.00641(19)	0.00623(16)	0.0067(3)	0.00631(15)	0.00561(17)
B	*x*	0.10917(15)	0.10894(12)	0.10884(18)	0.10917(10)	0.10977(12)
	y	2*x*	2*x*	2*x*	2*x*	2*x*
	z	0.4541(5)	0.4541()	0.4530(7)	0.4533(4)	0.4530(5)
	U_{eq}	0.0102(6)	0.0083(5)	0.0078(8)	0.0082(4)	0.0092(6)
O(*1*)[d]	*x*	0.0167(7)	0.0106(12)	0.0116(13)	0.0118(8)	0.0147(7)
	y	½*x*	½*x*	½*x*	½*x*	½*x*
	z	0.7822(7)	0.7790(6)	0.7775(9)	0.7795(5)	0.7862(7)
	U_{eq}	0.0213(18)	0.0169(18)	0.011(2)	0.0150(14)	0.0146(17)
O(*1*)[o]	*x*	0	0	0	0	0
	y	0	0	0	0	0
	z	0.7822(7)	0.7789(6)	0.7776(9)	0.7795(5)	0.7862(7)
	U_{eq}	0.0406(12)	0.0241(9)	0.0201(13)	0.0245(8)	0.0298(11)
O(2)[d]	*x*	0.0520(4)	0.0534(3)	0.0537(6)	0.0533(3)	0.0529(3)
	y	0.1198(4)	0.12088(15)	0.1199(3)	0.12105(14)	0.12214(16)
	z	0.4860(4)	0.4898(3)	0.4895(5)	0.4874(3)	0.4816(3)
	U_{eq}	0.0118(7)	0.0095(6)	0.0110(9)	0.0106(5)	0.0101(6)
O(*2*)[o]	*x*	0.05987(9)	0.06042(8)	0.05994(12)	0.06052(7)	0.06106(8)
	y	2*x*	2*x*	2*x*	2*x*	2*x*
	z	0.4859(4)	0.4897(3)	0.4894(5)	0.4873(3)	0.4815(3)
	U_{eq}	0.0173(6)	0.0139(4)	0.0144(7)	0.0152(4)	0.0163(5)
O(*3*)	*x*	0.2651(2)	0.26336(18)	0.2618(3)	0.26405(15)	0.26786(17)
	y	½*x*	½*x*	½*x*	½*x*	½*x*
	z	0.5088(3)	0.5077(3)	0.5073(5)	0.5079(2)	0.5095(3)
	U_{eq}	0.0134(5)	0.0129(4)	0.0126(7)	0.0128(4)	0.0103(4)

APPENDIX A.2.1. (CON'T)

		SHW8	SHM1	SHM2	SHM3	SHM3a
O(*4*)	*x*	0.09296(10)	0.09377(8)	0.09391(13)	0.09373(7)	0.09347(8)
	y	2*x*	2*x*	2*x*	2*x*	2*x*
	z	0.0742(4)	0.0736(3)	0.0728(5)	0.0730(3)	0.0715(3)
	U_{eq}	0.0121(5)	0.0105(4)	0.0113(6)	0.0103(3)	0.0106(4)
O(*5*)	*x*	0.1855(2)	0.18684(16)	0.1868(3)	0.18685(14)	0.18682(16)
	y	½*x*	½*x*	½*x*	½*x*	½*x*
	z	0.0961(3)	0.0951(3)	0.0949(5)	0.0943(2)	0.0929(3)
	U_{eq}	0.0125(5)	0.0102(4)	0.0114(6)	0.0110(3)	0.0100(4)
O(*6*)	*x*	0.19481(12)	0.19473(10)	0.19454(16)	0.19517(9)	0.19661(10)
	y	0.18459(12)	0.18430(10)	0.18407(16)	0.18506(9)	0.18691(10)
	z	0.7750(3)	0.7746(2)	0.7747(4)	0.77503(19)	0.7753(2)
	U_{eq}	0.0095(3)	0.0082(3)	0.0086(4)	0.0088(2)	0.0088(3)
O(*7*)	x	0.28610(12)	0.28604(10)	0.28601(16)	0.28607(8)	0.28572(10)
	y	0.28564(11)	0.28568(9)	0.28577(15)	0.28574(8)	0.28583(9)
	z	0.0784(2)	0.07701(19)	0.0762(3)	0.07739(17)	0.0796(2)
	U_{eq}	0.0084(3)	0.0076(3)	0.0081(4)	0.0077(2)	0.0073(3)
O(*8*)	*x*	0.20954(12)	0.20974(10)	0.20941(17)	0.20971(9)	0.21008(11)
	y	0.26979(13)	0.27012(11)	0.27006(17)	0.27028(9)	0.27091(11)
	z	0.4390(2)	0.4383(2)	0.4372(3)	0.43848(18)	0.4403(2)
	U_{eq}	0.0091(3)	0.0079(3)	0.0083(4)	0.0085(2)	0.0091(3)
H(*3*)	*x*	0.254(3)	0.250(3)	0.252(5)	0.245(2)	0.262(3)
	y	½*x*	½*x*	½*x*	½*x*	½*x*
	z	0.376(3)	0.376(3)	0.371(2)	0.378(3)	0.377(3)
	U_{eq}	0.015*	0.015*	0.015*	0.015*	0.015*

APPENDIX A.2.1. (CON'T)

		SHM3e	SHM5	SHP1	SHP2	SHP3
X	*x*	0	0	0	0	0
	y	0	0	0	0	0
	z	0.2238(3)	0.2239(4)	0.2298(4)	0.2288(6)	0.2276(9)
	U_{eq}	0.0254(7)	0.0263(9)	0.0248(8)	0.0255(13)	0.0312(19)
Y	*x*	0.12037(5)	0.12064(6)	0.12173(6)	0.12110(9)	0.12114(13)
	y	½*x*	½*x*	½*x*	½*x*	½*x*
	z	0.63822(11)	0.63815(14)	0.63581(14)	0.63407(18)	0.6333(3)
	U_{eq}	0.0114(2)	0.0120(3)	0.0106(3)	0.0115(4)	0.0125(5)
Z	*x*	0.29691(3)	0.29688(3)	0.29690(3)	0.29708(5)	0.29720(8)
	y	0.26031(3)	0.26024(4)	0.26018(3)	0.26048(5)	0.26055(8)
	z	0.60845(9)	0.60845(10)	0.60926(9)	0.60962(14)	0.6099(2)
	U_{eq}	0.00847(10)	0.00897(11)	0.00722(11)	0.00710(18)	0.0070(2)
T	*x*	0.19146(3)	0.19143(3)	0.19172(3)	0.19174(4)	0.19168(7)
	y	0.18956(3)	0.18959(3)	0.18973(3)	0.18983(4)	0.18983(7)
	z	0	0	0	0	0
	U_{eq}	0.00720(13)	0.00767(14)	0.00625(13)	0.0061(2)	0.0065(3)
B	*x*	0.10922(8)	0.10917(10)	0.10901(9)	0.10916(14)	0.1090(2)
	y	2*x*	2*x*	2*x*	2*x*	2*x*
	z	0.4535(3)	0.4535(3)	0.4544(3)	0.4541(5)	0.4526(8)
	U_{eq}	0.0090(4)	0.0094(4)	0.0082(4)	0.0084(6)	0.0094(10)
O(*1*)[d]	*x*	0.0109(7)	0.0105(9)	0.0147(5)	0.0154(7)	0.0168(12)
	y	½*x*	½*x*	½*x*	½*x*	½*x*
	z	0.7790(4)	0.7788(5)	0.7806(5)	0.7811(7)	0.7813(12)
	U_{eq}	0.0146(11)	0.0155(13)	0.0112(11)	0.0120(17)	0.013(3)
O(*1*)[o]	*x*	0	0	0	0	0
	y	0	0	0	0	0
	z	0.7790(4)	0.7788(5)	0.7806(5)	0.7810(7)	0.7815(12)
	U_{eq}	0.0227(6)	0.0229(7)	0.0262(7)	0.0286(12)	0.033(2)
O(2)[d]	*x*	0.0535(3)	0.0533(3)	0.0529(2)	0.0524(4)	0.0515(5)
	y	0.12051(11)	0.12063(13)	0.12085(12)	0.1210(2)	0.1212(3)
	z	0.4883(2)	0.4885(3)	0.4885(2)	0.4858(4)	0.4845(6)
	U_{eq}	0.0118(4)	0.0117(5)	0.0099(4)	0.0116(7)	0.089(10)
O(*2*)[o]	*x*	0.06025(5)	0.06031(6)	0.06040(6)	0.06052(10)	0.06056(14)
	y	2*x*	2*x*	2*x*	2*x*	2*x*
	z	0.4881(2)	0.4884(3)	0.4884(2)	0.4856(4)	0.4844(6)
	U_{eq}	0.0158(3)	0.0160(4)	0.0150(4)	0.0175(6)	0.0164(9)
O(*3*)	*x*	0.26317(12)	0.26298(15)	0.26454(14)	0.2656(2)	0.2661(3)
	y	½*x*	½*x*	½*x*	½*x*	½*x*
	z	0.5077(2)	0.5077(2)	0.5077(2)	0.5085(3)	0.5085(5)
	U_{eq}	0.0133(3)	0.0135(3)	0.0127(3)	0.0130(5)	0.0139(9)

APPENDIX A.2.1. (CON'T)

		SHM3e	SHM5	SHP1	SHP2	SHP3
O(*4*)	*x*	0.09393(6)	0.09390(7)	0.09375(6)	0.09360(9)	0.09353(14)
	y	2*x*	2*x*	2*x*	2*x*	2*x*
	z	0.0731(2)	0.0732(3)	0.0728(2)	0.0720(4)	0.0708(5)
	U_{eq}	0.0119(3)	0.0129(3)	0.0103(3)	0.0097(5)	0.0099(8)
O(*5*)	*x*	0.18671(12)	0.18678(14)	0.18700(12)	0.1869(2)	0.1869(3)
	y	½*x*	½*x*	½*x*	½*x*	½*x*
	z	0.0945(2)	0.0949(2)	0.0947(2)	0.0941(3)	0.0944(5)
	U_{eq}	0.0122(3)	0.0124(3)	0.0104(3)	0.0107(5)	0.0099(7)
O(*6*)	*x*	0.19477(7)	0.19469(8)	0.19516(7)	0.19578(12)	0.19598(19)
	y	0.18460(7)	0.18446(8)	0.18494(7)	0.18557(13)	0.18559(17)
	z	0.77474(16)	0.77471(18)	0.77484(17)	0.7750(3)	0.7749(4)
	U_{eq}	0.00947(19)	0.0098(2)	0.0086(2)	0.0088(3)	0.0091(5)
O(*7*)	x	0.28601(7)	0.28599(8)	0.28603(7)	0.28573(12)	0.28562(18)
	y	0.28577(7)	0.28578(8)	0.28572(7)	0.28589(11)	0.28591(16)
	z	0.07708(14)	0.07681(17)	0.07771(15)	0.0788(2)	0.0784(4)
	U_{eq}	0.00871(18)	0.0090(2)	0.00746(19)	0.0077(3)	0.0080(5)
O(*8*)	*x*	0.20960(7)	0.20968(9)	0.20964(8)	0.20986(13)	0.20995(19)
	y	0.27014(8)	0.27019(9)	0.27017(8)	0.27051(13)	0.27064(19)
	z	0.43802(15)	0.43796(17)	0.43881(16)	0.4397(3)	0.4392(4)
	U_{eq}	0.00933(19)	0.0098(2)	0.0081(2)	0.0087(3)	0.0087(5)
H(*3*)	*x*	0.251(2)	0.251(2)	0.255(2)	0.252(4)	0.239(4)
	y	½*x*	½*x*	½*x*	½*x*	½*x*
	z	0.379(2)	0.377(3)	0.375(3)	0.377(3)	0.380(4)
	U_{eq}	0.015*	0.015*	0.015*	0.015*	0.015*

APPENDIX A.2.2.

FULL ANISOTROPIC DISPLACEMENT FACTORS ($Å^2$) FOR ALL TOURMALINE CRYSTALS

APPENDIX A.2.2. FULL ANISOTROPIC DISPLACEMENT FACTORS (Å^2) FOR ALL TOURMALINES

		LID1	LID2	LID4	LID5	LID6
X	U_{11}	0.0184(4)	0.0159(4)	0.0171(4)	0.0149(4)	0.0150(3)
	U_{22}	0.0184(4)	0.0159(4)	0.0171(4)	0.0149(4)	0.0150(3)
	U_{33}	0.0157(6)	0.0149(5)	0.0153(5)	0.0132(5)	0.0134(5)
	U_{23}	0	0	0	0	0
	U_{13}	0	0	0	0	0
	U_{12}	0.0092(2)	0.00797(17)	0.0085(2)	0.00744(17)	0.00748(17)
	U_{eq}	0.0175(3)	0.0156(3)	0.0165(3)	0.0143(3)	0.0145(3)
Y	U_{11}	0.0114(5)	0.0115(5)	0.0122(5)	0.0094(6)	0.0112(6)
	U_{22}	0.0091(4)	0.0092(4)	0.0087(4)	0.0100(5)	0.0101(5)
	U_{33}	0.0141(5)	0.0149(5)	0.0143(5)	0.0153(6)	0.0162(6)
	U_{23}	-	-	-	-0.0009(2)	-0.0008(2)
	U_{13}	-0.0013(3)	-0.0014(4)	-0.0021(4)	-0.0017(4)	-0.0016(4)
	U_{12}	0.0057(2)	0.0058(3)	0.0061(3)	0.0047(3)	0.0056(3)
	U_{eq}	0.0113(3)	0.0116(3)	0.0114(3)	0.0117(40	0.0124(4)
Z	U_{11}	0.0066(2)	0.0064(2)	0.0067(2)	0.0065(2)	0.0067(2)
	U_{22}	0.0079(2)	0.0078(2)	0.0081(3)	0.0080(2)	0.0078(2)
	U_{33}	0.00465(19)	0.00561(18)	0.00523(19)	0.00546(18)	0.00524(18)
	U_{23}	0.00048(17)	0.00072(16)	0.00081(18)	0.00073(17)	0.00065(17)
	U_{13}	-	0.00027(16)	0.00023(18)	-	0.00013(17)
	U_{12}	0.00417(18)	0.00399(17)	0.00422(19)	0.00416(18)	0.00416(18)
	U_{eq}	0.00617(11)	0.00638(11)	0.00647(11)	0.00637(11)	0.00633(11)
T	U_{11}	0.0054(2)	0.0049(2)	0.0052(2)	0.0050(2)	0.0050(2)
	U_{22}	0.0051(2)	0.00453(19)	0.0046(2)	0.00485(19)	0.00471(19)
	U_{33}	0.00434(17)	0.00551(17)	0.00528(18)	0.00537(17)	0.00511(17)
	U_{23}	-	-	0.00002(15)	-	-
	U_{13}	0.00018(16)	0.00010(15)	0.00022(16)	0.00014(15)	-
	U_{12}	0.00256(15)	0.00214(14)	0.00219(15)	0.00242(14)	0.00232(14)
	U_{eq}	0.00496(10)	0.00506(9)	0.00515(10)	0.00511(9)	0.00500(9)
B	U_{11}	0.0077(8)	0.0070(7)	0.0084(8)	0.0084(8)	0.0068(7)
	U_{22}	0.0090(11)	0.0100(11)	0.0091(11)	0.0096(11)	0.0105(11)
	U_{33}	0.0028(9)	0.0044(9)	0.004(1)	0.004(1)	0.004(1)
	U_{23}	-0.0006(8)	-0.0002(8)	-0.0000(8)	-0.0009(8)	-0.0006(8)
	U_{13}	-0.0003(4)	-0.0001(4)	-0.0000(4)	-0.0005(4)	-0.0003(4)
	U_{12}	0.0045(6)	0.0050(5)	0.0045(6)	0.0048(6)	0.0053(6)
	U_{eq}	0.0064(4)	0.0068(4)	0.0072(4)	0.0075(4)	0.0068(4)

APPENDIX A.2.2. (CON'T)

		LID1	LID2	LID4	LID5	LID6
O(1)[d]	U_{11}	0.0148(11)	0.014(1)	0.0144(11)	0.0151(11)	0.0145(11)
O(1)[o]	U_{11}	0.078(2)	0.077(2)	0.073(2)	0.076(2)	0.075(2)
	U_{22}	0.078(2)	0.077(2)	0.073(2)	0.076(2)	0.075(2)
	U_{33}	0.0137(17)	0.0119(16)	0.0141(18)	0.0134(16)	0.0113(16)
	U_{23}	0	0	0	0	0
	U_{13}	0	0	0	0	0
	U_{12}	0.0391(11)	0.0386(11)	0.0367(11)	0.0380(11)	0.0376(10)
	U_{eq}	0.0567(14)	0.0554(13)	0.0536(13)	0.0551(13)	0.0540(13)
O(2)[d]	U_{11}	0.0087(5)	0.0102(5)	0.0088(5)	0.0088(5)	0.0092(5)
O(2)[o]	U_{11}	0.0271(9)	0.0278(9)	0.0250(9)	0.0256(9)	0.02609(9)
	U_{22}	0.0051(9)	0.0278(9)	0.0250(9)	0.0256(9)	0.0261(9)
	U_{33}	0.0119(9)	0.0138(9)	0.0250(9)	0.0132(9)	0.0129(9)
	U_{23}	0.0009(7)	-0.0002(3)	0.0250(9)	0.0001(3)	-0.0002(3)
	U_{13}	0.0004(3)	0.0002(3)	0.0250(9)	-0.0001(3)	0.0002(3)
	U_{12}	0.0025(4)	0.025(1)	0.0250(9)	0.0236(9)	0.0234(9)
	U_{eq}	0.0171(5)	0.0183(5)	0.0250(9)	0.0167(4)	0.0171(4)
O(3)	U_{11}	0.0192(9)	0.0186(9)	0.020(1)	0.0199(9)	0.0212(9)
	U_{22}	0.0092(6)	0.0095(6)	0.0091(6)	0.0099(6)	0.0094(6)
	U_{33}	0.0049(8)	0.0051(7)	0.0048(8)	0.0047(7)	0.0044(7)
	U_{23}	-0.0003(3)	-0.0004(3)	-0.0006(3)	-0.0002(3)	0.0000(3)
	U_{13}	-0.0006(7)	-0.0007(6)	-0.0012(7)	-0.0004(6)	0.0000(7)
	U_{12}	0.0096(5)	0.0093(4)	0.0100(5)	0.0100(5)	0.0106(5)
	U_{eq}	0.0100(3)	0.0100(3)	0.0101(4)	0.0104(3)	0.0103(3)
O(4)	U_{11}	0.0062(5)	0.0064(5)	0.0062(6)	0.0063(5)	0.0074(5)
	U_{22}	0.0117(9)	0.0117(8)	0.0127(9)	0.0131(9)	0.0113(8)
	U_{33}	0.0081(7)	0.0079(7)	0.0080(7)	0.0090(7)	0.0079(7)
	U_{23}	-0.0010(6)	-0.0014(6)	-0.0017(6)	-0.0012(6)	-0.0013(6)
	U_{13}	-0.0005(3)	-0.00071	-0.0009(3)	-0.0006(3)	-0.0007(3)
	U_{12}	0.0058(4)	0.00582	0.0063(4)	0.0066(4)	0.0056(4)
	U_{eq}	0.0080(3)	0.0081(3)	0.0082(3)	0.0087(3)	0.0084(3)
O(5)	U_{11}	0.0144(9)	0.0133(8)	0.0154(9)	0.0128(8)	0.0142(9)
	U_{22}	0.0075(5)	0.0072(5)	0.0074(5)	0.0072(5)	0.0072(5)
	U_{33}	0.0049(7)	0.0074(7)	0.0069(7)	0.0065(7)	0.0065(7)
	U_{23}	0.0002(3)	0.0005(3)	0.0000(3)	-0.0000(3)	0.0002(3)
	U_{13}	0.0005(6)	0.0010(6)	0.0000(6)	-0.0001(6)	0.0004(6)
	U_{12}	0.0072(4)	0.0066(4)	0.0077(5)	0.0064(4)	0.0071(4)
	U_{eq}	0.0082(3)	0.0086(3)	0.0090(3)	0.0082(3)	0.0085(3)

APPENDIX A.2.2. (CON'T)

		LID1	LID2	LID4	LID5	LID6
O(6)	U_{11}	0.0077(5)	0.0069(5)	0.0072(5)	0.0069(5)	0.0067(5)
	U_{22}	0.0088(5)	0.0086(5)	0.0079(6)	0.0084(5)	0.0082(5)
	U_{33}	0.0040(5)	0.0050(5)	0.0053(5)	0.0051(5)	0.0048(5)
	U_{23}	0.0006(4)	0.0003(4)	-0.0001(4)	-0.0002(4)	0.0002(4)
	U_{13}	0.0006(4)	0.0010(4)	0.0006(4)	0.0007(4)	0.0003(4)
	U_{12}	0.0029(4)	0.0028(4)	0.0025(4)	0.0031(4)	0.0025(4)
	U_{eq}	0.0074(2)	0.0073(2)	0.0074(2)	0.0071(2)	0.0071(2)
O(7)	U_{11}	0.0055(5)	0.0053(5)	0.0061(5)	0.0053(5)	0.0061(5)
	U_{22}	0.0060(5)	0.0056(5)	0.0057(5)	0.0063(5)	0.0052(5)
	U_{33}	0.0056(5)	0.0059(5)	0.0059(5)	0.0058(5)	0.0060(5)
	U_{23}	-0.0008(4)	-0.0002(4)	-0.0003(4)	-0.0006(4)	-0.0008(4)
	U_{13}	0.0004(4)	0.0008(4)	0.0008(4)	0.0004(4)	0.0003(4)
	U_{12}	0.0015(4)	0.0012(4)	0.0019(4)	0.0016(4)	0.0013(4)
	U_{eq}	0.0063(2)	0.0063(2)	0.0064(2)	0.0064(2)	0.0064(2)
O(8)	U_{11}	0.0065(5)	0.0060(5)	0.0050(5)	0.0054(5)	0.0060(5)
	U_{22}	0.0096(6)	0.0094(5)	0.0101(6)	0.0096(6)	0.0090(6)
	U_{33}	0.0073(5)	0.0085(5)	0.0083(5)	0.0077(5)	0.0081(5)
	U_{23}	0.0029(4)	0.0025(4)	0.0032(4)	0.0028(4)	0.0023(4)
	U_{13}	0.0006(4)	0.0003(4)	0.0010(4)	0.0008(4)	0.0005(4)
	U_{12}	0.0046(5)	0.0043(4)	0.0042(5)	0.0039(4)	0.0042(4)
	U_{eq}	0.0076(2)	0.0077(2)	0.0076(2)	0.0075(2)	0.0076(2)
H(3)*	U_{eq}	0.015	0.015	0.015	0.015	0.015

* Fixed during refinement

APPENDIX A.2.2. (CON'T)

		LID7	LID11	LID12	LID13	LID15
X	U_{11}	0.0153(3)	0.0176(4)	0.0164(4)	0.0171(5)	0.0155(4)
	U_{22}	0.0153(3)	0.0176(4)	0.0164(4)	0.0171(5)	0.0155(4)
	U_{33}	0.0125(4)	0.0169(5)	0.0153(5)	0.0142(6)	0.0094(5)
	U_{23}	0	0	0	0	0
	U_{13}	0	0	0	0	0
	U_{12}	0.00765(16)	0.0088(2)	0.00821(18)	0.0086(2)	0.0077(2)
	U_{eq}	0.0144(3)	0.0173(3)	0.0160(3)	0.0161(4)	0.0134(3)
Y	U_{11}	0.0119(6)	0.0097(5)	0.0111(5)	0.0081(6)	0.0116(8)
	U_{22}	0.0091(4)	0.0085(4)	0.0090(4)	0.0104(5)	0.0112(6)
	U_{33}	0.0138(6)	0.0146(5)	0.0151(5)	0.0139(6)	0.0112(8)
	U_{23}	-	-	-	-0.0011(2)	-0.0010(2)
	U_{13}	-0.0014(4)	-0.0012(3)	-0.0017(3)	-0.0021(4)	-0.0020(5)
	U_{12}	0.0059(3)	0.0049(2)	0.0055(2)	0.0040(3)	0.0058(4)
	U_{eq}	0.0113(3)	0.0108(3)	0.0115(3)	0.0110(4)	0.0113(5)
Z	U_{11}	0.0065(2)	0.0063(2)	0.0067(2)	0.0066(2)	0.0074(3)
	U_{22}	0.0081(2)	0.0076(2)	0.0082(2)	0.0078(3)	0.0090(3)
	U_{33}	0.00522(17)	0.00531(18)	0.00543(18)	0.0052(2)	0.0026(2)
	U_{23}	0.00081(16)	0.00071(16)	0.00067(16)	0.00071(19)	0.00063(18)
	U_{13}	0.00022(15)	0.00018(16)	0.00009(16)	0.00022(19)	0.00017(18)
	U_{12}	0.00418(16)	0.00413(17)	0.00428(17)	0.0041(2)	0.0046(2)
	U_{eq}	0.00640(10)	0.00609(11)	0.00653(10)	0.00631(12)	0.00608(13)
T	U_{11}	0.00506(19)	0.0048(2)	0.0052(2)	0.0054(2)	0.0061(2)
	U_{22}	0.00483(18)	0.00469(18)	0.00467(18)	0.0054(2)	0.0059(2)
	U_{33}	0.00530(16)	0.00537(17)	0.00532(16)	0.00528(19)	0.0030(2)
	U_{23}	-	-	-	-	-
	U_{13}	0.00008(14)	0.00019(15)	0.00019(14)	0.00032(17)	0.00020(17)
	U_{12}	0.00222(13)	0.00242(14)	0.00216(14)	0.00258(16)	0.00282(16)
	U_{eq}	0.00518(9)	0.00493(9)	0.00518(9)	0.00539(11)	0.00509(12)
B	U_{11}	0.0071(7)	0.0080(7)	0.0081(7)	0.0076(9)	0.0084(8)
	U_{22}	0.0099(10)	0.0090(10)	0.0085(10)	0.0094(12)	0.0116(12)
	U_{33}	0.0046(9)	0.0041(9)	0.0044(9)	0.0054(11)	0.0011(11)
	U_{23}	-0.0002(7)	-0.0018(8)	-0.0011(7)	-0.0006(9)	-0.0010(8)
	U_{13}	-0.0001(4)	-0.0009(4)	-0.0006(4)	-0.0003(5)	-0.0005(4)
	U_{12}	0.0049(5)	0.0045(5)	0.0042(5)	0.0047(6)	0.0058(6)
	U_{eq}	0.0069(4)	0.0069(4)	0.0069(4)	0.0073(5)	0.0067(5)

APPENDIX A.2.2. (CON'T)

		LID7	LID11	LID12	LID13	LID15
O(1)[d]	U_{11}	0.014(1)	0.014(1)	0.0122(9)	0.0158(12)	0.0148(12)
O(1)[o]	U_{11}	0.0718(19)	0.085(3)	0.076(2)	0.075(2)	0.072(2)
		0.0718(19)	0.085(3)	0.076(2)	0.075(2)	0.072(2)
	U_{33}	0.0129(15)	0.0132(17)	0.0119(16)	0.0128(18)	0.012(2)
	U_{23}	0	0	0	0	0
	U_{13}	0	0	0	0	0
	U_{12}	0.036(1)	0.0426(13)	0.03817	0.0377(12)	0.0360(12)
	U_{eq}	0.0522(12)	0.0612(16)	0.0549(14)	0.0546(15)	0.0522(15)
O(2)[d]	U_{11}	0.0095(4)	0.0090(5)	0.0088(4)	0.0090(5)	0.0082(5)
O(2)[o]	U_{11}	0.0253(8)	0.028(1)	0.0280(9)	0.026(1)	0.027(1)
	U_{22}	0.0253(8)	0.028(1)	0.0280(9)	0.026(1)	0.027(1)
	U_{33}	0.0137(8)	0.0132(9)	0.0125(9)	0.012(1)	0.0091(10)
	U_{23}	0.0001(3)	0.0001(3)	-0.0002(3)	-0.0004(4)	-0.0004(4)
	U_{13}	-0.0001(3)	-0.0001(3)	0.0002(3)	0.0004(4)	0.0004(4)
	U_{12}	0.0228(9)	0.0263(10)	0.026(1)	0.0229(10)	0.0234(11)
	U_{eq}	0.0169(4)	0.0180(5)	0.0176(5)	0.0167(5)	0.0164(5)
O(3)	U_{11}	0.0211(9)	0.0171(9)	0.0196(9)	0.0190(10)	0.0225(10)
	U_{22}	0.0094(5)	0.0085(5)	0.0090(5)	0.0092(6)	0.0108(6)
	U_{33}	0.0045(7)	0.0046(7)	0.0057(7)	0.0050(8)	0.0020(8)
	U_{23}	0.0001(3)	0.0001(3)	-0.0005(3)	-0.0003(4)	-0.0001(4)
	U_{13}	0.0002(6)	0.0002(6)	-0.0010(6)	-0.0005(70	-0.0002(7)
	U_{12}	0.0105(4)	0.0085(4)	0.0098(4)	0.0095(5)	0.0112(5)
	U_{eq}	0.0104(3)	0.0091(3)	0.0102(3)	0.0100(4)	0.0105(4)
O(4)	U_{11}	0.0065(5)	0.0059(5)	0.0072(5)	0.0073(6)	0.0073(6)
	U_{22}	0.0121(8)	0.0115(8)	0.0122(8)	0.0120(9)	0.015(1)
	U_{33}	0.0087(7)	0.0080(7)	0.0078(7)	0.0078(8)	0.0053(8)
	U_{23}	-0.0015(6)	-0.0012(6)	-0.0016(6)	-0.0010(7)	-0.0005(7)
	U_{13}	-0.0007(3)	-0.0006(3)	-0.0008(3)	-0.0005(4)	-0.0003(4)
	U_{12}	0.0060(4)	0.0057(4)	0.0061(4)	0.0060(5)	0.0075(5)
	U_{eq}	0.0085(3)	0.0078(3)	0.0085(3)	0.0085(4)	0.0084(4)
O(5)	U_{11}	0.0142(8)	0.0133(8)	0.0146(8)	0.0119(9)	0.0144(9)
	U_{22}	0.0071(5)	0.0069(5)	0.0080(5)	0.0072(6)	0.0081(6)
	U_{33}	0.0064(6)	0.0061(6)	0.0061(6)	0.0078(8)	0.0033(8)
	U_{23}	0.0003(3)	0.0000(3)	0.0002(3)	0.0005(3)	0.0004(3)
	U_{13}	0.0005(5)	0.0000(6)	0.0003(6)	0.0010(7)	0.0009(6)
	U_{12}	0.0071(4)	0.0067(4)	0.0073(4)	0.0060(5)	0.0072(5)

APPENDIX A.2.2. (CON'T)

		LID7	LID11	LID12	LID13	LID15
	U_{eq}	0.0085(3)	0.0081(3)	0.0088(3)	0.0085(3)	0.0079(3)
O(6)	U_{11}	0.0067(5)	0.0069(5)	0.0066(5)	0.0074(6)	0.0083(6)
	U_{22}	0.0084(5)	0.0083(5)	0.0084(5)	0.0087(6)	0.0098(60
	U_{33}	0.0049(4)	0.0046(5)	0.0049(5)	0.0048(5)	0.0026(6)
	U_{23}	0.0001(4)	0.0000(4)	0.0001(4)	0.0005(4)	-0.0001(4)
	U_{13}	0.0009(4)	0.0008(4)	0.0004(4)	0.0007(4)	0.0005(4)
	U_{12}	0.0027(4)	0.0022(4)	0.0022(4)	0.0033(5)	0.0038(5)
	U_{eq}	0.0071(2)	0.0073(2)	0.0073(2)	0.0073(2)	0.0072(3)
O(7)	U_{11}	0.0063(5)	0.0056(5)	0.0061(5)	0.0062(6)	0.0065(6)
	U_{22}	0.0065(5)	0.0046(5)	0.0056(5)	0.0059(6)	0.0074(6)
	U_{33}	0.0054(5)	0.0064(5)	0.0056(5)	0.0056(6)	0.0028(6)
	U_{23}	-0.0003(4)	-0.0011(4)	-0.0007(4)	-0.0008(4)	-0.0013(4)
	U_{13}	0.0009(4)	0.0002(4)	0.0004(4)	0.0001(4)	-0.0001(4)
	U_{12}	0.0022(4)	0.0009(4)	0.0015(4)	0.0022(5)	0.0018(5)
	U_{eq}	0.0065(2)	0.0062(2)	0.0064(2)	0.0063(2)	0.0063(2)
O(8)	U_{11}	0.0060(5)	0.0060(5)	0.0062(5)	0.0058(6)	0.0073(6)
	U_{22}	0.0097(5)	0.0099(5)	0.0112(5)	0.0092(6)	0.0107(6)
	U_{33}	0.0072(5)	0.0077(5)	0.0080(5)	0.0080(6)	0.0052(6)
	U_{23}	0.0026(4)	0.0033(4)	0.0032(4)	0.0033(5)	0.0033(5)
	U_{13}	0.0011(4)	0.0012(4)	0.0008(4)	0.0010(5)	0.0010(5)
	U_{12}	0.0043(4)	0.0044(4)	0.0050(4)	0.0039(5)	0.0049(5)
	U_{eq}	0.0074(2)	0.0076(2)	0.0082(2)	0.0076(3)	0.0076(3)
H(3)*	U_{eq}	0.015	0.015	0.015	0.015	0.015

* Fixed during refinement

APPENDIX A.2.2. (CON'T)

		LID16	LID17	LID18	LID19	LID20
X	U_{11}	0.0150(3)	0.0152(3)	0.0147(3)	0.0145(3)	0.0146(4)
	U_{22}	0.0150(3)	0.0152(3)	0.0147(3)	0.0145(3)	0.0146(4)
	U_{33}	0.0125(4)	0.0141(5)	0.0127(4)	0.0132(4)	0.0116(5)
	U_{23}	0	0	0	0	0
	U_{13}	0	0	0	0	0
	U_{12}	0.00752(15)	0.00759(17)	0.00733(16)	0.00726(17)	0.00730(18)
	U_{eq}	0.0142(2)	0.0148(3)	0.0140(3)	0.0141(3)	0.0136(3)
Y	U_{11}	0.0109(5)	0.0103(6)	0.0110(6)	0.0094(6)	0.0105(7)
	U_{22}	0.0080(4)	0.0089(4)	0.0089(5)	0.0098(5)	0.0077(5)
	U_{33}	0.0131(6)	0.0142(60	0.0139(6)	0.0136(6)	0.0136(7)
	U_{23}	-	-	-0.0011(2)	-0.0011(2)	-0.0013(2)
	U_{13}	-0.0026(4)	-0.0024(4)	-0.0022(4)	-0.0022(4)	-0.0026(5)
	U_{12}	0.0055(3)	0.0051(3)	0.0055(3)	0.0047(30	0.0053(3)
	U_{eq}	0.0103(3)	0.0110(3)	0.0110(4)	0.0110(4)	0.0103(4)
Z	U_{11}	0.00612(18)	0.0063(2)	0.0064(2)	0.0061(2)	0.0062(2)
	U_{22}	0.00745(19)	0.0076(2)	0.0073(2)	0.0076(2)	0.0074(2)
	U_{33}	0.00517(15)	0.00514(17)	0.00562(16)	0.00520(17)	0.00472(18)
	U_{23}	0.00071(14)	0.00062(16)	0.00060(15)	0.00074(15)	0.00064(17)
	U_{13}	0.00025(14)	-	0.00016(15)	-	-
	U_{12}	0.00377(14)	0.00381(16)	0.00383(16)	0.00387(16)	0.00381(17)
	U_{eq}	0.00608(9)	0.00616(10)	0.00626(10)	0.00609(10)	0.00590(10)
T	U_{11}	0.00478(17)	0.00520(19)	0.00512(18)	0.00461(18)	0.0047(2)
	U_{22}	0.00468(16)	0.00493(18)	0.00474(17)	0.00491(18)	0.00450(19)
	U_{33}	0.00503(14)	0.00549(16)	0.00580(16)	0.00570(16)	0.00455(16)
	U_{23}	-	-	-	-	-
	U_{13}	0.00007(12)	0.00026(14)	0.00004(14)	0.00027(14)	0.00024(15)
	U_{12}	0.00214(11)	0.00232(13)	0.00233(13)	0.00233(13)	0.00203(14)
	U_{eq}	0.00493(8)	0.00530(9)	0.00528(9)	0.00509(9)	0.00471(9)
B	U_{11}	0.0071(6)	0.0075(7)	0.0077(7)	0.0072(7)	0.0083(8)
	U_{22}	0.0094(9)	0.0090(10)	0.009(1)	0.009(1)	0.0092(11)
	U_{33}	0.0048(8)	0.0055(9)	0.0042(9)	0.0052(9)	0.004(1)
	U_{23}	-0.0002(6)	-0.0015(7)	-0.0007(7)	-0.0011(7)	-0.0002(8)
	U_{13}	-0.0001(3)	-0.0008(4)	-0.0003(4)	-0.0006(4)	-0.0001(4)
	U_{12}	0.0047(4)	0.0045(5)	0.0046(5)	0.0045(5)	0.0046(5)
	U_{eq}	0.0068(3)	0.0071(4)	0.0069(4)	0.0069(4)	0.0070(4)

APPENDIX A.2.2. (CON'T)

		LID16	LID17	LID18	LID19	LID20
O(1)[d]	U_{11}	0.0131(9)	0.015(1)	0.013(1)	0.014(1)	0.0138(11)
O(1)[o]	U_{11}	0.0674(17)	0.0718(19)	0.0659(18)	0.0716(19)	0.0675(19)
	U_{22}	0.0674(17)	0.0718(19)	0.0659(18)	0.0716(19)	0.0675(19)
	U_{33}	0.0128(14)	0.0128(15)	0.0130(15)	0.0121(15)	0.0122(16)
	U_{23}	0	0	0	0	0
	U_{13}	0	0	0	0	0
	U_{12}	0.0337(9)	0.0359(9)	0.0329(9)	0.036(1)	0.0338(9)
	U_{eq}	0.0492(10)	0.0521(12)	0.0482(11)	0.0518(12)	0.0491(12)
O(2)[d]	U_{11}	0.0093(4)	0.0091(4)	0.0092(4)	0.0089(4)	0.0086(5)
O(2)[o]	U_{11}	0.0243(7)	0.0244(8)	0.0241(8)	0.0243(8)	0.0236(8)
	U_{22}	0.0243(7)	0.0244(8)	0.0241(8)	0.0243(8)	0.0236(8)
	U_{33}	0.0135(8)	0.0125(8)	0.0124(8)	0.0129(8)	0.0122(9)
	U_{23}	-0.0001(3)	-0.0002(3)	-0.0003(3)	-0.0001(3)	0.0002(3)
	U_{13}	0.0001(3)	0.0002(3)	0.0003(3)	0.0001(3)	-0.0002(3)
	U_{12}	0.0218(8)	0.0216(9)	0.0212(8)	0.0219(8)	0.0210(9)
	U_{eq}	0.0164(4)	0.0162(4)	0.0161(4)	0.0162(4)	0.0157(4)
O(3)	U_{11}	0.0222(8)	0.0220(9)	0.0220(9)	0.0208(8)	0.0210(9)
	U_{22}	0.0097(5)	0.0096(5)	0.0102(5)	0.0092(5)	0.0097(6)
	U_{33}	0.0043(6)	0.0045(7)	0.0049(7)	0.0052(7)	0.0043(7)
	U_{23}	-0.0004(3)	0.0000(3)	-0.0004(3)	-0.0007(3)	-0.0008(3)
	U_{13}	-0.0008(5)	-0.0001(6)	-0.0008(6)	-0.0014(6)	-0.0015(7)
	U_{12}	0.0111(4)	0.0110(4)	0.0110(4)	0.0104(4)	0.0105(5)
	U_{eq}	0.0107(3)	0.0106(3)	0.0111(3)	0.0105(3)	0.0104(3)
O(4)	U_{11}	0.0065(4)	0.0067(5)	0.0067(5)	0.0066(5)	0.0063(5)
	U_{22}	0.0122(7)	0.0136(8)	0.0132(8)	0.0117(8)	0.0108(8)
	U_{33}	0.0083(6)	0.0070(6)	0.0071(6)	0.0078(6)	0.0073(7)
	U_{23}	-0.0009(5)	-0.0013(6)	-0.0007(6)	-0.0010(6)	-0.0016(6)
	U_{13}	-0.0005(3)	-0.0007(3)	-0.0004(3)	-0.0005(3)	-0.0008(3)
	U_{12}	0.0061(3)	0.0068(4)	0.0066(4)	0.0059(4)	0.0054(4)
	U_{eq}	0.0084(3)	0.0084(3)	0.0083(3)	0.0081(3)	0.0077(3)
O(5)	U_{11}	0.0144(7)	0.0141(8)	0.0140(8)	0.0123(8)	0.0147(9)
	U_{22}	0.0073(4)	0.0078(5)	0.0068(5)	0.0076(5)	0.0065(5)
	U_{33}	0.0056(6)	0.0066(7)	0.0069(6)	0.0066(6)	0.0049(7)
	U_{23}	0.0004(2)	0.0001(3)	0.0003(3)	0.0001(3)	0.0002(3)
	U_{13}	0.0007(5)	0.0003(5)	0.0006(5)	0.0003(5)	0.0003(6)
	U_{12}	0.0072(4)	0.0070(4)	0.0070(4)	0.0062(4)	0.0073(4)
	U_{eq}	0.0083(3)	0.0088(3)	0.0085(3)	0.0083(3)	0.0078(3)

APPENDIX A.2.2. (CON'T)

		LID16	LID17	LID18	LID19	LID20
O(6)	U_{11}	0.0068(4)	0.0071(5)	0.0072(5)	0.0065(5)	0.0064(5)
	U_{22}	0.0081(4)	0.0077(5)	0.0089(5)	0.0081(5)	0.0073(5)
	U_{33}	0.0048(4)	0.0053(4)	0.0049(4)	0.0051(4)	0.0046(5)
	U_{23}	0.0002(3)	0.0000(4)	-0.0001(4)	0.0000(4)	-0.0001(4)
	U_{13}	0.0007(3)	0.0009(4)	0.0006(4)	0.0005(4)	0.0009(4)
	U_{12}	0.0024(4)	0.0026(4)	0.0029(4)	0.0028(4)	0.0019(4)
	U_{eq}	0.00718(18)	0.0072(2)	0.0075(2)	0.0070(2)	0.0068(2)
O(7)	U_{11}	0.0053(4)	0.0057(4)	0.0056(5)	0.0058(5)	0.0056(5)
	U_{22}	0.0057(4)	0.0053(5)	0.0054(5)	0.0057(5)	0.0056(5)
	U_{33}	0.0053(4)	0.0054(5)	0.0060(5)	0.0054(5)	0.0048(5)
	U_{23}	-0.0011(3)	-0.0004(4)	-0.0010(3)	-0.0007(3)	-0.0008(4)
	U_{13}	0.0005(3)	0.0003(4)	-0.0001(3)	0.0000(3)	0.0010(4)
	U_{12}	0.0014(3)	0.0013(4)	0.0017(4)	0.0016(4)	0.0015(4)
	U_{eq}	0.00602(17)	0.00614(19)	0.00616(19)	0.00618(19)	0.0059(2)
O(8)	U_{11}	0.0052(4)	0.0050(5)	0.0052(5)	0.0052(5)	0.0057(5)
	U_{22}	0.0096(5)	0.0095(5)	0.0094(5)	0.0091(5)	0.0089(5)
	U_{33}	0.0077(4)	0.0078(5)	0.0079(4)	0.0077(5)	0.0069(5)
	U_{23}	0.0034(3)	0.0032(4)	0.0033(4)	0.0033(4)	0.0035(4)
	U_{13}	0.0010(4)	0.0012(4)	0.0010(4)	0.0010(4)	0.0005(4)
	U_{12}	0.0041(4)	0.0038(4)	0.0038(4)	0.0039(4)	0.0041(4)
	U_{eq}	0.00735(19)	0.0074(2)	0.0074(2)	0.0072(2)	0.0069(2)
H(3)*	U_{eq}	0.015	0.015	0.015	0.015	0.015

* Fixed during refinement

APPENDIX A.2.2. (CON'T)

		LID21	LID22	LID23	LID24	LID25
X	U_{11}	0.0160(4)	0.0128(5)	0.0149(3)	0.0145(3)	0.0155(4)
	U_{22}	0.0160(4)	0.0128(5)	0.0149(3)	0.0145(3)	0.0155(4)
	U_{33}	0.0121(5)	0.0150(7)	0.0124(4)	0.0124(4)	0.0123(5)
	U_{23}	0	0	0	0	0
	U_{13}	0	0	0	0	0
	U_{12}	0.00797(19)	0.0064(2)	0.00744(16)	0.00723(16)	0.0077(2)
	U_{eq}	0.0147(3)	0.0135(4)	0.0141(3)	0.0138(3)	0.0144(3)
Y	U_{11}	0.0089(6)	0.0071(9)	0.0096(6)	0.0102(6)	0.0088(6)
	U_{22}	0.0100(5)	0.0057(7)	0.0085(4)	0.0095(5)	0.0086(5)
	U_{33}	0.0123(6)	0.0154(9)	0.0135(6)	0.0144(6)	0.0120(6)
	U_{23}	-	-0.0015(3)	-	-0.0012(2)	-0.0010(2)
	U_{13}	-0.0026(4)	-0.0029(6)	-0.0023(4)	-0.0024(4)	-0.0020(4)
	U_{12}	0.0045(3)	0.0036(4)	0.0048(3)	0.0051(3)	0.0044(3)
	U_{eq}	0.0105(4)	0.0093(6)	0.0104(4)	0.0113(4)	0.0098(4)
Z	U_{11}	0.0064(2)	0.0042(3)	0.00607(18)	0.0064(2)	0.0063(2)
	U_{22}	0.0076(2)	0.0061(3)	0.00743(19)	0.0075(2)	0.0080(2)
	U_{33}	0.00444(17)	0.0074(3)	0.00514(15)	0.00524(17)	0.00451(19)
	U_{23}	0.00040(16)	0.0008(2)	0.00079(14)	0.00073(16)	0.00078(17)
	U_{13}	-	0.0003(2)	0.00017(14)	0.00010(16)	0.00002(17)
	U_{12}	0.00397(17)	0.0030(2)	0.00381(15)	0.00403(16)	0.00411(18)
	U_{eq}	0.00592(10)	0.00570(16)	0.00602(9)	0.00617(10)	0.00601(11)
T	U_{11}	0.0051(2)	0.0030(3)	0.00466(17)	0.00493(19)	0.0049(2)
	U_{22}	0.00481(19)	0.0029(3)	0.00472(16)	0.00479(18)	0.0048(2)
	U_{33}	0.00456(16)	0.0076(3)	0.00550(15)	0.00520(16)	0.00450(18)
	U_{23}	-	-	-	-	-
	U_{13}	0.00003(15)	0.0001(2)	0.00013(13)	0.00038(14)	0.00007(15)
	U_{12}	0.00225(14)	0.00137(19)	0.00218(12)	0.00225(13)	0.00225(14)
	U_{eq}	0.00494(9)	0.00454(15)	0.00503(8)	0.00505(9)	0.00480(10)
B	U_{11}	0.0075(7)	0.0059(10)	0.0071(6)	0.0069(7)	0.0082(8)
	U_{22}	0.0097(11)	0.0074(15)	0.0093(9)	0.008(1)	0.0101(11)
	U_{33}	0.0038(9)	0.0070(14)	0.0048(8)	0.0051(9)	0.002(1)
	U_{23}	-0.0012(8)	-0.000(1)	-0.0014(7)	-0.0008(7)	-0.0002(8)
	U_{13}	-0.0006(4)	-0.0001(5)	-0.0007(3)	-0.0004(4)	-0.0001(4)
	U_{12}	0.0048(5)	0.0037(7)	0.0046(5)	0.0042(5)	0.0050(6)
	U_{eq}	0.0068(4)	0.0066(6)	0.0068(4)	0.0067(4)	0.0065(4)

APPENDIX A.2.2. (CON'T)

		LID21	LID22	LID23	LID24	LID25
O(1)[d]	U_{11}	0.0152(11)	0.0129(14)	0.0140(9)	0.013(1)	0.0125(10)
O(1)[o]	U_{11}	0.073(2)	0.068(3)	0.0681(17)	0.0693(18)	0.074(2)
	U_{22}	0.073(2)	0.068(3)	0.0681(17)	0.0693(18)	0.074(2)
	U_{33}	0.0131(16)	0.012(2)	0.0139(15)	0.0108(15)	0.0106(16)
	U_{23}	0	0	0	0	0
	U_{13}	0	0	0	0	0
	U_{12}	0.0363(1)	0.0340(14)	0.0341(9)	0.0347(9)	0.0368(11)
	U_{eq}	0.0527(12)	0.0494(17)	0.0500(11)	0.0498(11)	0.0526(14)
O(2)[d]	U_{11}	0.0089(5)	0.0103(7)	0.0088(4)	0.0087(4)	0.0079(5)
O(2)[o]	U_{11}	0.0255(8)	0.0230(12)	0.0242(7)	0.0242(8)	0.0250(9)
	U_{22}	0.0255(8)	0.0230(12)	0.0242(7)	0.0242(8)	0.0250(9)
	U_{33}	0.0126(9)	0.0169(13)	0.0135(8)	0.0126(8)	0.0107(9)
	U_{23}	0.0000(3)	-0.0004(4)	-0.0003(3)	-0.0001(3)	0.0000(3)
	U_{13}	0.0000(3)	0.0004(4)	0.0003(3)	0.0001(3)	0.0000(3)
	U_{12}	0.0231(9)	0.0212(12)	0.0221(8)	0.0219(8)	0.023(1)
	U_{eq}	0.0166(4)	0.0167(6)	0.0162(4)	0.0160(4)	0.0157(5)
O(3)	U_{11}	0.0208(9)	0.0184(12)	0.0208(8)	0.0205(9)	0.0197(9)
	U_{22}	0.0095(6)	0.0076(8)	0.0090(5)	0.0099(5)	0.0092(6)
	U_{33}	0.0040(7)	0.0074(10)	0.0054(6)	0.0046(7)	0.0040(8)
	U_{23}	-0.0002(3)	-0.0004(4)	-0.0005(3)	-0.0002(3)	-0.0004(3)
	U_{13}	-0.0003(6)	-0.0008(9)	-0.0009(5)	-0.0005(6)	-0.0008(7)
	U_{12}	0.0104(5)	0.0092(6)	0.0104(4)	0.0103(4)	0.0099(5)
	U_{eq}	0.0102(3)	0.0100(5)	0.0104(3)	0.0105(3)	0.0098(3)
O(4)	U_{11}	0.0066(5)	0.0055(7)	0.0060(4)	0.0065(5)	0.0061(5)
	U_{22}	0.0119(8)	0.0112(11)	0.0127(7)	0.0122(8)	0.0122(9)
	U_{33}	0.0073(7)	0.0078(9)	0.0082(6)	0.0074(6)	0.0077(7)
	U_{23}	-0.0018(6)	-0.0007(8)	-0.0008(5)	-0.0012(6)	-0.0012(6)
	U_{13}	-0.0009(3)	-0.0004(4)	-0.0004(3)	-0.0006(3)	-0.0006(3)
	U_{12}	0.0059(4)	0.0056(6)	0.0063(4)	0.0061(4)	0.0061(4)
	U_{eq}	0.0080(3)	0.0075(4)	0.0082(3)	0.0081(3)	0.0080(3)
O(5)	U_{11}	0.0134(8)	0.0126(12)	0.0134(7)	0.0139(8)	0.0138(9)
	U_{22}	0.0083(5)	0.0059(7)	0.0072(4)	0.0071(5)	0.0068(5)
	U_{33}	0.0059(7)	0.009(1)	0.0065(6)	0.0063(7)	0.0054(7)
	U_{23}	0.0000(3)	0.0007(4)	0.0003(2)	0.0003(3)	0.0002(3)
	U_{13}	0.0000(6)	0.0013(8)	0.0005(5)	0.0005(5)	0.0005(6)
	U_{12}	0.0067(4)	0.0063(6)	0.0067(4)	0.0070(4)	0.0069(4)
	U_{eq}	0.0086(3)	0.0084(4)	0.0083(3)	0.0083(3)	0.0079(3)

APPENDIX A.2.2. (CON'T)

		LID21	LID22	LID23	LID24	LID25
O(6)	U_{11}	0.0079(5)	0.0045(7)	0.0068(4)	0.0069(5)	0.0075(5)
	U_{22}	0.0082(5)	0.0061(7)	0.0082(5)	0.0083(5)	0.0086(6)
	U_{33}	0.0041(5)	0.0071(7)	0.0045(4)	0.0053(4)	0.0029(5)
	U_{23}	0.0000(4)	0.0002(5)	0.0002(3)	0.0001(4)	-0.0003(4)
	U_{13}	0.0005(4)	0.0006(5)	0.0005(3)	0.0012(4)	0.0001(4)
	U_{12}	0.0033(4)	0.0011(6)	0.0028(4)	0.0026(4)	0.0029(4)
	U_{eq}	0.0071(2)	0.0066(3)	0.00692(19)	0.0074(2)	0.0068(2)
O(7)	U_{11}	0.0061(50	0.0038(7)	0.0053(4)	0.0057(5)	0.0063(5)
	U_{22}	0.0059(5)	0.0045(7)	0.0052(4)	0.0059(5)	0.0054(5)
	U_{33}	0.0044(5)	0.0085(7)	0.0058(4)	0.0056(5)	0.0051(5)
	U_{23}	-0.0007(4)	-0.0007(5)	-0.0013(3)	-0.0007(4)	-0.0008(4)
	U_{13}	0.0001(4)	0.0006(5)	0.00012(3)	0.0007(4)	0.0003(4)
	U_{12}	0.0017(40	0.0009(6)	0.0012(3)	0.0016(4)	0.0016(4)
	U_{eq}	0.0061(2)	0.0061(3)	0.00607(18)	0.0063(2)	0.0062(2)
O(8)	U_{11}	0.0058(5)	0.0039(7)	0.0057(4)	0.0056(5)	0.0065(5)
	U_{22}	0.0100(5)	0.0083(8)	0.0087(5)	0.0093(5)	0.0099(6)
	U_{33}	0.0068(5)	0.0103(7)	0.0084(4)	0.0077(5)	0.0070(5)
	U_{23}	0.0033(4)	0.0035(5)	0.0033(3)	0.0039(4)	0.0033(4)
	U_{13}	0.0009(4)	0.0017(6)	0.0015(4)	0.0011(4)	0.0010(4)
	U_{12}	0.0043(4)	0.0038(6)	0.0041(4)	0.0038(4)	0.0048(5)
	U_{eq}	0.0074(2)	0.0072(3)	0.00736(19)	0.0075(2)	0.0075(2)
H(3)*	U_{eq}	0.015	0.015	0.015	0.015	0.015

* Fixed during refinement

APPENDIX A.2.2. (CON'T)

		LID26	LID27	LID28	SHW1	SHW2
X	U_{11}	0.0152(4)	0.0154(4)	0.0164(3)	0.0194(7)	0.0168(7)
	U_{22}	0.0152(4)	0.0154(4)	0.0164(3)	0.0194(7)	0.0168(7)
	U_{33}	0.0134(5)	0.0133(5)	0.0131(4)	0.0161(9)	0.018(1)
	U_{23}	0	0	0	0	0
	U_{13}	0	0	0	0	0
	U_{12}	0.00760(19)	0.00768(18)	0.00819(17)	0.0097(3)	0.0084(3)
	U_{eq}	0.0146(3)	0.0147(3)	0.0153(3)	0.0183(5)	0.0170(5)
Y	U_{11}	0.0099(6)	0.0119(6)	0.0096(5)	0.0093(5)	0.0089(6)
	U_{22}	0.0105(5)	0.0094(5)	0.0091(4)	0.0076(4)	0.0085(4)
	U_{33}	0.0145(7)	0.0132(6)	0.0127(5)	0.0141(5)	0.0140(6)
	U_{23}	-0.0011(2)	-0.0012(2)	-	-	-
	U_{13}	-0.0021(4)	-0.0025(4)	-0.0019(4)	-0.0026(3)	-0.0029(4)
	U_{12}	0.0050(3)	0.0059(3)	0.0048(3)	0.0046(2)	0.0045(3)
	U_{eq}	0.0117(4)	0.0112(4)	0.0104(3)	0.0102(3)	0.0104(4)
Z	U_{11}	0.0062(2)	0.0064(2)	0.0062(2)	0.0064(2)	0.0076(2)
	U_{22}	0.0075(3)	0.0079(2)	0.0078(2)	0.0080(2)	0.0085(2)
	U_{33}	0.00527(19)	0.00482(18)	0.00507(16)	0.00576(17)	0.0063(2)
	U_{23}	0.00036(18)	0.00077(17)	0.00056(15)	0.00035(15)	0.00036(16)
	U_{13}	-	0.00024(17)	0.00003(15)	-	-
	U_{12}	0.00406(19)	0.00409(17)	0.00390(16)	0.00394(16)	0.00441(17)
	U_{eq}	0.00606(11)	0.00613(10)	0.00619(10)	0.00660(11)	0.00727(12)
T	U_{11}	0.0048(2)	0.0051(2)	0.00506(18)	0.0051(2)	0.0058(2)
	U_{22}	0.0046(2)	0.00476(19)	0.00471(17)	0.0049(2)	0.0058(2)
	U_{33}	0.00528(18)	0.00499(17)	0.00512(15)	0.00554(19)	0.0060(2)
	U_{23}	-	-	-	-	-
	U_{13}	0.00004(16)	0.00021(15)	0.00004(14)	-	-
	U_{12}	0.00235(15)	0.00238(14)	0.00228(13)	0.00191(14)	0.00255(15)
	U_{eq}	0.00490(10)	0.00500(9)	0.00504(9)	0.00540(14)	0.00598(15)
B	U_{11}	0.0062(8)	0.0062(7)	0.0075(7)	0.0073(7)	0.0081(7)
	U_{22}	0.0089(11)	0.0097(11)	0.009(1)	0.010(1)	0.0098(10)
	U_{33}	0.0040(10)	0.005(1)	0.0043(9)	0.0050(9)	0.0069(11)
	U_{23}	0.0000(8)	0.0001(8)	-0.0008(7)	0.0003(7)	-0.0004(8)
	U_{13}	0.0000(4)	0.0000(4)	-0.0004(4)	0.0001(4)	-0.0002(4)
	U_{12}	0.0044(6)	0.0048(5)	0.0043(5)	0.0048(5)	0.0049(5)
		0.0061(4)	0.0067(4)	0.0067(4)	0.0070(4)	0.0081(4)

APPENDIX A.2.2. (CON'T)

		LID26	LID27	LID28	SHW1	SHW2
O(1)[d]	U_{11}	0.0037(10)	0.0131(10)	0.0144(9)	0.0084(10)	0.0095(12)
O(1)[o]	U_{11}	0.072(2)	0.070(2)	0.0732(19)	0.0428(14)	0.0427(15)
	U_{22}	0.072(2)	0.070(2)	0.0732(19)	0.0428(14)	0.0427(15)
	U_{33}	0.0156(18)	0.0113(16)	0.0138(15)	0.0077(14)	0.0091(17)
	U_{23}	0	0	0	0	0
	U_{13}	0	0	0	0	0
	U_{12}	0.0361(11)	0.035(1)	0.036(1)	0.0214(7)	0.0213(7)
	U_{eq}	0.0533(13)	0.0502(12)	0.0534(12)	0.0311(9)	0.0315(9)
O(2)[d]	U_{11}	0.0092(5)	0.0080(5)	0.0086(4)	0.0108(5)	0.0110(5)
O(2)[o]	U_{11}	0.0241(9)	0.0254(9)	0.0248(8)	0.0212(7)	0.0209(7)
	U_{22}	0.0241(9)	0.0254(9)	0.0248(8)	0.0074(7)	0.0066(7)
	U_{33}	0.0125(9)	0.0104(9)	0.0115(8)	0.0142(8)	0.0170(10)
	U_{23}	-0.0005(4)	-0.0004(3)	-0.0006(3)	0.0000(6)	-0.0003(6)
	U_{13}	0.0005(4)	0.0004(3)	0.0006(3)	0.0000(3)	-0.0002(3)
	U_{12}	0.022(1)	0.0228(9)	0.0221(9)	0.0037(4)	0.0033(4)
	U_{eq}	0.0160(4)	0.0159(4)	0.0160(4)	0.0158(4)	0.0164(4)
O(3)	U_{11}	0.019(1)	0.0209(9)	0.0201(8)	0.0247(9)	0.027(1)
	U_{22}	0.0086(6)	0.0098(6)	0.0091(5)	0.0101(5)	0.0110(5)
	U_{33}	0.0049(8)	0.0039(7)	0.0051(7)	0.0062(7)	0.0048(8)
	U_{23}	-0.0003(3)	-0.0003(3)	-0.0004(3)	-0.0008(3)	-0.0010(3)
	U_{13}	-0.0006(7)	-0.0007(6)	-0.0007(6)	-0.0017(6)	-0.0019(7)
	U_{12}	0.0097(5)	0.0105(5)	0.0100(4)	0.0124(5)	0.0134(5)
	U_{eq}	0.0098(4)	0.0103(3)	0.0102(3)	0.0121(3)	0.0125(3)
O(4)	U_{11}	0.0063(6)	0.0064(5)	0.0070(5)	0.0084(5)	0.0084(5)
	U_{22}	0.0126(9)	0.0128(8)	0.0121(8)	0.0124(8)	0.0142(8)
	U_{33}	0.0074(7)	0.0080(7)	0.0078(6)	0.0082(6)	0.0104(8)
	U_{23}	-0.0012(7)	-0.0016(6)	-0.0011(6)	-0.0012(6)	-0.0015(6)
	U_{13}	-0.0006(3)	-0.0008(3)	-0.0006(3)	-0.0006(3)	-0.0008(3)
	U_{12}	0.0063(5)	0.0064(4)	0.0060(4)	0.0062(4)	0.0071(4)
	U_{eq}	0.0081(3)	0.0083(3)	0.0084(3)	0.0092(3)	0.0104(3)
O(5)	U_{11}	0.0129(9)	0.0151(9)	0.0135(8)	0.0149(8)	0.0158(8)
	U_{22}	0.0072(5)	0.0074(5)	0.0075(5)	0.0088(5)	0.0093(5)
	U_{33}	0.0072(8)	0.0061(7)	0.0057(6)	0.0066(7)	0.0085(8)
	U_{23}	-0.0001(3)	0.0003(3)	0.0003(3)	0.0005(3)	0.0006(3)
	U_{13}	-0.0001(6)	0.0005(6)	0.0006(5)	0.0009(5)	0.0011(6)
	U_{12}	0.0065(5)	0.0076(4)	0.0067(4)	0.0075(4)	0.0079(4)
	U_{eq}	0.0085(3)	0.0087(3)	0.0082(3)	0.0094(3)	0.0105(3)

APPENDIX A.2.2. (CON'T)

		LID26	LID27	LID28	SHW1	SHW2
O(6)	U_{11}	0.0062(5)	0.0066(5)	0.0072(5)	0.0076(5)	0.0077(5)
	U_{22}	0.0083(6)	0.0082(5)	0.0080(5)	0.0088(5)	0.0095(5)
	U_{33}	0.0052(5)	0.0044(5)	0.0045(4)	0.0060(4)	0.0062(5)
	U_{23}	0.0000(4)	-0.0002(4)	-0.0001(4)	0.0000(4)	-0.0007(4)
	U_{13}	0.0008(4)	0.0000(4)	0.0007(3)	0.0005(4)	0.0005(4)
	U_{12}	0.0023(5)	0.0029(4)	0.0025(4)	0.0032(4)	0.0033(4)
	U_{eq}	0.0071(2)	0.0068(2)	0.0071(2)	0.0079(2)	0.0083(2)
O(7)	U_{11}	0.0060(5)	0.0055(5)	0.0056(4)	0.0067(5)	0.0077(5)
	U_{22}	0.0056(5)	0.0057(5)	0.0055(4)	0.0070(5)	0.0074(5)
	U_{33}	0.0055(5)	0.0057(5)	0.0060(4)	0.0058(4)	0.0063(5)
	U_{23}	-0.0013(4)	-0.0010(4)	-0.0013(3)	-0.0012(4)	-0.0014(4)
	U_{13}	0.0002(4)	0.0001(4)	-0.0001(3)	0.0002(4)	0.0001(4)
	U_{12}	0.0019(4)	0.0014(4)	0.0019(4)	0.0023(4)	0.0027(4)
	U_{eq}	0.0061(2)	0.0063(2)	0.00608(19)	0.00699(19)	0.0076(2)
O(8)	U_{11}	0.0054(6)	0.0052(5)	0.0057(5)	0.0054(5)	0.0064(5)
	U_{22}	0.0092(6)	0.0097(5)	0.0096(5)	0.0096(95)	0.0102(5)
	U_{33}	0.0079(5)	0.0077(5)	0.0077(4)	0.0084(5)	0.0088(5)
	U_{23}	0.0022(4)	0.0030(4)	0.0037(4)	0.0029(4)	0.0027(4)
	U_{13}	0.0002(5)	0.0011(4)	0.0011(4)	0.0002(4)	0.0006(4)
	U_{12}	0.0040(5)	0.0041(4)	0.0040(4)	0.0039(4)	0.0047(4)
	U_{eq}	0.0073(2)	0.0073(2)	0.0076(2)	0.0077(2)	0.0082(2)
H(3)*	U_{eq}	0.015	0.015	0.015	0.015	0.015

* Fixed during refinement

APPENDIX A.2.2. (CON'T)

		SHW3	SHW4	SHW5	SHW6	SHW7
X	U_{11}	0.0250(13)	0.0241(9)	0.0192(6)	0.0212(8)	0.0174(12)
	U_{22}	0.0250(13)	0.0241(9)	0.0192(6)	0.0212(8)	0.0174(12)
	U_{33}	0.0207(17)	0.0246(13)	0.0238(8)	0.0166(11)	0.0111(15)
	U_{23}	0	0	0	0	0
	U_{13}	0	0	0	0	0
	U_{12}	0.0125(6)	0.0121(4)	0.0096(3)	0.0106(4)	0.0087(6)
	U_{eq}	0.0236(10)	0.0243(7)	0.0208(5)	0.0197(7)	0.015(1)
Y	U_{11}	0.0145(7)	0.0136(5)	0.0124(5)	0.0092(5)	0.011(1)
	U_{22}	0.0112(5)	0.0102(4)	0.0096(4)	0.0078(4)	0.0081(7)
	U_{33}	0.0148(7)	0.0162(6)	0.0175(5)	0.0137(6)	0.013(1)
	U_{23}	-0.0015(3)	-	-	-	-0.0016(3)
	U_{13}	-0.0030(5)	-0.0027(4)	-0.0036(4)	-0.0019(4)	-0.0032(7)
	U_{12}	0.0073(4)	0.0068(3)	0.0062(3)	0.0046(3)	0.0053(5)
	U_{eq}	0.0131(4)	0.0129(3)	0.0129(3)	0.0101(3)	0.0104(6)
Z	U_{11}	0.0086(4)	0.0087(3)	0.0092(2)	0.0083(2)	0.0073(4)
	U_{22}	0.0117(4)	0.0110(3)	0.0107(2)	0.0099(2)	0.0099(4)
	U_{33}	0.0053(3)	0.0072(3)	0.00841(17)	0.00776(19)	0.0053(3)
	U_{23}	0.0008(3)	0.0009(2)	0.00089(15)	0.00061(17)	0.0004(3)
	U_{13}	0.0002(3)	0.0004(2)	0.00002(15)	0.00017(17)	-0.0005(3)
	U_{12}	0.0058(3)	0.006(2)	0.00534(16)	0.00490(17)	0.0051(3)
	U_{eq}	0.00824(19)	0.00867(13)	0.00929(10)	0.00850(11)	0.00717(18)
T	U_{11}	0.0059(4)	0.0065(3)	0.0071(2)	0.0066(2)	0.0054(4)
	U_{22}	0.0061(4)	0.0063(3)	0.0065(2)	0.0060(2)	0.0053(4)
	U_{33}	0.0046(3)	0.0069(3)	0.00744(19)	0.0073(2)	0.0057(3)
	U_{23}	-0.0005(3)	-	-	-	-0.0010(3)
	U_{13}	-0.0002(3)	-0.0002(2)	-	-	-0.0002(3)
	U_{12}	0.0026(3)	0.00285(18)	0.00294(14)	0.00252(15)	0.0021(3)
	U_{eq}	0.0057(2)	0.00670(17)	0.00722(13)	0.00692(14)	0.0057(2)
B	U_{11}	0.0108(14)	0.010(1)	0.0101(7)	0.0097(8)	0.0089(14)
	U_{22}	0.014(2)	0.0129(14)	0.0127(10)	0.0117(11)	0.013(2)
	U_{33}	0.0071(18)	0.0089(14)	0.0093(9)	0.0074(10)	0.0077(18)
	U_{23}	-0.0028(15)	-0.0010(11)	-0.0012(8)	-0.0025(8)	-0.0023(16)
	U_{13}	-0.0014(8)	-0.0005(5)	-0.0006(4)	-0.0012(4)	-0.0011(8)
	U_{12}	0.0072(10)	0.0065(7)	0.0064(5)	0.0059(5)	0.0063(10)
		0.0104(8)	0.0105(6)	0.0104(4)	0.0094(4)	0.0093(8)

APPENDIX A.2.2. (CON'T)

		SHW3	SHW4	SHW5	SHW6	SHW7
O(1)[d]	U_{11}	0.0165(19)	0.0170(14)	0.0217(11)	0.0097(12)	0.023(2)
O(1)[o]	U_{11}	0.078(4)	0.076(3)	0.0588(15)	0.0357(13)	0.052(3)
	U_{22}	0.078(4)	0.076(3)	0.0588(15)	0.0357(13)	0.052(3)
	U_{33}	0.017(3)	0.016(2)	0.0203(14)	0.0106(15)	0.023(3)
	U_{23}	0	0	0	0	0
	U_{13}	0	0	0	0	0
	U_{12}	0.0392(18)	0.0381(13)	0.0294(7)	0.0178(6)	0.0261(13)
	U_{eq}	0.058(2)	0.0560(16)	0.0459(9)	0.0273(8)	0.0426(16)
O(2)[d]	U_{11}	0.0102(8)	0.0109(6)	0.0125(5)	0.0122(5)	0.0105(9)
O(2)[o]	U_{11}	0.0290(15)	0.0276(11)	0.0240(7)	0.0206(7)	0.0229(13)
	U_{22}	0.0085(15)	0.0082(11)	0.0080(7)	0.0077(8)	0.0072(14)
	U_{33}	0.0121(15)	0.0138(12)	0.0170(8)	0.0171(9)	0.0138(15)
	U_{23}	-0.0022(12)	-0.0007(8)	-0.0003(6)	-0.0007(6)	0.0000(12)
	U_{13}	-0.0011(6)	-0.0003(4)	-0.0002(3)	-0.0003(4)	0.0000(6)
	U_{12}	0.0042(7)	0.0041(5)	0.0040(4)	0.0038(4)	0.0036(7)
	U_{eq}	0.0188(8)	0.0187(6)	0.0181(4)	0.0166(4)	0.0164(7)
O(3)	U_{11}	0.0231(16)	0.0228(12)	0.0277(9)	0.028(1)	0.0282(18)
	U_{22}	0.012(1)	0.0122(7)	0.0132(5)	0.0126(6)	0.0119(10)
	U_{33}	0.0029(12)	0.006(1)	0.0077(7)	0.0056(8)	0.0042(13)
	U_{23}	-0.0006(6)	0.0004(4)	-0.0004(3)	-0.0008(3)	-0.0015(6)
	U_{13}	-0.0011(11)	0.0008(8)	-0.0008(6)	-0.0016(7)	-0.0031(12)
	U_{12}	0.0116(8)	0.0114(6)	0.0138(5)	0.0141(5)	0.0141(9)
	U_{eq}	0.0113(6)	0.0124(4)	0.0146(3)	0.0137(4)	0.0130(6)
O(4)	U_{11}	0.010(1)	0.0096(7)	0.0104(5)	0.0104(6)	0.0104(10)
	U_{22}	0.0170(15)	0.0170(11)	0.0169(8)	0.0178(9)	0.0178(16)
	U_{33}	0.0090(12)	0.0101(9)	0.0118(7)	0.0104(7)	0.0083(12)
	U_{23}	-0.0004(11)	-0.0012(8)	-0.0007(6)	-0.0009(7)	0.0000(12)
	U_{13}	-0.0002(6)	-0.0006(4)	-0.0003(3)	-0.0005(3)	0.0000(6)
	U_{12}	0.0085(8)	0.0085(5)	0.0085(4)	0.0089(4)	0.0089(8)
	U_{eq}	0.0111(6)	0.0114(4)	0.0123(3)	0.0120(3)	0.0114(6)
O(5)	U_{11}	0.0137(14)	0.0157(11)	0.0178(8)	0.0166(9)	0.0144(15)
	U_{22}	0.0098(9)	0.0097(7)	0.0113(5)	0.0109(5)	0.0090(9)
	U_{33}	0.0112(13)	0.0116(10)	0.0111(7)	0.0112(8)	0.0114(14)
	U_{23}	0.0000(5)	0.0005(4)	-0.0000(3)	0.0004(3)	0.0003(6)
	U_{13}	0.0001(11)	0.0011(8)	-0.0001(6)	0.0007(6)	0.0005(11)
	U_{12}	0.0068(7)	0.0079(5)	0.0089(4)	0.0083(4)	0.0072(8)
	U_{eq}	0.0111(6)	0.0117(4)	0.0127(3)	0.0123(3)	0.0110(6)

APPENDIX A.2.2. (CON'T)

		SHW3	SHW4	SHW5	SHW6	SHW7
O(6)	U_{11}	0.0103(9)	0.0098(7)	0.0099(5)	0.0088(5)	0.0093(9)
	U_{22}	0.0107(9)	0.0108(7)	0.0112(5)	0.0103(5)	0.011(1)
	U_{33}	0.0057(8)	0.0068(6)	0.0082(4)	0.0077(5)	0.0067(8)
	U_{23}	-0.0004(7)	0.0000(5)	0.0000(4)	-0.0008(4)	-0.0010(8)
	U_{13}	0.0006(7)	0.0001(5)	0.0007(4)	-0.0001(4)	0.0011(7)
	U_{12}	0.0040(8)	0.0036(5)	0.0039(4)	0.0037(4)	0.0044(8)
	U_{eq}	0.0094(4)	0.0098(3)	0.0104(2)	0.0094(2)	0.0092(4)
O(7)	U_{11}	0.0068(9)	0.0074(6)	0.0085(5)	0.0079(5)	0.0071(9)
	U_{22}	0.0086(9)	0.0082(6)	0.0084(5)	0.0078(5)	0.0077(9)
	U_{33}	0.0051(8)	0.0076(6)	0.0083(5)	0.0083(5)	0.0062(8)
	U_{23}	-0.0015(7)	-0.0013(5)	-0.0005(4)	-0.0012(4)	-0.0010(7)
	U_{13}	-0.0006(7)	0.0000(5)	-0.0002(4)	-0.0001(4)	-0.0006(7)
	U_{12}	0.0022(7)	0.0021(5)	0.0026(4)	0.0026(4)	0.0024(7)
	U_{eq}	0.0076(4)	0.0085(3)	0.0091(2)	0.0086(2)	0.0076(4)
O(8)	U_{11}	0.0094(9)	0.0087(6)	0.0081(5)	0.0075(5)	0.0070(9)
	U_{22}	0.012(1)	0.0125(7)	0.0114(5)	0.0110(5)	0.010(1)
	U_{33}	0.0101(9)	0.0113(7)	0.0108(5)	0.0108(5)	0.0094(9)
	U_{23}	0.0037(7)	0.0037(5)	0.0031(4)	0.0027(4)	0.0041(7)
	U_{13}	0.0011(8)	0.0020(6)	0.0011(4)	0.0009(4)	0.0018(8)
	U_{12}	0.0061(8)	0.0063(6)	0.0053(4)	0.0052(4)	0.0049(8)
	U_{eq}	0.0103(4)	0.0104(3)	0.0099(2)	0.0095(2)	0.0087(4)
H(3)*	U_{eq}	0.015	0.015	0.015	0.015	0.015

* Fixed during refinement

APPENDIX A.2.2 (CON'T)

		SHW8	SHM1	SHM2	SHM3	SHM3A
X	U_{11}	0.0162(9)	0.0258(14)	0.027(2)	0.0249(11)	0.0279(12)
	U_{22}	0.0162(9)	0.0258(14)	0.027(2)	0.0249(11)	0.0279(12)
	U_{33}	0.0129(11)	0.0174(17)	0.022(3)	0.020(14)	0.0264(18)
	U_{23}	0	0	0	0	0
	U_{13}	0	0	0	0	0
	U_{12}	0.0081(4)	0.0129(7)	0.0137(11)	0.0124(5)	0.0139(6)
	U_{eq}	0.0151(7)	0.0230(11)	0.0258(18)	0.0233(9)	0.027(1)
Y	U_{11}	0.0097(8)	0.0089(6)	0.0100(9)	0.0115(4)	0.0129(4)
	U_{22}	0.0076(6)	0.0100(4)	0.0072(6)	0.0095(3)	0.0096(3)
	U_{33}	0.0148(8)	0.0136(6)	0.0142(9)	0.0140(4)	0.0145(4)
	U_{23}	-0.0015(3)	-0.0013(2)	-0.0013(3)	-	-
	U_{13}	-0.0030(5)	-0.0026(4)	-0.0026(6)	-0.0033(3)	-0.0038(3)
	U_{12}	0.0048(4)	0.0044(3)	0.0050(4)	0.0057(2)	0.00647(18)
	U_{eq}	0.0105(5)	0.0109(3)	0.0102(5)	0.0115(3)	0.0120(2)
Z	U_{11}	0.0081(3)	0.0077(3)	0.0074(4)	0.0080(2)	0.0067(3)
	U_{22}	0.0103(3)	0.0084(3)	0.0082(4)	0.0088(2)	0.0082(3)
	U_{33}	0.0072(3)	0.0055(2)	0.0069(4)	0.00628(19)	0.0066(3)
	U_{23}	0.0007(2)	0.0004(2)	0.0008(3)	0.00055(17)	0.0009(2)
	U_{13}	-0.0001(2)	-0.0004(2)	-0.0004(3)	-	0.0004(2)
	U_{12}	0.0053(3)	0.0041(2)	0.0037(3)	0.00442(18)	0.0042(2)
	U_{eq}	0.00826(15)	0.00718(13)	0.0075(2)	0.00757(12)	0.00694(13)
T	U_{11}	0.0058(3)	0.0062(3)	0.0077(5)	0.0062(2)	0.0051(3)
	U_{22}	0.0057(3)	0.0065(3)	0.0053(4)	0.0064(2)	0.0050(3)
	U_{33}	0.0068(3)	0.0056(2)	0.0065(4)	0.0059(2)	0.0065(3)
	U_{23}	-0.0009(2)	-	-0.0008(3)	-	-
	U_{13}	-0.0002(2)	0.00016(19)	0.0000(3)	0.00007(16)	-0.0003(2)
	U_{12}	0.0022(2)	0.00294(18)	0.0028(3)	0.00283(16)	0.00239(18)
	U_{eq}	0.00641(19)	0.00623(16)	0.0067(3)	0.00631(15)	0.00561(17)
B	U_{11}	0.0100(11)	0.0081(9)	0.0064(14)	0.0089(8)	0.009(1)
	U_{22}	0.0130(16)	0.0102(13)	0.0098(19)	0.0117(11)	0.0110(13)
	U_{33}	0.0086(14)	0.0073(12)	0.0084(18)	0.005(1)	0.0077(13)
	U_{23}	-0.0010(12)	-0.0011(10)	0.0000(15)	-0.0007(8)	-0.0009(11)
	U_{13}	-0.0005(6)	-0.0006(5)	0.0000(8)	-0.0004(4)	-0.0005(5)
	U_{12}	0.0065(8)	0.0051(7)	0.005(1)	0.0059(6)	0.0055(7)
		0.0102(6)	0.0083(5)	0.0078(8)	0.0082(4)	0.0092(6)

APPENDIX A.2.2. (CON'T)

		SHW8	SHM1	SHM2	SHM3	SHM3A
O(1)[d]	U_{11}	0.0213(18)	0.0169(18)	0.011(2)	0.0150(14)	0.0146(17)
O(1)[o]	U_{11}	0.0428(14)	0.0286(14)	0.025(2)	0.0301(12)	0.0383(17)
	U_{22}	0.0428(14)	0.0286(14)	0.025(2)	0.0301(12)	0.0383(17)
	U_{33}	0.0077(14)	0.0152(19)	0.011(3)	0.0133(16)	0.013(2)
	U_{23}	0	0	0	0	0
	U_{13}	0	0	0	0	0
	U_{12}	0.0214(7)	0.0143(7)	0.012(1)	0.0151(6)	0.0192(8)
	U_{eq}	0.0311(9)	0.0241(9)	0.0201(13)	0.0245(8)	0.0298(11)
O(2)[d]	U_{11}	0.0118(7)	0.0095(6)	0.0110(9)	0.0106(5)	0.0101(6)
O(2)[o]	U_{11}	0.0212(7)	0.0190(8)	0.0176(13)	0.0202(7)	0.0233(9)
	U_{22}	0.0074(7)	0.0077(9)	0.0071(15)	0.0072(8)	0.007(1)
	U_{33}	0.0142(8)	0.011(1)	0.0149(16)	0.0138(9)	0.0130(11)
	U_{23}	0.0000(6)	-0.0002(8)	0.0016(12)	-0.0003(6)	-0.0010(8)
	U_{13}	0.0000(3)	-0.0001(4)	0.0008(6)	-0.0001(3)	-0.0005(4)
	U_{12}	0.0037(4)	0.0038(5)	0.0035(7)	0.0036(4)	0.0037(5)
	U_{eq}	0.0158(4)	0.0139(4)	0.0144(7)	0.0152(4)	0.0163(5)
O(3)	U_{11}	0.0267(14)	0.0270(12)	0.0247(18)	0.0251(10)	0.0194(11)
	U_{22}	0.0125(8)	0.0121(7)	0.0109(10)	0.0116(6)	0.0103(7)
	U_{33}	0.0059(11)	0.0047(9)	0.0067(14)	0.0062(8)	0.0043(9)
	U_{23}	-0.0007(5)	0.0000(4)	-0.0006(6)	-0.0004(3)	-0.0007(4)
	U_{13}	-0.001(1)	0.0000(8)	-0.0012(12)	-0.0008(7)	-0.0014(8)
	U_{12}	0.0133(7)	0.0135(6)	0.0123(9)	0.0126(5)	0.0097(5)
	U_{eq}	0.0134(5)	0.0129(4)	0.0126(7)	0.0128(4)	0.0103(4)
O(4)	U_{11}	0.0103(8)	0.0097(7)	0.0100(11)	0.0093(6)	0.0093(7)
	U_{22}	0.0176(13)	0.0142(10)	0.0150(16)	0.0139(9)	0.0143(10)
	U_{33}	0.0108(10)	0.0090(9)	0.0105(14)	0.0093(7)	0.0097(9)
	U_{23}	-0.0016(9)	-0.0024(8)	-0.0012(12)	-0.0021(6)	-0.0004(8)
	U_{13}	-0.0008(5)	-0.0012(4)	-0.0006(6)	-0.0011(3)	-0.0002(4)
	U_{12}	0.0088(6)	0.0071(5)	0.0075(8)	0.0070(4)	0.0072(5)
	U_{eq}	0.0121(5)	0.0105(4)	0.0113(6)	0.0103(3)	0.0106(4)
O(5)	U_{11}	0.0166(13)	0.0159(11)	0.0175(17)	0.0162(9)	0.0133(10)
	U_{22}	0.0108(8)	0.0092(6)	0.010(1)	0.0102(5)	0.0075(6)
	U_{33}	0.0119(11)	0.0076(9)	0.0087(14)	0.0085(8)	0.011(1)
	U_{23}	0.0005(4)	0.0003(4)	0.0000(6)	-0.0001(3)	0.0002(4)
	U_{13}	0.0010(9)	0.0007(7)	0.0000(11)	-0.0002(6)	0.0004(8)
	U_{12}	0.0083(6)	0.0080(5)	0.0088(8)	0.0081(4)	0.0067(5)
	U_{eq}	0.0125(5)	0.0102(4)	0.0114(6)	0.0110(3)	0.0100(4)

APPENDIX A.2.2. (CON'T)

		SHW8	SHM1	SHM2	SHM3	SHM3A
O(6)	U_{11}	0.0094(7)	0.0087(6)	0.0082(9)	0.0087(5)	0.0086(6)
	U_{22}	0.0095(8)	0.0102(6)	0.009(1)	0.0104(5)	0.0095(6)
	U_{33}	0.0077(7)	0.0053(5)	0.0072(9)	0.0063(5)	0.0066(6)
	U_{23}	-0.0005(6)	-0.0006(5)	0.0000(8)	-0.0002(4)	-0.0001(5)
	U_{13}	0.0004(6)	0.0002(5)	0.0009(7)	0.0007(4)	0.0002(5)
	U_{12}	0.0033(6)	0.0043(5)	0.0035(8)	0.0041(4)	0.0033(5)
	U_{eq}	0.0095(3)	0.0082(3)	0.0086(4)	0.0088(2)	0.0088(3)
O(7)	U_{11}	0.0079(7)	0.0077(6)	0.0082(9)	0.0069(5)	0.0065(6)
	U_{22}	0.0074(7)	0.0079(6)	0.0074(9)	0.0076(5)	0.0067(6)
	U_{33}	0.0074(7)	0.0056(6)	0.0075(9)	0.0068(5)	0.0070(6)
	U_{23}	-0.0010(6)	-0.0010(5)	-0.0004(7)	-0.0009(4)	-0.0015(5)
	U_{13}	-0.0003(6)	0.0004(5)	0.0007(8)	0.0003(4)	-0.0003(5)
	U_{12}	0.0019(6)	0.0028(5)	0.0029(8)	0.0023(4)	0.0020(5)
	U_{eq}	0.0084(3)	0.0076(3)	0.0081(4)	0.0077(2)	0.0073(3)
O(8)	U_{11}	0.0080(7)	0.0063(6)	0.0058(9)	0.0064(5)	0.0070(6)
	U_{22}	0.0102(8)	0.0101(6)	0.009(1)	0.0105(5)	0.0106(7)
	U_{33}	0.0099(7)	0.0075(6)	0.011(1)	0.0086(5)	0.0108(7)
	U_{23}	0.0038(6)	0.0027(5)	0.0032(7)	0.0027(4)	0.0026(5)
	U_{13}	0.0016(6)	0.0002(5)	0.0015(8)	0.0008(4)	0.0015(6)
	U_{12}	0.0050(6)	0.0043(5)	0.0043(8)	0.0044(4)	0.0051(5)
	U_{eq}	0.0091(3)	0.0079(3)	0.0083(4)	0.0085(2)	0.0091(3)
H(3)*	U_{eq}	0.015	0.015	0.015	0.015	0.015

* Fixed during refinement

APPENDIX A.2.2. (CON'T)

		SHM3E	SHM5	SHP1	SHP2	SHP3
X	U_{11}	0.0264(9)	0.0282(11)	0.0273(11)	0.0268(16)	0.031(2)
	U_{22}	0.0264(9)	0.0282(11)	0.0273(11)	0.0268(16)	0.031(2)
	U_{33}	0.023(12)	0.0224(14)	0.0197(13)	0.023(2)	0.032(4)
	U_{23}	0	0	0	0	0
	U_{13}	0	0	0	0	0
	U_{12}	0.0132(5)	0.0141(5)	0.0136(5)	0.0134(8)	0.0154(12)
	U_{eq}	0.0254(7)	0.0263(9)	0.0248(8)	0.0255(13)	0.0312(19)
Y	U_{11}	0.0111(3)	0.0121(4)	0.0098(4)	0.0109(6)	0.0137(8)
	U_{22}	0.0091(3)	0.0097(3)	0.0094(3)	0.0081(4)	0.0088(6)
	U_{33}	0.0146(4)	0.0150(4)	0.0126(4)	0.0163(6)	0.0167(9)
	U_{23}	-	-	-	-	-0.0013(3)
	U_{13}	-0.0032(2)	-0.0030(3)	-0.0029(3)	-0.0031(4)	-0.0026(7)
	U_{12}	0.00554(17)	0.0061(2)	0.0049(2)	0.0054(3)	0.0069(4)
	U_{eq}	0.0114(2)	0.0120(3)	0.0106(3)	0.0115(4)	0.0125(5)
Z	U_{11}	0.00844(18)	0.0090(2)	0.00760(19)	0.0071(3)	0.0066(5)
	U_{22}	0.00947(19)	0.0106(2)	0.0091(2)	0.0079(3)	0.0081(5)
	U_{33}	0.00761(16)	0.00762(19)	0.00531(17)	0.0065(3)	0.0060(4)
	U_{23}	0.00067(13)	0.00091(16)	0.00063(14)	0.0007(2)	0.0009(4)
	U_{13}	-	0.00001(16)	-	0.0000(2)	0.0003(4)
	U_{12}	0.00456(15)	0.00514(17)	0.00442(16)	0.0038(3)	0.0033(4)
	U_{eq}	0.00847(10)	0.00897(11)	0.00722(11)	0.00710(18)	0.0070(2)
T	U_{11}	0.0071(2)	0.0078(2)	0.0064(2)	0.0062(3)	0.0069(6)
	U_{22}	0.00672(19)	0.0073(2)	0.0067(2)	0.0052(3)	0.0058(5)
	U_{33}	0.00714(18)	0.0071(2)	0.00524(18)	0.0065(3)	0.0065(4)
	U_{23}	-	-	-	-0.0005(2)	-0.0002(4)
	U_{13}	-	-	-	-0.0001(2)	0.0004(4)
	U_{12}	0.00299(13)	0.00324(15)	0.00302(14)	0.0026(2)	0.0029(4)
	U_{eq}	0.00720(13)	0.00767(14)	0.00625(13)	0.0061(2)	0.0065(3)
B	U_{11}	0.0093(6)	0.0096(7)	0.0085(7)	0.0084(11)	0.011(2)
	U_{22}	0.0108(9)	0.0125(10)	0.011(1)	0.0105(15)	0.010(3)
	U_{33}	0.0073(8)	0.007(1)	0.0060(9)	0.0070(14)	0.008(2)
	U_{23}	-0.0011(7)	-0.0005(8)	-0.0006(7)	-0.0007(11)	-0.001(2)
	U_{13}	-0.0005(3)	-0.0002(4)	-0.0003(4)	-0.0004(6)	-0.0006(11)
	U_{12}	0.0054(4)	0.0062(5)	0.0054(5)	0.0052(8)	0.0049(13)
		0.0090(4)	0.0094(4)	0.0082(4)	0.0084(6)	0.0094(10)

APPENDIX A.2.2. (CON'T)

		SHM3E	SHM5	SHP1	SHP2	SHP3
O(1)[d]	U_{11}	0.0146(11)	0.0155(13)	0.0112(11)	0.0120(17)	0.013(3)
O(1)[o]	U_{11}	0.0272(9)	0.0270(11)	0.0344(11)	0.037(2)	0.042(3)
	U_{22}	0.0272(9)	0.0270(11)	0.0344(11)	0.037(2)	0.042(3)
	U_{33}	0.0137(12)	0.0146(15)	0.0097(13)	0.012(2)	0.013(4)
	U_{23}	0	0	0	0	0
	U_{13}	0	0	0	0	0
	U_{12}	0.0136(4)	0.0135(5)	0.0172(6)	0.018(1)	0.0212(16)
	U_{eq}	0.0227(6)	0.0229(7)	0.0262(7)	0.0286(12)	0.033(2)
O(2)[d]	U_{11}	0.0118(4)	0.0117(5)	0.0099(4)	0.0116(7)	0.0089(11)
O(2)[o]	U_{11}	0.0199(6)	0.0205(7)	0.0211(6)	0.0236(11)	0.0252(18)
	U_{22}	0.0079(6)	0.0081(8)	0.0079(7)	0.0057(11)	0.0060(18)
	U_{33}	0.0157(7)	0.0153(9)	0.0117(8)	0.0172(13)	0.0117(19)
	U_{23}	-0.0001(5)	-0.0004(6)	0.0007(5)	-0.0007(9)	0.0024(16)
	U_{13}	-0.0001(2)	-0.0002(3)	0.0003(3)	-0.0004(4)	0.0012(8)
	U_{12}	0.0040(3)	0.0040(4)	0.0039(4)	0.0023(6)	0.0030(9)
	U_{eq}	0.0158(3)	0.0160(4)	0.0150(4)	0.0175(6)	0.0164(9)
O(3)	U_{11}	0.0256(8)	0.0260(9)	0.0260(9)	0.0262(14)	0.027(2)
	U_{22}	0.0127(5)	0.0124(6)	0.0120(5)	0.0120(8)	0.0123(14)
	U_{33}	0.0059(6)	0.0066(7)	0.0048(7)	0.0055(10)	0.0072(19)
	U_{23}	-0.0006(3)	-0.0007(3)	-0.0005(3)	-0.0006(5)	-0.0004(8)
	U_{13}	-0.0012(5)	-0.0014(6)	-0.0011(6)	-0.0012(9)	-0.0008(17)
	U_{12}	0.0128(4)	0.0130(5)	0.0130(4)	0.0131(7)	0.0135(12)
	U_{eq}	0.0133(3)	0.0135(3)	0.0127(3)	0.0130(5)	0.0139(9)
O(4)	U_{11}	0.0107(5)	0.0116(6)	0.0090(5)	0.0083(8)	0.0091(13)
	U_{22}	0.0161(7)	0.0176(9)	0.0151(8)	0.0121(11)	0.015(2)
	U_{33}	0.0108(6)	0.0113(7)	0.0088(6)	0.010(1)	0.0079(16)
	U_{23}	-0.0015(5)	-0.0011(6)	-0.0017(6)	-0.0012(9)	-0.0012(15)
	U_{13}	-0.0008(3)	-0.0005(3)	-0.0008(3)	-0.0006(4)	-0.0006(7)
	U_{12}	0.0080(4)	0.0088(4)	0.0076(4)	0.0060(6)	0.007(1)
	U_{eq}	0.0119(3)	0.0129(3)	0.0103(3)	0.0097(5)	0.0099(8)
O(5)	U_{11}	0.0173(7)	0.0173(9)	0.0160(8)	0.0163(12)	0.014(2)
	U_{22}	0.0112(4)	0.0114(5)	0.0104(5)	0.0091(7)	0.0104(13)
	U_{33}	0.0102(6)	0.0106(8)	0.0069(7)	0.0091(10)	0.0068(17)
	U_{23}	0.0007(3)	0.0005(3)	0.0004(3)	-0.0002(4)	0.0001(7)
	U_{13}	0.0013(5)	0.0010(6)	0.0008(5)	-0.0004(8)	0.0002(14)
	U_{12}	0.0087(4)	0.0086(4)	0.0080(4)	0.0081(6)	0.007(1)
	U_{eq}	0.0122(3)	0.0124(3)	0.0104(3)	0.0107(5)	0.0099(7)

APPENDIX A.2.2. (CON'T)

		SHM3E	SHM5	SHP1	SHP2	SHP3
O(6)	U_{11}	0.0093(4)	0.0099(5)	0.0087(5)	0.0083(7)	0.0112(13)
	U_{22}	0.0112(4)	0.0113(5)	0.0109(5)	0.0111(8)	0.0097(12)
	U_{33}	0.0074(4)	0.0070(5)	0.0052(4)	0.0065(7)	0.0064(10)
	U_{23}	-0.0004(3)	-0.0008(4)	-0.0008(4)	0.0002(6)	0.0005(10)
	U_{13}	0.0000(3)	-0.0001(4)	-0.0004(3)	0.0009(5)	0.0011(10)
	U_{12}	0.0048(4)	0.0046(4)	0.0042(4)	0.0046(6)	0.0052(11)
	U_{eq}	0.00947(19)	0.0098(2)	0.0086(2)	0.0088(3)	0.0091(5)
O(7)	U_{11}	0.0085(4)	0.0088(5)	0.0082(4)	0.0064(7)	0.0089(12)
	U_{22}	0.0084(4)	0.0086(5)	0.0074(4)	0.0066(7)	0.0054(12)
	U_{33}	0.0073(4)	0.0078(5)	0.0054(4)	0.0077(7)	0.0085(11)
	U_{23}	-0.0007(3)	-0.0012(4)	-0.0014(3)	-0.0011(6)	-0.0006(9)
	U_{13}	0.0008(3)	0.0001(4)	-0.0002(4)	0.0000(6)	0.001(1)
	U_{12}	0.0028(3)	0.0028(4)	0.0029(4)	0.0014(6)	0.003(1)
	U_{eq}	0.00871(18)	0.0090(2)	0.00746(19)	0.0077(3)	0.0080(5)
O(8)	U_{11}	0.0070(4)	0.0077(5)	0.0067(4)	0.0061(7)	0.0078(12)
	U_{22}	0.0104(4)	0.0117(5)	0.0107(5)	0.0100(8)	0.0123(13)
	U_{33}	0.0108(4)	0.0108(5)	0.0076(4)	0.0101(7)	0.0076(12)
	U_{23}	0.0026(3)	0.0025(4)	0.0032(3)	0.0031(5)	0.002(1)
	U_{13}	0.0013(3)	0.0010(4)	0.0005(4)	0.0015(6)	0.001(1)
	U_{12}	0.0046(4)	0.0055(4)	0.0049(4)	0.0042(6)	0.0063(11)
	U_{eq}	0.00933(19)	0.0098(2)	0.0081(2)	0.0087(3)	0.0087(5)
H(3)*	U_{eq}	0.015	0.015	0.015	0.015	0.015

* Fixed during refinement

APPENDIX A.3

SELECTED INTERATOMIC DISTANCES (Å)

APPENDIX A.3. SELECTED INTERATOMIC DISTANCES (Å).

		L1	L2	L4	L5	L6
X–*O*(*2*)	x3	2.389(2)	2.381(2)	2.386(2)	2.381(2)	2.381(2)
X–*O*(*4*)	x3	2.797(2)	2.795(2)	2.795(2)	2.790(2)	2.789(2)
X–*O*(*5*)	x3	2.737(2)	2.730(2)	2.733(2)	2.729(2)	2.726(2)
<*X*–*O*>		2.641	2.635	2.638	2.633	2.632
Y–*O*(*1*)^{d}	$x\,\frac{1}{3}$	1.781(4)	1.776(4)	1.776(4)	1.771(4)	1.770(4)
Y–*O*(*1*)^{d}	$x\,\frac{2}{3}$	2.189(3)	2.183(3)	2.178(3)	2.174(3)	2.170(3)
Y–*O*(*2*)^{d}		1.885(3)	1.884(3)	1.889(3)	1.892(3)	1.893(3)
Y–*O*(*2*)^{d}		2.107(3)	2.107(3)	2.101(3)	2.109(3)	2.109(3)
Y–*O*(*3*)		2.179(2)	2.180(2)	2.179(2)	2.182(2)	2.189(2)
Y–*O*(*6*)	x2	2.009(1)	2.001(1)	2.000(2)	1.995(2)	1.990(2)
<*Y*–*O*^{d}>^{a}		2.040	2.037	2.036	2.035	2.035
Y–*O*(*1*)^{o}		2.037(3)	2.031(2)	2.029(3)	2.024(3)	2.022(2)
Y–*O*(*2*)^{o}	x2	1.994(2)	1.993(2)	1.993(2)	1.998(2)	2.000(2)
Y–*O*(*3*)		2.178(2)	2.180(2)	2.178(3)	2.182(2)	2.189(2)
Y–*O*(*6*)	x2	2.008(2)	2.001(2)	2.000(2)	1.994(2)	1.990(2)
<*Y*–*O*^{o}>		2.037	2.033	2.032	2.032	2.032
Z–*O*(*3*)		1.949(1)	1.944(1)	1.947(1)	1.943(1)	1.942(1)
Z–*O*(*6*)		1.848(1)	1.847(1)	1.849(1)	1.849(1)	1.847(1)
Z–*O*(*7*)		1.883(1)	1.884(1)	1.885(1)	1.886(1)	1.887(1)
Z–*O*(*7*)		1.960(1)	1.961(1)	1.958(1)	1.961(1)	1.961(1)
Z–*O*(*8*)		1.886(1)	1.887(1)	1.887(1)	1.887(1)	1.887(1)
Z–*O*(*8*)		1.906(1)	1.906(1)	1.905(1)	1.902(1)	1.902(1)
<*Z*–*O*>		1.905	1.905	1.905	1.905	1.904
T–*O*(*4*)		1.626(1)	1.627(1)	1.626(1)	1.628(1)	1.627(1)
T–*O*(*5*)		1.642(1)	1.642(1)	1.642(1)	1.644(1)	1.643(1)
T–*O*(*6*)		1.594(1)	1.593(1)	1.593(1)	1.592(1)	1.592(1)
T–*O*(*7*)		1.607(1)	1.607(1)	1.608(1)	1.605(1)	1.605(1)
<*T*–*O*>		1.617	1.617	1.617	1.617	1.617
B–*O*(*2*)		1.362(3)	1.367(3)	1.359(3)	1.360(3)	1.360(3)
B–*O*(*8*)	x2	1.384(2)	1.382(2)	1.385(2)	1.386(2)	1.385(2)
<*B*–*O*>		1.377	1.377	1.376	1.377	1.377

a, calculated as: [0.333 x $Y\text{-}O(1)_{short}$ + 0.667 x $Y\text{-}O(1)_{long}$ + $Y\text{-}O(2)_{long}$ + $Y\text{-}O(2)_{short}$ + Y-O(2) + 2 x Y-O(5)] / 6

APPENDIX A.3. (CON'T)

		L7	L11	L12	L13	L15
X–O(*2*)	x3	2.379(2)	2.386(2)	2.384(2)	2.397(2)	2.386(2)
X–O(*4*)	x3	2.786(2)	2.803(2)	2.799(2)	2.787(2)	2.780(2)
X–O(*5*)	x3	2.723(2)	2.742(2)	2.736(2)	2.724(2)	2.716(2)
<*X–O*>		2.629	2.644	2.640	2.636	2.627
Y–O(*1*)[d]	$x\,\frac{1}{3}$	1.771(4)	1.778(4)	1.782(4)	1.768(5)	1.765(5)
Y–O(*1*)[d]	$x\,\frac{2}{3}$	2.165(3)	2.206(3)	2.192(3)	2.165(4)	2.153(4)
Y–O(*2*)[d]		1.895(3)	1.882(3)	1.881(3)	1.895(3)	1.894(3)
Y–O(*2*)[d]		2.106(3)	2.111(3)	2.108(3)	2.108(3)	2.112(3)
Y–O(*3*)		2.187(2)	2.179(2)	2.179(2)	2.179(3)	2.189(3)
Y–O(*6*)	x2	1.987(1)	2.016(1)	2.010(2)	1.990(2)	1.976(2)
<*Y–O*[d]>[a]		2.033	2.045	2.041	2.032	2.028
Y–O(*1*)[o]		2.019(2)	2.045(4)	2.039(3)	2.018(3)	2.010(3)
Y–O(*2*)[o]	x2	1.999(2)	1.994(2)	1.992(2)	1.999(2)	2.000(2)
Y–O(*3*)		2.186(2)	2.178(2)	2.178(3)	2.179(3)	2.187(3)
Y–O(*6*)	x2	1.987(2)	2.016(2)	2.010(2)	1.989(2)	1.975(2)
<*Y–O*[o]>		2.030	2.041	2.037	2.029	2.025
Z–O(*3*)		1.941(1)	1.950(1)	1.947(1)	1.944(1)	1.939(1)
Z–O(*6*)		1.848(1)	1.846(1)	1.846(1)	1.849(1)	1.853(2)
Z–O(*7*)		1.885(1)	1.883(1)	1.885(1)	1.886(1)	1.887(1)
Z–O(*7*)		1.960(1)	1.960(1)	1.960(1)	1.962(1)	1.963(1)
Z–O(*8*)		1.888(1)	1.885(1)	1.886(1)	1.884(1)	1.888(1)
Z–O(*8*)		1.903(1)	1.906(1)	1.906(1)	1.904(1)	1.899(1)
<*Z–O*>		1.904	1.905	1.905	1.905	1.905
T–O(*4*)		1.626(1)	1.627(1)	1.626(1)	1.628(1)	1.627(1)
T–O(*5*)		1.642(1)	1.642(1)	1.642(1)	1.643(1)	1.642(1)
T–O(*6*)		1.592(1)	1.594(1)	1.595(2)	1.594(1)	1.589(2)
T–O(*7*)		1.606(1)	1.607(1)	1.607(1)	1.604(1)	1.602(1)
<*T–O*>		1.617	1.618	1.618	1.617	1.615
B–O(*2*)		1.358(3)	1.363(3)	1.360(3)	1.363(4)	1.361(4)
B–O(*8*)	x2	1.384(2)	1.383(2)	1.385(2)	1.383(2)	1.383(2)
<*B–O*>		1.375	1.376	1.377	1.376	1.376

APPENDIX A.3. (CON'T)

		L16	L17	L18	L19	L20
X–*O*(*2*)	x3	2.379(2)	2.388(2)	2.382(2)	2.385(2)	2.382(2)
X–*O*(*4*)	x3	2.781(2)	2.782(2)	2.780(2)	2.779(2)	2.779(2)
X–*O*(*5*)	x3	2.718(2)	2.718(2)	2.717(2)	2.720(2)	2.715(2)
<*X*–*O*>		2.626	2.629	2.626	2.628	2.625
Y–*O*(*1*)[d]	$x\,\frac{1}{3}$	1.770(3)	1.764(4)	1.772(4)	1.767(4)	1.768(4)
Y–*O*(*1*)[d]	$x\,\frac{2}{3}$	2.156(3)	2.158(3)	2.153(3)	2.157(3)	2.151(3)
Y–*O*(*2*)[d]		1.899(3)	1.897(3)	1.901(3)	1.900(3)	1.898(3)
Y–*O*(*2*)[d]		2.105(2)	2.103(3)	2.105(3)	2.107(3)	2.103(3)
Y–*O*(*3*)		2.186(2)	2.185(2)	2.185(2)	2.185(2)	2.192(2)
Y–*O*(*6*)	x2	1.979(1)	1.982(1)	1.977(1)	1.978(1)	1.979(2)
<*Y*–*O*[d]>[a]		2.029	2.029	2.029	2.029	2.029
Y–*O*(*1*)[o]		2.013(2)	2.012(2)	2.012(2)	2.013(2)	2.009(2)
Y–*O*(*2*)[o]	x2	2.000(1)	1.998(2)	2.001(2)	2.001(2)	1.999(2)
Y–*O*(*3*)		2.185(2)	2.185(2)	2.184(2)	2.184(2)	2.191(3)
Y–*O*(*6*)	x2	1.978(1)	1.981(2)	1.977(2)	1.978(2)	1.978(2)
<*Y*–*O*[o]>		2.026	2.026	2.025	2.026	2.026
Z–*O*(*3*)		1.940(1)	1.941(1)	1.941(1)	1.941(1)	1.941(1)
Z–*O*(*6*)		1.850(1)	1.849(1)	1.848(1)	1.851(1)	1.850(1)
Z–*O*(*7*)		1.886(1)	1.885(1)	1.886(1)	1.887(1)	1.885(1)
Z–*O*(*7*)		1.961(1)	1.961(1)	1.960(1)	1.963(1)	1.960(1)
Z–*O*(*8*)		1.888(1)	1.889(1)	1.888(1)	1.887(1)	1.890(1)
Z–*O*(*8*)		1.901(1)	1.901(1)	1.901(1)	1.901(1)	1.900(1)
<*Z*–*O*>		1.904	1.904	1.904	1.905	1.904
T–*O*(*4*)		1.627(1)	1.627(1)	1.627(1)	1.628(1)	1.627(1)
T–*O*(*5*)		1.643(1)	1.643(1)	1.643(1)	1.643(1)	1.644(1)
T–*O*(*6*)		1.591(1)	1.592(1)	1.592(1)	1.591(1)	1.591(1)
T–*O*(*7*)		1.605(1)	1.605(1)	1.606(1)	1.604(1)	1.606(1)
<*T*–*O*>		1.617	1.617	1.617	1.617	1.617
B–*O*(*2*)		1.360(3)	1.359(3)	1.359(3)	1.363(3)	1.359(3)
B–*O*(*8*)	x2	1.385(1)	1.385(2)	1.385(2)	1.385(2)	1.385(2)
<*B*–*O*>		1.377	1.376	1.376	1.378	1.376

APPENDIX A.3. (CON'T)

		L21	L22	L23	L24	L25
X–*O*(*2*)	x3	2.391(2)	2.379(3)	2.380(2)	2.381(2)	2.387(2)
X–*O*(*4*)	x3	2.783(2)	2.780(3)	2.783(2)	2.783(2)	2.784(2)
X–*O*(*5*)	x3	2.719(2)	2.718(3)	2.716(2)	2.716(2)	2.720(2)
<*X*–*O*>		2.631	2.626	2.626	2.627	2.630
Y–*O*(*1*)[d]	x ⅓	1.767(4)	1.767(6)	1.773(4)	1.769(4)	1.768(4)
Y–*O*(*1*)[d]	x ⅔	2.159(3)	2.154(4)	2.158(3)	2.156(3)	2.169(3)
Y–*O*(*2*)[d]		1.895(3)	1.904(5)	1.899(3)	1.898(3)	1.895(3)
Y–*O*(*2*)[d]		2.109(3)	2.100(4)	2.108(2)	2.107(3)	2.110(3)
Y–*O*(*3*)		2.184(2)	2.182(3)	2.182(2)	2.186(2)	2.184(2)
Y–*O*(*6*)	x2	1.984(1)	1.978(2)	1.979(1)	1.979(1)	1.987(2)
<*Y*–*O*[d]>[a]		2.031	2.028	2.029	2.029	2.033
Y–*O*(*1*)[o]		2.013(3)	2.011(3)	2.016(2)	2.013(2)	2.020(3)
Y–*O*(*2*)[o]	x2	1.999(2)	2.000(2)	2.001(1)	2.001(2)	2.000(2)
Y–*O*(*3*)		2.179(3)	2.181(3)	2.181(2)	2.185(2)	2.183(3)
Y–*O*(*6*)	x2	1.983(2)	1.977(2)	1.978(1)	1.979(2)	1.987(2)
<*Y*–*O*[o]>		2.026	2.024	2.026	2.026	2.030
Z–*O*(*3*)		1.943(1)	1.941(1)	1.940(1)	1.940(1)	1.943(1)
Z–*O*(*6*)		1.849(1)	1.849(2)	1.849(1)	1.848(1)	1.848(1)
Z–*O*(*7*)		1.887(1)	1.886(2)	1.886(1)	1.885(1)	1.886(1)
Z–*O*(*7*)		1.961(1)	1.959(2)	1.962(1)	1.961(1)	1.962(1)
Z–*O*(*8*)		1.885(1)	1.888(2)	1.888(1)	1.889(1)	1.887(1)
Z–*O*(*8*)		1.902(1)	1.902(2)	1.900(1)	1.901(1)	1.902(1)
<*Z*–*O*>		1.905	1.904	1.904	1.904	1.905
T–*O*(*4*)		1.627(1)	1.627(1)	1.627(1)	1.627(1)	1.628(1)
T–*O*(*5*)		1.643(1)	1.644(1)	1.644(1)	1.644(1)	1.644(1)
T–*O*(*6*)		1.593(1)	1.593(2)	1.592(1)	1.593(1)	1.592(1)
T–*O*(*7*)		1.604(1)	1.605(2)	1.604(1)	1.605(1)	1.605(1)
<*T*–*O*>		1.617	1.617	1.617	1.617	1.617
B–*O*(*2*)		1.361(3)	1.358(4)	1.362(3)	1.359(3)	1.363(3)
B–*O*(*8*)	x2	1.386(2)	1.384(2)	1.385(2)	1.383(2)	1.385(2)
<*B*–*O*>		1.378	1.375	1.377	1.375	1.378

APPENDIX A.3. (CON'T)

		L26	L27	L28	SHW1	SHW2
X–*O*(*2*)	x3	2.387(2)	2.383(2)	2.383(2)	2.450(2)	2.445(2)
X–*O*(*4*)	x3	2.783(2)	2.780(2)	2.784(2)	2.778(2)	2.776(2)
X–*O*(*5*)	x3	2.718(2)	2.719(2)	2.722(2)	2.717(2)	2.715(2)
<*X*–*O*>		2.629	2.627	2.630	2.648	2.645
Y–*O*(*1*)[d]	$x\,\frac{1}{3}$	1.773(4)	1.770(4)	1.776(4)	1.782(5)	1.782(5)
Y–*O*(*1*)[d]	$x\,\frac{2}{3}$	2.155(3)	2.160(3)	2.175(3)	2.098(3)	2.094(4)
Y–*O*(*2*)[d]		1.900(2)	1.894(3)	1.895(3)	1.882(3)	1.886(3)
Y–*O*(*2*)[d]		2.103(3)	2.110(3)	2.106(3)	2.059(3)	2.062(3)
Y–*O*(*3*)		2.190(2)	2.189(2)	2.176(2)	2.148(2)	2.146(2)
Y–*O*(*6*)	x2	1.985(2)	1.985(2)	1.990(1)	1.971(1)	1.961(1)
<*Y*–*O*[d]>[a]		2.032	2.032	2.033	2.004	2.001
Y–*O*(*1*)[o]		2.013(3)	2.016(2)	2.027(2)	1.983(2)	1.981(3)
Y–*O*(*2*)[o]	x2	1.999(2)	2.000(2)	1.999(1)	1.969(1)	1.972(2)
Y–*O*(*3*)		2.187(3)	2.188(3)	2.175(2)	2.147(2)	2.145(2)
Y–*O*(*6*)	x2	1.985(2)	1.985(2)	1.989(2)	1.971(1)	1.961(1)
<*Y*–*O*[o]>		2.028	2.029	2.030	2.002	1.999
Z–*O*(*3*)		1.943(1)	1.940(1)	1.942(1)	1.9506(8)	1.9497(9)
Z–*O*(*6*)		1.849(1)	1.848(1)	1.848(1)	1.856(1)	1.857(1)
Z–*O*(*7*)		1.885(1)	1.886(1)	1.885(1)	1.882(1)	1.881(1)
Z–*O*(*7*)		1.959(1)	1.962(1)	1.961(1)	1.945(1)	1.945(1)
Z–*O*(*8*)		1.887(1)	1.887(1)	1.887(1)	1.880(1)	1.879(1)
Z–*O*(*8*)		1.901(1)	1.901(1)	1.902(1)	1.898(1)	1.896(1)
<*Z*–*O*>		1.904	1.904	1.904	1.902	1.901
T–*O*(*4*)		1.627(1)	1.627(1)	1.627(1)	1.6148(7)	1.6176(7)
T–*O*(*5*)		1.643(1)	1.643(1)	1.642(1)	1.6303(8)	1.6304(9)
T–*O*(*6*)		1.590(1)	1.592(1)	1.592(1)	1.595(1)	1.595(1)
T–*O*(*7*)		1.607(1)	1.604(1)	1.605(1)	1.600(1)	1.602(1)
<*T*–*O*>		1.617	1.617	1.617	1.610	1.611
B–*O*(*2*)		1.354(3)	1.357(3)	1.362(3)	1.357(3)	1.361(3)
B–*O*(*8*)	x2	1.388(2)	1.386(2)	1.383(2)	1.379(2)	1.382(2)
<*B*–*O*>		1.377	1.376	1.376	1.372	1.375

APPENDIX A.3. (CON'T)

		SHW3	SHW4	SHW5	SHW6	SHW7
X–O(*2*)	x3	2.445(4)	2.453(3)	2.461(2)	2.453(3)	2.437(4)
X–O(*4*)	x3	2.802(3)	2.797(3)	2.775(2)	2.790(2)	2.787(4)
X–O(*5*)	x3	2.744(3)	2.738(3)	2.716(2)	2.726(2)	2.726(3)
<*X–O*>		2.664	2.663	2.651	2.656	2.650
Y–O(*1*)[d]	x ⅓	1.778(7)	1.778(5)	1.785(5)	1.790(6)	1.79(1)
Y–O(*1*)[d]	x ⅔	2.188(5)	2.177(4)	2.113(3)	2.075(4)	2.085(8)
Y–O(*2*)[d]		1.871(5)	1.874(4)	1.886(3)	1.889(4)	1.887(6)
Y–O(*2*)[d]		2.094(5)	2.087(4)	2.072(3)	2.053(4)	2.076(6)
Y–O(*3*)		2.167(4)	2.163(3)	2.145(2)	2.141(2)	2.158(4)
Y–O(*6*)	x2	2.007(2)	2.005(2)	1.967(1)	1.954(1)	1.957(3)
<*Y–O*[d]>[a]		2.033	2.030	2.007	1.995	2.004
Y–O(*1*)[o]		2.034(4)	2.027(3)	1.993(2)	1.972(2)	1.978(4)
Y–O(*2*)[o]	x2	1.980(2)	1.978(2)	1.977(1)	1.970(1)	1.980(3)
Y–O(*3*)		2.167(4)	2.163(3)	2.144(2)	2.140(2)	2.158(4)
Y–O(*6*)	x2	2.007(2)	2.005(2)	1.967(1)	1.954(1)	1.957(3)
<*Y–O*[o]>		2.029	2.026	2.004	1.993	2.002
Z–O(*3*)		1.952(2)	1.952(1)	1.9488(9)	1.9572(9)	1.953(2)
Z–O(*6*)		1.848(2)	1.853(2)	1.861(1)	1.862(1)	1.857(2)
Z–O(*7*)		1.886(2)	1.884(2)	1.884(1)	1.883(1)	1.884(2)
Z–O(*7*)		1.960(2)	1.959(2)	1.951(1)	1.943(1)	1.947(2)
Z–O(*8*)		1.882(2)	1.882(2)	1.883(1)	1.881(1)	1.882(2)
Z–O(*8*)		1.911(2)	1.909(2)	1.900(1)	1.898(1)	1.899(2)
<*Z–O*>		1.907	1.907	1.905	1.904	1.904
T–O(*4*)		1.623(1)	1.6220(9)	1.6194(7)	1.6156(7)	1.621(1)
T–O(*5*)		1.640(2)	1.639(1)	1.6346(8)	1.6327(8)	1.637(1)
T–O(*6*)		1.603(2)	1.598(2)	1.595(1)	1.600(1)	1.6042(2)
T–O(*7*)		1.608(2)	1.607(1)	1.604(1)	1.605(1)	1.607(2)
<*T–O*>		1.619	1.617	1.613	1.613	1.617
B–O(*2*)		1.365(6)	1.365(4)	1.368(3)	1.366(3)	1.366(6)
B–O(*8*)	x2	1.386(3)	1.384(2)	1.381(2)	1.381(2)	1.384(3)
<*B–O*>		1.379	1.378	1.377	1.376	1.378

APPENDIX A.3. (CON'T)

		SHW8	SHM1	SHM2	SHM3	SHM3a
X–*O*(*2*)	x3	2.445(3)	2.493(4)	2.503(6)	2.503(3)	2.476(4)
X–*O*(*4*)	x3	2.775(3)	2.792(3)	2.780(4)	2.786(2)	2.807(3)
X–*O*(*5*)	x3	2.711(3)	2.727(3)	2.711(4)	2.722(2)	2.750(3)
<*X*–*O*>		2.644	2.671	2.665	2.670	2.678
Y–*O*(*1*)[d]	x ⅓	1.779(9)	1.81(1)	1.79(2)	1.79(1)	1.80(1)
Y–*O*(*1*)[d]	x ⅔	2.078(6)	2.009(8)	2.00(1)	2.002(6)	2.055(7)
Y–*O*(*2*)[d]		1.891(5)	1.882(4)	1.883(8)	1.886(4)	1.902(4)
Y–*O*(*2*)[d]		2.074(5)	2.042(4)	2.029(8)	2.049(4)	2.087(5)
Y–*O*(*3*)		2.147(3)	2.151(3)	2.134(4)	2.177(2)	2.235(3)
Y–*O*(*6*)	x2	1.950(2)	1.958(2)	1.951(3)	1.979(2)	2.026(2)
<*Y*–*O*[d]>[a]		1.998	1.989	1.980	2.000	2.041
Y–*O*(*1*)[o]		1.970(3)	1.940(3)	1.927(4)	1.927(2)	1.959(3)
Y–*O*(*2*)[o]	x2	1.981(2)	1.960(2)	1.955(3)	1.967(2)	1.993(2)
Y–*O*(*3*)		2.147(3)	2.150(3)	2.133(4)	2.176(2)	2.234(3)
Y–*O*(*6*)	x2	1.950(2)	1.958(2)	1.950(3)	1.979(2)	2.026(2)
<*Y*–*O*[o]>		1.997	1.988	1.978	1.999	2.039
Z–*O*(*3*)		1.953(1)	1.959(1)	1.964(2)	1.961(1)	1.960(1)
Z–*O*(*6*)		1.862(2)	1.866(2)	1.870(3)	1.865(1)	1.852(2)
Z–*O*(*7*)		1.885(2)	1.888(2)	1.882(2)	1.884(1)	1.884(2)
Z–*O*(*7*)		1.944(2)	1.942(1)	1.936(2)	1.943(1)	1.958(2)
Z–*O*(*8*)		1.880(2)	1.882(2)	1.879(2)	1.881(1)	1.879(2)
Z–*O*(*8*)		1.900(2)	1.897(2)	1.898(3)	1.900(1)	1.912(2)
<*Z*–*O*>		1.904	1.906	1.905	1.906	1.908
T–*O*(*4*)		1.617(1)	1.6163(9)	1.608(1)	1.6153(8)	1.623(1)
T–*O*(*5*)		1.634(1)	1.628(1)	1.626(2)	1.6290(9)	1.636(1)
T–*O*(*6*)		1.600(2)	1.605(2)	1.600(3)	1.601(2)	1.607(2)
T–*O*(*7*)		1.603(2)	1.601(1)	1.600(2)	1.603(1)	1.611(2)
<*T*–*O*>		1.614	1.613	1.609	1.612	1.619
B–*O*(*2*)		1.373(5)	1.359(4)	1.366(6)	1.361(4)	1.365(5)
B–*O*(*8*)	x2	1.377(3)	1.381(2)	1.377(3)	1.380(2)	1.383(3)
<*B*–*O*>		1.376	1.374	1.373	1.374	1.377

APPENDIX A.3. (CON'T)

		SHM3e	SHM5	SHP1	SHP2	SHP3
X–*O*(*2*)	x3	2.503(2)	2.505(3)	2.477(3)	2.475(4)	2.475(6)
X–*O*(*4*)	x3	2.786(2)	2.785(2)	2.800(2)	2.802(3)	2.802(5)
X–*O*(*5*)	x3	2.716(2)	2.716(2)	2.735(2)	2.740(3)	2.736(4)
<*X*–*O*>		2.668	2.669	2.671	2.672	2.671
Y–*O*(*1*)[d]	x ⅓	1.798(8)	1.81(1)	1.787(6)	1.785(9)	1.77(1)
Y–*O*(*1*)[d]	x ⅔	1.992(5)	1.991(7)	2.051(4)	2.059(6)	2.080(9)
Y–*O*(*2*)[d]		1.885(3)	1.883(4)	1.876(3)	1.874(5)	1.869(7)
Y–*O*(*2*)[d]		2.040(3)	2.042(4)	2.051(3)	2.062(5)	2.073(7)
Y–*O*(*3*)		2.161(2)	2.155(2)	2.156(2)	2.173(3)	2.178(5)
Y–*O*(*6*)	x2	1.968(1)	1.963(1)	1.971(1)	1.995(2)	1.995(3)
<*Y*–*O*[d]>[a]		1.991	1.989	1.998	2.011	2.014
Y–*O*(*1*)[o]		1.9249(15)	1.927(2)	1.957(2)	1.961(3)	1.966(5)
Y–*O*(*2*)[o]	x2	1.961(1)	1.961(1)	1.962(1)	1.967(2)	1.969(3)
Y–*O*(*3*)		2.160(2)	2.154(2)	2.155(2)	2.172(3)	2.177(5)
Y–*O*(*6*)	x2	1.968(1)	1.963(1)	1.971(1)	1.995(2)	1.994(3)
<*Y*–*O*[o]>		1.990	1.988	1.996	2.010	2.012
Z–*O*(*3*)		1.9621(7)	1.9607(9)	1.9585(9)	1.962(1)	1.959(2)
Z–*O*(*6*)		1.869(1)	1.868(1)	1.861(1)	1.859(2)	1.850(3)
Z–*O*(*7*)		1.882(1)	1.883(1)	1.885(1)	1.879(2)	1.884(3)
Z–*O*(*7*)		1.942(1)	1.942(1)	1.943(1)	1.949(2)	1.946(3)
Z–*O*(*8*)		1.880(1)	1.879(1)	1.881(1)	1.881(2)	1.875(3)
Z–*O*(*8*)		1.899(1)	1.898(1)	1.900(1)	1.901(2)	1.906(3)
<*Z*–*O*>		1.906	1.905	1.905	1.905	1.903
T–*O*(*4*)		1.6130(6)	1.6122(8)	1.6157(7)	1.617(1)	1.612(2)
T–*O*(*5*)		1.6282(7)	1.6288(9)	1.6293(8)	1.632(1)	1.630(2)
T–*O*(*6*)		1.601(1)	1.602(1)	1.601(1)	1.602(2)	1.608(3)
T–*O*(*7*)		1.603(1)	1.602(1)	1.602(1)	1.606(2)	1.604(3)
<*T*–*O*>		1.611	1.611	1.612	1.614	1.614
B–*O*(*2*)		1.368(3)	1.367(3)	1.359(3)	1.361(5)	1.359(9)
B–*O*(*8*)	x2	1.377(2)	1.378(2)	1.380(2)	1.383(3)	1.385(4)
<*B*–*O*>		1.374	1.374	1.373	1.376	1.376

APPENDIX A.4.1

CHEMICAL COMPOSITION (wt. %) AND UNIT FORMULAE (*apfu*) FOR SINGLE CRYSTALS

APPENDIX A.4,1. CHEMICAL COMPOSITION (wt. %) AND UNIT FORMULAE (*apfu*) FOR SINGLE CRYSTALS

	L1	L2	L4	L5	L6	L7	L11
SiO_2	36.81	37.01	37.30	37.25	37.28	37.63	36.88
TiO_2	0.03	0.01	0.02	0.01	0.01	0.02	0.00
Al_2O_3	38.35	38.08	38.24	38.19	38.25	38.82	37.83
B_2O_3	10.85	10.84	10.92	10.88	10.89	11.01	10.81
Fe_2O_3	0.07	0.01	0.06	0.01	0.01	0.03	0.02
FeO	0.76	0.11	0.63	0.15	0.14	0.32	0.18
MgO	0.00	0.00	0.43	0.00	0.00	0.01	0.00
MnO	2.67	2.42	1.74	1.54	1.34	1.00	3.89
CaO	2.84	3.28	3.03	3.67	3.75	3.76	2.56
PbO	0.50	0.60	0.48	0.53	0.53	0.46	0.58
ZnO	0.00	0.00	0.00	0.00	0.00	0.00	0.00
Na_2O	1.40	1.14	1.25	0.96	0.93	0.92	1.51
Li_2O	2.00	2.26	2.18	2.47	2.50	2.51	1.98
H_2O	3.08	3.09	3.21	3.10	3.10	3.12	3.10
F	1.40	1.37	1.17	1.39	1.38	1.42	1.34
O=F	–0.59	–0.58	–0.49	–0.59	–0.58	–0.60	–0.56
Σ	100.17	99.64	100.17	99.56	99.53	100.43	100.12
Ca^{2+}	0.487	0.563	0.517	0.628	0.641	0.636	0.441
Na^{+}	0.435	0.354	0.386	0.297	0.288	0.282	0.471
Pb^{2+}	0.022	0.026	0.021	0.023	0.023	0.020	0.025
□	0.056	0.057	0.076	0.052	0.048	0.062	0.063
Σ*X*	1.000	1.000	1.000	1.000	1.000	1.000	1.000
^{Y}Al	1.238	1.194	1.174	1.187	1.193	1.224	1.166
Ti	0.004	0.001	0.002	0.001	0.001	0.002	0.000
Fe^{3+}	0.009	0.001	0.007	0.002	0.002	0.004	0.002
Fe^{2+}	0.101	0.015	0.084	0.019	0.018	0.042	0.025
Mn^{2+}	0.362	0.329	0.235	0.208	0.181	0.134	0.530
Mg^{2+}	0.000	0.000	0.102	0.000	0.000	0.002	0.000
Zn	---	---	---	---	---	---	---
Li	1.286	1.460	1.396	1.583	1.605	1.592	1.277
Σ*Y*	3.000	3.000	3.000	3.000	3.000	3.000	3.000
^{Z}Al	6.000	6.000	6.000	6.000	6.000	6.000	6.000
B	3.000	3.000	3.000	3.000	3.000	3.000	3.000
Si	5.895	5.933	5.937	5.948	5.948	5.942	5.927
B	---	---	---	---	---	---	---
Al	---	---	---	---	---	---	---
Σ*T*	5.895	5.933	5.937	5.948	5.948	5.942	5.927
OH^{-}	3.291	3.306	3.411	3.298	3.304	3.291	3.319
F^{-}	0.709	0.694	0.589	0.702	0.696	0.709	0.681
Σ(*V*+*W*)	4.000	4.000	4.000	4.000	4.000	4.000	4.000

APPENDIX A.4.1. (CON`T)

	L12	L13	L15	L16	L17	L18	L19
SiO_2	36.59	37.69	37.98	37.43	37.45	37.35	37.50
TiO_2	0.01	0.08	0.01	0.02	0.04	0.02	0.02
Al_2O_3	37.70	38.87	39.35	39.08	39.21	39.36	39.20
B_2O_3	10.74	11.05	11.11	10.99	11.01	10.99	11.00
Fe_2O_3	0.02	0.13	0.02	0.04	0.07	0.02	0.03
FeO	0.18	1.38	0.21	0.42	0.78	0.24	0.32
MgO	0.00	0.26	0.00	0.00	0.00	0.00	0.00
MnO	3.09	0.25	0.24	0.26	0.23	0.24	0.21
CaO	2.94	3.46	4.15	4.04	3.81	4.06	4.03
PbO	0.59	0.14	0.23	0.24	0.21	0.20	0.20
ZnO	0.00	0.00	0.00	0.00	0.00	0.00	0.00
Na_2O	1.30	1.13	0.75	0.80	0.92	0.78	0.81
Li_2O	2.09	2.36	2.67	2.54	2.45	2.51	2.56
H_2O	3.01	3.19	3.19	3.14	3.12	3.10	3.16
F	1.47	1.30	1.35	1.37	1.43	1.46	1.34
O=F	–0.62	–0.55	–0.57	–0.58	–0.60	–0.61	–0.56
Σ	99.11	100.74	100.69	99.79	100.13	99.72	99.82
Ca^{2+}	0.510	0.583	0.696	0.685	0.645	0.688	0.682
Na^{+}	0.408	0.345	0.228	0.245	0.282	0.239	0.248
Pb^{2+}	0.026	0.006	0.010	0.010	0.009	0.009	0.009
□	0.056	0.066	0.066	0.060	0.064	0.064	0.061
Σ*X*	1.000	1.000	1.000	1.000	1.000	1.000	1.000
^{Y}Al	1.190	1.209	1.258	1.286	1.297	1.335	1.297
Ti	0.001	0.009	0.001	0.002	0.005	0.002	0.002
Fe^{3+}	0.002	0.016	0.002	0.005	0.009	0.003	0.004
Fe^{2+}	0.025	0.181	0.027	0.055	0.102	0.031	0.042
Mn^{2+}	0.424	0.033	0.032	0.035	0.031	0.032	0.028
Mg^{2+}	0.000	0.061	0.000	0.000	0.000	0.000	0.000
Zn	---	---	---	---	---	---	---
Li	1.358	1.491	1.680	1.617	1.556	1.597	1.627
Σ*Y*	3.000	3.000	3.000	3.000	3.000	3.000	3.000
^{Z}Al	6.000	6.000	6.000	6.000	6.000	6.000	6.000
B	3.000	3.000	3.000	3.000	3.000	3.000	3.000
Si	5.921	5.931	5.944	5.921	5.913	5.906	5.923
B	---	---	---	---	---	---	---
Al	---	---	---	---	---	---	---
Σ*T*	5.921	5.931	5.944	5.921	5.913	5.906	5.923
OH^{-}	3.248	3.353	3.332	3.315	3.286	3.270	3.331
F^{-}	0.752	0.647	0.668	0.685	0.714	0.730	0.669
Σ(*V*+*W*)	4.000	4.000	4.000	4.000	4.000	4.000	4.000

APPENDIX A.4.1. (CON`T)

	L20	L21	L22	L23	L24	L25	L26
SiO_2	37.77	37.62	37.71	37.12	37.64	38.16	37.33
TiO_2	0.02	0.06	0.03	0.03	0.01	0.06	0.08
Al_2O_3	39.58	39.04	38.99	39.06	39.33	38.71	38.25
B_2O_3	11.10	11.03	11.04	10.94	11.05	11.10	10.89
Fe_2O_3	0.04	0.09	0.04	0.04	0.03	0.08	0.06
FeO	0.37	0.92	0.45	0.39	0.26	0.85	0.65
MgO	0.01	0.06	0.11	0.09	0.00	0.25	0.00
MnO	0.18	0.23	0.26	0.25	0.35	0.45	0.42
CaO	4.12	3.78	4.05	4.08	4.06	3.64	3.86
PbO	0.14	0.13	0.15	0.17	0.30	0.16	0.12
ZnO	0.00	0.00	0.00	0.00	0.00	0.00	0.00
Na_2O	0.77	0.93	0.81	0.78	0.78	1.06	0.88
Li_2O	2.56	2.47	2.58	2.45	2.56	2.56	2.57
H_2O	3.18	3.17	3.20	3.13	3.13	3.20	3.35
F	1.37	1.34	1.28	1.35	1.43	1.34	0.86
O=F	–0.58	–0.56	–0.54	–0.57	–0.60	–0.56	–0.36
Σ	100.63	100.31	100.16	99.31	100.33	101.06	98.96
Ca^{2+}	0.691	0.638	0.683	0.695	0.684	0.610	0.660
Na^{+}	0.234	0.284	0.247	0.240	0.238	0.322	0.272
Pb^{2+}	0.006	0.006	0.006	0.007	0.013	0.007	0.005
□	0.069	0.072	0.064	0.058	0.065	0.061	0.063
Σ*X*	1.000	1.000	1.000	1.000	1.000	1.000	1.000
^{Y}Al	1.307	1.251	1.238	1.316	1.293	1.141	1.193
Ti	0.002	0.007	0.004	0.004	0.001	0.007	0.010
Fe^{3+}	0.004	0.011	0.005	0.005	0.003	0.010	0.008
Fe^{2+}	0.049	0.121	0.059	0.052	0.035	0.111	0.086
Mn^{2+}	0.024	0.031	0.035	0.034	0.047	0.060	0.057
Mg^{2+}	0.002	0.014	0.026	0.021	0.000	0.058	0.000
Zn	---	---	---	---	---	---	---
Li	1.612	1.565	1.633	1.568	1.621	1.613	1.646
Σ*Y*	3.000	3.000	3.000	3.000	3.000	3.000	3.000
^{Z}Al	6.000	6.000	6.000	6.000	6.000	6.000	6.000
B	3.000	3.000	3.000	3.000	3.000	3.000	3.000
Si	5.916	5.929	5.939	5.899	5.922	5.973	5.956
B	---	---	---	---	---	---	---
Al	---	---	---	---	---	---	---
Σ*T*	5.916	5.929	5.939	5.899	5.922	5.973	5.956
OH^{-}	3.321	3.332	3.362	3.322	3.288	3.337	3.566
F^{-}	0.679	0.668	0.638	0.678	0.712	0.663	0.434
Σ(*V*+*W*)	4.000	4.000	4.000	4.000	4.000	4.000	4.000

APPENDIX A.4.1. (CON`T)

	L27	L28	SHW1	SHW2	SHW3	SHW4	SHW5
SiO_2	37.19	37.36	37.64	37.25	36.48	36.31	36.46
TiO_2	0.14	0.10	0.21	0.02	0.67	0.64	0.12
Al_2O_3	38.86	38.57	41.84	41.71	37.20	37.31	40.90
B_2O_3	10.95	10.97	12.18	12.32	10.92	10.93	11.73
Fe_2O_3	0.10	0.08	---	---	0.29	0.27	---
FeO	1.08	0.86	0.25	0.04	4.95	4.58	0.22
MgO	0.07	0.29	0.00	0.00	0.00	0.00	0.00
MnO	0.43	0.52	0.33	0.46	0.18	0.20	0.64
CaO	3.61	3.71	1.21	1.65	0.33	0.44	1.40
PbO	0.13	0.17	---	---	---	---	---
ZnO	0.00	0.00	0.00	0.00	0.08	0.08	0.00
Na_2O	1.01	1.10	1.84	1.78	2.89	2.85	2.04
Li_2O	2.32	2.39	2.16	2.22	1.76	1.80	2.16
H_2O	3.18	3.13	3.50	3.50	3.05	2.95	3.15
F	1.26	1.38	0.86	0.85	1.38	1.58	1.39
O=F	–0.53	–0.58	–0.36	–0.36	–0.58	–0.67	–0.59
Σ	99.80	100.05	101.65	101.44	99.60	99.28	99.63
Ca^{2+}	0.614	0.630	0.199	0.272	0.057	0.076	0.236
Na^{+}	0.311	0.338	0.547	0.531	0.906	0.895	0.662
Pb^{2+}	0.006	0.007	---	---	---	---	---
□	0.069	0.025	0.254	0.197	0.037	0.029	0.102
Σ*X*	1.000	1.000	1.000	1.000	1.000	1.000	1.000
^{Y}Al	1.271	1.202	1.566	1.561	1.035	1.059	1.506
Ti	0.017	0.012	0.024	0.002	0.081	0.078	0.014
Fe^{3+}	0.012	0.010	---	---	0.035	0.033	---
Fe^{2+}	0.143	0.114	0.032	0.005	0.669	0.622	0.029
Mn^{2+}	0.058	0.070	0.043	0.060	0.025	0.027	0.085
Mg^{2+}	0.017	0.068	---	---	---	---	---
Zn	---	---	0.000	0.000	0.010	0.010	0.000
Li	1.482	1.524	1.333	1.373	1.144	1.172	1.367
Σ*Y*	3.000	3.000	2.998	3.001	2.999	3.001	3.001
^{Z}Al	6.000	6.000	6.000	6.000	6.000	6.000	6.000
B	3.000	3.000	3.000	3.000	3.000	3.000	3.000
Si	5.904	5.919	5.775	5.729	5.898	5.881	5.736
B	---	---	0.225	0.271	0.048	0.059	0.186
Al	---	---	–	–	0.054	0.056	0.078
Σ*T*	5.904	5.919	6.000	6.000	6.000	6.000	6.000
OH^{-}	3.367	3.309	3.583	3.587	3.289	3.187	3.308
F^{-}	0.633	0.691	0.417	0.413	0.706	0.809	0.692
Σ(*V*+*W*)	4.000	4.000	4.000	4.000	4.000	4.000	4.000

APPENDIX A.4.1. (CON`T)

	SHW6	SHW7	SHW8	SHM1	SHM2	SHM3	SHM3a
SiO_2	35.96	36.39	35.27	36.65	34.86	35.06	36.24
TiO_2	0.00	0.03	0.03	---	---	0.47	0.60
Al_2O_3	42.09	42.41	42.71	43.03	44.10	41.61	36.40
B_2O_3	11.83	12.19	12.90	12.63	13.94	13.42	11.88
Fe_2O_3	---	---	---	---	---	0.43	3.47
FeO	0.01	0.01	0.01	---	---	1.90	3.85
MgO	0.00	0.00	0.00	---	---	---	---
MnO	0.03	0.27	0.22	0.57	0.70	0.99	1.92
CaO	1.16	1.93	2.38	0.27	0.62	0.56	0.23
PbO	---	---	0.00	---	---	---	---
ZnO	0.00	0.00	0.00	---	---	---	---
Na_2O	1.82	1.56	1.41	1.94	1.72	1.99	2.43
Li_2O	2.06	2.17	2.12	1.80	1.58	1.51	1.47
H_2O	3.34	3.33	3.32	3.83	3.89	3.87	3.66
F	0.99	1.15	1.19	0.14	0.08	0.02	0.26
O=F	–0.42	–0.48	-0.50	–0.06	–0.03	–0.01	–0.11
Σ	98.87	100.96	101.06	100.80	101.45	101.62	101.99
Ca^{2+}	0.196	0.320	0.394	0.045	0.101	0.093	0.039
Na^{+}	0.556	0.468	0.422	0.579	0.509	0.596	0.747
Pb^{2+}	---	---	---	---	---	---	---
□	0.248	0.212	0.184	0.376	0.390	0.311	0.213
Σ*X*	1.000	1.000	1.000	1.000	1.000	1.000	1.000
^{Y}Al	1.691	1.610	1.651	1.810	1.938	1.581	0.806
Ti	0.000	0.003	0.003	---	---	0.055	0.072
Fe^{3+}	---	---	---	---	---	0.050	0.414
Fe^{2+}	0.001	0.001	0.001	---	---	0.246	0.511
Mn^{2+}	0.004	0.035	0.029	0.074	0.091	0.130	0.258
Mg^{2+}	---	---	---	---	---	---	---
Zn	0.000	0.000	0.000	---	---	---	---
Li	1.305	1.349	1.316	1.116	0.971	0.939	0.940
Σ*Y*	3.001	2.998	3.000	3.000	3.000	3.000	2.998
^{Z}Al	6.000	6.000	6.000	6.000	6.000	6.000	6.000
B	3.000	3.000	3.000	3.000	3.000	3.000	3.000
Si	5.663	5.627	5.444	5.642	5.324	5.419	5.749
B	0.216	0.254	0.437	0.358	0.676	0.581	0.252
Al	0.121	0.119	0.119	---	---	---	---
Σ*T*	6.000	6.000	6.000	6.000	6.000	6.000	6.000
OH^{-}	3.507	3.438	3.419	3.932	3.961	3.990	3.870
F^{-}	0.493	0.562	0.581	0.068	0.039	0.010	0.130
Σ(*V*+*W*)	4.000	4.000	4.000	4.000	4.000	4.000	4.000

APPENDIX A.4.1. (CON`T)

	SHM3e	SHM5	SHP1	SHP2	SHP3
SiO_2	34.40	33.54	37.68	36.06	36.90
TiO_2	0.39	0.87	0.04	0.68	0.35
Al_2O_3	42.87	41.81	42.17	40.44	40.91
B_2O_3	14.08	14.17	11.98	12.59	10.80
Fe_2O_3	0.32	---	---	---	---
FeO	1.15	1.18	0.19	0.56	0.43
MgO	---	---	---	---	---
MnO	0.87	1.08	1.00	3.24	3.26
CaO	0.56	0.93	0.16	0.40	0.20
PbO	---	---	---	---	---
ZnO	---	---	---	---	---
Na_2O	1.95	1.88	2.11	2.15	2.14
Li_2O	1.48	1.53	1.89	1.59	1.60
H_2O	3.84	3.66	3.68	3.74	3.87
F	0.16	0.43	0.43	0.23	0.00
O=F	–0.07	–0.19	–0.18	–0.10	–0.00
Σ	101.99	100.93	101.15	101.58	101.91
Ca^{2+}	0.092	0.155	0.026	0.067	0.033
Na^{+}	0.580	0.566	0.631	0.649	0.643
Pb^{2+}	---	---	---	---	---
□	0.328	0.279	0.343	0.284	0.324
Σ*X*	1.000	1.000	1.000	1.000	1.000
^{Y}Al	1.747	1.655	1.666	1.423	1.477
Ti	0.045	0.102	0.005	0.080	0.041
Fe^{3+}	0.036	0.026	---	---	---
Fe^{2+}	0.147	0.126	0.025	0.073	0.056
Mn^{2+}	0.113	0.142	0.131	0.428	0.428
Mg^{2+}	---	---	---	---	---
Zn	---	---	---	---	---
Li	0.911	0.948	1.173	0.996	0.998
Σ*Y*	3.000	3.000	3.000	3.000	3.000
^{Z}Al	6.000	6.000	6.000	6.000	6.000
B	3.000	3.000	3.000	3.000	3.000
Si	5.274	5.210	5.812	5.618	5.723
B	0.726	0.790	0.188	0.382	0.279
Al	---	---	---	---	---
Σ*T*	6.000	6.000	6.000	6.000	6.000
OH^{-}	3.922	3.789	3.790	3.897	4.000
F^{-}	0.078	0.211	0.210	0.103	0.000
Σ(*V*+*W*)	4.000	4.000	4.000	4.000	4.000

APPENDIX A.4.2

CHEMICAL COMPOSITION (wt. %) AND UNIT FORMULAE (*apfu*) FOR MAS NMR SAMPLES

APPENDIX A.4,2. CHEMICAL COMPOSITION (wt. %) AND UNIT FORMULAE (*apfu*) FOR MAS NMR SAMPLES

	AT06	AT07	AT09	AT10	AT11	AT13	AT14
SiO_2	38.00	37.53	37.09	38.45	38.95	36.96	32.62
TiO_2	---	---	---	---	0.00	0.99	---
Al_2O_3	41.55	39.22	43.87	41.91	39.82	31.40	47.46
B_2O_3*	11.17	11.02	11.11	---	---	10.94	12.85
V_2O_3	---	---	---	---	---	---	---
Cr_2O_3	---	---	---	---	---	---	---
FeO	0.04	1.60	0.02	---	---		0.58
MgO	---	---	---	0.05	0.48	12.71	0.01
MnO	0.05	---	0.07	---	0.10	0.00	0.05
CuO	---	---	---	---	---	---	---
CaO	2.05	3.21	0.13	---	0.29	2.47	1.76
PbO	---	---	---	---	---	---	---
ZnO	---	---	---	1.69	1.83	---	---
Na_2O	1.33	1.21	1.90	---	---	1.65	1.42
Li_2O*	2.18	2.23	1.44	2.02	2.43	0.00	0.88
K_2O	0.00	---	---	0.42	0.96	---	0.01
H_2O*	3.38	3.33	3.13	3.64	3.36	3.68	3.71
F	1.00	1.60	1.49	11.12	11.05	0.20	0.37
(O = F)	-0.42	-0.42	-0.63	-0.18	-0.40	-0.08	-0.16
Σ	100.33	100.53	99.62	99.12	98.87	100.92	101.56
Ca	0.342	0.542	0.022	0.000	0.049	0.421	0.291
Na	0.401	0.370	0.576	0.512	0.558	0.508	0.425
Pb	---	---	---	---	---	---	---
K	---	---	---	---	---	---	0.002
□	0.257	0.088	0.402	0.488	0.393	0.071	0.282
Σ*X*	1.000	1.000	1.000	1.000	1.000	1.000	1.000
Al	1.622	1.289	2.085	1.721	1.382	---	2.627
Ti^{4+}	---	---	---	---	---	0.118	0.003
Fe^{2+}	0.005	0.211	0.003	---	0.013	0.009	0.075
Mn^{2+}	0.007	0.084	0.009	0.007	0.064	0.000	0.007
Mg	0.000	0.000	---	---	---	2.892	0.002
Zn^{2+}	---	---	---	---	---	---	---
Li	1.366	1.416	0.903	1.272	1.541	---	0.545
Σ*Y*	3.000	3.000	3.000	3.000	3.000	3.019	3.259
Mg	---	---	---	---	---	0.119	---
Al	6.000	6.000	6.000	6.000	6.000	5.881	6.000
Σ*Z*	6.000	6.000	6.000	6.000	6.000	6.000	6.000
B	3.000	3.000	3.000	3.000	3.000	3.000	3.420
Si	5.915	5.918	5.800	6.010	6.126	5.873	5.031
B	---	---	---	---	---	---	---
Al	---	---	---	---	---	---	0.259
Σ*T*	5.915	5.918	5.800	6.010	6.126	5.873	5.290
OH	3.508	3.501	3.263	3.792	3.522	3.899	3.820
F	0.492	0.499	0.737	0.208	0.478	0.101	0.180
Σ (*V* + *W*)	4.000	4.000	4.000	4.000	4.000	4.000	4.000

APPENDIX A.4.2. (CON'T)

	AT16	AT17	AT18	AT19	AT20	AT21	AT23
SiO_2	37.92	37.09	38.58	38.40	38.67	38.75	38.14
TiO_2	---	---	---	---	---	---	---
Al_2O_3	39.80	39.47	39.43	38.89	39.23	38.94	39.03
B_2O_3*	11.10	10.99	11.22	11.08	11.22	11.18	11.11
V_2O_3	---	---	---	---	---	---	---
Cr_2O_3	---	---	---	---	---	---	---
FeO	0.04	1.35	0.01	---	---	0.01	0.09
MgO	---	0.01	---	---	---	---	---
MnO	0.15	0.87	0.20	0.11	0.12	0.09	0.41
CuO	---	---	---	---	---	---	---
CaO	3.68	2.86	4.33	3.77	4.52	0.01	4.26
PbO	---	---	---	---	---	---	---
ZnO	---	---	---	---	---	---	---
Na_2O	0.98	1.37	0.69	0.84	0.64	0.69	0.73
Li_2O*	2.59	2.02	2.84	2.85	2.93	2.95	2.76
K_2O	0.01	0.01	0.01	0.02	0.01	?	0.01
H_2O*	3.50	3.13	3.16	3.07	3.16	3.00	3.12
F	0.70	1.40	1.50	1.60	1.50	1.80	1.50
(O = F)	-0.29	-0.59	-0.63	-0.67	-0.63	-0.76	-0.63
Σ	100.18	99.98	101.34	99.96	101.37	96.66	100.53
Ca	0.617	0.485	0.719	0.633	0.750	0.695	0.714
Na	0.298	0.420	0.207	0.255	0.192	0.208	0.222
Pb	---	---	---	---	---	---	---
K	0.002	0.002	0.002	0.004	0.002	0.002	0.004
□	0.083	0.093	0.072	0.108	0.056	0.095	0.060
Σ*X*	1.000	1.000	1.000	1.000	1.000	1.000	1.000
Al	1.345	1.360	1.201	1.187	1.161	1.138	1.199
Ti^{4+}	---	---	---	---	---	---	---
Fe^{2+}	0.005	0.179	0.001	0.000	0.000	0.001	0.012
Mn^{2+}	0.020	0.117	0.026	0.015	0.016	0.012	0.054
Mg	0.000	0.024	0.000	0.000	0.000	0.000	0.000
Zn^{2+}	---	---	---	---	---	---	---
Li	1.630	1.287	1.771	1.798	1.822	1.848	1.734
Σ*Y*	3.000	2.967	2.999	3.000	2.999	2.999	2.999
Mg	---	---	---	---	---	---	---
Al	6.000	6.000	6.000	6.000	6.000	6.000	6.000
Σ*Z*	6.000	6.000	6.000	6.000	6.000	6.000	6.000
B	3.000	3.000	3.000	3.000	3.000	3.000	3.000
Si	5.937	5.868	5.978	6.021	5.989	6.027	5.969
B	---	---	---	---	---	---	---
Al	---	---	---	---	---	---	---
Σ*T*	5.937	5.868	5.978	6.021	5.989	6.027	5.969
OH	3.653	3.299	3.265	3.207	3.265	3.115	3.258
F	0.347	0.701	0.735	0.793	0.735	0.885	0.742
Σ (*V* + *W*)	4.000	4.000	4.000	4.000	4.000	4.000	4.000

APPENDIX A.4.2. (CON'T)

	AT25	AT28	AT47	AT48	AT49	AT50[a]	AT51
SiO_2	38.59	37.79	37.65	37.23	38.43		35.00
TiO_2	---	---	---	---	---		0.02
Al_2O_3	41.39	43.11	39.31	38.67	42.72		45.86
B_2O_3*	11.22	11.16	10.99	10.96	10.29		14.77
V_2O_3	---	---	---	---	---		---
Cr_2O_3	---	---	---	---	---		---
FeO	0.12	0.00	0.08	1.34	0.78		0.12
MgO	0.02	0.00	---	0.14	0.09		0.01
MnO	0.67	0.03	0.16	0.56	0.47		0.10
CuO	---	---	---	---	---		---
CaO	0.95	0.13	3.54	3.94	0.08		0.47
PbO	---	---	---	---	---		---
ZnO	---	---	---	---	---		---
Na_2O	1.83	2.00	0.90	0.94	2.04		1.81
Li_2O*	2.14	1.74	2.58	2.32	1.72		1.55
K_2O	0.02	0.00	0.02	0.01	0.02		0.00
H_2O*	3.26	3.36	3.03	3.07	3.52		3.94
F	1.30	0.00	1.60	1.50	0.80		0.20
(O = F)	-0.55	-0.44	-0.67	-0.63	-0.34		-0.08
Σ	100.96	98.88	99.19	100.05	100.62		103.77
Ca	0.158	0.022	0.600	0.669	0.013	0.093	0.075
Na	0.550	0.604	0.276	0.289	0.609	0.415	0.522
Pb	---	---	---	---	---	---	---
K	0.004	0.000	0.004	0.002	0.004	---	0.000
□	0.288	0.374	0.120	0.040	0.374	0.492	0.403
Σ*X*	1.000	1.000	1.000	1.000	1.000	1.000	1.000
Al	1.555	1.909	1.328	1.224	1.752	2.068	2.042
Ti^{4+}	---	0.000	---	---	---	---	0.002
Fe^{2+}	0.016	0.000	0.011	0.178	0.100	0.023	0.015
Mn^{2+}	0.088	0.004	0.021	0.075	0.061	0.016	0.013
Mg	0.000	0.000	0.000	0.033	0.021		0.002
Zn^{2+}	---	0.000	---	---	---	---	---
Li	1.336	1.087	1.639	1.480	1.065	0.892	0.926
Σ*Y*	2.995	3.000	2.999	2.990	2.999	3.000	3.000
Mg	---	---	---	---	---	---	---
Al	6.000	6.000	6.000	6.000	6.000	6.000	6.000
Σ*Z*	6.000	6.000	6.000	6.000	6.000	0.000	6.000
B	3.000	3.000	3.000	3.000	3.000	3.000	3.000
Si	5.977	5.883	5.955	5.901	5.917	5.553	5.208
B	---	---	---	---	---	0.447	0.792
Al	---	---	---	---	---	---	0.000
Σ*T*	5.977	5.883	5.955	5.901	5.917	6.000	6.000
OH	3.307	3.488	3.363	3.248	3.610	3.673	3.906
F	0.693	0.512	0.637	0.752	0.390	---	0.094
Σ (*V* + *W*)	4.000	4.000	4.000	4.000	4.000	0.000	4.000

a, original oxide data unavailable.

APPENDIX A.4.2. (CON'T)

	AT52	AT53	AT54	AT55	AT56	AT57	AT58
SiO_2	38.26	36.80	37.97	37.59	38.38	36.66	37.14
TiO_2	0.01	0.93	---	1.03	---	0.06	---
Al_2O_3	42.92	28.80	41.78	30.66	42.48	29.56	33.47
B_2O_3*	11.23	10.70	11.08	10.84	11.20	10.67	10.84
V_2O_3	---	---	---	---	---	0.56	---
Cr_2O_3	---	---	---	---	---	0.17	---
FeO	---	0.39	0.01	0.26	0.33	---	0.16
MgO	---	13.04	---	12.21	---	13.06	10.60
MnO	0.03	---	0.13	---	0.12	---	0.00
CuO	---	---	---	---	---	---	---
CaO	0.23	3.15	0.50	0.26	0.04	2.71	0.84
PbO	---	---	---	---	---	---	---
ZnO	---	---	---	---	---	---	---
Na_2O	1.69	1.30	1.61	2.83	1.71	1.27	2.02
Li_2O*	2.01	0.25	2.06	0.19	1.94	0.08	0.25
K_2O	0.01	0.03	---	---	---	0.01	---
H_2O*	3.67	3.23	3.40	3.74	3.70	2.98	3.67
F	0.44	0.98	0.88	---	0.34	1.48	0.14
(O = F)	-0.19	-0.41	-0.37	---	-0.14	-0.62	-0.06
Σ	100.31	99.19	99.05	99.61	100.10	98.65	99.07
Ca	0.038	0.548	0.084	0.072	0.007	0.476	0.144
Na	0.507	0.409	0.490	0.756	0.515	0.401	0.628
Pb	---	---	---	---	---	---	---
K	0.002	0.006	0.000	0.004	0.000	0.002	0.000
□	0.453	0.037	0.426	0.168	0.478	0.121	0.228
Σ*X*	1.000	1.000	1.000	1.000	1.000	1.000	1.000
Al	1.745	0.000	1.683	0.135	1.730	0.000	0.284
Ti^{4+}	0.001	0.114	0.000	0.028	0.000	0.007	0.000
Fe^{2+}	0.000	0.053	0.001	0.043	0.043	0.000	0.021
Mn^{2+}	0.004	0.000	0.017	0.000	0.016	0.000	0.000
Mg	0.000	2.648	0.000	2.681	0.000	2.815	2.535
Zn^{2+}	0.000	0.000	0.000	0.000	0.000	0.000	0.000
Li	1.250	0.162	1.299	0.113	1.211	0.083	0.160
Σ*Y*	3.000	2.977	3.000	3.000	3.000	3.000	3.000
Mg	---	0.510	---	---	---	0.356	---
Al	6.000	5.490	6.000	6.000	6.000	5.644	6.000
Σ*Z*	6.000	6.000	6.000	6.000	6.000	6.000	6.000
B	3.000	3.000	3.000	3.000	3.000	3.000	3.000
Si	5.919	5.977	5.957	6.005	5.958	5.970	5.957
B	---	---	---	---	---	---	---
Al	0.081	0.023	0.043	---	0.042	0.030	0.046
Σ*T*	6.000	6.000	6.000	6.005	6.000	6.000	6.003
OH	3.785	3.497	3.563	4.000	3.833	3.238	3.929
F	0.215	0.503	0.437	0.000	0.167	0.762	0.071
Σ (*V* + *W*)	4.000	4.000	4.000	4.000	4.000	4.000	4.000

APPENDIX A.4.2. (CON'T)

	AT59	AT60	AT61	AT62	AT63	AT64	AT65
SiO_2	34.47	34.06	34.48	38.38	37.66	35.89	39.86
TiO_2	0.23	0.28	0.29	---	0.42	0.77	---
Al_2O_3	30.42	31.92	30.49	39.48	34.03	35.80	41.31
B_2O_3*	10.58	10.66	10.66	11.05	11.06	10.64	11.35
V_2O_3	0.18	0.45	0.93	---	0.25	0.02	---
Cr_2O_3	0.04	0.05	0.08	---	0.06	0.96	---
FeO	0.03	---	0.06	0.49	0.05	7.71	---
MgO	13.58	12.79	13.53	---	10.44	0.63	---
MnO	---	---	---	2.06	0.02	0.65	0.16
CuO	0.03	---	---	---	---	---	---
CaO	4.33	4.40	4.40	0.77	1.05	0.96	0.41
PbO	---	---	---	---	---	---	---
ZnO	---	---	---	0.04	---	0.03	---
Na_2O	0.72	0.65	0.64	1.99	2.00	2.17	1.76
Li_2O*	0.08	0.17	0.08	2.10	0.36	1.28	2.48
K_2O	---	---	---	0.01	0.04	1.08	---
H_2O*	2.89	3.00	2.94	3.25	3.68	3.16	3.45
F	1.60	1.43	1.56	1.19	0.28	1.08	0.99
(O = F)	-0.67	-0.60	-0.66	-0.50	-0.12	-0.45	-0.42
Σ	98.51	99.26	99.48	100.31	101.28	102.38	101.35
Ca	0.762	0.768	0.769	0.130	0.177	0.168	0.067
Na	0.229	0.205	0.202	0.607	0.609	0.687	0.522
Pb	---	---	---	---	---	---	---
K	0.000	0.000	0.000	0.002	0.008	0.004	0.000
□	0.009	0.027	0.029	0.261	0.206	0.141	0.411
Σ*X*	1.000	1.000	1.000	1.000	1.000	1.000	1.000
Al	0.000	0.000	0.000	1.320	0.220	0.758	1.454
Ti^{4+}	0.028	0.034	0.036	0.000	0.050	0.095	0.000
Fe^{2+}	0.004	0.000	0.008	0.064	0.007	1.054	0.000
Mn^{2+}	0.000	0.000	0.000	0.275	0.003	0.090	0.021
Mg	2.879	2.789	2.774	0.000	2.446	0.153	0.000
Zn^{2+}	0.000	0.000	0.000	0.005	0.000	0.004	0.000
Li	0.056	0.112	0.050	1.336	0.236	0.842	1.527
Σ*Y*	3.000	3.000	3.000	3.000	3.000	3.000	3.002
Mg	0.447	0.318	0.516	---	---	---	---
Al	5.553	5.682	5.484	6.000	6.000	6.000	6.000
Σ*Z*	6.000	6.000	6.000	6.000	6.000	6.000	6.000
B	3.000	3.000	3.000	3.000	3.000	3.000	3.000
Si	5.663	5.551	5.623	6.038	5.918	5.864	6.103
B	---	---	---	---	---	---	---
Al	0.337	0.449	0.377	---	0.082	0.136	---
Σ*T*	6.000	6.000	6.000	6.038	6.000	6.000	6.103
OH	3.169	3.263	3.195	3.408	3.861	3.442	3.521
F	0.831	0.737	0.805	0.592	0.139	0.558	0.479
Σ (*V* + *W*)	4.000	4.000	4.000	4.000	4.000	4.000	4.000

APPENDIX A.4.2. (CON'T)

	AT66	AT67	AT68	AT70	AT71 NMR1	AT71 NMR7	AT71 NMR9
SiO_2	38.18	35.11	33.89	38.27	37.84	37.27	37.01
TiO_2	0.04	0.25	0.29	---	0.02	0.01	0.01
Al_2O_3	38.96	31.35	31.76	40.17	39.33	38.70	38.21
B_2O_3*	0.00	10.88	10.69	11.09	11.07	10.92	10.86
V_2O_3	0.02	0.45	0.96	---	---	---	---
Cr_2O_3	0.02	0.29	0.17	---	---	---	---
FeO	0.02	0.02	---	---	0.37	0.15	0.27
MgO	0.17	13.87	12.94	6.15	0.06	0.01	0.04
MnO	0.12	0.01	---	---	0.39	1.46	2.98
CuO	0.00	---	---	---	---	---	---
CaO	4.30	4.50	4.44	---	3.89	3.60	2.90
PbO	---	---	---	---	---	---	---
ZnO	0.69	0.01	---	---	---	---	---
Na_2O	0.00	0.74	0.64	0.70	0.87	1.02	1.41
Li_2O*	2.85	0.08	0.13	---	2.55	2.38	2.08
K_2O	1.66	0.01	---	---	0.01	---	---
H_2O*	3.05	2.77	2.94	3.82	3.07	2.85	2.79
F	11.11	2.06	1.57	---	1.65	1.94	2.01
(O = F)	-0.70	-0.87	-0.66	---	-0.69	-0.82	-0.85
Σ	100.49	101.52	99.76	100.20	100.43	99.49	99.72
Ca	0.721	0.770	0.774	---	0.654	0.614	0.497
Na	0.209	0.228	0.202	0.210	0.265	0.315	0.438
Pb	---	---	---	---	---	---	---
K	0.000	0.001	---	---	0.002	---	0.002
□	0.070	0.001	0.024	0.790	0.079	0.071	0.063
Σ*X*	1.000	1.000	1.000	1.000	1.000	1.000	1.000
Al	1.156	---	---	1.420	1.275	1.257	1.208
Ti^{4+}	0.005	0.030	0.035	---	0.002	0.001	0.001
Fe^{2+}	0.016	0.003	---	0.130	0.049	0.020	0.036
Mn^{2+}	0.023	0.001	---	---	0.052	0.197	0.404
Mg	0.000	2.820	2.738	1.440	0.014	0.002	0.010
Zn^{2+}	0.002	0.002	---	---	---	---	---
Li	1.793	0.050	0.080	0.000	1.608	1.523	1.341
Σ*Y*	3.000	3.000	3.000	2.990	3.000	3.000	3.000
Mg	---	0.484	0.400	---	---	---	---
Al	6.000	5.516	5.600	6.000	6.000	6.000	6.000
Σ*Z*	6.000	6.000	6.000	6.000	6.000	6.000	6.000
B	3.000	3.000	3.000	3.000	3.000	3.000	3.000
Si	5.973	5.611	5.512	6.000	5.938	5.930	5.924
B	---	---	---	---	---	---	---
Al	0.027	0.389	0.488	---	---	---	---
Σ*T*	6.000	6.000	6.000	6.000	5.938	5.930	5.924
OH	3.179	2.957	3.192	4.000	3.181	3.024	2.982
F	0.821	1.043	0.808	0.000	0.819	0.976	1.017
Σ (*V* + *W*)	4.000	4.000	4.000	4.000	4.000	4.000	4.000

APPENDIX A.4.2. (CON'T)

	AT71 NMR10	AT72	AT73 SHM1	AT73 SHM2	AT73 SHM3	AT75 SHW2	AT75 SHW1	AT76
SiO_2	36.41	37.24	36.65	34.86	35.06	37.25	37.64	35.62
TiO_2	0.01	0.42	---	---	0.47	0.02	0.21	0.18
Al_2O_3	37.75	32.41	43.03	44.10	41.61	41.71	41.84	41.32
B_2O_3*	10.71	10.95	12.63	13.94	13.32	12.31	12.18	10.83
V_2O_3	---	---	---	---	---	---	---	---
Cr_2O_3	---	---	---	---	---	---	---	---
FeO	0.24	0.16	---	---	2.28	0.04	0.25	0.02
MgO	0.05	12.43	---	---	---	---	---	---
MnO	3.73	---	0.57	0.70	0.99	0.46	0.33	5.44
CuO	---	---	---	---	---	---	---	---
CaO	2.51	0.64	0.27	0.62	0.56	1.65	1.21	0.10
PbO	---	---	---	---	---	---	---	---
ZnO	---	---	---	---	---	---	---	---
Na_2O	1.57	2.74	1.94	1.72	1.99	1.78	1.84	2.13
Li_2O*	1.87	---	1.80	1.58	1.47	2.22	2.17	0.65
K_2O	---	0.02	---	---	---	---	---	---
H_2O*	2.91	3.71	3.83	3.89	3.86	3.49	3.50	3.39
F	1.65	0.15	0.14	0.08	0.02	0.85	0.86	0.74
(O = F)	-0.69	-0.06	-0.06	-0.03	-0.01	-0.36	-0.36	-0.31
Σ	98.72	100.81	100.80	101.46	101.62	101.42	101.67	100.11
Ca	0.436	0.109	0.045	0.101	0.093	0.272	0.199	0.100
Na	0.494	0.846	0.579	0.509	0.598	0.531	0.547	0.663
Pb	---	---	---	---	---	---	---	---
K	---	0.004	---	---	---		---	---
□	0.017	0.041	0.376	0.390	0.309	0.197	0.254	0.237
Σ *X*	1.000	1.000	1.000	1.000	1.000	1.000	1.000	1.000
Al	1.220	0.475	1.810	1.938	1.603	1.562	1.565	1.815
Ti^{4+}	0.001	0.050	---	---	0.055	0.002	0.024	0.022
Fe^{2+}	0.033	0.021	---	---	0.296	0.005	0.032	0.003
Mn^{2+}	0.513	0.000	0.074	0.091	0.130	0.060	0.043	0.739
Mg	0.012	2.454	---	---	---	---	---	---
Zn^{2+}	---	---	---	---	---	---	---	---
Li	1.222	0.000	1.116	0.971	0.916	1.373	1.339	0.421
Σ *Y*	3.000	3.000	3.000	3.000	3.000	3.002	3.003	3.000
Mg	---	0.486	---	---	---	---	---	---
Al	6.000	5.514	6.000	6.000	6.000	6.000	6.000	6.000
Σ *Z*	6.000	6.000	6.000	6.000	6.000	6.000	6.000	6.000
B	3.000	3.000	3.000	3.000	3.000	3.000	3.000	3.000
Si	5.908	5.908	5.642	5.324	5.436	5.730	5.775	5.716
B	---	---	0.358	0.676	0.564	0.270	0.225	---
Al	---	---	---	---	---	---	---	---
Σ *T*	5.908	5.908	6.000	6.000	6.000	6.000	6.000	5.716
OH	3.153	3.925	3.932	3.961	3.989	3.581	3.582	3.624
F	0.847	0.075	0.068	0.039	0.011	0.414	0.418	0.376
Σ (*V* + *W*)	4.000	4.000	4.000	4.000	4.000	3.995	4.000	4.000

APPENDIX A.4.3.

OPTIMIZED SITE OCCUPANCIES (in *apfu*) FOR SELECTED TOURMALINE STRUCTURES IN TABLE 2.1 USING OccQP (WRIGHT *et al*. 2000)

APPENDIX A.4.3. OPTIMIZED SITE OCCUPANCIES (in *apfu*) FOR SELECTED TOURMALINE STRUCTURES IN TABLE 2.1.

Sample	gde	gen	gfj	BrgGE19	Drv3200	Drv4317	Drv4323
Ref.	[1]	[1]	[1]	[2]	[2]	[2]	[2]
Ca	0.030	0.000	0.480	0.040	0.350	0.180	0.090
Na	0.640	0.810	0.490	0.860	0.550	0.770	0.820
K	0.010	0.010	0.010	0.020	0.000	0.000	0.000
□	0.320	0.180	0.020	0.080	0.100	0.050	0.090
∑X	1.000	1.000	1.000	1.000	1.000	1.000	1.000
Al	0.922	0.750	0.000	0.793	0.431	0.610	1.243
Li	0.110	0.670	0.000	0.000	0.039	0.003	0.002
Ti^{4+}	0.070	0.032	0.200	0.086	0.050	0.039	0.120
Cr^{3+}	0.000	0.000	0.000	0.000	0.000	0.000	0.000
Fe^{3+}	0.280	0.000	1.106	1.619	0.610	0.811	0.030
Fe^{2+}	1.588	0.913	0.370	0.442	0.285	0.000	0.030
Mg	0.000	0.592	1.324	0.040	1.575	1.537	1.575
Mn^{2+}	0.000	0.017	0.000	0.020	0.010	0.000	0.000
Zn	0.030	0.028	0.000	0.000	0.000	0.000	0.000
V^{3+}	0.000	0.000	0.000	0.000	0.000	0.000	0.000
∑Y	3.000	3.000	3.000	3.000	3.000	3.000	3.000
Al	5.698	6.000	4.600	5.496	5.030	4.823	4.845
Ti^{4+}	0.000	0.000	0.000	0.000	0.000	0.000	0.000
Cr^{3+}	0.000	0.000	0.000	0.000	0.000	0.000	0.000
Fe^{3+}	0.000	0.000	0.004	0.044	0.000	0.113	0.000
Fe^{2+}	0.122	0.000	0.570	0.460	0.205	0.642	0.000
Mg	0.000	0.000	0.826	0.000	0.765	0.422	1.155
Mn^{2+}	0.180	0.000	0.000	0.000	0.000	0.000	0.000
Zn	0.000	0.000	0.000	0.000	0.000	0.000	0.000
V^{3+}	0.000	0.000	0.000	0.000	0.000	0.000	0.000
∑Z	6.000	6.000	6.000	5.999	6.001	6.000	6.000
Al	0.197	0.069	0.000	0.143	0.011	0.127	0.054
Si	5.803	5.931	6.000	5.857	5.989	5.873	5.946
∑T	6.000	6.000	6.000	6.000	6.000	6.000	6.000

APPENDIX A.4.3. (CON'T)

Sample Ref.	Drv4387 [2]	FuvGE19 [2]	PovGE19 [2]	Sch2672 [2]	Sch4935 [2]	SchCros [2]	uvt52210 [2]
Ca	0.300	0.628	0.000	0.010	0.000	0.000	0.540
Na	0.700	0.352	0.752	0.951	0.950	0.490	0.420
K	0.000	0.020	0.248	0.040	0.010	0.000	0.000
□	0.000	0.000	0.000	0.000	0.040	0.510	0.040
∑X	1.000	1.000	1.000	1.000	1.000	1.000	1.000
Al	0.352	0.149	0.000	0.000	0.872	0.780	0.712
Li	0.002	0.000	0.000	0.004	0.022	0.090	0.006
Ti^{4+}	0.070	0.312	0.000	0.400	0.210	0.000	0.000
Cr^{3+}	0.000	0.000	0.000	0.000	0.000	0.000	0.000
Fe^{3+}	0.690	0.728	2.246	0.830	0.110	0.680	0.000
Fe^{2+}	0.048	0.768	0.340	1.164	1.581	1.293	0.000
Mg	1.838	1.021	0.414	0.583	0.195	0.000	2.282
Mn^{2+}	0.000	0.023	0.000	0.020	0.010	0.080	0.000
Zn	0.000	0.000	0.000	0.000	0.000	0.076	0.000
V^{3+}	0.000	0.000	0.000	0.000	0.000	0.000	0.000
∑Y	3.000	3.000	3.000	3.000	3.000	3.000	3.000
Al	4.876	4.462	0.398	3.506	5.256	5.600	4.682
Ti^{4+}	0.000	0.000	0.000	0.000	0.000	0.000	0.060
Cr^{3+}	0.000	0.000	0.000	0.000	0.000	0.000	0.000
Fe^{3+}	0.000	0.000	4.061	1.210	0.000	0.000	0.000
Fe^{2+}	0.262	0.505	0.000	0.566	0.249	0.146	0.030
Mg	0.862	1.032	1.531	0.697	0.495	0.170	1.228
Mn^{2+}	0.000	0.000	0.000	0.000	0.000	0.000	0.000
Zn	0.000	0.000	0.000	0.000	0.000	0.084	0.000
V^{3+}	0.000	0.000	0.010	0.020	0.000	0.000	0.000
∑Z	6.000	5.999	6.000	5.999	6.000	6.000	6.000
Al	0.062	0.216	0.000	0.000	0.149	0.047	0.035
Si	5.938	5.784	5.927	6.000	5.851	5.953	5.965
∑T	6.000	6.000	5.999	6.000	6.000	6.000	6.000

APPENDIX A.4.3. (CON'T)

Sample	T72	T73	T74	T75	T76	T77	T78
Ref.	[3]	[3]	[3]	[3]	[3]	[3]	[3]
Ca	0.813	0.762	0.697	0.768	0.595	0.716	0.774
Na	0.173	0.229	0.288	0.205	0.362	0.255	0.202
K	0.000	0.000	0.000	0.000	0.000	0.000	0.000
□	0.014	0.009	0.015	0.027	0.043	0.029	0.024
∑X	1.000	1.000	1.000	1.000	1.000	1.000	1.000
Al	0.446	0.182	0.623	0.614	0.675	0.571	0.496
Li	0.132	0.000	0.076	0.197	0.133	0.058	0.080
Ti^{4+}	0.000	0.000	0.000	0.057	0.000	0.000	0.000
Cr^{3+}	0.000	0.000	0.000	0.000	0.000	0.000	0.000
Fe^{3+}	0.000	0.000	0.000	0.000	0.000	0.000	0.000
Fe^{2+}	0.000	0.000	0.000	0.000	0.000	0.000	0.000
Mg	2.422	2.818	2.301	2.091	2.132	2.285	2.425
Mn^{2+}	0.000	0.000	0.000	0.000	0.000	0.000	0.000
Zn	0.000	0.000	0.000	0.000	0.000	0.000	0.000
V^{3+}	0.000	0.000	0.000	0.041	0.061	0.086	0.000
∑Y	3.000	3.000	3.000	3.000	3.000	3.000	3.000
Al	4.864	5.422	5.228	5.198	4.916	4.951	5.105
Ti^{4+}	0.009	0.014	0.034	0.000	0.000	0.000	0.035
Cr^{3+}	0.000	0.000	0.000	0.019	0.000	0.000	0.022
Fe^{3+}	0.000	0.000	0.000	0.000	0.000	0.000	0.000
Fe^{2+}	0.000	0.000	0.000	0.000	0.000	0.000	0.000
Mg	1.120	0.561	0.693	0.750	1.070	0.933	0.713
Mn^{2+}	0.000	0.000	0.000	0.000	0.000	0.000	0.000
Zn	0.000	0.000	0.000	0.000	0.000	0.000	0.000
V^{3+}	0.008	0.002	0.044	0.033	0.014	0.116	0.125
∑Z	6.000	5.999	6.000	6.000	6.001	6.000	6.000
Al	0.188	0.336	0.113	0.378	0.178	0.402	0.488
Si	5.812	5.664	5.887	5.622	5.822	5.598	5.512
∑T	6.000	6.000	6.000	6.000	6.000	6.000	6.000

APPENDIX A.4.3. (CON'T)

Sample	T79	T80	Foit	CrTour	UviteO	Drav
Ref.	[3]	[3]	[4]	[5]	[6]	[7]
Ca	0.769	0.430	0.000	0.159	0.421	0.000
Na	0.202	0.400	0.250	0.820	0.392	0.814
K	0.000	0.000	0.000	0.022	0.000	0.014
□	0.029	0.170	0.750	0.000	0.187	0.172
∑X	1.000	1.000	1.000	1.000	1.000	1.000
Al	0.541	0.657	0.994	0.384	0.763	1.109
Li	0.056	0.000	0.220	0.000	0.000	0.000
Ti^{4+}	0.000	0.000	0.000	0.011	0.000	0.030
Cr^{3+}	0.000	0.000	0.000	1.096	0.000	0.005
Fe^{3+}	0.000	0.000	0.000	0.238	0.000	0.560
Fe^{2+}	0.000	0.000	1.690	0.000	0.000	0.000
Mg	2.403	2.343	0.000	1.248	2.237	1.293
Mn^{2+}	0.000	0.000	0.096	0.024	0.000	0.003
Zn	0.000	0.000	0.000	0.000	0.000	0.000
V^{3+}	0.000	0.000	0.000	0.000	0.000	0.000
∑Y	3.000	3.000	3.000	3.000	3.000	3.000
Al	4.945	5.770	5.806	3.269	5.725	5.030
Ti^{4+}	0.036	0.030	0.000	0.000	0.030	0.000
Cr^{3+}	0.010	0.042	0.000	1.378	0.042	0.001
Fe^{3+}	0.000	0.000	0.000	0.000	0.000	0.000
Fe^{2+}	0.000	0.003	0.000	0.142	0.003	0.051
Mg	0.887	0.094	0.050	1.210	0.200	0.918
Mn^{2+}	0.000	0.000	0.144	0.000	0.000	0.000
Zn	0.000	0.000	0.000	0.000	0.000	0.000
V^{3+}	0.122	0.061	0.000	0.000	0.000	0.000
∑Z	6.000	6.001	6.000	6.000	6.000	6.000
Al	0.364	0.002	0.090	0.670	0.049	0.000
Si	5.636	5.998	5.910	5.330	5.951	6.000
∑T	6.000	6.000	6.000	6.000	6.000	6.000

[1] Camara *et al*. (2002); [2] Grice & Ercit (1993a); [3] MacDonald & Hawthorne (1995a); [4] MacDonald *et al*. (1993); [5] Nuber & Schmetzer (1979); [6] Taylor *et al*. (1995); [7] Hawthorne *et al*. (1993).

APPENDIX A.5

SITE-SCATTERING VALUES FOR TOURMALINE CRYSTALS (*epfu*) DERIVED FROM SREF AND EMPA

APPENDIX A.5. SITE-SCATTERING VALUES FOR TOURMALINE CRYSTALS (epfu) DERIVED FROM SREF AND EMPA

	X-site		*Y*-site		*T*-site	
	SREF	EMPA	SREF	EMPA	SREF	EMPA
L1	16.9(1)	16.3	31.7(2)	32.0	---	---
L2	17.9(1)	17.3	28.7(2)	28.6	---	---
L4	17.2(1)	16.3	29.1(2)	29.0	---	---
L5	18.2(1)	17.7	26.5(2)	25.9	---	---
L6	18.3(1)	17.9	26.3(2)	25.4	---	---
L7	18.1(1)	17.5	25.6(2)	25.3	---	---
L11	16.9(1)	16.1	32.5(2)	32.9	---	---
L12	17.6(1)	16.8	30.5(2)	30.9	---	---
L13	16.3(1)	16.0	27.4(2)	27.1	---	---
L15	17.6(1)	17.2	23.8(3)	23.0	---	---
L16	17.6(1)	17.2	23.8(2)	24.1	---	---
L17	17.1(1)	16.7	25.0(2)	25.3	---	---
L18	17.5(1)	17.1	23.3(2)	23.9	---	---
L19	17.4(1)	17.1	23.8(2)	23.7	---	---
L20	17.4(1)	16.9	23.6(2)	23.9	---	---
L21	16.9(1)	16.4	25.5(2)	25.5	---	---
L22	17.3(1)	16.9	23.7(3)	24.0	---	---
L23	17.4(1)	17.1	23.8(2)	24.5	---	---
L24	17.8(1)	17.4	23.8(2)	23.9	---	---
L25	16.9(1)	16.3	25.4(2)	25.2	---	---
L26	17.1(1)	16.8	25.7(2)	26.9	---	---
L27	17.4(1)	16.2	25.2(2)	27.1	---	---
L28	17.2(1)	16.4	25.9(2)	23.9	---	---
<dev.>	0.6		0.5			
SHW1	10.8(1)	10.0	28.3(2)	26.8	81.4(3)	82.0
SHW2	12.0(1)	11.3	26.7(2)	26.1	81.5(4)	81.6
SHW3	12.4(2)	11.1	36.8(3)	37.7	81.3(5)	83.1
SHW4	12.3(1)	11.8	36.5(2)	37.0	81.6(4)	82.8
SHW5	12.4(1)	11.5	27.1(2)	27.0	80.6(3)	80.6
SHW6	10.1(1)	9.9	27.0(2)	26.3	79.0(3)	80.4
SHW7	11.0(2)	11.4	26.3(3)	26.2	80.0(5)	81.5
SHW8	12.2(1)	12.3	27.0(2)	26.4	79.3(4)	78.8
<dev.>	0.6		0.6		0.9	
SHM1	7.7(1)	7.2	30.6(3)	28.7	81.9(4)	80.8
SHM2	8.0(2)	7.6	32.1(5)	30.3	79.9(8)	77.9
SHM3	8.7(1)	8.4	37.4(3)	35.7	81.2(3)	78.9
SHM3a	10.34(9)	9.3	47.9(3)	47.1	82.9(4)	82.7
SHM3e	8.16(9)	8.3	34.85(7)	34.2	80.6(3)	77.5
SHM5	8.3(1)	9.4	33.9(1)	34.1	80.2(3)	76.9
SHP1	7.5(1)	7.5	29.9(2)	29.2	82.4(4)	82.3
SHP2	8.5(2)	8.5	37.3(3)	35.9	82.1(5)	80.6
SHP3	8.7(2)	7.7	38.6(3)	35.3	82.8(5)	81.5
<dev.>	0.5		1.5		1.7	

APPENDIX A.6

^{11}B AND ^{27}Al MAGIC ANGLE SPINNING NUCLEAR MAGNETIC RESONANCE (MAS NMR) SPECTRA[1]

[1] Some tourmalines were ground using mortar and pestle fabricated of sintered alumina. The resulting $^{[6]}$Al contamination gives rise to a peak at ~16 ppm. This peak is indicated in relevant spectra by the symbol, *A*.

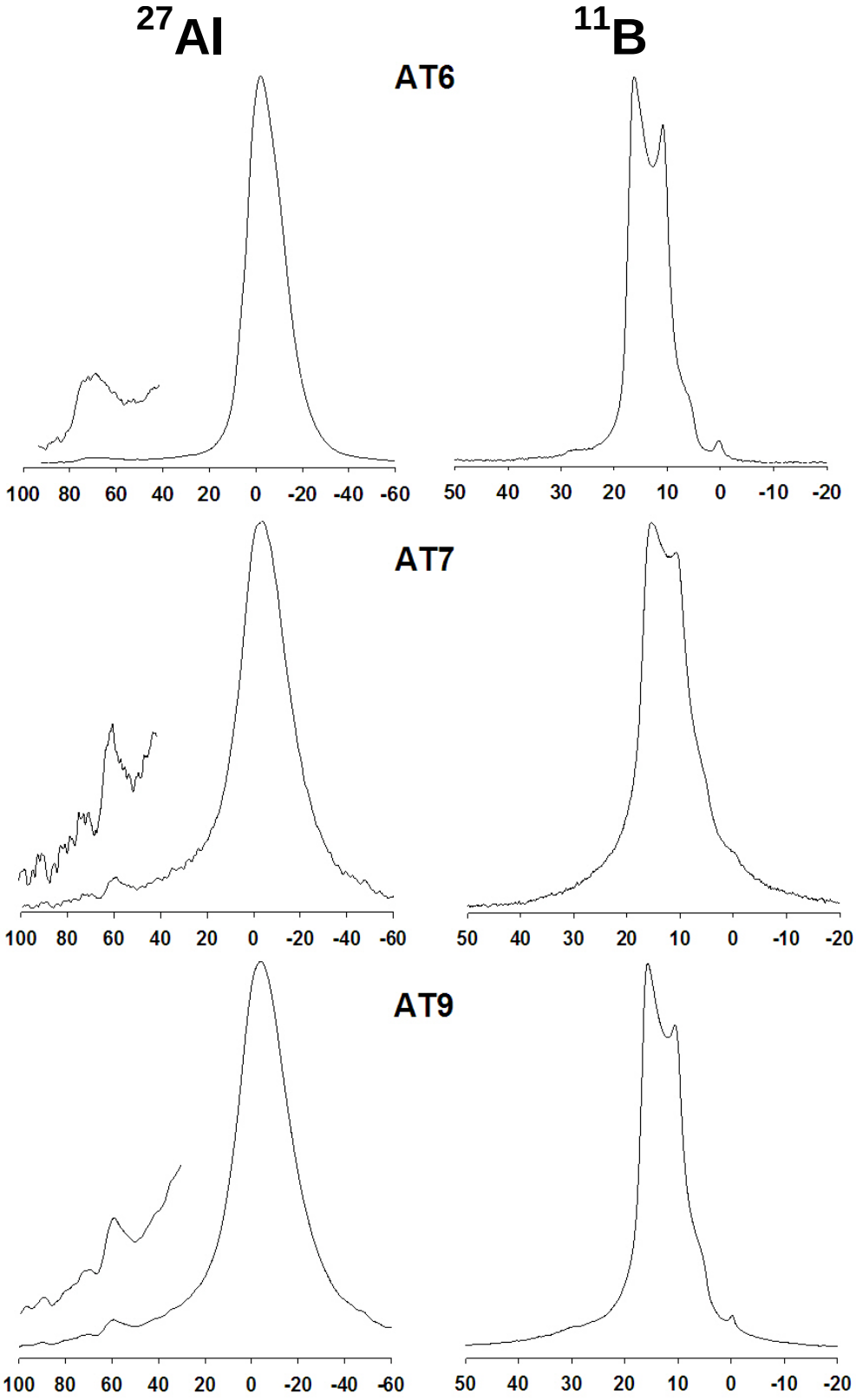
^{27}Al
^{11}B
AT6
AT7
AT9
100 80 60 40 20 0 -20 -40 -60
50 40 30 20 10 0 -10 -20

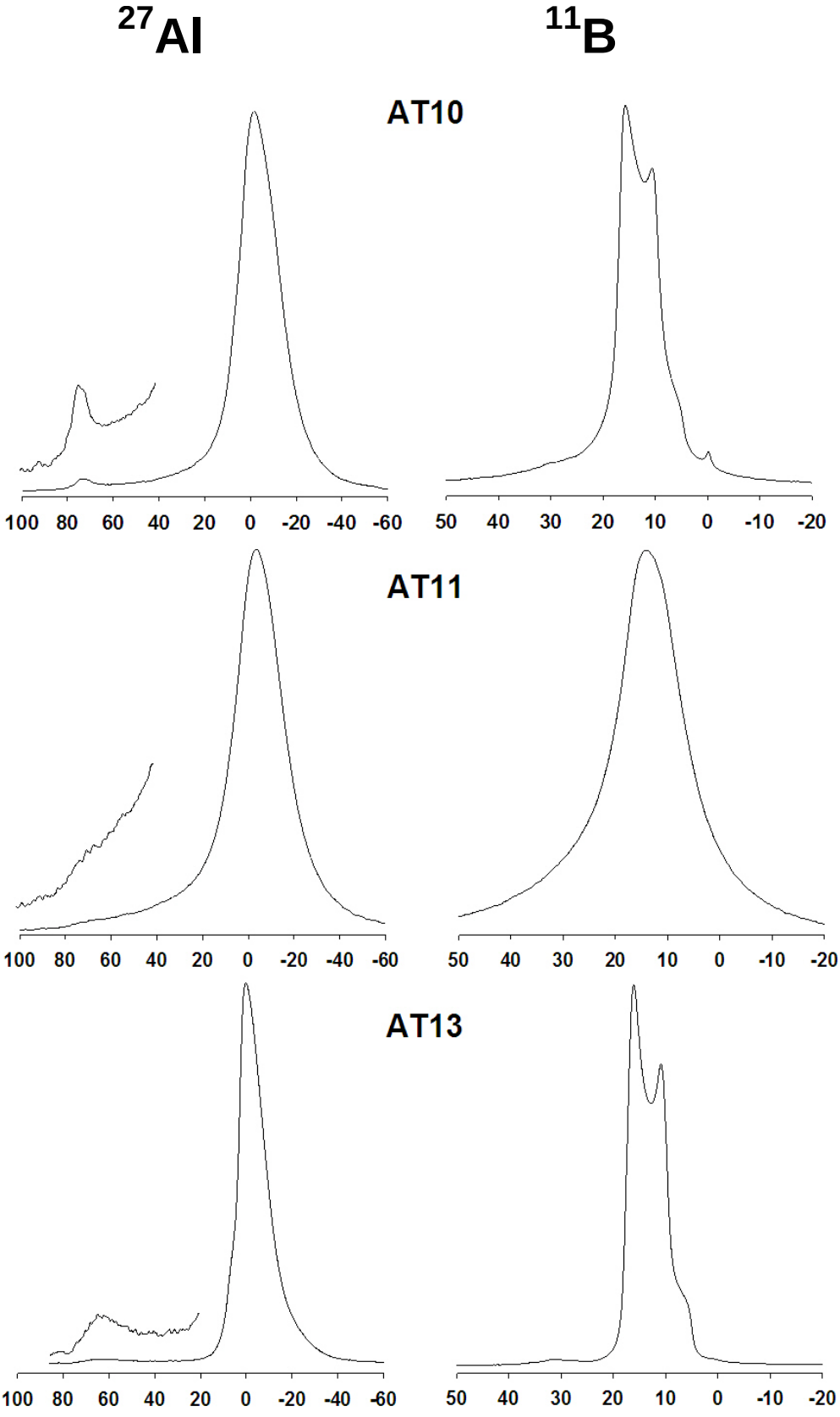
^{27}Al
^{11}B
AT10
AT11
AT13
100 80 60 40 20 0 -20 -40 -60
50 40 30 20 10 0 -10 -20

\\\\\

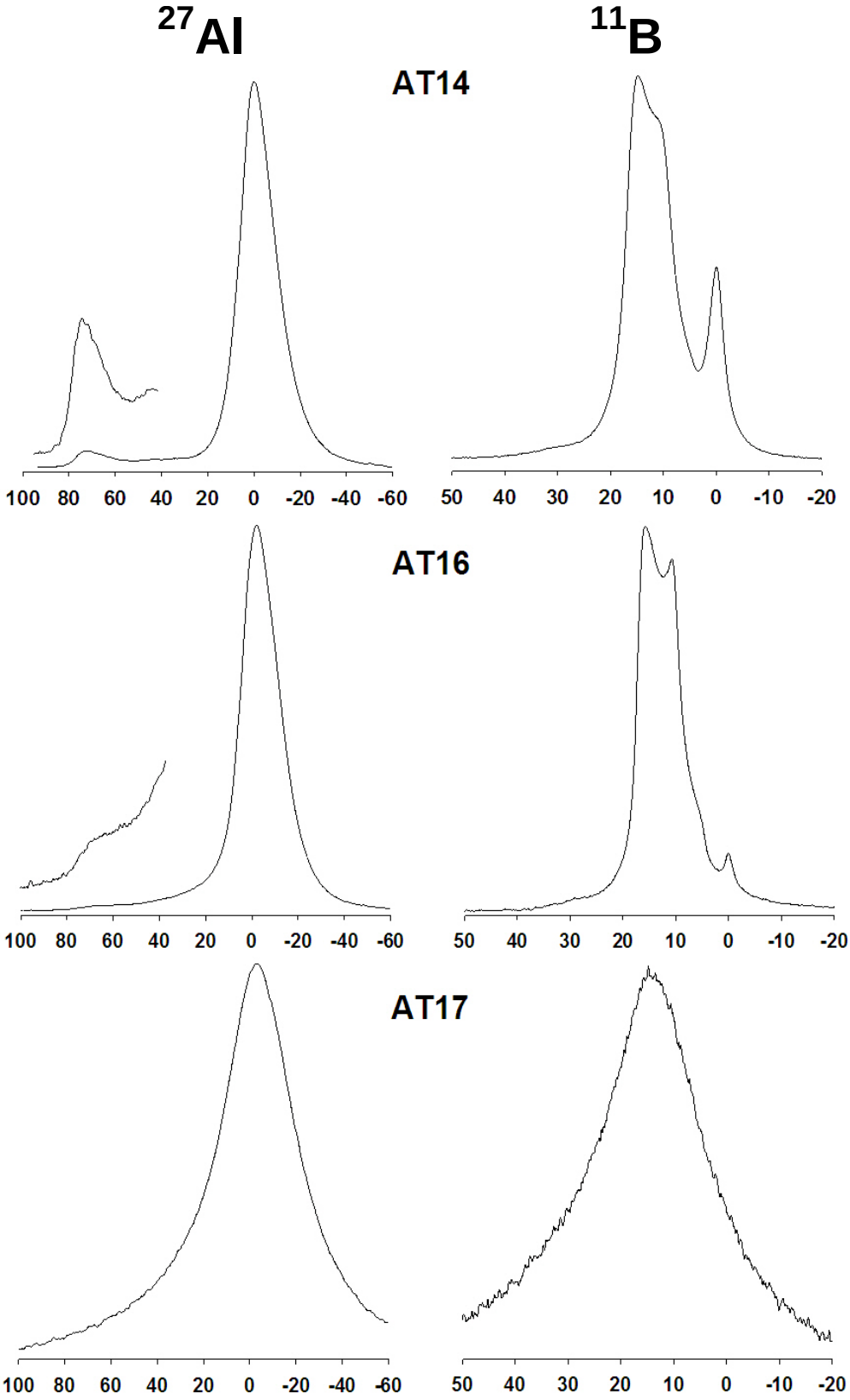
^{27}Al
^{11}B
AT14
AT16
AT17
100 80 60 40 20 0 -20 -40 -60
50 40 30 20 10 0 -10 -20

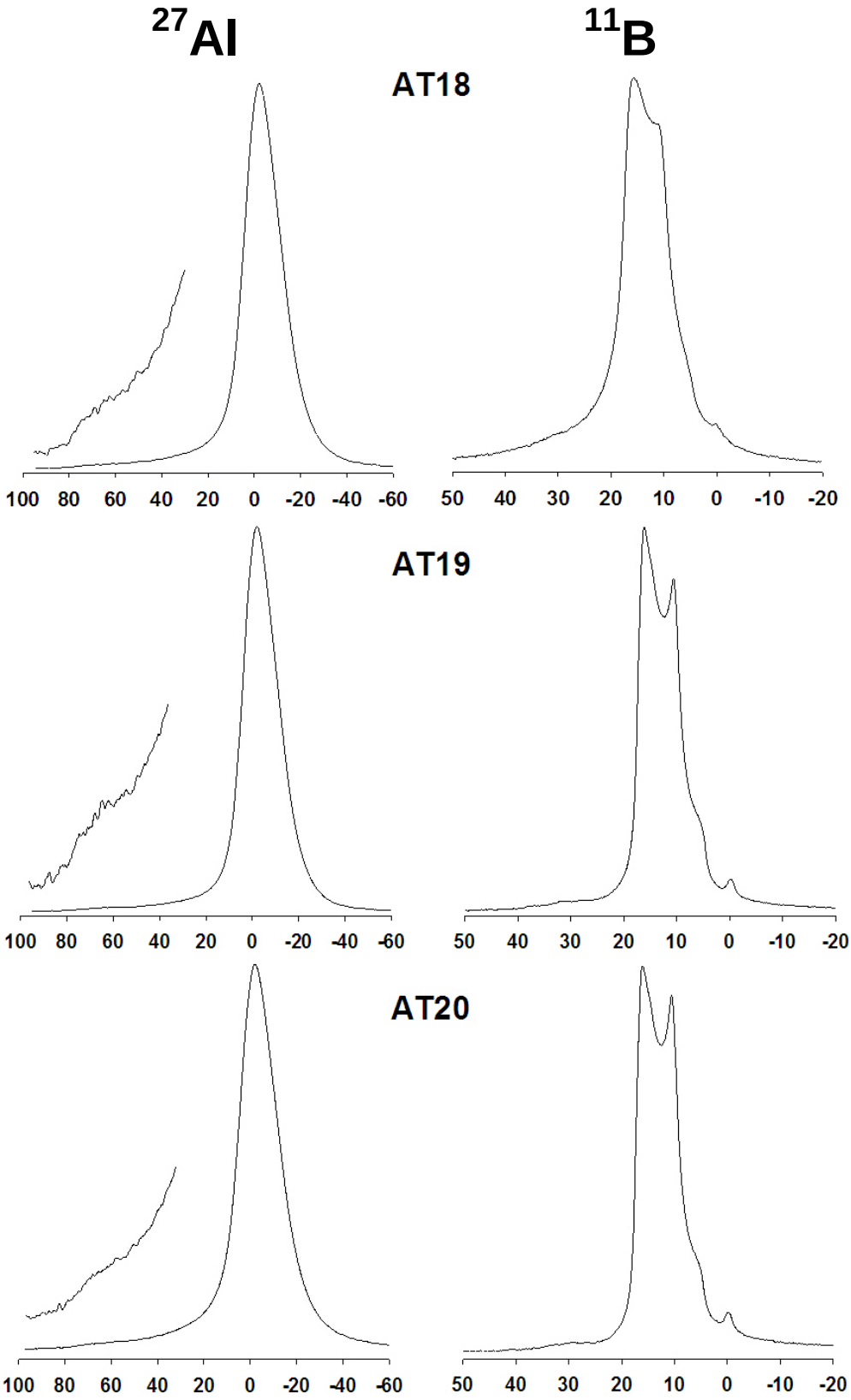
^{27}Al
^{11}B
AT18
AT19
AT20
100 80 60 40 20 0 -20 -40 -60
50 40 30 20 10 0 -10 -20

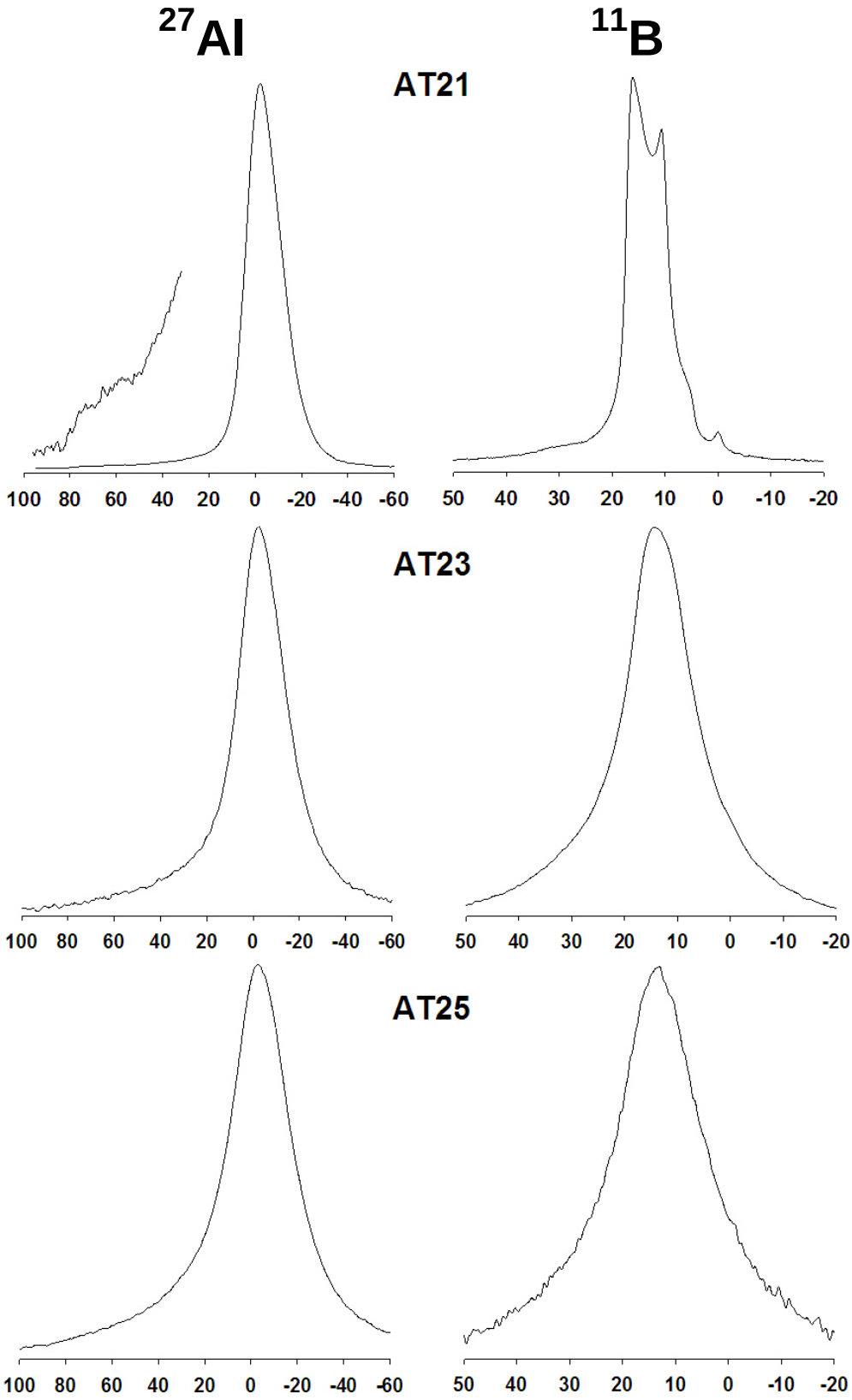
^{27}Al
^{11}B
AT21
AT23
AT25
100 80 60 40 20 0 -20 -40 -60
50 40 30 20 10 0 -10 -20

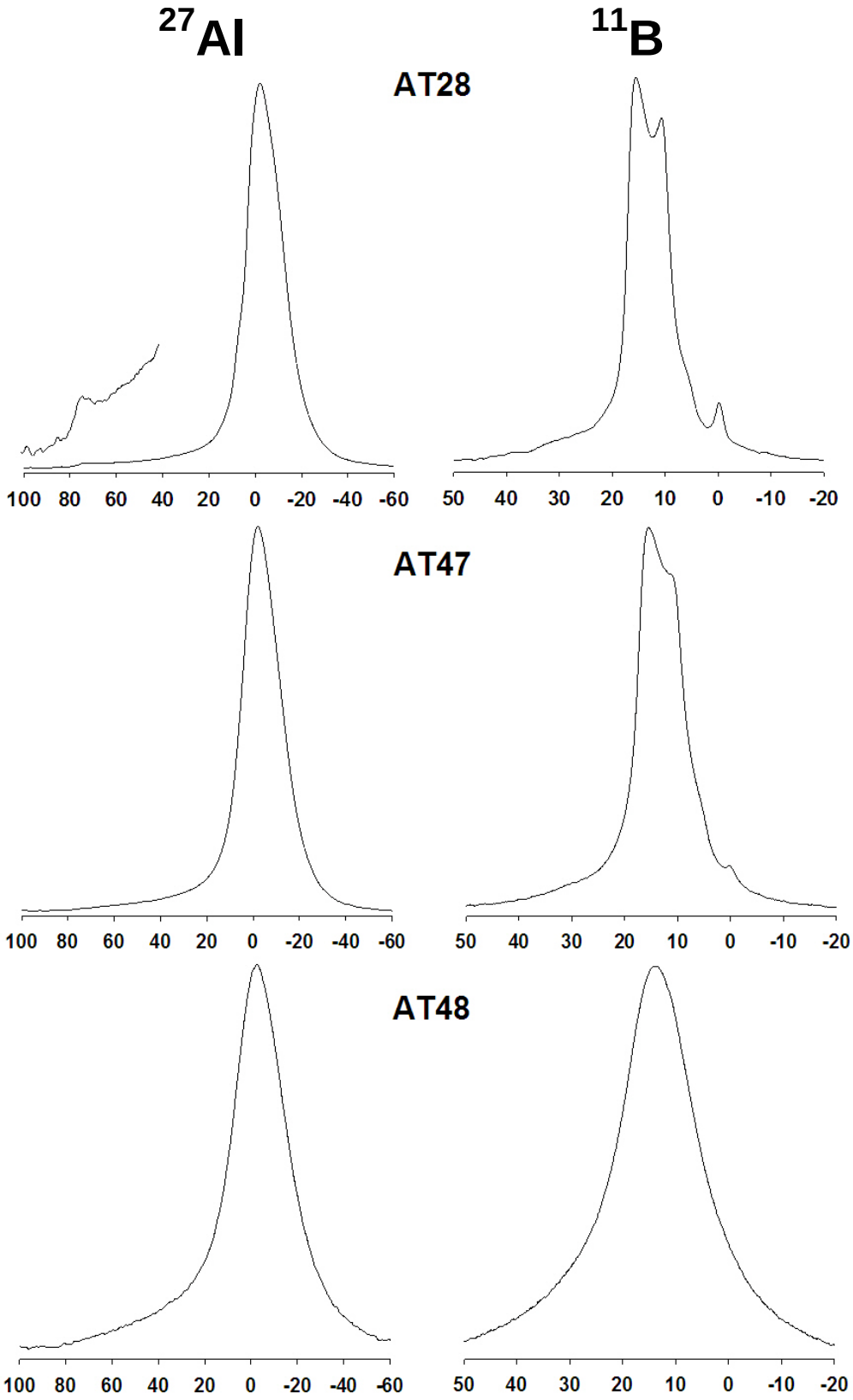
^{27}Al
^{11}B
AT28
AT47
AT48
100 80 60 40 20 0 -20 -40 -60
50 40 30 20 10 0 -10 -20

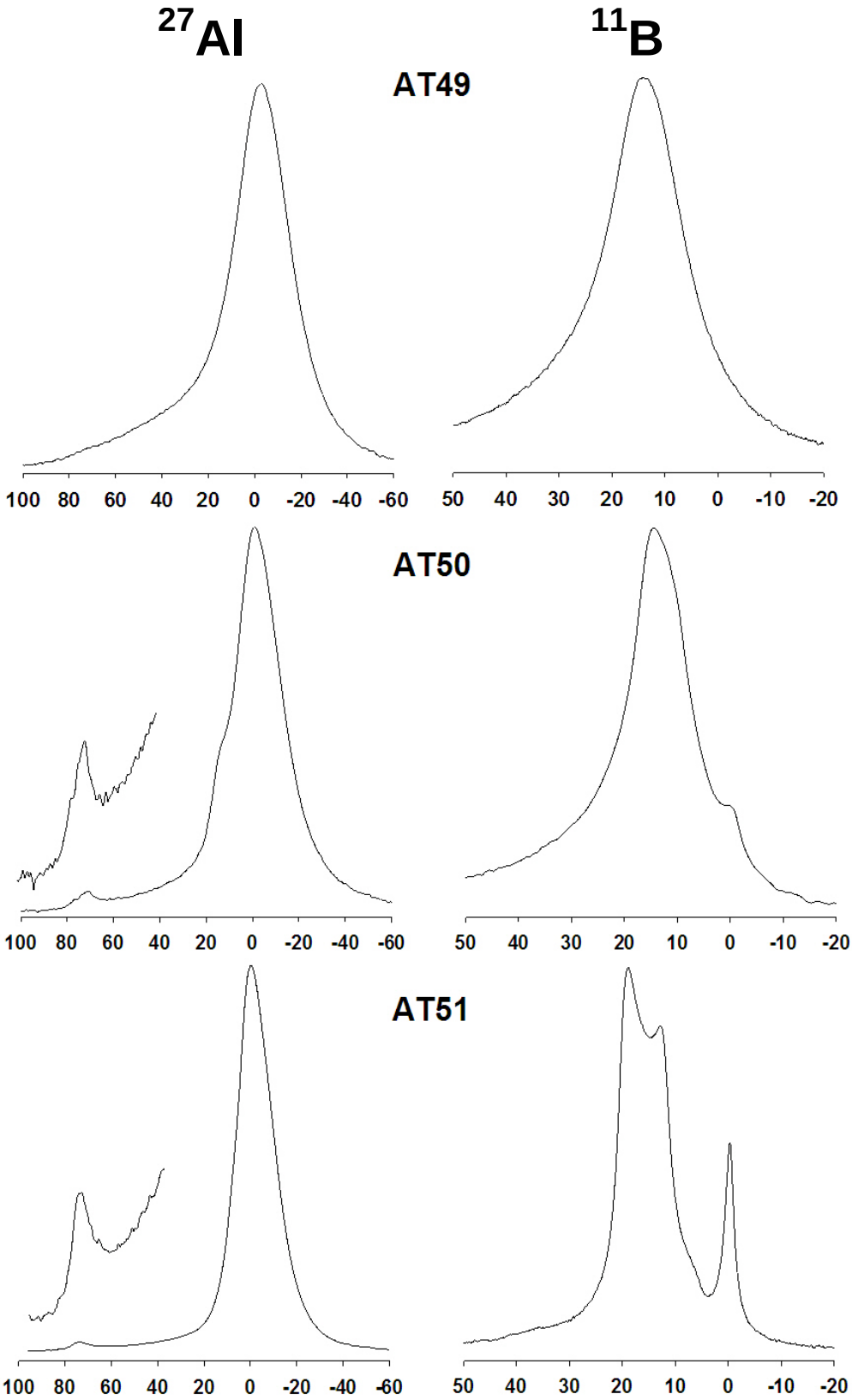
^{27}Al
^{11}B
AT49
100 80 60 40 20 0 -20 -40 -60
50 40 30 20 10 0 -10 -20
AT50
100 80 60 40 20 0 -20 -40 -60
50 40 30 20 10 0 -10 -20
AT51
100 80 60 40 20 0 -20 -40 -60
50 40 30 20 10 0 -10 -20

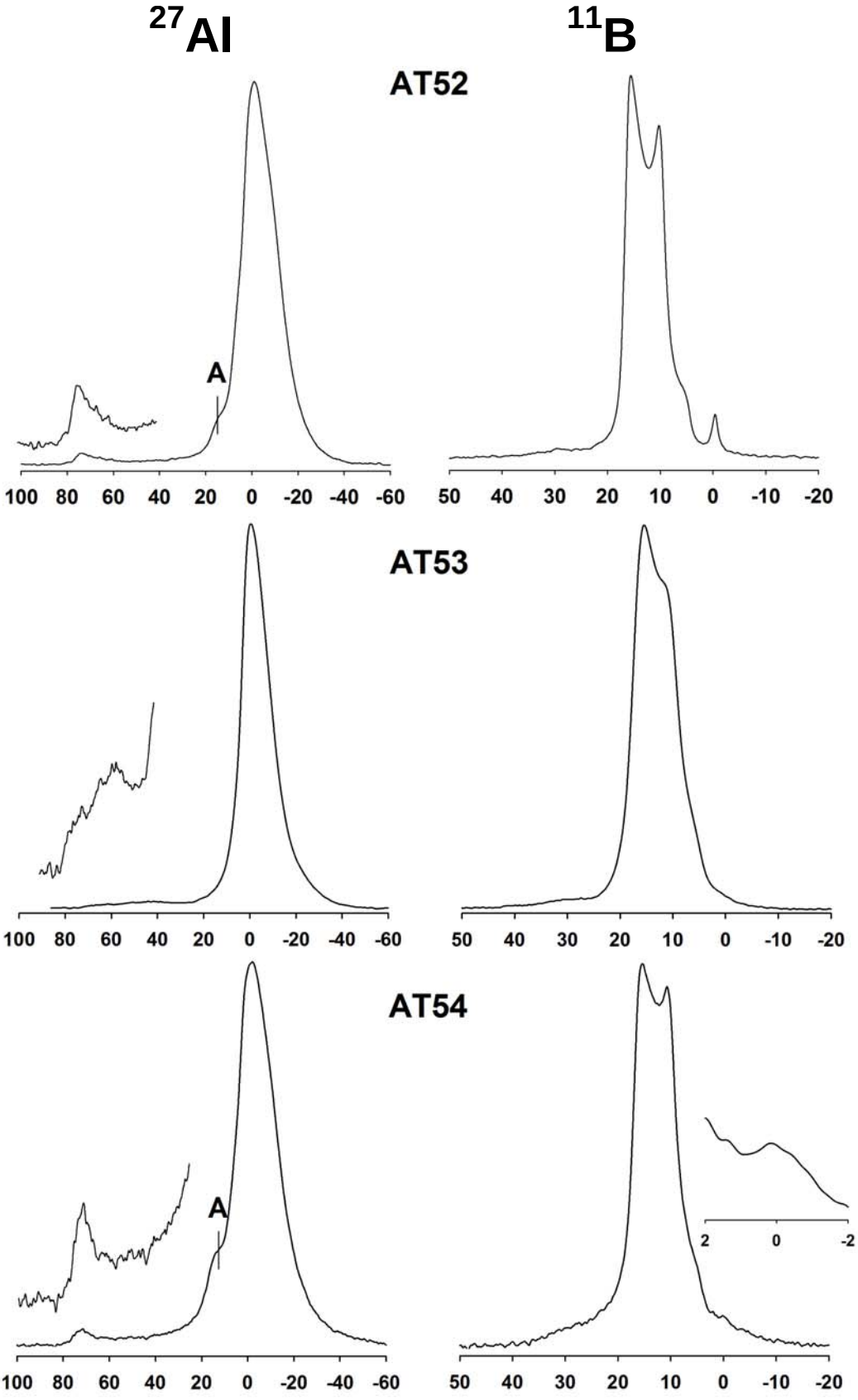
^{27}Al
^{11}B
AT52
A
100 80 60 40 20 0 -20 -40 -60
50 40 30 20 10 0 -10 -20
AT53
100 80 60 40 20 0 -20 -40 -60
50 40 30 20 10 0 -10 -20
AT54
A
100 80 60 40 20 0 -20 -40 -60
50 40 30 20 10 0 -10 -20
2 0 -2

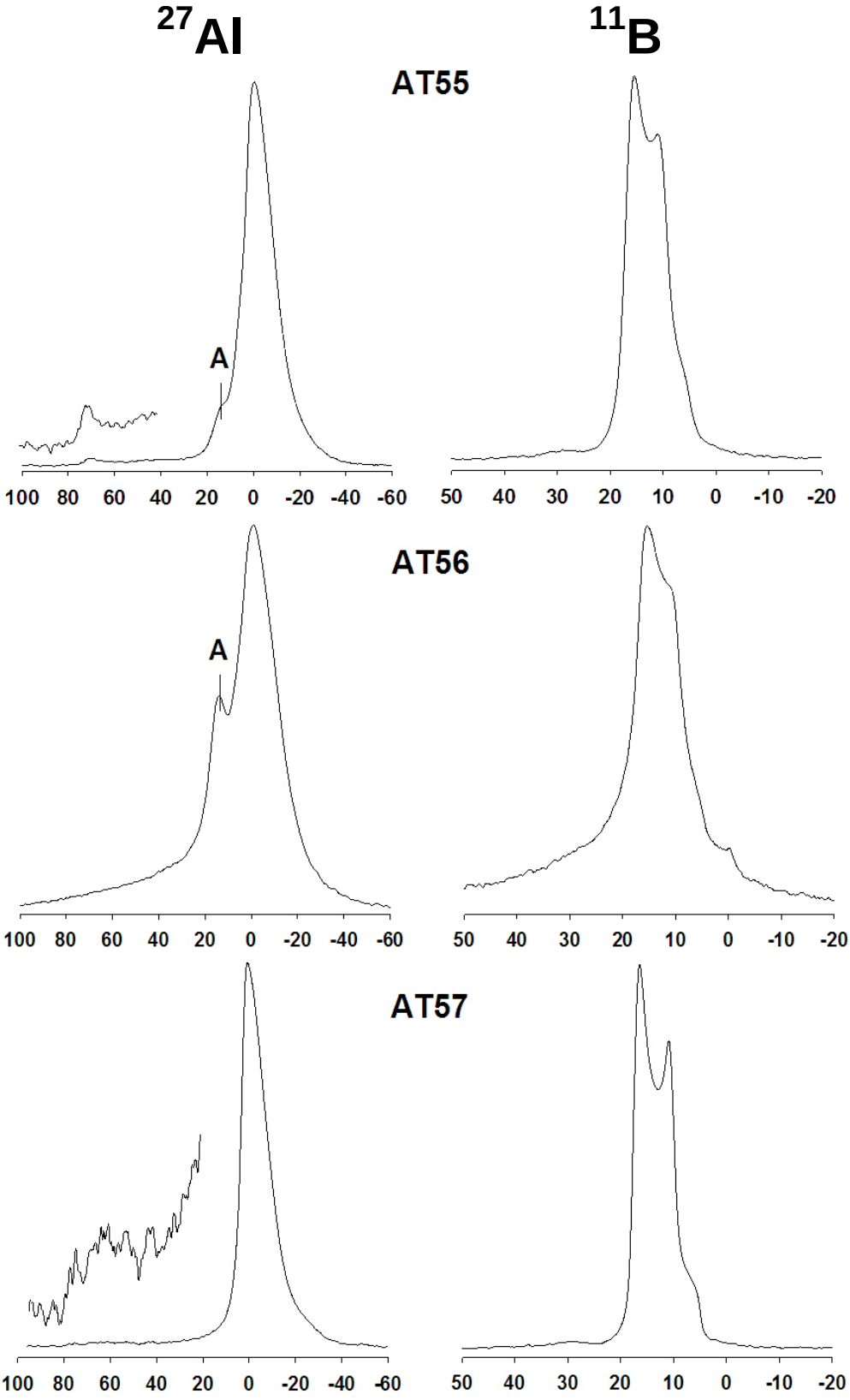
27Al
11B
AT55
A
100 80 60 40 20 0 -20 -40 -60
50 40 30 20 10 0 -10 -20
AT56
A
100 80 60 40 20 0 -20 -40 -60
50 40 30 20 10 0 -10 -20
AT57
100 80 60 40 20 0 -20 -40 -60
50 40 30 20 10 0 -10 -20

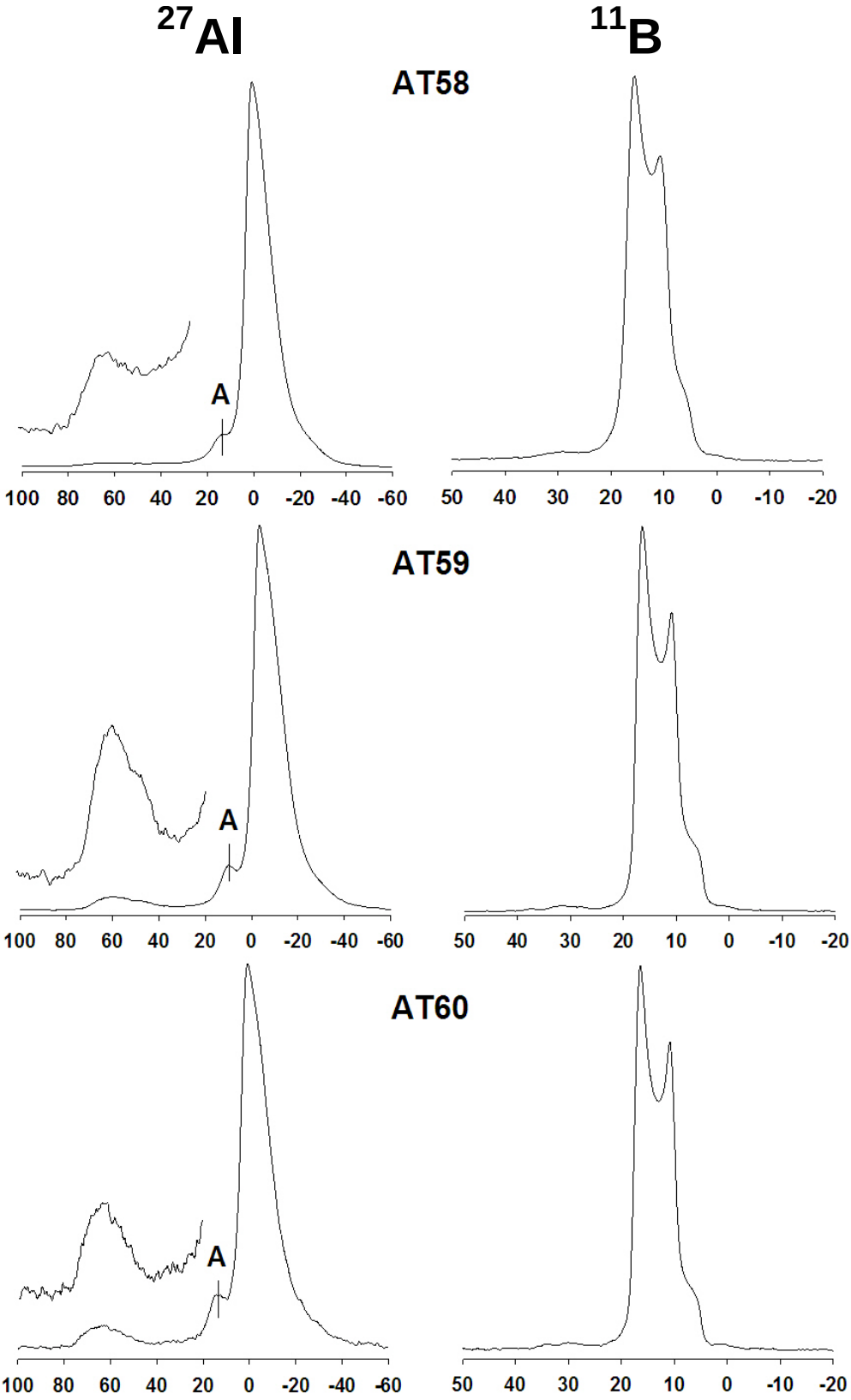
^{27}Al
^{11}B
AT58
AT59
AT60
A
100 80 60 40 20 0 -20 -40 -60
50 40 30 20 10 0 -10 -20

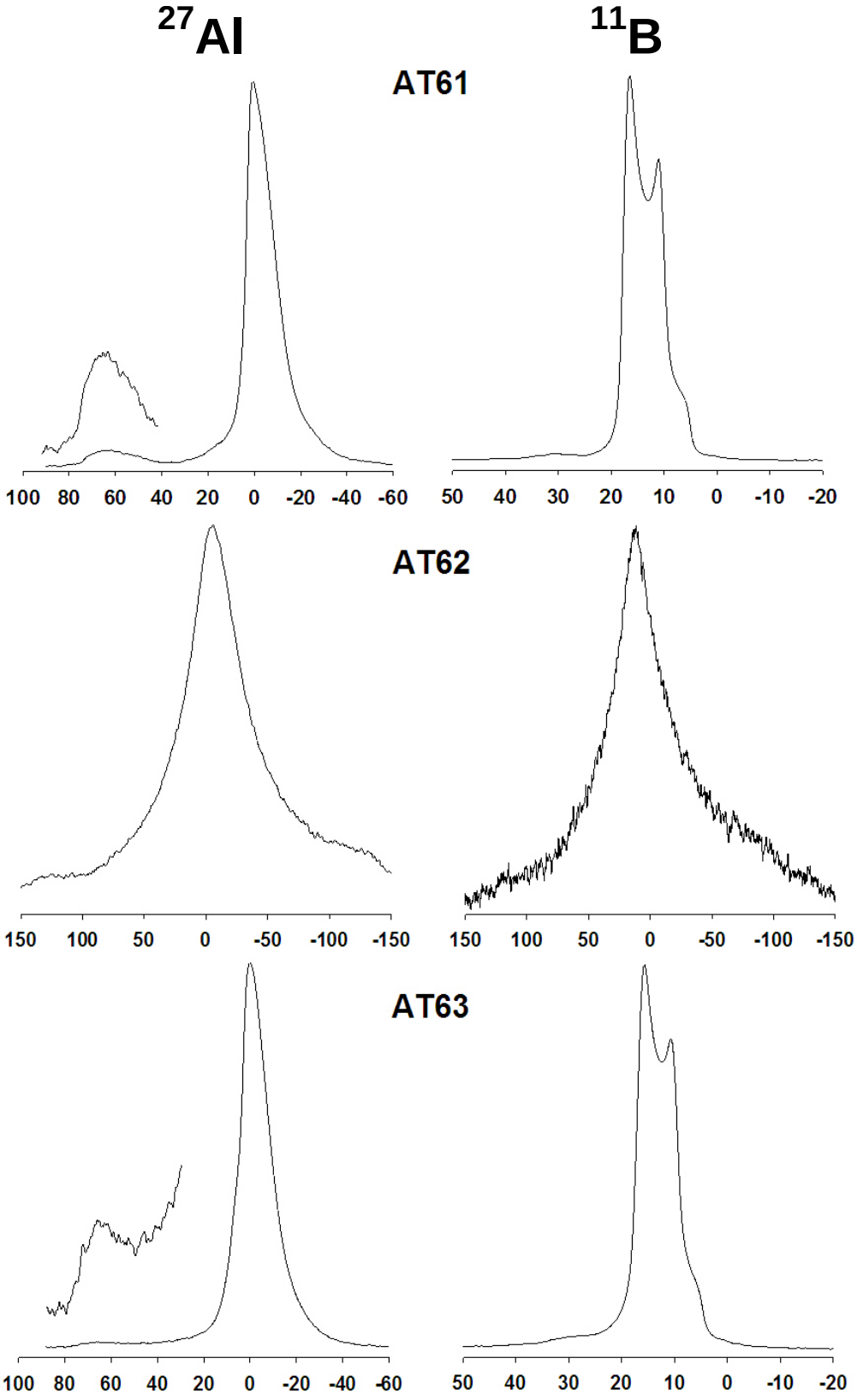
^{27}Al
^{11}B
AT61
100 80 60 40 20 0 -20 -40 -60
50 40 30 20 10 0 -10 -20
AT62
150 100 50 0 -50 -100 -150
150 100 50 0 -50 -100 -150
AT63
100 80 60 40 20 0 -20 -40 -60
50 40 30 20 10 0 -10 -20

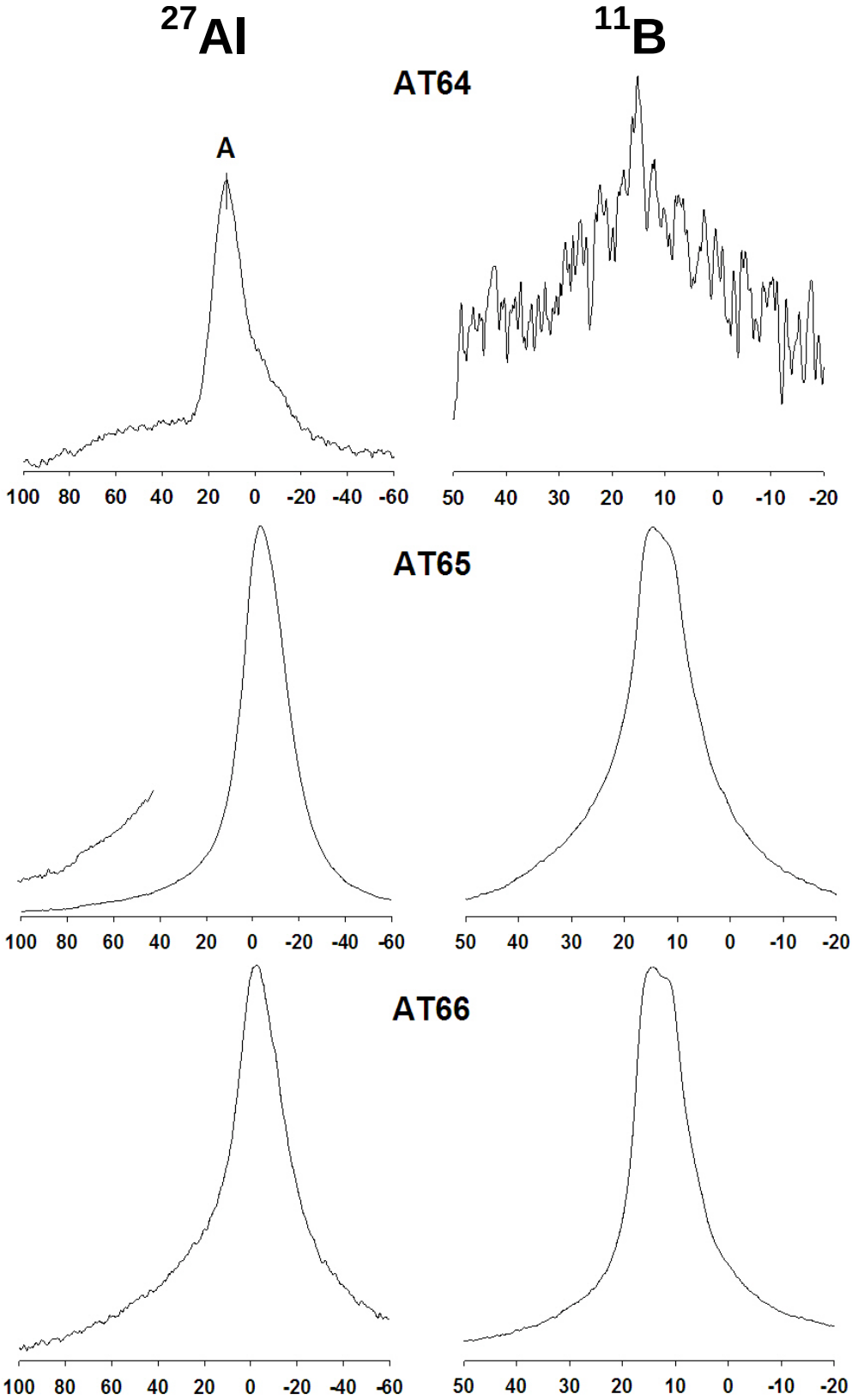
27Al
11B
AT64
A
100 80 60 40 20 0 -20 -40 -60
50 40 30 20 10 0 -10 -20
AT65
100 80 60 40 20 0 -20 -40 -60
50 40 30 20 10 0 -10 -20
AT66
100 80 60 40 20 0 -20 -40 -60
50 40 30 20 10 0 -10 -20

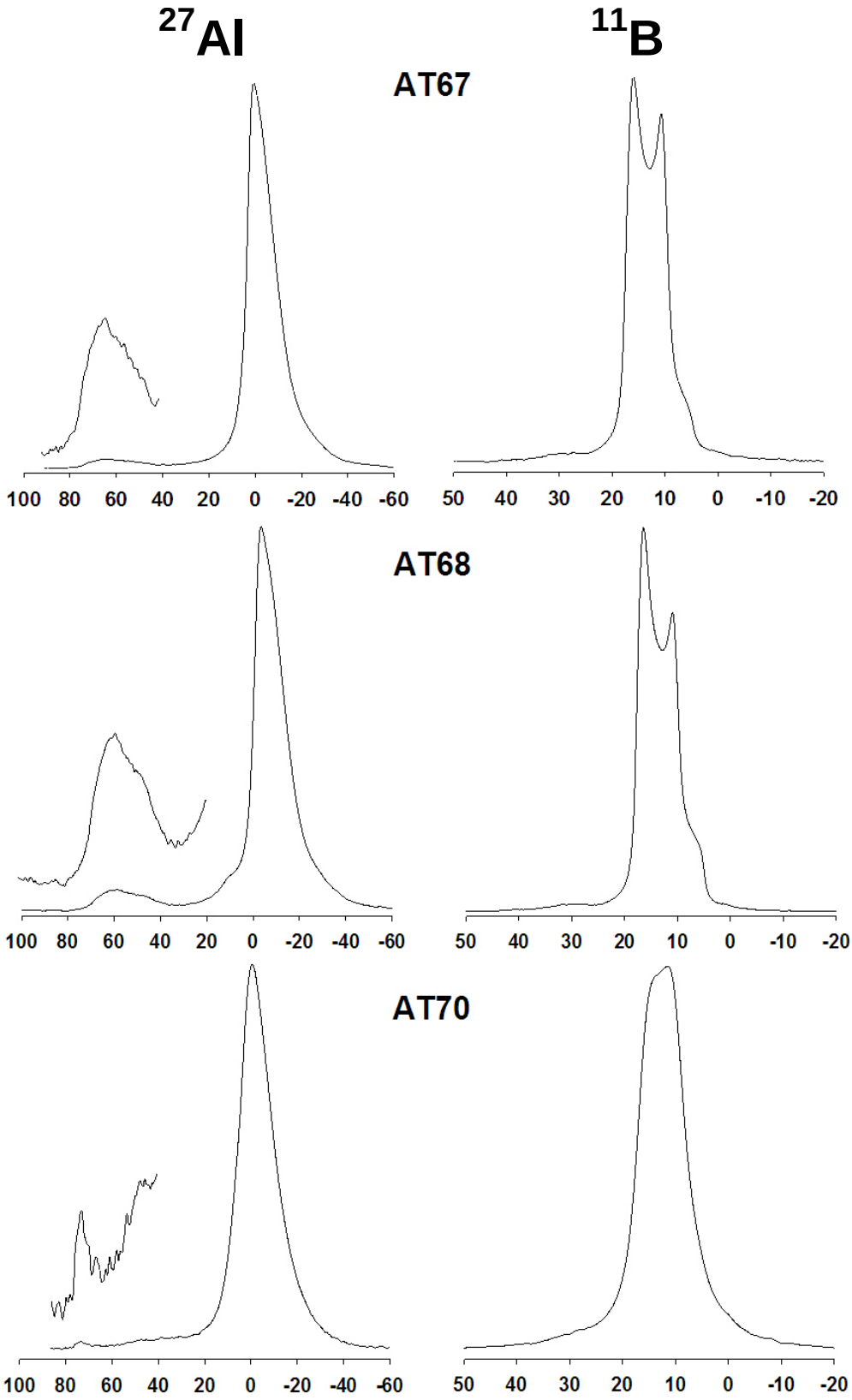
^{27}Al
^{11}B
AT67
AT68
AT70
100 80 60 40 20 0 -20 -40 -60
50 40 30 20 10 0 -10 -20

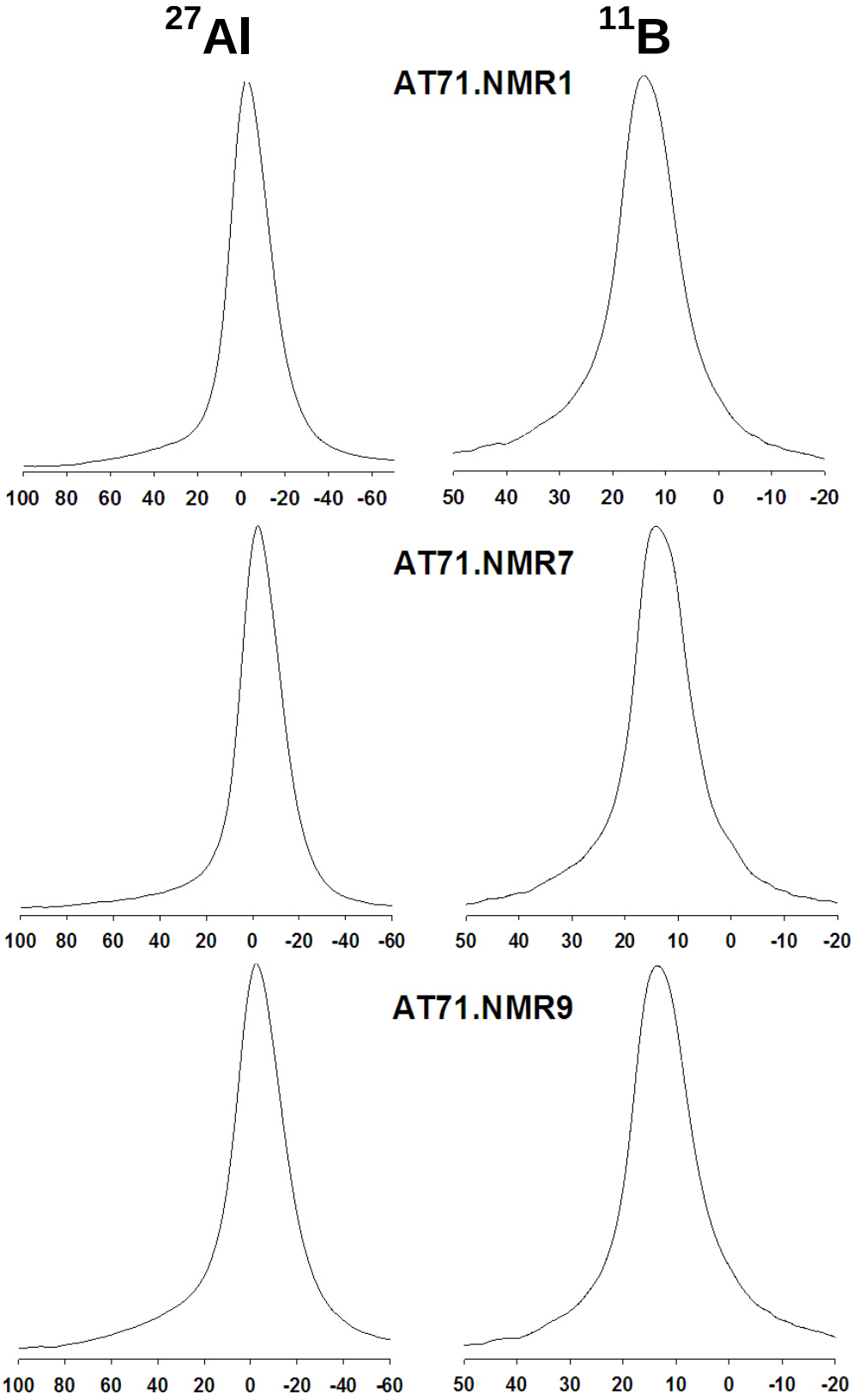
^{27}Al
^{11}B
AT71.NMR1
100 80 60 40 20 0 -20 -40 -60
50 40 30 20 10 0 -10 -20
AT71.NMR7
100 80 60 40 20 0 -20 -40 -60
50 40 30 20 10 0 -10 -20
AT71.NMR9
100 80 60 40 20 0 -20 -40 -60
50 40 30 20 10 0 -10 -20

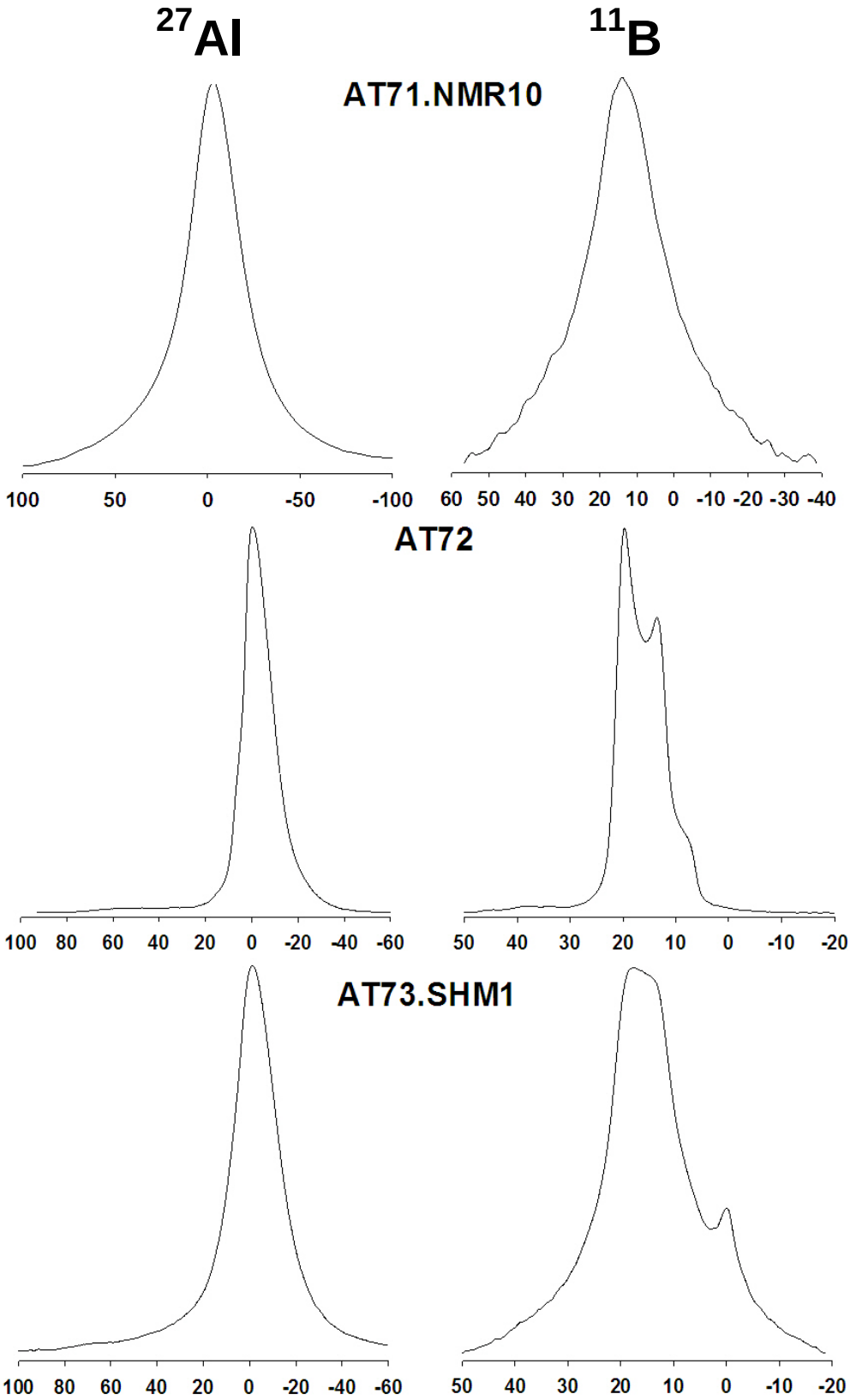
27Al
11B
AT71.NMR10
100 50 0 -50 -100
60 50 40 30 20 10 0 -10 -20 -30 -40
AT72
100 80 60 40 20 0 -20 -40 -60
50 40 30 20 10 0 -10 -20
AT73.SHM1
100 80 60 40 20 0 -20 -40 -60
50 40 30 20 10 0 -10 -20

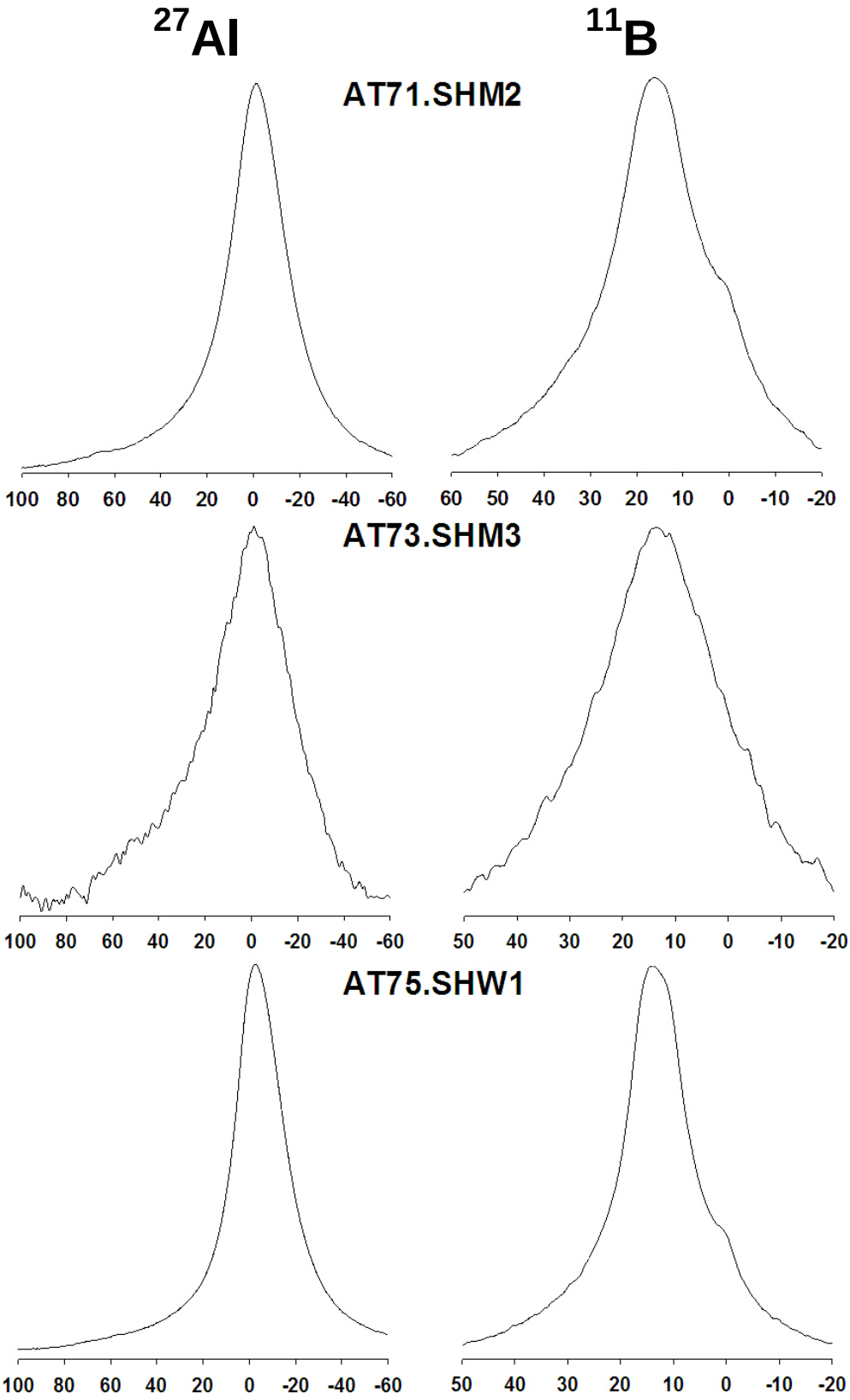
^{27}Al
^{11}B
AT71.SHM2
100 80 60 40 20 0 -20 -40 -60
60 50 40 30 20 10 0 -10 -20
AT73.SHM3
100 80 60 40 20 0 -20 -40 -60
50 40 30 20 10 0 -10 -20
AT75.SHW1
100 80 60 40 20 0 -20 -40 -60
50 40 30 20 10 0 -10 -20

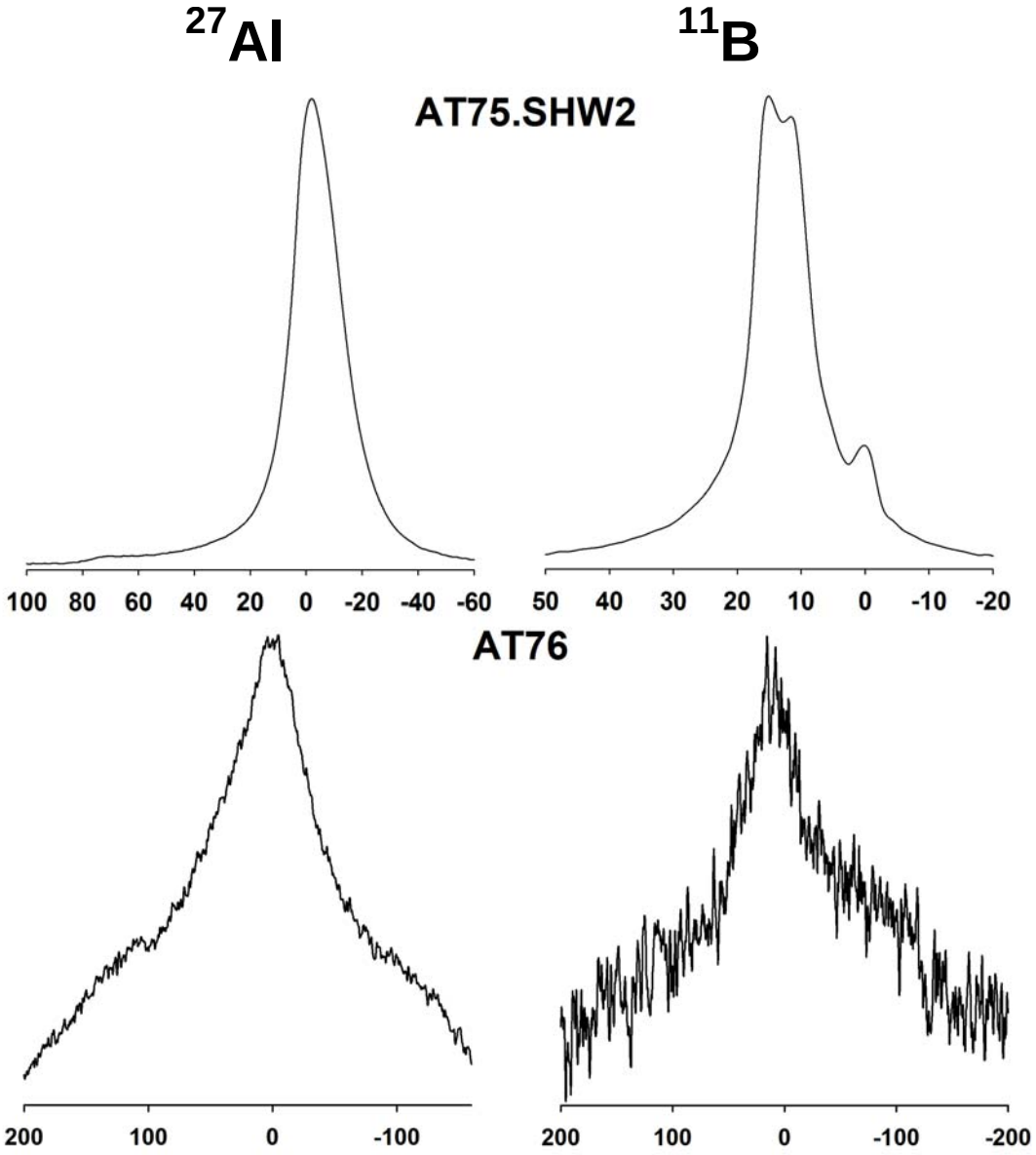
^{27}Al
^{11}B
AT75.SHW2
100 80 60 40 20 0 -20 -40 -60
50 40 30 20 10 0 -10 -20
AT76
200 100 0 -100
200 100 0 -100 -200